Heterodinuclear Cooperativity in Oxygenated Polymer Catalysis

Arron Craig Deacy



Trinity College

Department of Inorganic Chemistry

University of Oxford

May 2019

A thesis submitted in partial fulfilment of the requirements for the degree of Doctor of Philosophy in Chemistry

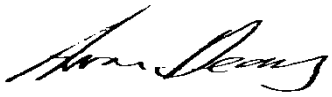
For my Friends and Family

‘Vitam Impendere Vero’

Declaration

The work presented in this thesis was conducted between October 2015 and August 2016 at Imperial College London and between September 2016 and May 2019 at the University of Oxford. This is the work of the author unless otherwise stated.

The copyright of this thesis rests with the author and is made available under a Creative Commons Attribution Non-Commercial No Derivatives licence. Researchers are free to copy, distribute or transmit the thesis on the condition that they attribute it, that they do not use it for commercial purposes and that they do not alter, transform or build-upon it. For any reuse or distribution, researchers must make clear to others the licence terms of this work.



Arron Deacy

Abstract

The following thesis describes the synthesis and characterisation of a series of heterodinuclear complexes derived from either a diphenolate macrocycle, or an *o*-vanillin derived dinucleating ligand. Their application as catalysts for the ring-opening copolymerisation of CO_2/epoxide, or anhydride/epoxide are investigated. **Chapter 2:** Explores the role of ionic Lewis acids, where a series of Group 1 and 2 metals with zinc (II) complexes are synthesised. All heterocomplexes are less active in the ROCOP of CO_2/CHO compared to the di-zinc analogue, with the exception of Mg(II)Zn(II). The chain-shuttling mechanistic hypothesis is advanced with the assignment of Mg(II) as the epoxide binder and Zn(II) as the carbonate donor. **Chapter 3:** Explores the role of covalent Lewis acids, where a series of Group 13 metals with zinc (II) complexes are synthesised. Activity and CO_2 uptake increases down the Group 13 homologues. All complexes are less active than the dizinc counterpart

Chapter 4: A Mg(II)Co(II) catalyst is synthesised and shows excellent activity, better than either di-Mg or di-Co analogues. Mg(II)Co(II) has a lower transition state Gibbs free energy vs. the homodinuclear analogues. Its superior performance arises from a combination of favourable entropy, provided by Mg(II) and reduced enthalpy, provided by Co(II). The experimental data supports a chain-shuttling mechanism, with epoxide coordination at Mg(II) and Co(II) accelerating carbonate attack. **Chapter 5:** A series of Zn(II) and Mg(II) dinucleating *o*-vanillin complexes with Na(I), Ca(II) and Cd(II) are reported. All zinc heterodinuclear catalysts are less active compared to the homodinuclear complex, where the converse is true for the magnesium complexes.

Acknowledgements

I would like to start by thanking Prof. Charlotte Williams for granting me the opportunity to carry out a DPhil in her group. I can only hope the following body of work goes someway to justifying that decision. I am grateful for your constant support and belief in my ability to succeed as an independent researcher and your positive outlook.

I would like to thank the staff members who have helped me collect data throughout my DPhil including: Dr. Andrew White (XRD) and Dr. Anna Regoutz (XPS) at Imperial College and Dr. Christopher Durr (XRD) and Dr. Alexander Kilpatrick (SQUID/CV) at the University of Oxford.

To the Williams group members, past and present, you have all made the DPhil experience both memorable and enjoyable. A huge thankyou to my team of break buddies, I couldn't have made it through the 4 years without them (Tim, Alice, Tom and Greg). I would like to thank all the Post-Docs (Jenni, Charles, Andres, Anish, Seb, Sumesh, Giulia, Chris, Leti, Duncan, Patrick, Caroline, George, Ryan and Andy) and students (Alice, Tom, Tim, Greg, Charlie, Arnaud, Ni, Gemma, Dom, Jameel, Peck, Said, Natalia, Wilf, Gloria and Lisa) for being an excellent team and creating an awesome working environment.

I would like to thank my parents who have supported me in my interest in science and encouraged extra-curricular activities which have helped shaped who I am today.

Abbreviations

Ar	Aryl
ATR-IR	Attenuated Total Reflectance Infrared
BDI	β-Diimine
Cat.	Catalyst
CC	Cyclic Carbonate
CHD	Cyclohexene-1,2-diol
CHO	Cyclohexene Oxide
CN	Coordination Number
COSY	Correlated Spectroscopy
Conv.	Conversion
C_p	Cyclopentadienyl
CTA	Chain Transfer Agent
CV	Cyclic Voltammetry
D	Diffusion Coefficient
Đ	Dispersity
1D	One-Dimensional
2D	Two-Dimensional
3D	Three-Dimensional
DCM	Dichloromethane
DEC	Diethyl Carbonate
DFT	Density Functional Theory
DMAP	4-dimethylaminopyridine
DMSO	Dimethyl sulfoxide

$\Delta G^{‡}$	Gibbs Free Energy of Transition
$\Delta H^{‡}$	Enthalpy of Transition
$\Delta S^{‡}$	Entropy of Transition
DOSY	Diffusion Ordered NMR Spectroscopy
ESI	Electrospray Ionisation
Eq.	Equation
eq.	Equivalent
Et	Ethyl
Fc	Ferrocene
GPC	Gel Permeation Chromatography
HMBC	Heteronuclear Multiple-Bond Coherence
HSQC	Heteronuclear Single Quantum Coherence Spectroscopy
IR	Infrared
k	Rate Constant
k_{obs}	Observed Rate Constant
L	Ligand
LHS	Left-Hand Side
LO	Limonene Oxide
m	Minute
M	Metal Centre
MA	Maleic Anhydride
MALDI	Matrix Assisted Laser Desorption Ionisation
Me	Methyl

MeCN	Acetonitrile
MeOH	Methanol
M_n	Number Average Molar Mass
MS	Mass Spectroscopy
MW	Molecular Weight
NA	Norbornene Anhydride
NMR	Nuclear Magnetic Resonance
Nu	Nucleophile
OAc	Acetate
OBz	Benzoate
o-Vanillin	Ortho-Vanillin
PA	Phthalic Anhydride
PC	Polycarbonate
PCHC	Poly(cyclohexene carbonate)
Ph	Phenyl
Polym.	Polymer
PO	Propylene Oxide
PPC	Poly(propylene carbonate)
ppm	Parts Per Million
PPN	Bis(triphenylphosphine)imine
PU	Polyurethane
RDS	Rate-Determining Step
RHS	Right-Hand Side
ROCOP	Ring-Opening Copolymerisation

ROP	Ring-Opening Polymerisation
RPKA	Reaction Progress Kinetic Analysis
RPM	Revolutions Per Minute
s	Second
SA	Succinic Anhydride
SEC	Size Exclusion Chromatography
SQUID	Superconducting Quantum Interference Device
t	Time
T	Temperature
τ	Structural Parameter
tBu	Tert-Butyl
TCE	1,1,2,2-Tetrachloroethane
Tg	Glass Transition Temperature
THF	Tetrahydrofuran
ToF	Time of Flight
TOF	Turnover Frequency
TON	Turnover Number
λ	Wavelength
XPS	X-ray Photoelectron Spectroscopy
XRD	X-ray Diffraction

List of Figures, Schemes, Tables and Equations

Chapter 1: Introduction

Figure 1.1	Global plastic production between 1950 and 2016.	29
Scheme 1.1	Polyether and polycarbonate derived polyurethane syntheses.	30
Scheme 1.2	Industrial process to producing polycarbonates	31
Scheme 1.3	Step-growth and chain-growth synthetic routes to polycarbonates	33
Table 1.1	Selected thermal and mechanical properties of common polycarbonates	33
Scheme 1.4	Catalytic cycle to polycarbonate, polyether and cyclic carbonate	35
Scheme 1.5	Potential side-reactions in CO_2/epoxide coupling	36
Scheme 1.6	Chain-transfer equilibria	36
Figure 1.2	Bimodality from co-ligand and diol initiation (Top). Monomodality from a catalyst featuring non-initiating co-ligands and diol (Bottom). (LHS:MALDI-ToF, RHS: Gel Permeation Chromatography)	37
Scheme 1.7	Bifunctional mechanisms (1) Dinuclear (2) Bicomponent	39
Figure 1.3	(a) Cr(III) salen catalyst structure. (b) Plot of initial rate versus catalyst loading for reactions with and without co-catalyst (M-MeIm). (c) Proposed mechanism where N-MeIm binds trans to the polymer chain end.	40
Figure 1.4	Co(III)salen structure and a series of co-catalysts and	41

	their interaction equilibrium.	
Figure 1.5	Catalysts screened by DFT	42
Figure 1.6	LHS, equilibrium between metal-epoxide/carbonate intermediates and a vacant metal centre. RHS, plot of TOF vs difference between metal-carbonate and epoxide dissociation energies.	43
Figure 1.7	Mechanistic hypothesis describing the relationship between the carbonate and epoxide dissociation energies.	43
Figure 1.8	Selected tether cobalt(III) salen catalysts.	44
Figure 1.9	LHS, binary Co(III) salen catalyst. RHS, bifunctional Co(III) salen catalyst	45
Figure 1.10	Energy barrier to polycarbonate and cyclic carbonate formation for a binery and bifunctional catalyst system	46
Figure 1.11	Neutral base tethered on a cobalt(III) salen catalyst system.	47
Scheme 1.8	Proposed mechanism for the tethered Co(III) catalyst system	48
Figure 1.12	Indium phosphasalen catalyst and polymerisation data.	49
Figure 1.13	Infrared data showing intermediates relevant to catalysis	50
Scheme 1.9	Mononuclear mechanism for CO_2/epoxide coupling.	51
Figure 1.14	Borane/PPNCl systems for CO_2/epoxide and COS/epoxide polymerisations.	52

Scheme 1.10	Lewis acid catalysed CO_2/epoxide copolymersation	52
Figure 1.15	Illustration of the potential energy surface for polycarbonate, polyether and cyclic carbonate formation	53
Scheme 1.11	Formation of poly(limonene carbonate) with an aluminium(III) trisphenolate catalyst.	54
Figure 1.16	Top; free energy profiles for the ROCOP of CO_2/CHO mediated by an Al(III)-trisphenolate catalyst showing a possible monometallic (Black) bimetallic (Red) and dimeric (Blue) mechanistic pathways. Bottom; catalytic cycles for the bimetallic and dimer-mediated pathways.	55
Scheme 1.12	Dinuclear mechanism for CO_2/epoxide copolymerisation	56
Figure 1.17	Dimeric, tethered and dinucleating catalysts	57
Figure 1.18	Activity of a zinc-β-diimine catalyst with change in ligand sterics	58
Figure 1.19	Proposed mechanism (Top LHS). Rate vs catalyst concentration (TOP RHS). Rate vs CO_2 pressure (Bottom LHS). Rate vs epoxide concentration (Bottom RHS).	59
Figure 1.20	Dinuclear zinc catalyst derived from pyrrolidine	60
Figure 1.21	Dinuclear cobalt(III) catalyst for CO_2/PO copolymersation	61
Figure 1.22	Dinuclear metal salen complexes bridged via the ortho-phenyl position	62
Scheme 1.13	Enantioselective homopolymerisation of propylene oxide using a dinuclear Co(III) salen catalyst	63

Figure 1.23	Dinuclear zinc catalysts derived from anilido-aldiimine ligands	64
Figure 1.24	(Top LHS) Di-zinc catalyst derived from a di-phenolate macrocyclic ligand. (Top RHS) A linear plot of initial rate vs. catalyst concentration. (Bottom LHS) Plot of initial rate vs pressure CO_2. (Bottom RHS) Linear plot of initial rate vs epoxide concentration.	65
Figure.1.25	Illustration of the potential energy surface for copolymerisation	66
Figure 1.26	Synthesis of a pure heterodinuclear Zn(II)Mg(II) catalyst	68
Figure 1.27	Tethered di-zinc-β-diimine catalyst for the copolymerisation of CO_2/CHO	69
Figure 1.28	Illustration of the potential energy surface for the ROCOP of CO_2/CHO for a tether di-zinc catalyst at 5 bar (blue) and 50 bar (red) CO_2 pressure.	70
Figure 1.29	Series of tris(salen)-multinuclear catalyst and proposed mechanism for the copolymerisation of CO_2/CHO	71

Chapter 2: Group 1 and 2, Zinc (II) Heterodinuclear Catalysts

Scheme 2.1	Overall synthetic strategies targeting Group 1 and 2 zinc heterodinuclear complexes **1-9**	82
Scheme 2.2	Synthesis of complexes **1-3**	83
Figure 2.1	^{1}H NMR spectra of complexes **1-3**.	84
Figure 2.2	2D DOSY NMR spectra of complexes **1-3**	85
Figure 2.3	ORTEP representation of crystallographic structures of	86

	complexes **1** and **2**.	
Scheme 2.3	Synthesis of di-zinc complexes **4a** and **4b**	87
Figure 2.4	^{1}H NMR spectra of complexes **4a** and **4b**	88
Figure 2.5	2D DOSY NMR spectra of complexes **4a** and **4b**	89
Figure 2.6	ORTEP representation of crystallographic structures of complexes **4a** and **4b**	90
Scheme 2.4	Metal redistribution reaction between homo-complexes (**1**-**3**) with di-zinc complex (**4a)**	91
Figure 2.7	Metal redistribution reaction of complex **1** with **4a** as followed by ^{1}H NMR spectroscopy	92
Figure 2.8	Metal redistribution reaction of complex **2** with **4a** as followed by ^{1}H NMR spectroscopy	93
Figure 2.9	Metal redistribution reaction of complex **3** with **4a** as followed by ^{1}H NMR spectroscopy	94
Scheme 2.5	Synthesis of complexes 5-7 by sequential metalation under themodynamic or kinetic conditions	95
Figure 2.10	Reactions of complex **5** with d_2-TCE solvent at 130 °C, as followed by ^{1}H NMR spectroscopy	96
Figure 2.11	COSY NMR of complex **5a**	97
Figure 2.12	^{1}H NMR spectrum of **6a** with 90 % heterodinuclear content.	98
Figure 2.13	Metal redistribution of complex **6a** towards complexes **2** and **4a**	98
Figure 2.14	COSY NMR of complex **5b**	99

Figure 2.15	^{1}H NMR spectrum of **7b**	100
Figure 2.16	2D DOSY NMR spectrum of complex **7b**	101
Figure 2.17	MALDI-ToF spectra of complexes **5b** and **7b**	101
Figure 2.18	ORTEP representation of crystallographic structure of complex **5b**	102
Scheme 2.6	Synthesis of complexes **8a** and **9a**	103
Figure 2.19	^{1}H NMR spectra of **8a** and **9a**	104
Figure 2.20	2D NMR spectra of complexes **8a** and **9a**	105
Figure 2.21	ORTEP representation of crystallographic structures of complexes **8a** and **9a**	107
Table 2.1	ROCOP of CO_2/CHO with catalysts **4a**-**9a**	108
Scheme 2.7	Proposed catalytic cycles rationalising formation of cis-cyclic carbonate, trans-cyclic carbonate and poly(cyclohexene carbonate)	109

Chapter 3: Group 13, Zinc (II) Heterodinuclear Catalysts

Scheme 3.1	Synthetic pathway to complexes **10**-**15**	118
Scheme 3.2	Synthesis of homodinuclear complex **10**	119
Figure 3.1	^{1}H and ^{13}C NMR spectra of complex **10**	120
Figure 3.2	ORTEP representation of crystallographic structure of **10**	121
Scheme 3.3	Synthesis of heterodinuclear complexes **11**-**13**	122
Figure 3.3	^{1}H NMR spectrum of di-zinc (**10**) and Zn(II)In(III) (**13**)	123
Figure 3.4	^{13}C NMR spectrum of di-zinc (**10**) and Zn(II)In(III) (**13**)	124
Figure 3.5	2D DOSY NMR spectra of complexes **11**-**13**	125

Figure 3.6	ORTEP representation of crystallographic structures of **11**-**13**	127
Table 3.1	ROCOP of CO_2/CHO with complexes **10**-**13**	128
Scheme 3.4	Proposed mechanism for the formation of polycarbonate, polyether and cyclic carbonate products.	129
Scheme 3.5	Synthesis of cationic hetero complex **14**	130
Figure 3.7	^{1}H NMR spectrum of complexes **13** and **14**	131
Figure 3.8	Synthesis of heterodinuclear complex **15**	132
Figure 3.9	^{1}H NMR spectrum of complex **13** and **15**	133
Figure 3.10	2D DOSY NMR spectrum of **15**	134
Figure 3.11	ORTEP representation of crystallographic structure of complex **15**	135

Chapter 4: Magnesium-Cobalt Heterodinuclear Catalyst

Figure 4.1	Isovalent and mixed valent di-cobalt complexes	140
Scheme 4.1	Synthesis of complexes **16**-**18**	142
Figure 4.2	MALDI-ToF spectrum of **18**	144
Equation 1	Determination of Binding Energy (Photoelectric effect)	145
Figure 4.3	XPS core level spectra of catalysts **16**-**18**	146
Figure 4.4	ORTEP representation of the molecular structure of **18**	147
Figure 4.5	Cyclic voltammagrapms of **16**-**18**	148
Table 4.1	Electrode potentials (E) vs $FeCp_2^{+/0}$ in THF	148
Table 4.2	Peak Potentials and limiting currents of complex **16**	149
Figure 4.6	Scan rate dependence of quasi-reversible redox couple	150
Figure 4.7	Temperature dependence of the field cooled and zero	151

	field cooled magnetic susceptibilities for complexes **16** and **18**. Field sweep of complex **18** showing no hysteresis	
Figure 4.8	Inverse susceptibility against temperature plot for **16** and **18**.	152
Equation 2	Curie-Weiss Law	152
Equation 3	Calculation of effective magnetic moment	153
Equation 4	Calculation of spin-only magnetic moment	153
Equation 5	Calculation of spin-orbit magnetic moment	153
Figure 4.9	Temperature dependence of observed magnetic moments of complexes **16** and **18** per cobalt centre.	153
Figure 4.10	Magnetic plotting effects for an octahedral Co(II) ion in an applied field along with thermal depopulation.	154
Figure 4.11	Field dependence of the magnetisation for complexes **16** and **18** per bimetallic complex	155
Equation 6	Calculation of magnetisation saturation	156
Equation 7	Calculation of the g-factor	156
Table 4.3	ROCOP of CO_2/CHO using complex **18** under different CTA loading, catalyst loading and stirring speed.	157
Table 4.3	ROCOP of CO_2/CHO using complex 18 at varying temperature	158
Figure 4.12	Catalysts with the highest reported activity for CO_2/CHO ROCOP in the literature.	159
Equation 8	Rate Law – Theoretical	160

Scheme 4.2	Chain-shuttling mechanistic proposal	160
Figure 4.13	Determination of k_{obs} *via in-situ* Infrared Spectroscopy Analysis	161
Equation 9	Rate Law – Homodinuclear complexes	162
Equation 10	Simplified Rate Law (k_{obs})	162
Equation 11	Integration of Equation 10	162
Equation 12	Determination of Catalyst concentration order	162
Equation 13	Rate Law – Catalysts order updated	162
Figure 4.14	Rate of CO_2/CHO processed under various normalised time to determine catalyst order	163
Equation 14	Rate Law – Epoxide concentration	164
Equation 15	Integration of Rate Law	164
Equation 16	Determination of epoxide order	164
Figure 4.15	Concentration of epoxide vs time plot for complex **18**	164
Equation 17	Rate Law – Epoxide order updated	165
Equation 18	Finalised Rate Law	165
Figure 4.16	Activity vs partial pressure of CO_2 using **18**	165
Figure 4.17	Activity vs Temperature of CO_2/CHO using **18** at 1 bar CO_2 pressure	166
Table 4.5	Effect of Temperature on CO_2/CHO copolymerisation at 1 bar pressure.	167
Equation 19	Henrys Law	168
Equation 20	Determination of Henrys Constant	168
Scheme 4.3	Mechanism shift due to lower solubility of CO_2 at	168

	elevated temperatures	
Figure 4.18	Activity vs temperature of CO_2/CHO using **18** at 20 bar CO_2 pressure.	169
Table 4.6	ROCOP of CO_2/CHO under varying temperature conditions	170
Figure 4.19	Highly active CO_2/CHO catalysts at elevated CO_2 pressure	171
Equation 21	Catalyst to polymer transition	172
Equation 22	Equilibrium between transition state, catalyst and monomers	172
Equation 23	Rate of reaction equated to transition state frequency	172
Equation 24	Rate Law	172
Equation 25	Rate equated to reaction equilibrium	173
Equation 26	Gibbs Energy Relationship to Chemical Equilibrium	173
Equation 27	Gibbs Energy Relationship to Enthalpy and Entropy	173
Equation 28	Chemical Equlibrium equated to Enthalpy and Entropy	173
Equation 29	Rate of reaction relationship to enthalpy and entropy (Eyring Equation)	173
Equation 30	Linearised Eyring Equation	173
Equation 31	Calculation of Enthalpy	173
Equation 32	Calculation of Entropy	173
Figure 4.20	[PCHC] vs time and ln[CHO] vs time plots.	174
Figure 4.21	Eyring plot for complexes **16-18**	175
Table 4.7	Summary of data from Eyring plot	175

Figure 4.23	Calculated Enthalpy and Entropy of Transition	176
Figure 4.24	Gibbs Free Energy vs temperature for **16**-**18**	177
Equation 33	Rate of reaction relationship with Gibbs free energy	178
Equation 34	Comparison of rates of reaction by difference in Gibbs free Energy	178
Figure 4.25	Series of anhydrides tested for ROCOP with CHO using **18**	179
Figure 4.26	Concentration vs time plots for ROCOP of anhydride/CHO using **18**	180
Table 4.8	ROCOP of anhydride/CHO using **18**	180
Figure 4.27	Series of catalysts active for ROCOP of anhydride CHO	181

Chapter 5: O-Vanillin Derived Heterodinuclear Catalysts

Scheme 5.1	ROCOP of anhydride/epoxide forming a polyester	188
Scheme 5.2	Synthesis of L_{1a}-L_{2b}	188
Table 5.1	Copolymerisation of PA/CHO	189
Scheme 5.3	Overall synthetic strategies targeting hetero- and homo-dinuclear Zn(II) and Mg(II) complexes.	191
Scheme 5.4	Synthesis of complexes **19** and **20**	192
Figure 5.1	^{1}H NMR spectra following the synthesis of complexes **19** and **20**	193
Figure 5.2	2D DOSY NMR spectra of complexes **19** and **20**	194
Figure 5.3	ORTEP representation of of complexes **19** (Top LHS), **20** (Bottom) and **21** (Top RHS).	196

Scheme 5.5	Synthesis of heterodinuclear complexes **22**, **23** and **24** via a monozinc species, **21**.	197
Figure 5.4	^{1}H NMR spectrum of complexes **22**-**25**	198
Figure 5.5	Macrocycle (LHS) and O-vanillin derived (RHS) ligands displaying the retention (blue) or break (red) in C_2 symmetry upon the addition of hetero-metals.	199
Figure 5.6	ORTEP representation of crystallographic structures of complexes **22** (Top LHS) **23** (TOP RHS) **24** (Bottom LHS) and **25** (Bottom RHS), obtained by single crystal X-ray diffraction.	201
Scheme 5.6	Synthesis of di-magnesium complex **25**.	202
Figure 5.7	^{1}H NMR spectra of complex **19** and **25**.	203
Figure 5.8	ORTEP representation of crystallographic structures of complexes **26** (RHS) and **27** (LHS), obtained by single crystal X-ray diffraction.	204
Scheme 5.7	Synthesis of mono-magnesium complex **28** and heterodinuclear complexes **29**, **30** and **31**.	205
Figure 5.9	^{1}H NMR spectra of complexes **28**-**31**	206
Figure 5.10	ORTEP representation of crystallographic structures of complexes **28** (LHS) and **30** (RHS), obtained by single crystal X-ray diffraction.	207
Table 5.2	Copolymerisation of PA and CHO	208
Scheme 5.8	Synthesis of a mono-cobalt complexes (**32**).	210

Figure 5.11	ORTEP representation of complex **32**, obtained by single crystal X-ray diffraction.	211

Chapter 6: Prospective and Future Work

Figure 6.1	Epoxides reported in literature for CO_2/coupling.	217
Figure 6.2	Conversion vs Time ploy for several Mg(II)TM(II)$(OAc)_2$ complexes for the ROCOP of CO_2/CHO	219
Figure 6.3	Proposed structural changes to the backbone of the Co(II) side of the macrocycle to enhance Co(II)-carbonate nucleophilicity	220
Figure 6.4	Proposed structural changes to determine effects of ligand rigidity	221
Figure 6.5	Crown-ether macrocycle to accommodate large ionic metal centres	222
Figure 6.6	Proposed ligand structures to increase the number of attacking nucleophiles per coordinated epoxide	223

Chapter 7: Experimental

Table 7.1	Diffusion coefficients of complexes in d8-THF along with corresponding molecular weights	230
Figure 7.1	LogD vs LogMW from the ^{1}H DOSY NMR data represented in Table 7.1	230
Equation 7.1	Estimation of MW from diffusion coefficients obtained in THF.	230

Chapter 8: Appendices

	See appendices for table of contents	255

Table of Contents

Heterodinuclear Cooperativity in Oxygenated Polymer Catalysis

	Declaration	2
	Abstract	3
	Acknowledgements	4
	List of Abbreviations	5
	List of Figures, Schemes, Tables and Equations	9
	Table of Contents	23

Chapter 1: Introduction

1.1.1	Polymers	29
1.1.2	Polyurethanes	30
1.1.3	Polycarbonates	31
1.1.4	CO_2/Epoxide ROCOP	34
1.1.5	Bifunctional/Two Component Catalysts	38
1.1.6	Metal – Salen Catalysts	40
1.1.7	Ionic Tethered Co-Catalysts	44
1.1.8	Neutral Tethered Co-Catalysts	47
1.1.9	Evidence of a Mononuclear Mechanism	49
1.2.0	Two component Catalysts (Organocatalysts)	52
1.2.1	Dinuclear Mechanisms	56
1.2.2	Type 1: Dimeric Catalysts	58
1.2.3	Type 2: Tethered Mononuclear Catalysts	61
1.2.4	Type 3: Dinucleating Catalysts	64
1.2.5	Multinuclear Catalysts	71

1.2.6 Aims and Objectives 72

1.2.7 References 74

Chapter 2: Group 1 and 2, Zinc (II) Heterodinuclear Catalysts

2.1.1 Introduction 80

2.1.2 Aims 81

2.1.3 Synthesis and Characterisation of Group 1 Homodinuclear Complexes 83

2.1.4 Synthesis and Characterisation of Homodinuclear Zinc Complexes 87

2.1.5 Group 1 Metal Redistribution Thermodynamics 91

2.1.6 Group 1-Zinc Sequential Metalation 95

2.1.7 Group 2-Zinc Sequential Metalation 103

2.1.8 Ring Opening Copolymerisation of CO_2 and Cyclohexene Oxide 108

2.1.9 Conclusions 111

2.2.0 References 112

Chapter 3: Group 13, Zinc (II) Heterodinuclear Catalysts

3.1.1 Introduction 117

3.1.2 Aims 118

3.1.3 Synthesis and Characterisation of di-zinc Chloride 119

3.1.4 Synthesis and Characterisation of Group 13 hetero-complexes 122

3.1.5 ROCOP of CO_2/CHO with complexes **10**-**13** 128

3.1.6 Zinc(II)/Indium(III) heterodinuclear derivative complexes 130

3.1.7	Conclusions	136
3.1.8	References	137

Chapter 4: Magnesium-Cobalt Heterodinuclear Catalyst

4.1.1	Introduction	140
4.1.2	Aims	141
4.1.3	Synthesis of Homo-and Hetero-complexes **16**,**17** and **18**	142
4.1.6	Mass Spectrometry	144
4.1.7	X-Ray Photoelectron Spectroscopy (XPS)	145
4.1.8	X-ray Crystallography	147
4.1.9	Cyclic Voltammetry	148
4.2.0	Superconducting Quatum Interference Device (SQUID) magnetometry	151
4.2.1	CO_2/epoxide Copolymerisation	157
4.2.2	Rate Law Determination Mg(II)Co(II)	160
4.2.3	CO_2 limit vs saturated ROCOP of CO_2/CHO	166
4.2.4	Gibbs Free Energy of Transition	172
4.2.6	Anhydride/CHO ROCOP catalysis	179
4.2.5	Conclusion	182
4.2.6	References	183

Chapter 5: O-Vanillin Derived Heterodinuclear Catalysts

5.1.1	Introduction	187
5.1.2	Aims	190
5.1.3	Synthesis and Characterisation of a Di-Zinc Complex	192
5.1.4	Synthesis and Characterisation of heterodinuclear Zn(II)	197

	Complexes.	
5.1.5	Synthesis and Characterisation of a Di-Magnesium Complex	202
5.1.6	Synthesis and Characterisation of heterodinuclear Mg(II) Complexes	205
5.1.7	ROCOP of Phthalic Anhydride and CHO	208
5.1.8	A Route to Co(II) Heterodinuclear Complexes	210
5.1.9	Conclusions	212
5.2.0	References	213

Chapter 6: Prospective and Future Work

6.1.1	Prospective and Challenges	216
6.1.2	Enthalpy Drive Catalyst Design	219
6.1.3	Entropy Driven Catalyst Design	222
6.1.4	References	224

Chapter 7: Experimental

7.1.0	General Comments	227
7.1.1	NMR Spectroscopy	228
7.1.2	Elemental analysis	228
7.1.3	Mass Spectroscopy	228
7.1.4	X-ray diffraction	228
7.1.5	Size Exclusion Chromatrography (SEC)	229
7.1.6	DOSY NMR Spectroscopy	230
7.1.7	CO_2 Polymerisations + ATR-IR Measurements	231
7.1.8	X-ray Photoelectron Spectroscopy (XPS)	232
7.1.9	Superconducting Quantum Interference Device	232

	Magnetometry	
7.2.0	Cyclic Voltammetry	232
7.2.1	Chapter 2: Group 1 and 2, Zinc (II) Heterodinuclear Catalysts	233
7.2.2	Chapter 3: Group 13, Zinc (II) Heterodinuclear Catalysts	240
7.2.3	Chapter 4: Mangesium-Cobalt Heterodinuclear Catalyst	246
7.2.4	Chapter 5: O-Vanillin Derived Heterodinuclear Catalysts	248

Chapter 8: Appendices

8.1.1	Chapter 2: Group 1 and 2, Zinc (II) Heterodinuclear Catalysts	262
8.1.2	Chapter 3: Group 12, Zinc (II) Heterodinuclear Catalysts	301
8.1.3	Chapter 4: Magnesium-Cobalt	322
8.1.4	Chapter 5: O-Vanillin Derived Heterodinuclear Catalysts	326

Chapter 1

Introduction

1.1.1 Polymers

The polymer revolution has become one of the most important scientific advancements of the 20th century, finding purpose in a plethora of applications such as packaging, construction, agriculture, medical and consumer goods. The impact of polymers on society can be highlighted through production increase from 1.65 million tons in 1950 to 335 million tons in 2016, with a 4 % rise per year expected (Figure 1.1).[1] Almost all polymeric materials are derived from crude oil. There is an increasing demand to improve the production, recycling and disposal of these materials in order to improve sustainability.

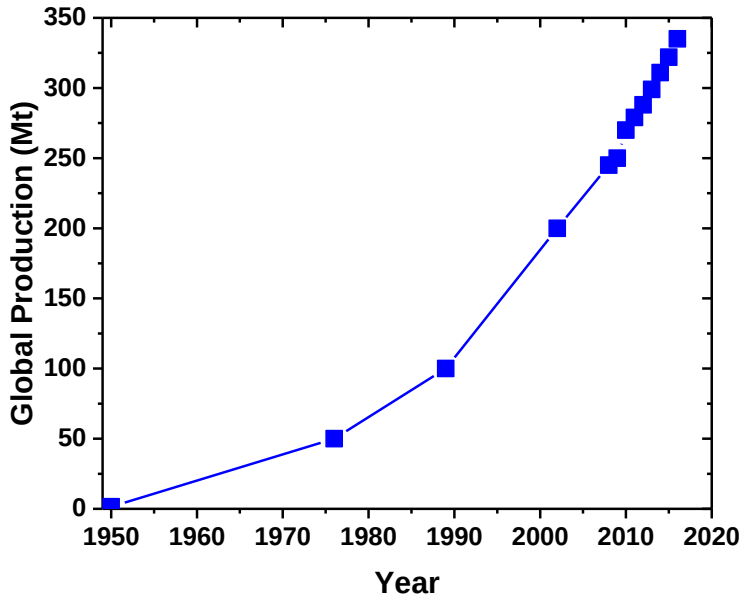
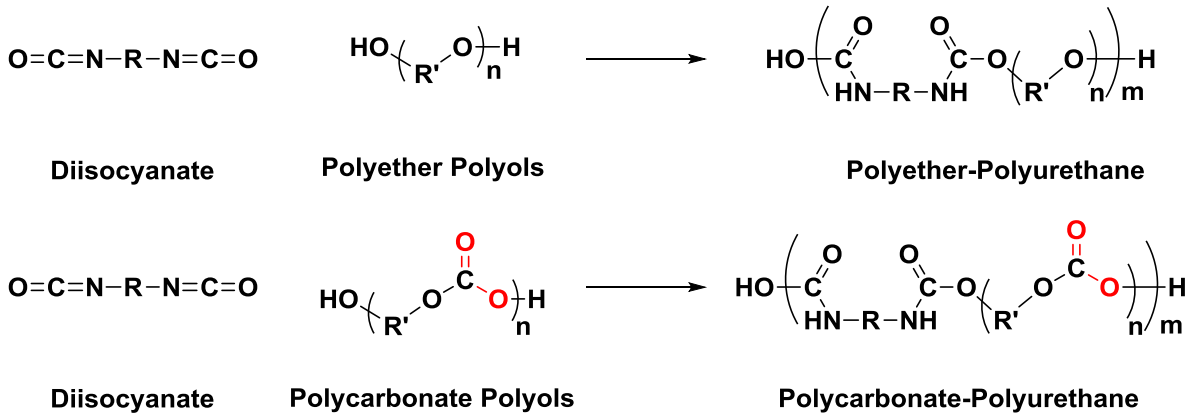


Figure 1.1: Global plastic production between 1950 and 2016 (million tons y^{-1}).[1]

1.1.2 Polyurethanes

Polyurethanes were first discovered by Otto Bayer in 1937 and make up 6 % of the total polymer market.[2] Global market forecasts estimates the polyurethanes industry to be worth up to $105 billion (USD) by 2025, with global production reaching 24 Mt per year by 2022, with its major applications being in rigid and flexible foams, coatings, adhesives and elastomers.[3] Polyurethanes are synthesised via a polycondensation reaction between a diol and diisocyanate, where the diol is typically a short chain, dihydroxy-terminated, polyol (Scheme 1.1). These polyols used can be segmented into 4 categories (market share 2011): polyether (71 %), polyester (21 %), Poly(THF) (5 %), acrylic (2 %) and polycarbonate (<1 %).[2]



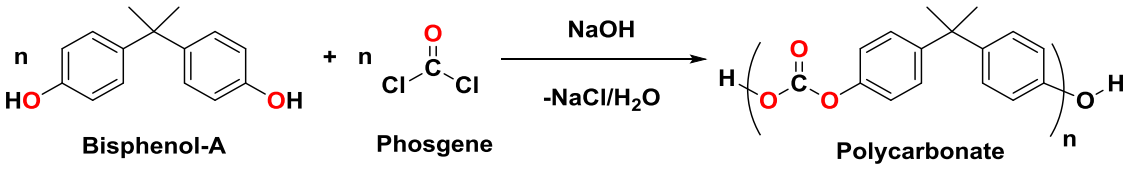
Scheme 1.1: Polyether and polycarbonate derived polyurethane syntheses.

Polyether polyols are by far the most commonly used polyol in the synthesis of polyurethanes, due to their low cost and good hydrolytic stability.[4] However, these materials can show lower thermal stability, modulus/strength and flammability in comparison to other major polyols.[4] These disadvantages are alleviated by polyester polyols, although they suffer from hydrolytic cleavage. Polycarbonate polyols currently have the smallest share of the polyurethane market, due to the current high

cost of synthesis (step-growth method, *vide infra*). These materials are often used for high performance applications due to their hydrolytic and oxidative stability, high modulus/strength and improved flame retardant properties.[4] Furthermore, a cradle to grave life cycle assessment of CO_2-derived polyethercarbonate polyols (20 wt % CO_2) shows that their use reduces both greenhouse gas emissions and fossil fuel consumption by 19 % and 16 %, respectively, in comparison to polyether polyols.[5]

1.1.3 Polycarbonates

Polycarbonates are polymers featuring [O-C(=O)-O] repeat units along the polymer backbone. The largest volume material in this class is made from bisphenol A and phosgene (Scheme 1.2). This polymer has a high glass transition temperature, T_g, 140-155 °C and is a transparent, thermoplastic material which is resistant to both impact and discolouration. It is used in applications including scratch resistant coatings, as a replacement for glass, in helmets and even in bulletproof windows.[6]



Scheme 1.2: Industrial process to producing polycarbonates.

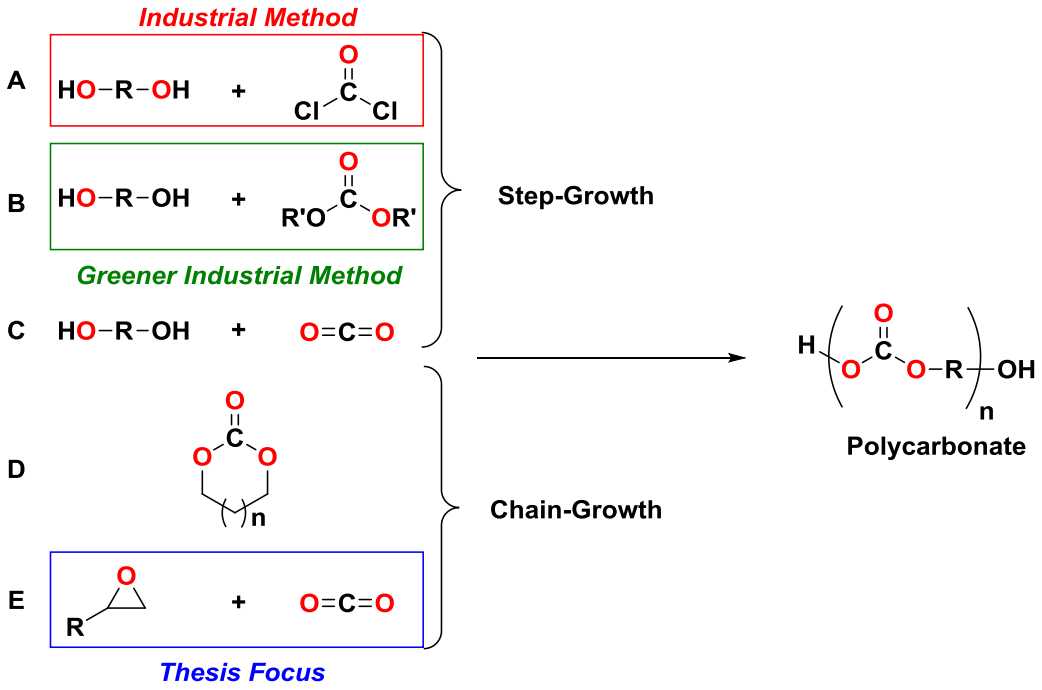
Phosgene is produced from the gaseous reaction between carbon monoxide and chlorine.[7] It is a highly reactive/toxic substrate which introduces carbonyl functionality and is used in the synthesis of acid chlorides, insecticides, isocyanates and polycarbonates. One drawback to the use of phosgene is the equimolar generation of chloride salts along with the copious volumes of chlorinated solvent waste generated during the synthesis of various carbonyl species.[8]

Several methods to make aliphatic polycarbonate polyols have been developed operating by step-growth or chain-growth polymerisation (Scheme 1.3). Step-growth methods involve reaction of a diol with a carbonyl fragment, through a polycondensation method (Scheme 1.3, A-C). Although this method allows access to polymers with either aliphatic or aromatic repeat units, it does not enable control over molecular weight. It also requires the removal of water, or other condensate, which is energy-intensive and precludes the synthesis of less thermally stable polymers.[9] In terms of chain-growth processes, the two most common are ring opening polymerisation (ROP) and ring opening copolymerisation (ROCOP).

Cyclic carbonate ROP is a viable route with good functional tolerance, however, polymerisations are dependent on a favourable Gibbs energy of polymerisation, ΔG_p, and a low monomer concentration at equilibrium, $[M]_{eq}$. Polymerisation thermodynamics are driven by ring-strain (enthalpy) and thus >5-membered rings such as trimethylene carbonate, are typically readily polymerised whereas 5-membered rings such as propylene carbonate are notoriously difficult. Furthermore, almost all the polymerisable cyclic carbonates are new monomers and, therefore, industry would have to successfully and economically scale their synthesis. The most commonly reported cyclic carbonate, trimethylene carbonate, is currently very expensive (£9400 kg^{-1}, Merck 2019) and is made via a condensation of 1,3-propanediol with ethylchloroformate (phosgene derivate).[10]

The ROCOP of CO_2 with epoxides has attracted considerable attention as a potential means to valorise waste carbon dioxide (Scheme 1.3, E). Many epoxides are already commercially produced at large scale and already used to make polymers, therefore it is feasible to design for a range of material properties. Thermodynamic constraints

are lifted as epoxide ring strain is sufficient to drive reactions to high conversions. Although there are a wide range of reported aliphatic polycarbonates, the most extensively studied are: polyethylene carbonate (PEC), polypropylene carbonate (PPC), polybutylene carbonate (PBC) and polycyclohexene carbonate (PCHC). PEC, PPC and PBC are potentially useful as plastics or elastomers, e.g. for packaging, due to their low T_g and high flexibility. In this thesis, PCHC is of particular interest due to its better thermal stability, rigidity and strength. Polyurethanes from PCHC, applications such as rigid foams or scratch resistant coatings are envisaged.[11]



Scheme 1.3: Step-growth and chain-growth synthetic routes to polycarbonates.

Table 1.1: Selected thermal and mechanical properties of common polycarbonates.[11]

	T_g (°C)	T_d (°C)	Tensile Strength (MPa)	Tensile Modulus (MPa)	Elongation to break (%)
PEC	10	229	-	-	-
PPC	42	252	7-30	700-1400	600-1200
PBC	9	241	-	-	-
PCHC	118	310	40-44	3500-3700	1.1-2.3
Bisphenol-A	149	458	43-51	2000-2800	15-75

1.1.4 CO_2/Epoxide ROCOP

The coupling of CO_2 and epoxides to make polycarbonate was first reported by Inoue in 1969.[12] The catalytic steps for the ring opening copolymerisation of CO_2/epoxide involves 4 processes: (1) initiation, (2) CO_2 insertion, (3) epoxide ring opening and (4) termination (Scheme 1.4).

(1) Initiation:

This step involves the ring opening of a coordinated epoxide by initiating group, X. The initiating group may be either a ligand, derived from the catalyst, or provided by a co-catalyst, **A**. The initiating group, X, is typically a halide, alkyl, carboxylate or alkoxide species. The reaction produces alkoxide intermediate, **B**.

(2) CO_2 insertion:

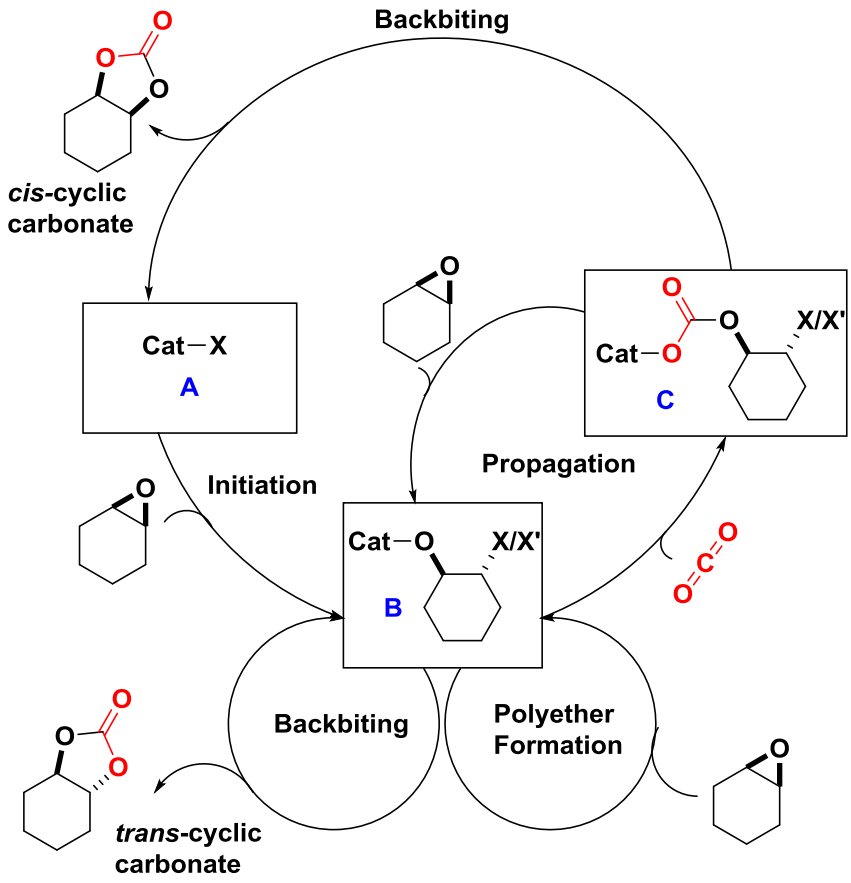
This step involves the rapid insertion of CO_2 into the metal-alkoxide, **B,** forming a metal-carbonate, **C**. For the catalysts in this thesis this step is not usually rate-determining.

(3) Epoxide Ring Opening:

The coordinated epoxide is attacked by the nucleophilic carbonate of **C**, which regenerates a metal-alkoxide, **B.** For catalysts in this thesis, this step is rate-determining.

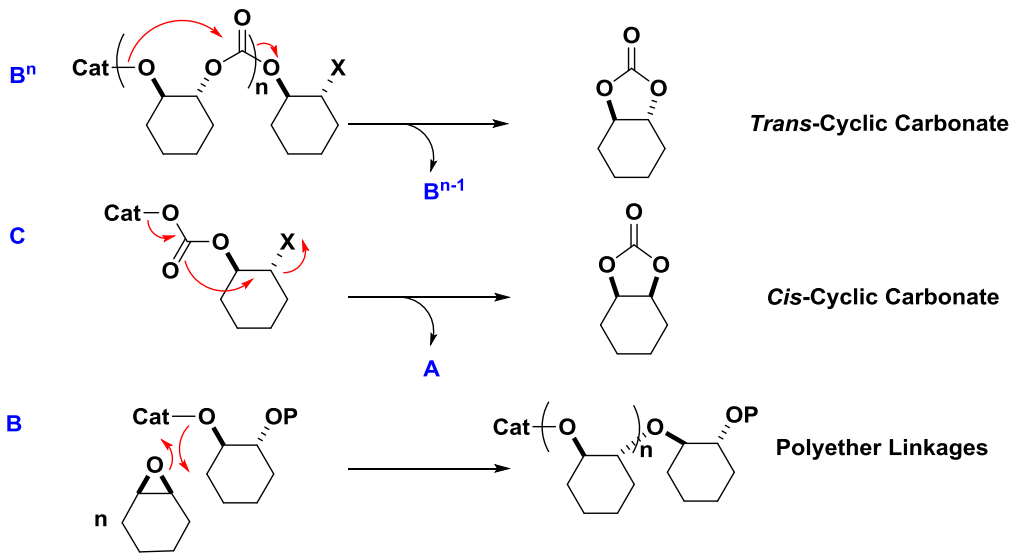
(4) Termination:

The addition of acidic or aqueous reagents hydrolyses the metal-alkoxide bond and terminates the reaction.



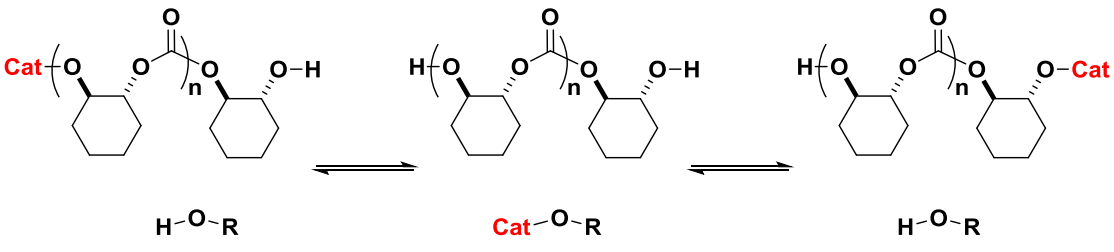
Scheme 1.4: Catalytic cycle to polycarbonate, polyether and cyclic carbonate products. X = initiating group (such as halide, alkoxide, acetate), X' = carbonate group during propagation.

Several side-reactions are feasible including backbiting to form a cyclic-carbonate species (Scheme 1.5). The cyclic carbonate is the thermodynamic product of CO_2/epoxide coupling and cannot re-enter the catalytic cycle. Backbiting reactions can occur at both **B** and **C**, but for cyclohexene oxide the stereochemistry differs depending on the process. Backbiting from **B** yields *trans*-cyclic carbonate whereas attack from **C** forms the *cis*-cyclic carbonate. Another side reaction is the sequential insertion of epoxide into metal-alkoxide **B,** leading to polyether linkages in the polymer chain.



Scheme 1.5: Potential side-reactions in CO_2/epoxide coupling

A living polymerisation shows a linear increase in molar mass (M_n) with conversion (%) where M_n is inversely proportional to the concentration of initiators, $1/[\text{initiator}]_0$. This results in narrow polydispersity provided the rate of initiation is faster than the rate of propagation, with the absence of chain-termination steps. The ROCOP reactions presented here are rarely true living polymerisations due to the presence of chain-transfer agents (CTAs). These are typically alcohols and are proposed to undergo exchange with the propagating metal-alkoxide species (Scheme 1.6). High control of polymerisation can be achieved provided the chain-transfer reactions are reversible and are faster than chain-propagation. This results in predictable molar mass, which is inversely proportional to the concentration of CTA, $1/[\text{CTA}]_0$.[13-14]



Scheme 1.6: Chain-transfer equilibria

In CO_2/epoxide ROCOP purification of both monomers, free of water, is important. A cobalt salen catalyst was shown to catalyse the hydrolysis of epoxide, prior to polymerisation.[15] Two distributions are observed in the mass spectrum, due to initiation from both catalyst and diol (Figure 1.2). Bimodality is observed in the GPC, with the diol distribution twice the MW of the catalyst distribution due to the bifunctionality of diol, where chains can grow from both ends.[16] One strategy to overcome this MW issue is by targeting non-initiating co-ligands, which exchange with the CTA, resulting in monomodal molecular weight distributions (Figure 1.2 Bottom).[16] Non-initiating co-ligands are usually alkyls or phenyls where their exchange with CTA results in irreversible CH bond formation.[16] The following discussion will focus on an overview of the most active catalysts and their mechanistic insights. For details of all catalytic systems, the reader is referred to comprehensive reviews.[6, 11, 17-20]

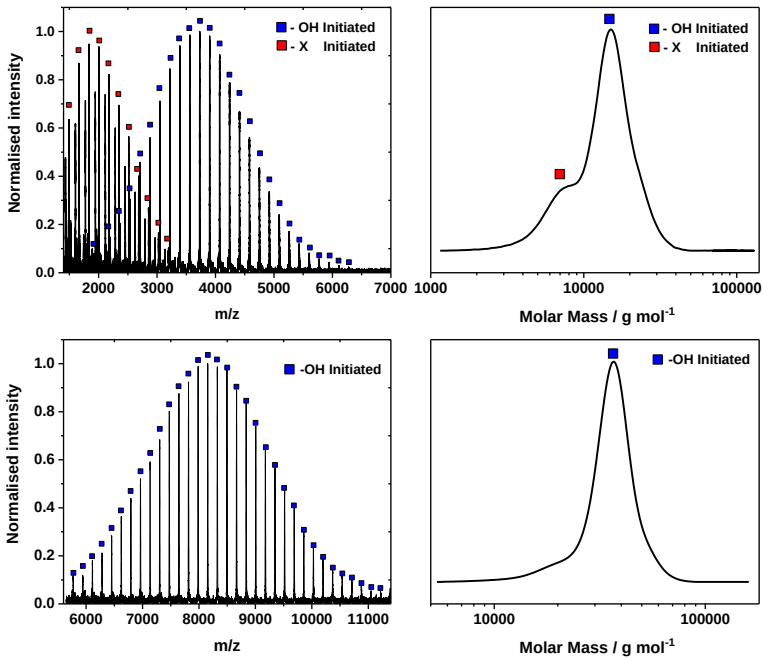


Figure 1.2: Bimodality from co-ligand and diol initiation (Top). Monomodality from a catalyst featuring non-initiating co-ligands and diol (Bottom). (LHS: MALDI-ToF, RHS: Gel Permeation Chromatography).

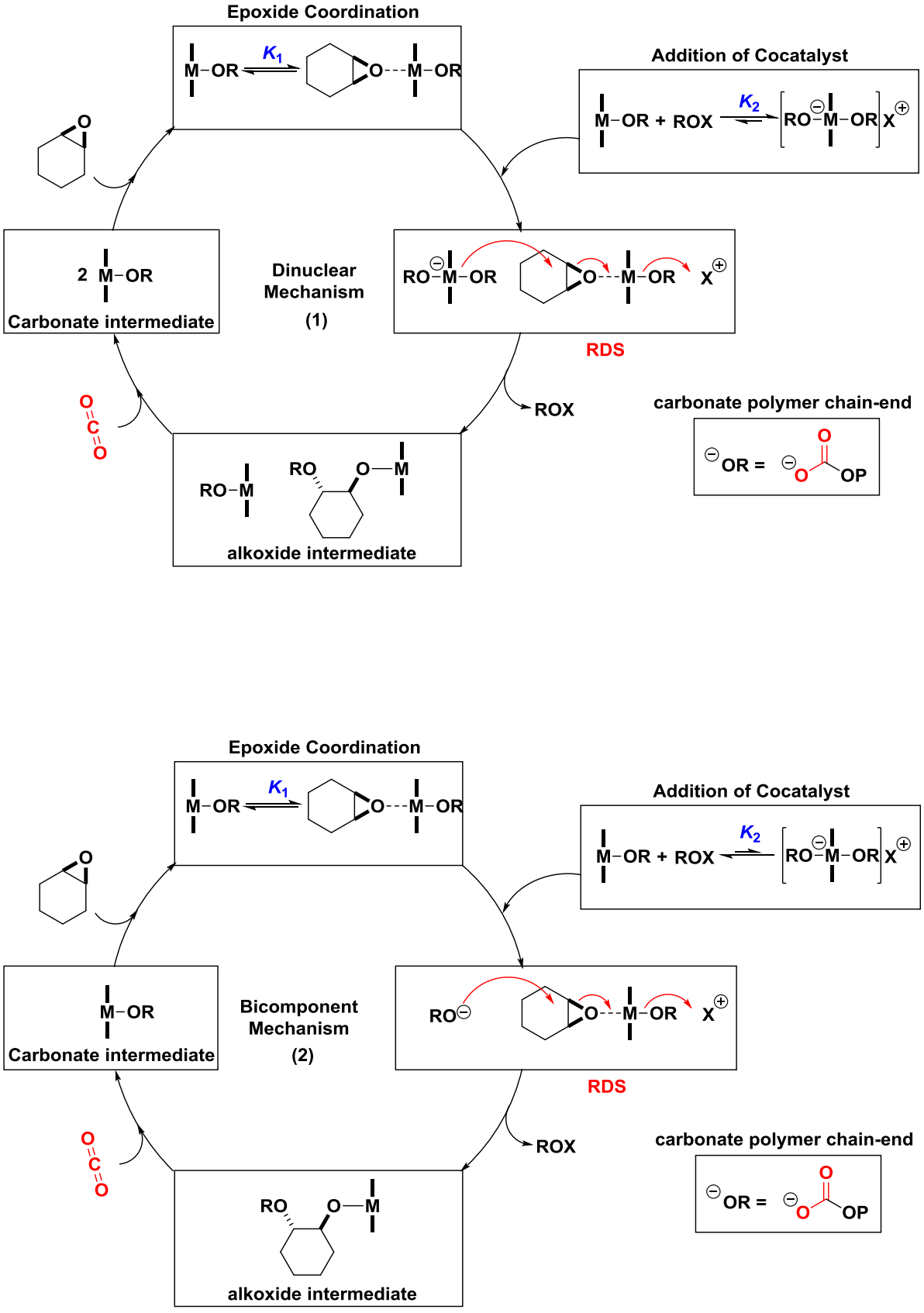
1.1.5 Bifunctional/Two Component Catalysis

Early ROCOP catalysis focused on two component catalyst systems: a combination of a metal catalyst (typically chromium/cobalt porphyrin/salans) and an organic co-catalyst (typically quaternary ammonium salts).[11, 18] Extensive mechanistic investigations on the roles of both catalyst and co-catalyst during polymerisation have been undertaken and is summarised here. A detailed discussion on these mechanistic investigations is presented in Sections 1.1.6-1.2.0. Two mechanisms are typically proposed for these bifunctional systems: (1) dinuclear and (2) bicomponent (Scheme 1.7).[18] Both mechanisms invoke similar solution equilibria. K_1 describes epoxide coordination to a metal centre. K_2 describes the interaction between metal catalyst and co-catalyst resulting in the formation of a hexacoordinate catalyst-co-catalyst ion pair.

In the dinuclear mechanism (1) K_2 lies towards the hexacoordinate metal complex which is proposed to be the 'active' nucleophilic species which attacks the 'activated' epoxide generating a reactive metal-alkoxide species. This results in an order in metal catalyst of 2.

In the bicomponent mechanism (2) K_2 lies towards the pentacoordinate metal complex, where the co-catalyst (ROX) provides the 'active' nucleophile to attack the activated epoxide. This results in an order in metal catalyst of 1.

In both cases, without co-catalyst, reactivity is lost presumably due to the lack of a reactive nucleophile. Furthermore, mononuclear metal salan catalysts typically report catalyst orders ranging between 1 and 2. This implies a combination of both mechanisms and the relative ratios are presumably affected by temperature of reaction and the concentration of both catalyst and co-catalyst.



Scheme 1.7: Bifunctional mechanisms (1) Dinuclear (2) Bicomponent. Where M = Metal Catalyst, X = Organic Co-Catalyst

1.1.6 Metal – Salen Catalysts

Darensbourg and co-workers was first to report an active Cr(III) salen catalyst for the ring opening copolymerisation of CO_2 and cyclohexene oxide (CHO).[21-22] The catalyst was shown to have a first order dependence on catalyst concentration, indicating a mononuclear mechanism (Figure 1.3). Activity was increased upon addition of a Lewis base (N-methyl imidazole). The imidazole was proposed to enhance the nucleophilicity of the carbonate chain end by coordinating *trans* to the growing polymer chain.

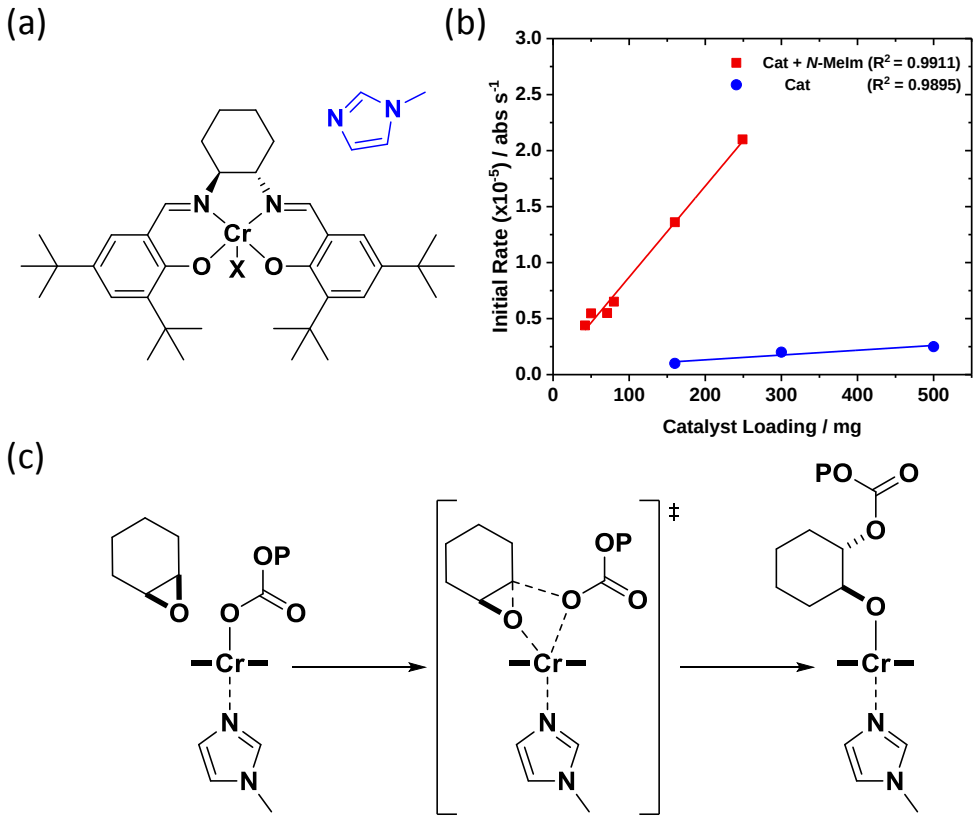
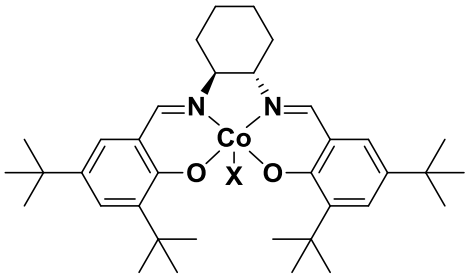


Figure 1.3: (a) Cr(III) salen catalyst structure. (b) Plot of initial rate versus catalyst loading for reactions with and without co-catalyst (N-MeIm). (c) Proposed mechanism where N-MeIm binds *trans* to the polymer chain end.[22]

PPNCl > $^{n}Hept_4NCl$ > $^{n}Bu_4NCl$ > $^{n}Et_4NCl$ > No Co-Catalyst



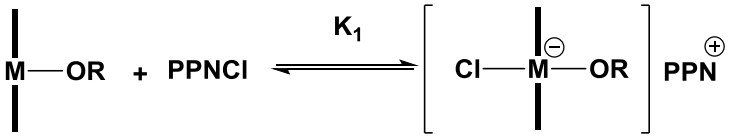


Figure 1.4: Co(III)salen structure and a series of co-catalysts and their interaction equilibrium.[23]

Subsequently, Coates and co-workers reported a Co(III) salen complex which was active without co-catalyst, for CO_2/propylene oxide (PO) ROCOP (25 °C, 20 bar, TOF = 80 h^{-1}). Increases in temperature severely decreased activity, to 17 h^{-1} (40°C).[23] Lu and co-workers reported that adding a co-catalyst to the Co(III) complex enhanced the rate, selectivity and reduced the temperature sensitivity of the polymerisation, resulting in a maximum activity of 371 h^{-1} (25 °C, 40 bar) and affording perfectly alternating copolymer (>99 %).[24] Further work showed that the Co(III) salen catalyst was more active with bis(triphenylphospine)iminium chloride (PPNCl) compared to other co-catalysts, and in the right ratios a maximum activity of 520 h^{-1} was feasible (Figure 1.4).[25] The ionic co-catalysts were proposed to stabilise the active species by forming a catalyst-co-catalyst ion pair preventing the decomposition of the catalyst to the inactive Co(II) salen.[25]

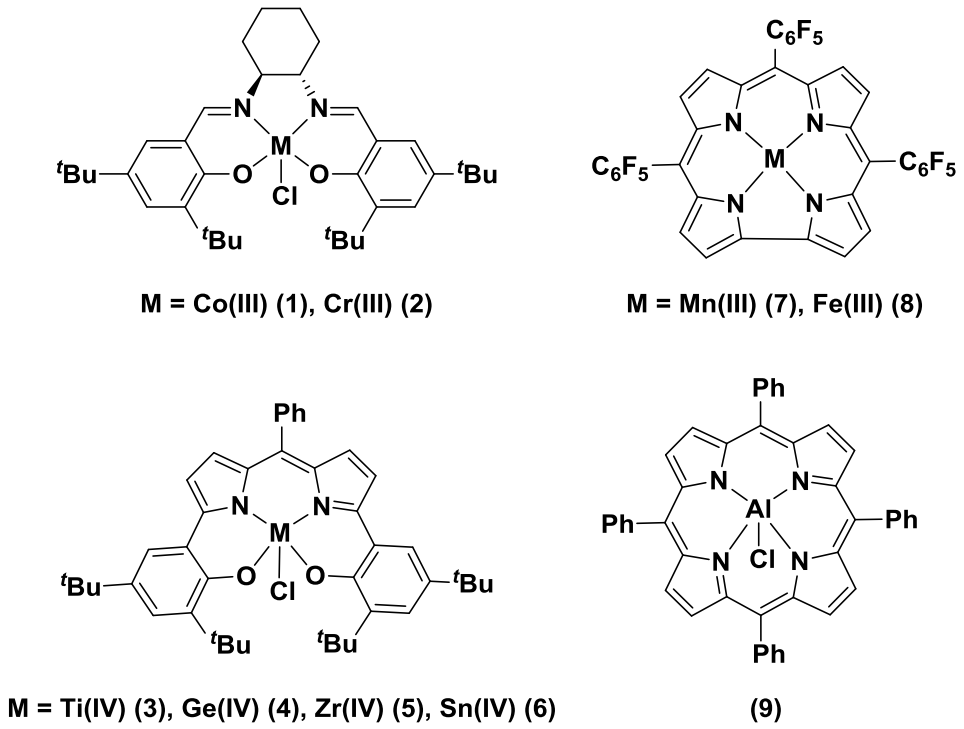


Figure 1.5: Catalysts screened by DFT.[26]

In 2014, Nozaki and co-workers reported a DFT study on a series of planar metal complexes all requiring a co-catalyst. The goal was to predict their propensity to form (1) polycarbonate (2) cyclic-carbonate and (3) polypropylene oxide (Figure 1.5).[26] For each catalyst the Gibbs dissociation energy for metal-epoxide (ΔG_{epx}), metal-alkoxide (ΔG_{alk}) and metal-carbonate (ΔG_{crb}) intermediates were determined. A negative correlation between the logarithm of TOF and (ΔG_{crb} - ΔG_{epx}) was observed (Figure 1.6). This was rationalised by maximum activity being observed when the dissociation equilibrium lies between metal-epoxide and metal-carbonate towards a vacant metal complex. It also suggested high polycarbonate (vs. cyclic carbonate) selectivity is observed when ΔG_{epx} is large. Under these conditions the attack of the metal-carbonate intermediate on an activated epoxide is favoured compared to its intramolecular backbiting reaction to form cyclic carbonate (Figure 1.7).[26]

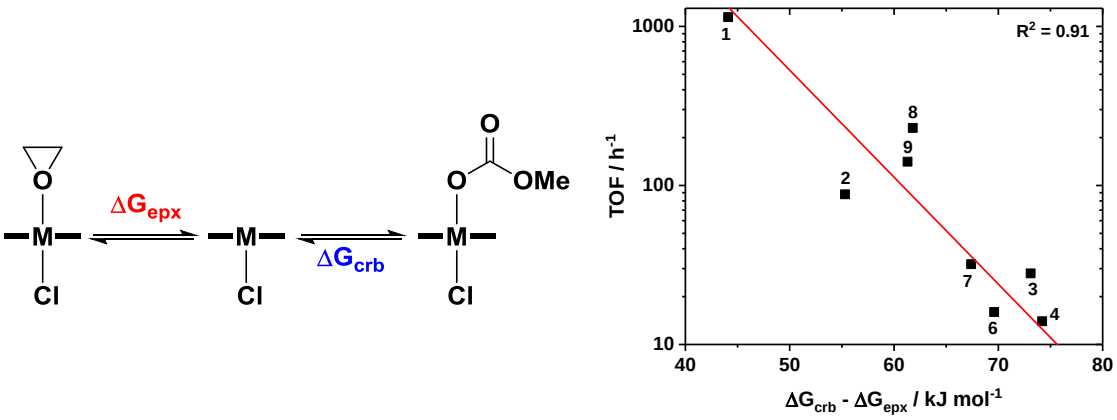


Figure 1.6: LHS, equilibrium between metal-epoxide/carbonate intermediates and a vacant metal centre. RHS, plot of TOF vs difference between metal-carbonate and epoxide dissociation energies.

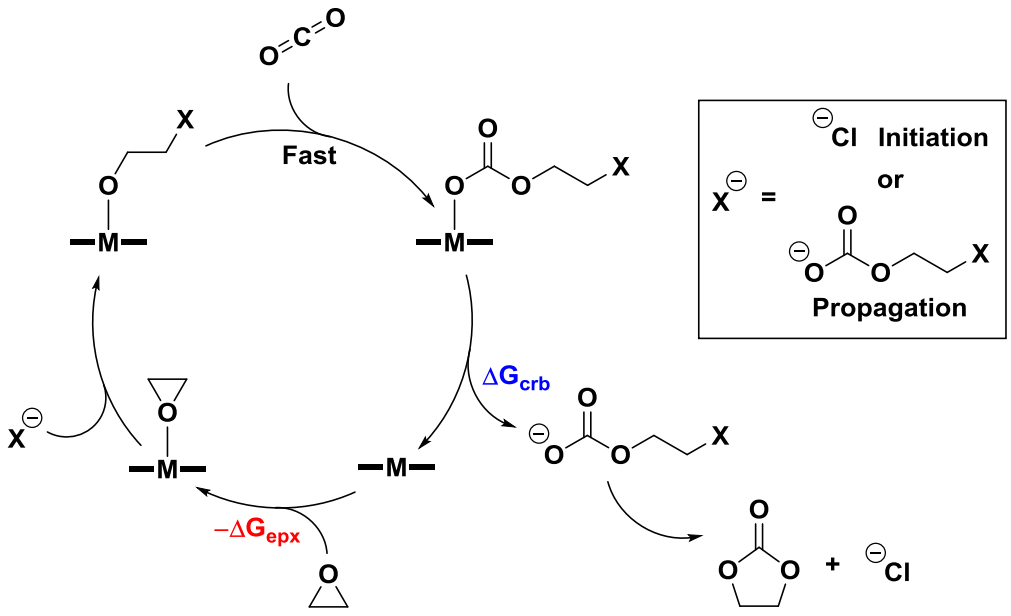


Figure 1.7: Mechanistic hypothesis describing the relationship between the carbonate and epoxide dissociation energies.

1.1.7 Ionic Tethered Co-Catalysts

The lack of activity at low catalyst loading and the concomitant production of cyclic carbonate at higher reaction temperatures are both significant limitations of simple salen catalysts. One solution has been to tether the co-catalyst to the ligand (Figure 1.8).

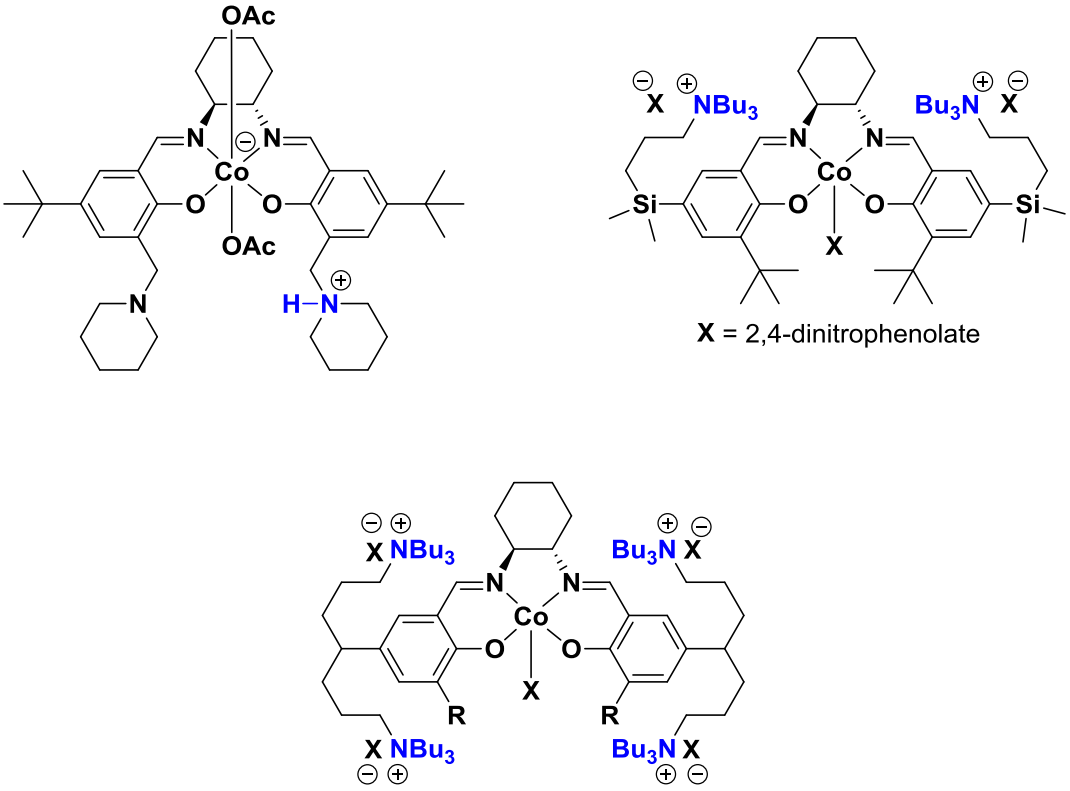


Figure 1.8: Selected tethered cobalt(III) salen catalysts.

Nozaki and co-workers were the first to report a Co(III) salen catalyst with a piperidinium moiety tethered to the *ortho*-position of the phenyl substituent. This catalyst displayed relatively high activity (250 h^{-1}), for CO_2/PO, at 25 °C, 14 bar CO_2, forming perfectly alternating copolymer (> 99 %). Increasing the temperature to 60 °C increased activity to 680 h^{-1}, whilst retaining high polymer selectivity (90 %). This increased thermal stability was proposed to be due to protonation of the polymer end

groups which dissociate from the metal centre, by the piperidium group, thereby reducing the propensity to backbite whilst maintaining CO_2 reactivity.[27]

Lee and co-workers subsequently reported a Co(III) salen catalyst with a silylammonium moiety tethered to the *para*-position of the phenyl substituent. This catalyst showed an activity of 3,500 h^{-1}, at low catalyst loading (0.0043 mol %) at 90 °C, 20 bar CO_2 pressure, maintaining excellent polymer selectivity (>90 %).[28] Further modification to the salen ligand, tethering four ammonium salts to the *para*-position of the phenyl substituents resulted in very high rates (26, 000 h^{-1}) affording perfectly alternating copolymer with excellent selectivity (> 99 %) at 80 °C, 20 bar CO_2 pressure, 0.001 mol % catalyst loading.[29] As the activity is retained at high dilution, these modifications appear to imply the catalysts operate by a bicomponent mechanism (2).

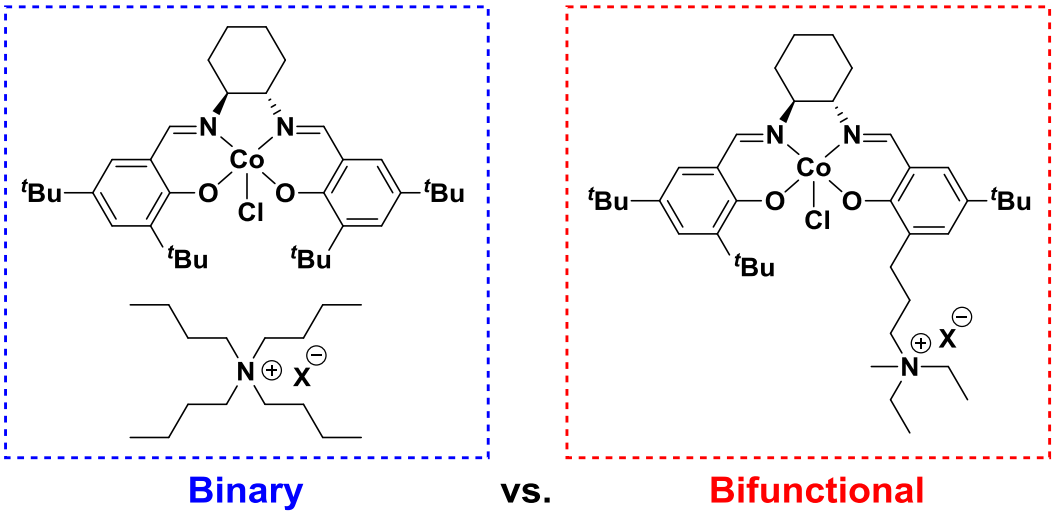


Figure 1.9: LHS, binary Co(III) salen catalyst. RHS, bifunctional Co(III) salen catalyst.

In 2013, Lu and co-workers reported a kinetic study comparing a binary and bifunctional Co(III) salen catalyst systems (Figure 1.9).[30] The binary system was reported to show a rate order in catalyst concentration of 1.61, indicating a complex

mechanistic pathway and some dependence on dinuclear pathways. In contrast, the bifunctional system showed a first order dependence on catalyst concentration indicating a mononuclear pathway. The activation energies for both polymer (E_a PPC) and cyclic carbonate (E_a CPC) (Figure 1.10) were compared and the bifunctional system showed a lower polymerisation barrier (33.8 vs. 29.5 kJ mol^{-1}) potentially due to an increase in the dissociation energy of the carbonate intermediate. Concurrently, the bifunctional system showed an increased barrier to cyclic carbonate formation (50.1 vs. 77.0 kJ mol^{-1}) which accounts for the better stability at elevated temperatures. The increased barrier to cyclic carbonate formation was proposed to be due to the carbonate chain ends being in close proximity to the metal, whereas in the binary system, due to dilution effects, the carbonate chain ends may exist as free anions and are more likely to undergo backbiting reactions. The stability of the bifunctional system towards backbiting may also be a result of the >1 order dependency of the binary catalyst concentration, where the barrier to cyclic carbonate formation maybe lowered due to the reaction proceeding via a dinuclear mechanism.[30]

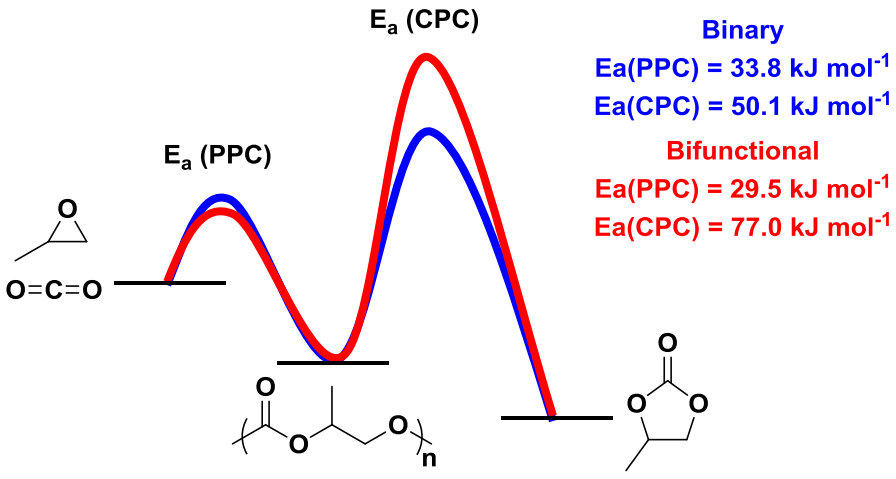


Figure 1.10: Energy barrier to polycarbonate and cyclic carbonate formation for a binary and bifunctional catalyst system.

1.1.8 Neutral Tethered Co-Catalysts

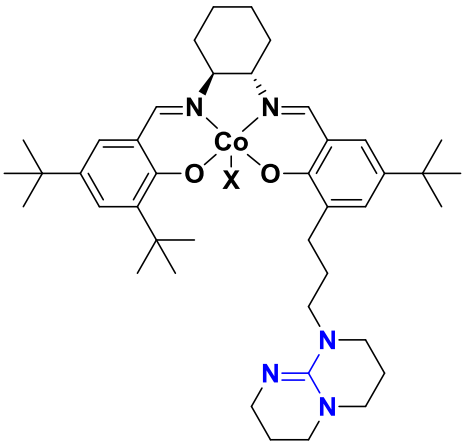
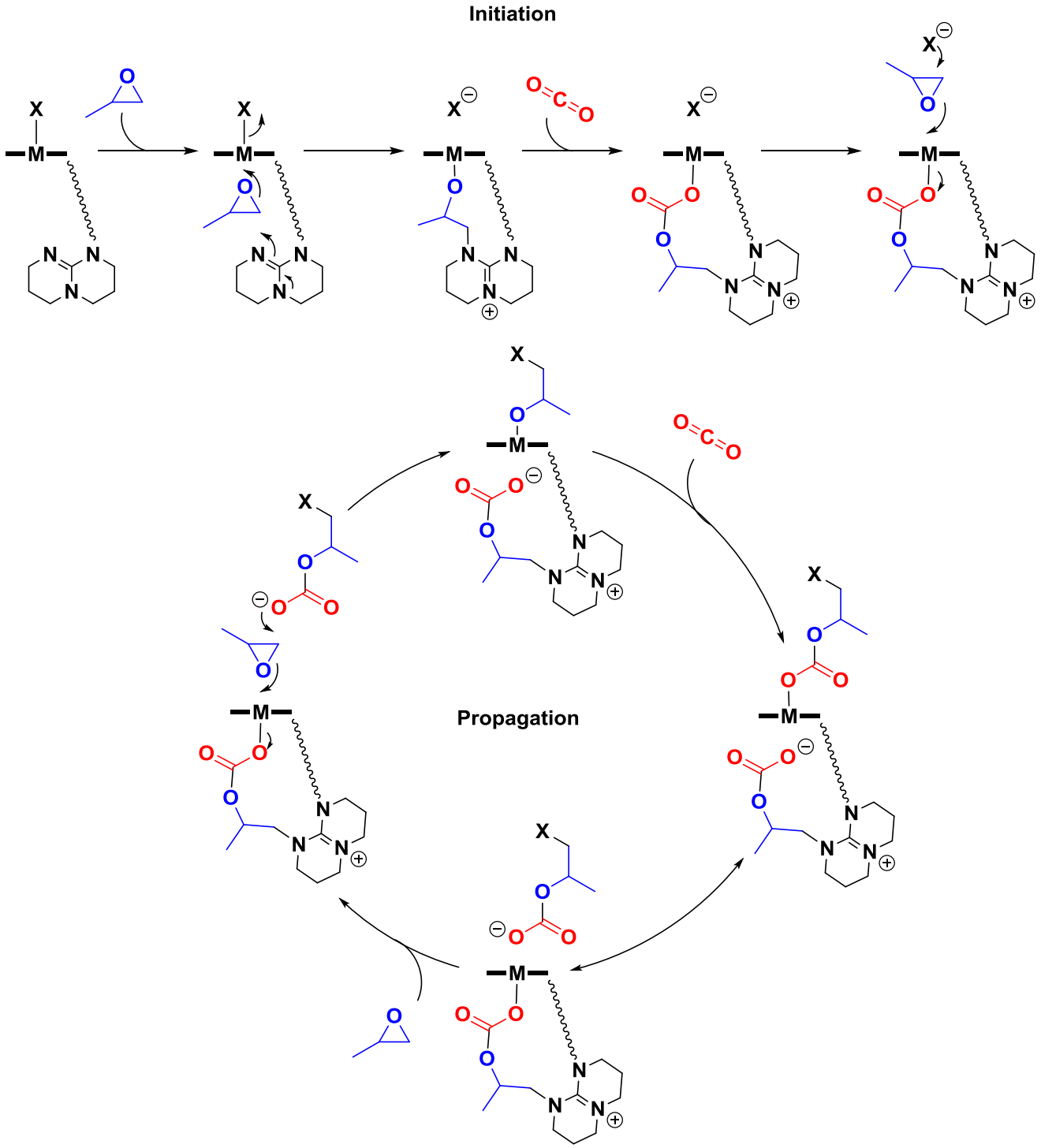


Figure 1.11 Neutral base tethered on a cobalt(III) salen catalyst system.

In 2009, Lu and co-workers reported an asymmetric Co(III) salen complex with a sterically hindered organic base tethered to the *ortho*-phenolate site (Figure 1.11). It showed an activity of 10,900 h^{-1} (100 °C, 25 bar CO_2) affording alternating PPC with high selectivity (97 %). This catalyst was 6 times as active as the non-tethered Co(III) salen system. The enhancement in rate was attributed to the increase in thermal stability of the Co(III) metal centre, limiting reduction to an inactive Co(II) centre. The activities were maintained when diluted (0.01 mol %). It was proposed to operate *via* a bicomponent mechanism, whereby the growing polymer chain dissociates from the metal and acts as a nucleophile (Scheme 1.8).[31]



Scheme 1.8: Proposed mechanism for the tethered Co(III) catalyst system.

1.1.9 Evidence of a Mononuclear Mechanism

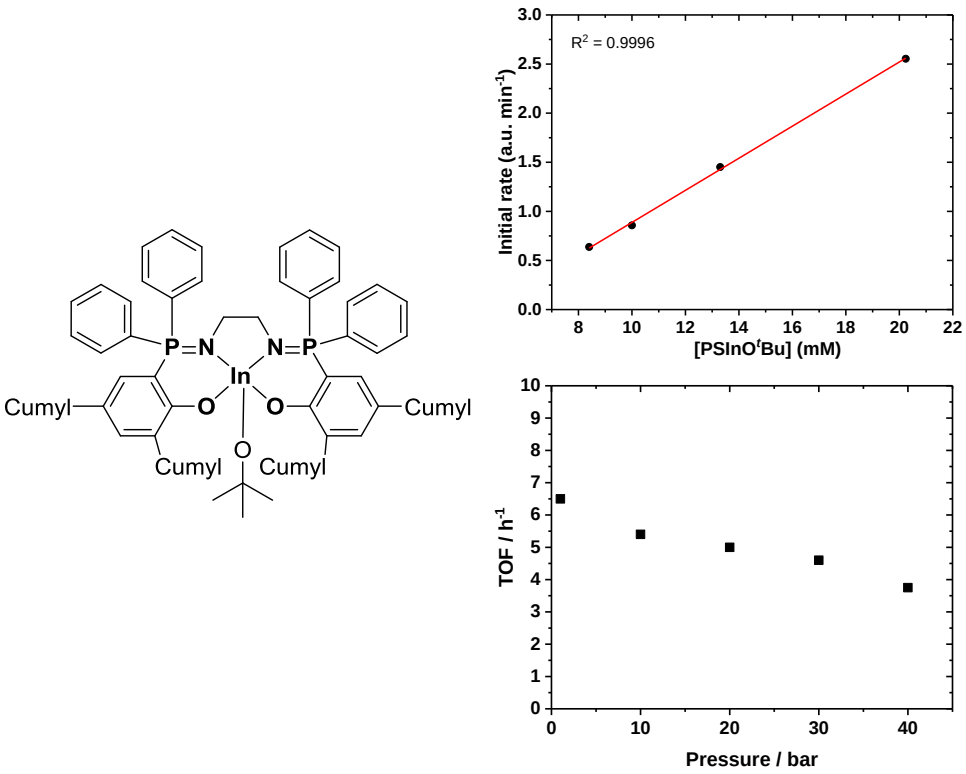


Figure 1.12: Indium phosphasalen catalyst and polymerisation data.

Until recently, all catalysts were proposed to operate by either dinuclear or bicomponent mechanisms, more often than not requiring the addition of a co-catalyst such as (PPNCl). In 2018, Williams and co-workers reported a series of mononuclear indium catalysts, coordinated by phosphasalen ligands (Figure 1.12). These catalysts showed low activity but without any co-catalyst, at 1 bar CO_2 pressure (15 h^{-1}) and produced perfectly alternating copolymer (>99 %) with little cyclic carbonate (<5 %). Kinetic studies, using *in-situ* ATIR-infrared spectroscopy, led to a rate law which was first order in catalyst concentration and zero order in CO_2 pressure, hence a dinuclear mechanism was less likely (generally catalyst order = 1-2). Dilution of neat CHO with diethylcarbonate, to determine epoxide order, resulted in the selective formation of *cis*-cyclic carbonate due to poor epoxide coordination at the carbonate intermediate.

The reaction mechanism was probed by in-*situ* IR spectroscopy (Figure 1.13). The indium alkoxide was exposed to 1 bar CO_2 and the immediate formation of a metal carbonate species formed with asymmetric and symmetric C-O stretches observed at 1560 and 1400 cm^{-1}. The difference between the asymmetric and symmetric C-O vibration frequency is indicative of the binding mode of the carbonyl species, with $\Delta > 200$ cm^{-1} observed for κ^1-coordination, $\Delta < 200$ cm^{-1} observed for κ^2-coordination. A difference of 160 cm^{-1} was measured for the metal-carbonate species, indicating κ^2-coordination. DMAP was added as a model for epoxide coordination which resulted in a shift of the C-O frequencies to 1618 and 1400 cm^{-1}, a difference of 218 cm^{-1} indicated κ^1-coordination. The formation of dissociated carbonate anions was not observed (expected at 1570 and 1415 cm^{-1}). Together with the kinetic data, the catalysts appear to operate via *cis*-coordination of an epoxide with respect to the carbonate chain which enables insertion to occur at a single metal centre without the need for a co-catalyst.

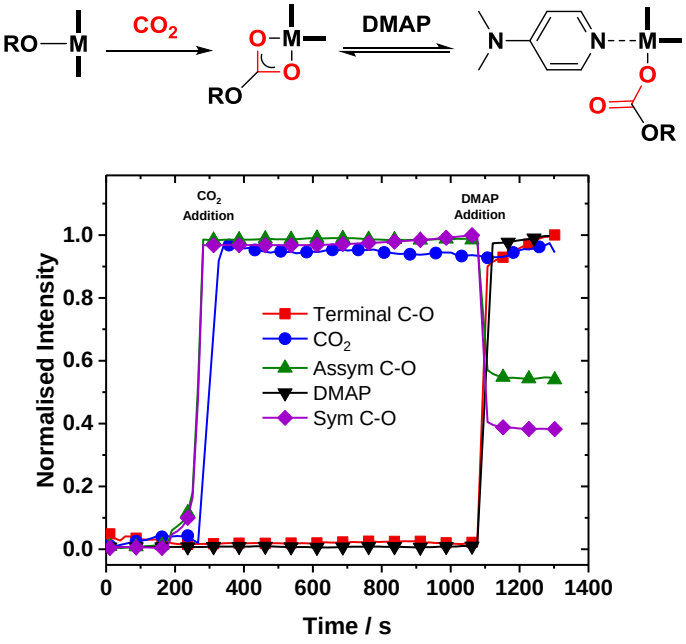
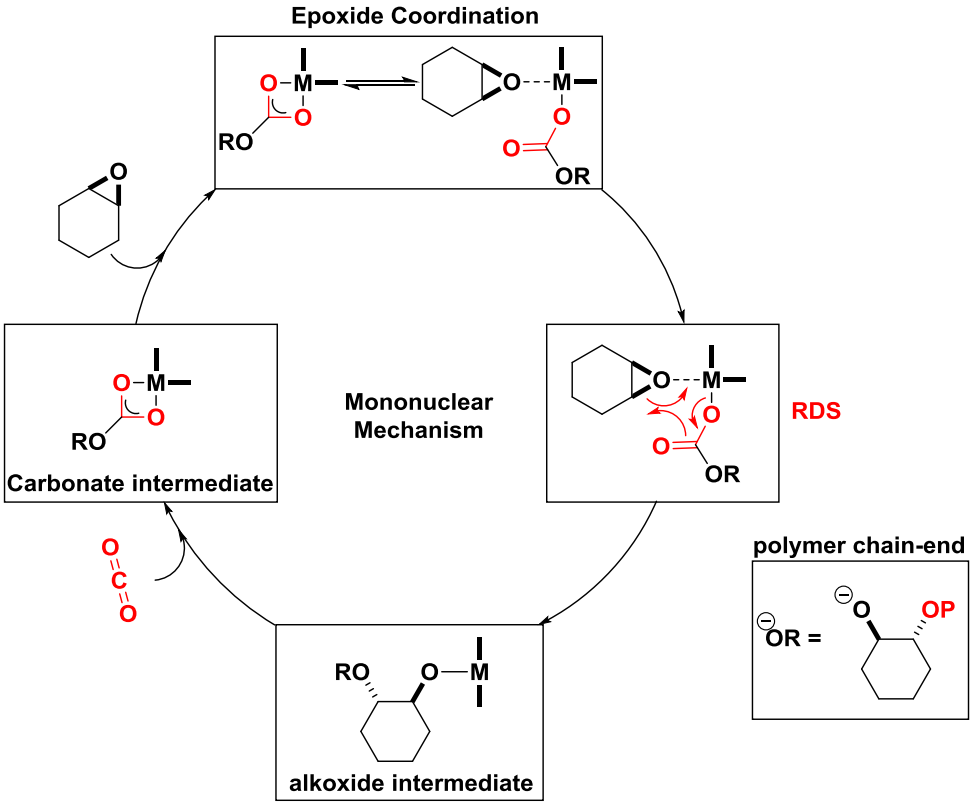


Figure 1.13: IR data showing intermediates relevant to catalysis.

A new mononuclear mechanistic hypothesis was advanced as illustrated in Scheme 1.9. The structure-activity studies indicated that successful catalysts must balance Lewis acidity with carbonate nucleophilicity. Increased Lewis acidity enhances epoxide coordination, but also results in a more stable metal-carbonate chelate and appears to increase the barrier to ring opening of the epoxide. On the other hand, a more nucleophilic metal carbonate enhances epoxide ring opening but may reduce epoxide coordination. It is proposed that the catalyst achieves this balance through the use of the electron donating phosphasalen ligand which reduces Lewis acidity at the In(III) centre, in comparison to the In(III) salen which showed negligible activity.[32]



Scheme 1.9: Mononuclear mechanism for CO_2/epoxide coupling

1.2.0 Two component Catalysts (Organocatalysts)

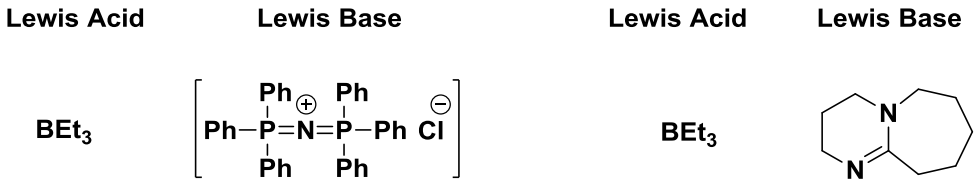
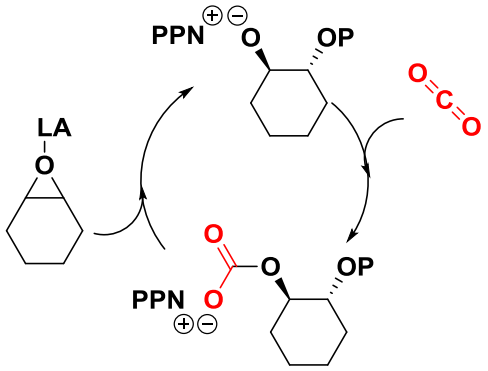


Figure 1.14: Borane/PPNCl systems for CO_2/epoxide and COS/epoxide polymerisations.

In 2016, Feng and co-workers reported systems comprising trialkylboranes, PPNCl and alcohol for PO or CHO ROCOP (Figure 1.14). The borane was proposed to activate epoxide and the copolymerisation involved both alkoxide and carbonate anions associated with the cationic co-catalyst (Scheme 1.10). This catalyst system produced perfectly alternating copolymer (>99 %) at 10 bar, 60 °C, showing a TOF of 49 h^{-1} and 600 h^{-1} for PO and CHO, respectively.[33]



Scheme 1.10: Lewis acid catalysed CO_2/epoxide copolymerisation.

A DFT study suggested the borane activates the epoxide in both initiation and propagation steps, lowering the activate barrier to ring opening of the epoxide by 93.3 and 54.4 kJ mol^{-1}, respectively (Figure 1.15).[34] The polycarbonate, polyether, and cyclic carbonate Gibbs free energy barriers were calculated to be 90.0, 119.7 and 210.9 kJ mol^{-1}, respectively.[34] This is in good agreement with experimental selectivity, with polycarbonate measured to be highly selective (> 99 %). However,

the borane is also suggested to stabilise the carbonate chain-end, with the rate-determining step shown to include two equivalents of borane (stabilised carbonate, activate epoxide), which would suggested a second order dependence on borane concentration. The consideration of the role of PPN^+ is not included in the study, although catalytic activity and selectivity is lost when removed. It is likely the PPN^+ stabilises the carbonate chain-end with borane activating epoxide. The determination of the rate law would help to clarify the role of the borane in the catalysis.[34]

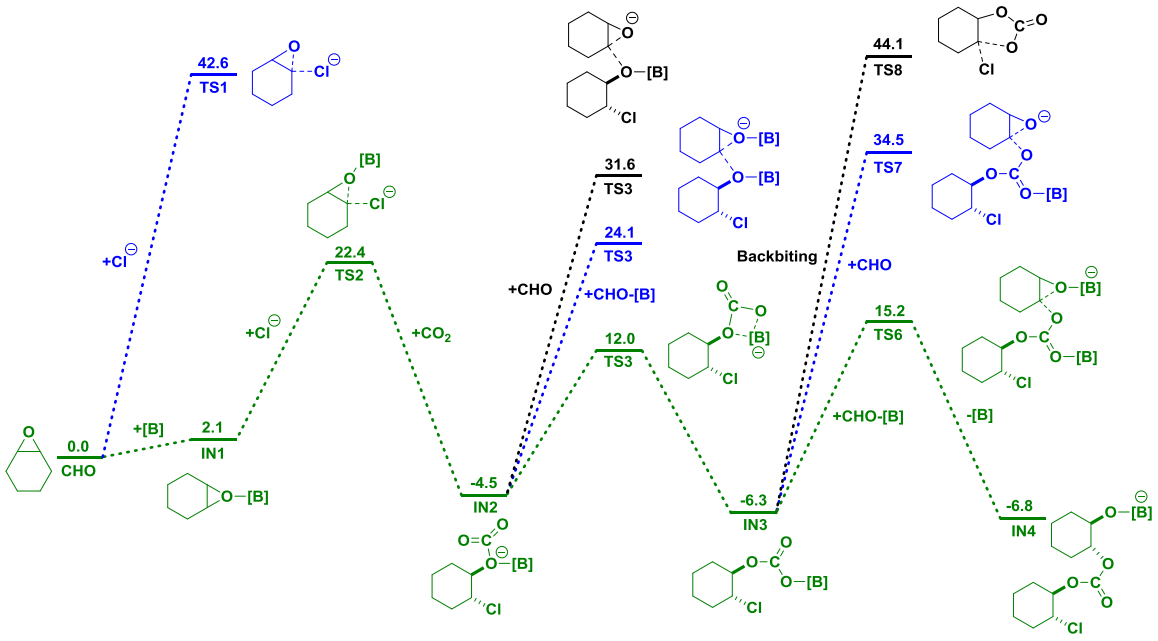
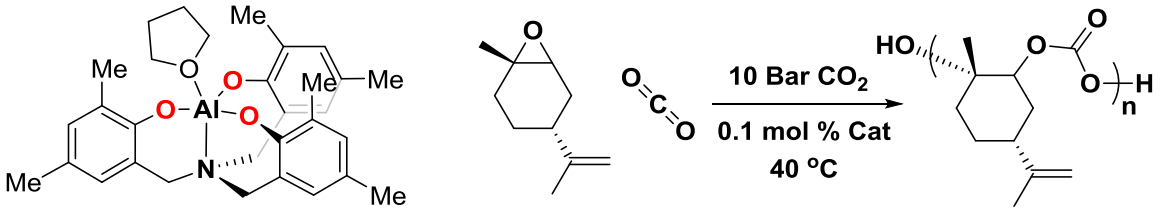


Figure 1.15: Illustration of the potential energy surface for polycarbonate, polyether and cyclic carbonate formation.

Subsequently, a trialkyl aluminium and LiBr system was reported although lower activity for CO_2/CHO copolymerisation (12 h^{-1}) was observed in comparison to the boron system. This was attributed to the reduced Lewis acidity of aluminium compared to boron and the higher stability of lithium carbonate verses the quaternary ammonium analogue.[35]



Scheme 1.11: Formation of poly(limonene carbonate) with an aluminium(III) trisphenolate catalyst.

In 2015, Kleij and co-workers synthesised poly(limonene carbonate) using either iron or aluminium trisphenolate catalyst systems, with PPNCl (Scheme 1.11). Previously Coates and co-workers were first to make poly(limonene carbonate), using a zinc-*β*-diimine catalyst. The trisphenolate catalysts preferentially copolymerise the *trans*-limonene oxide with a selectivity of over 70 %. The aluminium catalyst was almost twice as fast as the iron catalyst proposed to be due to its higher Lewis acidity. The aluminium trisphenolate catalyst showed a TOF of 3 h^{-1} (40 °C, 0.1 mol %, 10 bar) and without cyclic carbonate or ether linkage formation. A DFT investigation of CO_2/CHO ROCOP indicated a mechanism requiring catalyst dimerization to reduce the barrier to epoxide ring opening (64.0 kJ mol^{-1}) (Figure 1.16).[36] Although the study suggests a dimeric mechanism, the role of co-catalyst is not considered which is curious because it is essential to have present for active copolymerisation. Furthermore, there was no kinetic analysis which would be useful to distinguish a dimeric mechanism which should exhibit a second order dependence on catalyst concentration.

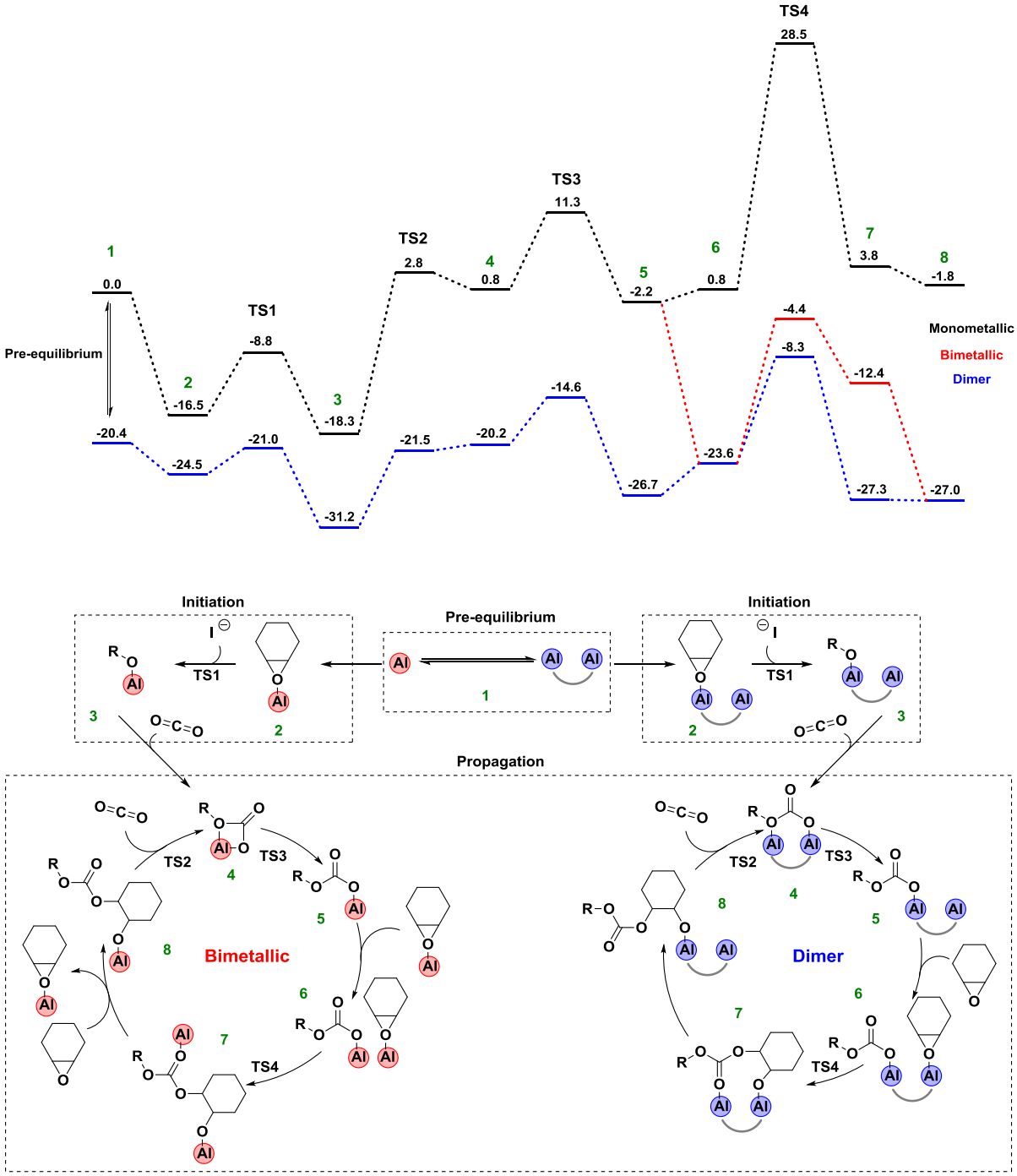
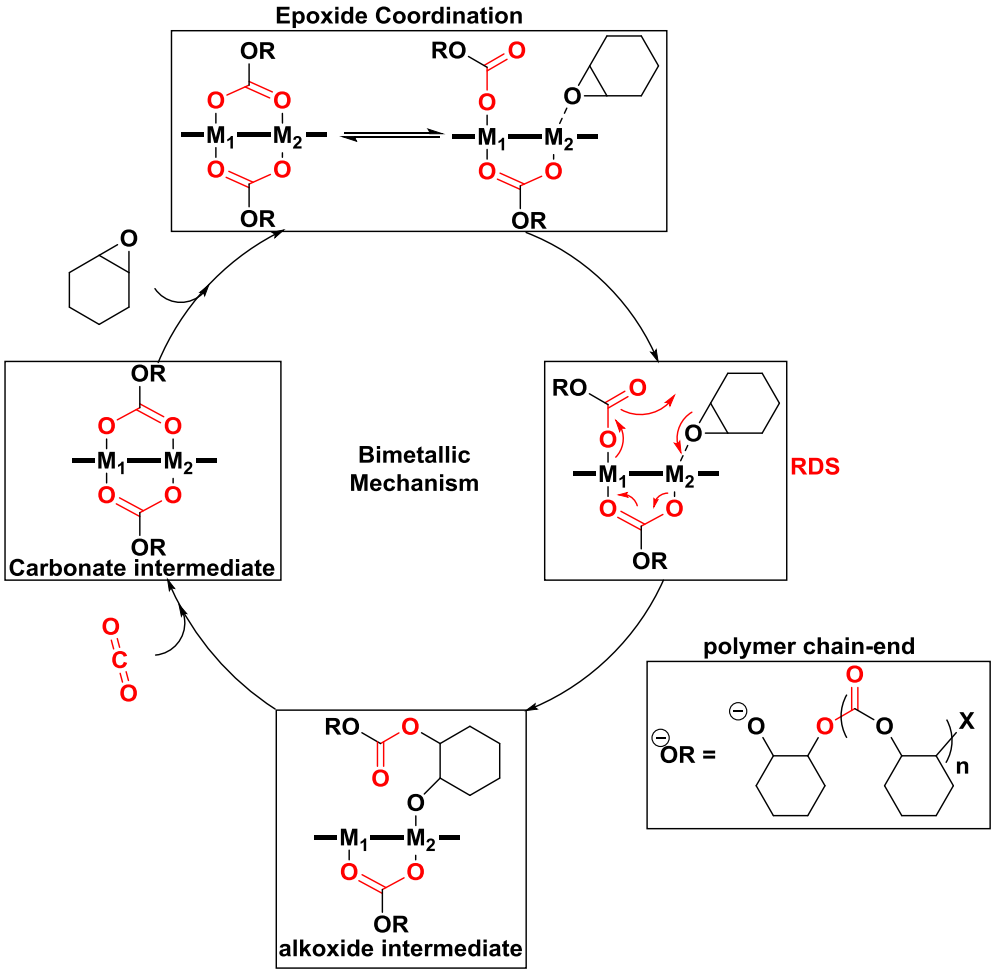


Figure 1.16: Top; free energy profiles for the ROCOP of CO_2/CHO mediated by an Al(III)-trisphenolate catalyst showing a possible monometallic (black) bimetallic (red) and dimeric (blue) mechanistic pathways. Bottom; Catalytic cycles for the bimetallic and dimer-mediated pathways.

1.2.1 Dinuclear Mechanisms

The mononuclear catalysts typically show rate laws with orders in catalyst ranging from 1.0-1.8. This finding has driven research towards dinuclear complexes. Dinuclear complexes are advantageous as they generally negate the need for a co-catalyst; this is beneficial to enable mechanistic insight and to obviate use of salts that are expensive and corrosive to steel, problematic to scale-up and commercialisation. Dinuclear catalysts also allow for activity to be retained under high dilution and if well designed may allow this without synthetically challenging ligands.



Scheme 1.12: Dinuclear mechanism for CO_2/epoxide copolymerisation.

In a typical dinuclear mechanism the two metal centres are separated by 3-4 Å. The RDS is nucleophilic epoxide ring opening by attack from a carbonate group. The RDS step involves both metals: one to active the epoxide and the other to provide the nucleophile (Scheme 1.12). The metal alkoxide inserts CO_2 forming a metal-carbonate intermediate, as the catalyst resting state.

Three different designs have been employed in preparing dinuclear catalysts (Figure 1.17):

A) Type 1,

Two mononuclear complexes dimerise to form a bimetallic active site.

B) Type 2,

Two mononuclear ligands are tethered to form a bimetallic compound.

C) Type 3,

Two metals are coordinated in close proximity by a dinucleating ligand.

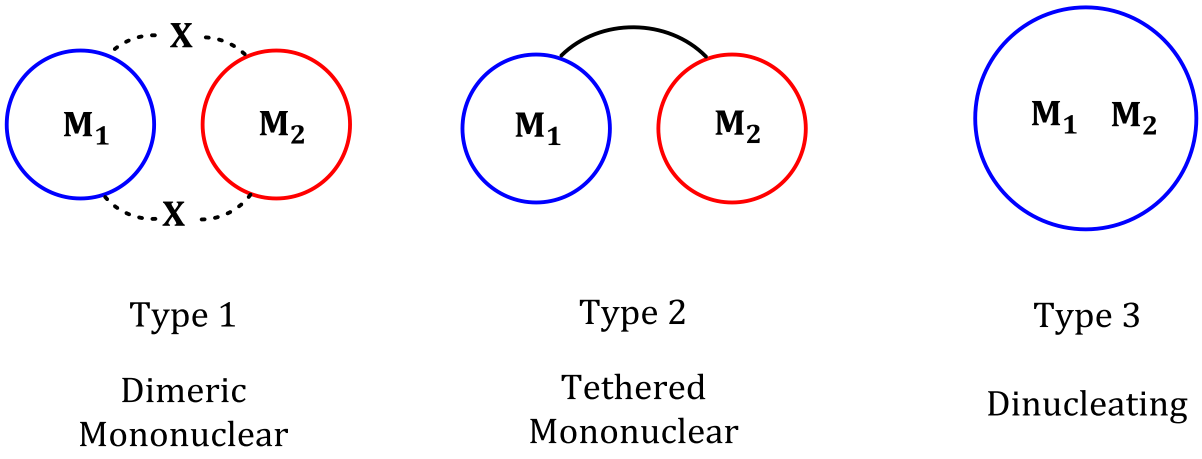
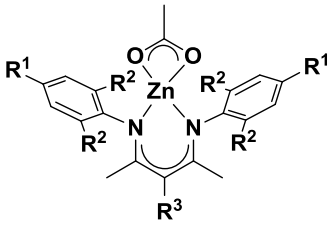


Figure 1.17: Dimeric, tethered and dinucleating catalysts.

1.2.2 Type 1: Dimeric Catalysts



	R^1	R^2	R^3	R^4
1	^{i}Pr	^{i}Pr	H	H
2	Et	Et	H	H
3	Me	Me	H	H
4	Et	Et	^{t}Bu	H
5	^{i}Pr	Et	H	H
6	^{i}Pr	^{i}Pr	^{t}Bu	H
7	Et	Et	H	CN

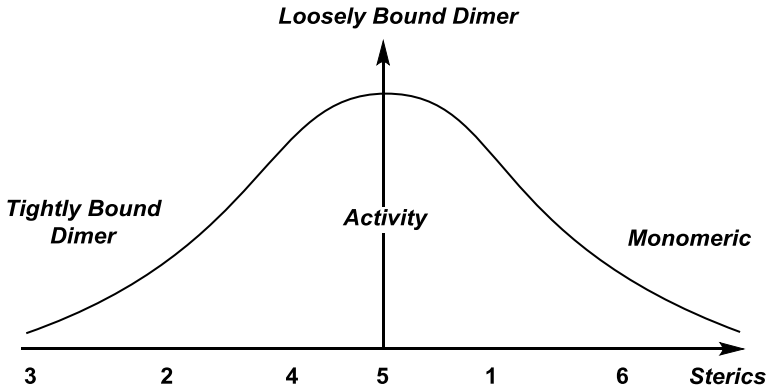


Figure 1.18: Activity of a zinc-β-diimine catalyst with change in ligand sterics.

Coates and co-workers pioneered highly active zinc-*β*-diimine (Zn-BDI) catalysts for CHO/CO_2 ROCOP, showing high CO_2 selectivity (> 96 %) and activity: 247 h^{-1} (50 °C, 7 bar CO_2) (Figure 1.18).[37-38] Complexes featuring cyano- substituents to the BDI showed excelled activity (2290 h^{-1}), whilst maintaining high CO_2 selectivity (90 %). This was rationalised on the basis that a more electron deficient Zn(II) centre promotes epoxide binding and hence increases the rate of polymerisation.[39-40] There is an equilibrium between monomeric and dimeric complexes in solution which is influenced by temperature, concentration and the size of the R substituents on the *ortho*- and *para*-phenyl positions of the BDI.[41] Varying the R substituents resulted in significant changes to the rate. Reduced rates were observed when R is small (Me), rationalised by the formation of a tightly bound dimer. Rates were also reduced when R was large (^{i}Pr) rationalised by the formation of a discrete monomeric species.[41]

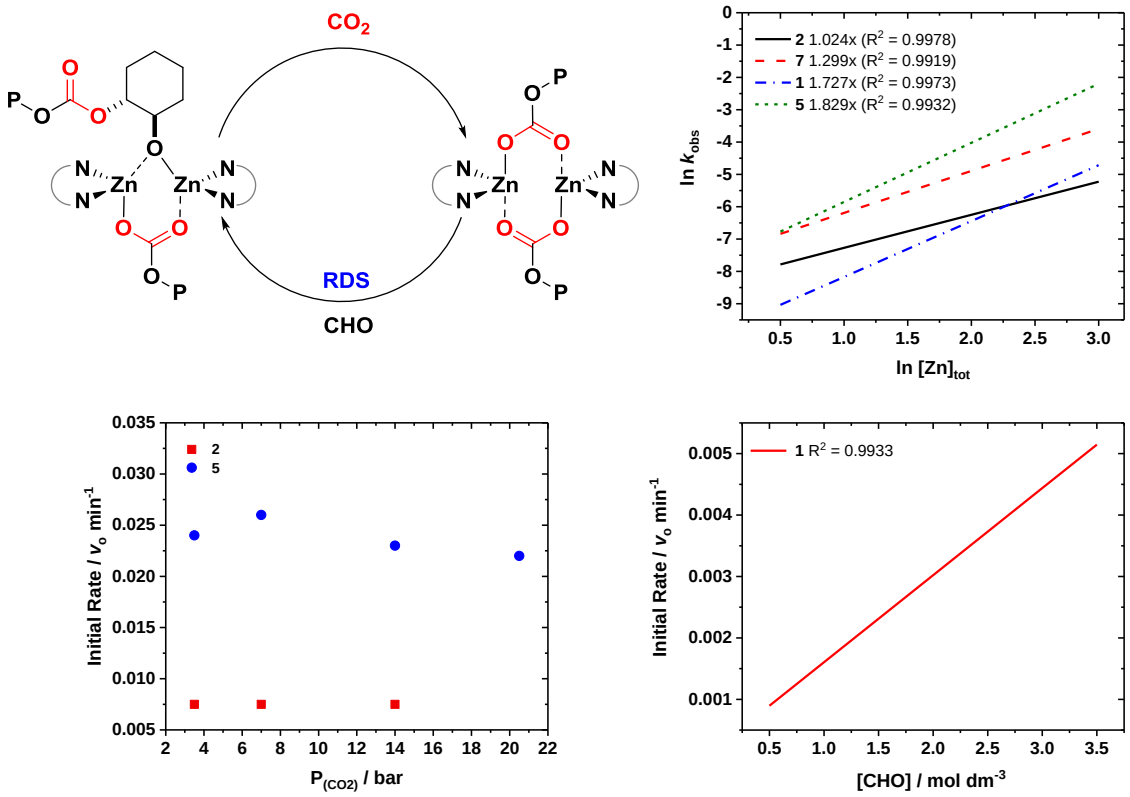


Figure 1.19: Proposed mechanism (Top LHS). Rate vs catalyst concentration (TOP RHS). Rate vs CO_2 pressure (Bottom LHS). Rate vs epoxide concentration (Bottom RHS).

The rate law showed a zero order dependence in CO_2 pressure, a first order dependence in epoxide concentration, and an order in catalyst concentration between 1.0 and 1.8 depending on the ligand substituents (Figure 1.19). The rate was clearly influenced by the monomer-dimer equilibrium and a mechanism was proposed where the best catalysts are loosely associated dimers.[41]

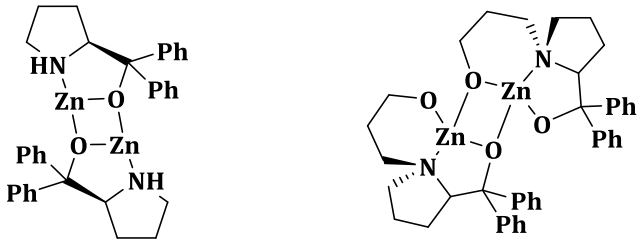


Figure 1.20: Dinuclear zinc catalysts derived from pyrrolidine.

Nozaki and co-workers reported an asymmetric copolymerisation of a racemic mixture of (R,R)- and (S,S)-cyclohexene oxide, with CO_2 using a chiral diphenylpyrroridinyl-zinc complex (Figure 1.20 LHS). This resulted in an enantiomeric excess (e.e) of 73 % in favour of the (R,R)-enantiomer.[42-43]

Nearly 20 years later, Meyer and co-workers reported a modified di-zinc catalyst that was active at 1 bar CO_2 (Figure 1.20 RHS). X-ray crystallography shows the complex is a tetramer with Zn-Zn distances in the range 2.9-3.2 Å. The catalysts showed an activity of 149 h^{-1} (80 °C, 1 bar CO_2), but the catalyst does not feature an initiating group and co-catalyst is not added, so it is unclear how the polymerisation initiates. Initiation may be from adventitious water or the ligand itself.[44]

1.2.3 Type 2: Tethered Mononuclear catalysts

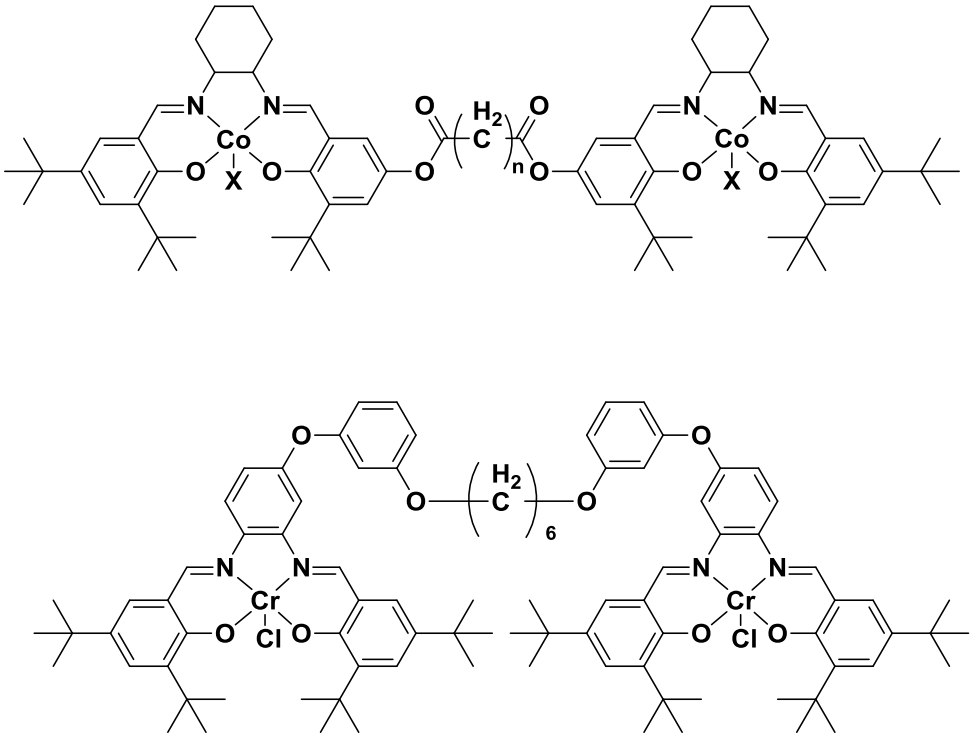


Figure 1.21: Dinuclear Cobalt(III) catalyst for CO_2/PO copolymerisation.

Nozaki and co-workers developed a series of dinuclear cobalt salen complexes for CO_2/PO ROCOP (Figure 1.21 Top).[45] Rieger and co-workers reported very similar tethered dinuclear chromium salphen catalysts which showed a TOF of 82 h^{-1} (60 °C, 40 bar) (Figure 1.21 Bottom).[46] The dinuclear complexes displayed 10-fold rate enhancement, without any co-catalyst, compared to monometallic homologues, especially at high dilution. The activity increased upon decreasing the spacer linker length and the maximum TOF was 180 h^{-1} (22 °C, 50 bar). Under these conditions, the reaction is proposed to proceed *via* a bimetallic mechanism.[45]

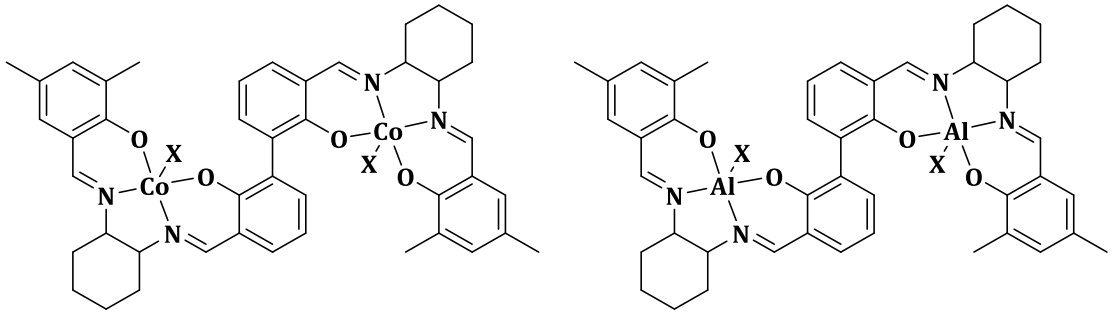
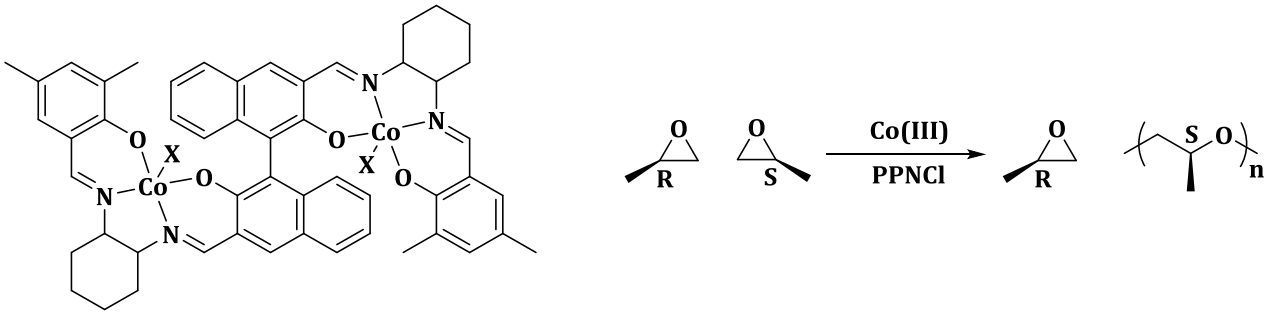


Figure 1.22: Dinuclear metal salen complexes bridged via the *ortho*-phenyl position.

In 2013, Lu reported a tethered dinuclear Co(III) salen catalyst for the asymmetric copolymerisation of cyclopentene oxide (CPO) and cyclohexene oxide (CHO) (Figure 1.22 LHS).[47] Previously, a system comprising mononuclear Co(III) salen, with PPNCl, enabled 96 % *ee* but required low temperature conditions and the addition of (S)-proylene oxide, with low activities observed, 3 h^{-1}.[48] The dinuclear catalyst displayed significantly higher rates at 25 °C, 20 bar, with TOFs of 650 h^{-1} and 1410 h^{-1} for CPO and CHO, respectively.[47] The polymerisation yielded perfectly alternating copolymer (>99%) with *e.e* exceeding >95 %.

Further investigations with this catalyst included the asymmetric copolymerisation of *meso*-epoxides and anhydrides, although PPNCl was required to prevent polyether formation.[49] Curiously, the dinuclear cobalt and chromium catalysts completely failed but the aluminium analogue showed good activity (Figure 1.22 RHS).[49] This demonstrates the subtle differences between the ROCOP of CO_2/epoxide against anhydride/epoxide, despite often being described as operating via the same mechanism.[49-50] The maximum activity of ROCOP for CHO with phthalic anhydride was 750 h^{-1} (50 °C, CHO/PA/Catalyst/PPNCl = 1000/250/1/2), which is one of the highest in this field. [49]



Scheme 1.13: Enantioselective homopolymerisation of propylene oxide using a dinuclear Co(III) salen catalyst.

As a side note, Coates and co-workers reported the enantioselective homopolymerisation of epoxides using a biaryl-linked Co(III) salen catalyst (Scheme 1.13).[51] This produced isotactic polyethers with ee above 99 %, at 0 °C. For this bimetallic catalyst, the addition of a co-catalyst was essential to observe both high activity and selectivity and thus the mechanism was proposed as a bifunctional, dinuclear mechanism.[51]

1.2.4 Type 3: Dinucleating Catalysts

Lee and co-workers were the first to report deliberately dinuclear zinc catalysts for the ROCOP of CO_2/CHO (Figure 1.23).[52] The two zinc centres were separated by 4.86(7) Å. Unlike in dimeric zinc-β-diimines catalysts, these catalysts maintained high activity at high catalyst dilution. The TOF was 312 h^{-1} (80°C, 12 bar) with excellent polycarbonate selectivity (94 %). The addition of electron-withdrawing ligand substituents increased activity to 2860 h^{-1} however, polycarbonate selectivity was decreased to 88 %, with significant polyether formation.[53]

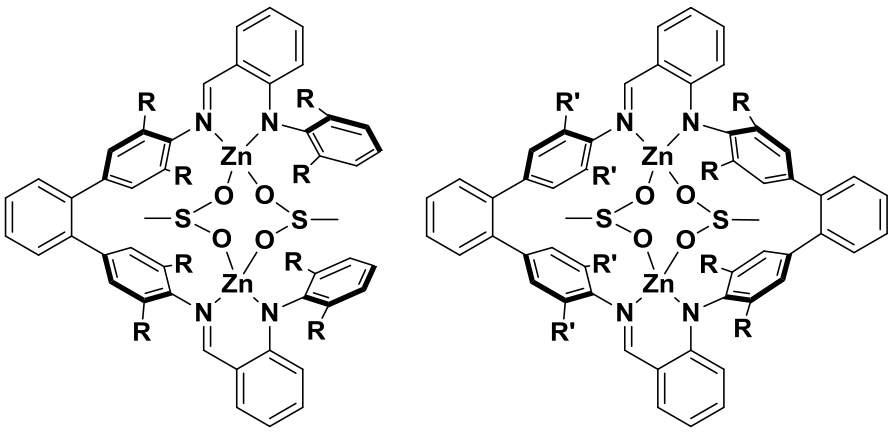


Figure 1.23: Dinuclear zinc catalysts derived from anilido-aldiimine ligands.

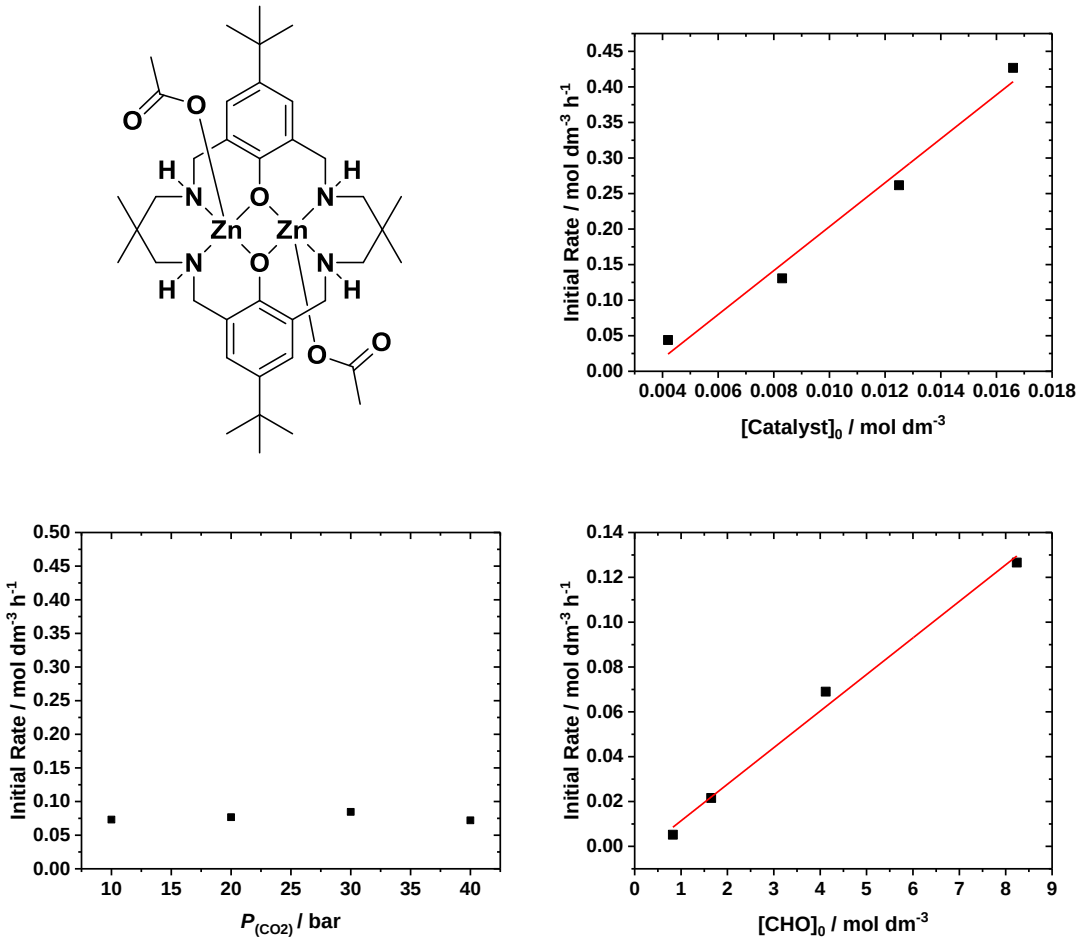


Figure 1.24: (Top LHS) Di-zinc catalyst derived from a di-phenolate macrocyclic ligand. (Top RHS) A linear plot of initial rate vs. catalyst concentration. (Bottom LHS) Plot of initial rate vs. partial pressure CO_2. (Bottom RHS) Linear plot of initial rate vs epoxide concentration.[54]

In 2009, Williams and co-workers reported the first reasonable activity catalyst for the ROCOP of CO_2/CHO at 1 bar CO_2 pressure (Figure 1.24).[55] The activity was 18 h^{-1} (80 °C) affording perfectly alternating polycarbonate (> 99 %). A bimolecular rate law was determined, showing a first order dependence in both catalyst and epoxide concentrations and a zero order dependence on CO_2 pressure.[54] This suggested the rate determining step is the nucleophilic ring opening of epoxide, as observed for several other catalytic systems.[54]

Detailed computational and structure activity studies led to a proposed 'chain-shuttling' mechanism where the growing polymer chain alternates between the two metal centres (Figure 1.25).[54, 56] The RDS was the ring opening of the epoxide with a free energy barrier of 98.3 kJ mol^{-1}, in-line with the experimental barrier (107.5 kJ mol^{-1}). Sequential epoxide enchainment was calculated to have a free energy barrier of 164.4 kJ mol^{-1}; significantly higher than for the alternating copolymer and complements the high selectivity of the catalyst (> 99 %) with respect to ether linkage formation.[56] The DFT study suggests that the two metals cooperate to ring open the epoxide, one binding the epoxide and the other providing the nucleophile. A clear outcome from the proposed mechanism is that a heterodinuclear catalyst may be more active, since each metal plays a distinct role in the catalytic cycle.

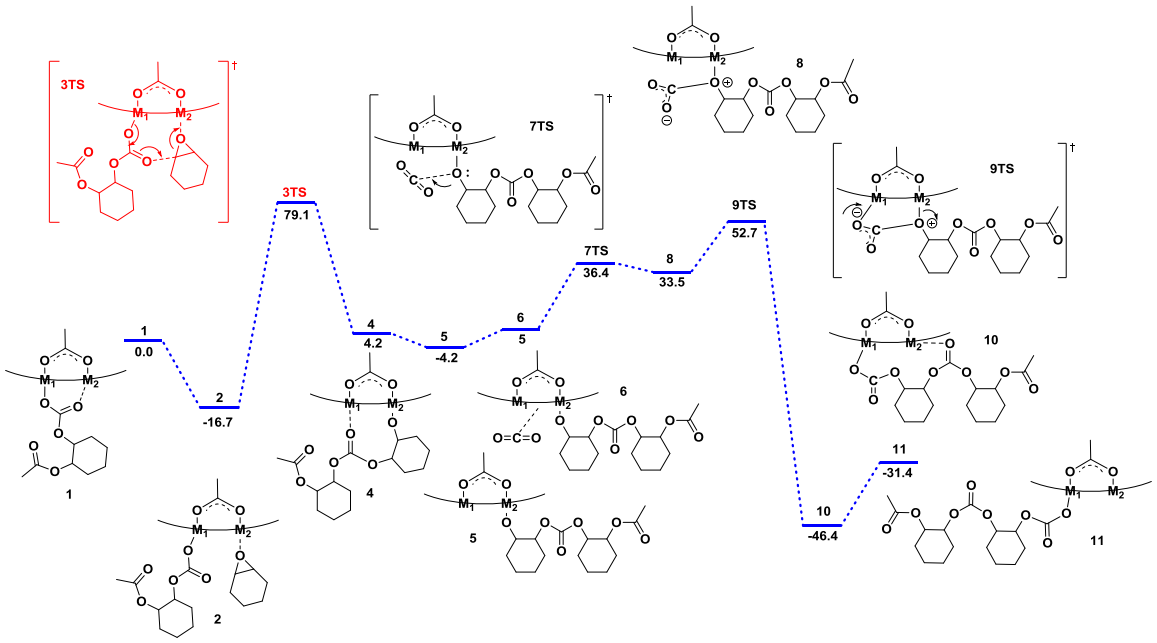


Figure 1.25: Illustration of the potential energy surface for copolymerisation.

A range of homodinuclear catalysts was explored including Co(II)/Co(III), Fe(III)/Fe(III), Mg(II)Mg(II) and Zn(II)Zn(II).[55, 57-60] The di-cobalt catalyst was significantly more active than the di-zinc analogue, showing a TOF of 200 h^{-1} (80 °C, 1 bar CO_2) affording perfectly alternating polycarbonate (99 %).[57, 60] The increase in rate was attributed to the increased nucleophilicity of the cobalt carbonate intermediate and analogy was drawn to enzymatic systems where substitution of Zn(II) for Co(II) has resulted in enhanced activity.[61-63]

In 2012, the di-magnesium analogue was shown to be approximately twice as active as the di-zinc counterpart showing an activity of 35 h^{-1} (80 °C, 1 bar CO_2).[59] Although this catalyst was significantly slower than the di-cobalt complex, it was more robust, with no ether linkages or cyclic carbonate formation observed at elevated temperatures.[59] Furthermore, it was tolerant to the use of CO_2 gas containing impurities such as oxygen, methane, hydrogen sulphide, sulphur oxides (SO_x) and nitrogen oxides (NO_x).[64] Such impurities are present in CO_2 gas streams obtained from carbon capture plants.[64] This catalyst was the first example of a Group 2 metal catalyst and is notable because various Mg(II) and Ca(II) complexes were previously reported as inactive, highlighting the importance of the macrocyclic ligand.

Next, investigations focused on a Zn(II)Mg(II) heterodinuclear catalyst, due to the track record of these metals in this catalysis and the ability to use NMR spectroscopy to characterise the catalysts.[65] Initially, it was difficult to isolate a pure heterodinuclear complex but a statistical mixture of hetero- and homo-dinuclear complexes could be prepared. The mixture was significantly more active than a 50:50 mixture of homodinuclear species, showing an activity of 80 h^{-1} versus an activity of 40 h^{-1}, respectively.[65] The synthesis of the pure heterodinuclear Zn(II)Mg(II) catalyst

was achieved by control of reaction conditions (Figure 1.26).[66] Specifically, by controlling the reaction concentration, temperature and rate of reagent addition a pure heterodinuclear complex in very high yield was isolated. The Zn(II)Mg(II) catalyst displayed a 5-fold rate enhancement compared to the dizinc analogue. The increased activity was attributed to a synergic relationship, whereby Zn(II) was proposed to bind the epoxide and Mg(II) provide the carbonate nucleophile.[66]

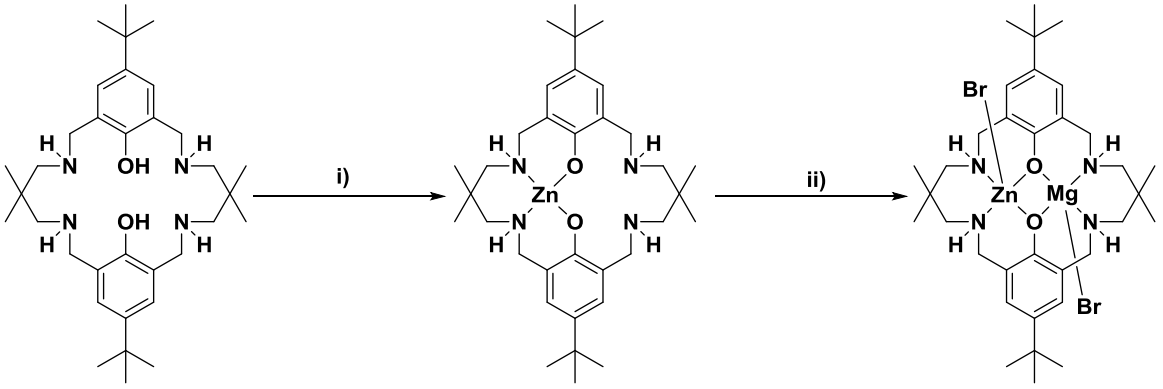


Figure 1.26: Synthesis of a pure heterodinuclear zinc/magnesium catalyst. i) $ZnEt_2$, THF, 25 °C, 24 h; ii) $MgBr_2$, THF:Pyridine, -78 °C to 25 °C, 1 h.[66]

From the proposed mechanism, one co-ligand remains bound to the metal and served to counter balance polymer chain growth on the opposite face. A series of Zn(II)Mg(II) catalysts featuring substituted benzoate co-ligands revealed a minimal effect on the activity of CO_2/CHO ROCOP, with observed rate constants, k_{obs}, ranging (2.8-3.8) $x10^{-5}$ s^{-1}.[67] The exception was a Zn(II)Mg(II) catalyst featuring a penta-fluoro benzoate which showed a significantly reduced rate (k_{obs} = 1.4 $x10^{-5}$ s^{-1}). This was rationalised by its highly electron withdrawing nature (evidenced by ^{13}C NMR spectroscopy) and by the chain-shuttling mechanism of the co-ligand. A significant effect upon initiation rates was observed, with halides having longest initiation times (160 min) and both benzoate and acetates initiating much faster (30-80 mins).[67] This was rationalised by the increased nucleophilicity of the carboxylate co-ligands.[67]

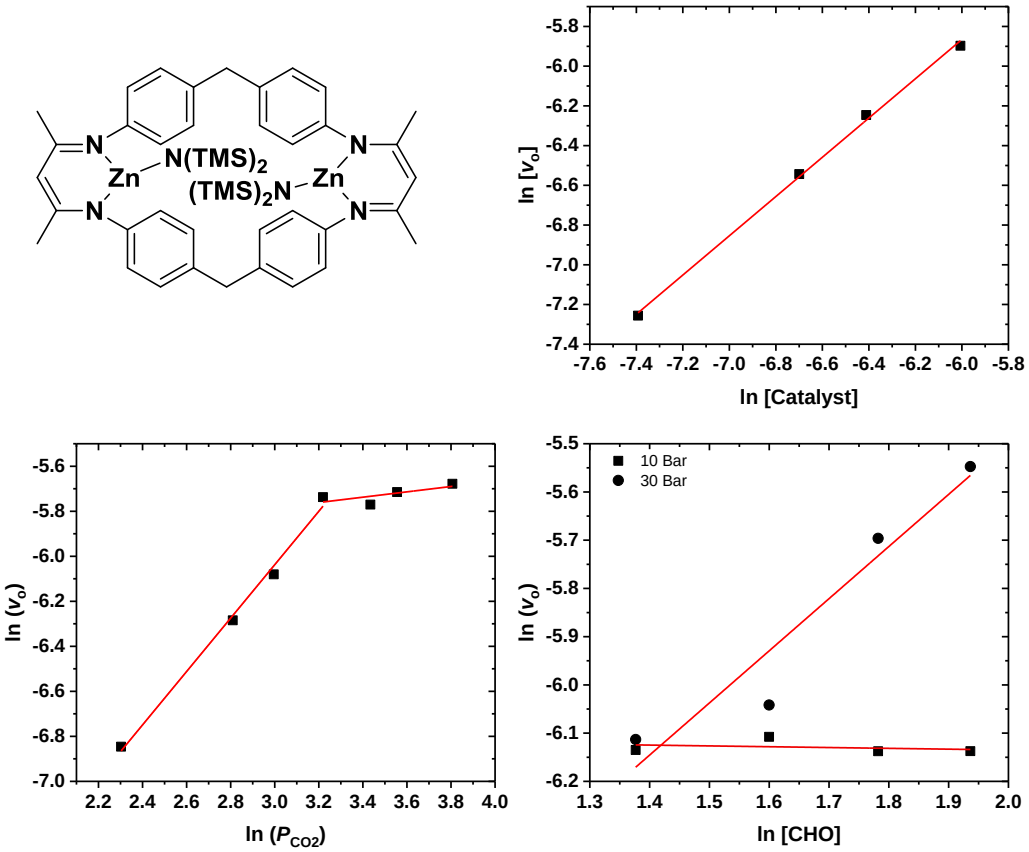


Figure 1.27: Tethered di-zinc-β-diimine catalyst for the copolymerisation of CO_2/CHO.

In 2013, Rieger and co-workers reported a tethered zinc β-diimine catalyst which showed an activity of 9130 h^{-1} (40 bar, 100 °C) and high polycarbonate selectivity (> 99) (Figure 1.27).[68] Two rate laws were reported at different CO_2 pressures: 5-25 bar CO_2, a first order dependence CO_2 pressure and catalyst concentration and a zero order dependence on epoxide concentration was reported. Between 25-45 bar CO_2, a first order dependence on both catalyst and epoxide concentration and a zero order dependence on CO_2 concentration was reported.[68-69]

A computational study led to a mechanistic proposal similar to the chain-shuttling mechanism proposed by Williams and co-workers (Figure 1.28).[56, 68] The free energies of both reaction intermediates and transition states were compared at 5 and 50 bar CO_2 pressure. At higher CO_2 pressure the barrier to CO_2 insertion decreased from 102.4 to 95.3 kJ mol^{-1}, whereas the barrier to epoxide ring opening remained constant at 101.0 kJ mol^{-1}. This was proposed to rationalise the experimental observation of a change in rate determining step from low pressure to high pressure CO_2.[68]

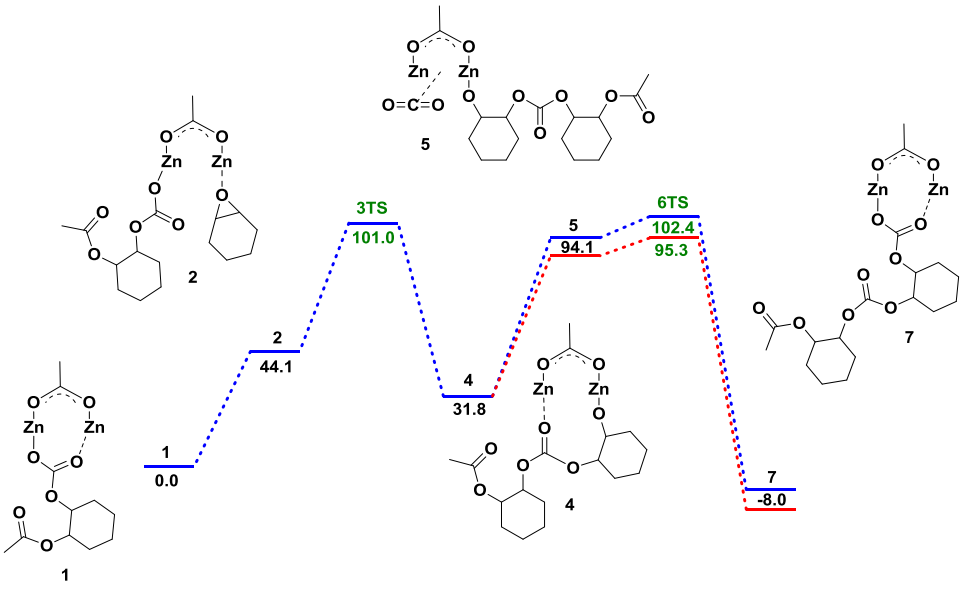


Figure 1.28: Illustration of the potential energy surface for the ROCOP of CO_2/CHO for a tether di-zinc catalyst at 5 bar (blue) and 50 bar (red) CO_2 pressure.[68]

Structure-activity studies suggested a correlation between ligand rigidity and activity; by substitution of the ligand with electron-withdrawing groups the activity increased to 155,000 h^{-1} (30 bar, 100 °C, 0.0125 mol % cat.).[70] This produced polycarbonate with 88 % selectivity with a significant quantity of polyether linkages. The reduction of CO_2 pressure to 1 bar resulted in a significant loss of activity and polycarbonate selectivity, 930 h^{-1} and 49 %, respectively.[70]

1.2.5 Multinuclear Catalysts

In 2018, Okuda and Mashima reported a series of tris(salen)-trizinc-lanthanide multinuclear catalysts which showed high activity (413 h^{-1}) under low pressure of CO_2 (3 bar) affording perfectly alternating PCHC (> 99 %) (Figure 1.29).[71] The ligand backbone was important, with L^1 and L^2 showing the highest activity of ~ 70 h^{-1}, followed by L^4 and L^5 with reduced activities (17 h^{-1} and 5 h^{-1} respectively) and L^3 showing no activity. The authors proposed a reaction mechanism akin to the 'chain-shuttling' mechanism proposed by Williams and co-workers whereby the growing polymer chain exchanges between the two metal centres during propagation.[71]

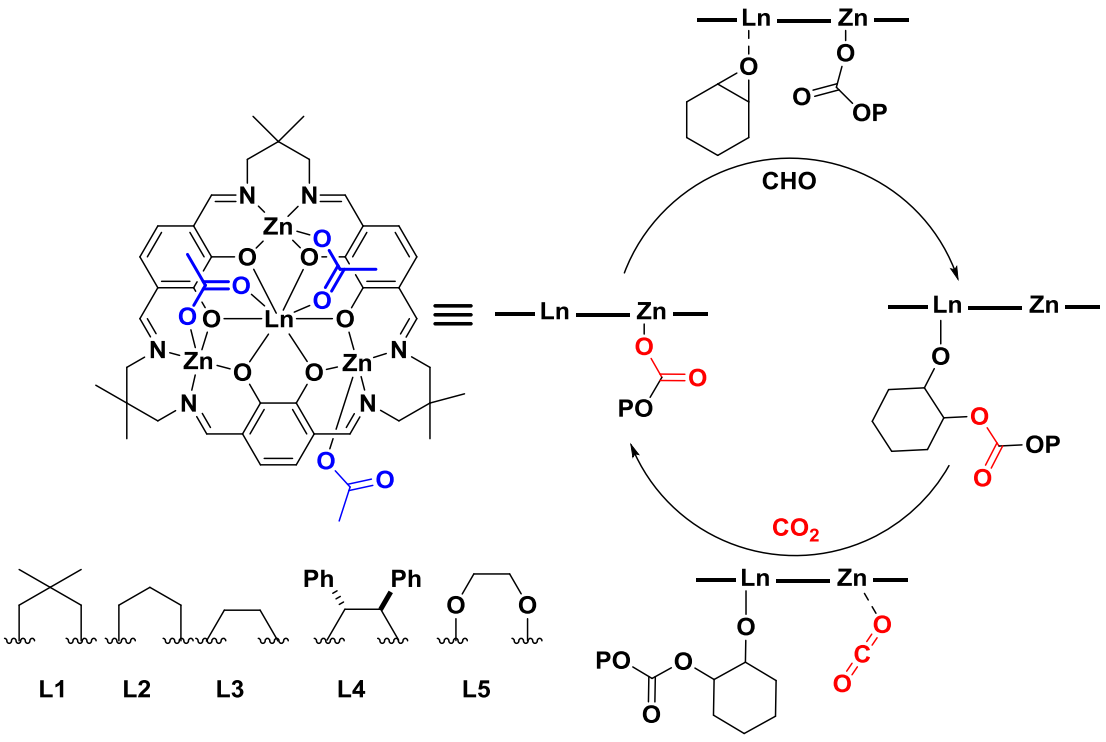
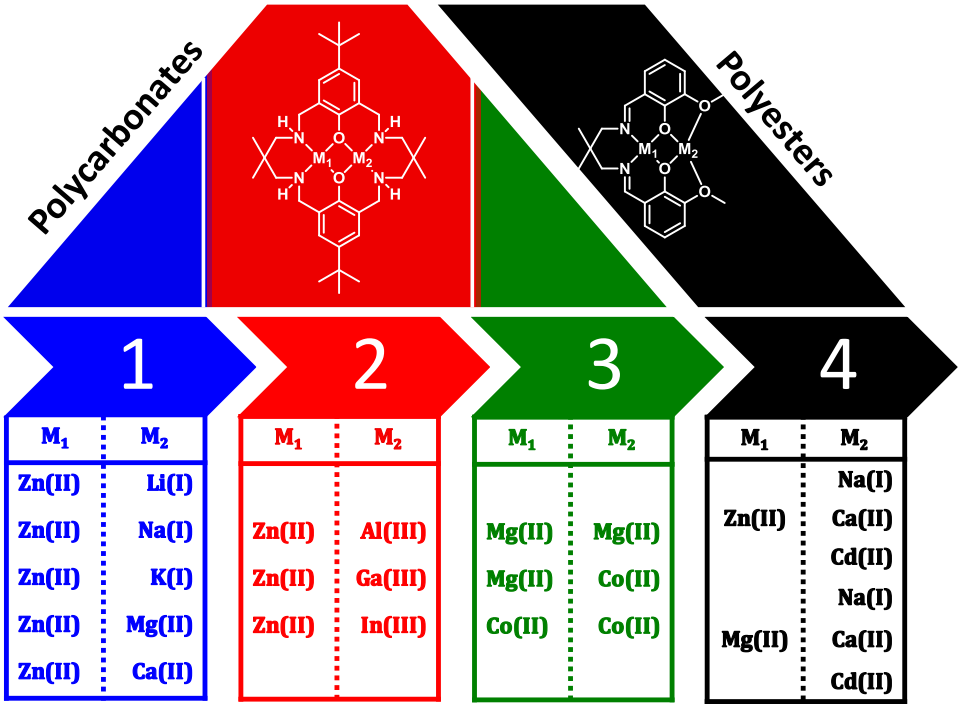


Figure 1.29: Series of tris(salen)-multinuclear catalyst and proposed mechanism for the copolymerisation of CO_2/CHO.[71]

1.2.6 Aims and Objectives

This thesis aims to optimise the metal selection in heterodinuclear catalysts where the design parameters are inspired by the Chain-shuttling mechanism which hypothesises that two metals play distinctly different roles to facilitate nucleophilic ring opening of an epoxide. The work presented in Chapters 2-4 follows on from a Zn(II)Mg(II) catalyst reported by Williams and co-workers,[66] with the following questions to investigate:

1. Is Mg(II) essential to the activity observed in CO_2/CHO ROCOP or can it be replaced by alkali/alkaline earth metals such as Li(I), Na(I), K(I) and Ca(II)?
2. Is the role of Mg(II) in catalysis determined by its ionic character or high Lewis acidity? Will a more covalent Lewis acid, such as Al(III), prove active?
3. Is Zn(II) essential to the high activity observed in CO_2/CHO ROCOP or can it be replaced by other transition metals such as Co(II)?
4. Can heterodinuclear design be applied to other ligand systems?



Questions 1 and 2 will be addressed in Chapters 2 and 3. This will be investigated by utilising the mono-Zn(II) complex reported in the synthesis of Zn(II)Mg(II) and subsequently reacted with a series of alkali and alkaline earth metals (Chapter 2) or Group 13 metals (Chapter 3) and tested in CO_2/CHO ROCOP. Heterodinuclear purity will be assessed by NMR spectroscopy, mass spectrometry and X-ray crystallography where possible. Catalyst performance will be established by comparing both activity (TOF) and selectivity (CO_2/Polym %).

Question 3 will be addressed in Chapter 4 with the first hurdle to synthesis a mono-Mg(II) species. Once achieved, subsequent metalation with Co(II) will be targeted, where Co(II) is chosen as the homodinuclear Co(II)Co(II) remains the most active homodinuclear catalyst for CO_2/CHO ROCOP. The determination of heterodinuclear purity will be challenging as NMR spectroscopy will not provide useful information, therefore alternative methods such as X-ray photoelectron spectroscopy, superconducting quantum interference device (SQUID) magnetometry and cyclic voltammetry will be used. Currently, the comparison of catalysts use point kinetics (TOFs), but does not take into account initiation effects, the potential for catalyst death, mechanical changes (i.e solution viscosity) or catalyst concentration. A more meaningful comparison should be the propagating rate coefficient, with a proper understanding of the rate law. This chapter aims to uncover this kinetic data so as to better understand mechanisms, properly compare rates and allow for rational catalyst optimisation and improvement.

Question 4 will be addressed in Chapter 5 where a series of Zn(II) and Mg(II) heterodinuclear complexes with Na(I), Ca(II) and Cd(II) are targeted and tested in the ROCOP of Anhydride/CHO.

1.2.7 References

1. Global plastic production from 1950 to 2016. https://www.statista.com/statistics/282732/global-production-of-plastics-since-1950/ (accessed 2018).
2. Sonnenschein, M. F., *Polyurethanes. Science, Techonolgy, Markets and Trends, The DOW Chemical Company*. Midland, MI, USA, 2014.
3. https://www.grandviewresearch.com/industry-analysis/polyurethane-pu-market?utm_source=google&utm_medium=cpc&utm_campaign=AdWords_PolyurethanePU_Type2_CMFE&gclid=Cj0KCQjw4fHkBRDcARIsACV58_HJqh-emfBYqOLWNndm8Stl8AgEGVCfEOKrvitY5DDq23YKRnQMgYAaAh3dEALw_wcB (accessed 27/03/19).
4. Akindoyo, J. O.; Beg, M. D. H.; Ghazali, S.; Islam, M. R.; Jeyaratnam, N.; Yuvaraj, A. R., Polyurethane types, synthesis and applications – a review, *RSC Advances,* **2016,** *6*, (115), 114453.
5. von der Assen, N.; Bardow, A., Life cycle assessment of polyols for polyurethane production using CO_2 as feedstock: insights from an industrial case study, *Green Chem.,* **2014,** *16*, (6), 3272.
6. Wang, Y.; Darensbourg, D. J., Carbon dioxide-based functional polycarbonates: Metal catalyzed copolymerization of CO_2 and epoxides, *Coord. Chem. Rev.,* **2018,** *372*, 85.
7. Schneider, W.; Diller, W., Phosgene. In *Ullmann's Encyclopedia of Industrial Chemistry*, Germany, Wiley-VCH, **2000**.
8. Gong, J.; Ma, X.; Wang, S., Phosgene-free approaches to catalytic synthesis of diphenyl carbonate and its intermediates, *Applied Catalysis A: General,* **2007,** *316*, (1), 1.
9. Zhang, X.; Fevre, M.; Jones, G. O.; Waymouth, R. M., Catalysis as an Enabling Science for Sustainable Polymers, *Chem. Rev.,* **2018,** *118*, (2), 839.
10. Duda, A.; Kowalski, A., *Handbook of Ring-Opening Polymerisation*. WILEY-VCH GmbH & Co. KGaA: Weinhein, Germany, 2009.
11. Kember, M. R.; Buchard, A.; Williams, C. K., Catalysts for CO_2/epoxide copolymerisation, *Chem. Commun.,* **2011,** *47*, (1), 141.
12. Inoue, S.; Koinuma, H.; Tsuruta, T., Copolymerization of carbon dioxide and epoxide, *J. Polym. Sci., Part A: Polym. Lett.,,* **1969,** *7*, (4), 287.
13. Williams, C. K.; Hillmyer, M. A., Polymers from Renewable Resources: A Perspective for a Special Issue of Polymer Reviews, *Polym. Rev.,* **2008,** *48*, (1), 1.
14. Penczek, S.; Pretula, J.; Lewiński, P., Dormant Polymers and Their Role in Living and Controlled Polymerizations; Influence on Polymer Chemistry, Particularly on the Ring Opening Polymerization, **2017,** *9*, (12), 646.
15. Wu, G.-P.; Darensbourg, D. J., Mechanistic Insights into Water-Mediated Tandem Catalysis of Metal-Coordination CO_2/Epoxide Copolymerization and Organocatalytic Ring-Opening Polymerization: One-Pot, Two Steps, and Three Catalysis Cycles for Triblock Copolymers Synthesis, *Macromolecules,* **2016,** *49*, (3), 807.
16. Zhu, Y.; Romain, C.; Williams, C. K., Selective Polymerization Catalysis: Controlling the Metal Chain End Group to Prepare Block Copolyesters, *J. Am. Chem. Soc.,* **2015,** *137*, (38), 12179.

17. Trott, G.; Saini, P. K.; Williams, C. K., Catalysts for CO_2/epoxide ring-opening copolymerization*, Phil. Trans. R. Soc. A.,* **2016,** *374*.
18. Klaus, S.; Lehenmeier, M. W.; Anderson, C. E.; Rieger, B., Recent advances in CO_2/epoxide copolymerization—New strategies and cooperative mechanisms*, Coord. Chem. Rev.,* **2011,** *255*, (13), 1460.
19. Darensbourg, D. J., Making Plastics from Carbon Dioxide: Salen Metal Complexes as Catalysts for the Production of Polycarbonates from Epoxides and CO_2*, Chem. Rev.,* **2007,** *107*, (6), 2388.
20. Aresta, M.; Zhang, S.; Zhang, W.-Z.; Rintjema, J.; Kraus, S.; Brill, M.; Lu, X.-B.; Romain, C.; Rieger, B.; Lazreg, F.; Ma, R.; Thevenon, A.; Carrodeguas, L. P.; Angelini, A.; He, L.-N.; Laserna, V.; Saini, P. K.; Cazin, C. S. J.; Nolan, S. P.; Sopeña, S.; Williams, C. K.; Kleij, A. W., *Carbon Dioxide and Organometallics*. 1 ed.; Springer International Publishing: 2016; p 308.
21. Paddock, R. L.; Nguyen, S. T., Chemical CO_2 Fixation: Cr(III) Salen Complexes as Highly Efficient Catalysts for the Coupling of CO_2 and Epoxides*, J. Am. Chem. Soc.,* **2001,** *123*, (46), 11498.
22. Darensbourg, D. J.; Yarbrough, J. C., Mechanistic Aspects of the Copolymerization Reaction of Carbon Dioxide and Epoxides, Using a Chiral Salen Chromium Chloride Catalyst*, J. Am. Chem. Soc.,* **2002,** *124*, (22), 6335.
23. Qin, Z.; Thomas, C. M.; Lee, S.; Coates, G. W., Cobalt-Based Complexes for the Copolymerization of Propylene Oxide and CO_2: Active and Selective Catalysts for Polycarbonate Synthesis*, Angew. Chem. Int. Ed.,* **2003,** *42*, (44), 5484.
24. Lu, X.-B.; Wang, Y., Highly Active, Binary Catalyst Systems for the Alternating Copolymerization of CO_2 and Epoxides under Mild Conditions*, Angew. Chem. Int. Ed.,* **2004,** *43*, (27), 3574.
25. Cohen, C. T.; Chu, T.; Coates, G. W., Cobalt Catalysts for the Alternating Copolymerization of Propylene Oxide and Carbon Dioxide: Combining High Activity and Selectivity*, J. Am. Chem. Soc.,* **2005,** *127*, (31), 10869.
26. Ohkawara, T.; Suzuki, K.; Nakano, K.; Mori, S.; Nozaki, K., Facile Estimation of Catalytic Activity and Selectivities in Copolymerization of Propylene Oxide with Carbon Dioxide Mediated by Metal Complexes with Planar Tetradentate Ligand*, J. Am. Chem. Soc.,* **2014,** *136*, (30), 10728.
27. Nakano, K.; Kamada, T.; Nozaki, K., Selective Formation of Polycarbonate over Cyclic Carbonate: Copolymerization of Epoxides with Carbon Dioxide Catalyzed by a Cobalt(III) Complex with a Piperidinium End-Capping Arm*, Angew. Chem. Int. Ed.,* **2006,** *45*, (43), 7274.
28. Noh, E. K.; Na, S. J.; S, S.; Kim, S.-W.; Lee, B. Y., Two Components in a Molecule: Highly Efficient and Thermally Robust Catalytic System for CO2/Epoxide Copolymerization*, J. Am. Chem. Soc.,* **2007,** *129*, (26), 8082.
29. S, S.; Min, J. K.; Seong, J. E.; Na, S. J.; Lee, B. Y., A Highly Active and Recyclable Catalytic System for CO2/Propylene Oxide Copolymerization*, Angew. Chem. Int. Ed.,* **2008,** *47*, (38), 7306.
30. Liu, J.; Ren, W.-M.; Liu, Y.; Lu, X.-B., Kinetic Study on the Coupling of CO_2 and Epoxides Catalyzed by Co(III) Complex with an Inter- or Intramolecular Nucleophilic Cocatalyst*, Macromolecules,* **2013,** *46*, (4), 1343.
31. Ren, W.-M.; Liu, Z.-W.; Wen, Y.-Q.; Zhang, R.; Lu, X.-B., Mechanistic Aspects of the Copolymerization of CO2 with Epoxides Using a Thermally Stable Single-Site Cobalt(III) Catalyst*, J. Am. Chem. Soc.,* **2009,** *131*, (32), 11509.

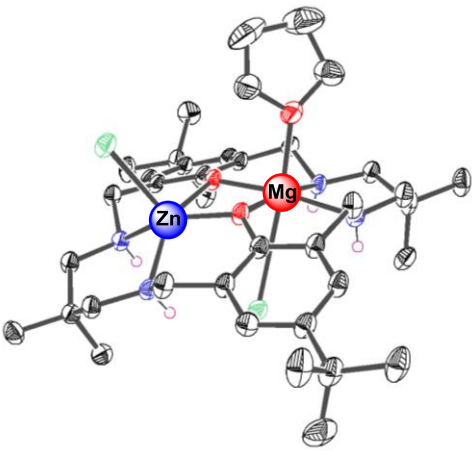
32. Thevenon, A.; Cyriac, A.; Myers, D.; White, A. J. P.; Durr, C. B.; Williams, C. K., Indium Catalysts for Low-Pressure CO_2/Epoxide Ring-Opening Copolymerization: Evidence for a Mononuclear Mechanism?*, J. Am. Chem. Soc.,* **2018,** *140*, (22), 6893.
33. Zhang, D.; Boopathi, S. K.; Hadjichristidis, N.; Gnanou, Y.; Feng, X., Metal-Free Alternating Copolymerization of CO_2 with Epoxides: Fulfilling "Green" Synthesis and Activity*, J. Am. Chem. Soc.,* **2016,** *138*, (35), 11117.
34. Zhang, D.-D.; Feng, X.; Gnanou, Y.; Huang, K.-W., Theoretical Mechanistic Investigation into Metal-Free Alternating Copolymerization of CO2 and Epoxides: The Key Role of Triethylborane*, Macromolecules,* **2018,** *51*, (15), 5600.
35. Zhang, D.; Zhang, H.; Hadjichristidis, N.; Gnanou, Y.; Feng, X., Lithium-Assisted Copolymerization of CO_2/Cyclohexene Oxide: A Novel and Straightforward Route to Polycarbonates and Related Block Copolymers*, Macromolecules,* **2016,** *49*, (7), 2484.
36. Peña Carrodeguas, L.; González-Fabra, J.; Castro-Gómez, F.; Bo, C.; Kleij, A. W., AlIII-Catalysed Formation of Poly(limonene)carbonate: DFT Analysis of the Origin of Stereoregularity*, Chem. Eur. J.,* **2015,** *21*, (16), 6115.
37. Cheng, M.; Lobkovsky, E. B.; Coates, G. W., Catalytic Reactions Involving C1 Feedstocks: New High-Activity Zn(II)-Based Catalysts for the Alternating Copolymerization of Carbon Dioxide and Epoxides*, J. Am. Chem. Soc.,* **1998,** *120*, (42), 11018.
38. Cheng, M.; Moore, D. R.; Reczek, J. J.; Chamberlain, B. M.; Lobkovsky, E. B.; Coates, G. W., Single-Site β-Diiminate Zinc Catalysts for the Alternating Copolymerization of CO_2 and Epoxides: Catalyst Synthesis and Unprecedented Polymerization Activity*, J. Am. Chem. Soc.,* **2001,** *123*, (36), 8738.
39. Allen, S. D.; Moore, D. R.; Lobkovsky, E. B.; Coates, G. W., High-Activity, Single-Site Catalysts for the Alternating Copolymerization of CO_2 and Propylene Oxide*, J. Am. Chem. Soc.,* **2002,** *124*, (48), 14284.
40. Moore, D. R.; Cheng, M.; Lobkovsky, E. B.; Coates, G. W., Electronic and Steric Effects on Catalysts for CO_2/Epoxide Polymerization: Subtle Modifications Resulting in Superior Activities*, Angew. Chem. Int. Ed.,* **2002,** *41*, (14), 2599.
41. Moore, D. R.; Cheng, M.; Lobkovsky, E. B.; Coates, G. W., Mechanism of the Alternating Copolymerization of Epoxides and CO_2 Using β-Diiminate Zinc Catalysts: Evidence for a Bimetallic Epoxide Enchainment*, J. Am. Chem. Soc.,* **2003,** *125*, (39), 11911.
42. Nozaki, K.; Nakano, K.; Hiyama, T., Optically Active Polycarbonates: Asymmetric Alternating Copolymerization of Cyclohexene Oxide and Carbon Dioxide*, J. Am. Chem. Soc.,* **1999,** *121*, (47), 11008.
43. Nakano, K.; Nozaki, K.; Hiyama, T., Asymmetric Alternating Copolymerization of Cyclohexene Oxide and CO_2 with Dimeric Zinc Complexes*, J. Am. Chem. Soc.,* **2003,** *125*, (18), 5501.
44. Mike, S.; Sebastian, D.; Franc, M., Highly Active and Readily Accessible Proline-Based Dizinc Catalyst for CO_2/Epoxide Copolymerization*, Chem. Eur. J.,* **2017,** *23*, (65), 16472.
45. Nakano, K.; Hashimoto, S.; Nozaki, K., Bimetallic mechanism operating in the copolymerization of propylene oxide with carbon dioxide catalyzed by cobalt–salen complexes*, Chem. Sci.,* **2010,** *1*, (3), 369.
46. Vagin, S. I.; Reichardt, R.; Klaus, S.; Rieger, B., Conformationally Flexible Dimeric Salphen Complexes for Bifunctional Catalysis*, J. Am. Chem. Soc.,* **2010,** *132*, (41), 14367.

47. Liu, Y.; Ren, W.-M.; Liu, J.; Lu, X.-B., Asymmetric Copolymerization of CO_2 with meso-Epoxides Mediated by Dinuclear Cobalt(III) Complexes: Unprecedented Enantioselectivity and Activity*, Angew. Chem. Int. Ed.,* **2013,** *52*, (44), 11594.
48. Wu, G.-P.; Ren, W.-M.; Luo, Y.; Li, B.; Zhang, W.-Z.; Lu, X.-B., Enhanced Asymmetric Induction for the Copolymerization of CO2 and Cyclohexene Oxide with Unsymmetric Enantiopure SalenCo(III) Complexes: Synthesis of Crystalline CO_2-Based Polycarbonate*, J. Am. Chem. Soc.,* **2012,** *134*, (12), 5682.
49. Li, J.; Liu, Y.; Ren, W.-M.; Lu, X.-B., Asymmetric Alternating Copolymerization of Meso-epoxides and Cyclic Anhydrides: Efficient Access to Enantiopure Polyesters*, J. Am. Chem. Soc.,* **2016,** *138*, (36), 11493.
50. Romain, C.; Zhu, Y.; Dingwall, P.; Paul, S.; Rzepa, H. S.; Buchard, A.; Williams, C. K., Chemoselective Polymerizations from Mixtures of Epoxide, Lactone, Anhydride, and Carbon Dioxide*, J. Am. Chem. Soc.,* **2016,** *138*, (12), 4120.
51. Ahmed, S. M.; Poater, A.; Childers, M. I.; Widger, P. C. B.; LaPointe, A. M.; Lobkovsky, E. B.; Coates, G. W.; Cavallo, L., Enantioselective Polymerization of Epoxides Using Biaryl-Linked Bimetallic Cobalt Catalysts: A Mechanistic Study*, J. Am. Chem. Soc.,* **2013,** *135*, (50), 18901.
52. Lee, B. Y.; Kwon, H. Y.; Lee, S. Y.; Na, S. J.; Han, S.-i.; Yun, H.; Lee, H.; Park, Y.-W., Bimetallic Anilido-Aldimine Zinc Complexes for Epoxide/CO_2 Copolymerization*, J. Am. Chem. Soc.,* **2005,** *127*, (9), 3031.
53. Bok, T.; Yun, H.; Lee, B. Y., Bimetallic Fluorine-Substituted Anilido–Aldimine Zinc Complexes for CO2/(Cyclohexene Oxide) Copolymerization*, Inorg. Chem.,* **2006,** *45*, (10), 4228.
54. Jutz, F.; Buchard, A.; Kember, M. R.; Fredriksen, S. B.; Williams, C. K., Mechanistic Investigation and Reaction Kinetics of the Low-Pressure Copolymerization of Cyclohexene Oxide and Carbon Dioxide Catalyzed by a Dizinc Complex*, J. Am. Chem. Soc.,* **2011,** *133*, (43), 17395.
55. Kember, M. R.; Knight, P. D.; Reung, P. T. R.; Williams, C. K., Highly Active Dizinc Catalyst for the Copolymerization of Carbon Dioxide and Cyclohexene Oxide at One Atmosphere Pressure*, Angew. Chem. Int. Ed.,* **2009,** *48*, (5), 931.
56. Buchard, A.; Jutz, F.; Kember, M. R.; White, A. J. P.; Rzepa, H. S.; Williams, C. K., Experimental and Computational Investigation of the Mechanism of Carbon Dioxide/Cyclohexene Oxide Copolymerization Using a Dizinc Catalyst*, Macromolecules,* **2012,** *45*, (17), 6781.
57. Kember, M. R.; White, A. J. P.; Williams, C. K., Highly Active Di- and Trimetallic Cobalt Catalysts for the Copolymerization of CHO and CO_2 at Atmospheric Pressure*, Macromolecules,* **2010,** *43*, (5), 2291.
58. Buchard, A.; Kember, M. R.; Sandeman, K. G.; Williams, C. K., A bimetallic iron(III) catalyst for CO_2/epoxide coupling*, Chem. Commun.,* **2011,** *47*, (1), 212.
59. Kember, M. R.; Williams, C. K., Efficient Magnesium Catalysts for the Copolymerization of Epoxides and CO_2; Using Water to Synthesize Polycarbonate Polyols*, J. Am. Chem. Soc.,* **2012,** *134*, (38), 15676.
60. Kember, M. R.; Jutz, F.; Buchard, A.; White, A. J. P.; Williams, C. K., Di-cobalt(ii) catalysts for the copolymerisation of CO_2 and cyclohexene oxide: support for a dinuclear mechanism?*, Chem. Sci.,* **2012,** *3*, (4), 1245.
61. Badarau, A.; Damblon, C.; Page, M. I., The activity of the dinuclear cobalt-beta-lactamase from Bacillus cereus in catalysing the hydrolysis of beta-lactams*, Biochem. J.,* **2007,** *401*, (1), 197.

62. Crawford, P. A.; Yang, K.-W.; Sharma, N.; Bennett, B.; Crowder, M. W., Spectroscopic Studies on Cobalt(II)-Substituted Metallo-β-lactamase ImiS from Aeromonas veronii bv. sobria*, Biochemistry,* **2005,** *44*, (13), 5168.
63. Hu, Z.; Periyannan, G.; Bennett, B.; Crowder, M. W., Role of the Zn1 and Zn2 sites in Metallo-β-lactamase L1*, J. Am. Chem. Soc.,* **2008,** *130*, (43), 14207.
64. Chapman, A. M.; Keyworth, C.; Kember, M. R.; Lennox, A. J. J.; Williams, C. K., Adding Value to Power Station Captured CO_2: Tolerant Zn and Mg Homogeneous Catalysts for Polycarbonate Polyol Production*, ACS Catal.,* **2015,** *5*, (3), 1581.
65. Saini, P. K.; Romain, C.; Williams, C. K., Dinuclear metal catalysts: improved performance of heterodinuclear mixed catalysts for CO_2-epoxide copolymerization*, Chem. Commun.,* **2014,** *50*, (32), 4164.
66. Garden, J. A.; Saini, P. K.; Williams, C. K., Greater than the Sum of Its Parts: A Heterodinuclear Polymerization Catalyst*, J. Am. Chem. Soc.,* **2015,** *137*, (48), 15078.
67. Trott, G.; Garden, J. A.; Williams, C. K., Heterodinuclear zinc and magnesium catalysts for epoxide/CO2 ring opening copolymerizations*, Chem. Sci.,* **2019**.
68. Lehenmeier, M. W.; Kissling, S.; Altenbuchner, P. T.; Bruckmeier, C.; Deglmann, P.; Brym, A.-K.; Rieger, B., Flexibly Tethered Dinuclear Zinc Complexes: A Solution to the Entropy Problem in CO_2/Epoxide Copolymerization Catalysis?*, Angew. Chem. Int. Ed.,* **2013,** *52*, (37), 9821.
69. Kissling, S.; Altenbuchner, P. T.; Lehenmeier, M. W.; Herdtweck, E.; Deglmann, P.; Seemann, U. B.; Rieger, B., Mechanistic Aspects of a Highly Active Dinuclear Zinc Catalyst for the Co-polymerization of Epoxides and CO_2*, Chem. Eur. J.,* **2015,** *21*, (22), 8148.
70. Kissling, S.; Lehenmeier, M. W.; Altenbuchner, P. T.; Kronast, A.; Reiter, M.; Deglmann, P.; Seemann, U. B.; Rieger, B., Dinuclear zinc catalysts with unprecedented activities for the copolymerization of cyclohexene oxide and CO_2*, Chem. Commun.,* **2015,** *51*, (22), 4579.
71. Nagae, H.; Aoki, R.; Akutagawa, S.; Kleemann, J.; Tagawa, R.; Schindler, T.; Choi, G.; Spaniol, T. P.; Tsurugi, H.; Okuda, J.; Mashima, K., Lanthanide Complexes Supported by a Trizinc Crown Ether as Catalysts for Alternating Copolymerization of Epoxide and CO_2: Telomerization Controlled by Carboxylate Anions*, Angew. Chem. Int. Ed.,* **2018,** *57*, (9), 2492.

Chapter 2:

Groups 1, 2 and Zn(II) Heterodinuclear Catalysts for CO_2/Epoxide Ring Opening Copolymerisation.



Epoxide Activation
Mg(II)

Nucleophile Donor
Zn(II)

Heterodinuclear Complexes
Thermodynamic Product ☑

Rate of CO_2/CHO
Mg(II) > Zn (II) > Li (I) > K(I) ☑

Coligand Controls
Product Selectivity ☑

A.C. Deacy, C. B. Durr, J. A. Garden, A. J. P. White and C. K. Williams, *Inorg. Chem.*, **2018**, 57, 15575

2.1.1 Introduction

Heterodinuclear cooperativity is a potential means to enhance catalytic activity beyond conventional ligand design.[1-2] Synergic interactions between two different metals has been proposed to enhance activity in homogeneous catalysts ranging from metalation,[3] CH bond activation,[4-6] and CF bond activation,[7-9] lactone ring opening polymerisation(ROP),[10-12] olefin polymerisation[13-17] and the ring opening copolymerisation (ROCOP) of CO_2 and epoxides.[18-22]

The viability of CO_2/epoxide ROCOP depends on the selection of the metal catalyst which in turn controls rates, polymer molar mass and polymer composition (selectivity).[23-26] Amongst the highest performing catalysts are dinuclear, dimeric or bicomponent metal complexes.[27-34] For highly active dinuclear catalysts, it is commonly proposed that one metal activates the epoxide whilst the other provides the attacking nucleophile.[26] Following this hypothesis, we have reported a series of (homo)dinuclear Zn(II), Mg(II), Co(II/III) and Fe(III) catalysts, coordinated by a macrocyclic ancillary ligand, which showed promising activities at 1 bar CO_2 pressure (i.e. at low pressure).[35-38] Detailed kinetic, mechanistic and theoretical studies suggested the catalysts operated by a 'chain-shuttling' mechanism and that the rate-limiting step is metal-carbonate attack on coordinated epoxide.[39-40] Building from this mechanistic hypothesis, a Zn(II)/Mg(II) heterodinuclear catalysts showed a 5-fold higher rate than either di-zinc or di-magnesium counterparts, or combinations of them.[19]

Here, a range of new complexes combining metals from Groups 1 or 2 with zinc are targeted. The selection of the metals is driven by the strong track record for zinc in this field of polymerisation catalysts. In contrast, although there are a few reports of

testing of alkaline earth metals, specifically Ca(II), none were found to be active for polymerisation.[41-43] Nonetheless, metals from Groups 1 and 2 are interesting candidates for further investigation because they are highly Lewis acidic, which should enhance epoxide coordination, and may be expected to form labile metal-carbonate bonds, which could accelerate the rate limiting step. One potential pitfall may be their propensity to form labile, ionic complexes which may result in metal redistribution side-reactions.

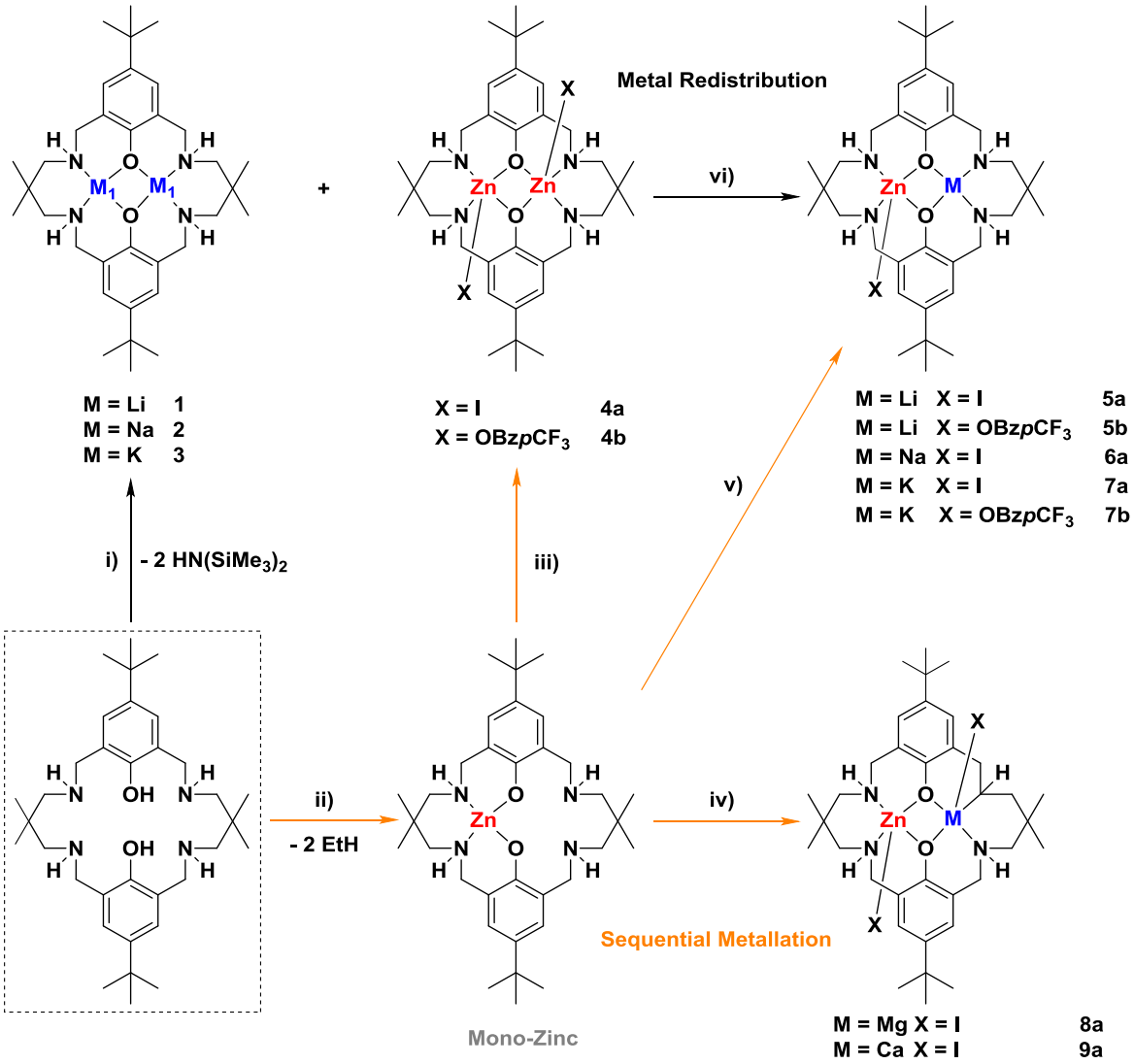
2.1.2 Aims

The primary objective of this chapter is to synthesise and test a range of heterodinuclear complexes derived from Groups 1 and 2 with zinc for the ROCOP of CO_2 with cyclohexene oxide in order to gain a better understanding of the factors involved for effective catalysis and improve upon the rate already achieved by the Zn(II)/Mg(II) complex.

In order to do this, its necessary first to establish the thermodynamic stability of the heterodinuclear complex compared to its homodinuclear analogues. Another key target is to gain further insight into metal roles in the catalytic cycle, especially with the highly active Zn(II)/Mg(II) complex.

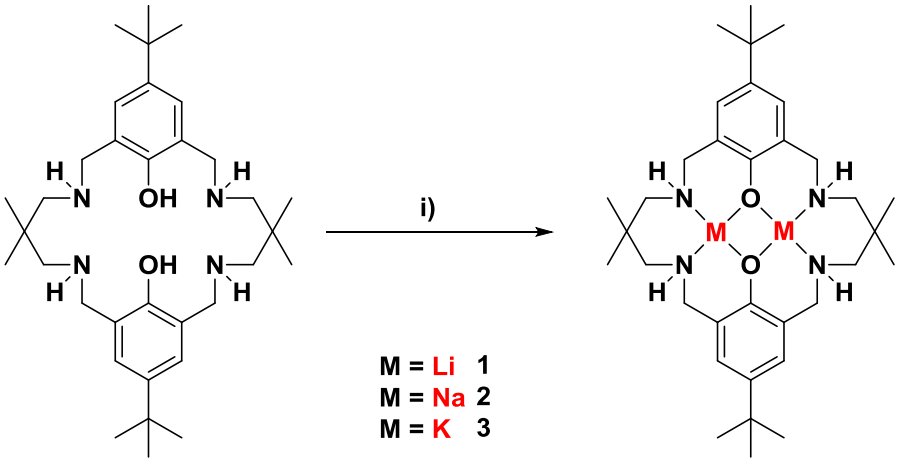
An outline of the synthetic pathways to each catalyst is shown below (Scheme 2.1). Two strategies are employed to synthesise well-defined heterodinuclear complexes: (1) a one-pot reaction between the two homodinuclear complexes (metal redistribution reaction) or (2) sequential reaction of the ligand with first one metal, to produce a mono-metalated intermediate which is subsequently reacted with the second metal (sequential metalation). One-pot syntheses are synthetically attractive

but the under-pinning principle is that the heterodinuclear complex should be the thermodynamic product, however, until now such stability is unknown. On the other hand, sequential metalation reactions are synthetically challenging but careful control of the reaction conditions, such as solvents, rate of reagent addition and temperature, allows control over the formation of thermodynamic or kinetic reaction products. Here, both synthetic methods are applied to evaluate the complex stabilities and to assess the best synthetic routes to heterodinuclear complexes.



Scheme 2.1: Overall synthetic strategies targeting Group 1 and 2 zinc heterocomplexes **1**-**9**. i) $M(N(SiCH_3)_3)_2$), THF, 25 °C, 4h, >75 %, ii) $ZnEt_2$, THF, 25 °C, 16 h, iii) ZnX_2, THF, 25 °C, 4 h, iv) MX_2, THF, 100 °C, 16 h, v) MX, THF, 100 °C, 16 h, vi) 100 °C 16 h.

2.1.3 Synthesis and Characterisation of Group 1 Homodinuclear Complexes



Scheme 2.2: Synthesis of complexes **1**-**3**. i) $M(N(Si(CH_3)_3)_2)$, THF, 25 °C, 4 h, > 75 %

Firstly, homodinuclear Group 1 complexes, **1-3,** were synthesised by reaction between the macrocyclic ligand and the corresponding metal (I) amide precursor, in THF at 25 °C (Scheme 2.2). The products were isolated as white powders in high yields (> 75 %) and were characterised, in solution, using NMR spectroscopy (Figure S1-S13). Single crystals of complexes **1** and **2** were also characterised using X-ray crystallography (Figure S14-S15).

Di-lithium and di-potassium complexes **1** and **3** displayed similar proton splitting patterns in their respective ^1H NMR spectra (Figure 2.1), where weak couplings were observed between the benzylic, methylene and amine proton environments at 3.58 ppm, 2.35 ppm and 1.42 ppm, respectively. On the other hand, di-sodium complex **2** displayed strong diastereotopic couplings between each of the respective proton resonance pairs indicating a strong interaction between metal and ligand framework. Interestingly, a strong up field shift of the NH proton resonance for complex **2** was observed in comparison to complexes **1** and **3,** as a result of the strong interaction between the amine and the electropositive sodium centre.

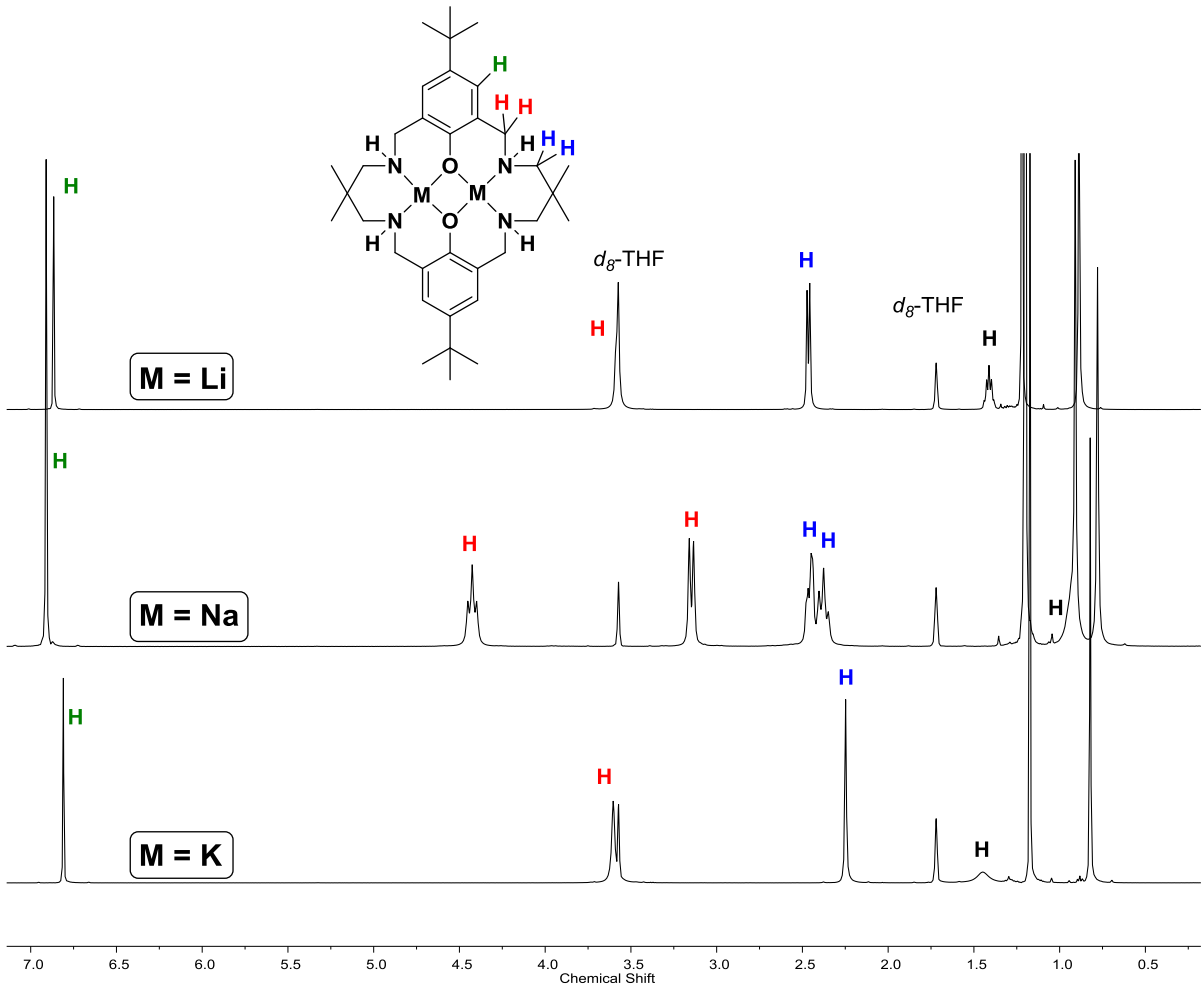


Figure 2.1: ^{1}H NMR spectra of complexes **1**, **2** and **3**. Phenyl, benzylic, methylene and amine protons are coloured green, red, blue and black, respectively.

2D DOSY NMR experiments for complexes **1-3** all showed a single species present in solution with diffusion coefficients of -9.173, -9.274 and -9.195 log (m^2s^{-1}) for complexes **1-3** respectively (Figure 2.2). Applying a linear calibration between molecular mass and diffusion coefficient, molecular masses of 922, 1394 and 1009 g mol^{-1} were calculated, indicating complexes **1** and **3** exist in 'monomer-dimer' equilibrium, whereas complex **2** exists as a dimer in the solution state.

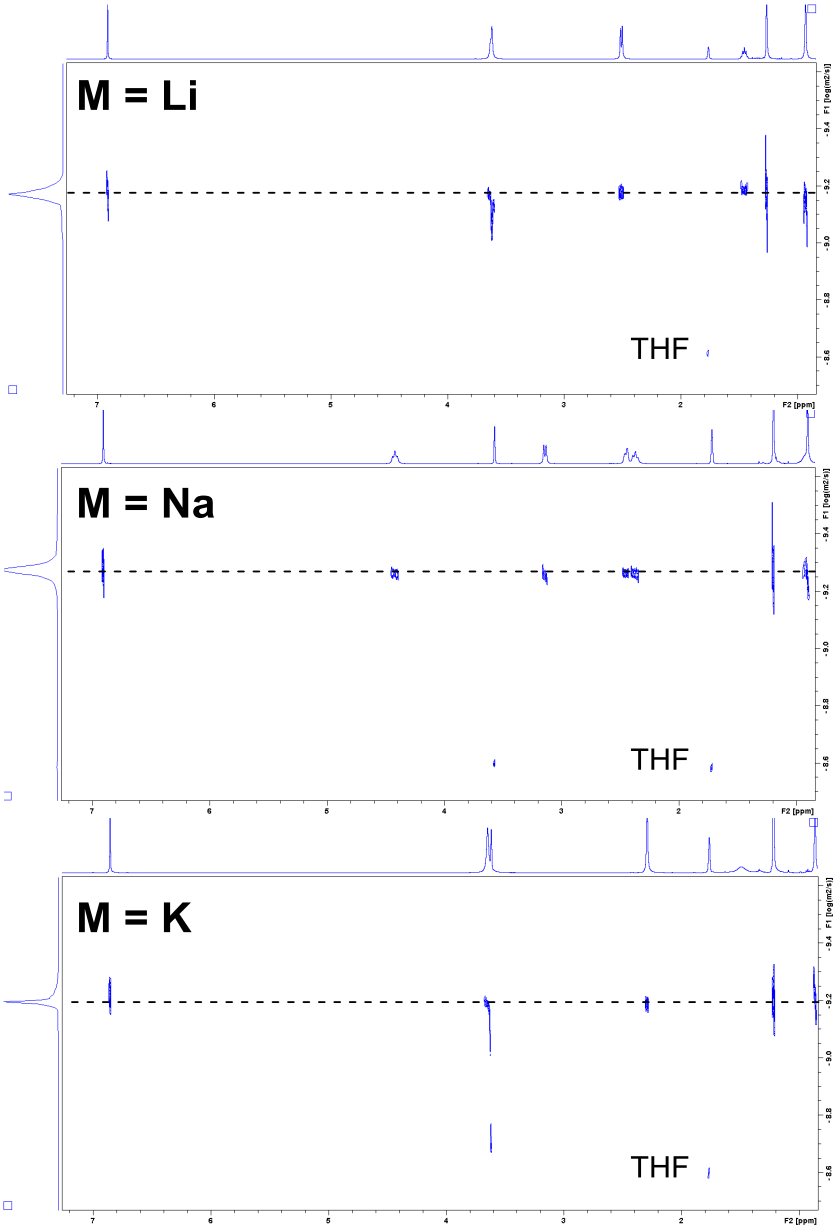


Figure 2.2: 2D DOSY NMR spectra of complexes **1**, **2** and **3** respectively.

Single crystals of complex **1** and **2** suitable for X-ray crystallography were obtained *via* slow evaporation of a saturated solution of each complex, in THF at -40 °C (Figure 2.3). Structural elucidation revealed a dimeric structure for both complexes **1** and **2** in the solid state, with **1** displaying a distorted cubane (Li_4O_4) structure, whereby each lithium centre adopts a tetrahedral geometry. Li(1) and Li(2) centres favour bonding towards phenolic-oxygen centres over amino-nitrogen centres, where the

converse is true for lithium centres (3) and (4). On the other hand, the sodium atoms in **2** adopt a pentacoordinate, square based pyramidal geometry ($\tau = 0.02$) forming a cubane structure (N_4O_4). Each sodium centre is bound by two amino-nitrogen centres and three phenolic-oxygen centres. The cubane structure formed by **2,** may indicate why **2** is the thermodynamic product with respect to the heterodinuclear complex targeted (*vide infra*). The metal-metal distances are measured at 2.518(4) Å and 2.630(4) Å for Li(1)-Li(2) and Li(3)-Li(4) and 3.136(15) Å for Na(1)-Na(2) and Na(3)-Na(4) respectively.

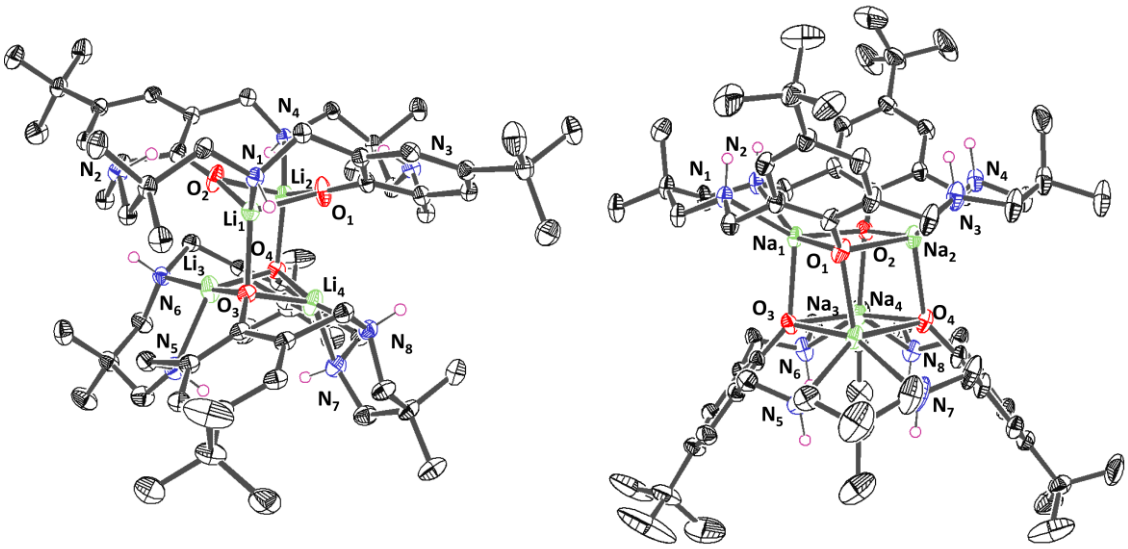
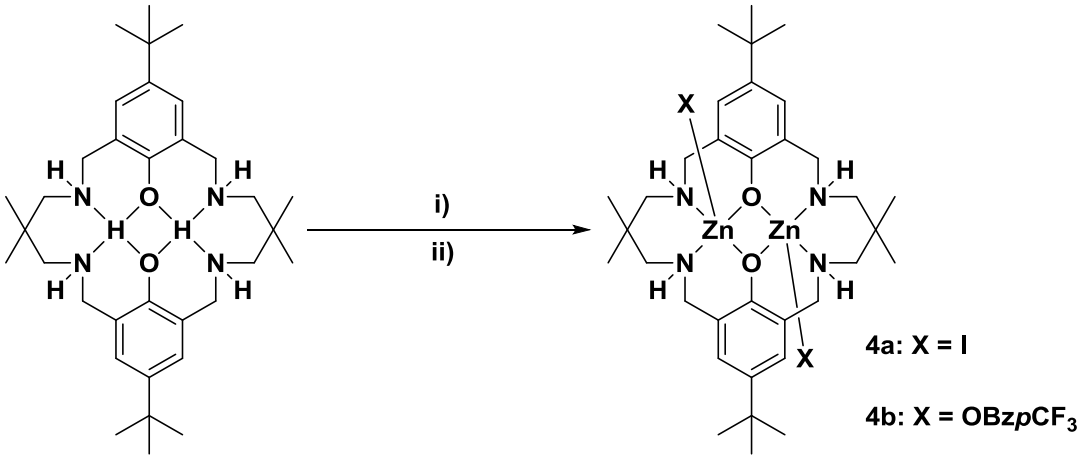


Figure 2.3: ORTEP representation of crystallographic structures of complexes 1 (LHS) and 2 (RHS), obtained by single crystal X-ray diffraction. Disorder and H-atoms (excluding NH) have been omitted for clarity, with thermal ellipsoids represented at 40 % probability. Selected bond lengths (Å) and angles (°) for complex 1 and 2 (Table S1-S2).

2.1.4 Synthesis and Characterisation of Homodinuclear Zinc complexes



Scheme 2.3: Synthesis of di-zinc complexes **4a** and **4b**. i) $ZnEt_2$, THF, 25 °C, 16 h. ii) ZnX_2 (Where X = I and OBz*p*CF_3), THF, 25 °C, 2 h.

Di-zinc complexes **4a** and **4b**, were synthesised by reaction between the macrocyclic ligand and one equivalent of diethyl zinc, immediately followed by the addition of an equivalent of zinc iodide or zinc benzoate (Scheme 2.3). The products were isolated as white powders in >76 % yield and characterised by NMR spectroscopy (Figure S19-S27), mass spectrometry (Figure S28-S29) and X-ray crystallography (Figure S30).

The sequential metalation synthetic procedure proved useful in homodinuclear complex synthesis as a much cleaner reaction was afforded with minimal purification requirements. Previous methods; using two equivalents of a zinc (II) salt, required rigorous purification to remove acidic by-products, such as HI and HOBz*p*CF_3. These acidic impurities, if not fully removed, could act as chain-transfer reagents forming multimodal polymeric materials, a problem negated with the sequential metalation procedure.

For both complexes, the ^{1}H NMR spectra, in d_8-THF, were complex and showed many coupled, broadened resonances indicative of fluxional processes (Figure 2.4). In contrast, the ^{1}H NMR spectra determined in tetrachloroethane (TCE) at 403 K, are coalesced and therefore are assigned; they show characteristic resonances for homodinuclear complex formation including diastereotopic benzylic (4.79 ppm and 3.34 ppm) and methylene (2.88 ppm and 2.46 ppm) protons and single resonances for the phenyl ring (7.00 ppm) and amine (2.95 ppm) protons.

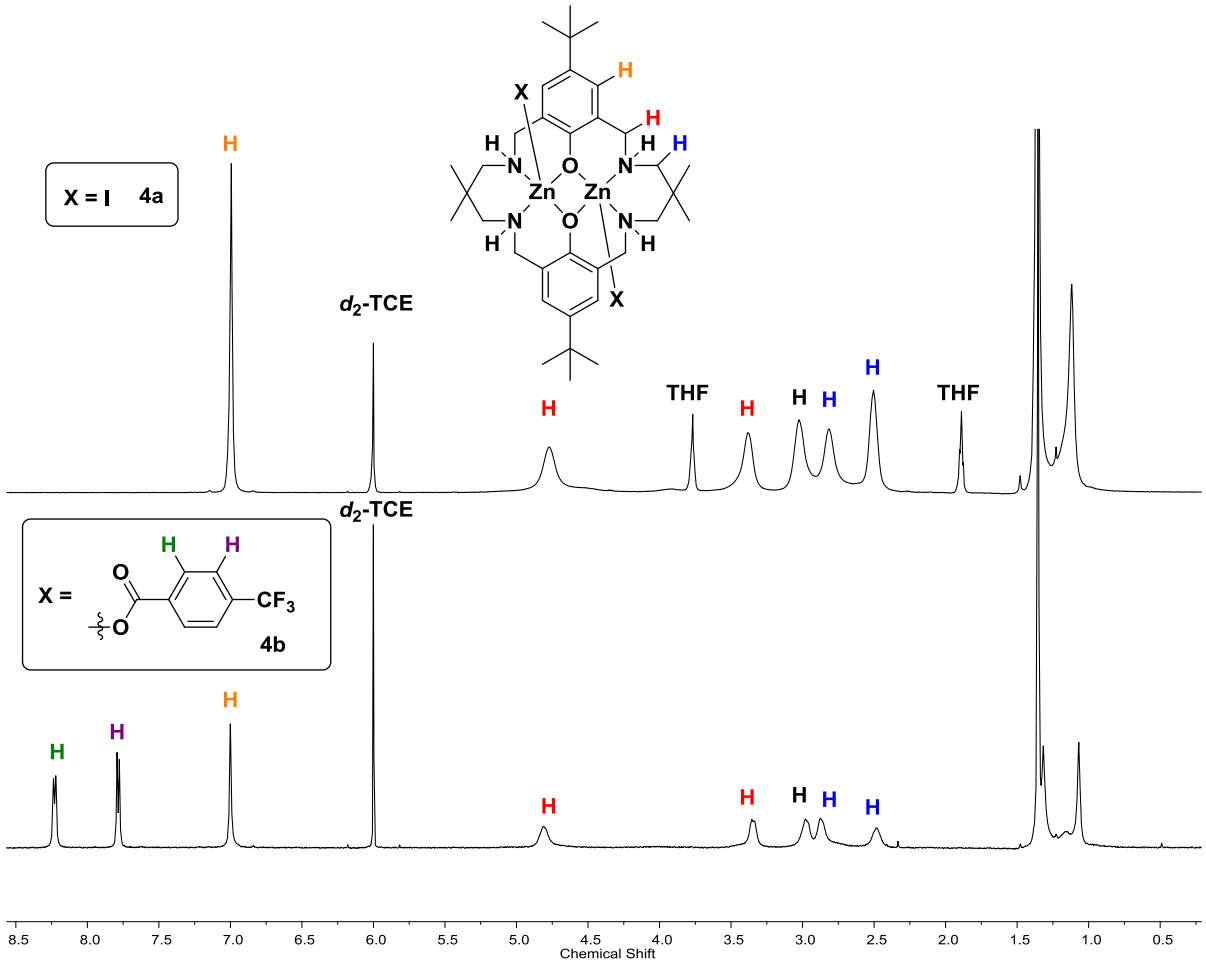


Figure 2.4: ^{1}H NMR spectra of complexes **4a** and **4b** in d_2-TCE, 403 K.

MALDI-ToF mass spectrometry of complexes **4a** and **4b** displayed peaks at 808 *m/z* and 868 *m/z* corresponding to the molecular cations $[LZn_2(I)]^+$ and $[LZn_2(OBzpCF_3)]^+$ respectively, with isotropic patterns matching the predicted values. 2D DOSY NMR experiments for complexes **4a** and **4b** displayed a single, monomeric, species present in solution with diffusion coefficients of -9.142 and -9.215 log (m^2s^{-1}) for complexes **4a** and **4b,** respectively (Figure 2.5).

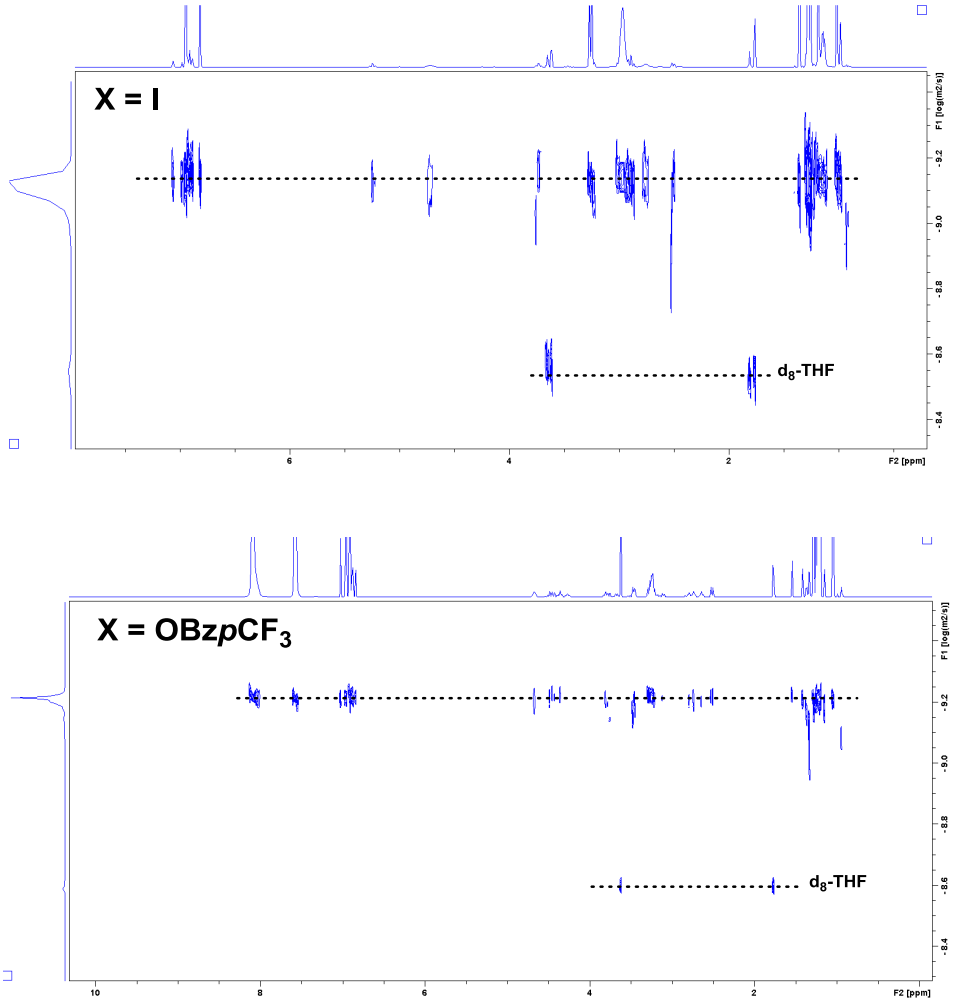


Figure 2.5: 2D DOSY NMR of complexes **4a** and **4b**. (**4a** -9.142 log (m^2s^{-1}), **4b** -9.215 log (m^2s^{-1}))

Single crystals of **4a** and **4b** were isolated *via* vapour diffusion of an antisolvent (**4a**: methanol, **4b**: pentane) into a saturated solution of complex in THF at -40 °C (Figure 2.6). Structural elucidation reveals both **4a** and **4b** are monomeric in the solid state with **4a** adopting a 'bowl' and **4b** an 'S-shape' conformation. Based on the structure of **4a** the polymerisation mechanism may be expected to occur on the 'open face' of the complex to minimise steric effects. The intermetallic separation was measured at 3.0996(5) Å and 3.19204(11) Å for **4a** and **4b**, respectively.

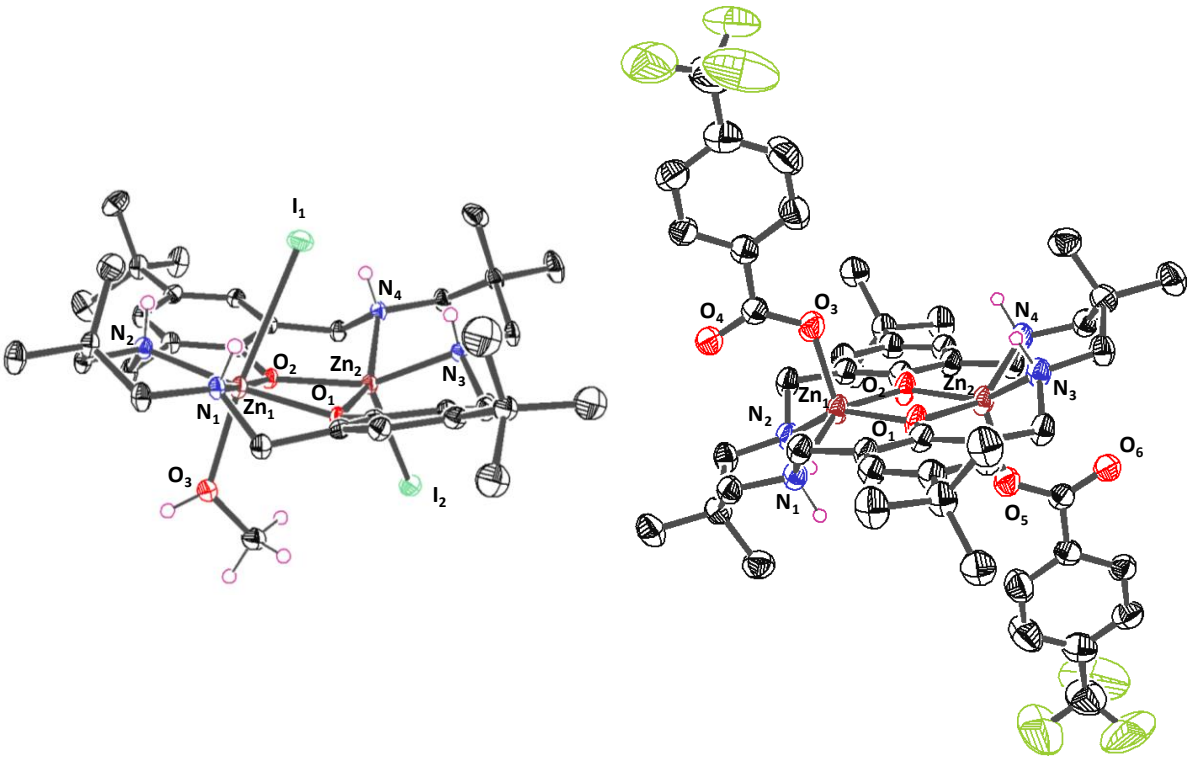
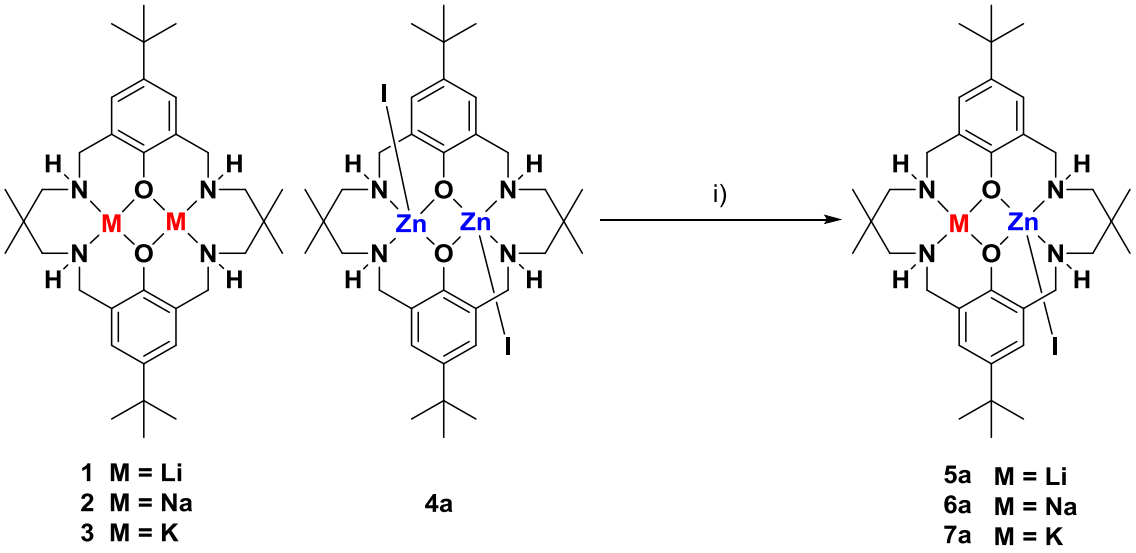


Figure 2.6: ORTEP representation of crystallographic structures of complexes **4a** (LHS) and **4b** (RHS), obtained by single crystal X-ray diffraction. Disorder and H-atoms (excluding NH) have been omitted for clarity, with thermal ellipsoids represented at 40 % probability. Selected bond lengths (Å) and angles (°) for complex **4a** and **4b** (Table S3-S4).

2.1.5 Group 1 Metal Redistribution Thermodynamics



Scheme 2.4: Metal redistribution reaction between Group 1 homodinuclear complexes, **1**-**3**, with the di-zinc iodide complex **4a**. i) THF, 100 °C.

The metal redistribution synthesis was investigated as a route to prepare Group 1/Zn heterodinuclear complexes **5a**, **6a** and **7a** (Scheme 2.4). The NMR scale reaction involved heating, at 100 °C, an equimolar mixture of the respective homodinuclear Group 1 complex **1**-**3** with the di-zinc complex **4a**, in d_8-THF. The reaction was monitored periodically using ^{1}H NMR spectroscopy (Figure S32-S33).

For di-lithium complex **1** and the di-zinc complex **4a**, no reaction was observed after 16 hours at 25 °C (Figure 2.7). Upon heating to 100 °C for 16 hours, a reduction in the 1H NMR proton resonances for complexes **1** and **4a** was observed alongside the appearance of new proton resonances. 2D COSY NMR experiments resolved $^{4}J_{HH}$ coupling between the phenyl proton resonances, indicating heterodinuclear complex formation (Figure S34).

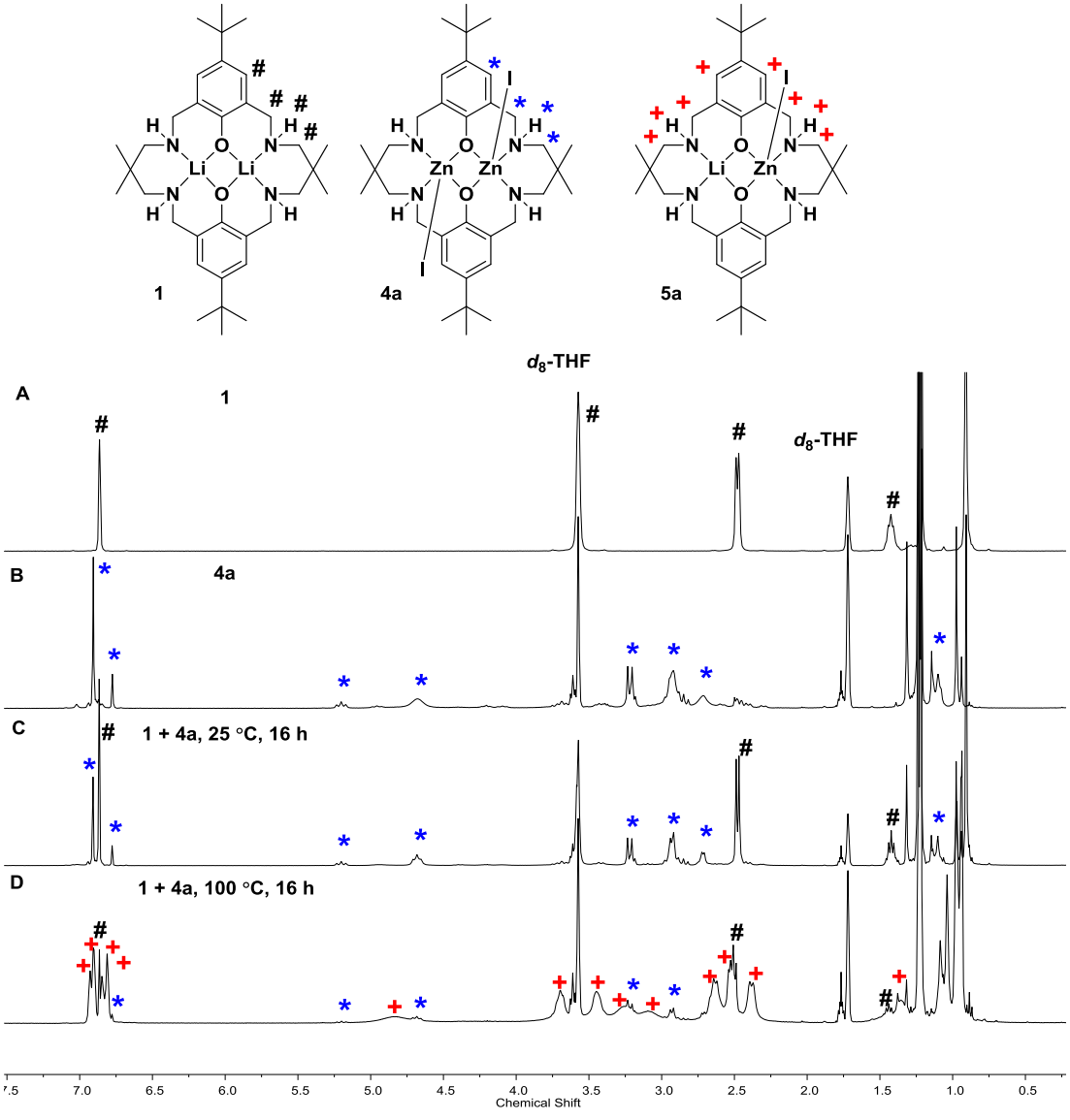


Figure 2.7: Metal redistribution reaction of complex **1** with **4a** as followed by ^{1}H NMR spectroscopy. A) Reference spectrum of di-lithium complex **1** (#). B) Reference spectrum of di-zinc complex **4a** (*). C) di-lithium and di-zinc complexes **1** and **4a** reaction at 25 °C, 16 h. D) di-lithium and di-zinc complexes **1** and **4a** reaction at 100 °C, 16 h forming a new species (+).

Addition of di-sodium complex **2** with the di-zinc complex **4a** resulted in no reaction even after heating to 100 °C for 48 hours (Figure 2.8). The lack of a thermodynamic driving force for the formation of heterodinuclear complex **6a**, maybe due to the strong chelating dimer, observed in both solid and solution state, of the di-sodium complex **2**, acting as a thermodynamic sink (*vide supra*).

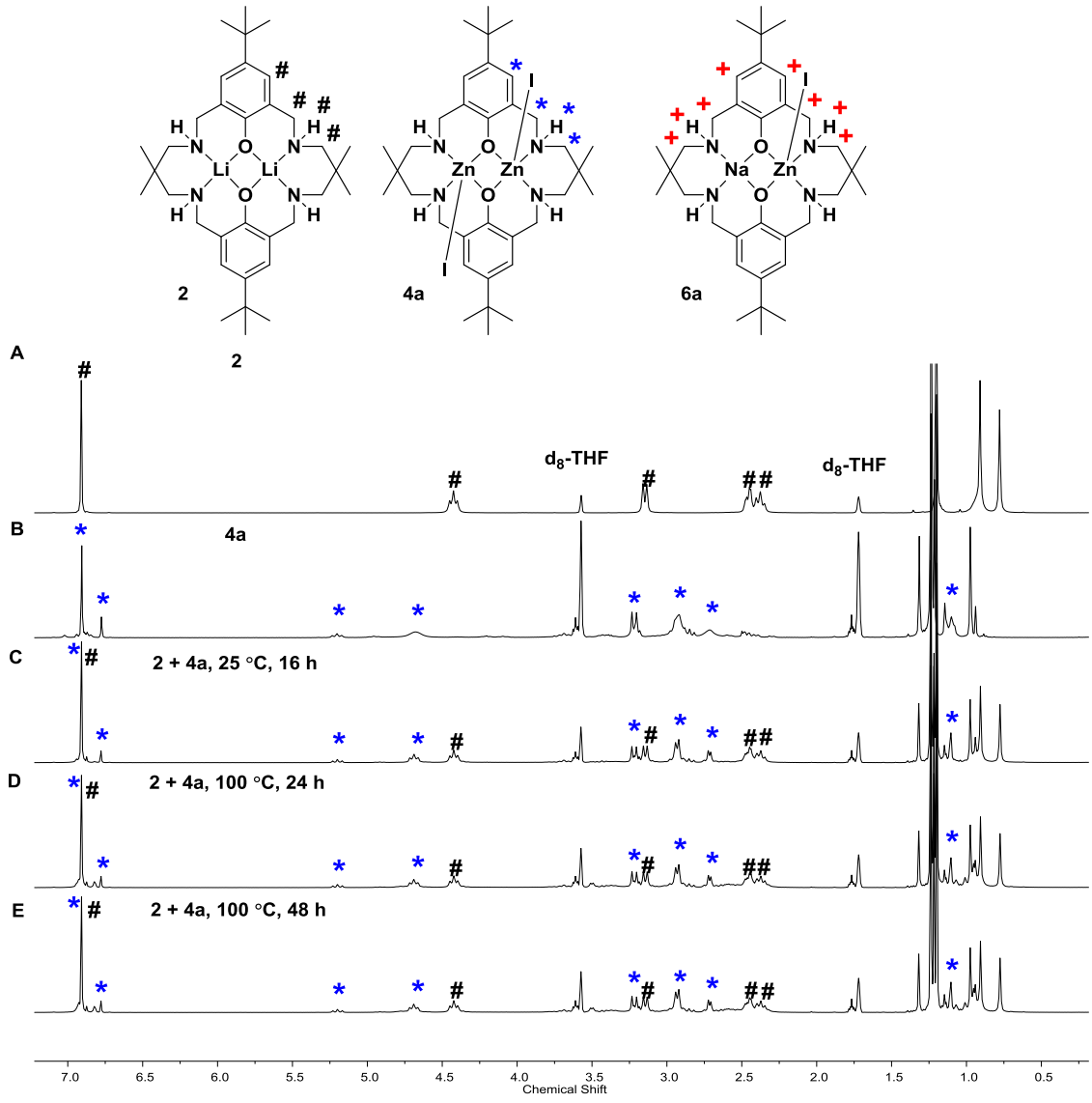


Figure 2.8: Metal redistribution reaction of complex **2** with **4a** as followed by ^{1}H NMR spectroscopy. A) Reference spectrum of di-sodium complex **2** (#). B) Reference spectrum of di-zinc complex **4a** (*). C) Di-sodium and di-zinc complexes **2** and **4a** reaction at 25 °C, 16 h. D) Di-sodium and di-zinc complexes **2** and **4a** reaction at 100 °C, 24 h. E) Di-sodium and di-zinc complexes **2** and **4a** reaction at 100 °C, 48 h.

Addition of di-potassium complex **3** to the di-zinc complex **4a** saw the disappearance of the proton resonances of **3** and **4a** and the formation of new proton environments at 25 °C in 16 hours (Figure 2.9). This ^{1}H NMR spectrum showed no change after heating to 100 °C for 16 h. Unfortunately, due to the broad proton resonances observed for **7a**, a COSY NMR provided limited information to the heterodinuclear nature of the newly formed species in the ^{1}H NMR spectrum.

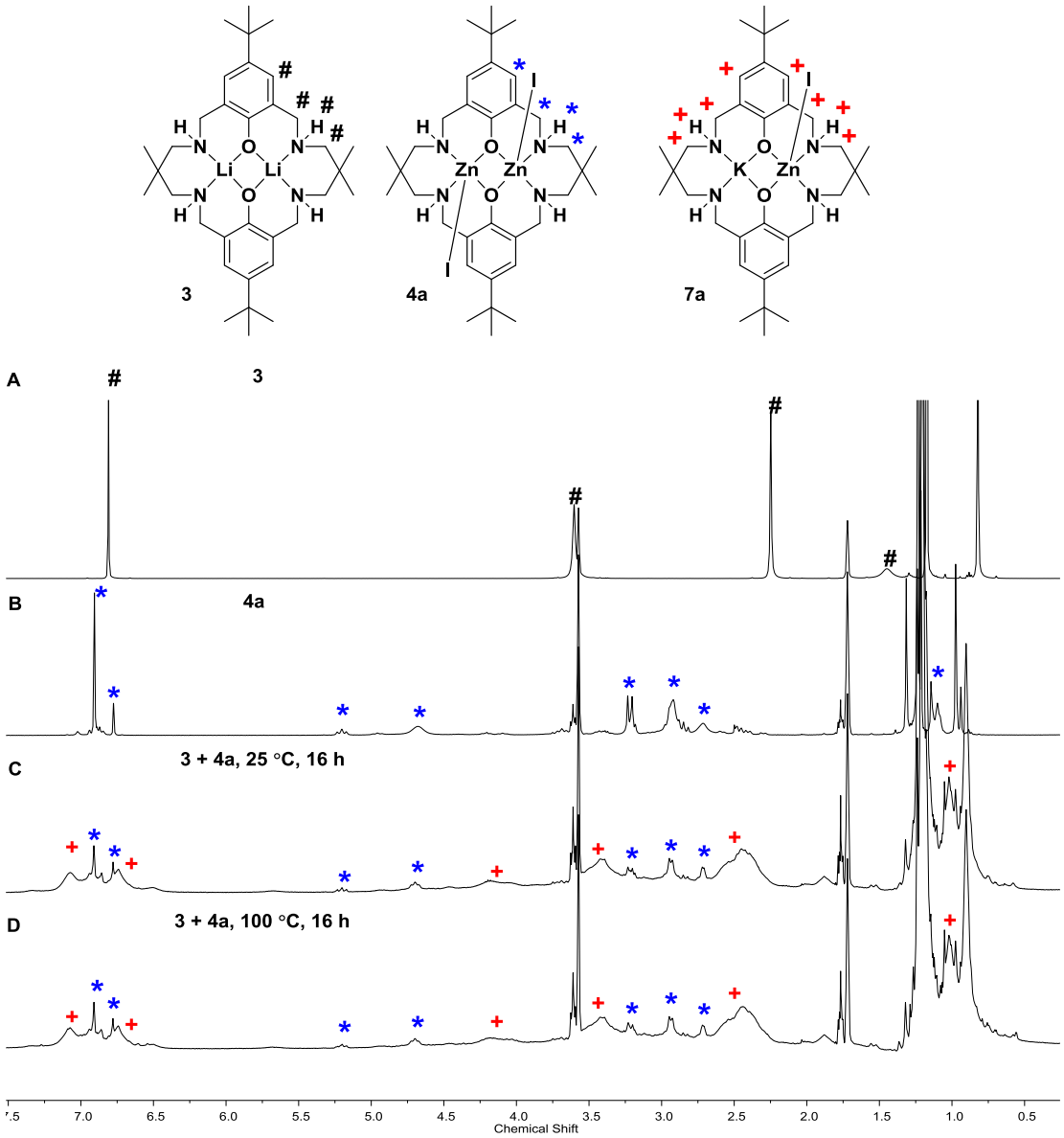
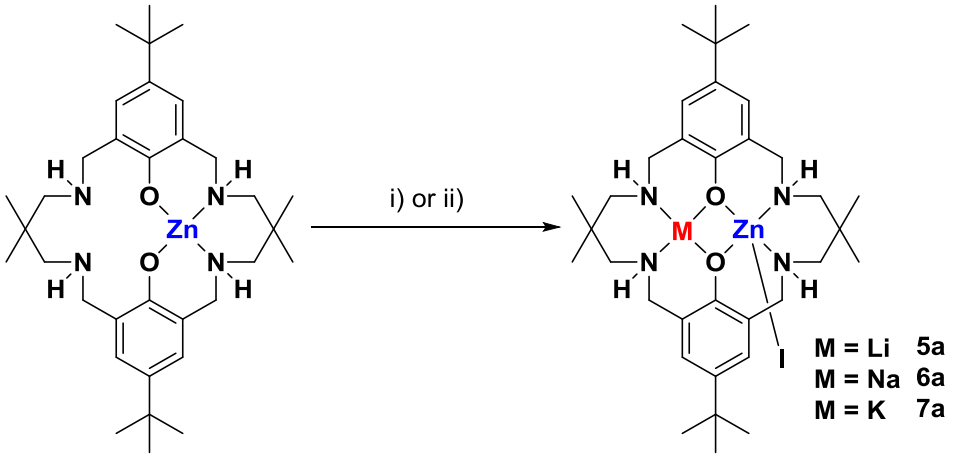


Figure 2.9; Metal redistribution reaction of complex **3** with **4a** as followed by ^{1}H NMR spectroscopy. A) Reference spectrum of di-potassium complex **3** (#). B) Reference spectrum of di-zinc complex **4a** (*). C) Di-potassium and di-zinc complexes **3** and **4a** reaction at 25 °C, 16 h, formation of new species (+). D) Di-potassium and di-zinc complexes **3** and **4a** reaction at 100 °C, 24 h.

2.1.6 Group 1-Zinc Sequential Metalation



Scheme 2.5: Synthesis of complexes **5**, **6** and **7** by sequential mono metalation under thermodynamic or kinetic conditions. i) MI, THF, 100 °C, 298 K, 16 h, for **5a** and **7a**. ii) MI, THF, -78 °C, 4 h for **6a**.

Next, the sequential metalation synthesis was investigated (Scheme 2.5), using the previously reported mono-zincation strategy which involved reaction of the ligand with diethyl zinc to generate a mono-zinc intermediate.[19] This intermediate was not isolated but was reacted *in situ* with the appropriate metal (I) iodide precursor, in THF at 100 °C for 16 hours. In each case, the ^{1}H NMR and 2D NMR spectra are identical to those obtained by the metal redistribution synthesis (Figure S36-S50). Due to the fluxionality of the complexes, NMR characterisation proved difficult. The initial approach of simplifying the ^{1}H NMR spectra by using TCE at 403 K, successful for di-zinc complexes **4a** and **4b**, proved unsuccessful in this case (Figure 2.10). The initial NMR spectra displayed multiplicities (doublet doublet) in the phenyl region, indicative of a heterodinuclear complex, along with proton resonances ascribed to methylene and benzylic proton pairs. However, prolonged analysis at 403 K, in TCE, resulted in a decrease in the intensity of the resonances assigned to the heterodinuclear complex and in the evolution of resonances corresponding to di-zinc iodide (**4a**) and protonated ligand. Thus, it was concluded the heterodinuclear

complex reacted with the NMR solvent, with the precipitation of lithium chloride driving the decomposition. Hence, chlorinated solvents were not suitable for Group 1 metal complex analysis.

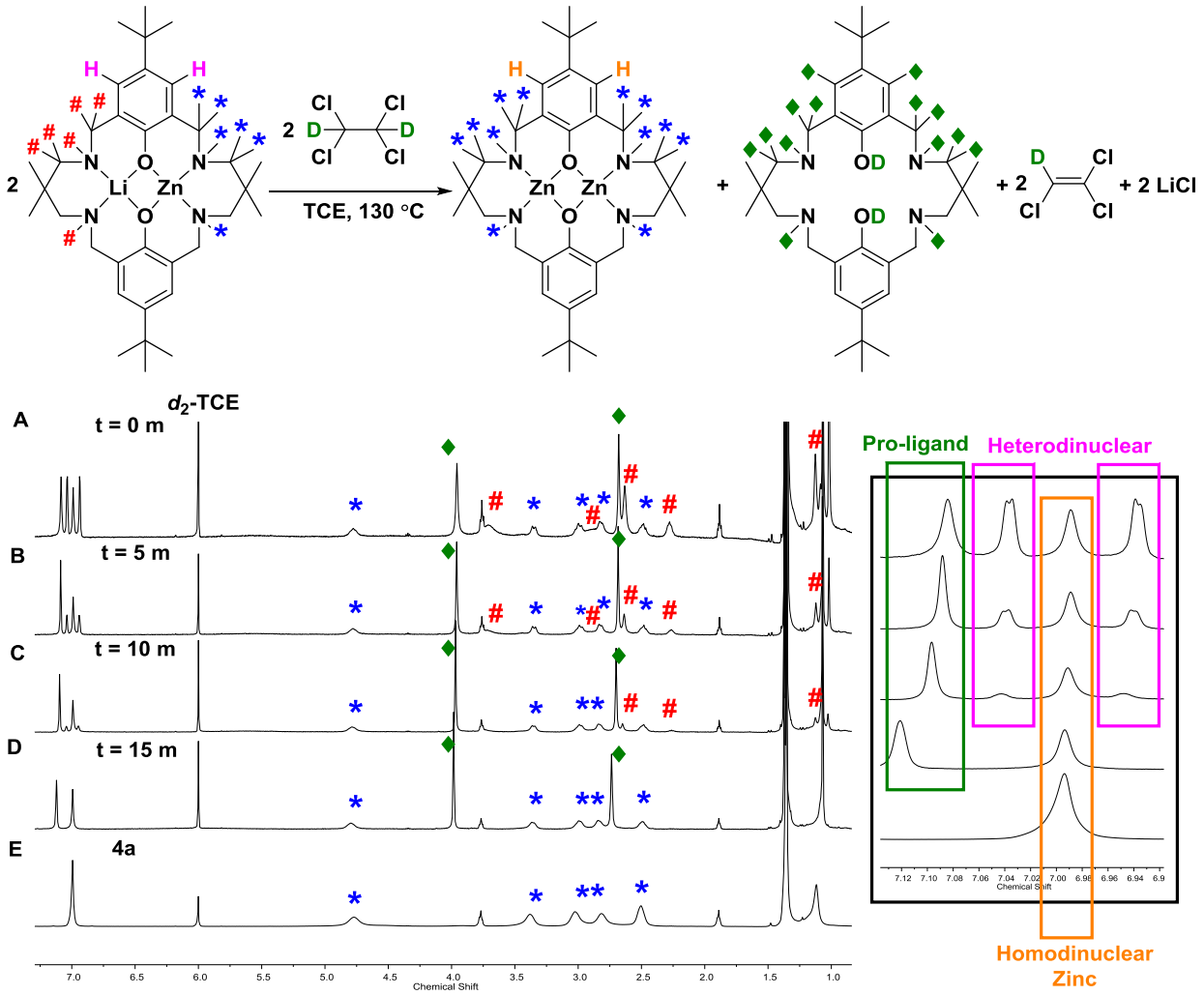


Figure 2.10: Reaction of complex **5** with d_2-TCE solvent at 130 °C, as followed by ^{1}H NMR spectroscopy.

Other solvents were used in an attempt to simplify the ^{1}H NMR spectrum such as toluene, pyridine, dimethylsulphoxide and 1,4-dioxane. All displayed very broad proton resonances which were difficult to assign. However, the ^{1}H NMR of complex **5a** in pyridine displayed clear coupling in the COSY NMR spectrum between the

phenyl proton resonances, indicative of heterodinuclear complex formation (Figure 2.11).

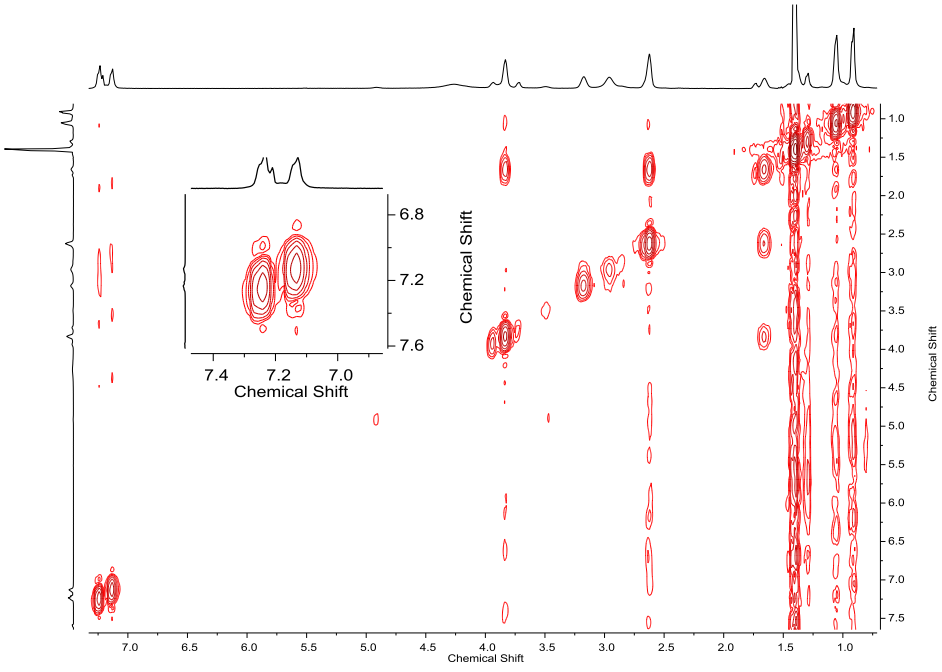


Figure 2.11: COSY NMR of complex **5a** (d_5-pyridine, 403 K)

Although NMR spectroscopy did not allow unambiguous confirmation of the heterodinuclear nature of complexes **5a** and **7a**, molecular cation peaks corresponding to $[LZnLi]^+$ and $[LZnK]^+$, at 623 m/z and 654 m/z, respectively, were observed in the MALDI-ToF mass spectra. Purity was also confirmed by elemental analysis.

Once again, the synthesis of complex **6a** was not feasible and resulted instead in the formation of mixtures of homodinuclear complexes **2** and **4a**. Complex **6a** could be isolated by careful temperature control (-78 °C) and slow addition of a sodium iodide solution (0.1 M in THF) to a dilute solution of 'mono-zinc' (11 mM in THF). Under these conditions, ^{1}H NMR spectroscopy indicated a 90 % conversion to heterodinuclear complex (Figure 2.12).

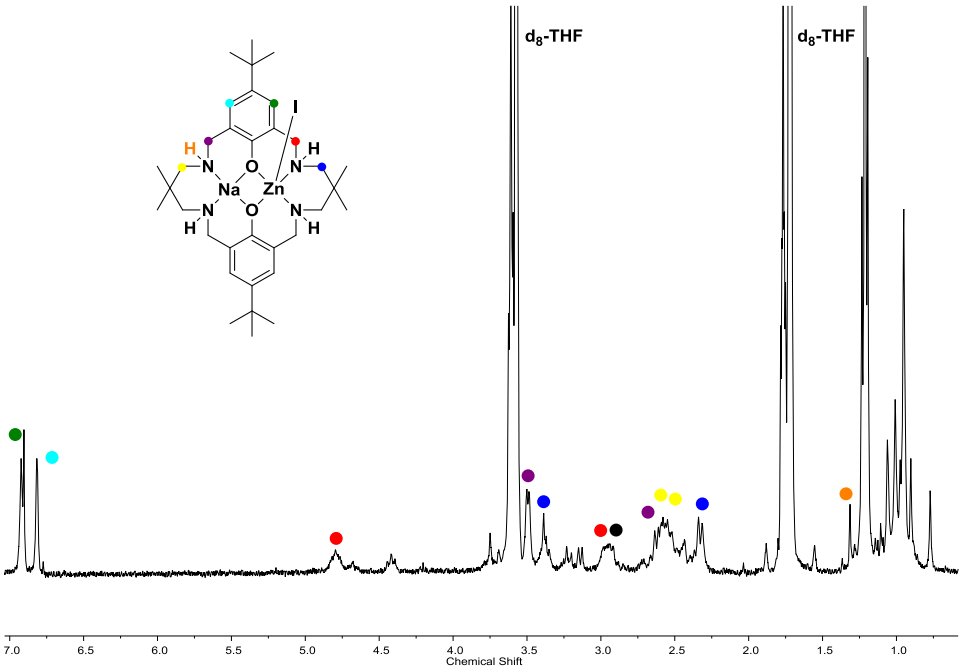


Figure 2.12: ^{1}H NMR spectrum of **6** with 90 % heterodinuclear content (d_8-THF, 298 K)

Nonetheless, the complex was unstable at 25 °C, and resulted in a reduction in the heterodinuclear content to 25 % after 16 h (Figure 2.13). These findings suggest that **6a** is accessed at low temperatures and hence will be unsuitable for CO_2/epoxide polymerisation catalysis since reactions are conducted at temperatures > 80 °C.

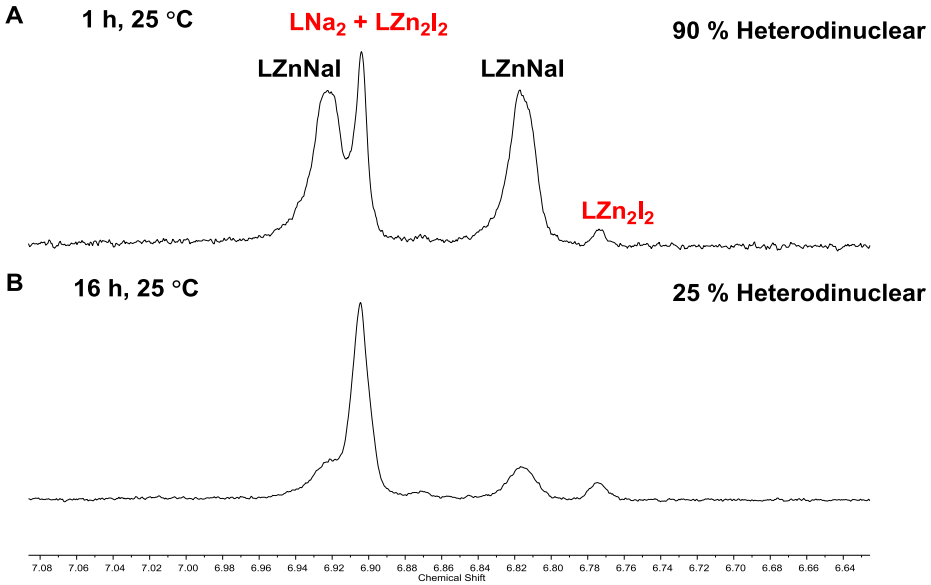


Figure 2.13: Metal redistribution of complex **6a** towards complexes **2** and **4a**.

Complexes **5b** and **7b** were also synthesised in the same manner as complexes **5a** and **7a**; characterised by multinuclear NMR spectroscopy and mass spectrometry with complex **5b** further characterised by single crystal X-ray diffraction. In the same manner as **5a**, **5b** could not be fully assigned due to the formation of multiple species in solution although coupling between the phenyl protons was observed, in the COSY NMR spectrum of **5a** at elevated temperatures, which indicates heterodinuclear complex formation (figure 2.14). The synthesis of **6b** was not targeted due to the relative instability of **6a**.

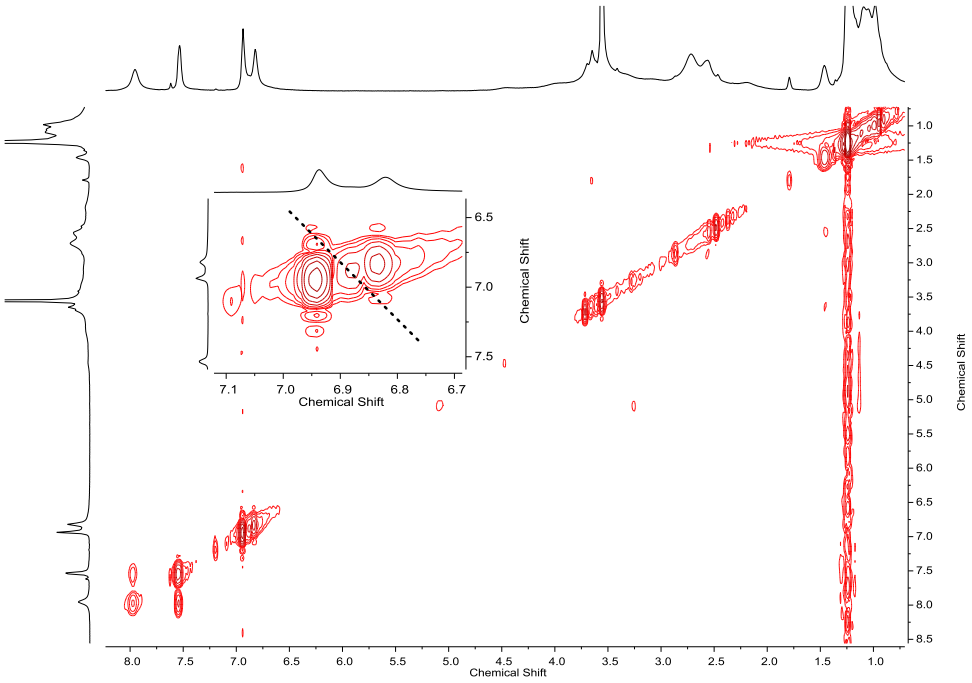


Figure 2.14: COSY NMR of complex **5b** (d_8-1,4-dioxane, 403 K)

In contrast to complex **7a**, **7b** displayed sharp proton resonances in its ^{1}H NMR spectrum, in d_8-THF at 25 °C (Figure 2.15). It may be that benzoate chelation provides additional stabilisation and thus reduces solution fluxionalality. In this spectrum, the benzylic and methylene resonances were assigned using COSY NMR spectroscopy.

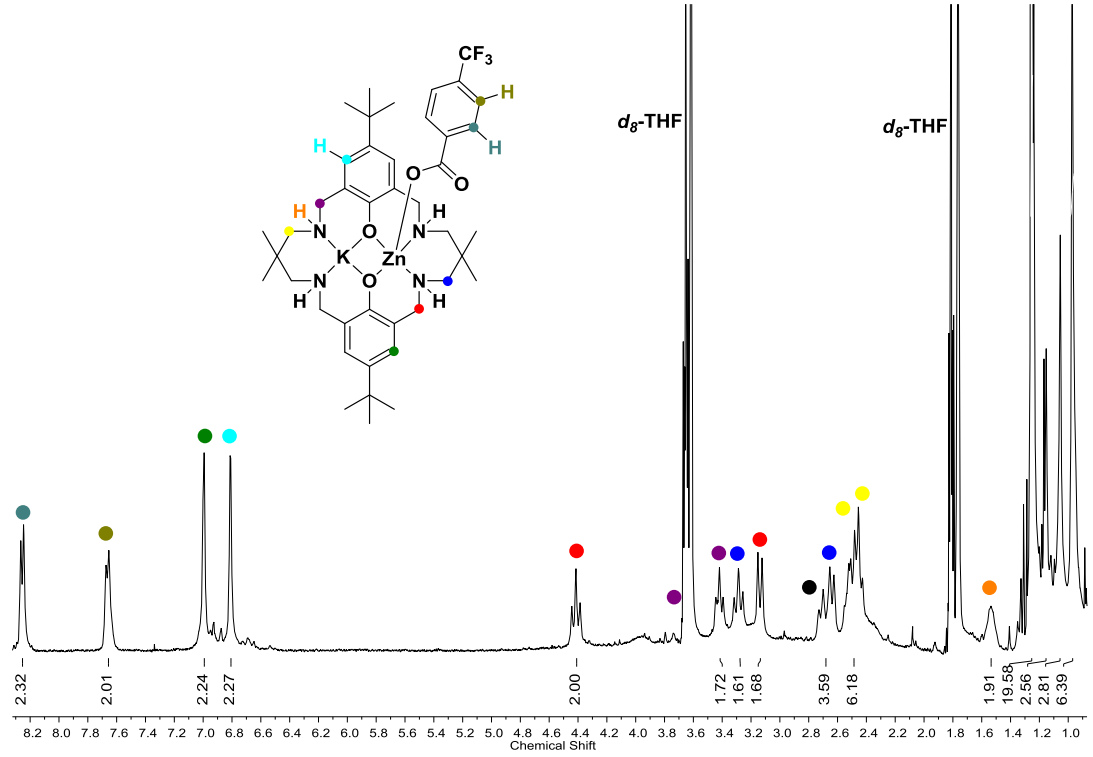


Figure 2.15: ^{1}H NMR of **7b** (d_8-THF, 298 K).

2D DOSY NMR experiment measured a diffusion coefficient of -9.250 log(m^2s^{-1}) indicating a single, monomeric species in the solution state (Figure 2.16).

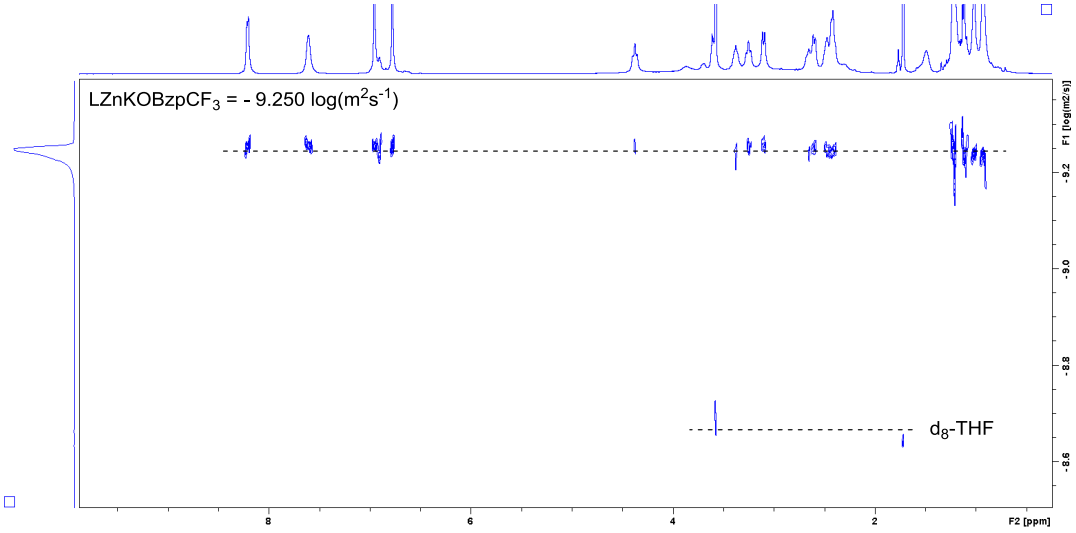


Figure 2.16: 2D DOSY NMR spectrum of complex **7b** (d_8-THF, 298 K).

The MALDI-ToF mass spectra of complexes **5b** and **7b** displayed peaks at 623 *m/z* and 654 *m/z* corresponding to the molecular cations $[LZnLi]^+$ and $[LZnK]^+$ respectively (Figure 2.17, S53-S54).

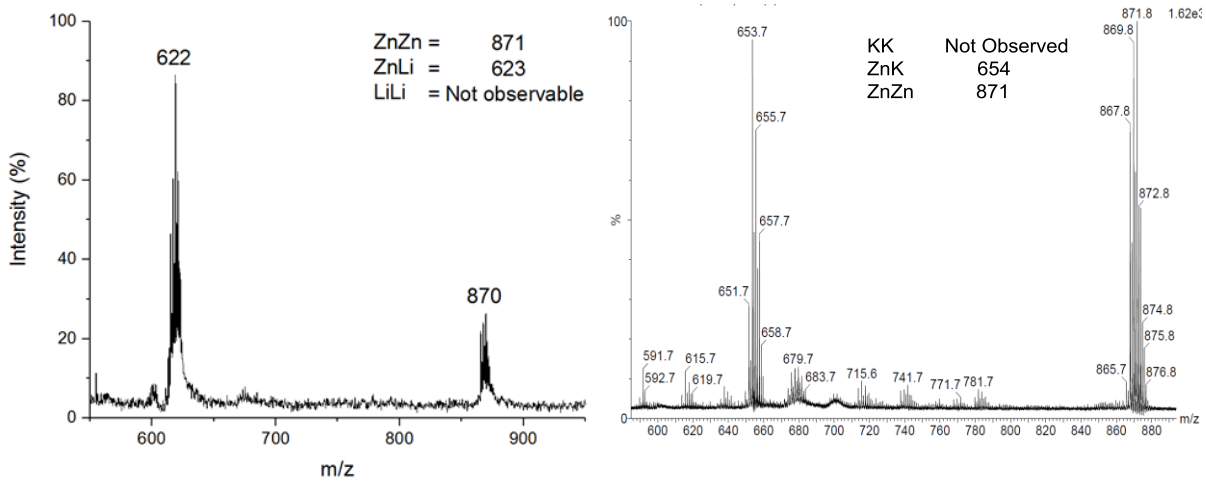


Figure 2.17: MALDI-ToF mass spectrum of complexes **5b** and **7b,** respectively

A single crystal of **5b** was isolated *via* recrystallization from DMSO and structural elucidation by X-ray crystallography showed the complex was monomeric in the solid state (Figure 2.18, S55). The ligand adopts an unusual 'crown-shape' conformation, with NH bonds alternating their direction around the macrocycle. The metal centres in the structure cannot be assigned as zinc or lithium due to their positional disorder, however, heterodinuclear complex formation is strongly indicated as only one co-ligand is present. In contrast, the di-lithium complex is dimeric with no co-ligands and the di-zinc complex has two co-ligands (Figure 2.15). Both metals adopt a pentacoordinate, square based pyramidal geometries (M_1 τ = 0.18, M_2 τ = 0.22). The intermetallic separation was measured to be 2.8612(8) Å.

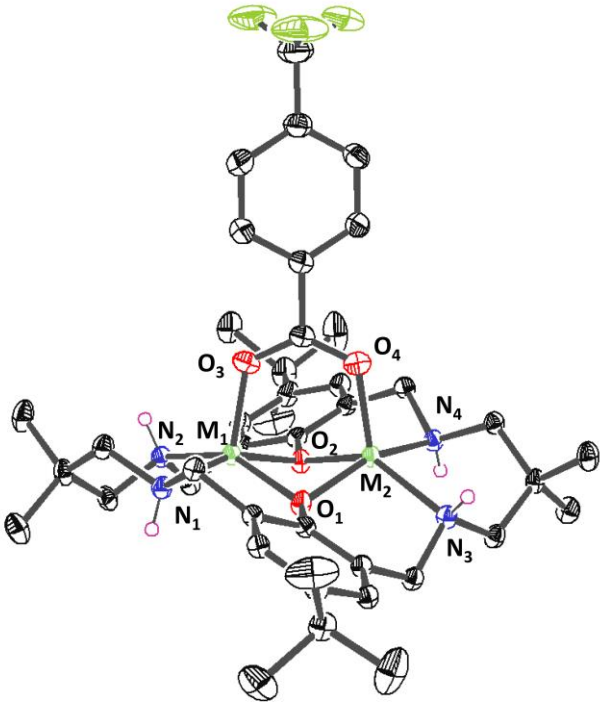
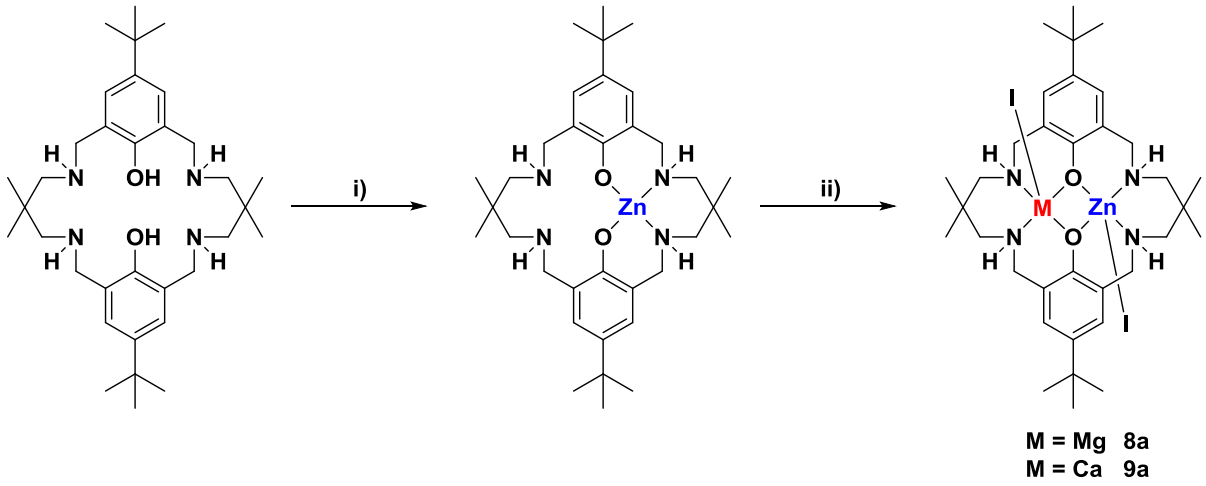


Figure 2.18: ORTEP representation of crystallographic structure of complex **5b** obtained by single crystal X-ray diffraction. Disorder and H-atoms (excluding NH) have been omitted for clarity, with thermal ellipsoids represented at 40 % probability. Selected bond lengths (Å) and angles (°) for complex 5b (Table S5).

2.1.7 Group 2-Zinc Sequential Metalation



Scheme 2.6: Synthesis of complexes **8a** and **9a**. i) $ZnEt_2$, THF, 25 °C. ii) MI_2 (M = Mg or Ca), THF, 100 °C, 16 h, > 70 %.

The analogous Group 2/Zn complexes **8a** and **9a** were successfully synthesised *via* the sequential metalation procedure (Scheme 2.6). In these cases, the monozinc intermediate was reacted *in situ* with the respective bis(iodide) metal (II) precursor, in THF at 100 °C. The complexes were isolated after 16 hours as white solids, in > 70 % yield. Complexes **8a** and **9a** were characterised by multinuclear NMR spectroscopy (Figure S56-S65), mass spectrometry (Figure S66-S67) and X-ray crystallography (Figure S68-S69), and bulk purity was confirmed by elemental analysis.

The ^{1}H NMR spectra of **8a** and **9a** displayed ten resonances between 2.0 and 5.2 ppm, assigned to the diastereotopic benzylic and methylene protons of the ligand (Figure 2.19). Chemical shifts common to both **8a** and **9a** were assigned to the zinc half of the macrocycle. Overall, proton resonances for **9a** are significantly broader compared to those for complex **8a**. This is perhaps due to a weaker complexation of calcium compared to magnesium due to its increased ionic radius (*vide infra*).

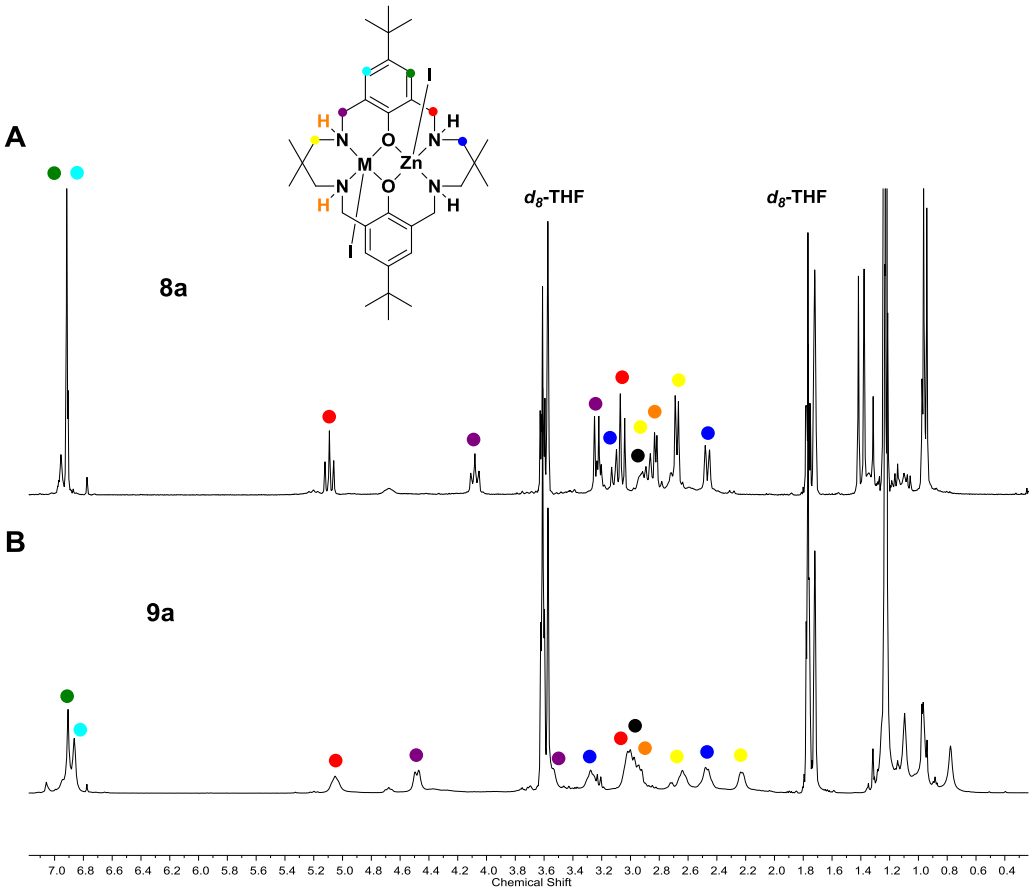


Figure 2.19: ^{1}H NMR spectra of A) complex **8a** and B) complex **9a**.

2D DOSY NMR experiments (Figure 2.20) confirmed all proton resonances diffuse with the same diffusion coefficient, indicating a single species in solution (figure 2.20). Values of -9.120 and -9.198 log(m^2s^{-1}) were determined for complexes **8a** and **9a**, both correspond to monomeric species in the solution state. MALDI-ToF mass spectrometry showed molecular cation peaks at 765 and 781 m/z, assigned to $[LZnMgI]^+$ and $[LZnCaI]^+$, respectively and with isotopic distributions matching predicted values.

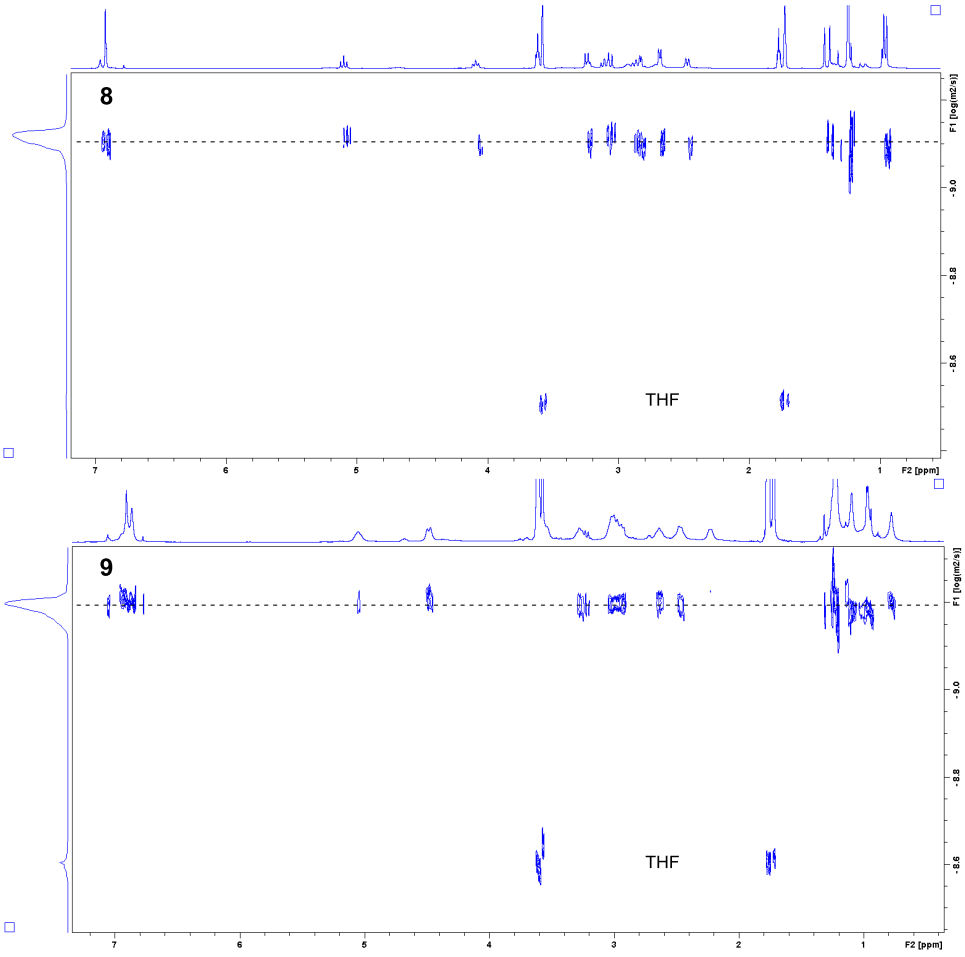


Figure 2.20: 2D DOSY NMR spectra of complexes **8a** and **9a,** respectively.

Single crystals of **8a** and **9a** were isolated *via* vapour diffusion of pentane into a saturated solution of complex in THF at –40 °C, under nitrogen (Figure 2.21). Both structures confirm the formation of discrete heterodinuclear complexes in the solid state. The ancillary ligand adopts slightly different coordination types, for **8a** a 'bowl' shape is observed in which all NH substituents are located on the same side of the complex, whereas for **9a** an 'S-shaped' conformation is revealed with only two NH substituents on the same face. In both structures, the zinc atoms are pentacoordinate and adopt a slightly distorted square based pyramidal coordination geometry (**8a**: τ = 0.09, **9a**: τ = 0.06). For complex **8a**, the magnesium centre is hexacoordinate and adopts an octahedral geometry and coordination by a THF molecule is observed (crystallization solvent). The coordination of THF is interesting since it provides a realistic model for epoxide coordination which is clearly relevant to the catalysis. Since the THF molecule is coordinated to the magnesium centre, it may indicate that in the catalytic reaction it is magnesium which activates the epoxide and zinc which provides the carbonate group. For complex **9a,** the calcium centre is heptacoordinate and adopts a capped-trigonal prismatic geometry and coordinates two THF molecules. The calcium atom also protrudes significantly, 1.300 Å, from the ligand coordination plane (formed by N(3)N(4)O(1)O(2)), particularly when compared to the analogous magnesium centre in complex **8a**, 0.153 Å. This lack of planarity in calcium coordination likely arises due to its larger ionic radius and expanded coordination number. The metal-zinc distances are 3.0616(17) and 3.3534(12) Å for complexes **8a** and **9a,** respectively, and sit within the range proposed as optimal for dinuclear ROCOP catalysis.[36, 44-45]

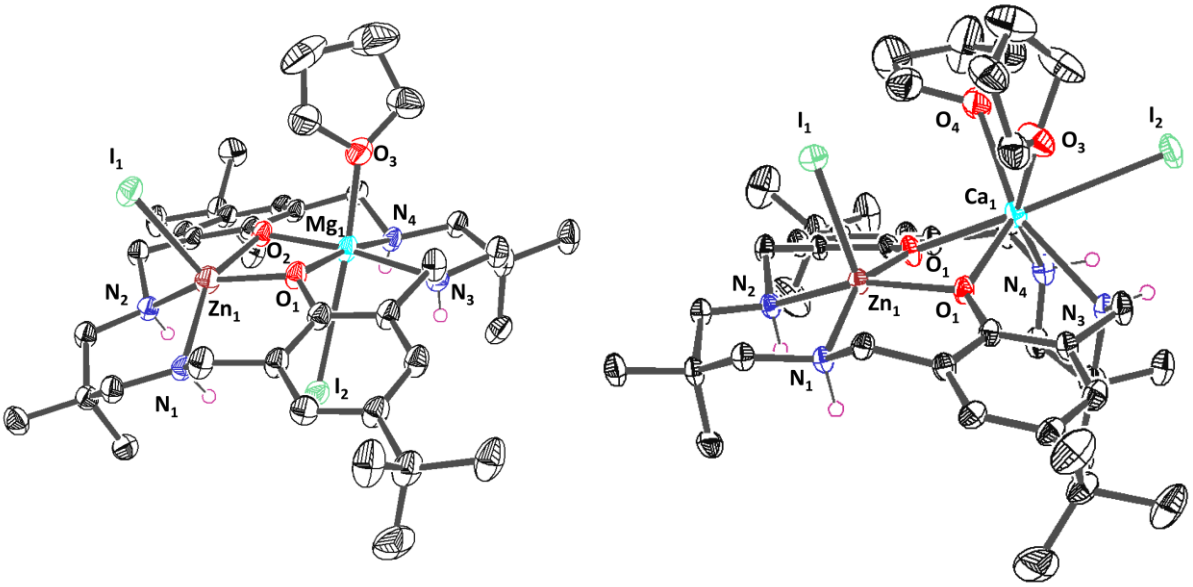


Figure 2.21: ORTEP representations of molecular structures of complexes **8a** (LHS) and **9a** (RHS), obtained by single crystal X-ray diffraction. Disorder and H-atoms (excluding NH) have been omitted for clarity, with thermal ellipsoides represented at 40 % probability. Selected bond lengths (Å) and angles (°) for complex 8a and 9a (Table S6-S7).

2.1.8 Ring Opening Copolymerization of CO_2 and Cyclohexene Oxide

Di-zinc complexes, **4**, and the new heterodinuclear complexes, **5-9**, were each tested in the ROCOP of CO_2 with CHO (Table 2.1). The polymerizations were carried out at 80 °C, using a 0.1 mol % catalyst loading and at 1 bar CO_2 pressure. Complexes **1-3**, were totally inactive, probably due to the lack of an initiating group. Nonetheless, this result is useful as it rules out the likelihood of any initiation from the ligand.

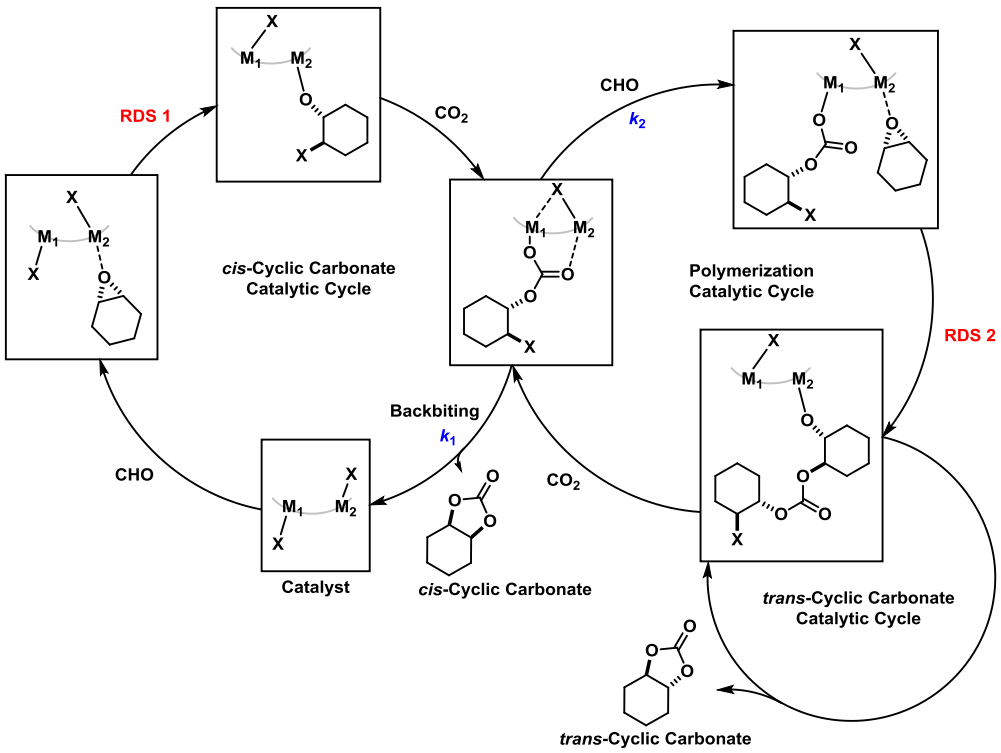
Table 2.1: ROCOP of CO_2 - CHO with catalysts **4a - 9a.**[a]

(M/M)	Cat.	Time (d)	TON[b]	TOF[c] (h^{-1})	CO_2[d] (%)	Polymer[e] (%)	Cyclic Carbonate	M_n [Đ][f]
(Zn/Zn)	**4a**	3	441	11	> 99	96	*4% Trans*	9800 [1.05] 4000 [1.09]
	4b	1	470	20	> 99	> 99	*<1% Trans*	11300 [1.05] 4900 [1.13]
(Zn/Li)	**5a**	3	20	0.4	> 99	0	*>99% Cis*	*n.d*
	5b	3	281	10	> 99	98	*2% Trans*	11000 [1.08] 4400 [1.13]
(Zn/K)	**7a**	3	27	0.6	> 99	0	*>99% Cis*	*n.d*
	7b	3	138	4	> 99	96	*4% Trans*	5600 [1.06] 2100 [1.11]
(Zn/Mg)	**8a**	0.25	430	72	> 99	99	*1% Trans*	17700 [1.03] 7600 [1.12]
(Zn/Ca)	**9a**	3	35	0.5	> 99	0	*>99% Cis*	*n.d*

[a]Copolymerisation conditions: cat : CHO 0.1 mol %, 1 bar CO_2. [b]Turnover number (TON) = number of moles of cyclohexene oxide consumed / number of moles of catalyst. [c]Turnover frequency (ToF) = TON / Time (h) for the final 24 h of reaction. [d]Expressed as a percentage of CO_2 uptake vs the theoretical maximum (100 %), determined by comparison of the relative integrals of the ^{1}H NMR resonances due to carbonate (δ 4.65 ppm) and ether (δ 3.45 ppm) linkages in the polymer backbone. [e]Expressed as a percentage of polymer formation vs. the theoretical maximum (100 %), determined by comparison of the relative integrals of the ^{1}H NMR proton resonances due to polymer (4.65 ppm), cis-cyclic carbonate (4.68 ppm) and trans-cyclic carbonate (4.00 ppm) (Fig. S71-S72). [f]Determined by SEC, in THF, using narrow-M_n polystyrene standards as the calibrant; dispersity is given in brackets.

All catalysts (**4a-9a**) displayed excellent selectivity towards CO_2 (> 99 %) with no ether linkages observed by ^{1}H NMR spectroscopy. Catalysts **4a, 4b, 8a** and **8b** showed a high selectivity for polycarbonate formation (> 96 %). Overall, heterodinuclear complex **8a** is six times more active than di-zinc **4a**, a finding that is in line with previous observations made using a heterodinuclear complex featuring

bromide co-ligands.[19] The polycarbonates have lower molar masses than theoretically calculated with bimodal distributions, in line with many other catalysts in the literature and consistent with initiation from both iodide and 1,2-cyclohexanediol groups, the latter forming by hydrolysis of the epoxide.[35, 38, 46-54]



Scheme 2.7: Proposed catalytic cycles rationalizing formation of *cis*-cyclic carbonate, *trans*-cyclic carbonate and/or poly(cyclohexene oxide). Where M1 = Li(I), K(I), Mg(II), Ca(II) and M2 = Zn(II); X = I or $OBzpCF_3$; and the macrocyclic ligand is abbreviated to a light grey 'bowl' shape, as commonly observed in the solid state structures. Where RDS stands for rate determining step.

A mechanistic hypothesis can be proposed to rationalise the formation of both *cis*-cyclic carbonate and poly(cyclohexene carbonate) products (Scheme 2.7). Accordingly, the reaction selectivity depends upon the relative rates of the backbiting reaction (k_1) vs. binding of the epoxide (k_2). The backbiting reaction is favoured by: (1) more ionic metal-oxygen bonds and (2) the presence of a good leaving group (X). One the other hand, epoxide binding and subsequent copolymerisation is favoured by: (1) highly Lewis acidic metals and (2) covalent metal-oxygen bond.

In accordance with this hypothesis, heterodinuclear complexes **5a**, **7a** and **9a** are selective for *cis*-cyclic carbonate formation (> 99 %). This selectivity results from the iodide ligand, which initiates ring-opening but subsequently becomes a good leaving group and accelerates the backbiting reaction. An additional driver may be the increased ionic character imparted to the metal carbonate bonds which may result in partial dissociation of the growing chain from the metal centre. In the ROCOP catalysis field, it has previously been proposed that ionic/metal-dissociated carbonate/alkoxide-polymer chains undergo faster back-biting reactions.[24-25, 55-57]

On the other hand, hetero-complexes **5b** and **7b** are very selective for polycarbonate formation and show a high uptake of CO_2 in the backbone, with no detectable ether linkages (Table 2.1). Indeed, complexes **4b, 5b, 7b** and **8b** all show high selectivity for polymer formation (> 96 %) which clearly demonstrates the importance of co-ligand selection. In addition to the altered selectivity, the activity of **5b** and **7b** is also significantly greater than the analogous complexes featuring iodide ligands, **5a** and **7a**. This is proposed to result from a change in rate limiting step from nucleophilic attack by an iodide on the epoxide (RDS 1) to metal-carbonate attack on the coordinated epoxide in the propagation cycle for the benzoate co-ligands (RDS 2). The activity is also higher for the lighter homologues in both Group 1 and Group 2 (i.e. for Li and Mg) perhaps due to its increased Lewis acidity and optimised coordination geometry (CN 5/6) for the rate determining epoxide ring-opening transition states. Considering the best catalyst in the series, Zn(II)/Mg(II) combinations lead to both the highest rates and selectivity for polymer formation and shows a solid state structure with THF coordinated at Mg(II) and thus it is proposed that Mg(II) coordinates epoxide (Lewis acid) which is attacked by a Zn(II) carbonate.

2.1.9 Conclusions

The efficient synthesis of a series of stable heterodinuclear complexes whereby, Zn(II) is coordinated with Li(I), K(I), Mg(II) and Ca(II) by a symmetrical macrocycle, were reported. The complexes were synthesised either by a sequential metalation or by heating the homodinuclear analogues for extended periods. Both approaches indicate that the heterodinuclear complexes are more thermodynamically stable than the homodinuclear counterparts. Such findings are in line with recent results demonstrating unexpected stability for other heteronuclear transition metal/main group combinations.[58] In terms of CO_2/epoxide polymerisation catalysis, the most active and selective catalyst features Mg(II)/Zn(II) with all the other hetero-combinations being much less active. The solid state structure of the Mg(II)/Zn(II) catalyst suggests epoxide coordination may occur at the magnesium centre, with the zinc carbonate attacking it. Catalytic reactivity trends highlight the subtle factors controlling rate, since replacing magnesium with any other Lewis acidic metals reduces rate. There is a clear opportunity for more detailed study of other Mg(II)/Zn(II) complexes and to moderate selectivity through appropriate co-ligand selection. More generally, these stable heterodinuclear complexes warrant investigation for other catalytic transformations, particularly those with mechanisms requiring substrate activation by a Lewis acidic site and subsequent labile metal-heteroatom bond attack. For example, these complexes could be of interest as catalysts for lactone ring-opening polymerisations, phosphate ester hydrolysis or even hydroamination/etherification reactions. An additional incentive for their development for catalysis is the relatively high abundance, low cost and low toxicity of the alkali or alkaline earth metals.

2.2.1 References

1. van der Vlugt, J. I.,Cooperative Catalysis with First-Row Late Transition Metals*, Eur. J. Inorg. Chem.,* **2012,** *2012*, (3), 363.
2. Mata, J. A.; Hahn, F. E.; Peris, E.,Heterometallic complexes, tandem catalysis and catalytic cooperativity*, Chem. Sci.,* **2014,** *5*, (5), 1723.
3. Hevia, E.; Chua, J. Z.; García-Álvarez, P.; Kennedy, A. R.; McCall, M. D.,Exposing the hidden complexity of stoichiometric and catalytic metathesis reactions by elucidation of Mg-Zn hybrids*, Proc. Natl. Acad. Sci.,* **2010,** *107*, (12), 5294.
4. Andrikopoulos, P. C.; Armstrong, D. R.; Barley, H. R. L.; Clegg, W.; Dale, S. H.; Hevia, E.; Honeyman, G. W.; Kennedy, A. R.; Mulvey, R. E.,Sodium Dialkyl-amidozincates: Alkyl or Amido Bases? An Experimental and Theoretical Case Study*, J. Am. Chem. Soc.,* **2005,** *127*, (17), 6184.
5. Mulvey, R. E.; Mongin, F.; Uchiyama, M.; Kondo, Y.,Deprotonative Metalation Using Ate Compounds: Synergy, Synthesis, and Structure Building*, Angew. Chem. Int. Ed.,* **2007,** *46*, (21), 3802.
6. Martínez-Martínez, A. J.; Kennedy, A. R.; Mulvey, R. E.; O'Hara, C. T.,Directed ortho-meta′- and meta-meta′-dimetalations: A template base approach to deprotonation*, Science,* **2014,** *346*, (6211), 834.
7. Crimmin, M. R.; Coates, G.; Bakewell, C.; Ward, B.; White, A.,Reactions of Fluoroalkanes with Mg-Mg Bonds: Scope, $sp^3{}_{C\text{-}F}$ / $sp^2{}_{C\text{-}F}$ Coupling and Mechanism*, Chem. Eur. J.,* **2018,** *24, 16282*.
8. Bakewell, C.; White, A. J. P.; Crimmin, M. R.,Reactions of Fluoroalkenes with an Aluminium(I) Complex*, Angew. Chem. Int. Ed.,* **2018,** *57*, (22), 6638.
9. Bakewell, C.; Ward, B. J.; White, A. J. P.; Crimmin, M. R.,A combined experimental and computational study on the reaction of fluoroarenes with Mg–Mg, Mg–Zn, Mg–Al and Al–Zn bonds*, Chem. Sci.,* **2018,** *9*, (8), 2348.
10. Chen, H.-Y.; Liu, M.-Y.; Sutar, A. K.; Lin, C.-C.,Synthesis and Structural Studies of Heterobimetallic Alkoxide Complexes Supported by Bis(phenolate) Ligands: Efficient Catalysts for Ring-Opening Polymerization of l-Lactide*, Inorg. Chem.,* **2010,** *49*, (2), 665.
11. Maudoux, N.; Roisnel, T.; Carpentier, J.-F.; Sarazin, Y.,Aluminum, Indium, and Mixed Yttrium–Lithium Complexes Supported by a Chiral Binap-Based Fluorinated Dialkoxide: Structural Features and Heteroselective ROP of Lactide*, Organometallics,* **2014,** *33*, (20), 5740.
12. Char, J.; Brulé, E.; Gros, P. C.; Rager, M.-N.; Guérineau, V.; Thomas, C. M.,Synthesis of heterotactic PLA from rac-lactide using hetero-bimetallic Mg/Zn–Li systems*, J. Organomet. Chem.,* **2015,** *796*, 47.
13. Kuwabara, J.; Takeuchi, D.; Osakada, K.,Early-late heterobimetallic complexes as initiator for ethylene polymerization. Cooperative effect of two metal centers to afford highly branched polyethylene*, Chem. Commun.,* **2006,** (36), 3815.
14. Li, H.; Marks, T. J.,Nuclearity and cooperativity effects in binuclear catalysts and cocatalysts for olefin polymerization*, Proc. Natal. Acad. Sci.,* **2006,** *103*, (42), 15295.
15. Delferro, M.; Marks, T. J.,Multinuclear Olefin Polymerization Catalysts*, Chem. Rev.,* **2011,** *111*, (3), 2450.

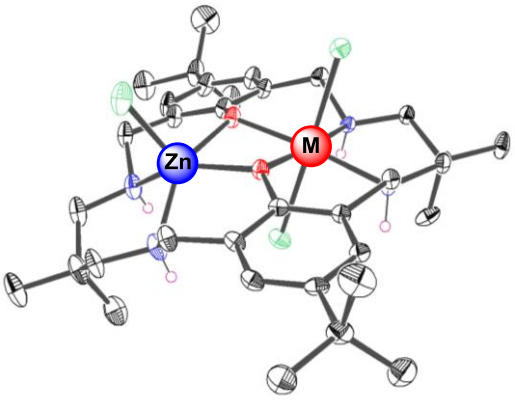
16. Liu, S.; Motta, A.; Delferro, M.; Marks, T. J.,Synthesis, Characterization, and Heterobimetallic Cooperation in a Titanium–Chromium Catalyst for Highly Branched Polyethylenes*, J. Am. Chem. Soc.,* **2013,** *135*, (24), 8830.
17. Mandal, S. K.; Roesky, H. W.,Assembling Heterometals through Oxygen: An Efficient Way To Design Homogeneous Catalysts*, Acc. Chem. Res.,* **2010,** *43*, (2), 248.
18. Saini, P. K.; Romain, C.; Williams, C. K.,Dinuclear metal catalysts: improved performance of heterodinuclear mixed catalysts for CO_2-epoxide copolymerization*, Chem. Commun.,* **2014,** *50*, (32), 4164.
19. Garden, J. A.; Saini, P. K.; Williams, C. K.,Greater than the Sum of Its Parts: A Heterodinuclear Polymerization Catalyst*, J. Am. Chem. Soc.,* **2015,** *137*, (48), 15078.
20. Garden, J. A.; White, A. J. P.; Williams, C. K.,Heterodinuclear titanium/zinc catalysis: synthesis, characterization and activity for CO_2/epoxide copolymerization and cyclic ester polymerization*, Dalton Transactions,* **2017,** *46*, (8), 2532.
21. Qin, J.; Xu, B.; Zhang, Y.; Yuan, D.; Yao, Y.,Cooperative rare earth metal–zinc based heterometallic catalysts for copolymerization of CO_2 and cyclohexene oxide*, Green Chem.,* **2016,** *18*, (15), 4270.
22. Nagae, H.; Aoki, R.; Akutagawa, S.; Kleemann, J.; Tagawa, R.; Schindler, T.; Choi, G.; Spaniol, T. P.; Tsurugi, H.; Okuda, J.; Mashima, K.,Lanthanide Complexes Supported by a Trizinc Crown Ether as Catalysts for Alternating Copolymerization of Epoxide and CO_2: Telomerization Controlled by Carboxylate Anions*, Angew. Chem. Int. Ed.,* **2018,** *57*, (9), 2492.
23. Trott, G.; Saini, P. K.; Williams, C. K.,Catalysts for CO_2/epoxide ring-opening copolymerization*, Philos. Trans. A. Math. Phys. Eng. Sci.,* **2016,** *374*, (2061).
24. Darensbourg, D. J.,Making Plastics from Carbon Dioxide: Salen Metal Complexes as Catalysts for the Production of Polycarbonates from Epoxides and CO_2*, Chem. Rev.,* **2007,** *107*, (6), 2388.
25. Lu, X. B.; Ren, W. M.; Wu, G. P.,CO_2 Copolymers from Epoxides: Catalyst Activity, Product Selectivity, and Stereochemistry Control*, Acc. Chem. Res.,* **2012,** *45*, (10), 1721.
26. Romain, C.; Thevenon, A.; Saini, P. K.; Williams, C. K., Dinuclear Metal Complex-Mediated Formation of CO_2-Based Polycarbonates. In *Carbon Dioxide and Organometallics*, Lu, X.-B., Ed. Springer International Publishing: Cham, 2016; pp 101.
27. Stößer, T.; Li, C.; Unruangsri, J.; Saini, P. K.; Sablong, R. J.; Meier, M. A. R.; Williams, C. K.; Koning, C.,Bio-derived polymers for coating applications: comparing poly(limonene carbonate) and poly(cyclohexadiene carbonate)*, Polym. Chem.,* **2017,** *8*, (39), 6099.
28. Lehenmeier, M. W.; Kissling, S.; Altenbuchner, P. T.; Bruckmeier, C.; Deglmann, P.; Brym, A.-K.; Rieger, B.,Flexibly Tethered Dinuclear Zinc Complexes: A Solution to the Entropy Problem in CO_2/Epoxide Copolymerization Catalysis?*, Angew. Chem. Int. Ed.,* **2013,** *52*, (37), 9821.
29. Kissling, S.; Lehenmeier, M. W.; Altenbuchner, P. T.; Kronast, A.; Reiter, M.; Deglmann, P.; Seemann, U. B.; Rieger, B.,Dinuclear zinc catalysts with unprecedented activities for the copolymerization of cyclohexene oxide and CO_2*, Chem. Commun.,* **2015,** *51*, (22), 4579.
30. Moore, D. R.; Cheng, M.; Lobkovsky, E. B.; Coates, G. W.,Mechanism of the Alternating Copolymerization of Epoxides and CO_2 Using β-Diiminate Zinc Catalysts: Evidence for a Bimetallic Epoxide Enchainment*, J. Am. Chem. Soc.,* **2003,** *125*, (39), 11911.

31. Nakano, K.; Nozaki, K.; Hiyama, T.,Asymmetric Alternating Copolymerization of Cyclohexene Oxide and CO_2 with Dimeric Zinc Complexes*, J. Am. Chem. Soc.,* **2003,** *125*, (18), 5501.
32. Peña Carrodeguas, L.; González-Fabra, J.; Castro-Gómez, F.; Bo, C.; Kleij, A. W.,AlIII-Catalysed Formation of Poly(limonene)carbonate: DFT Analysis of the Origin of Stereoregularity*, Chem. Eur. J.,* **2015,** *21*, (16), 6115.
33. González-Fabra, J.; Castro-Gómez, F.; Kleij, A. W.; Bo, C.,Mechanistic Insights into the Carbon Dioxide/Cyclohexene Oxide Copolymerization Reaction: Is One Metal Center Enough?*, ChemSusChem,* **2017,** *10*, (6), 1233.
34. Thevenon, A.; Cyriac, A.; Myers, D.; White, A. J. P.; Durr, C. B.; Williams, C. K.,Indium Catalysts for Low-Pressure CO_2/Epoxide Ring-Opening Copolymerization: Evidence for a Mononuclear Mechanism?*, J. Am. Chem. Soc.,* **2018,** *140*, (22), 6893.
35. Kember, M. R.; Knight, P. D.; Reung, P. T. R.; Williams, C. K.,Highly Active Dizinc Catalyst for the Copolymerization of Carbon Dioxide and Cyclohexene Oxide at One Atmosphere Pressure*, Angew. Chem. Int. Ed.,* **2009,** *48*, (5), 931.
36. Kember, M. R.; White, A. J. P.; Williams, C. K.,Highly Active Di- and Trimetallic Cobalt Catalysts for the Copolymerization of CHO and CO_2 at Atmospheric Pressure*, Macromolecules,* **2010,** *43*, (5), 2291.
37. Buchard, A.; Kember, M. R.; Sandeman, K. G.; Williams, C. K.,A bimetallic iron(iii) catalyst for CO_2/epoxide coupling*, Chem. Commun.,* **2011,** *47*, (1), 212.
38. Kember, M. R.; Williams, C. K.,Efficient Magnesium Catalysts for the Copolymerization of Epoxides and CO2; Using Water to Synthesize Polycarbonate Polyols*, J. Am. Chem. Soc.,* **2012,** *134*, (38), 15676.
39. Jutz, F.; Buchard, A.; Kember, M. R.; Fredriksen, S. B.; Williams, C. K.,Mechanistic Investigation and Reaction Kinetics of the Low-Pressure Copolymerization of Cyclohexene Oxide and Carbon Dioxide Catalyzed by a Dizinc Complex*, J. Am. Chem. Soc.,* **2011,** *133*, (43), 17395.
40. Buchard, A.; Jutz, F.; Kember, M. R.; White, A. J. P.; Rzepa, H. S.; Williams, C. K.,Experimental and Computational Investigation of the Mechanism of Carbon Dioxide/Cyclohexene Oxide Copolymerization Using a Dizinc Catalyst*, Macromolecules,* **2012,** *45*, (17), 6781.
41. Xiao, Y.; Wang, Z.; Ding, K.,Intramolecularly Dinuclear Magnesium Complex Catalyzed Copolymerization of Cyclohexene Oxide with CO_2 under Ambient CO_2 Pressure: Kinetics and Mechanism*, Macromolecules,* **2006,** *39*, (1), 128.
42. Piesik, D. F. J.; Range, S.; Harder, S.,Bimetallic Calcium and Zinc Complexes with Bridged β-Diketiminate Ligands: Investigations on Epoxide/CO_2 Copolymerization*, Organometallics,* **2008,** *27*, (23), 6178.
43. Range, S.; Piesik, D. F. J.; Harder, S.,Binuclear Magnesium, Calcium and Zinc Complexes Based on Bis(salicylaldimine) Ligands with Rigid Bridges*, Eur. J. Inorg. Chem.,* **2008,** (22), 3442.
44. Moore, D. R.; Cheng, M.; Lobkovsky, E. B.; Coates, G. W.,Electronic and Steric Effects on Catalysts for CO_2/Epoxide Polymerization: Subtle Modifications Resulting in Superior Activities*, Angew. Chem. Int. Ed.,* **2002,** *41*, (14), 2599.
45. Klaus, S.; Lehenmeier, M. W.; Anderson, C. E.; Rieger, B.,Recent advances in CO_2/epoxide copolymerization—New strategies and cooperative mechanisms*, Coord. Chem. Rev.,* **2011,** *255*, (13), 1460.
46. Nakano, K.; Nakamura, M.; Nozaki, K.,Alternating Copolymerization of Cyclohexene Oxide with Carbon Dioxide Catalyzed by (salalen)CrCl Complexes*, Macromolecules,* **2009,** *42*, (18), 6972.

47. Lu, X.-B.; Darensbourg, D. J.,Cobalt catalysts for the coupling of CO_2 and epoxides to provide polycarbonates and cyclic carbonates*, Chem. Soc. Rev.,* **2012,** *41*, (4), 1462.
48. Wu, G.-P.; Darensbourg, D. J.,Mechanistic Insights into Water-Mediated Tandem Catalysis of Metal-Coordination CO2/Epoxide Copolymerization and Organocatalytic Ring-Opening Polymerization: One-Pot, Two Steps, and Three Catalysis Cycles for Triblock Copolymers Synthesis*, Macromolecules,* **2016,** *49*, (3), 807.
49. Lee, B. Y.; Kwon, H. Y.; Lee, S. Y.; Na, S. J.; Han, S. I.; Yun, H.; Lee, H.; Park, Y. W.,Bimetallic Anilido-Aldimine Zinc Complexes for Epoxide/CO_2 Copolymerization*, J. Am. Chem. Soc.,* **2005,** *127*, (9), 3031.
50. Sugimoto, H.; Kuroda, K.,The Cobalt Porphyrin−Lewis Base System: A Highly Selective Catalyst for Alternating Copolymerization of CO_2 and Epoxide under Mild Conditions*, Macromolecules,* **2008,** *41*, (2), 312.
51. Nakano, K.; Kobayashi, K.; Nozaki, K.,Tetravalent Metal Complexes as a New Family of Catalysts for Copolymerization of Epoxides with Carbon Dioxide*, J. Am. Chem. Soc.,* **2011,** *133*, (28), 10720.
52. Nakano, K.; Kobayashi, K.; Ohkawara, T.; Imoto, H.; Nozaki, K.,Copolymerization of Epoxides with Carbon Dioxide Catalyzed by Iron−Corrole Complexes: Synthesis of a Crystalline Copolymer*, J. Am. Chem. Soc.,* **2013,** *135*, (23), 8456.
53. Kember, M. R.; Copley, J.; Buchard, A.; Williams, C. K.,Triblock copolymers from lactide and telechelic poly(cyclohexene carbonate)*, Polym. Chem.,* **2012,** *3*, (5), 1196.
54. Decortes, A.; Haak, R. M.; Martín, C.; Belmonte, M. M.; Martin, E.; Benet-Buchholz, J.; Kleij, A. W.,Copolymerization of CO_2 and Cyclohexene Oxide Mediated by Yb(salen)-Based Complexes*, Macromolecules,* **2015,** *48*, (22), 8197.
55. Darensbourg, D. J.; Wei, S. H.,Depolymerization of Polycarbonates Derived from Carbon Dioxide and Epoxides to Provide Cyclic Carbonates. A Kinetic Study*, Macromolecules,* **2012,** *45*, (15), 5916.
56. Darensbourg, D. J.; Moncada, A. I.; Wei, S. H.,Aliphatic Polycarbonates Produced from the Coupling of Carbon Dioxide and Oxetanes and Their Depolymerization via Cyclic Carbonate Formation*, Macromolecules,* **2011,** *44*, (8), 2568.
57. Wu, G.-P.; Wei, S.-H.; Ren, W.-M.; Lu, X.-B.; Li, B.; Zu, Y.-P.; Darensbourg, D. J.,Alternating copolymerization of CO_2 and styrene oxide with Co(iii)-based catalyst systems: differences between styrene oxide and propylene oxide*, Energy Environ. Sci.,* **2011,** *4*, (12), 5084.
58. Butler, M. J.; Crimmin, M. R.,Magnesium, zinc, aluminium and gallium hydride complexes of the transition metals*, Chem. Commun.,* **2017,** *53*, (8), 1348.

Chapter 3:

Group 13-Zinc(II) Heterodinuclear Catalysts for CO_2/Epoxide Ring Opening Copolymerisation.



Rate of CO_2/CHO

Zn(II) > In(III) > Ga(III)> Al(III)

High Heterodinuclear Purity (> 90 %) ☑

Polyether Linkages
Al(III) > Ga(III) > In(III) > Zn(II) ☑

Cationic Complex
Selectively Polyether Linkages ☑

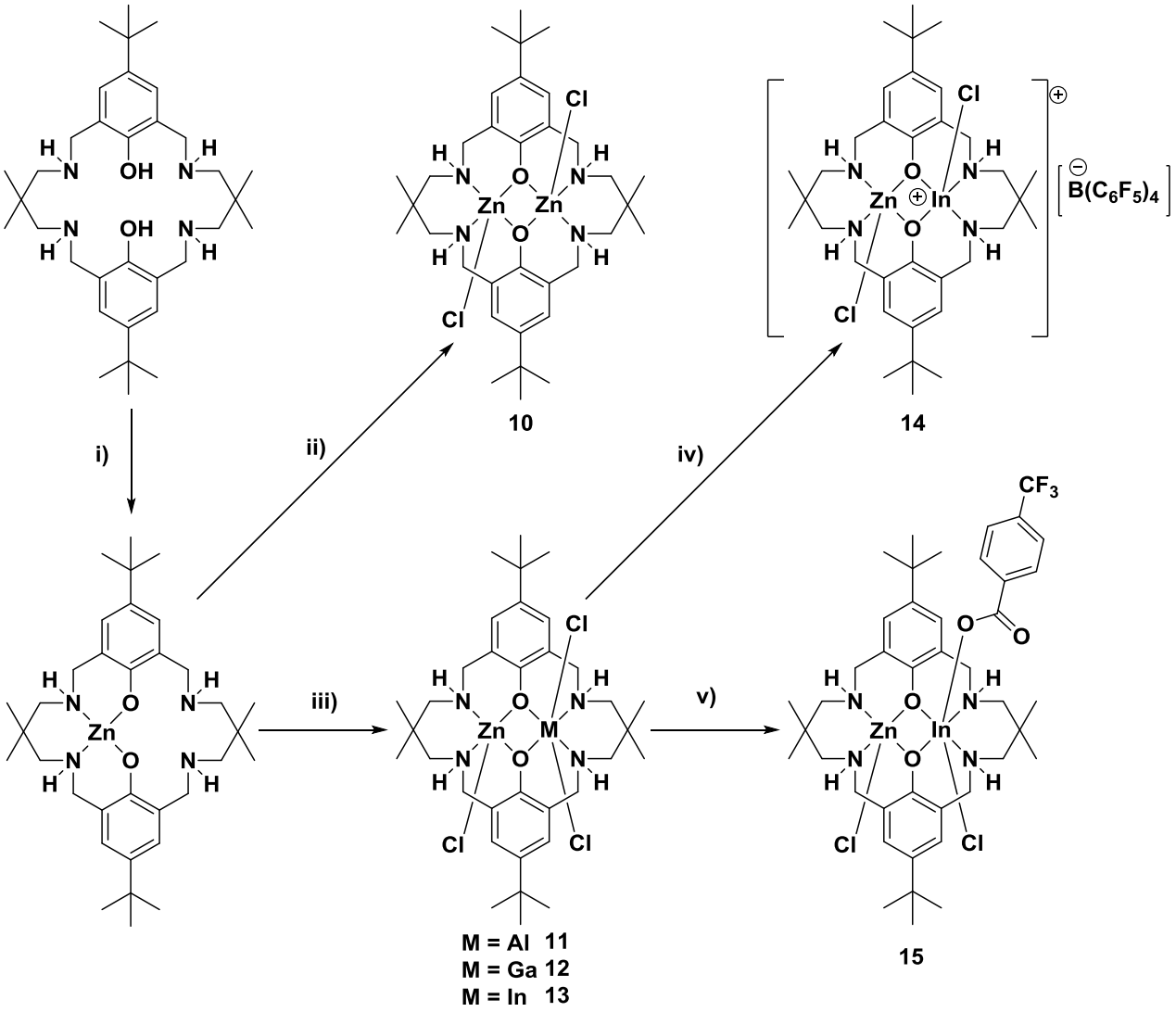
3.1.1. Introduction

Chapter 2 presents a range of heterodinuclear metal complexes featuring Zn(II) with alkali or alkaline-earth metals, but none were especially notable and all showed lower activity and selectivity than the di-zinc analogue.[1] The key design criteria are that catalysts should feature a highly Lewis acidic metal, together with a metal centre with a labile carbonate bond. Furthermore, all bonds should be covalent as increased ionic character results in backbiting to form cyclic carbonate. [2-8] Here, heterodinuclear complexes of Zn(II) with Group 13 elements are targeted because these metals should show sufficiently small radii ($r < 80$ pm) to enable successful in-plane coordination of both metals in the macrocycle cavity.

Group 13 elements have a track record as effective metal sites for this catalysis, although remain generally less researched than transition metal analogues. Al(III) complexes, coordinated by salen,[7] porphyrin[8-10] or trisphenolate[11-12] ligands, are all active for CO_2/epoxide polymerisations. In all cases ionic co-catalysts, such as PPNCl, must be added to ensure acceptable rates and selectivity. Very recently, the first In(III) catalysts showed activity, without co-catalyst, under 1 bar CO_2 pressure.[13]

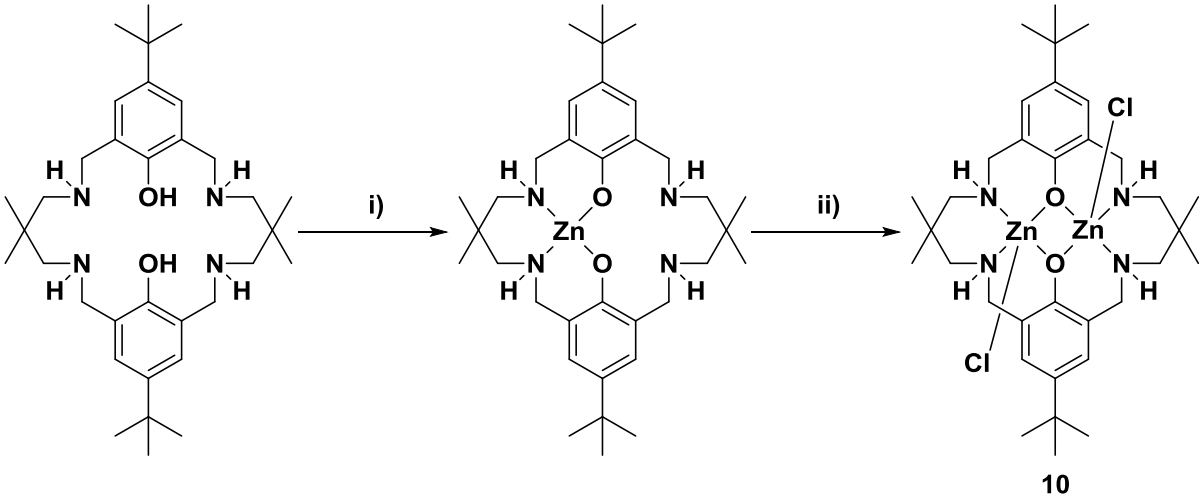
3.1.2 Aims

An outline of the synthetic routes and targeted catalysts, **10**-**15**, are shown in Scheme 3.1. The thermodynamic sequential metalation method (Chapter 2) is utilised to synthesise the heterodinuclear complexes due to the likelihood of the heterodinuclear complexes being the thermodynamic product.



Scheme 3.1: Synthetic pathway to synthesise complexes 10-15. i) $ZnEt_2$, THF, 25 °C, 16 h. ii) $ZnCl_2$, THF, 100 °C, 16 h, 81 % iii) MCl_3 (where M = Al (95 %), Ga (72 %) or In (86 %)), THF, 100 °C, 16 h. iv) $K[B(C_6F_5)_4]$, THF, 25 °C, 16 h, 90 %. v) KOBz*p*CF_3, MeOH, 25 °C, 16 h, 95 %.

3.1.3 Synthesis and characterisation of di-zinc chloride



Scheme 3.2: Synthesis of homodinuclear complex **10**. i) $ZnEt_2$, THF, 25 °C, 16 h. ii) $ZnCl_2$, THF, 100 °C, 16 h, 81 %.

Firstly, the di-zinc complex (**10**) was prepared as a necessary bench mark to allow for comparison with the new heterodinuclear chloride complexes. The ligand was deprotonated with diethyl zinc, in THF at 25 °C, to yield, *in situ*, the mono-zinc complex. This species was reacted *in situ* with further addition of $ZnCl_2$, in THF, and the reaction was heated to 100 °C for 16 h. The complex was isolated, without further purification, as a white powder in > 80 % isolated yield. It was characterised by NMR spectroscopy (Figure S70-S71), mass spectrometry (Figure S72) and X-ray crystallography (Figure S73) with purity determined by elemental analysis.

The ^{1}H NMR spectrum of (**10**), in TCE at 403 K, displays five resonances between 2.2 ppm and 5.0 ppm, assigned to the benzylic, methylene and amine diastereotopic protons. A single resonance at 7.00 ppm corresponding to the phenyl protons indicates a symmetrical macrocyclic complex. The ^{13}C{^{1}H} NMR spectrum displays two signals at 58.7 and 64.5 ppm, corresponding to the benzylic and methylene carbon atoms, and two phenyl carbon signals at 125.5 ppm and 128.4 ppm, assigned to the *ortho*- and *meta*- phenyl carbon environments. The ^{1}H and ^{13}C{^{1}H} NMR spectra are in-line with other di-zinc complexes including with acetate, phenyl, benzoate and iodide coligands. The MALDI-ToF mass spectrum displays a peak at 717 m/z, corresponding to the molecular cation $[LZn_2(Cl)]^+$.

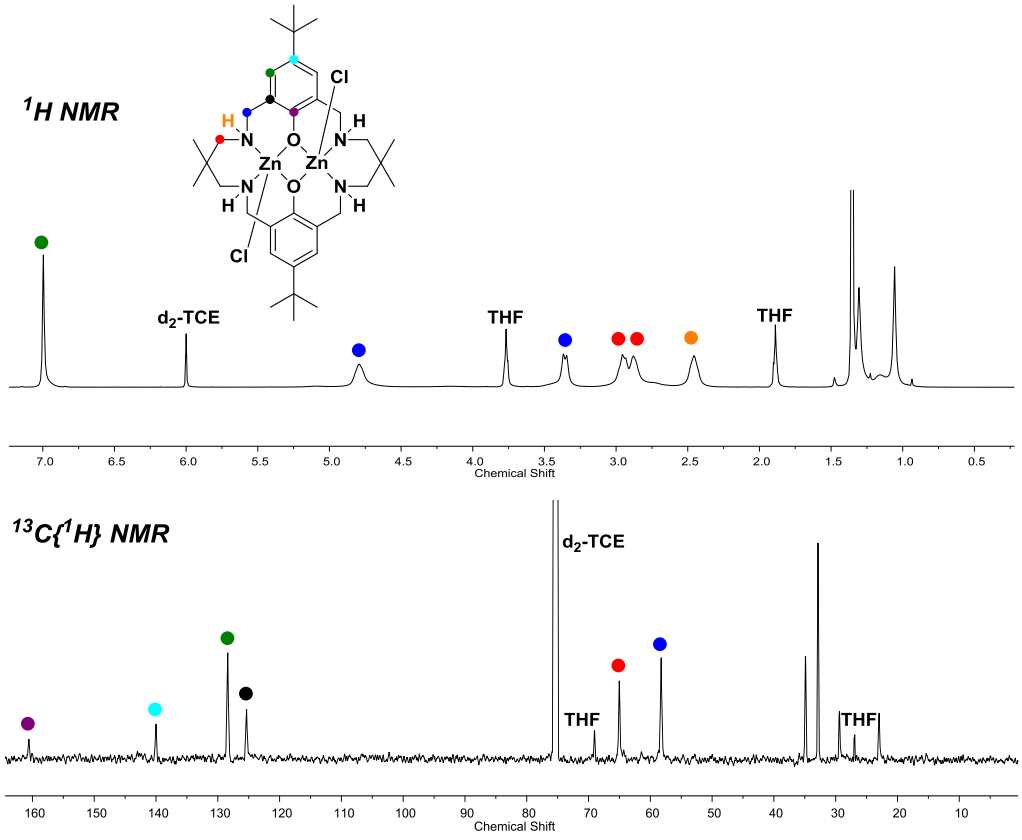


Figure 3.1: Top: ^{1}H, Bottom: ^{13}C{^{1}H}, NMR spectra of complex **10** (d_2-TCE, 403 K).

A single crystal of complex (**10**), suitable for X-ray crystallography, was isolated by vapour diffusion of pentane into a saturated solution of the complex, in acetonitrile, at -40 °C. Structural elucidation reveals a monomeric structure where the ligand adopts a 'bowl' conformation. Both zinc (II) centres adopt a pentacoordinate, square based pyramidal, geometries (τ = 0.35 Zn_1, τ = 0.15 Zn_2). The intermetallic distance is 3.0405(3) Å and is typical of other di-zinc complexes.[14-16]

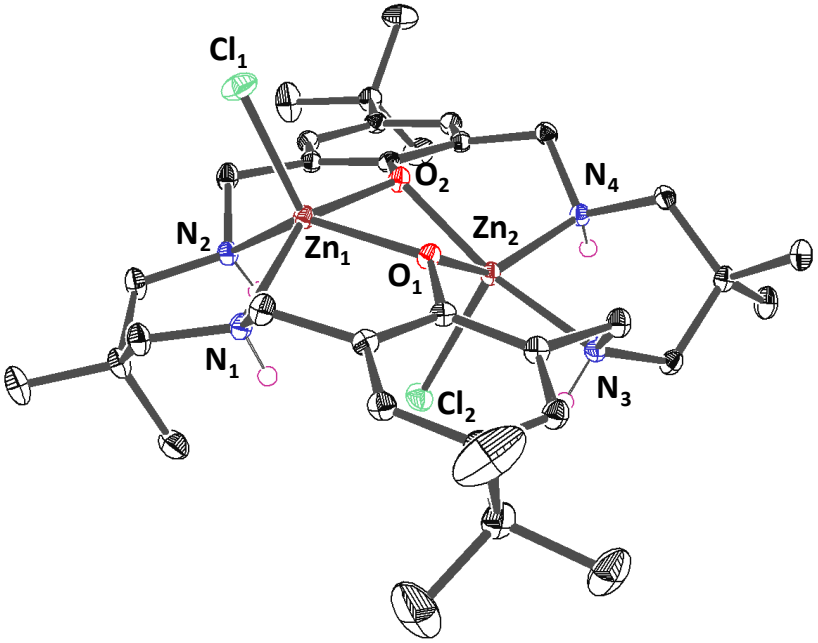
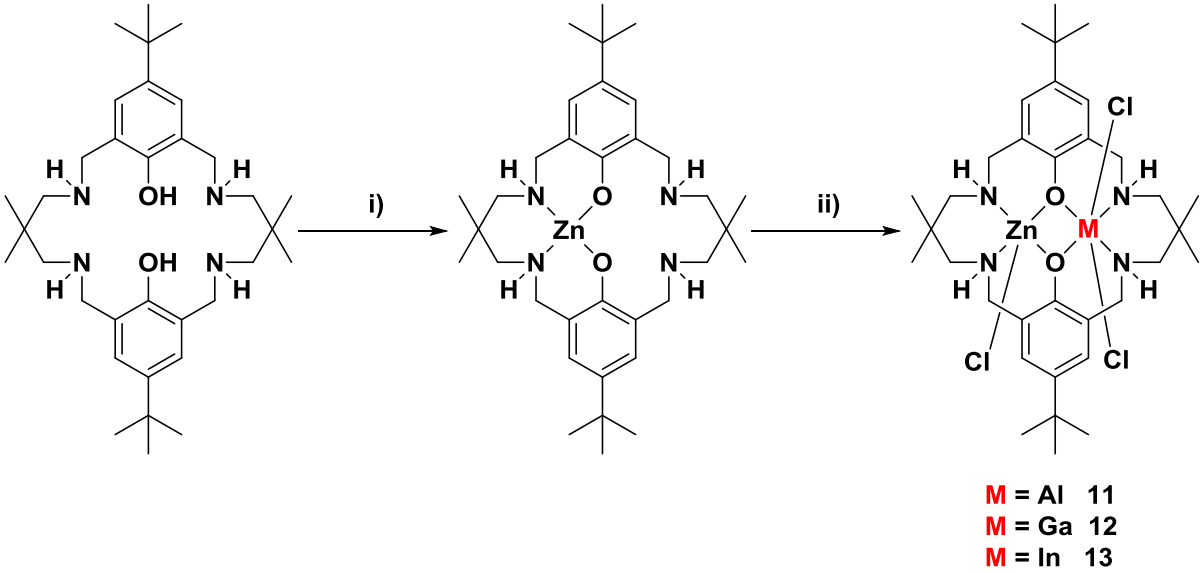


Figure 3.2: ORTEP representation of the crystallographic structure of complex **10**, obtained by single crystal X-ray diffraction. Disorder and H-atoms (excluding N-H) have been omitted for clarity, with thermal ellipsoids represented at 40 % probability. Selected bond lengths (Å) and angles (°) for complex 10 (Table S8).

3.1.4 Synthesis a characterisation of Group 13 hetero-complexes



Scheme 3.3: Synthesis of heterodinuclear complexes **11-13**. i) $ZnEt_2$, THF, 25 °C, 16 h. ii) MCl_3, THF, 100 °C, 16 h, (M = Al; 95 %, M = Ga; 72 %, M = In; 86 %).

Heterodinuclear complexes **11-13** were synthesised using the sequential mono metalation synthetic procedure. The ligand was reacted with diethyl zinc, in THF at 25 °C, followed by the addition of MCl_3 (where M = Al, Ga or In) in THF, and the mixture was heated to 100 °C for 16 h. The complexes were isolated as white powders in > 70 % yield and were all characterised by NMR spectroscopy (Figure S74-S94), mass spectrometry (Figure S78, S86 and S93) and X-ray crystallography (Figure S80, S87 and S94), with purity confirmed by elemental analysis.

NMR spectroscopy is used to determine the success of heterodinuclear synthesis by comparison with the homodinuclear di-zinc complex (**10**). The heterodinuclear complex lacks C_2 symmetry and thus all the phenyl, benzylic, amine and methylene protons are observed. Coupling between the two phenyl protons resonances, at 7.00 ppm, is observed in the 2D COSY NMR spectrum, indicative of a heterodiunclear complex. The ^{1}H NMR spectrum was also used to infer an approximate heterodinuclear purity, by comparing the integrals assigned to the di-zinc and heterodinuclear complexes, respectively. This analysis indicates that the heterodinuclear complexes are formed as the major product in all cases, with values of 90 %, 95 % and > 99 % for complexes **11**, **12** and **13**, respectively.

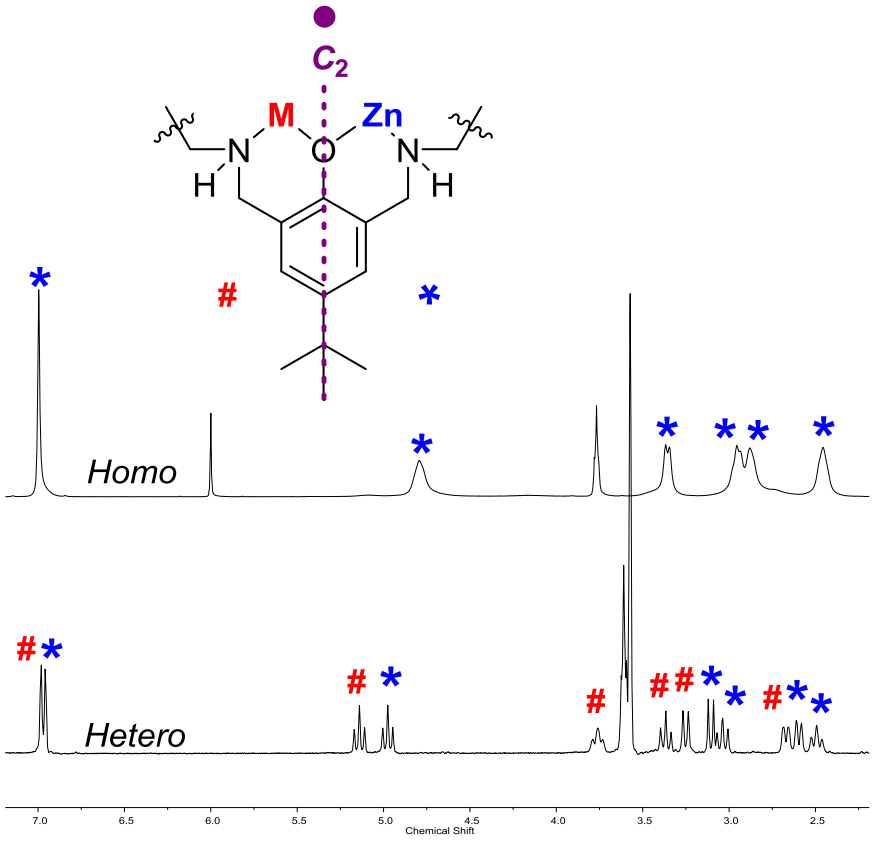


Figure 3.3: ^{1}H NMR of the homodinuclear zinc complex (**10**, d_2-TCE) and heterodinuclear indium complex (**13**, d_8 THF).

The $^{13}C\{^1H\}$ NMR spectrum also shows all the methylene, benzylic, *ortho*-phenyl and *meta*-phenyl carbon environments. Diagnostic evidence for the heterodinuclear complex is the single resonance for each of the *ipso*-phenyl and *para*-phenyl carbon environments at approx. 160 ppm and 140 ppm, respectively. A mixture of homodinuclear complexes would display two signals each for these carbon centres.

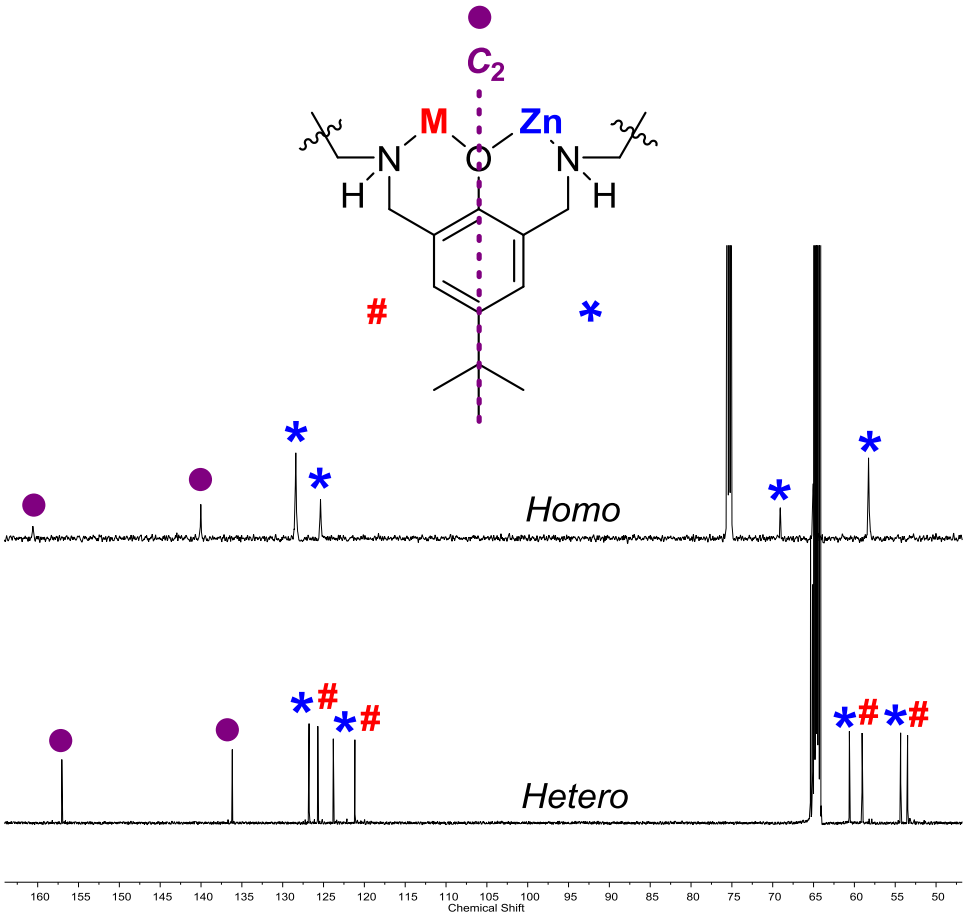


Figure 3.4: $^{13}C\{^1H\}$ NMR spectrum of homodinuclear zinc complex (**10**) and heterodinuclear indium complex (**13**). (d_8-THF)

2D DOSY NMR spectroscopy showed a single diffusion coefficient (-8.962 - -9.176 log(m^2s^{-1})), consistent with a discrete heterodinuclear complex in solution. MALDI-ToF mass spectra showed molecular ions corresponding to the cation $[LZnM(Cl)_2]^+$ at 714 m/z, 755 m/z and 800 m/z, where M = Al, Ga and In for complexes **11**, **12** and **13**, respectively.

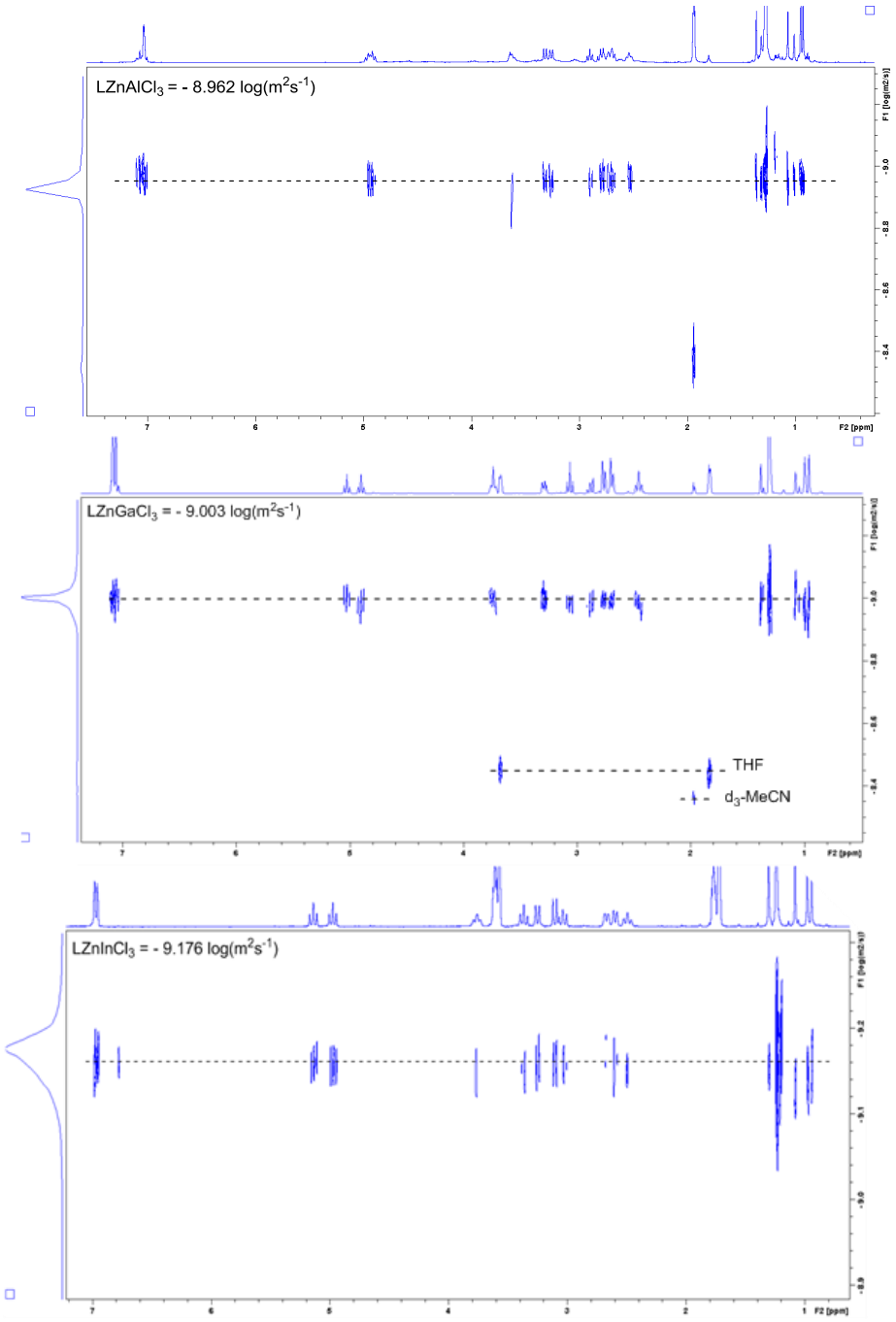


Figure 3.5: 2D DOSY NMR of complexes **11**, **12** (d_3-MeCN) and **13** (d_8-THF).

Single crystals of complexes **11**-**13** suitable for X-ray crystallography were isolated by diffusion of pentane into a saturated solution of the complex in acetonitrile (**11** and **12**) or THF (**13**), at -40 °C in a glovebox. Structural elucidation confirmed the formation of heterodinuclear complexes, which are monomeric in the solid state, and contain three chloride co-ligands. All are isostructural, with the macrocycle adopting a 'bowl' shape conformation and each zinc centre adopting a pentacoordinate, distorted square based pyramidal geometry (τ = 0.07 Zn_1 (**11**), τ = 0.02 Zn_1 (**12**), τ = 0.01 Zn_1 (**13**)) bound by two amino-nitrogen centres, two phenolic-oxygen centres and a chloride co-ligand. The Group 13 metals occupy an octahedral coordination geometry and are coordinated by two amino-nitrogen centres, two phenolic-oxygen centres and an two chloride co-ligands to balance charge. In complexes **11**-**13**, one of the chloride ligands bridges between the two metal centres, indicating a κ^2 binding mode. The Zn-Cl_1 bond distances are 2.29(8) Å, 2.11(1) Å and 2.06(1) Å compared with Zn-Cl_3 distances of 3.38(7) Å, 3.28(1) Å and 3.42(1) Å for complexes **11**, **12** and **13**, respectively. The intermetallic distances may suggest a trend increasing down the Group 13 elements, however, all are within error: 3.02297(3) Å, 3.123(2) Å and 3.15788(10) Å for **11**, **12** and **13**, respectively. All distances fall within the range of values reported for other successful dinuclear CO_2/epoxide polymerisation catalysts.[16-17]

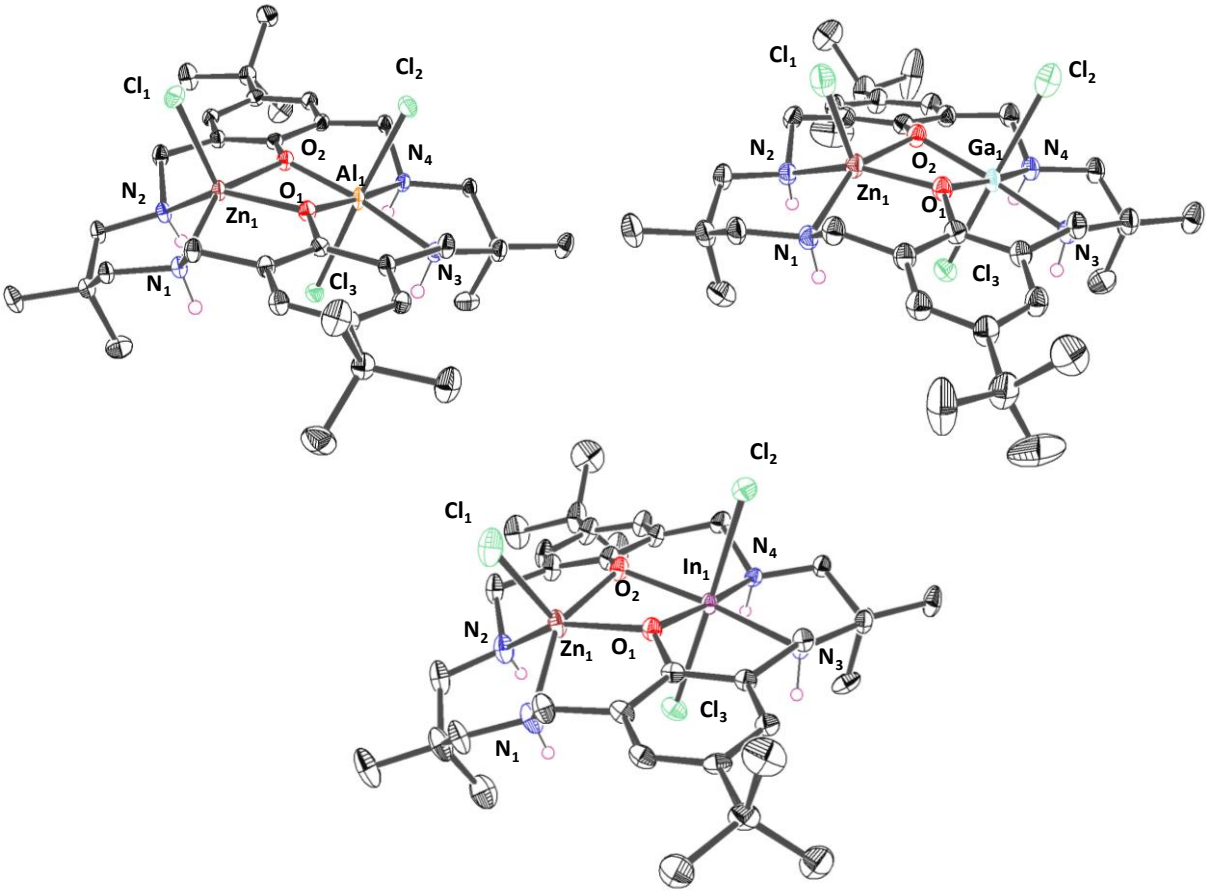


Figure 3.6: ORTEP representation of crystallographic structures of complexes **11** (Top LHS), **12** (TOP RHS) and **13** (Bottom), obtained by single crystal X-ray diffraction. Disorder and H-atoms (excluding NH) have been omitted for clarity, with thermal ellipsoids represented at 40 % probability. Selected bond lengths (Å) and angles (°) for complexes 11-13 (Table S9-S11).

3.1.5 ROCOP of CO_2-CHO with complexes 10-13

All heterocomplexes, **11-13**, were investigated as catalysts for CO_2/CHO ROCOP and compared against the di-zinc catalyst (**10**). Conditions were standardised to 80 °C, 0.1 mol % catalyst loading and tested at 1 bar CO_2 pressure, as has been established to obtained good activities with other catalysts using the same macrocyclic ligand.

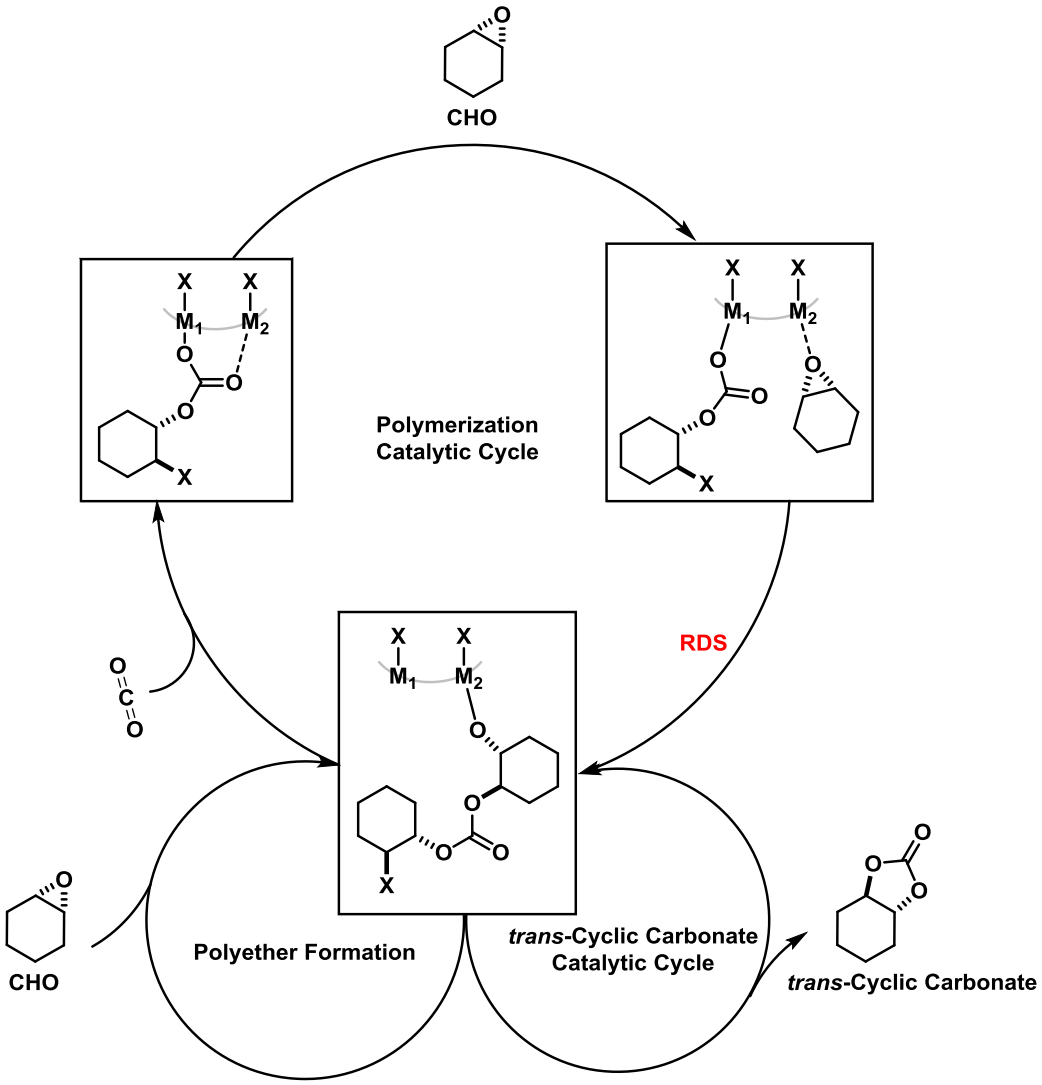
Table 3.1: ROCOP of CO_2/CHO with complexes **10-13**.

Cat.	Time (d)	TON [b]	ToF (h^{-1}) [c]	CO_2 (%) [d]	Polymer (%) [e]	M_n [Đ] [f]
ZnZn	2	417	17	> 99	98	20500 [1.04] 8800 [1.13]
ZnAl	3	24	1	68	88	*n.d*
ZnGa	3	69	2	85	95	*n.d*
ZnIn	3	399	9	85	91	16800 [1.07] 6600 [1.07] 2700 [1.12]

[a]Catalysis conditions: catalyst : CHO 1:1000, 80 °C. [b]Turnover number (TON) = number of moles of cyclohexene oxide consumed / number of moles of catalyst. [c]Turnover frequency (ToF) = TON / Time (h) for the final 24 h of reaction. [d]Expressed as a percentage of CO_2 uptake vs the theoretical maximum (100 %), determined by comparison of the relative integrals of the ^{1}H NMR proton resonances due to carbonate (δ 4.65 ppm) and ether (δ 3.45 ppm) linkages in the polymer backbone. [e]Expressed as a percentage of polymer formation vs the theoretical maximum (100 %), determined by comparison of the relative integrals of the ^{1}H NMR proton resonances due to polymer (4.65 ppm) and trans-cyclic carbonate (4.00 ppm). [f]Determined by SEC, in THF, calibrated using narrow-Mn polystyrene standards.

Di-zinc catalyst (**10**) demonstrates the highest activity (17 h^{-1}) and yields a polycarbonate material with high carbonate linkages and polymer selectivity (>98 %). Indeed, its performance is equivalent to previously reported di-zinc analogues using this macrocycle.[1, 18] Complexes (**11-13**) showed low activity (<10 h^{-1}) and formed polymers with significant ether linkages (up to 32 %). Such ether linkages form by sequential epoxide enchainment. The quantity of ether linkages decreases, descending the homologous series Al (III) to In (III), and is proposed to result from the decrease in metal Lewis acidity. In addition, the covalent metal-oxygen bond

enables high selectivity for polymer in all cases, with low formation of cyclic carbonate by product (< 15 %). The catalytic activity increases, descending Group 13, from 1 h^{-1} to 9 h^{-1} but overall values are low compared to the highest performing catalysts in this field.[15, 19-21] Multimodal polymer molecular weight distributions were obtained, as determined by gel permutation chromatography. This is probably due to the formation of both polyether and polycarbonate polymers and to chains initiated from 1,2-dihydroxycyclohexenol, as well as from chloride.

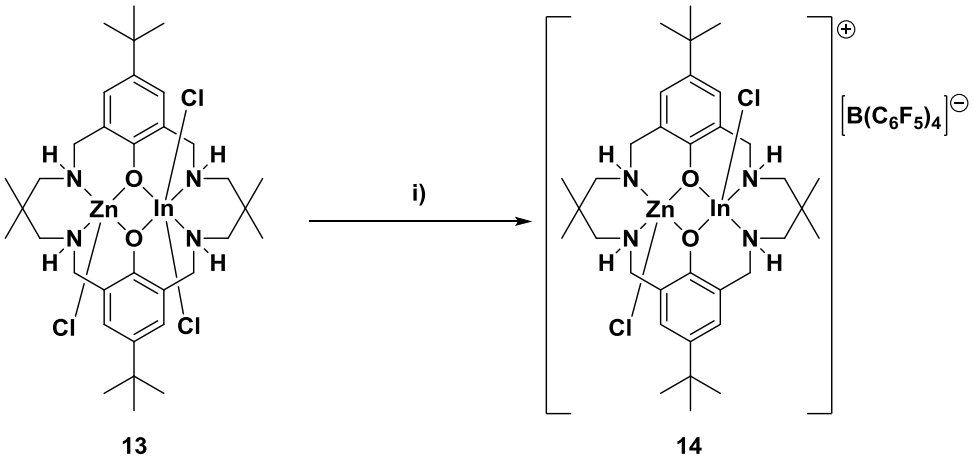


Scheme 3.4: Proposed mechanism for the formation of polycarbonate, polyether and cyclic carbonate products.

3.1.6 Zinc(II)/Indium (III) heterodinuclear derivative complexes

One potential reason for the low reactivity of the Group 13/ zinc (II), heterodinuclear complexes could be the lack of a free coordination site for epoxide binding.

In an effort to alleviate this problem, a coordination site would become available by abstracting a chloride co-ligand. Complex **13** was chosen to investigate chloride abstraction reactions as it was the most active heterodinuclear catalyst in the series.



Scheme 3.5: Synthesis of cationic heterodinuclear complex **14**. i) $K[B(C_6F_5)_4]$, THF, 25 °C, 16 h, 90 %.

The chloride abstraction reaction involved the addition of one equivalent of $K(B(C_6F_5)_4)$ to an equivalent of complex **13**, in THF, at 25 °C. A precipitate was removed by filtration, next the solvent reduced in *vacuo*, with the product washed with pentane to afford an off-white powder at 65 % yield. The complex was characterised by NMR spectroscopy (Figure S95-S99).

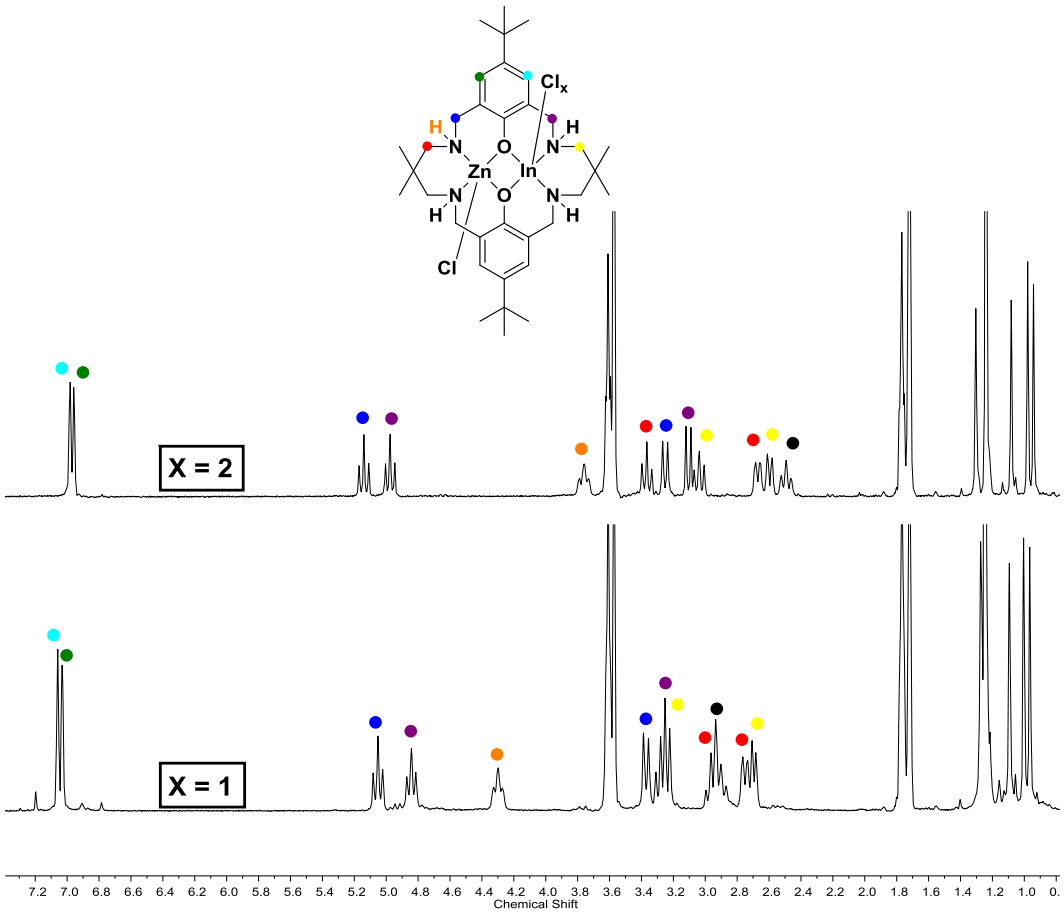


Figure 3.7: ^{1}H NMR spectrum of heterodinuclear complex **13** and cationic heterodinuclear complex **14** (d_8-THF, 298 K).

The cationic complex showed a large upfield shift in the NH proton resonances, by 0.55 ppm and 0.44 ppm, for the indium and zinc NH protons, respectively. ^{1}H NMR spectroscopy indicates retention of the heterodinuclear complex with no observable proton resonances corresponding to either homodinuclear complexes as a result of metal redistribution reactions. Both ^{11}B and ^{19}F NMR spectra indicate a single species is formed.

The cationic complex **14** was tested in the ROCOP of CO_2/CHO under the standard conditions tested for dinuclear complexes **10**-**13** (Table 3.1). Visually, after 3 hours the polymerisation solution became viscous. ^{1}H NMR spectroscopy showed the formation of only polyether linkages (> 99 %) with no polycarbonate linkages.

Cations have been known to catalyse the polymerisation of epoxide forming polyether, by cationic ROP.

An alternative approach to enhance copolymerisation selectivity was to replace the chloride co-ligands with benzoates; similar to the strategy applied in Chapter 2. This modification may also improve the observed rate as co-ligands have a large effect on the initiation time of the reaction.[22] Interestingly, only a single chloride substitution presented a discernible ^{1}H NMR spectrum. Addition of further equivalents of potassium benzoate salts resulted in multiple, complex, proton environments.

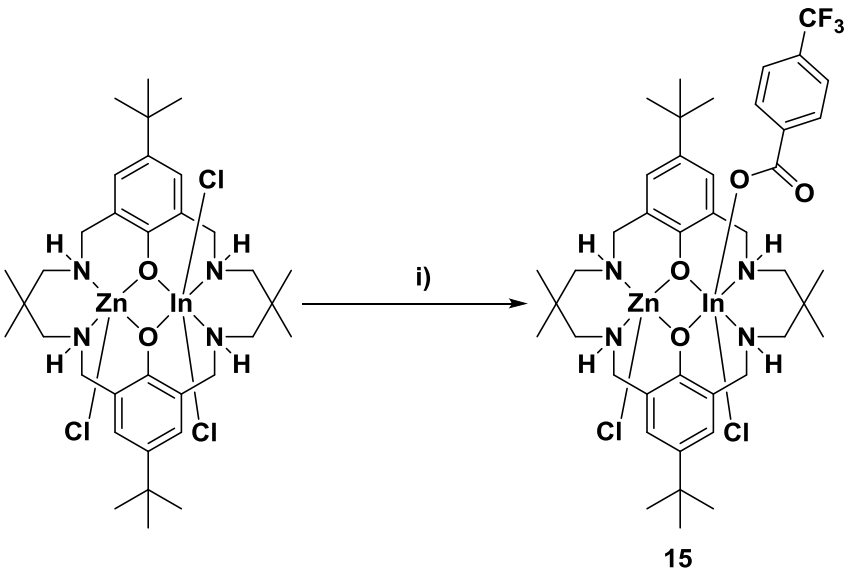


Figure 3.8: Synthesis of heterodinuclear complex 15. i) KOBzpCF$_3$, MeOH, 25 °C, 16 h, 95 %.

Complex **15** was synthesised via salt metathesis of complex **13** with potassium benzoate in MeOH, at 25 °C. The product was isolated as a white solid at 95 % yield. Its ^{1}H NMR spectrum shows a highly symmetrical splitting pattern, indicating the metathesis occurs at the bridging chloride (*vide infra*). Furthermore, retention of the heterodinuclear content is observed as no resonances are observed corresponding to the dizinc complex (**4b** or **10**). NH proton resonances are not observed in the ^{1}H NMR

spectrum of complex **15** perhaps due to hydrogen-deuterium exchange processes occurring between the complex and the solvent (Figure S100-S103). Interestingly, a major and minor set of proton environments are observed for the benzoate protons, with the minor resonances observed slightly downfield, at 7.63 and 8.04 ppm. This isomerism could be due to the benzoate binding in a κ_1 *vs.* κ_2 coordination mode, as has been previously observed for benzoate complexes for the heterodinuclear magnesium(II)/zinc(II) in methanol.[22]

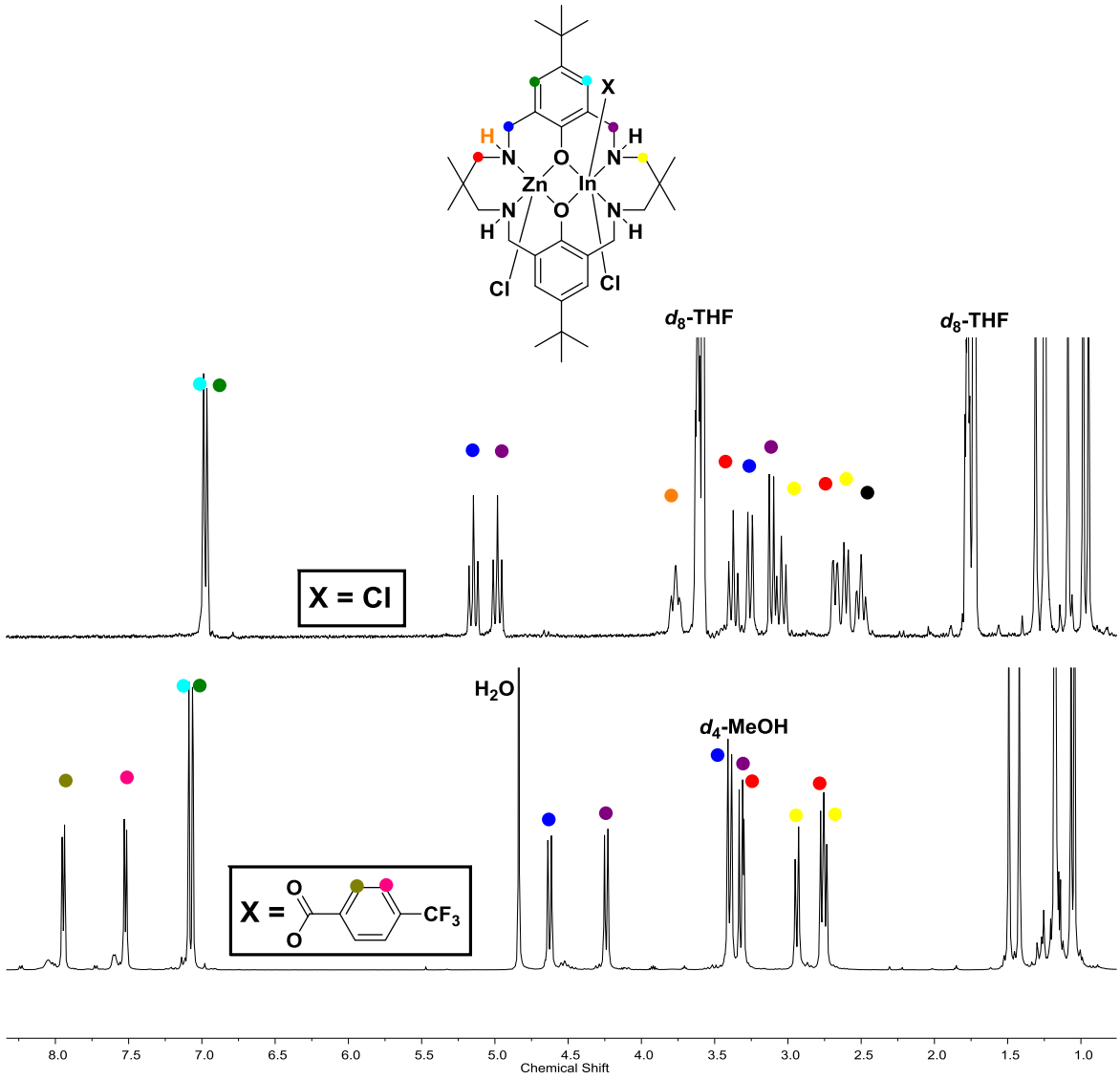


Figure 3.9: ^{1}H NMR spectrum of heterodinuclear complex **13** (d_8-THF) with **15** (d_4-MeOH) at 298 K.

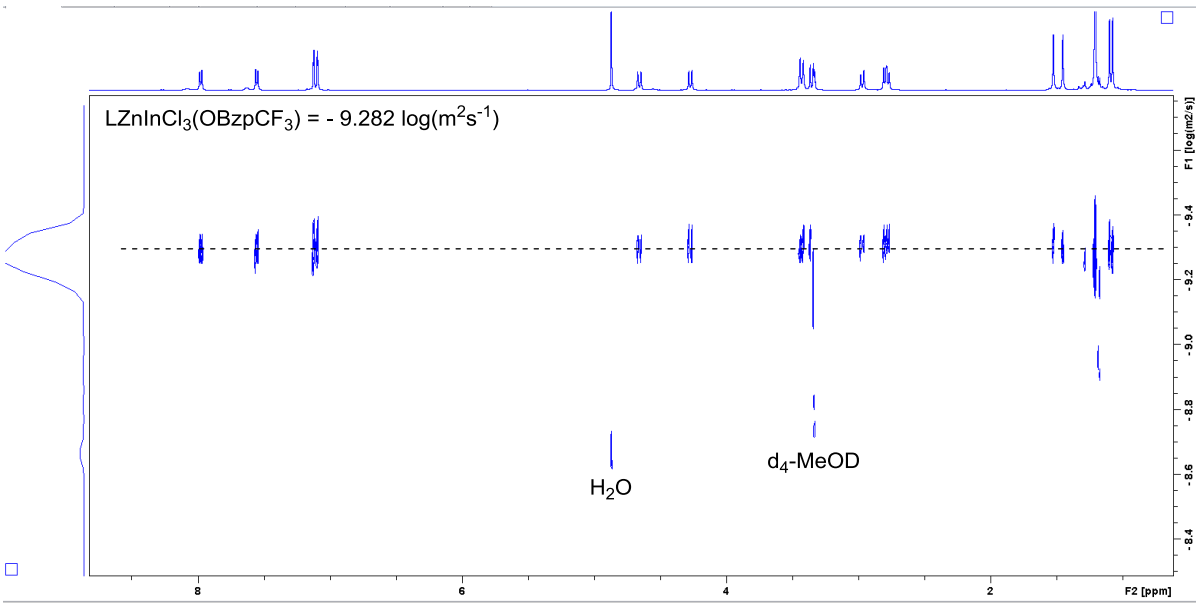


Figure 3.10: 2D DOSY NMR spectrum of **15** (d_4-MeOD, 298 K)

2D DOSY NMR revealed each proton resonance diffused with identical diffusion coefficient, *D*, evidence for a single molecular species, with a coefficient of – 9.292 log(m^2s^{-1}).

A single crystal of **15** suitable for X-ray diffraction was isolated via vapour diffusion of pentane into a saturated solution of complex, in THF, at -40 °C (Figure S104). Structural elucidation revealed a monomeric structure where the ligand adopts the 'bowl' shape conformation. Both zinc(II) and indium(III) centres adopt a hexacoordinate, octahedral, geometry. The structure confirms the selective substitution of the bridging chloride ligand for the benzoate. Furthermore, there is an extension of 0.24(4) Å in the Zn_1-Cl_1 bond and a reduction of 0.34(9) Å in the In_1-Cl_2 bond in complex **15** when compared to complex **13**. This could be due to the bridging benzoate strengthening the In-Cl bond and weakening the Zn-Cl bond. The intermetallic separation is measured at 3.16(7) Å.

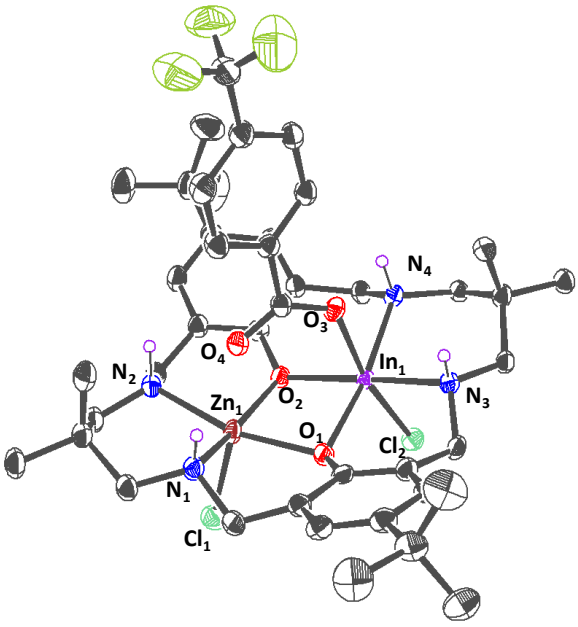


Figure 3.11: ORTEP representation of crystallographic structure of complex **15**, obtained by single crystal X-ray diffraction. Disorder and H-atoms (excluding NH) have been omitted for clarity, with thermal ellipsoids represented at 40 % probability. Selected bond lengths (Å) and angles (°) for complex 15 (Table S12).

3.1.7 Conclusions

The synthesis of a series of heterodinuclear Group 13-zinc(II) complexes (**10**-**15**), coordinated by a symmetrical macrocycle, were reported. Complexes **10**-**13** were synthesised via the thermodynamic sequential metalation procedure developed in Chapter 2. Complexes **14** and **15** were synthesised by salt metathesis and chloride abstraction reactions with complex **13**. All heterocomplexes were found to be the thermodynamic products with no evidence of contamination with di-zinc (**10**), in-line with the findings reported in Chapter 2. The CO_2/epoxide polymerisations were all lower in activity than the di-zinc catalyst (**10**). This was proposed to be due to the saturation of the coordination sphere for both the Group 13 metal centre and zinc(II), suggesting that the M(II)M(III) metal combination is not a useful design target for these catalysts.

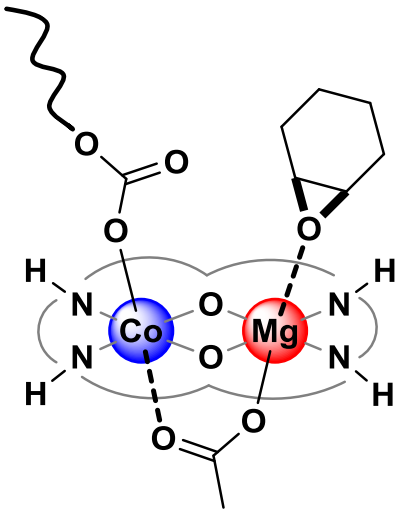
3.1.8 References

1. Deacy, A. C.; Durr, C. B.; Garden, J. A.; White, A. J. P.; Williams, C. K., Groups 1, 2 and Zn(II) Heterodinuclear Catalysts for Epoxide/CO_2 Ring-Opening Copolymerization, *Inorg. Chem.,* **2018,** *57*, (24), 15575.
2. Darensbourg, D. J., Making Plastics from Carbon Dioxide: Salen Metal Complexes as Catalysts for the Production of Polycarbonates from Epoxides and CO_2, *Chem. Rev.,* **2007,** *107*, (6), 2388.
3. Darensbourg, D. J.; Moncada, A. I.; Wei, S.-H., Aliphatic Polycarbonates Produced from the Coupling of Carbon Dioxide and Oxetanes and Their Depolymerization via Cyclic Carbonate Formation, *Macromolecules,* **2011,** *44*, (8), 2568.
4. Wu, G.-P.; Wei, S.-H.; Ren, W.-M.; Lu, X.-B.; Li, B.; Zu, Y.-P.; Darensbourg, D. J., Alternating copolymerization of CO_2 and styrene oxide with Co(III)-based catalyst systems: differences between styrene oxide and propylene oxide, *Energy Environ. Sci.,* **2011,** *4*, (12), 5084.
5. Darensbourg, D. J.; Wei, S.-H., Depolymerization of Polycarbonates Derived from Carbon Dioxide and Epoxides to Provide Cyclic Carbonates. A Kinetic Study, *Macromolecules,* **2012,** *45*, (15), 5916.
6. Lu, X.-B.; Ren, W.-M.; Wu, G.-P., CO_2 Copolymers from Epoxides: Catalyst Activity, Product Selectivity, and Stereochemistry Control, *Acc. Chem. Res.,* **2012,** *45*, (10), 1721.
7. Darensbourg, D. J.; Billodeaux, D. R., Aluminum Salen Complexes and Tetrabutylammonium Salts: A Binary Catalytic System for Production of Polycarbonates from CO2 and Cyclohexene Oxide, *Inorg. Chem.,* **2005,** *44*, (5), 1433.
8. Chatterjee, C.; Chisholm, M. H., The Influence of the Metal (Al, Cr, and Co) and the Substituents of the Porphyrin in Controlling the Reactions Involved in the Copolymerization of Propylene Oxide and Carbon Dioxide by Porphyrin Metal(III) Complexes. 1. Aluminum Chemistry, *Inorg. Chem.,* **2011,** *50*, (10), 4481.
9. Chen, P.; Chisholm, M. H.; Gallucci, J. C.; Zhang, X.; Zhou, Z., Binding of Propylene Oxide to Porphyrin− and Salen−M(III) Cations, Where M = Al, Ga, Cr, and Co, *Inorg. Chem.,* **2005,** *44*, (8), 2588.
10. Norikazu, T.; Shohei, I., Polymerization of 1,2-epoxypropane and copolymerization with carbon dioxide catalyzed by metalloporphyrins, *Die Makromolekulare Chemie,* **1978,** *179*, (5), 1377.
11. González-Fabra, J.; Castro-Gómez, F.; Kleij, A. W.; Bo, C., Mechanistic Insights into the Carbon Dioxide/Cyclohexene Oxide Copolymerization Reaction: Is One Metal Center Enough?, *ChemSusChem,* **2017,** *10*, (6), 1233.
12. Peña Carrodeguas, L.; González-Fabra, J.; Castro-Gómez, F.; Bo, C.; Kleij, A. W., AlIII-Catalysed Formation of Poly(limonene)carbonate: DFT Analysis of the Origin of Stereoregularity, *Chem. Eur. J.,* **2015,** *21*, (16), 6115.
13. Thevenon, A.; Cyriac, A.; Myers, D.; White, A. J. P.; Durr, C. B.; Williams, C. K., Indium Catalysts for Low-Pressure CO_2/Epoxide Ring-Opening Copolymerization: Evidence for a Mononuclear Mechanism?, *J. Am. Chem. Soc.,* **2018,** *140*, (22), 6893.
14. Kember, M. R.; White, A. J. P.; Williams, C. K., Highly Active Di- and Trimetallic Cobalt Catalysts for the Copolymerization of CHO and CO_2 at Atmospheric Pressure, *Macromolecules,* **2010,** *43*, (5), 2291.

15. Moore, D. R.; Cheng, M.; Lobkovsky, E. B.; Coates, G. W., Electronic and Steric Effects on Catalysts for CO_2/Epoxide Polymerization: Subtle Modifications Resulting in Superior Activities*, Angew. Chem. Int. Ed.,* **2002,** *41*, (14), 2599.
16. Klaus, S.; Lehenmeier, M. W.; Anderson, C. E.; Rieger, B., Recent advances in CO_2/epoxide copolymerization—New strategies and cooperative mechanisms*, Coord. Chem. Rev.,* **2011,** *255*, (13), 1460.
17. Kember, M. R.; Buchard, A.; Williams, C. K., Catalysts for CO_2/epoxide copolymerisation*, Chem. Commun.,* **2011,** *47*, (1), 141.
18. Kember, M. R.; Knight, P. D.; Reung, P. T. R.; Williams, C. K., Highly Active Dizinc Catalyst for the Copolymerization of Carbon Dioxide and Cyclohexene Oxide at One Atmosphere Pressure*, Angew. Chem. Int. Ed.,* **2009,** *48*, (5), 931.
19. Nagae, H.; Aoki, R.; Akutagawa, S.; Kleemann, J.; Tagawa, R.; Schindler, T.; Choi, G.; Spaniol, T. P.; Tsurugi, H.; Okuda, J.; Mashima, K., Lanthanide Complexes Supported by a Trizinc Crown Ether as Catalysts for Alternating Copolymerization of Epoxide and CO_2: Telomerization Controlled by Carboxylate Anions*, Angew. Chem. Int. Ed.,* **2018,** *57*, (9), 2492.
20. Kissling, S.; Lehenmeier, M. W.; Altenbuchner, P. T.; Kronast, A.; Reiter, M.; Deglmann, P.; Seemann, U. B.; Rieger, B., Dinuclear zinc catalysts with unprecedented activities for the copolymerization of cyclohexene oxide and CO_2*, Chem. Commun.,* **2015,** *51*, (22), 4579.
21. Kember, M. R.; Jutz, F.; Buchard, A.; White, A. J. P.; Williams, C. K., Di-cobalt(ii) catalysts for the copolymerisation of CO_2 and cyclohexene oxide: support for a dinuclear mechanism?*, Chem. Sci.,* **2012,** *3*, (4), 1245.
22. Trott, G. Heterodinuclear catalysts for CO_2/epoxide copolymerisations. University of Oxford, 2018.

Chapter 4:

Magnesium-Cobalt Heterodinuclear Complex for Epoxide/CO_2 ROCOP



$\Delta G^{\ddagger} = \Delta H^{\ddagger} - T\Delta S^{\ddagger}$

Entropic Control Mg(II)

Enthalpic Control Co(II)

One-pot Synthesis
High Heterodinuclear Purity ☑

High CO_2/Epoxide Activity
TOF = >12,400 h^{-1} ☑

High Thermal Stability
and Selectivity ☑

4.1.1 Introduction

The research into Group 1 or 2, zinc(II) heterodinuclear catalysts (Chapter 2) showed that not all hetero-combinations enhance reaction rates. X-ray crystallographic evidence hints that the Group 1 and 2 metals may be the epoxide binding site with the zinc-carbonate being the nucleophile.[1] As the Zn(II)Mg(II) catalyst was the best hetero-combination, in this chapter the Mg(II) centre is maintained as the best epoxide binder and the optimal metal-carbonate nucleophile is investigated through substituting Zn(II) for other first row transition metals.

In 2010, Williams and co-workers reported a di-cobalt(II) and mixed valent di-cobalt (II)/(III) catalysts, which were both highly active in the ROCOP of CO_2/CHO (Figure 4.1).[2] The mixed valent Co(II)Co(III) complex was slightly more active than the Co(II)Co(II) complex and this finding was rationalised by the greater Lewis acidity of the Co(III) centre, versus a Co(II) centre, and thus better epoxide binding. The mixed valent system shows an activity of 480 h^{-1} at 100 °C, 1 bar CO_2 pressure and remains the most active low CO_2 pressure catalyst reported in the literature.[3]

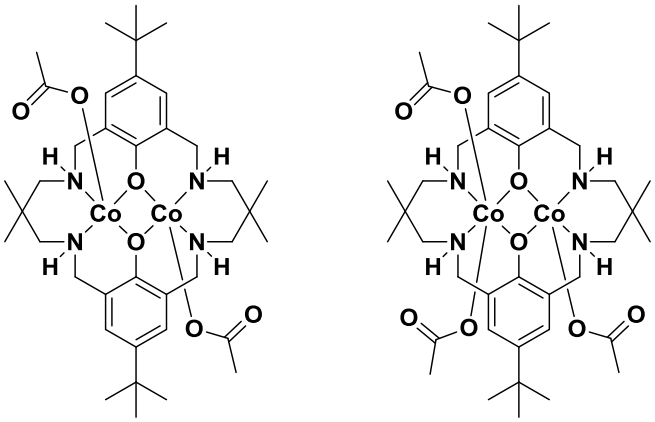


Figure 4.1: Isovalent and mixed valent di-cobalt complexes.

4.1.2 Aims

Leading on from the homodinuclear catalysts, here, the target is a heterodinuclear Mg(II)Co(II) catalyst. We reasoned that Co(II)-carbonate should be more labile than the zinc(II) counterpart.

In terms of developing a synthetic route to the target compound, due to the paramagnetism of Co(II), determination of heterodinuclear content will be significantly more challenging than for the complexes synthesised in Chapters 2 and 3 due to the lack of useful NMR spectroscopic data. Other characterisation techniques such as magnetic, electrochemical and elemental composition will be explored.

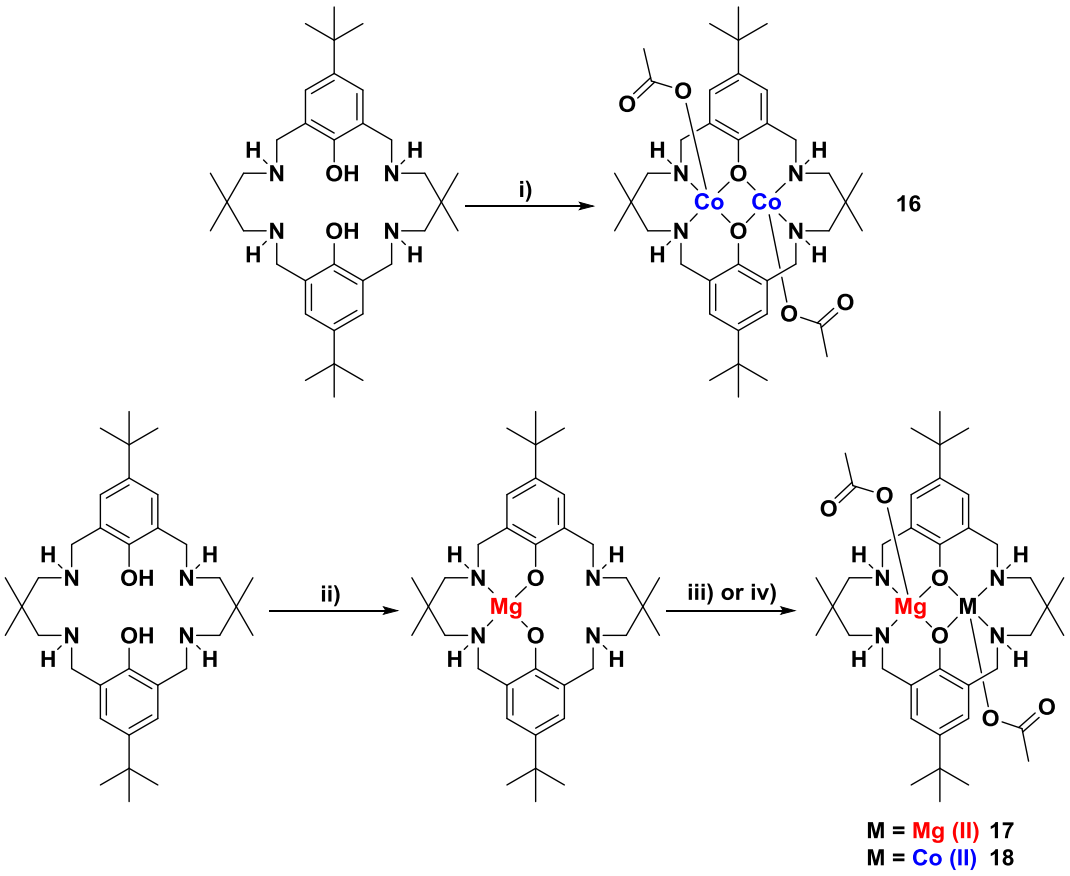
To establish whether activity is enhanced, its rate law will be determined and compared to those determined for the respective homodinuclear di-magnesium and di-cobalt complexes. It will be important to observe whether the rate determining step is the same and hence whether the same mechanism should apply.

The chapter also targets improved understanding of any cooperative effect between the two metals. This may be interrogated by experimentally determining the Gibbs free energy of transition of the heterocomplex in comparison to the homocomplexes, in order to gain insight into the thermodynamic influences of entropy and enthalpy.

Finally, the Mg(II)Co(II) catalyst should be generally applicable to other ROCOP, so monomers such as epoxides and anhydrides will be investigated. This study seeks to understand the generality of the catalysis.

4.1.3 Synthesis of homo- and hetero- complexes 16, 17 and 18

The targeting of a heterodinuclear transition metal complex presents several new challenges. 1) Sensitivity to oxidation and 2) determination of heterodinuclear content without the availability of useful NMR spectroscopic analysis techniques as utilised in chapters 2 and 3. The thermodynamic sequential metalation procedure will be utilised in synthesising complex **18** due to most heterodinuclear complexes synthesised so far being the thermodynamic product (Scheme 4.1). The oxidation state will be determined using X-ray Photoelectron spectroscopy (XPS), super conducting quantum interference device (SQUID) magnetic measurements and cyclic voltammetry (CV). Furthermore, CV analysis may provide evidence of successful heterodinuclear complex synthesis.



Scheme 4.1: Synthesis of complexes **16**, **17** and **18**. i) $Co(OAc)_2$, THF, 100 °C, 16 h, 74 %. ii)$Mg(N(Si(CH_3)_3)_2)_2$, THF, 25 °C, 4 h. iii) $Mg(OAc)_2$, THF, 100 °C, 16 h, 68 %. iv) $Co(OAc)_2$, THF, 100 °C, 16 h, 78 %.

The di-cobalt complex, **16**, was synthesised by adding two equivalents of cobalt acetate to the macrocyclic ligand in THF and heating to 100 °C for 16 hours. The acetic acid evolved during the reaction was azeotropically removed with toluene and the product dried in *vacuo* to afford a pink solid with good yield (74 %).

The di-magnesium complex, **17**, and heterodinuclear Mg(II)/Co(II) complex **18** were synthesised using the sequential monometallation procedure developed in Chapter 2.[1] A mono-magnesium intermediate was synthesised *in-situ* by addition of one equivalent of $Mg(N(Si(CH_3)_3)_2)_2$ to the pro-ligand, in THF at 25 °C (Figure S105). This was followed by the addition of either magnesium(II) or cobalt(II) acetate salts and heating at 100 °C for 16 h. The products were then dried in *vacuo* and isolated in good yields, 68 % and 78 % respectively.

Complexes **16**, **17** and **18** were characterised by NMR spectroscopy (Figure S106), mass spectrometry and purity determined by elemental analysis. Complexes **16** and **18** were further characterised XPS, CV and SQUID magnetometry. Complex **18** was further characterised by X-ray crystallography.

4.1.6 Mass Spectrometry

The MALDI-ToF analysis of complex **18** was prepared by addition of a solution of complex (0.02 M) with a solution of matrix (0.02 M) in THF (Figure 4.2).

Molecular cation peaks at 655, 690 and 725 m/z were observed, corresponding to $[LMg_2(OAc)]^+$, $[LMgCo(OAc)]^+$ and $[LCo_2(OAc)]^+$, respectively. Signals for the homodinuclear complexes were observed and may be due to either some contamination during synthesis (N.B compounds in chapters 2 and 3 showed 90-99 % selectivity) or due to metal scrambling occurring during the ionisation.

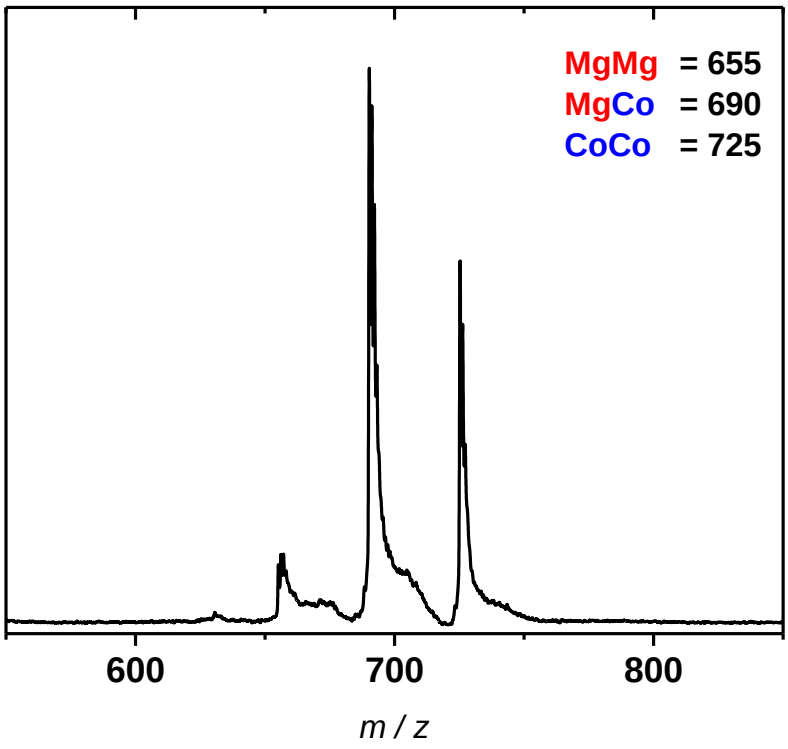


Figure 4.2: MALDI-ToF mass spectrum of MgCo.

4.1.7 X-Ray Photoelectron Spectroscopy (XPS)

X-ray photoelectron spectroscopy (XPS) is a surface sensitive technique typically used to investigate surface elemental composition along with providing evidence for metal oxidation states.[4]

$$KE = hv - BE - \Phi_s \quad (1)$$

The technique utilises the photoelectric effect (1) by irradiating a solid in *vacuo* with monochromatic X-rays (hv) and measuring the kinetic energy of the emitted electrons (KE). By accounting for the work function of the spectrometer (Φ_s) the binding energy (BE) of the electron can be calculated. The data is presented as the number of detected electrons per energy interval versus their kinetic energy. Each element produces a characteristic set of XPS peaks, at diagnostic binding energy values, and hence XPS is used to provide elemental surface composition data. The experiments were conducted by Dr. Anna Regoutz at Imperial College London.

X-ray photoelectron spectroscopy (XPS) was used in order to analyse the oxidation states of the cobalt centres and the elemental composition of the catalysts. The core orbital levels of complexes **16**-**18** were normalised and are shown as slightly stacked plots to avoid complete overlap (Figure 4.3). The Mg 1s core level is at an energy consistent with other compounds and shows a binding energy (BE) of 1303.1 eV (Figure 4.3(a)).[5] The Co $2p_{1/2}$ and Co $2p_{3/2}$ core levels, observed in both **16** and **18**, show a BE of 780.2 eV and 796.2 eV, respectively (Figure 4.3(b)).[6] The spin-orbit coupling between $2p_{1/2}$ and $2p_{3/2}$ is 16 eV, consistent with a Co(II) centre (15 eV is

typical for Co(III)).[7-9] In addition, satellite features at 3 – 5 eV higher BE (784.9 eV and 801.9 eV), are observed and are indicative of a Co(II) centre. [6] It is notable that a Co(III) species would not result in these satellite features.[6, 10] From peak fitting of the Mg 1*s* and Co $2p_{3/2}$ core levels, a Mg:Co ratio of 1:1 was determined for the heterocomplex, **18**. The C 1*s*, N 1*s* and O 1*s* core level show BE features expected from the ligand, including C-O, C-C, N-H and O-C chemical environments.[9]

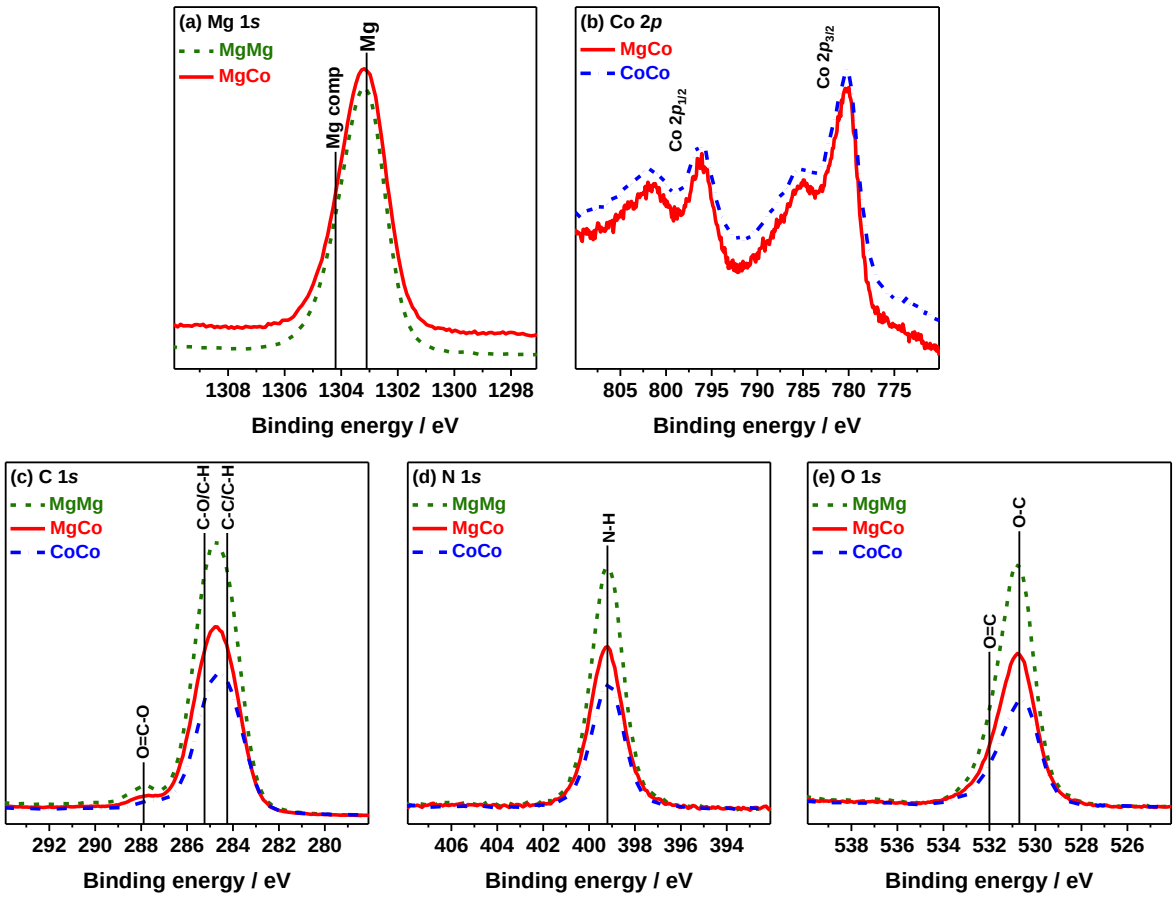


Figure 4.3: XPS core level spectra of the catalyst, including (a) Mg 1*s*, (b) Co 2*p*, (c) C 1*s*, (d) N 1*s* and (e) O 1*s*. The two metal core levels have standard normalisation and stacking applied to them, whilst C, N and O 1*s* levels have been normalised to the total areas of Mg and Co peaks.

4.1.8 X-Ray Crystallography

A single crystal suitable for X-ray crystallography of **18** was obtained *via* slow evaporation of saturated solution of complex in toluene, at -40 °C. Structural elucidation reveals a dimeric structure with each ligand scaffold adopting the 'bowl' shape (Figure 4.4). The recrystallization allowed ingress of water which coordinated to one of the metals and partly cleaved the dimer. The disruption of the dimer may be somewhat similar to processes occurring during catalysis when epoxide is present in excess and coordinates to the catalyst. Due to positional disordering, elucidation of each metal site for magnesium and cobalt, specifically, could not be achieved. The metal-metal distance was measured to be 3.037(3) Å.

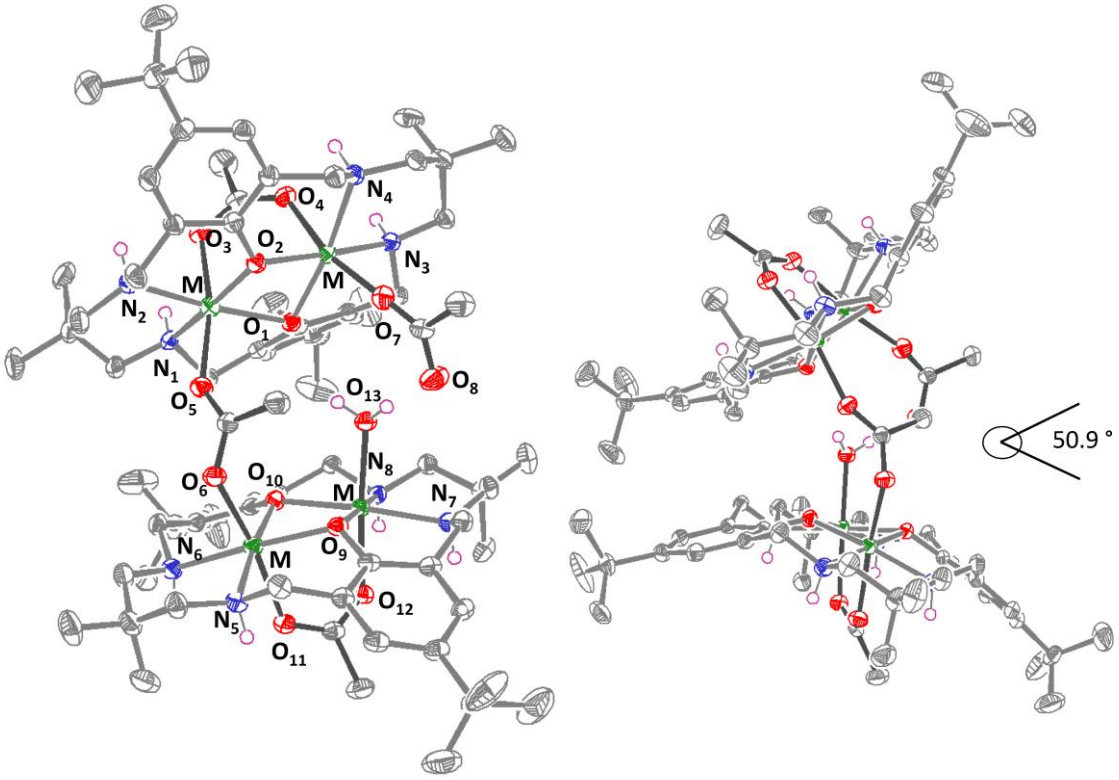


Figure 4.4: ORTEP representation of the molecular structure of MgCo, obtained by single crystal X-ray diffraction. Disorder and H-atoms (excluding NH) have been omitted for clarity, with thermal ellipsoids represented at 40 % probability.

4.1.9 Cyclic Voltammetry

To gain further insight into the heterodinuclear nature of complex **18**, the electrochemical behaviour of complexes **16**, **17** and **18** were studied by cyclic voltammetry. Experiments were conducted over a range of different scan rates, in THF containing 0.1 M [$^{n}Bu_4N$][PF_6] as the supporting electrolyte. The electrochemical responses were referenced internally to Fc^{+}/Fc, by adding ferrocene (ca. 1 mg) to the sample solution (Figure 4.5 and Table 4.1).

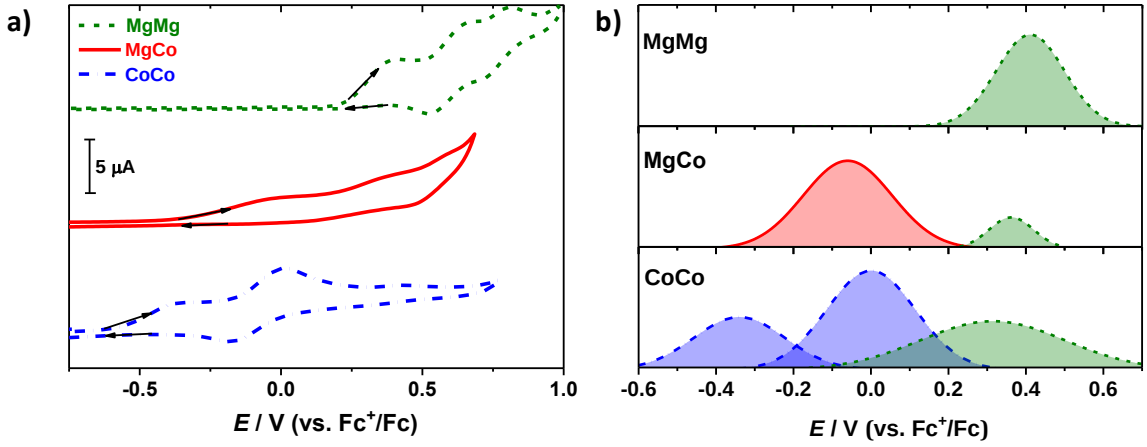


Figure 4.5: (LHS) Cyclic voltammagrams of **MgMg** (Green, dotted), **MgCo** (red, line) and **CoCo** (blue, dot-dash) in THF, 0.1 M [$^{n}Bu_4N$][PF_6] at 100 mV s^{-1}. (RHS) Deconvoluted oxidation potential for **MgMg**, **MgCo** and **CoCo** displaying ligand oxidations (Green dotted), Co(II) to Co(III) oxidations for **MgCo** (red, line) and **CoCo** (Blue, dot-dash).

Table 4.1: Electrode potentials (E) vs $FeCp_2^{+/0}$ in THF, 0.1 M [nBu4N][PF_6] at 100 mV s^{-1}.

Complex	$E_{1/2}$ / V	E_{pp}/ V
MgMg	$E_{pa}^{(I)}$ = +0.39	-
	$E_{1/2}^{(II)}$ = +0.60	+0.24
	$E_{1/2}^{(III)}$ = +0.78	+0.21
MgCo	$E_{pa}^{(I)}$ = -0.06	-
	$E_{pa}^{(II)}$ = +0.35	-
CoCo	$E_{pa}^{(I)}$ = -0.34	-
	$E_{1/2}^{(II)}$ = -0.10	+0.21
	$E_{pa}^{(III)}$ = +0.32	-

The cyclic voltammogram of **17** shows a series of oxidations above +0.39 V (Figure 4.5, green dotted). Assuming magnesium is not oxidised, these processes are assigned to phenolate ring oxidation to phenoxyl radicals. The separate oxidation processes for each phenolate moiety suggest some degree of delocalisation over both phenol rings in the oxidised form, which has been reported for related complexes with phenolate ligands.[11-15]

The cyclic voltammogram of **16** show two principle redox processes (Figure 4.5, blue dot-dash). An irreversible oxidation at E_{pa} = -0.34 V, and a quasi-reversible oxidation centres at $E_{1/2}$ = -0.10 V. These are assigned to the $[Co^{II}Co^{II}]/[Co^{II}Co^{III}]^{+}$ and $[Co^{II}Co^{III}]^{+}/[Co^{III}Co^{III}]^{2+}$ oxidation processes. The second Co(II) oxidation process occurs at a lower potential than in Mg(II)Co(II), possibly indicating a cooperative process increasing the stability of the oxidised species.

Table 4.2: Peak potentials (Ep vs. $FeCp_2^{+/0}$) and limiting currents (ip) for CoCo in THF / 0.1 M $[nBu_4N][PF_6]$ at variable scan rates.

Scan Rate / mVs^{-1}	E_{pa} / mV	E_{pc} / mV	ΔE_{pp} / mV	i_{pa} / mA	i_{pc} / mA	$\lvert i_{pa}/i_{pc} \rvert$
50	-120	+260	380	-0.515	+0.722	0.7
100	-200	+230	430	-1.437	+1.452	1.0
200	-190	+320	510	-2.159	+2.682	0.8
300	-200	+370	570	-2.667	+3.275	0.8
400	-220	+390	610	-3.124	+3.530	0.9
500	-210	+400	610	-3.665	+3.698	1.0
1000	-170	+440	610	-3.935	+3.228	1.2

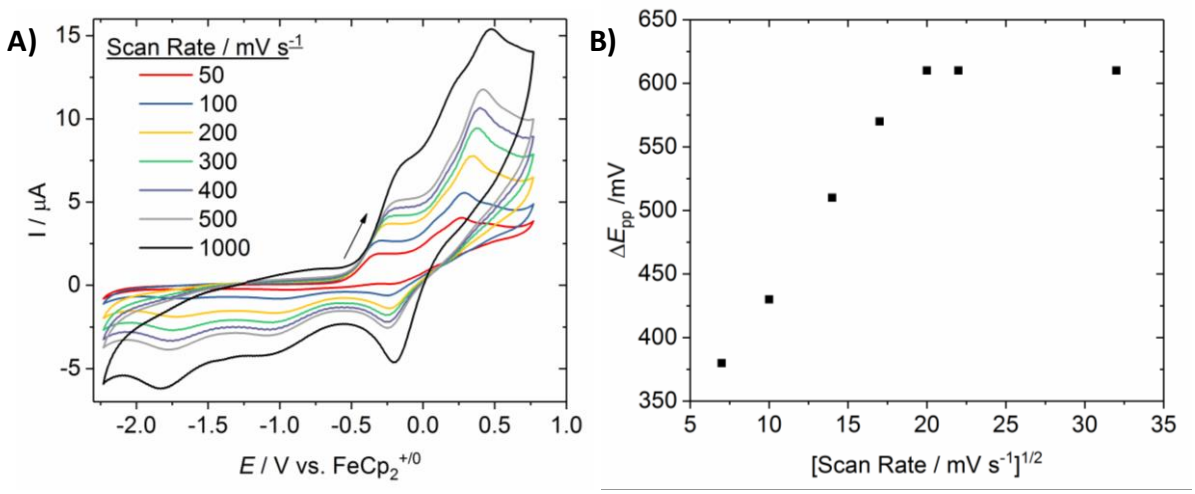


Figure 4.6: A) Scan rate dependence of the voltammetry in the reduction for Process III of complex CoCo in THF, 0.1 M [^{n}Bu$_4$N][PF$_6$]. B) Scan rate dependence of the peak-to-peak separation (ΔE_{pp}) for Process III of complex CoCo in THF, 0.1 M [^{n}Bu$_4$N][PF$_6$].

The ratio of oxidative and reductive peak currents for $E_{1/2}$ (i_{pa}/i_{pc}) for complex **16** is close to unity, signifying a quasi-reversible process.[16] The peak-to-peak separation (ΔE_{pp}) is comparable to that for ferrocene under the same conditions (ca. 180 mV) indicating a single electron transfer. These results suggest that the second oxidation product, $[Co^{III}Co^{III}]^{2+}$ is more stable than the $[Co^{II}Co^{III}]^{+}$ under the conditions and timescale of the experiment.

The cyclic voltammogram of **18** shows an oxidation at E_{pa} = -0.06 V, with no associated reduction in the reverse scan (Figure 4.5, LHS red line). Similar potential values have been reported for other mono-Co(II) complexes, and hence is assigned to the $[Mg^{II}Co^{II}]/[Mg^{II}Co^{III}]^{+}$ oxidation.[17] Its irreversible behaviour suggests that the $[Mg^{II}Co^{III}]^{+}$ product is unstable under the conditions and timescale of the experiment. The observation of a single oxidation process for complex **18** compared to two oxidation processes observed for **16** provides evidence of successful heterodinuclear complex synthesis (Figure 4.5, RHS).

4.2.0 Superconducting Quantum Interference Device (SQUID) Magnetometry

The magnetic susceptibilities of **16** and **18** were studied in the solid state using SQUID, at an applied magnetic field of 0.1 Tesla and over the temperature range 2 – 300 K. The experiments were conducted by Dr. Alexander Kilpatrick at Oxford University. For each complex, the observed magnetic susceptibility per mole of bimetallic complex (χ_m) at each temperature was identical for zero-field cooled (ZFC) and field cooled (FC) measurements. These findings indicate the complexes are magnetically dilute, hence only ZFC data are shown. Both complexes **16** and **18** behave as typical paramagnets over the temperature range measured (Figure 4.7). Furthermore, no evidence was found for magnetic hysteresis at 4 K.

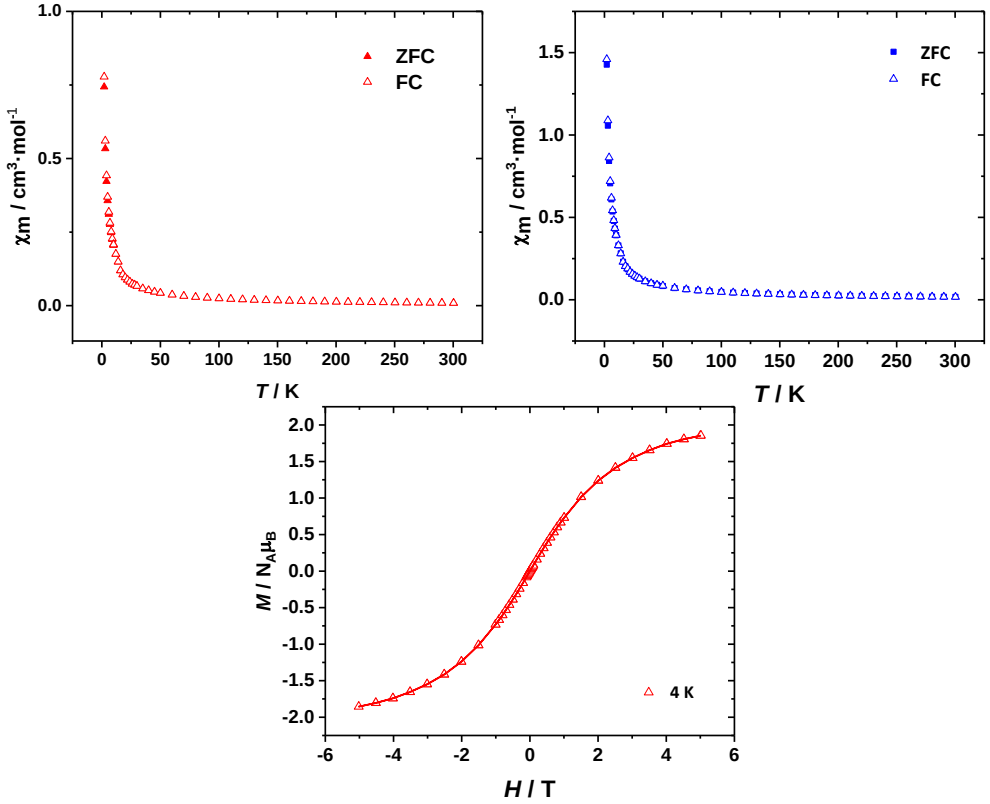


Figure 4.7: Temperature dependence of the Field-Cooled (FC) and Zero-Field-Cooled (ZFC) magnetic susceptibilities, χ_m, of MgCo (Top LSH) and CoCo (Top RHS) per bimetallic complex at 0.1 Tesla. Field sweep for MgCo at 4 K, showing no hysteresis of the magnetisation (Bottom).

Values of the magnetic susceptibility were corrected for the underlying diamagnetic increment by using tabulated Pascal constants,[18] per bimetallic complex unit: **16** (χ_{dia} = -4.83 x 10^{-4} emu mol^{-1}) and **18** (χ_{dia} = -4.76 x 10^{-4} emu mol^{-1}). The mass magnetic susceptibility, χ_g, was multiplied by the molar mass for **16** (786.8 g mol^{-1}) and **18** (752.2 g mol^{-1}) to obtained the magnetic susceptibility per mole of bimetallic complex, χ_m.

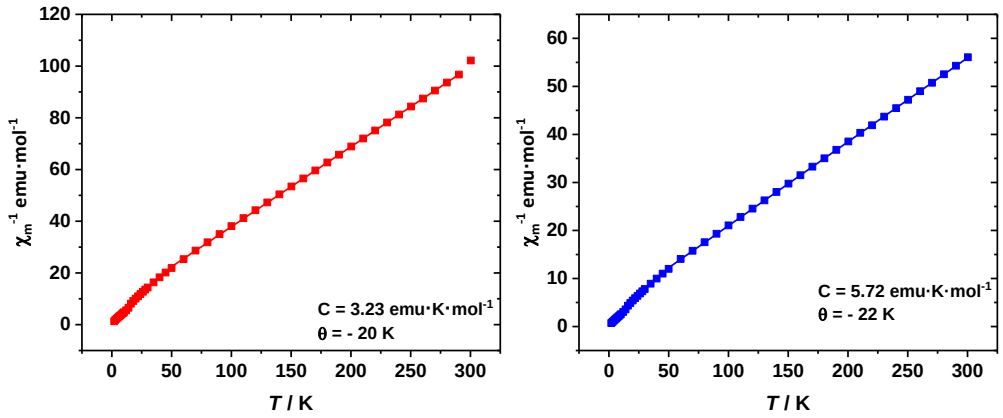


Figure 4.8: Inverse susceptibility against temperature, χ_m^{-1} vs T, plot for **18** (LHS) and **16** (RHS). Linear fitting (50 – 300 K).

The temperature dependence of the inverse of molar susceptibility, χ_m^{-1}, for both **16** and **18** are fit by the linear Curie-Weiss law between 50 K and 300 K (Figure 4.8). Curie constants, C, of 5.72 emu K mol^{-1} and 3.23 emu K mol^{-1} were determined for complexes **16** and **18,** respectively (2). The Weiss constant, θ, of ~ -21 K for both complexes indicates antiferromagnetic interactions.

$$\chi_m = \frac{C}{T - \theta} \qquad (2)$$

The temperature dependence of the χ_mT product per bimetallic complex has a similar form for both complexes **16** and **18**, so they will be discussed together. At room temperature, the χ_mT product for complex **16** is equal to 6.55 cm^3 mol^{-1} K and for complex **18** is equal to 2.82 cm^3 mol^{-1} K. The corresponding effective magnetic

moments per cobalt ion (μ_{eff} per Co(II)) for **16** and **18** are 4.63 and 4.75 μ_B, respectively (3). These values are greater than the spin-only value (4) for a high spin cobalt(II) centre (μ_{SO} = 3.87 μ_B, for S= 3/2, g = 2), suggesting there is significant spin-orbit coupling in both complexes. Such spin-orbit coupling is typically observed in high-spin Co(II) centres, in an octahedral geometry, due to the degeneracy of the triplet ground state, $^4T_{1g}$. The maximum effective magnetic moment, spin-orbit coupled (5), for each Co(II) centre is μ_{S+L} = 5.20 μ_B (for S = 3/2, L = 3, g = 2).

$$\mu_{eff} = 2.828\sqrt{\chi_m T} \quad (3)$$

$$\mu_{SO} = \sqrt{4S(S+1)} \quad (4)$$

$$\mu_{S+L} = \sqrt{4S(S+1) + L(L+1)} \quad (5)$$

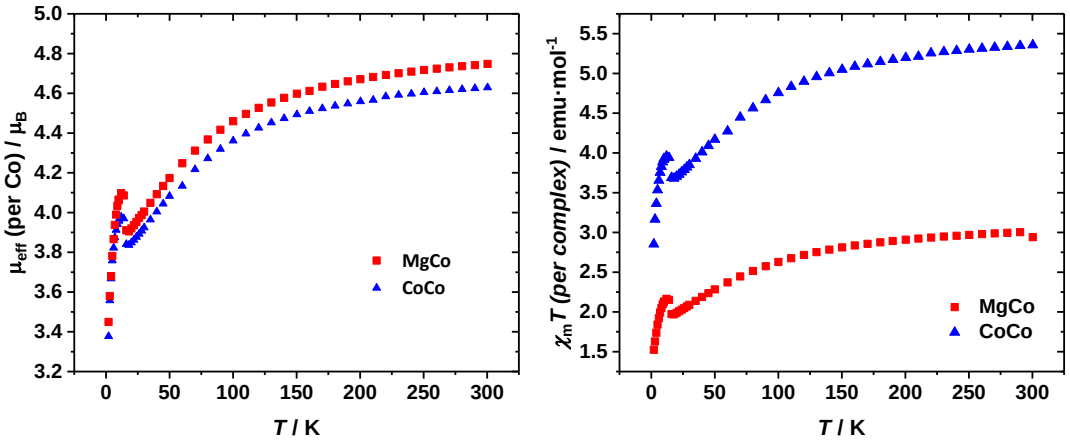


Figure 4.9: Temperature dependence of observed μ_{eff} per cobalt centre for MgCo (square) and CoCo (triangle) at 0.1 Tesla (LHS). Temperature dependence of observed $\chi_m T$ per complex for MgCo (square) and CoCo (triangle) at 0.1 Tesla (RHS).

Upon cooling, $\chi_m T$ decreases reaching a local minima at 18 K of 3.68 $cm^3\ mol^{-1}\ K$ for complex **16** and 1.91 $cm^3\ mol^{-1}\ K$ for complex **18** (Figure 4.9). Upon cooling further there is a sharp increase reaching a local maximum at 12 K of 3.96 $cm^3\ mol^{-1}\ K$ and 2.10 $cm^3\ mol^{-1}\ K$ for complexes **16** and **18**, respectively. Below this temperature, $\chi_m T$ decreases abruptly to reach a minimum of 3.85 $cm^3\ mol^{-1}\ K$ and 1.49 $cm^3\ mol^{-1}\ K$ for **16** and **18** at 2 K.

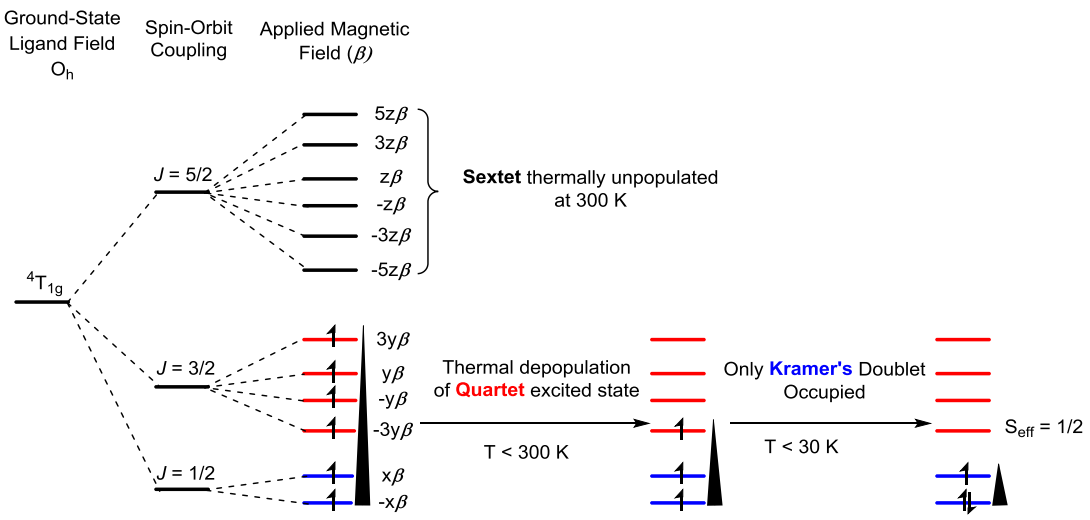


Figure 4.10: Magnetic splitting effects for an octahedral Co(II) ion in an applied magnetic field along with thermal depopulation.[19]

The decrease of $\chi_m T$ in the high temperature regime is due to the depopulation of the higher energy quartet and Kramer's doublet of the Co(II) ion (Figure 4.10). The increase in $\chi_m T$ on cooling after the local minimum at 12 K may be attributed to an intermolecular ferromagnetic interaction between the high-spin Co(II) ions in adjacent molecules.

Increases in $\chi_m T$ at low temperature have been observed in previously reported cobalt(II) complexes, and have been explained in terms of intramolecular ferromagnetic interactions between the cobalt(II) ions, mediated by bridging acetate ligands.[20] Assuming both **16** and **18** exist as acetate-bridged dimers in the solid state, as indicated by X-ray crystallography, both intramolecular (monomeric) and intermolecular (dimeric) interactions could occur between the cobalt(II) centres. Notably, complex **18** shows similar $\chi_m T$ vs T features as **16** between 2 – 18 K, however, for this complex intramolecular coupling is not possible (the magnesium(II) ion being diamagnetic). If a ferromagnetic interaction between Co(II) centres is causing the low temperature magnetic behaviour in **18** then intermolecular

interactions within the dimer, mediated by the bridging acetate ligands are assumed. The second shortest intermetallic distance in **18** is 5.75(5) Å (shortest intermolecular metal-metal distance in dimer), which lies within the reported range of Co-Co distances for complexes showing exchange interactions.[20-21] The final decrease of $\chi_m T$ at very low temperatures is due to intermolecular antiferromagnetic interactions and/or zero-field splitting effects of the ground state resulting from the antiparallel alignment of the interacting local spins.[20]

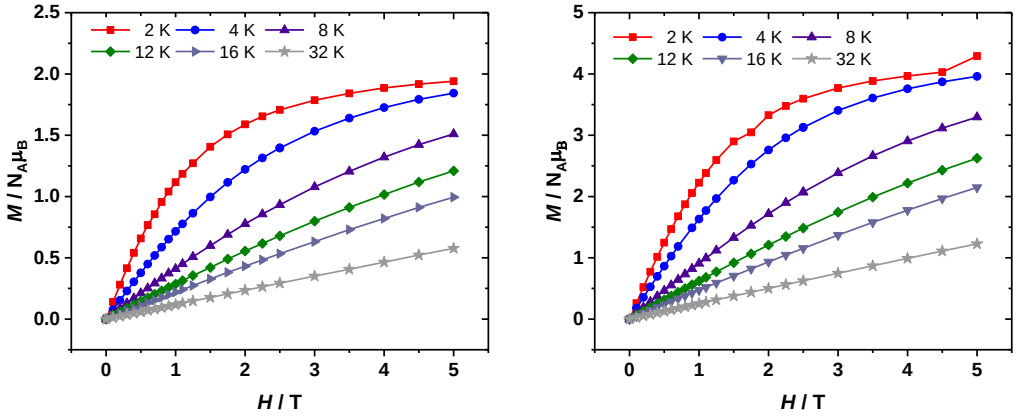


Figure 4.11: Field dependence of the magnetisation for complexes **16** (RHS) and **18** (LHD) per bimetallic complex.

Magnetisation, M, versus applied field, H, experiments of polycrystalline samples of **16** and **18** were measured ranging 2 – 32 K and is displayed per bimetallic complex (Figure 4.11). At 5 Tesla, **16** shows a saturation magnetisation (M_{sat}) of 4.29 μ_B (2.15 μ_B per Co(II) centre) and complex **18** shows a saturation value of 1.94 μ_B, at 2 K respectively. These values are smaller than the expected saturation value of 3 μ_B (6) for a high-spin Co(II) centre (where g = 2, S = 3/2). However, any difference may be consistent with population of the ground-state Kramer's doublet at T < 30 K, thus resulting in an effective spin S_{eff} = 1/2 (due to the single unpaired electron). Due to the octahedral symmetry of the Co(II) centre, the g factor is isotropic and thus has a

range of 4.4 – 4.0 (where α = 1.5 – 1.0, orbital reduction factor) (7), resulting in a maximum magnetic saturation of 2.2 μ_B which is in-line with experimental data for complexes **16** and **18** and with several other Co(II) complexes.[22-24]

$$M_{sat} = gS\ (\mu_B) \tag{6}$$

$$g_0 = \frac{10 + 2\alpha}{3} \tag{7}$$

4.2.1 CO_2/Epoxide Copolymerisations

Table 4.3: ROCOP of CO_2/CHO using the heterodinuclear MgCo catalyst.[a]

Entry	Cat. Loading (mol %)	Stirring (RPM)	CTA (eq)	Conv. (%)	TON[b]	TOF (h^{-1})[c]	M_n [Đ][d]
1	0.100	350	0	21	208	139	20500 [1.27] 8800 [1.13]
2	0.100	350	10	30	298	198	2800 [1.14]
3	0.100	350	20	41	409	272	1500 [1.12]
4	0.100	1400	20	51	510	340	2000 [1.13]
5	0.050	1400	20	32	648	432	2500 [1.11]
6	0.025	1400	20	15	606	404	2500 [1.16]

[a]Copolymerisation conditions: 80°C, 1 bar CO_2, 90 min, neat CHO (9.9 M). All reactions displayed >99 % CO_2 and polymer selectivity. [b]Turnover number (TON) = number of moles of cyclohexene oxide consumed / number of moles of catalyst. [c]Turnover frequency (ToF) = TON / Time (h).[d]Determined by SEC, in THF, using narrow-M_n polystyrene standards as the calibrant; dispersity is given in brackets.

The CO_2/CHO copolymerisation reactions were carried out using complex **18** at 80 °C, for 90 minutes, at 1 bar CO_2 pressure and in neat epoxide (9.9 M) (Table 4.3). All polymerisations displayed both excellent CO_2 selectivity (> 99 %) and polymer selectivity (> 99 %), with no polyether linkages or cyclic carbonate by-products observed by ^{1}H NMR spectroscopy. An initial study into the effects of adding chain transfer agent (CTA) was carried out using the bifunctional trans-1,2-cyclohexenediol to form dihydroxy-terminated, telechelic, polyols (Entry 1-3). As the amount of CTA is increased from 0 to 20 equivalents (vs catalyst), the activity increased two-fold from 139 h^{-1} to 272 h^{-1}. The increased activity is attributed to the decrease in solution viscosity as a result of the reduced molecular weight polyols (2000 g mol^{-1}). The activity was also increased by changing the stirring speed of the reaction from 350 RPM to 1400 RPM. This is attributed to mass transfer limitations. To further reduce the viscosity and find a region beyond mass transfer limit, the catalyst loading was reduced whilst maintaining CTA loading (Entry 4-6). A further increase in activity

was observed upon decreasing catalyst loading from 0.1 to 0.05 mol % (340 h^{-1} vs 432 h^{-1}). Decreasing the catalyst loading further to 0.025 mol % did not increase the rate of polymerisation further which indicated it is a safe region in which to study reaction kinetics.

Table 4.4: ROCOP of CO_2/CHO under varying temperature conditions.[a]

Cat.	Temp (°C)	Time (min)	CO_2 (%)[b]	Polym. (%)[c]	TON[d]	TOF (h^{-1})[e]	M_n [Đ][f]
MgCo	80	60	> 99	> 99	455	455	1700 [1.13]
MgCo	100	40	> 99	> 99	465	699	1600 [1.15]
MgCo	120	25	> 99	99	502	1205	2100 [1.24]
CoCo	120	60	> 99	96	712	712	2500 [1.20]
MgMg	120	60	> 99	> 99	368	368	1800 [1.16]
LIn(O^{t}Bu)^g	80	2880	> 99	95	350	15	3400 [1.32]
LZn$_3$Ce(OAc)$_3$^{h}	100	180	> 99	> 99	900	300	15000 [1.20]
LCo(X)^i	100	180	> 99	> 99	1315	263	48200 [1.12]
L$_2$Zn$_2$^{j}	80	1440	> 99	98	1684	149	2700 [1.28]

[a]Copolymerisation conditions: cat : CHO 0.05 mol %, 1 bar CO_2, neat CHO (9.98 M). [b]Expressed as a percentage of CO_2 uptake vs the theoretical maximum (100 %), determined by comparison of the relative integrals of the ^{1}H NMR resonances due to carbonate (δ 4.65 ppm) and ether (δ 3.45 ppm) linkages in the polymer backbone. [c]Expressed as a percentage of polymer formation vs. the theoretical maximum (100 %), determined by comparison of the relative integrals of the ^{1}H NMR proton resonances due to polymer (4.65 ppm), cis-cyclic carbonate (4.68 ppm) and trans-cyclic carbonate (4.00 ppm). [d]Turnover number (TON) = number of moles of cyclohexene oxide consumed / number of moles of catalyst. [e]Turnover frequency (ToF) = TON / Time (h). [f]Determined by SEC, in THF, using narrow-M_n polystyrene standards as the calibrant; dispersity is given in brackets .[g]0.1 mol % catalyst loading.[h]0.05 mol % catalyst loading, 3 bar CO_2 pressure [i]0.02 mol % catalyst loading, 1 bar CO_2. [j]0.1 mol % catalyst loading.

After this activity evaluation, complex **18** was tested using new standard conditions: 0.05 mol % catalyst loading, 1400 RPM stirring speed, 1 bar CO_2 pressure with 20 equivalents CTA (Table 4.4). All polymerisations retained excellent CO_2 and polymer selectivity (>96 %) over the temperature range 80 – 120 °C, with only trace amounts of *trans*-cyclic carbonate observed at 120 °C. An increase in activity from 455 h^{-1} to 1205 h^{-1} was observed with increasing temperature. In comparison, complexes **16** and **17** produced activities of 712^{-1} and 368 h^{-1}, under equivalent conditions. These results strongly suggest there is a heterodinuclear rate enhancement, similar to that

observed with Mg(II)Zn(II), and highlight also the improved performance of Mg(II)Co(II) as a metal combination.[25]

To provide context to the values, the best activity of 1205 h^{-1} is six times higher than the highest 1 bar CO_2 pressure catalyst reported to date, forming perfectly alternating poly(cyclohexene carbonate) (Table 4.4). Some of the most active catalysts for the ROCOP of CO_2/CHO at 1 bar CO_2 pressure are illustrated below (Figure 4.12). In general, multi-metallic catalysts are significantly more active than monometallic systems. These results support a bimetallic mechanism favouring the concerted attack of a nucleophile to ring open the epoxide.

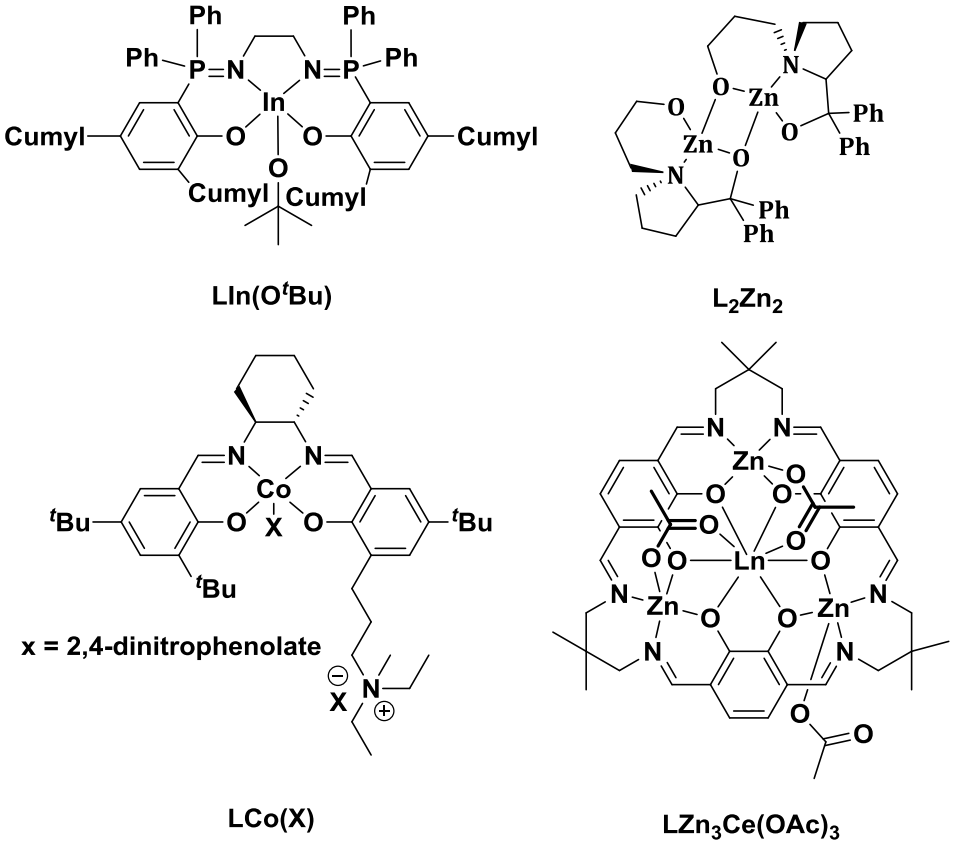


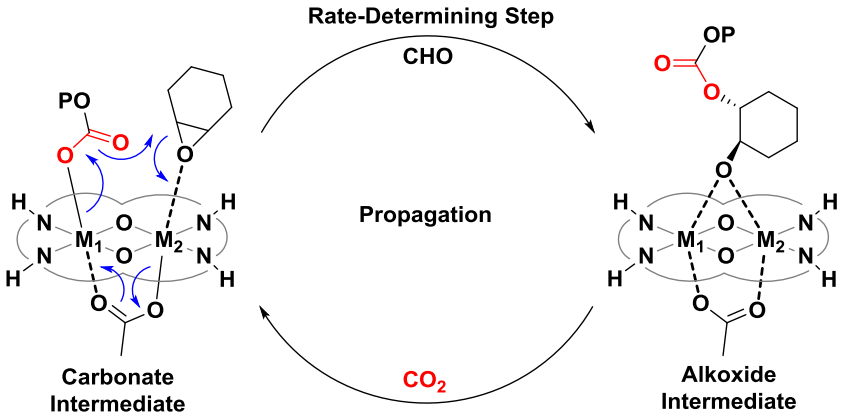
Figure 4.12: Catalysts with the highest reported activity for the ROCOP of CO_2/CHO reported in the literature, per metal centre.[26-29]

4.2.2 Rate Law Determination Mg(II)Co(II)

The homodinuclear complexes di-zinc, di-magnesium and di-cobalt were determined to show the rate law (8):

$$rate = k[Cat]^1[CHO]^1[CO_2]^0 \quad (8)$$

A 'chain-shuttling' mechanistic hypothesis was proposed where the rate determining step (RDS) is the ring opening of a metal bound epoxide by the adjacent metal bound carbonate (Scheme 4.2).[30-31] To understand the performance, it was important to determine the rate law for Mg(II)Co(II). In particular, understanding the RDS is important to identify any potential effects of metal synergy.



Scheme 4.2: 'Chain-shuttling' mechanistic proposal

Kinetic experiments to determine the order of each reaction component were carried out at 100 °C. Catalyst and epoxide orders were determined using *in-situ* infrared spectroscopy, at 1 bar CO_2 pressure. The order in CO_2 (fugacity) was determined using a high pressure reactor vessel equipped with an *in-situ* infrared probe.

For in *situ* IR measurements, reactions were monitored by following the change in intensity (absorbance) of a signal at 988, 1160 and 1330 cm^{-1} (Figure 4.13(a) and (b)). The absorbance was calibrated for monomer conversion by ^{1}H NMR spectroscopy (Figure 4.13 (c)) and the k_{obs} values (gradient) were calculated by a liner fit of the logarithm of epoxide concentrations vs. time (Figure 4.13 (d)). A standard error of ±2.2 % was determined.

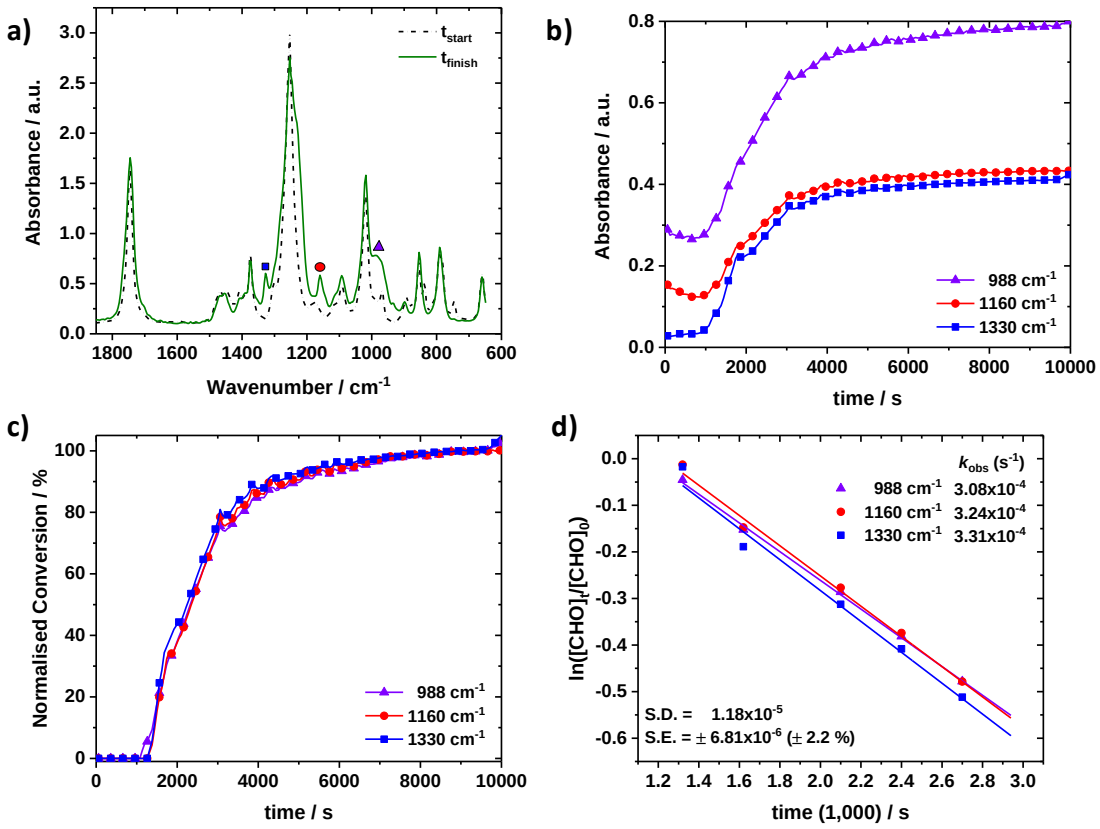


Figure 4.13: (a) ReactIR spectrum recorded at the start and finish of the polymerisation. Three peaks associated with PCHC were analysed: 988 (▲), 1160 (●) and 1330 cm^{-1} (■). (b) Absorbance vs. time plot for the three PCHC wavenumbers (every 5th point displayed). (c) Normalised conversion vs. time plot for the three PCHC wavenumbers (every 5th point displayed). (d) Logarithm of epoxide concentration vs. time for the three PCHC wavenumbers. k_{obs} (s^{-1}) approximately similar for each wavenumber monitored.

Reaction Order Catalyst: The order in [catalyst]^x was determined over the range 0.43 mM to 1.67 mM in diethylcarbonate, with 3.33 M CHO, at 100 °C and 1 bar CO_2 pressure. The order in catalyst was determined by applying a normalised time method, reported by Bures.[32]

The rate law for CO_2/epoxide copolymerisation can be described by (9).

$$rate = k[Cat]^x[CHO]^y[CO_2]^z \quad (9)$$

Simplification of this rate law to determine order of catalyst is given by (10).

$$-\frac{d[CHO]}{dt} = k_{obs}[Cat]^x \quad (10)$$

$Where\ k_{obs} = k[CHO]^y[CO_2]^z$

Integration of equation (10) results in a simplified equation (12) and plotting [CHO] *vs.* [Cat]^X T for a series of catalyst concentrations allows determination of the order in catalyst (Figure 4.14). For each analysis, the value of 'X' was systematically changed.

$$\frac{1}{k_{obs}}\int_{[CHO]_0}^{[CHO]_t} d[CHO] = \int_0^T [Cat]^X\, dt \quad (11)$$

$$[CHO]_{\Delta T} = -k_{obs}[Cat]^X T \quad (12)$$

A first order dependence on the catalyst concentration is clearly indicated by the overlap of [epoxide] vs normalised time over the range of catalyst concentrations measured. The first order dependence is in agreement with the rate law determined for previous catalysts, including both the dinuclear magnesium and cobalt catalysts.[3, 30]

$$rate = k[Cat]^1[CHO]^y[CO_2]^z \quad (13)$$

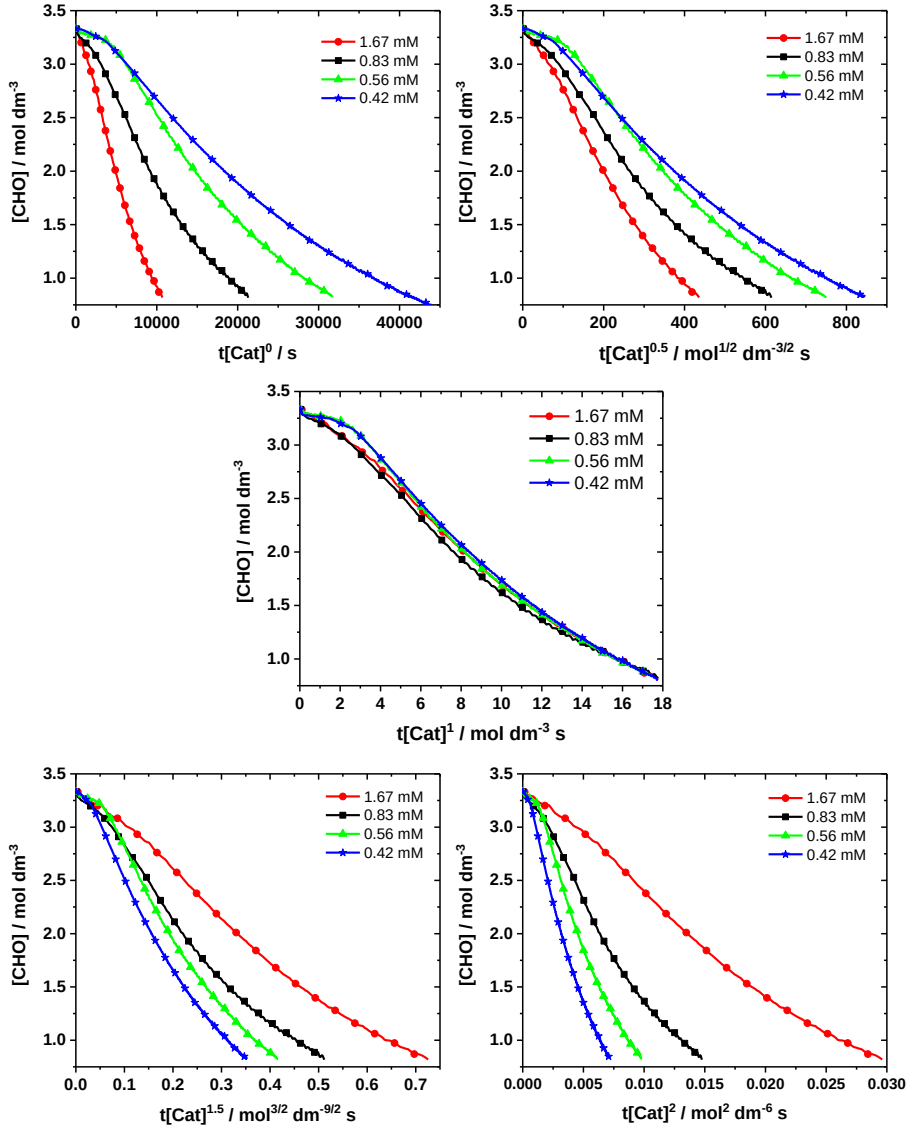


Figure 4.14: Rate of CO_2/CHO ROCOP processed under various orders of [catalyst] (0^{th} Top LHS, 0.5^{th} Top RHS, 1^{st} Middle, 1.5^{th} Bottom LHS, 2^{nd} Bottom RHS). Every 10^{th} point presented.

When the catalyst concentration exceeded 1.67 mM the catalyst order diverged from one towards a second order dependence. Increasing the catalyst concentration could favour the formation of dimers/aggregates in solution, as indicated by X-ray crystallography, and therefore, may result in a second order dependence. All further investigations were carried out at catalyst concentrations less than 1.67 mM, as this is the region of highest interest for any application.

Reaction Order Epoxide (CHO): The reaction order in epoxide concentration was determined over the range 1 to 5 M in diethylcarbonate, at a catalyst loading of 0.05 mol %, at 100 °C and at 1 bar CO_2 pressure (Figure 4.15).

A first order rate dependence in epoxide concentration would take the form (14):

$$-\frac{d[CHO]}{dt} = k_{obs}[CHO]^y \tag{14}$$

$$where\ k_{obs} = k[Cat]^x[CO_2]^y$$

$$\int_{[CHO]_o}^{[CHO]} \frac{d[CHO]}{[CHO]} = -k_{obs}\int_{t=0}^{t=t} dt \tag{15}$$

$$\ln[CHO] = \ln[CHO]_0 - k_{obs}t \tag{16}$$

This expression can be integrated (15) to give the exponential for the integrated rate law (16). By analysing the semi-logarithmic relationship between epoxide concentration and time, a linear fit indicates the first order dependence. The rate constant can be calculated by the gradient of the fit.

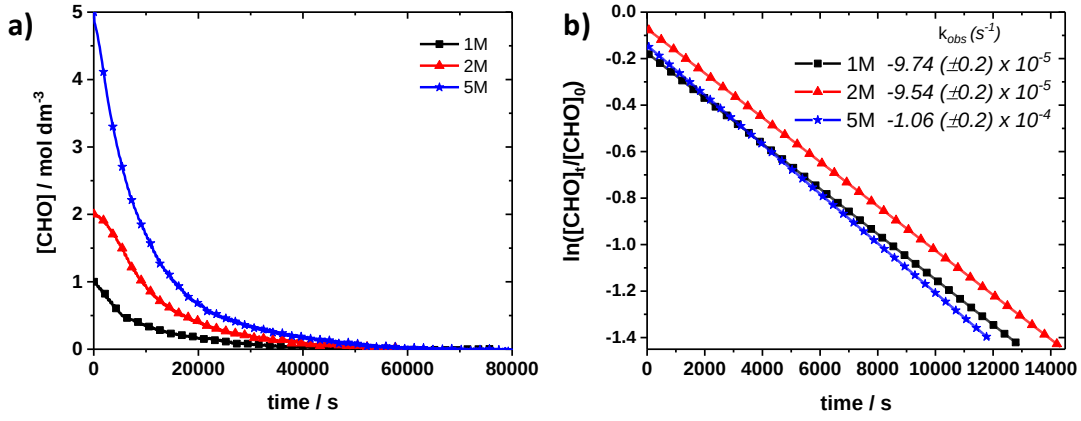


Figure 4.15: ROCOP of CO_2/CHO using MgCo. Concentration vs time plot (LHS) every 30th point plotted. Logarithm of Concentration vs Time(RHS) every 30th point plotted.

The data is analysed in each case from 5-75 % conversion and clearly shows a first order dependence on the concentration of epoxide. The overall rate law of (17) for complex **18** can be updated.

$$rate = k[Cat]^1[CHO]^1[CO_2]^z \quad (17)$$

Reaction Order CO_2: The rate dependence on the partial pressure of carbon dioxide was determined from 10 to 40 bar, in 3.33 M CHO, 0.05 mol % catalyst loading in diethylcarbonate, and at 100 °C (Figure 4.16). An initial rates method was used where by the intial rate (5-15 % conversion) is plotted against partial pressure of CO_2. There was not a strong correlation suggesting a zero order dependence on $P_{(CO2)}$. The slight negative curvature may be due to the gas expansion in the sub-critical regime, which has previously been observed for CO_2 at pressure >30 bar. The overall rate law is represented by equation (18).

$$rate = k[Cat]^1[CHO]^1[CO_2]^0 \quad (18)$$

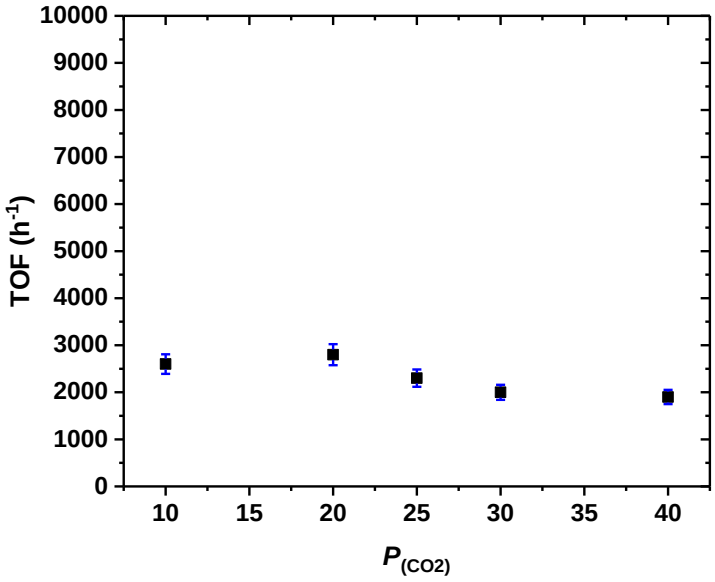


Figure 4.16: Activity vs. partial pressure of CO_2 for the ROCOP of CO_2/CHO using catalyst **18**.

4.2.3 CO_2 limit vs saturated ROCOP of CO_2/CHO

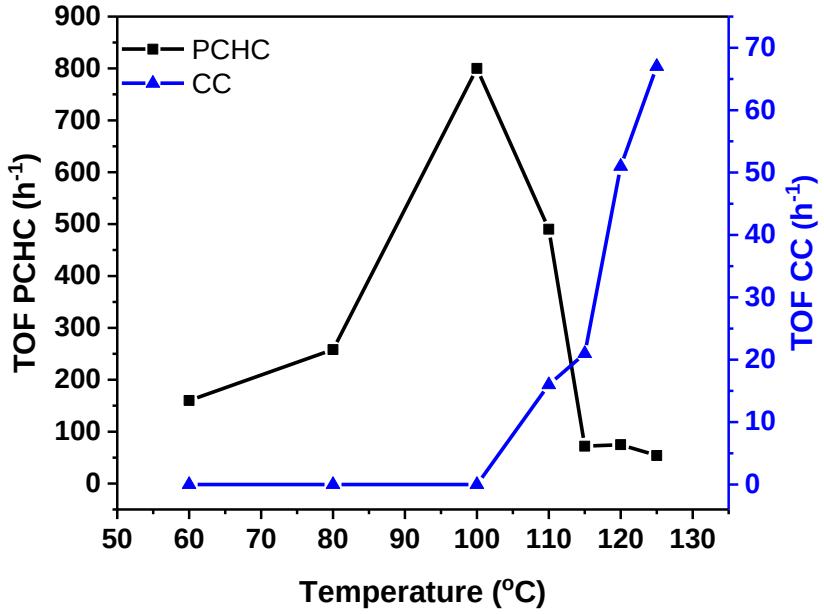


Figure 4.17: Activity vs temperature for the formation of polycarbonate (PCHC, Square) and cyclic carbonate (CC, triangle) at 1 bar CO_2.

The effect of temperature on the rate of polycarbonate (PCHC) and cyclic carbonate (CC) formation was investigated over the temperature range 60 to 125 °C in 3.33 M CHO solution in diethylcarbonate, 0.05 mol % catalyst loading and 1 bar CO_2 pressure (Figure 4.17). From 60 - 100 °C the polymerisation activity increased (160 h^{-1} to 800 h^{-1}). Above 100 °C, there is an exponential decrease in rate of polymer formation (800 h^{-1} to 54 h^{-1}) and the concurrent increase in the rate of cyclic carbonate formation from 0 h^{-1} to 67 h^{-1} resulting in a decrease in the polymer selectivity from >99 % to 49 % (Table 4.5).

Table 4.5: Effect of temperature on CO_2/CHO copolymerisation, at 1 bar CO_2.[a]

Temp (°C)	Time (h)	CO_2 (%)[b]	Polym. (%)[c]	TON[d]	TOF (PCHC) (h^{-1})[e]	TOF (CC) (h^{-1})
60	3.9	> 99	> 99	300	160	-
80	0.7	> 99	> 99	300	418	-
100	0.3	> 99	> 99	300	800	-
110	0.5	> 99	92	380	490	16
115	4.7	> 99	75	600	72	21
120	3.5	> 99	70	460	75	51
125	3.5	> 99	49	240	54	67

[a]Copolymerisation conditions: cat : CHO 0.05 mol %, 20 equiv. 1,2-cyclohexane diol, 1 bar CO_2. [b]Expressed as a percentage of CO_2 uptake vs the theoretical maximum (100 %), determined by comparison of the relative integrals of the ^{1}H NMR resonances due to carbonate (δ 4.65 ppm) and ether (δ 3.45 ppm) linkages in the polymer backbone. [c]Expressed as a percentage of polymer formation vs. the theoretical maximum (100 %), determined by comparison of the relative integrals of the ^{1}H NMR proton resonances due to polymer (4.65 ppm), cis-cyclic carbonate (4.68 ppm) and trans-cyclic carbonate (4.00 ppm). [d]Turnover number (TON) = number of moles of cyclohexene oxide consumed / number of moles of catalyst. [e]Turnover frequency (ToF) = TON / Time (h).

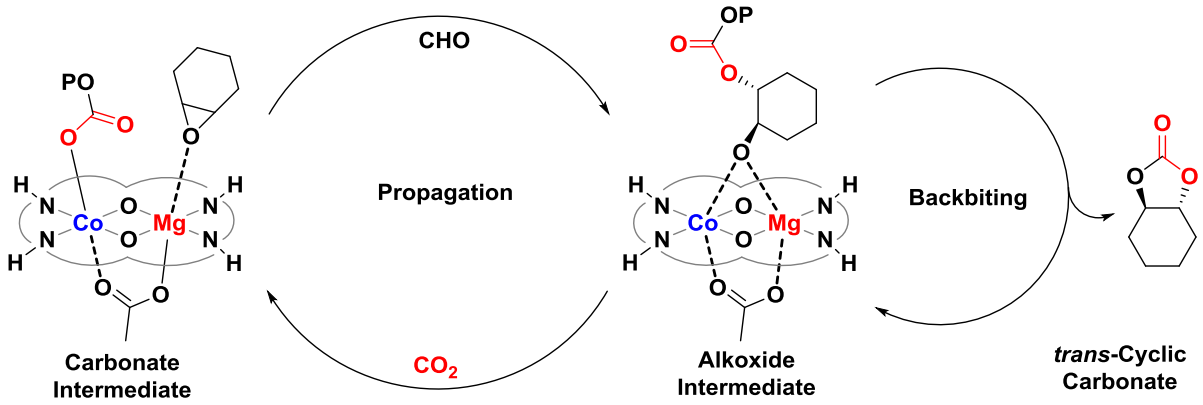
These observations were rationalised by the decreasing CO_2 solubility in epoxide at increasing temperatures. Indeed gas solubility is expressed by Henry's Law (19), where C_{CO2} is the concentration of CO_2 in solution, P_{CO2} is the partial pressure of CO_2 and $K_H(T)$ is Henry's constant.

The temperature-dependence of Henry's constant can be expressed by equation (20) due to the small temperature range considered (ΔT <20 °C), where ΔH_H and ΔS_H are the enthalpy and entropy of phase change and R is the gas constant. With an increase in temperature there is a decrease in $K_H(T)$, and a reduced concentration of CO_2 in solution (C_{CO2}) at a fixed pressure (P_{CO2}).

As a result, the rate of CO_2 insertion may become diffusion limited at higher temperatures and the catalytic resting state is the metal alkoxide species (Scheme 4.3). The alkoxide intermediate may undergo both propagation (dependent on CO_2 pressure) and backbiting reactions to form cyclic carbonate. Since the back-biting reaction does not depend on CO_2 concentration, its rate increases at elevated temperature.

$$C_{CO2} = P_{CO2}\, x\, K_H(T) \tag{19}$$

$$ln\, K_H(T) = \left(\frac{-\Delta H_H}{R}\right)\left(\frac{1}{T}\right) + \frac{\Delta S_H}{R} \tag{20}$$



Scheme 4.3: Mechanism shift due to lower solubility of CO_2 at higher temperature

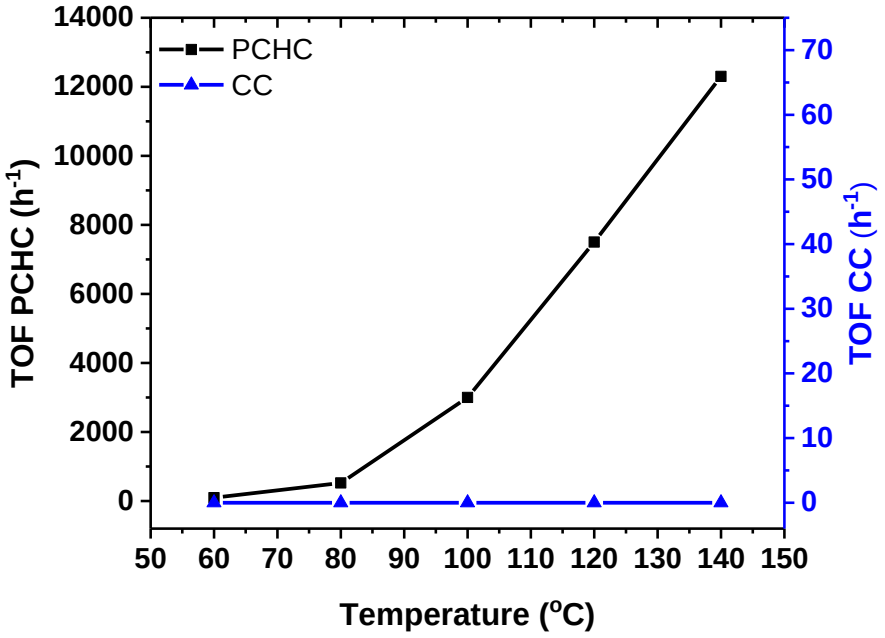


Figure 4.18: Activity vs temp for the formation of polycarbonate (PCHC, square) and cyclic carbonate (CC, triangle) at 20 bar CO_2.

To overcome CO_2 solubility and achieve higher rates of polymerisation, the study was carried out at a partial pressure of 20 bar (Figure 4.18). Reactions were carried out in 3.33 M CHO in diethylcarbonate, catalyst loading of 0.05 mol %. Over the entire temperature range, there is an increase in the initial rate (5-10 % conversion) of polycarbonate formation from 78 h^{-1} at 60 °C to 12,462 h^{-1} at 140 °C (10-20 % conversion). Furthermore, near complete selectivity for polycarbonate (>99 %) is observed with no cyclic carbonate being observed by either in-*situ* infrared spectroscopy or ^{1}H NMR spectroscopy.

Table 4.6 ROCOP of CO_2/CHO under varying temperature conditions.[a]

Cat.	Temp (°C)	CO_2 (%)[b]	Polym. (%)[c]	TON[d]	ToF (h^{-1})[e]	k_p ($dm^3\ mol^{-1}\ s^{-1}$)[e]	k_{rel}[f]
MgCo	60	> 99	> 99	240	78	0.0151	14
MgCo	80	> 99	> 99	400	510	0.0931	85
MgCo	100	> 99	> 99	320	3200	0.4289	390
MgCo	120	> 99	> 99	480	7200	1.2312	1120
MgCo	140	> 99	> 99	360	12462	1.7844	1622
MgMg	120	> 99	> 99	300	1059	0.2697	245
CoCo	120	> 99	> 99	240	4200	0.5592	508
ZnZn	80	> 99	92	530	22	0.0011	1
MgZn[h]	120	> 99	> 99	-	-	0.5140	467
BEt_3 PPNCl[i]	80	> 99	> 99	3600	600	-	-
CrSalen PPNCl[j]	80	> 99	> 99	2686	1153	-	-
LCo_2X PPNX[k]	25	> 99	> 99	339	1356	-	-
LCo_2X[k]	25	> 99	> 99	400	200	-	-
LFeCl $^nBu_4NCl$[l]	80	> 99	> 99	400	400	0.0056	5

*[a]Copolymerisation conditions: cat : CHO 0.05 mol %, 20 bar CO_2. All entries report >99 CO_2 selectivity vs. theoretical maximum (100 %), determined by comparison of the relative integrals of the ^1H NMR resonances due to carbonate (δ 4.65 ppm) and ether (δ 3.45 ppm) linkages in the polymer backbone. [b]Expressed as a percentage of polymer formation vs. the theoretical maximum (100 %), determined by comparison of the relative integrals of the ^1H NMR proton resonances due to polymer (4.65 ppm), cis-cyclic carbonate (4.68 ppm) and trans-cyclic carbonate (4.00 ppm). [c]Turnover number (TON) = number of moles of cyclohexene oxide consumed / number of moles of catalyst. [d]Turnover frequency (ToF) = TON / Time (h) (measured between 5-20 % conversion). [e]$k = k_{obs}$ / [cat]^1, k_{obs} determined from the gradient of $\ln([CHO]_t/[CHO]_0)$ vs. time plot [cat] = 1.67 mM. [f]Rate constant relative to **ZnZn** at 80 °C, $k_{rel} = k/0.0011$. [h]0.1 mol% cat, 20 bar CO_2. [i]0.03mol% cat, 0.015 mol% PPNCl, 10 bar CO_2. [j]0.043 mol %, 35 bar CO_2. [k]0.1 mol % cat, 0.2 mol % PPNCl, 20 bar CO_2. [l]0.1 mol% cat, 0.1mol% $^nBu_4N$, 10 bar CO_2.*

At elevated CO_2 pressure (20 bar) high selectivity for both CO_2 uptake and polymer (> 99 %) is retained with an increase in temperature. Increasing the temperature from 60-140 °C for complex **18**, there is over a 100-fold increase in catalytic activity, with a maximum TOF of 12,462 h^{-1} and a rate constant (k_p) of 1.7844 $dm^3\ mol^{-1}\ s^{-1}$.

The higher activity observed for the heterodinuclear complex **18** compared to the homodinuclear complexes **16** and **17** at 1 bar CO_2 pressure (Table 4.6) is once again observed at 20 bar pressure with activities of 7200, 4200 and 1056 h^{-1} for **18**, **16** and **17**, respectively, at 120 °C.

Furthermore, complex **18** is significantly more active than homodinuclear complex **17** and the heterodinuclear MgZn complex reported, with rate constants of 1.2312,

0.5140 and 0.2697 dm^3 mol^{-1} s^{-1}, at 120 °C. This may be due to the increased nucleophilicity of the Co-carbonate in comparison to Zn- and Mg-carbonate to enhance epoxide ring opening.

Catalyst activities are typically reported in terms of a point-kinetic TOF value. Furthermore, catalysts are often measured under different catalytic conditions and thus making fair comparisons is often challenging. From the catalysts activities reported, the MgCo complex is by far the most active when comparing the TOF values, albeit under both higher temperature and dilution.

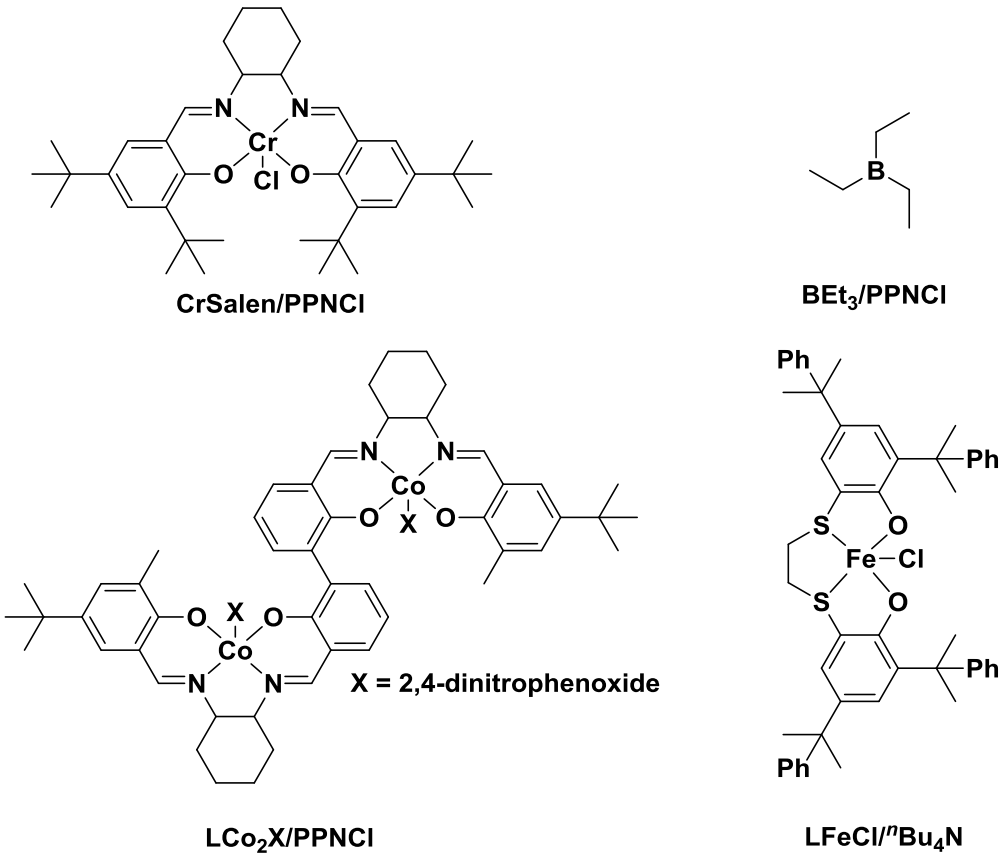


Figure 4.19: Highly active CO_2/CHO catalysts at elevated CO_2 pressure.

4.2.4 Gibbs Free Energy of Transition

As the rate laws for **16**-**18** are identical, it allows a common mechanistic rational. To further understand the rate enhancement for the heterocomplex **18**, over both complexes **16** and **17,** an investigation into the transition state thermodynamic parameters was undertaken. The Gibbs free energy for the RDS was determined by analysis of rate versus temperature behaviours, i.e. an Eyring analysis.

The kinetics of CO_2/CHO copolymerisation suggest the RDS is a bimolecular reaction passing through a transition state (21), where K‡ is the equilibrium constant (22).

$$catalyst + Monomer = Transition\ State^{\ddagger} \rightarrow Polymer \tag{21}$$

$$K^{\ddagger} = \frac{[Transition\ State]^{\ddagger}}{[Catalyst][Monomer]} \tag{22}$$

The rate of a reaction can be described in several ways. (a) the concentration of species at the transition state multiplied by the frequency of which the transition state species form the product (23) and (b), the concentration of the molecular components multiplied by a rate constant (24).

$$rate = \nu[Transition\ State]^{\ddagger} = \nu[Catalyst][Monomer]K^{\ddagger} \tag{23}$$

$$rate = k[Catalyst][Monomer] \tag{24}$$

Equating the two equations, the rate constant is equal to the frequency of vibration, *ν*, multiplied by the equilibrium constant $K^{\ddagger}$ (25).

$$k = \nu K^{\ddagger} = \frac{k_B T}{h} K^{\ddagger} \tag{25}$$

$$where\ \nu = \frac{k_B T}{h}$$

The Gibbs Free Energy of Transition, $\Delta G^{\ddagger}$, can be expressed as a function of the equilibrium constant (26) or in terms of enthalpy and entropy (27). Equating these equations (28) and solving for the rate constant, k, results in the Eyring Equation (29). A linear form of the Eyring equation can be expressed by equation (30) where plotting ln(k/T) vs 1/T results in the enthalpy term as the gradient (31) and the entropy term is proportional to the y-intercept (32).

$$\Delta G^{\ddagger} = -RT ln K^{\ddagger} \tag{26}$$

$$\Delta G^{\ddagger} = \Delta H^{\ddagger} - T\Delta S^{\ddagger} \tag{27}$$

$$ln K^{\ddagger} = -\frac{\Delta H^{\ddagger}}{RT} + \frac{\Delta S^{\ddagger}}{R} \tag{28}$$

$$k = \frac{k_B T}{h} e^{-\frac{\Delta H^{\ddagger}}{RT}} e^{\frac{\Delta S^{\ddagger}}{R}} \tag{29}$$

$$ln\frac{k}{T} = -\frac{\Delta H^{\ddagger}}{R}\left(\frac{1}{T}\right) + ln\frac{k_B}{h} + \frac{\Delta S^{\ddagger}}{R} \tag{30}$$

Gradient $$-\frac{\Delta H^{\ddagger}}{R} \tag{31}$$

Y-intercept $$\frac{\Delta S^{\ddagger}}{R} + ln\frac{k_B}{h} \tag{32}$$

Experiments were conducted using an initial CHO concentration of 3.33 M in diethylcarbonate, a catalyst concentration of 1.67 mM and at 20 bar CO_2 pressure

(Figure 4.20). Reactions were tested at 20 °C increments, over the range 60 – 120 °C. The higher pressure of CO_2 was used in order to avoid the backbiting side reaction forming cyclic carbonate as discussed in 4.2.3.

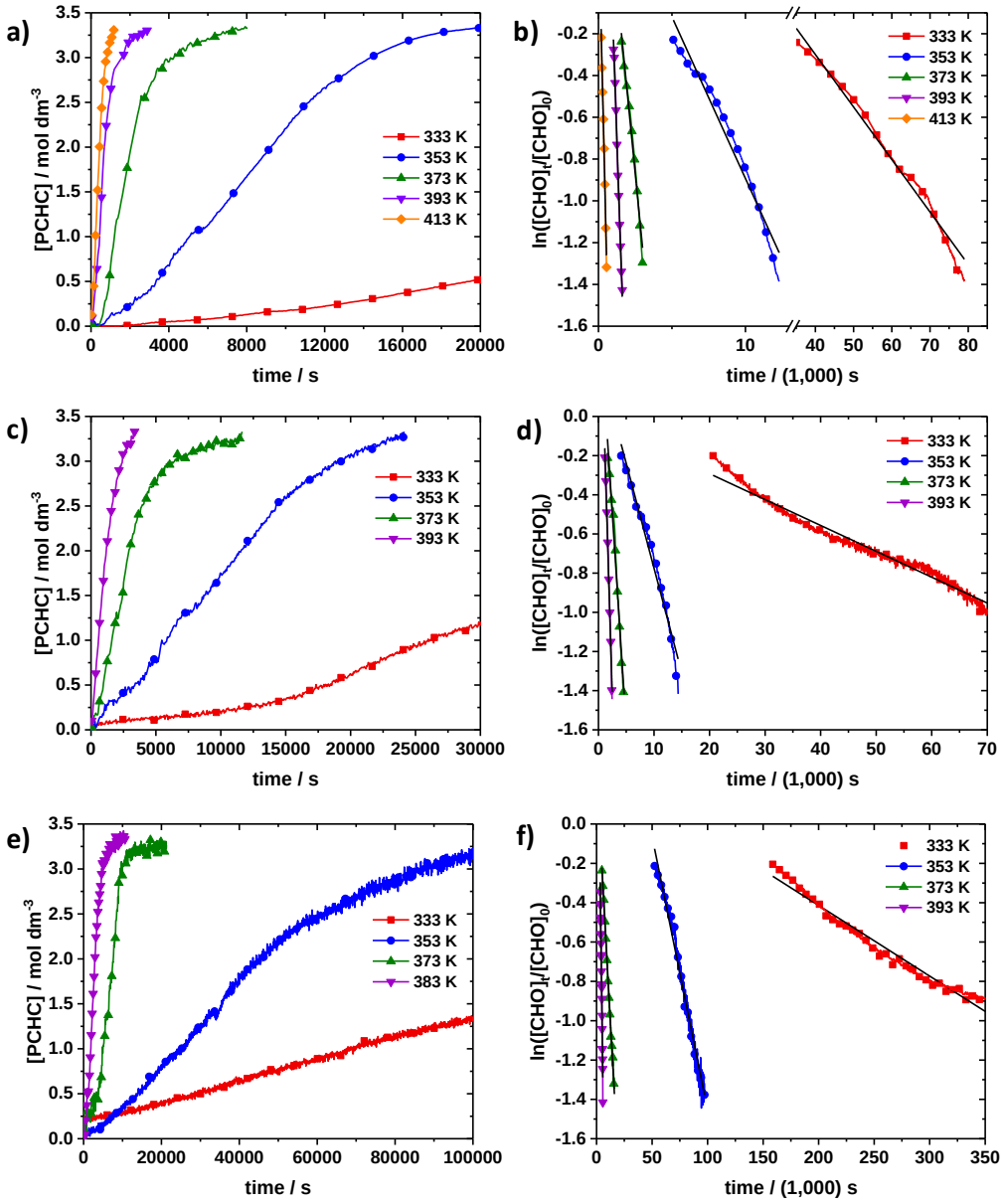


Figure 4.20. (a)/(c)/(d) formation of PCHC vs time plots for **MgCo**, **CoCo** and **MgMg** and various temperatures. (b)/(d)/(f) Logarithm of CHO concentration vs time plot for **MgCo**, **CoCo** and **MgMg** at various temperatures. (Table S13-S15)

An Eyring analysis (ln(k/T) vs 1/T) was used to determine the enthalpic and entropic contributions for **16**-**18** (Figure 4.21, Table 4.7).

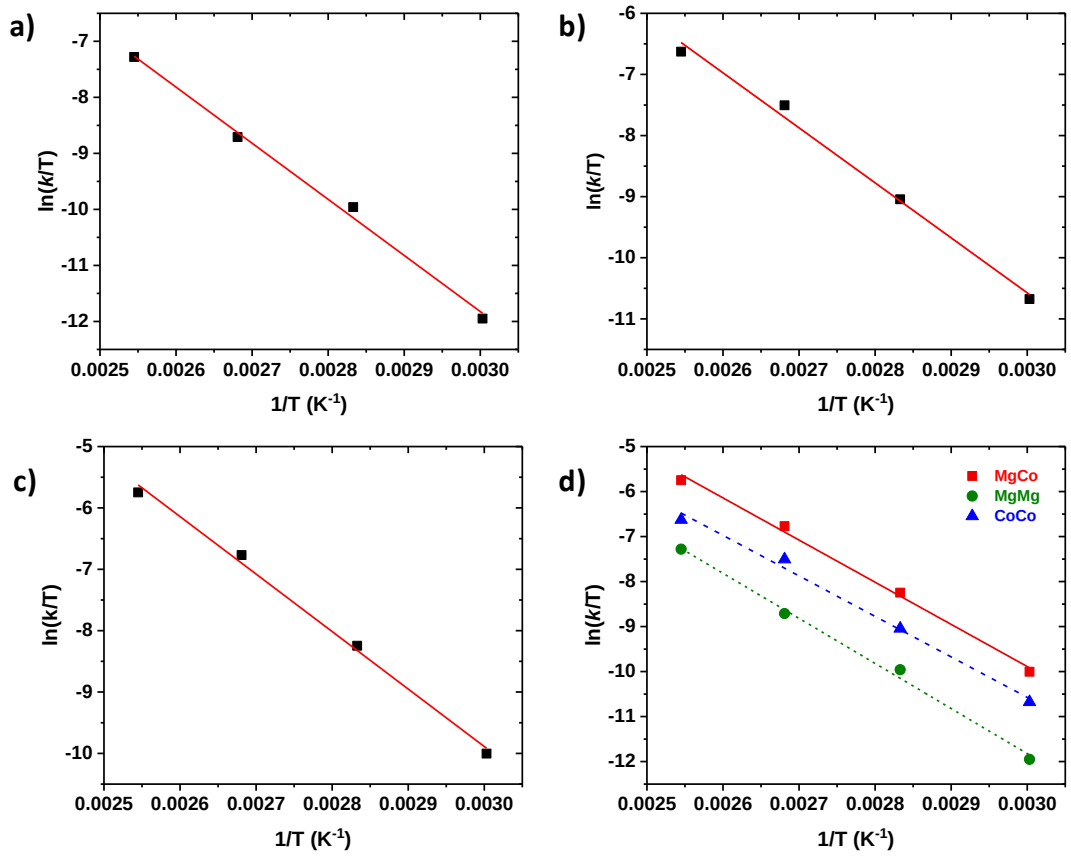


Figure 4.21 Eyring plots (ln(k/T) vs 1/T) for **MgCo** (a), **CoCo** (b) and **MgMg** (c), respectively. (d) Combined Eyring Analysis for **MgCo (■), CoCo(▲)** and **MgMg(●)**.

Figure 4.22: Eyring plots for complexes **16-18** over the temperature range 60 °C to 120 °C under 20 bar CO_2 pressure.

Table 4.7: Summarises data from Eyring plot in figure 4.15

Catalyst	y = mx + c	R^2	$\Delta H^{\ddagger}$ (kJ mol^{-1})	$\Delta S^{\ddagger}$ (J mol^{-1} k^{-1})	$\frac{\sigma(\Delta S^{\ddagger})}{\sigma(\Delta H^{\ddagger})}$
MgMg	10090 x + 18.41	0.9978	+83.3(±1.3)	-45.4(±3.7)	0.00285
CoCo	9002 x + 16.43	0.9965	+74.9(±1.5)	-60.2(±4.2)	0.00280
MgCo	9368 x + 18.21	0.9978	+77.3(±1.2)	-46.1(±3.4)	0.00283

Linear fits were applied to the data and in all cases R^2 exceeded 0.9965. Standard errors, σ, were calculated using the least squares fitting method where the division of

σ(ΔS‡) by σ(ΔH‡) equates approximately to inverse of the average temperature, $1/T_{average} = 0.00274\ K^{-1}$.[33]

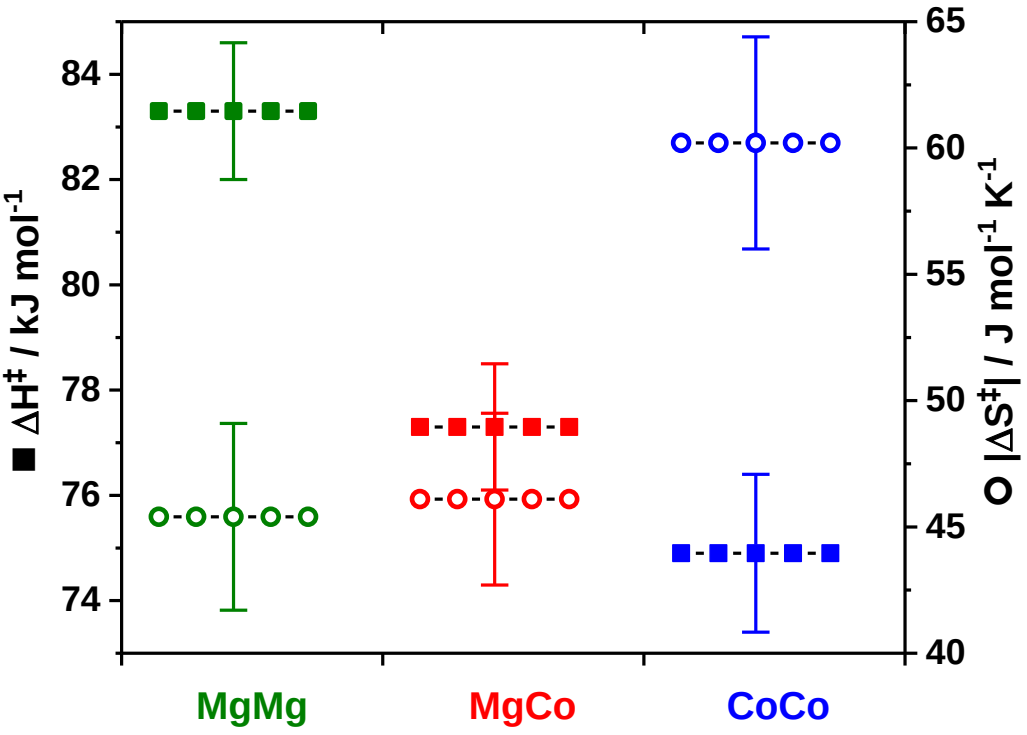


Figure 4.23: Calculated values of ΔH‡ (■, ±1.3) and ΔS‡ (O, ±3.7) for **MgMg**, **CoCo** and **MgCo**.

The transition state enthalpy, ΔH‡, decreases from the di-magnesium to the di-cobalt catalyst by 8.4 kJ mol^{-1} (Figure 4.23). Concurrently, the transition state entropy, ΔS‡, decreases by 14.8 J mol^{-1}. The heterodinuclear magnesium-cobalt complex, **18**, shows both a similar enthalpy to the di-cobalt complex (77.3 kJ mol^{-1}) and entropy to the di-magnesium complex (-46.1 J mol^{-1} K^{-1}). Considering the chain-shuttling mechanism, the RDS is the ring opening of the epoxide. Together with X-ray crystallographic evidence, it is hypothesised that the magnesium binds the epoxide (a significant entropic event) whereas the cobalt centre provides the carbonate nucleophile (a significant enthalpic event). The favourable increase in entropy caused by the

substitution of the cobalt centre for a magnesium centre may be due to the increased ionic character of the epoxide binding process and thus a decrease in the directionality of the adduct formed. This may result in an increase in the number of available microstates/degrees of freedom at the transition state. It is hypothesised a further increase in entropy may be observed with a more ionic metal centre such as sodium or potassium, although this ligand was shown to be unsuitable for those metals due to the size of the ligand binding cavity, as described in Chapter 2.

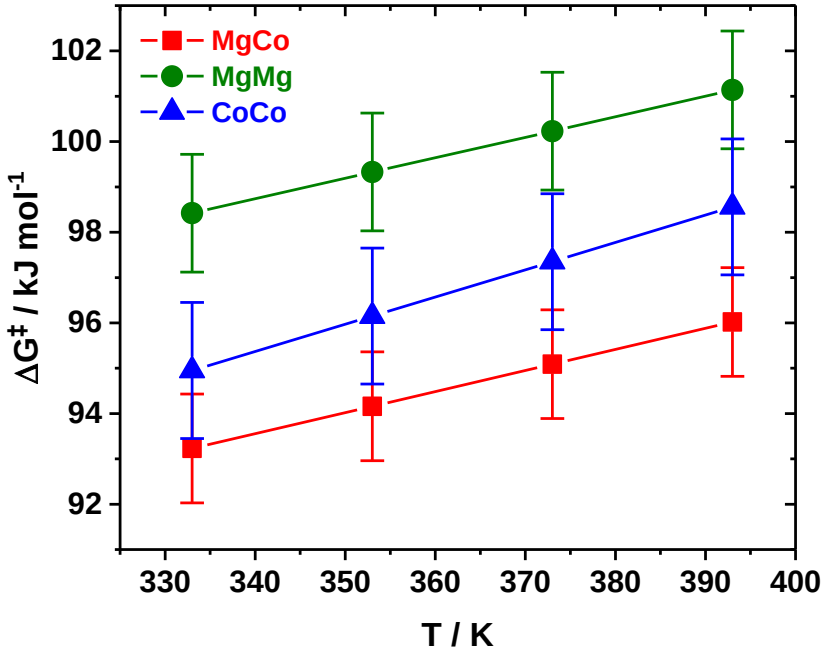


Figure 4.24: Plot of Gibbs Free Energy of Transition (ΔG‡) vs. temperature (K) **MgMg** (●, ±1.3) **CoCo** (▲, ±1.5) and **MgCo** (■, ±1.2) across the temperature range 333-393 K.

The transition state Gibbs free energy ($\Delta G^{\ddagger}$, T = 373 K) values are 94.5(±1.2), 97.3(±1.5) and 100.2(±1.3) kJ mol^{-1} for **18**, **16** and **17**, respectively (Figure 4.24). Over the series of catalysts, the transition state barrier decreases by 5.7 kJ mol^{-1} which correlates well with the observed 8-fold increase in rate for the heterodinuclear catalyst (34). The analogous dizinc catalyst (**ZnZn**) shows $\Delta G^{\ddagger}$ = 107

kJ mol^{-1} (T = 373 K) and accordingly **18** is ~84-times faster; these findings clearly demonstrate the benefit of targeting the right metal combinations and synergies.

$$k = \frac{k_B T}{h} e^{-\frac{\Delta G^{\ddagger}}{RT}} \quad (33)$$

$$\frac{k_1}{k_2} = e^{-\frac{\Delta\Delta G^{\ddagger}}{RT}} \quad (34)$$

4.2.6 Anhydride/CHO ROCOP catalysis

The heterodinuclear complex **18** was tested in the ROCOP of a series of anhydrides with cyclohexene oxide. Monomers include: maleic anhydride (MA), succinic anhydride (SA), phthalic anhydride (PA) and norbornene anhydride (NA) (Figure 4.25).

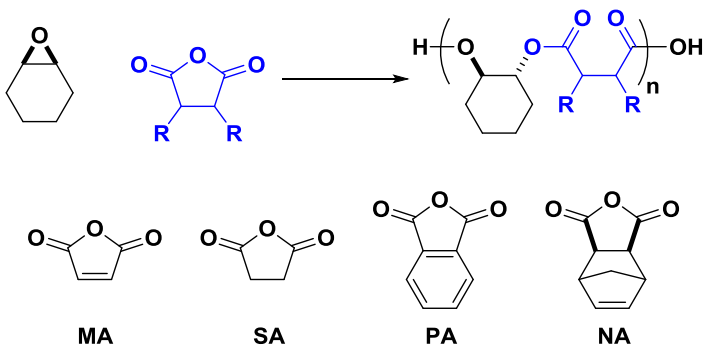


Figure 4.25: Series of anhydride tested for the ROCOP with CHO

The reactions were tested under the following conditions: 0.025 mol % catalyst loading (1 eq.), 0.5 M anhydride (200 eq.) 0.5 M CHD (20 eq.) in neat cyclohexene oxide (4000 eq.) at 120 °C (60 °C was used for MA to prevent cross-linking of the alkene groups). The reaction progress was monitored by *in-situ* infrared spectroscopy by analysis of changes to anhydride resonances at ~ 1780 cm^{-1} (Figure 4.26 and Table 4.8).

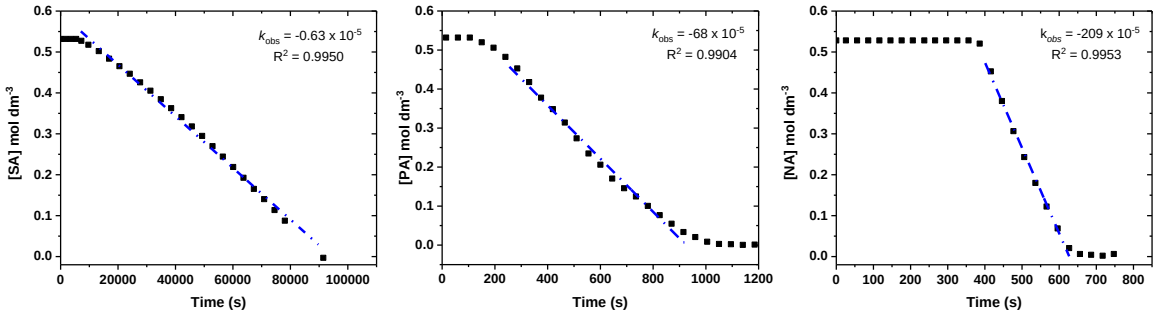


Figure 4.26: Concentration vs time plots for the ROCOP of anhydrides with CHO using catalyst **18**. Succinic anhydride (LHS), phthalic anhydride (Centre), norbornene anhydride (RHS).

Table 4.8: ROCOP of anhydride with CHO using heterodinuclear complex **18**.

M	Cat.	Time (min)	Temp (°C)	TON	TOF (h^{-1})	k_{obs} (x10^{-5}) (s^{-1})	M_n [Đ] (g mol^{-1})
MA[a]	**18**	1440	60	-	-	-	-
SA	**18**	1440	120	400	8	0.63	-
PA	**18**	20	120	400	925	68	2200 [1.14]
	a	90	100	188	125	-	6200 [1.12]
	b	15	100	295	1180	-	7800 [1.25]
NA	**18**	13	120	400	2992	209	2400 [1.17]
	a	90	100	155	103	-	3500 [1.32]
	c	300	110	243	48	-	3000 [1.02]
	d	15	110	243	970	-	11900 [1.28]

Catalysts (Figure 4.23) **a** Chromium salen.[34] **b** di-Iron triphenolate.[35] **c** Chromiun salphen.[36] **d** (ONSO)Chromium.[37]

The reaction of MA with CHO, at 60 °C, resulted in no conversion, as observed by ^{1}H NMR spectroscopy, after 24 h. This is expected as CO_2/CHO ROCOP reactions with **18** were typically active > 80 °C. In this case, a higher temperature could not be used due to the side-reaction whereby the alkene group cross-links at elevated temperature.

The reactions of SA, PA and NA each with CHO were all very fast at 120 °C, with increasing activity (8 h^{-1} vs 2992 h^{-1}). This rate may be rationalised by the increased nucleophilicity for more sterically hindered anhydrides. A similar kinetic trend was previously reported by Coates and co-workers using a mononuclear aluminium salan catalyst in anhydride/PO ROCOP reactions.[38-39]

Comparing the rate of **18** for PA/CHO with other reported catalysts shows it is in one of the most active at 925 h^{-1}. The most active is a di-iron tris-phenolate catalyst (**c**) with an activity of 1180 h^{-1} at 100 °C.[35] **18** is significantly more active than the commercial chromium salan catalyst (**a**), with PPNCl co-catalyst, with an activity reported at 125 h^{-1} at 100 °C.[34]

Catalyst **18** also proved highly active for NA/CHO ROCOP, showing a 30-fold increase in activity with respect to the commercial chromium salan catalyst (**a**).[34] The next highest reported activity for the ROCOP of NA/CHO is 970 h^{-1}, by a (ONSO)chromium catalyst (**d**), but complex **18** is 3-times more active that this and sets a new highest value.[37]

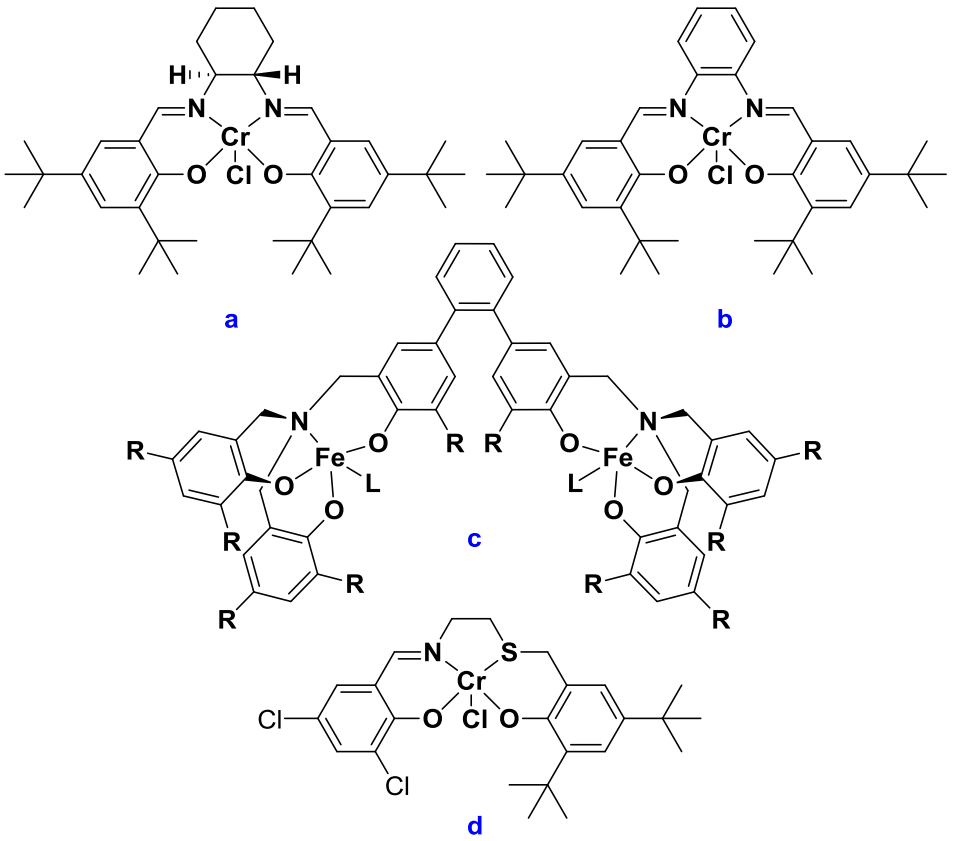


Figure 4.27: Series of catalysts active in the ROCOP of anhydride/CHO reported in the literature.

4.2.5 Conclusion

The one-pot synthesis of a stable heterodinuclear Mg(II)Co(II) complex along with homodinuclear analogues Mg(II)Mg(II) and Co(II)Co(II) coordinated by a dinucleating macrocyclic ligand were reported. The heterocomplex was characterised by cyclic voltammetry whereby only one oxidation is observed as opposed to two oxidations for the di-cobalt complex. Mg(II)Co(II) displayed high activities for the ROCOP of CO_2/epoxide, at 1 bar CO_2 pressure, with an activity of 1205 h^{-1} forming perfectly alternating copolymer. Increasing the CO_2 pressure to bar, resulted in a TOF of over 12,000 h^{-1}, three times higher than the next best catalyst, producing perfectly alternating copolymer. The polymerisation rate was CO_2 diffusion limited at high temperature using 1 bar CO_2 pressure but this is easily solved by increasing CO_2 pressure to 20 bar (where no diffusion limit was observed). The Gibbs free energy was determined for Mg(II)Co(II), Mg(II)Mg(II) and Co(II)Co(II), with the heterocomplex having the lowest energy transition state (94 kJ mol^{-1}, 373 K). We hypothesise that the role of each metal is optimised in this catalyst with cobalt showing the lowest TS‡ enthalpy whilst magnesium optimises the entropy. This mechanistic rationale could be explored in future both to increase reactivity and to apply the catalyst to other reactions.

4.2.6 References

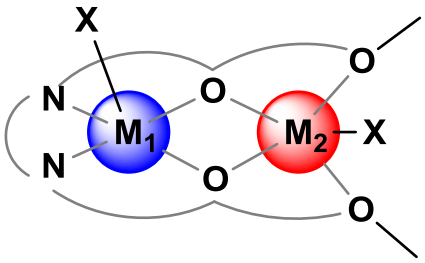
1. Deacy, A. C.; Durr, C. B.; Garden, J. A.; White, A. J. P.; Williams, C. K., Groups 1, 2 and Zn(II) Heterodinuclear Catalysts for Epoxide/CO_2 Ring-Opening Copolymerization, *Inorg. Chem.,* **2018,** *57*, (24), 15575.
2. Kember, M. R.; White, A. J. P.; Williams, C. K., Highly Active Di- and Trimetallic Cobalt Catalysts for the Copolymerization of CHO and CO_2 at Atmospheric Pressure, *Macromolecules,* **2010,** *43*, (5), 2291.
3. Kember, M. R.; Jutz, F.; Buchard, A.; White, A. J. P.; Williams, C. K., Di-cobalt(ii) catalysts for the copolymerisation of CO_2 and cyclohexene oxide: support for a dinuclear mechanism?, *Chem. Sci.,* **2012,** *3*, (4), 1245.
4. Moulder, J. F.; Sitickle, W. F.; Sobol, P. E.; Bomben, K. D., *Handbook of X-ray Photoelectron Spectroscopy*. Perkin Elmer Corporation: Eden Prairie, Minnesota, USA, 1979.
5. Corneille, J. S.; He, J.-W.; Goodman, D. W., XPS characterization of ultra-thin MgO films on a Mo(100) surface, *Surf. Sci.,* **1994,** *306*, (3), 269.
6. Borod'ko, Y. G.; Vetchinkin, S. I.; Zimont, S. L.; Ivleva, I. N.; Shul'ga, Y. M., Nature of satellites in x-ray photoelectron spectra XPS of paramagnetic cobalt (II) compounds, *Chem. Phys. Lett.,* **1976,** *42*, (2), 264.
7. Dillard, J. G.; Schenck, C. V.; Koppelman, M. H., Surface Chemistry of Cobalt in calcined cobalt-kaolinite materials, *Clays Clay Miner.,* **1983,** *31*, (1), 69.
8. Menezes, P. W.; Indra, A.; Gutkin, V.; Driess, M., Boosting electrochemical water oxidation through replacement of Oh Co sites in cobalt oxide spinel with manganese, *Chem. Commun.,* **2017,** *53*, (57), 8018.
9. Menezes, P. W.; Indra, A.; González-Flores, D.; Sahraie, N. R.; Zaharieva, I.; Schwarze, M.; Strasser, P.; Dau, H.; Driess, M., High-Performance Oxygen Redox Catalysis with Multifunctional Cobalt Oxide Nanochains: Morphology-Dependent Activity, *ACS Catal.,* **2015,** *5*, (4), 2017.
10. Natile, M. M.; Glisenti, A., Study of Surface Reactivity of Cobalt Oxides: Interaction with Methanol, *Chem. Mater.,* **2002,** *14*, (7), 3090.
11. Halfen, J. A.; Jazdzewski, B. A.; Mahapatra, S.; Berreau, L. M.; Wilkinson, E. C.; Que, L.; Tolman, W. B., Synthetic Models of the Inactive Copper(II)−Tyrosinate and Active Copper(II)−Tyrosyl Radical Forms of Galactose and Glyoxal Oxidases, *J. Am. Chem. Soc.,* **1997,** *119*, (35), 8217.
12. Bill, E.; Müller, J.; Weyhermüller, T.; Wieghardt, K., Intramolecular Spin Interactions in Bis(phenoxyl)metal Complexes of Zinc(II) and Copper(II), *Inorg. Chem.,* **1999,** *38*, (25), 5795.
13. Itoh, S.; Taki, M.; Kumei, H.; Takayama, S.; Nagatomo, S.; Kitagawa, T.; Sakurada, N.; Arakawa, R.; Fukuzumi, S., Model Complexes for the Active Form of Galactose Oxidase. Physicochemical Properties of Cu(II)− and Zn(II)−Phenoxyl Radical Complexes, *Inorg. Chem.,* **2000,** *39*, (16), 3708.
14. Mukherjee, A.; Lloret, F.; Mukherjee, R., Synthesis and Properties of Diphenoxo-Bridged CoII, NiII, CuII, and ZnII Complexes of a New Tripodal Ligand: Generation and Properties of MII-Coordinated Phenoxyl Radical Species, *Inorg. Chem.,* **2008,** *47*, (11), 4471.
15. DiCiccio, A. M.; Longo, J. M.; Rodríguez-Calero, G. G.; Coates, G. W., Development of Highly Active and Regioselective Catalysts for the Copolymerization of Epoxides with Cyclic Anhydrides: An Unanticipated Effect of Electronic Variation, *J. Am. Chem. Soc.,* **2016,** *138*, (22), 7107.

16. Compton, R. G.; Banks, C. E., *Understanding Voltammetry*. 2nd ed.; Imperial College Press: Covent Garden, London, UK, 2011.
17. Arora, H.; Philouze, C.; Jarjayes, O.; Thomas, F., CoII, NiII, CuII and ZnII complexes of a bipyridine bis-phenol conjugate: Generation and properties of coordinated radical species*, Dalton Trans.,* **2010,** *39*, (42), 10088.
18. Bain, G. A.; Berry, J. F., Diamagnetic Corrections and Pascal's Constants*, J. Chem. Educ.,* **2008,** *85*, (4), 532.
19. Lloret, F.; Julve, M.; Cano, J.; Ruiz-García, R.; Pardo, E., Magnetic properties of six-coordinated high-spin cobalt(II) complexes: Theoretical background and its application*, Inorg. Chim. Acta,* **2008,** *361*, (12), 3432.
20. Martin, E.; Tudor, V.; Madalan, A. M.; Maxim, C.; Tuna, F.; Lloret, F.; Julve, M.; Andruh, M., Heterometallic CoII-CoIII-MII alkoxido-bridged heptanuclear motifs (M=Cu, Zn). Syntheses, crystal structures and magnetic properties*, Inorg. Chim. Acta,* **2018,** *475*, 98.
21. De Munno, G.; Julve, M.; Lloret, F.; Faus, J.; Caneschi, A., 2,2′-Bipyrimidine (bipym)-bridged dinuclear complexes. *J. Chem. Soc., Dalton Trans.,* **1994,** (8), 1175.
22. Mishra, V.; Lloret, F.; Mukherjee, R., Coordination versatility of 1,3-bis[3-(2-pyridyl)pyrazol-1-yl]propane: Co(II) and Ni(II) complexes*, Inorg. Chim. Acta,* **2006,** *359*, (12), 4053.
23. Rodriguez, A.; Sakiyama, H.; Masciocchi, N.; Galli, S.; Gálvez, N.; Lloret, F.; Colacio, E., Hexacyanocobaltate(III) Anions as Precursors of Co(II)−Ni(II) Cyano-Bridged Multidimensional Assemblies: Hydrothermal Syntheses, Crystal and Powder X-ray Structures, and Magnetic Properties*, Inorg. Chem.,* **2005,** *44*, (23), 8399.
24. Herrera, J. M.; Bleuzen, A.; Dromzée, Y.; Julve, M.; Lloret, F.; Verdaguer, M., Crystal Structures and Magnetic Properties of Two Octacyanotungstate(IV) and (V)-Cobalt(II) Three-Dimensional Bimetallic Frameworks*, Inorg. Chem.,* **2003,** *42*, (22), 7052.
25. Garden, J. A.; Saini, P. K.; Williams, C. K., Greater than the Sum of Its Parts: A Heterodinuclear Polymerization Catalyst*, J. Am. Chem. Soc.,* **2015,** *137*, (48), 15078.
26. Thevenon, A.; Cyriac, A.; Myers, D.; White, A. J. P.; Durr, C. B.; Williams, C. K., Indium Catalysts for Low-Pressure CO_2/Epoxide Ring-Opening Copolymerization: Evidence for a Mononuclear Mechanism?*, J. Am. Chem. Soc.,* **2018,** *140*, (22), 6893.
27. Nagae, H.; Aoki, R.; Akutagawa, S.; Kleemann, J.; Tagawa, R.; Schindler, T.; Choi, G.; Spaniol, T. P.; Tsurugi, H.; Okuda, J.; Mashima, K., Lanthanide Complexes Supported by a Trizinc Crown Ether as Catalysts for Alternating Copolymerization of Epoxide and CO_2: Telomerization Controlled by Carboxylate Anions*, Angew. Chem. Int. Ed.,* **2018,** *57*, (9), 2492.
28. Mike, S.; Sebastian, D.; Franc, M., Highly Active and Readily Accessible Proline-Based Dizinc Catalyst for CO_2/Epoxide Copolymerization*, Chem. Eur. J.,* **2017,** *23*, (65), 16472.
29. Kissling, S.; Lehenmeier, M. W.; Altenbuchner, P. T.; Kronast, A.; Reiter, M.; Deglmann, P.; Seemann, U. B.; Rieger, B., Dinuclear zinc catalysts with unprecedented activities for the copolymerization of cyclohexene oxide and CO_2*, Chem. Commun.,* **2015,** *51*, (22), 4579.
30. Jutz, F.; Buchard, A.; Kember, M. R.; Fredriksen, S. B.; Williams, C. K., Mechanistic Investigation and Reaction Kinetics of the Low-Pressure Copolymerization of Cyclohexene Oxide and Carbon Dioxide Catalyzed by a Dizinc Complex*, J. Am. Chem. Soc.,* **2011,** *133*, (43), 17395.

31. Buchard, A.; Jutz, F.; Kember, M. R.; White, A. J. P.; Rzepa, H. S.; Williams, C. K., Experimental and Computational Investigation of the Mechanism of Carbon Dioxide/Cyclohexene Oxide Copolymerization Using a Dizinc Catalyst, *Macromolecules,* **2012,** *45*, (17), 6781.
32. Burés, J., A Simple Graphical Method to Determine the Order in Catalyst, *Angew. Chem. Int. Ed.,* **2016,** *55*, (6), 2028.
33. Lente, G.; Fábián, I.; Poë, A. J., A common misconception about the Eyring equation, *New J. Chem.,* **2005,** *29*, (6), 759.
34. Stößer, T.; Williams, C. K., Selective Polymerization Catalysis from Monomer Mixtures: Using a Commercial Cr-Salen Catalyst To Access ABA Block Polyesters, **2018,** *57*, (21), 6337.
35. Shi, Z.; Jiang, Q.; Song, Z.; Wang, Z.; Gao, C., Dinuclear iron(iii) complexes bearing phenylene-bridged bis(amino triphenolate) ligands as catalysts for the copolymerization of cyclohexene oxide with carbon dioxide or phthalic anhydride, *Polym. Chem.,* **2018,** *9*, (38), 4733.
36. Baumgartner, R.; Song, Z.; Zhang, Y.; Cheng, J., Functional polyesters derived from alternating copolymerization of norbornene anhydride and epoxides, *Polym. Chem.,* **2015,** *6*, (19), 3586.
37. Han, B.; Zhang, L.; Yang, M.; Liu, B.; Dong, X.; Theato, P., Highly Cis/Trans-Stereoselective (ONSO)CrCl-Catalyzed Ring-Opening Copolymerization of Norbornene Anhydrides and Epoxides, *Macromolecules,* **2016,** *49*, (17), 6232.
38. Van Zee, N. J.; Sanford, M. J.; Coates, G. W., Electronic Effects of Aluminum Complexes in the Copolymerization of Propylene Oxide with Tricyclic Anhydrides: Access to Well-Defined, Functionalizable Aliphatic Polyesters, *J. Am. Chem. Soc.,* **2016,** *138*, (8), 2755.
39. Fieser, M. E.; Sanford, M. J.; Mitchell, L. A.; Dunbar, C. R.; Mandal, M.; Van Zee, N. J.; Urness, D. M.; Cramer, C. J.; Coates, G. W.; Tolman, W. B., Mechanistic Insights into the Alternating Copolymerization of Epoxides and Cyclic Anhydrides Using a (Salph)AlCl and Iminium Salt Catalytic System, *J. Am. Chem. Soc.,* **2017,** *139*, (42), 15222.

Chapter 5:

O-Vanillin Derived Heterodinuclear Catalysts



M_1 = Zn(II), Mg (II)
M_2 = Na(I), Ca(II) and Cd(II)

Mg(II) Derived Catalysts
Less Active than
Zn(II) Derived Catalysts

High Heterodinuclear Purity (> 99 %) ☑

Hight Polyester Selectivity (> 99 %) ☑

Zn(II)Zn(II) Highest activity ($150\ h^{-1}$) ☑

5.1.1 Introduction

Globally, the production of polyesters reached 77 Mt in 2016, with a market value of $110 billion (USD).[1] Polyesters are produced as four major segments: filaments (44%, clothing), PET Resins (28 %, bottles), staples (20%, insulation) and Films (5%, packaging).[1] Typically, step-growth polycondensation is used but there are three pitfalls:[2]

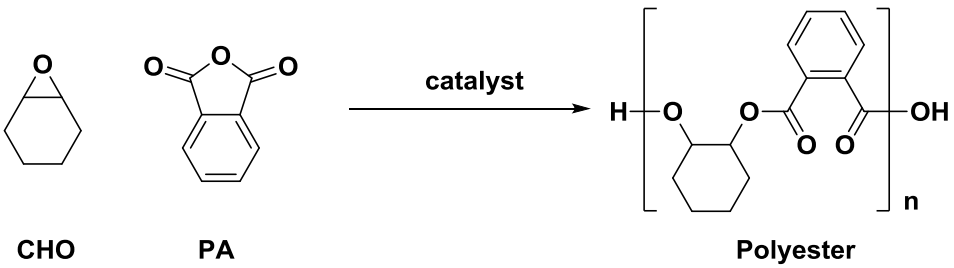
(1) Energy intensive process; high thermal conditions required to drive the formation of water/condensate.

(2) Uncontrolled polymerisation; unable to control molecular weight and high sensitivity to impurities therefore block polymers not easily accessed.

(3) lack of scope; unable to access a wide range of polyester materials, especially those derived from thermally unstable monomers.

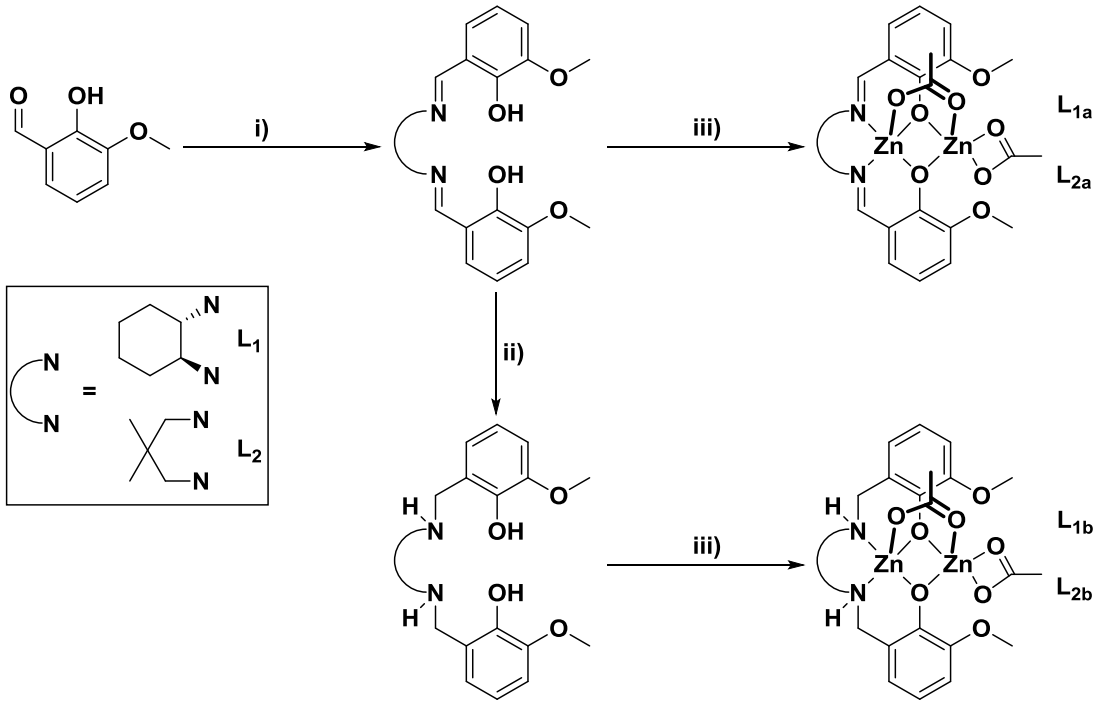
Epoxide/anhydride ROCOP provides an alternative which is applicable with a wide range of monomers and is well controlled. The high control of this catalysis enables predictable polymer MW and narrow dispersity.

The ROCOP of anhydride/epoxide is largely considered to operate by the same mechanism as the ROCOP of CO_2/epoxide,[3] with alteration between metal-alkoxide and metal-carboxylate catalytic intermediates. Typically, catalysts with good CO_2/epoxide activity display good activities for anhydride/epoxide.[2, 4-8] Dinuclear catalysts are currently the most active with an activity of 1100 h^{-1} for a di-iron(III) trisphenolate catalyst,[9] and 750 h^{-1} for a di-aluminium(III) salen catalyst for the ROCOP of phthalic anhydride/cyclohexene oxide at 100 °C.[7]



Scheme 5.1: Copolymerisation of anhydride/epoxide forming a polyester.

In 2015, a series of di-zinc catalysts derived from *o*-vanillin; an inexpensive, commercially available, bio-based ligand, were synthesised for the ROCOP of both CO_2/epoxide and anhydride/epoxide.[10] All complexes showed both low activity (0.1-3 h^{-1}) and selectivity (52-99%) in the ROCOP of CO_2/CHO at 1 bar pressure. An improvement in activity (44 h^{-1}) and selectivity (89-99%) was observed at 30 bar pressure, although are slow relative to the fastest CO_2/CHO ROCOP catalysts in the field.[11-15]



Scheme 5.2: Synthesis of catalysts L_{1a}-L_{2b}. i) 2 equiv. o-vanillin, 1 eq. diamine, MeOH, 25 °C, 4 h. ii) 3.5 eq. $NaBH_4$, MeOH, 25 °C, 2 h. H_2O, 25 °C, 16 h iii) 2 eq. $Zn(OAc)_2.2H_2O$, MeOH, 25 °C, 16 h.

Table 5.1: Copolymerisation of PA/CHO.[a]

Catalyst	Time (h)	Conv.(%)[b] and TON[c]	TOF (h^{-1})[d]	Polym. (%)[e]	M_n[f] [Đ][g] ($g\ mol^{-1}$)
L_{1a}	1.0	70	70	> 99	4400 [1.15]
L_{2a}	0.5	99	198	> 99	5300 [1.23]
L_{1b}	6.0	64	11	27	6400 [2.18]
L_{2b}	6.0	59	10	21	8200 [2.17]

[a]Copolymerisation conditions: Catalyst/PA/CHO = 1/100/800, 100, 100 °C. [b]Determined by ^{1}H NMR spectroscopy (DMSO-d_6) by integrating the normalized resonances for PA (7.97 ppm) and phenylene signals in polyester (7.30-7.83 ppm). [c]TON = number of moles of epoxide consumed per mole of catalyst. [d]TOF = TON/ h. [e]Determined by ^{1}H NMR spectroscopy (DMSO-d_6) by integrating the normalised resonances for ester linkages (4.80-5.26 ppm) and ether linkages (3.22-3.64 ppm). [f]Determined by SEC in THF calibrated using polystyrene standards.

Copolymerisations of PA/CHO were conducted at 100 °C with a catalyst/PA/CHO ratio of 1/100/800. Catalysts with an imine backbone showed significantly higher polyester selectivity (>99%) than those with an amine backbone (~25 %). This was rationalised by the more electron-donating imine, reducing the Lewis acidity of the metal centre, thus decreasing successive ring opening of epoxides.[10] Furthermore, catalyst L_{2a} displayed an activity of 198 h^{-1}, and was at that time amongst the highest activity for these monomers.[10]

Catalyst L_{2a} was further tested in terpolymerisation of PA/CHO/CO_2. At 100 °C, 30 bar CO_2 pressure in a mixture of 100/1000 PA/CHO. Complete selectivity to polyester formation was observed with no polycarbonate linkages as observed by ^{1}H NMR spectroscopy. Upon the complete consumption of PA, polycarbonate formation was observed. This selectivity is in-line with other di-zinc catalysts reported in terpolymerisation of anhydride/epoxide/CO_2, and thus can form poly(ester-block-carbonates) from a one-pot reaction mixture.[10]

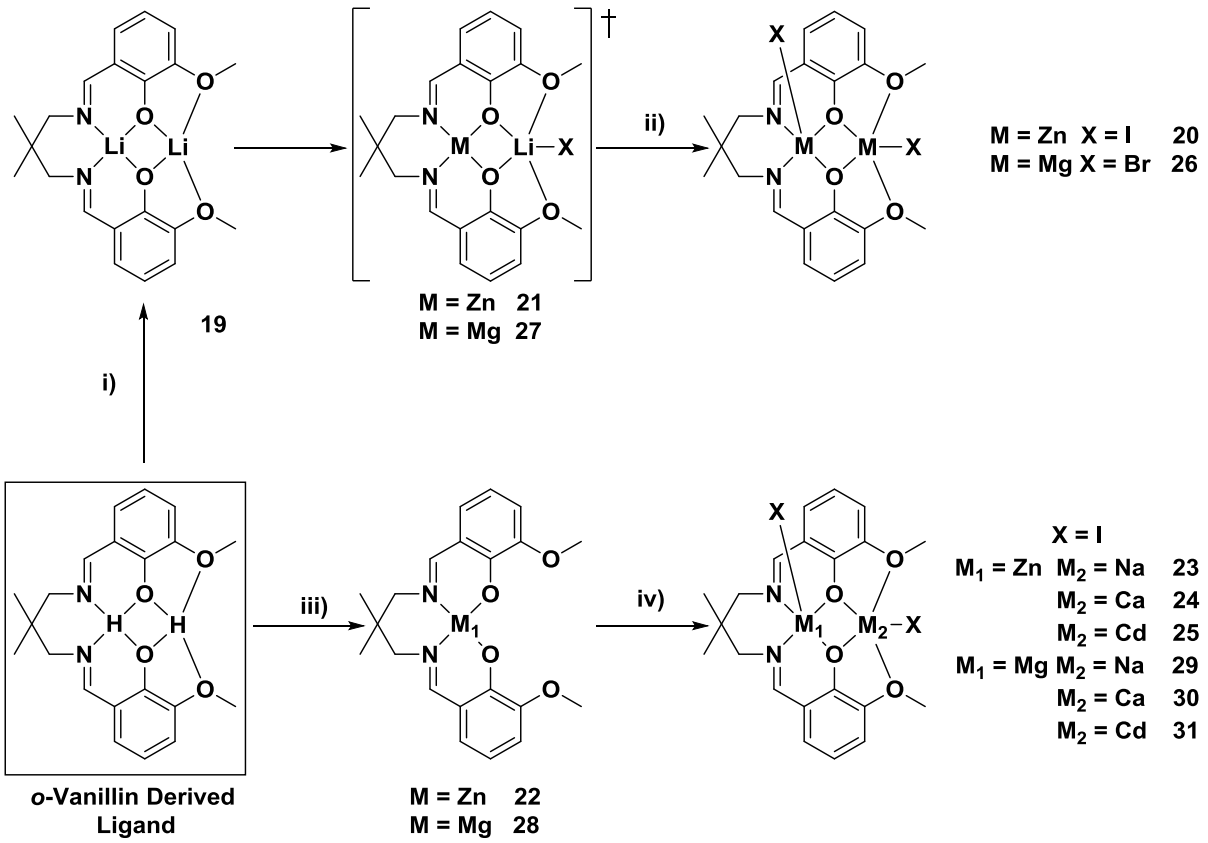
5.1.2 Aims

A series of heterodinuclear complexes are targeted for the ROCOP of anhydride/CHO (Scheme 5.2).[10] It was rationalised that heterodinuclear complexes may promote enhanced activities given the increase in rate observed for anhydride/CHO ROCOP of a Zn(II)Mg(II) complex versus their homodinuclear analogues for the macrocyclic ligand investigated in Chapters 2-4.[4]

As discussed in chapter 2 and 4, Group 1 and 2 metals are of significant interest due to their ionic character and may result in the lowering of the Gibbs free energy of transition for the ROCOP of CO_2/CHO. An issue for the macrocyclic ligand utilised in chapters 2-4, larger Group 1 and 2 elements were found to be too large to fit into the binding cavity and thus were not particularly effective. The utilisation of the *o*-vanillin derived ligand, the binding cavity is much larger and can therefore accommodate the larger Group 1 and 2 elements and thus heterodinuclear complexes with sodium and calcium are targeted.

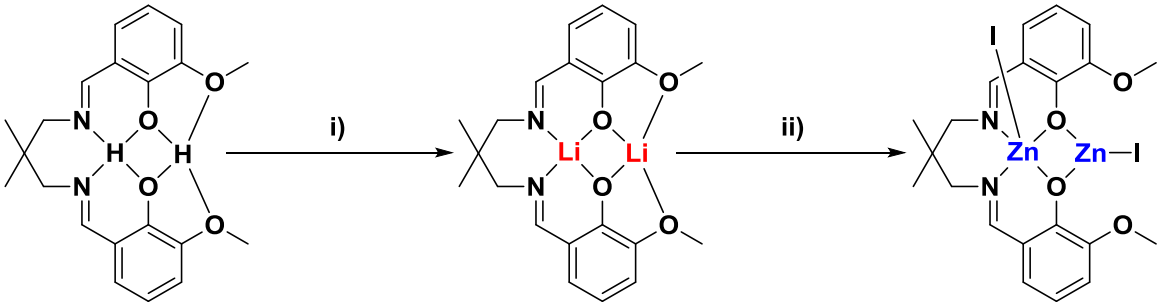
A series of heterodinuclear complexes derived from Mg(II) will also be targeted as higher activity for anhydride/CHO ROCOP was observed for the homodinuclear Mg(II) complex in comparison to the homodinuclear Zn(II) complex derived from the macrocycle utilised in Chapters 2-4.[2]

Finally, Cd(II) will be targeted for heterodinuclear synthesis due to it being NMR active and thus a possible probe for mechanistic insight. In comparison to Zn(II), Cd(II) is larger (74 pm vs. 95 pm), softer and less Lewis acidic and thus potentially provide a more labile nucleophile.



Scheme 5.3: Overall synthetic strategies targeting hetero- and homo-dinuclear Zn(II) and Mg(II) complexes **19**-**31**. i) 2 eq. $Li(N(Si(CH_3)_3)_2)$, THF, 25 °C, 4 h, 90 %. ii) 2 eq. MX_2 (where MX_2 = ZnI_2 or $MgBr_2$), THF, 25 °C, 16 h, > 80 %. iii) MX_2 (where MX_2 = $ZnEt_2$ or $Mg(N(Si(CH_3)_3)_2)_2$), THF, 25 °C, > 70 % iv) MI_n (Where M = Na(I), Ca(II) or Cd(II)), THF, 25 °C, > 70 %.

5.1.3 Synthesis and Characterisation of a Di-Zinc Complex



Scheme 5.4: Synthesis of complexes **19** and **20**. i) 2 eq. Li(N(Si(CH$_3$)$_3$)$_2$), THF, 25 °C, 4 h, 90 %. ii) 2 eq. ZnI$_2$, THF, 25 °C, 16 h, 82 %.

The di-lithium complex, **19**, was synthesised via deprotonation of the pro-ligand using a lithium (I) amide salt, in THF at 25 °C (Scheme 5.1). The di-zinc iodide complex, **20**, was synthesised by addition of two equivalents of zinc (II) iodide to complex **19**, in THF at 25 °C (Scheme 5.1). The products were isolated as white powders in high yields (> 80 %) and were characterised by multinuclear NMR spectroscopy (Figure S107-SS113) and X-ray crystallography (Figure S111 and S120-S121), with purity confirmed by elemental analysis.

Successful deprotonation of the ligand was confirmed by monitoring the loss of the phenolic proton resonance of the pro-ligand at 13.40 ppm in the ^{1}H NMR spectrum (Figure 5.1). A significant up field shift, 0.5 ppm, of the imine proton resonance was observed, indicative of metal coordination due to the relative electropositivity of the metal centres with respect to a proton. The addition of zinc (II) iodide caused anisotropic splitting of the methylene and methyl proton resonances centred at 3.75 ppm and 0.75 ppm, respectively, in the ^{1}H NMR spectrum. This anisotropic splitting is indicative of zinc (II) coordination due to the adoption of a pentacoordinate geometry.

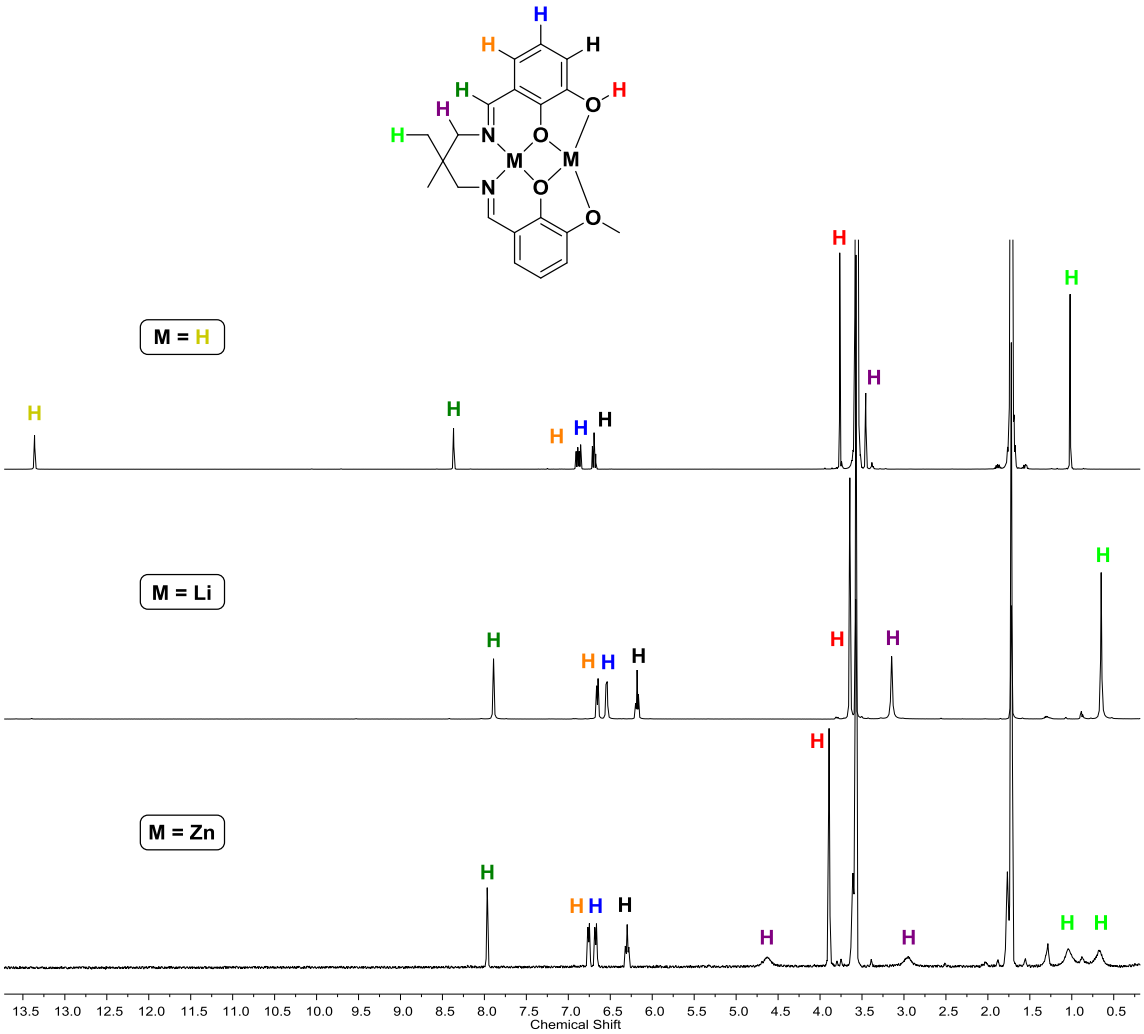


Figure 5.1: ^{1}H NMR spectra following the synthesis of complexes **19** and **20**.

2D DOSY NMR analysis of complexes **19** and **20** show all proton resonances diffuse with identical diffusion coefficient, indicating a single species present in solution (Figure 5.2). A diffusion coefficient of -9.14 log (m^2s^{-1}) was measure for complex **19**, producing an estimated molecular mass of 778 g mol^{-1}, indicating a dimeric species in the solution state. In contrast, a diffusion coefficient of -9.02 log (m^2s^{-1}) was measured for complex **20**, producing an estimated molecular mass of 499 g mol^{-1}, indicating a monomeric species in the solution state.

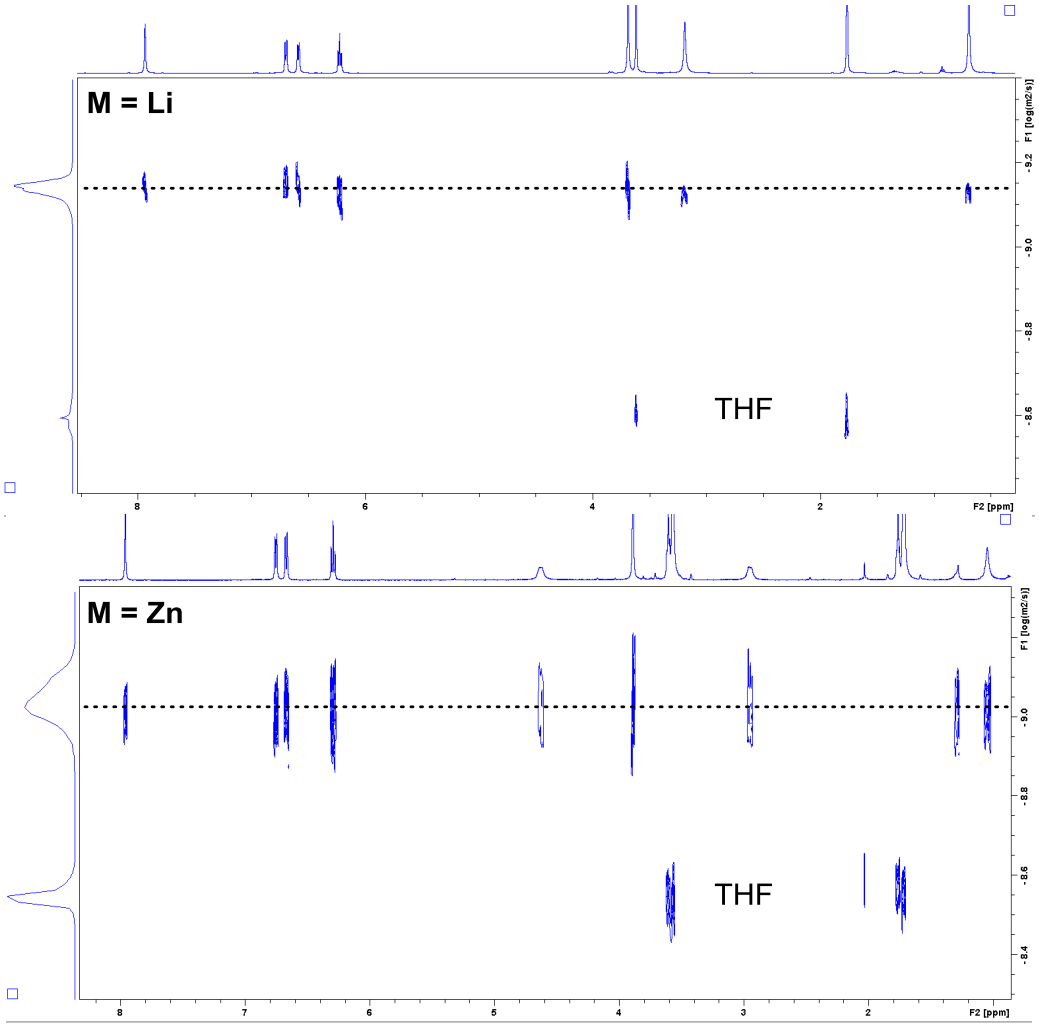


Figure 5.2: 2D DOSY NMR spectra of complex **19** and **20**, respectively.

Single crystals of complexes (**19**) and (**20**) along with an intermediate structure (**21**), suitable for X-ray crystallography were isolated *via* vapour diffusion of pentane into a saturated solution of each complex, in THF at -40 °C. Structural elucidation revealed complex (**19**) to exist as a dimer in the solid state with each lithium centre adopting a pentacoordinate, square-based pyramidal geometry (τ = 0.06) with the four lithium centres and and four phenolic-oxygen centres forming a stable cubane structure (Li_4O_4). Upon the addition of zinc (II) iodide, a step-wise metal substitution takes place, displacing the imine-bound lithium centre first, forming complex (**21**). This structure exists as a monomeric species in the solid state with both zinc and lithium centres adopting pentacoordinate, square based pyramidal geometries (Zn τ = 0.14, Li τ = 0.01). The lithium centre is further coordinated by a THF molecule (recrystallization solvent). The addition of a second equivalent of zinc (II) iodide resulted in the second metal substitution forming di-zinc complex (**20**). In this example, Zn_1 retains its pentacoordinate geometry (τ = 0.13). On the other hand, Zn_2 adopts a tetrahedral geometry and is coordinated by a THF molecule in a similar manner to complex **19**. The coordinated THF would indicate Zn_2 is the more Lewis acidic site and thus could be the position for epoxide coordination in the catalysis. The intermetallic separation for complexes (**21**) and (**20**) are 3.070(4) Å and 3.21325(6) Å, respectively.

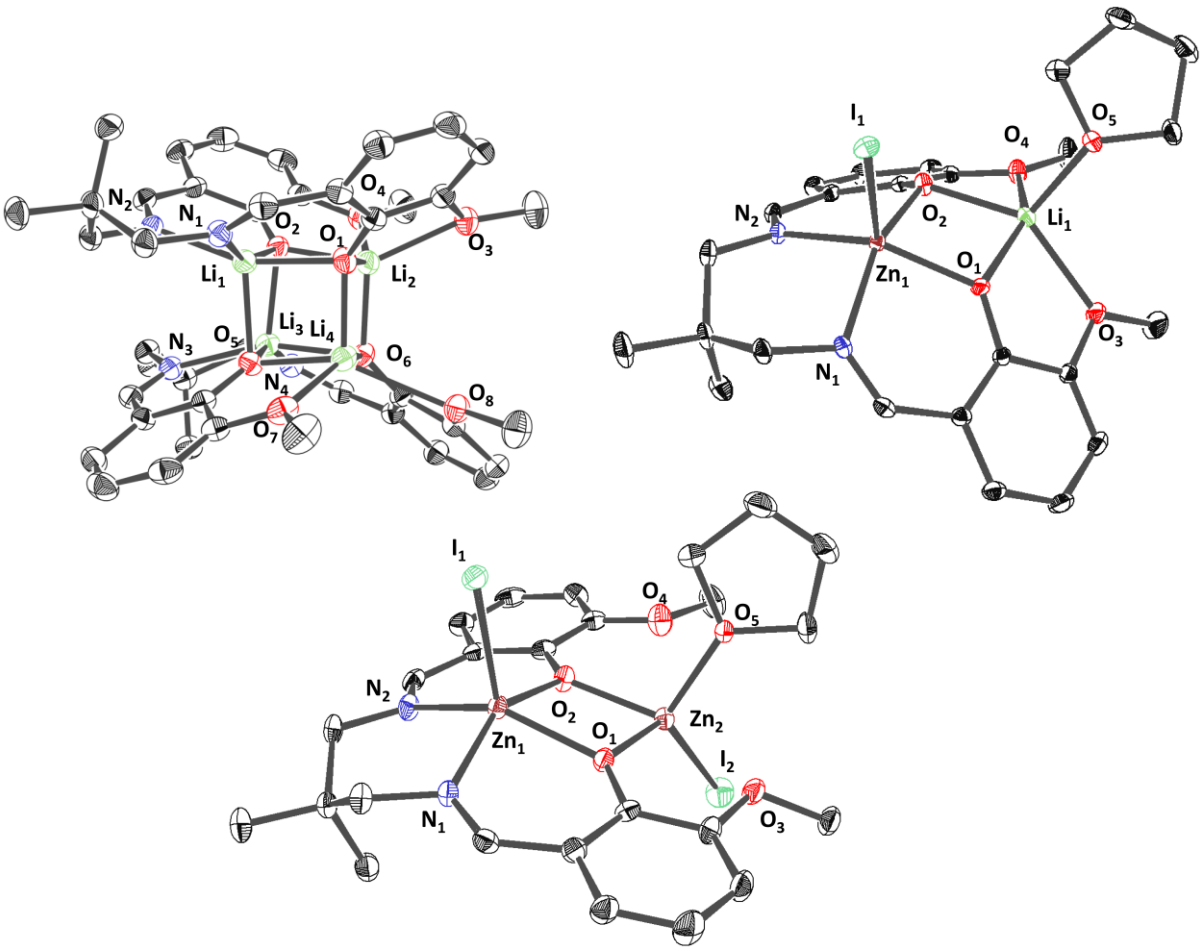
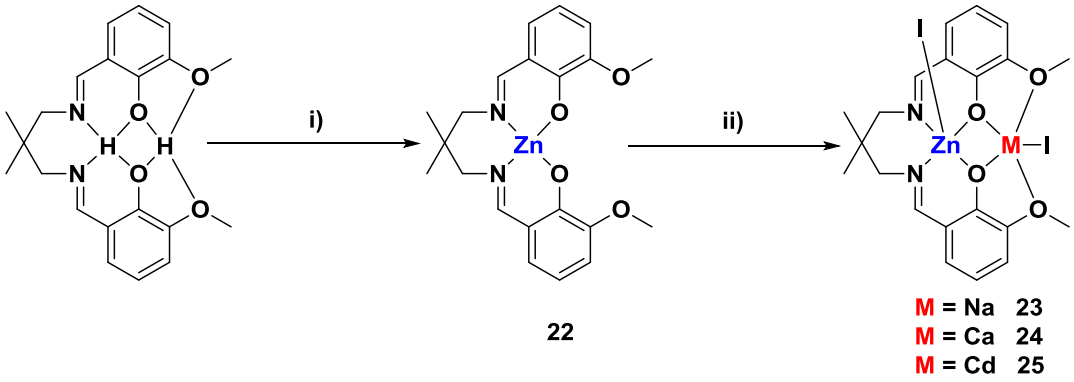


Figure 5.3: ORTEP representation of crystallographic structures of complexes **19** (Top LHS), **20** (bottom) and **21** (Top RHS), obtained by single crystal X-ray diffraction. Disorder and H-atoms have been omitted for clarity, with thermal ellipsoids represented at 40 % probability.

5.1.4 Synthesis and characterisation of heterodinuclear Zn(II) complexes.



Scheme 5.5: Synthesis of heterodinuclear complexes **22**, **23** and **24** via a monozinc species **21**. i) $ZnEt_2$, THF, 25 °C, 4 h, 90 %. ii) MI_x, THF, 25 °C, 16 h, >74 %.

The mono-zinc complex, **22**, was synthesised via deprotonation of the pro-ligand by diethyl zinc (II), in THF at 25 °C. Heterodinuclear complexes **23**, **24** and **25** were synthesised by addition of a metal (I)/(II) iodide salt to complex **22**, in THF at 25 °C. All complexes, **22-25,** were isolated in good yields (>74 %) and characterised by multinuclear NMR spectroscopy (Figure S121-134) and X-ray crystallography (Figure S124, S128, S131 and S135), with purity confirmed by elemental analysis.

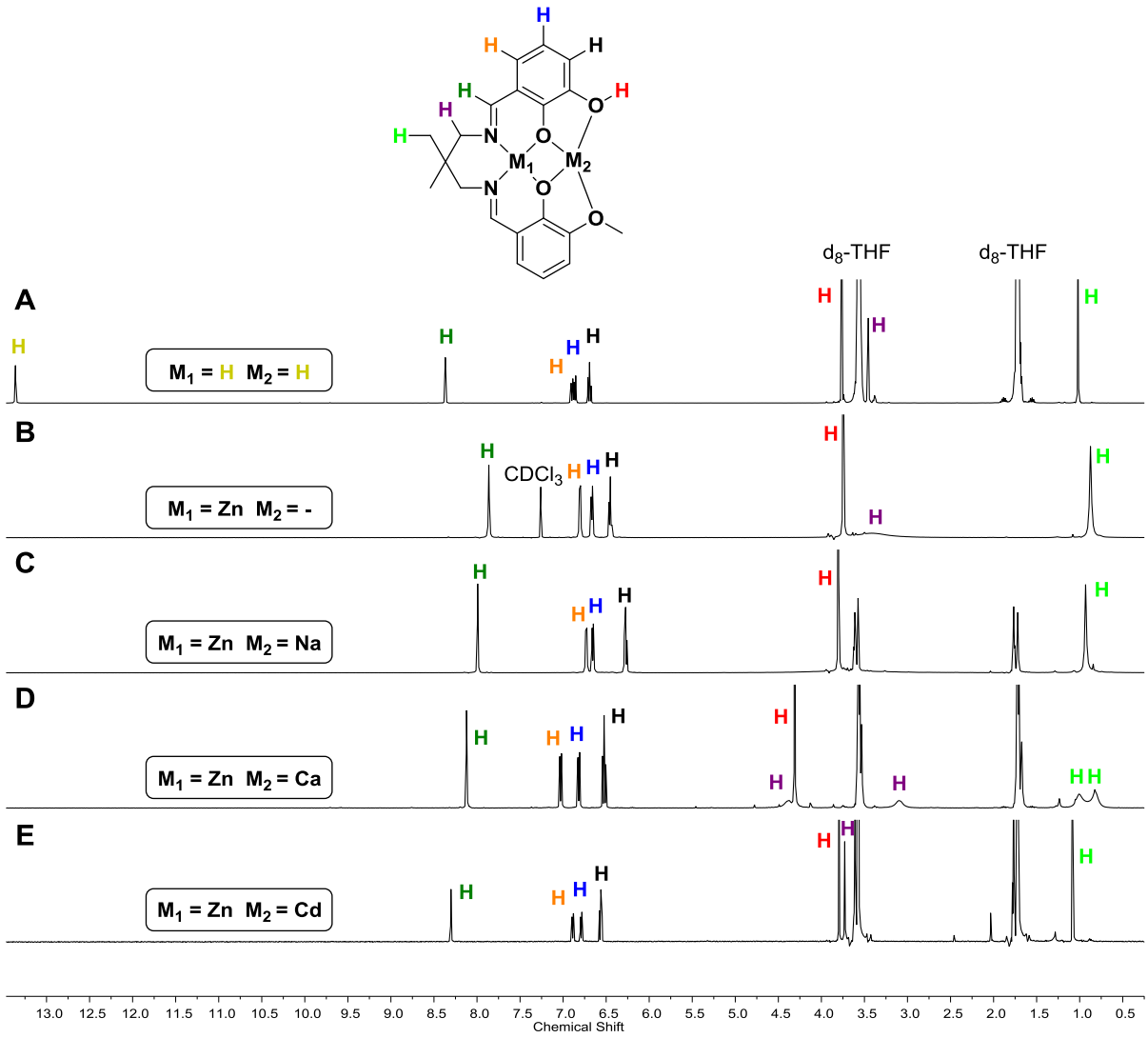


Figure 5.4: ^{1}H NMR spectrum of complexes **22**-**25**.

The successful deprotonation of the ligand by diethyl zinc (II) was characterised by the disappearance of the phenolic proton resonance at 13.4 ppm in the ^{1}H NMR spectrum (Figure 5.4). Complex **22** proved highly insoluble in THF and thus was characterised in $CDCl_3$. The addition of metal iodide salts to form complexes **23**, **24** and **25** resulted in minor changes to the ^{1}H NMR spectra. Unfortunately, NMR spectroscopy does not give conclusive evidence of heterodinuclear complex formation due to the C_2 symmetry being retained upon addition of the second (hetero)metal, unlike the macrocycle used in chapters 2-4 (Figure 5.5).

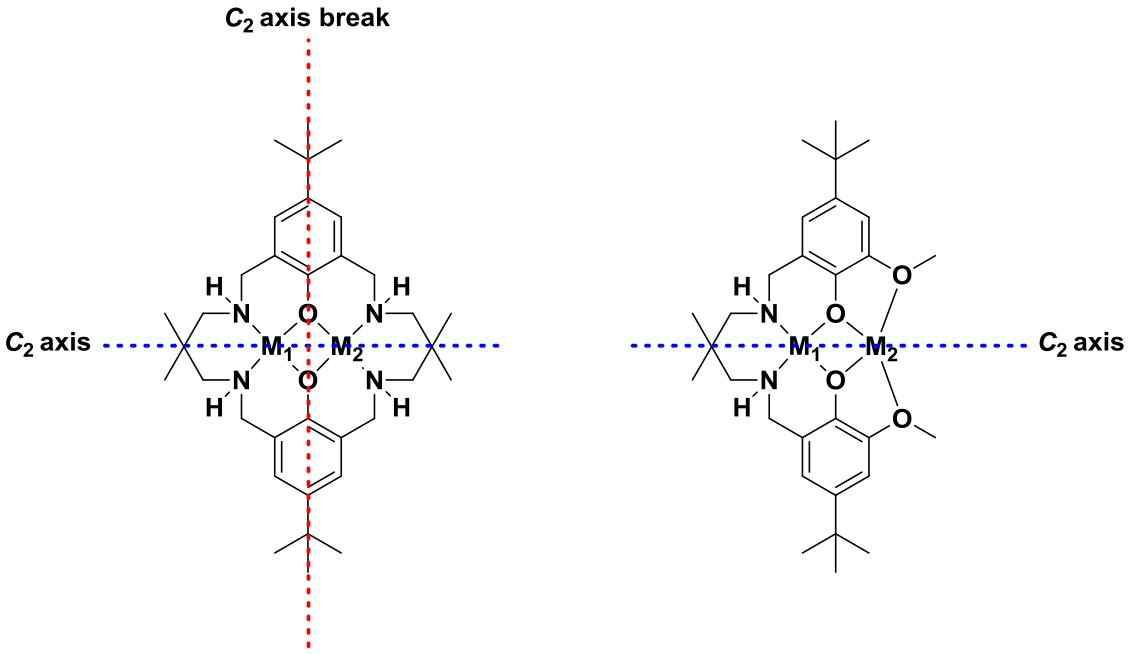


Figure 5.5: Macrocycle (LHS) and O-vanillin derived (RHS) ligands displaying the retention (blue) or break (red) in C_2 symmetry upon the addition of hetero metals.

A single crystal of the mono-zinc complex (**22**) was isolated via vapour diffusion of pentane into a saturated solution of complex in chloroform at 25 °C (Figure 5.6). Structural elucidation revealed it is dimeric in the solid state with the ligands perpendicular to one another to allow for the formation of a half-cubane structure (Zn_2O_2). Both zinc (II) centres are in identical environments, adopting a pentacoordinate, distorted trigonal bipyramidal geometry (τ = 0.53). The intermetallic distance was measured to be 3.1217(4) Å.

Single crystals of complexes (**23**) and (**24**) were isolated via vapour diffusion of pentane into a saturated solution of complex in THF at 25 °C (Figure 5.6). Structural elucidation revealed the complexes are monomeric in the solid state where both

complexes are isostructural. Both zinc (II) centres adopt a pentacoordinate, square based pyramidal geometry (**23** τ= 0.26, **24** τ = 0.09). Both alkali/alkaline earth metals adopt a heptacoordinate, pentagonal bipyramidal geometry, bound by two phenolic-oxygen centres and two methoxy-oxygen centres from the ligand. In the case of the sodium (I) centre, it is further coordinated by three THF molecules and for the calcium (II) centre, it is coordinated by two THF molecules and an iodide co-ligand to balance the additional charge. The intermetallic separations are 3.5461(13) Å and 3.5785(8) Å for complexes (**23**) and (**24**), respectively.

A single crystal of complex (**25**) was isolated via vapour diffusion of pentane in to a saturated solution of complex in THF at -40 °C (Figure 5.5). The zinc (II) centre adopts a hexacoordinate, octahedral geometry and is coordinated by two THF molecules (recrystallization solvent). The cadmium (II) centre adopts a tetrahedral geometry and coordinates the two iodide co-ligands. Interestingly, this structure coordinates THF on the imine-metallic centre in preference to the methoxy-metallic centre. This is due to the significant decrease in Lewis acidity of cadmium (II) centre in comparison to a zinc (II). The intermetallic distance is 3.4020(8) Å.

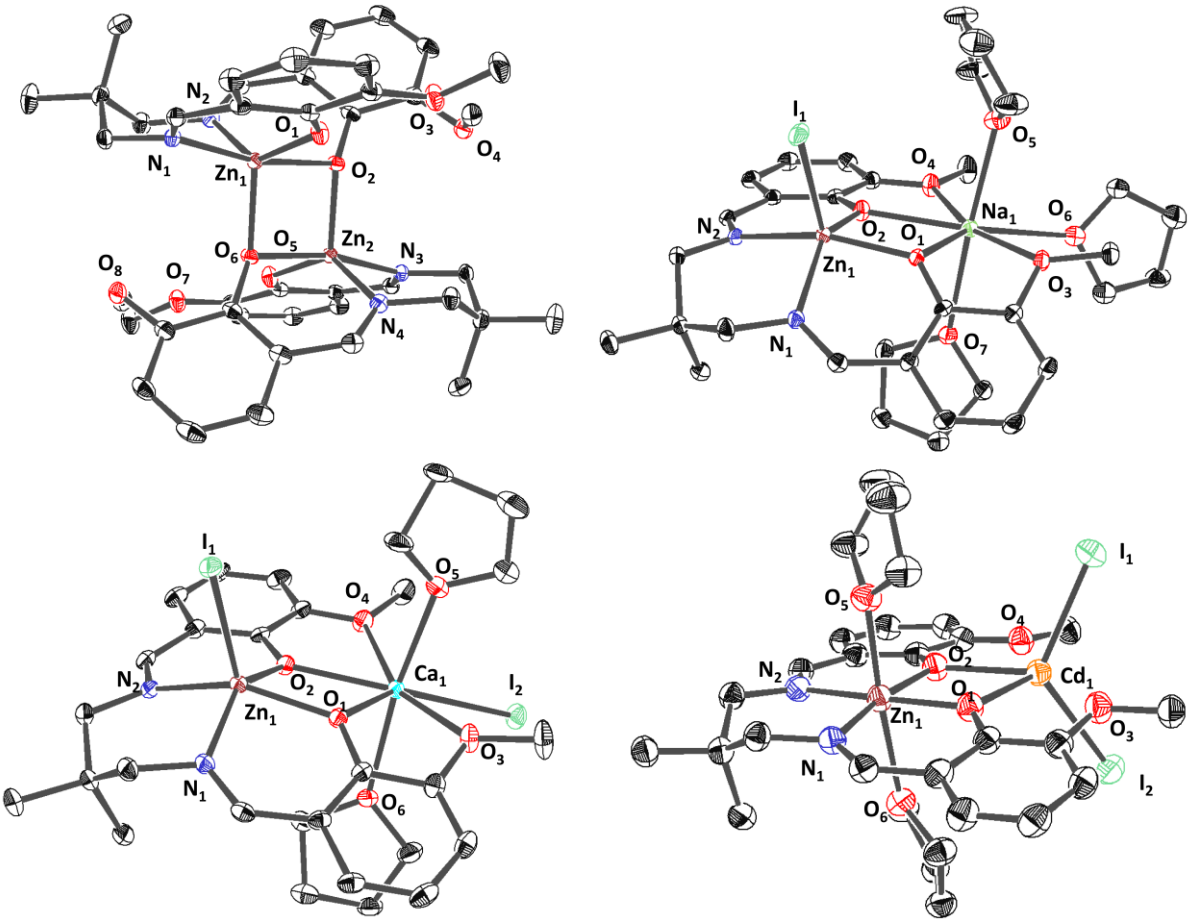
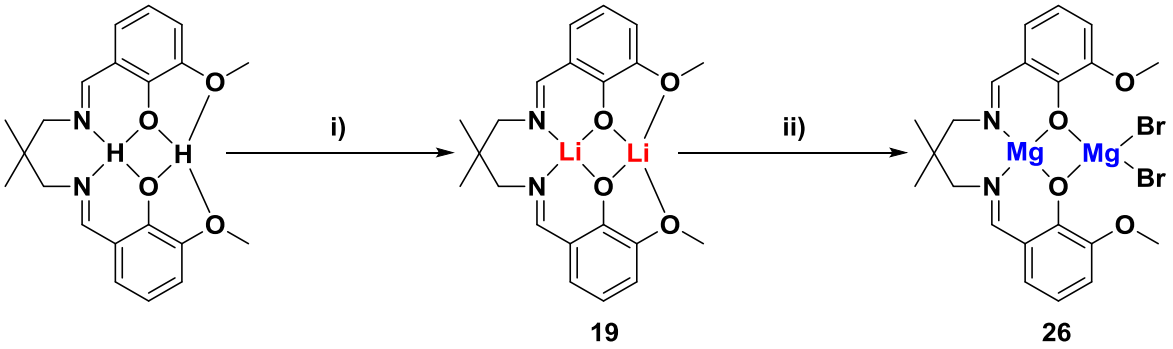


Figure 5.6: ORTEP representation of crystallographic structures of complexes **22** (Top LHS) **23** (TOP RHS) **24** (Bottom LHS) and **25** (Bottom RHS), obtained by single crystal X-ray diffraction. Disorder and H-atoms have been omitted for clarity, with thermal ellipsoids represented at 40 % probability.

5.1.5 Synthesis and Characterisation of a Di-Magnesium Complex



Scheme 5.6: Synthesis of di-magnesium complex **26**. i) Li(N(Si(CH$_3$)$_3$)$_2$), THF, 25 °C, 4h. ii) 2 eq Mg(II)Br$_2$, THF, 25 °C, 16 h, 82 %.

The di-magnesium bromide complex was synthesised by addition of two equivalents of magnesium (II) bromide to complex **19**, in THF at 25 °C (Scheme 5.3). The product was isolated as white powder in high yield (> 80 %) and was characterised by multinuclear NMR spectroscopy (Figure S136-138) and X-ray crystallography (Figure S139), with purity confirmed by elemental analysis. The bromide co-ligand was targeted, as magnesium (II) iodide was highly insoluble in a range of organic solvents and thus successful metalation of the ligand was not achieved.

In contrast to di-zinc complex **20**, di-magnesium complex **26** does not show diastereotopic splitting of the methylene and methyl proton resonances. This is presumably due to the zinc (II) centre tending to adopt a 5-coordinate geometry, causing a break in the C_2 axis, whereas the magnesium (II) centre adopts a 6-coordinate geometry (vide infra) and thus the C_2 symmetry plane is retained.

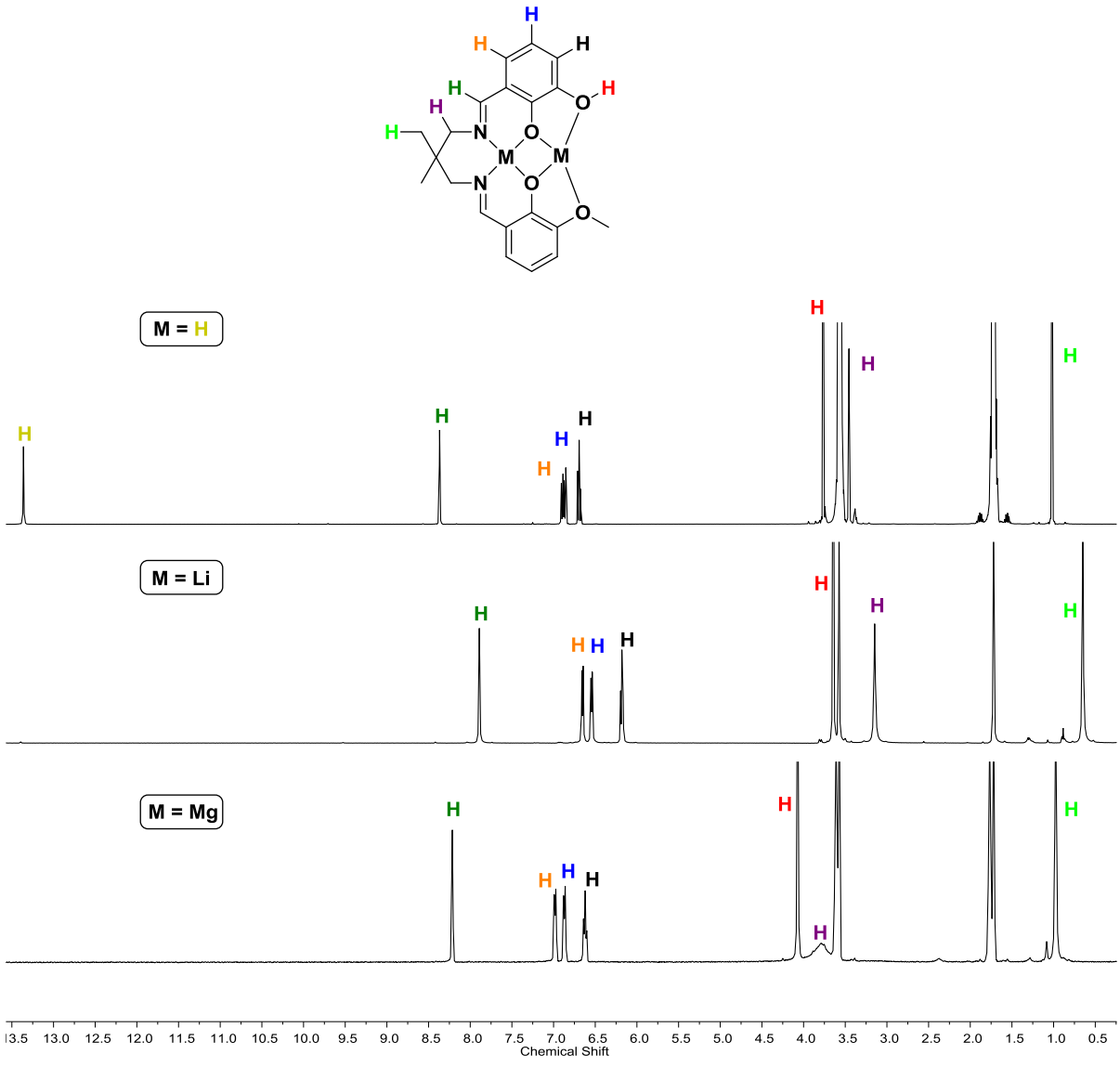


Figure 5.7: ^{1}H NMR spectra of complex **19** and **26** (d_8-THF, 298 K).

Single crystals of complexes (**26**) along with an intermediate structure (**27**) suitable for X-ray crystallography were isolated *via* vapour diffusion of pentane into a saturated solution of each complex, in THF at -40 °C (Figure 5.7). Structural elucidation reveals a step-wise metal-substitution mechanism in the same manner observed for the zinc analogue (**21**), and an isostructural intermediate was isolated. Complex (**27**) exists as a monomeric species in the solid state with both magnesium (II) and lithium (I) centres adopting a pentacoordinate, square based pyramidal geometries (Mg τ = 0.07, Li τ = 0.06). The addition of a second equivalent of magnesium (II) bromide resulted in the second metal substitution forming di-magnesium complex (**26**). Unlike the di-zinc complex (**20**), the Mg_1 centre adopts a hexacoordinate, octahedral geometry and is bound by two THF molecules. On the other hand, Mg_2 adopts a tetrahedral geometry and is coordinated by two bromide co-ligands. The intermetallic separation for complexes **26** and **27** are 3.117 Å and 3.001(2) Å, respectively.

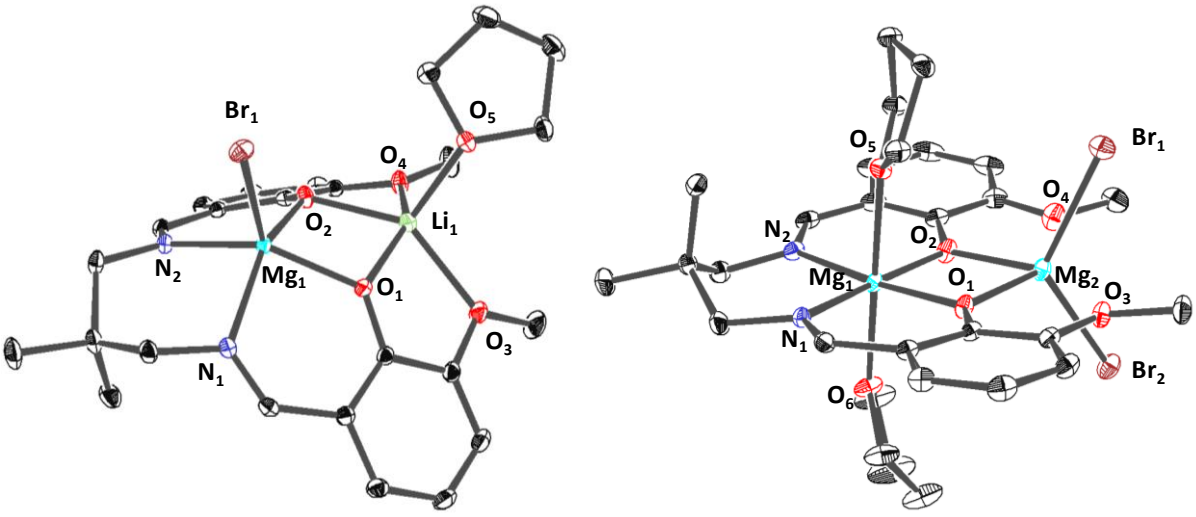
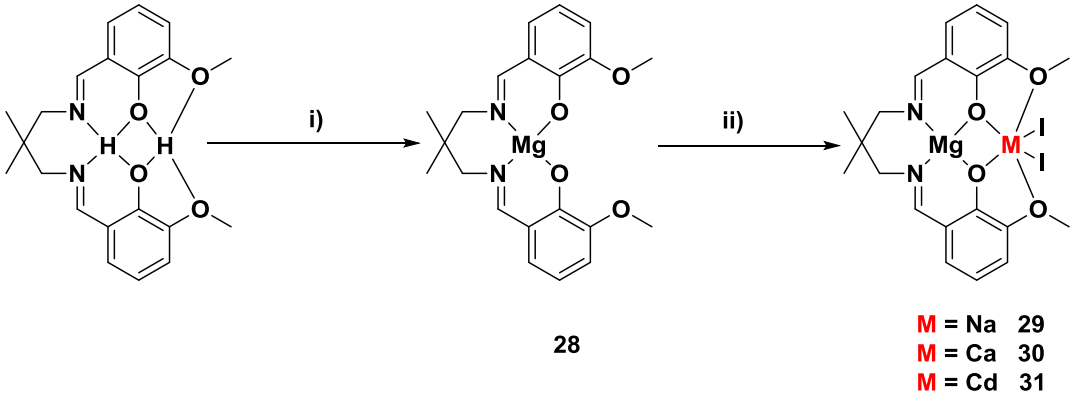


Figure 5.8: ORTEP representation of crystallographic structures of complexes **26** (RHS) and **27** (LHS), obtained by single crystal X-ray diffraction. Disorder and H-atoms have been omitted for clarity, with thermal ellipsoids represented at 40 % probability.

5.1.6 Synthesis and Characterisation of heterodinuclear Mg(II) Complexes



Scheme 5.7: Synthesis of mono-magnesium complex **28** and heterodinuclear complexes **29**, **30** and **31**. i) $Mg(N(Si(CH_3)_3)_2)_2$, THF, 25 °C, 4h, 80 %. ii) MI_x, THF, 25 °C, 16 h, >76 %.

The mono-magnesium complex, **28**, was synthesised by deprotonoation of the pro-ligand by a magnesium (II) amide salt, in THF at 25 °C. Heterodinuclear complexes **29**, **30** and **31** were synthesised by addition of a metal iodide salt to the mono-magnesium complex, **28**, in THF at 25 °C. All complexes were isolated as pale yellow powders and were characterised by multinuclear NMR spectroscopy (Figure S141-S145) and X-ray crystallography (Figure S141 and S146), with purity confirmed by elemental analysis.

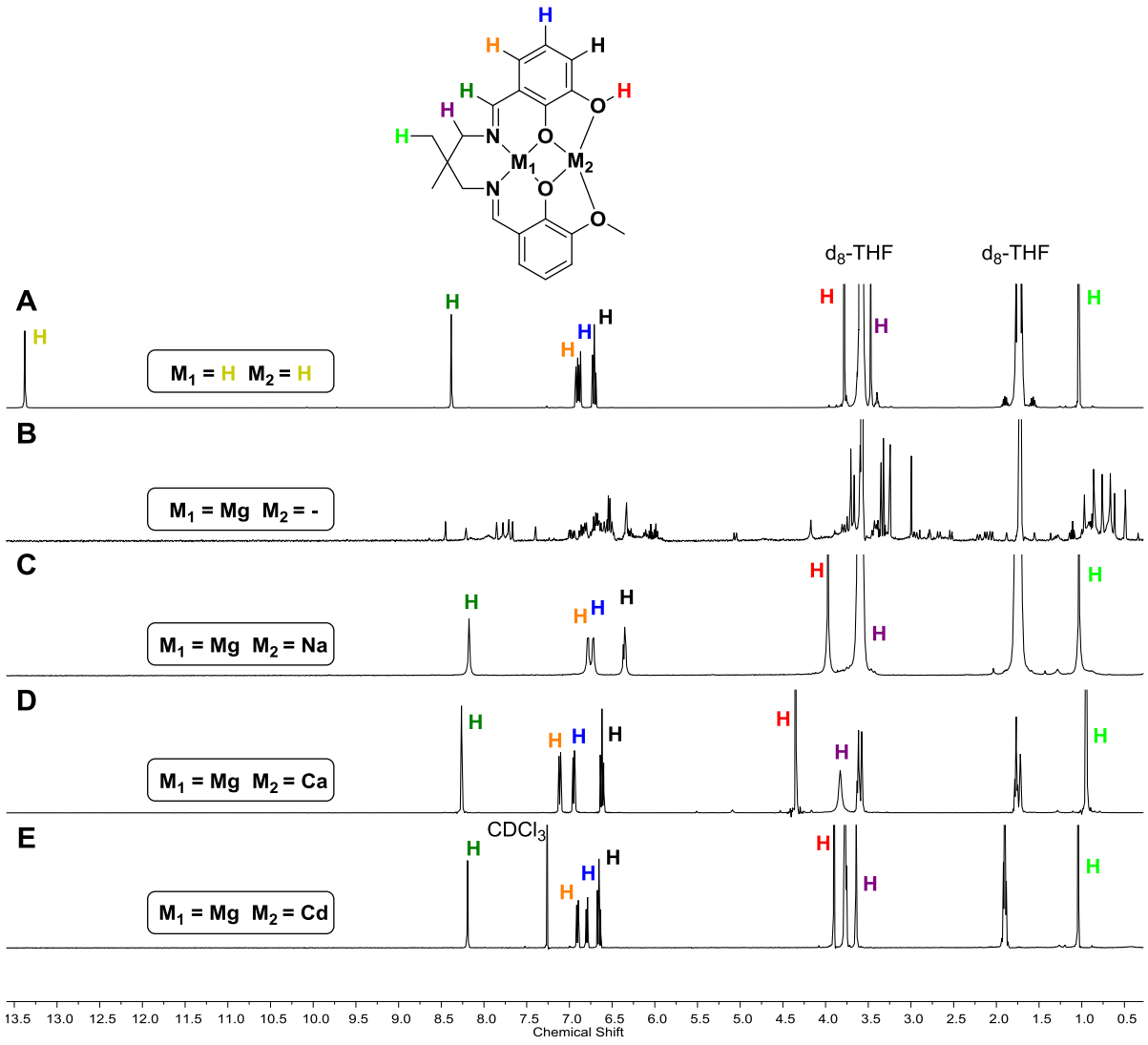


Figure 5.9: ^{1}H NMR spectra of complexes **28-31**.

The addition of Mg (II) amide to the pro-ligand resulted in an uncharacterisable proton NMR spectrum in d_8-THF at 25 °C. This could be due to the formation of multiple aggregate species as was observed in the solid state (vide infra). The addition of metal (I)/(II) iodide salt to the complex **28** resulted in a sharpening and a fully assignable ^{1}H NMR spectrum, due to the formation of a monomeric species.

A single crystal of complex **28** was obtained via evaporation of a solution of complex, in THF at 25 °C. Structural elucidation revealed a trimeric structure where each magnesium centre adopts a hexacoordinate, octahedral geometry. The formation of an aggregated species may explain the complex nature of the ^{1}H NMR spectrum observed in d_8-THF. A single crystal of complex **30** was obtained via vapour diffusion of pentane into a solution of complex, in THF at -40 °C. Structural elucidation revealed a monomeric species. The structure obtained was isostructural to complex **26** whereby the Mg (II) centre adopts a hexacoordinate, octahedral geometry, and the Ca (II) centre adopts a tetrahedral geometry bound by two iodide co-ligands. The intermetallic separation was measured at 3.3470(11) Å for complex **30**.

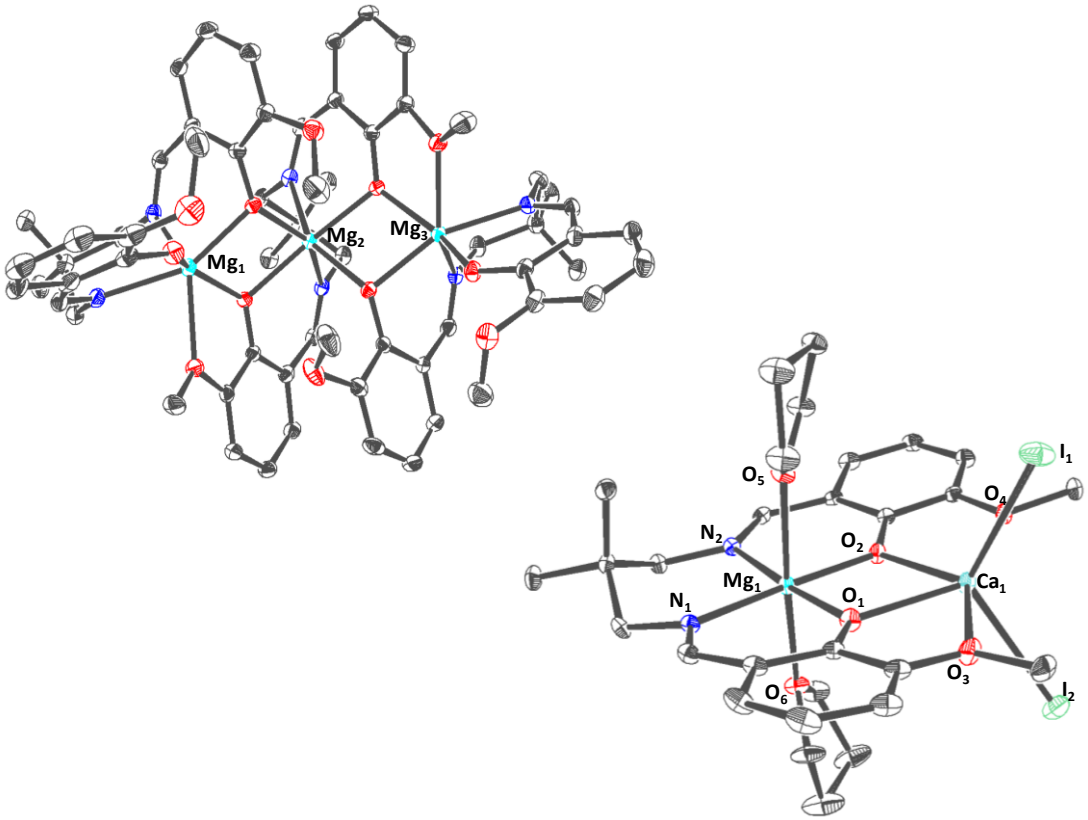


Figure 5.10: ORTEP representation of crystallographic structures of complexes **28** (LHS) and **30** (RHS), obtained by single crystal X-ray diffraction. Disorder and H-atoms have been omitted for clarity, with thermal ellipsoids represented at 40 % probability.

5.1.7 ROCOP of Phthalic Anhydride and CHO

Homodinuclear complexes **19**, **20** and **26**, mononuclear complexes **22** and **28** and heterodinuclear complexes **23**-**25** and **29**-**31** were each tested in the ROCOP of phthalic anhydride with cyclohexene oxide. The polymerisations were carried out at 100 °C, using 0.1 mol % catalyst loading with 100 equivalents of phthalic anhydride.

Table 5.2: Copolymerisation of PA and CHO.[a]

Catalyst	Time (h)	TON[b]	ToF (h^{-1})[c]	Polym. (%)[d]	k_{obs} (x10^{-5}) [R^2]	M_n [Đ][e]
LiLi	24	0	-	-	-	-
Zn	13.1	100	7	> 99	2.7 [0.99]	2300 [1.20]
Mg	19	100	5	> 99	1.3 [0.99]	6500 [1.30]
ZnZn	0.7	100	150	> 99	49.9 [0.98]	8500 [1.05] 18000 [1.03]
MgMg	2.8	100	35	> 99	13.9 [0.99]	8700 [1.11] 22500 [1.08]
ZnNa	2.9	100	35	> 99	13.3 [0.99]	7400 [1.14] 18500 [1.08]
ZnCa	1.0	41	41	> 99	-	5900 [1.10]
MgCa	1.0	19	19	> 99	-	-
ZnCd	1.4	100	70	> 99	23.9 [0.99]	5600 [1.23] 17000 [1.08]
MgCd	1.6	100	64	> 99	22.0 [0.99]	9200 [1.14] 24000 [1.07]

[a]Copolymerisation conditions: catalyst/PA/CHO = 1/100/800, 100 °C. [b]TON = number of molecules of epoxide consumed per mole of catalyst. [c]TOF = TON/h. [d]Determined by ^{1}H NMR spectroscopy (DMSO-d_6) by integrating the normalised resonances for ester linkages (4.80-5.26 ppm) and ether linkages (3.22-3.64 ppm). [e]Determined by SEC in THF calibrated using polystyrene standards.

All polymerisations displayed excellent selectivity for polyester formation (> 99 %) with no polyether linkages observed by ^{1}H NMR spectroscopy. Furthermore, the polymerisations appeared well controlled with polydispersity's measured between 1.03-1.30. However, bimodal distributions were observed due to the presence of chain transfer agent, 1,2-cyclohexane diol, as a result of ring opening of cyclohexene oxide by residual water.

As expected, no activity was observed by the homodinuclear lithium complex, due to the lack of an initiating species. However, some turn-over was observed with mononuclear zinc and magnesium complexes, where initiation may have been caused by water or ligand.

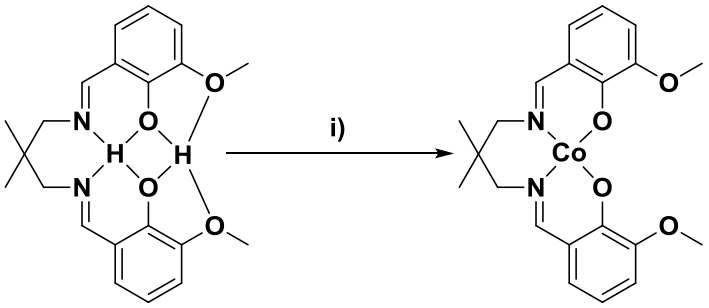
The Zn(II)Zn(II) complex proved 4 times more active than the Mg(II)Mg(II) complex, in contrast to the activity trend observed for the macrocyclic ligand.[2] In each case, the presence of THF in the crystal structures may suggest effective epoxide binding and thus the difference in rate may be attributed to the enhanced nucleophilicity of a zinc-carboxylate in comparison to a magnesium-carboxylate.

Zn(II)Na(I) (35 h^{-1}) showed higher activity than Zn(II)Ca(II) (20 h^{-1}) (per co-ligand), and maybe due to sodium being more ionic and hence enhancing epoxide coordination (chapter 4). Zn(II)Ca(II) shows twice the activity of Mg(II)Ca(II) and is also consistent with a greater nucleophilicity for a zinc-carboxylate versus a calcium-carboxylate.

Both Zn(II)Cd(II) and Mg(II)Cd(II) show equivalent activity, 70 h^{-1}. The molecular structure of Zn(II)Cd(II) is isostructural to that of Mg(II)Mg(II) and Mg(II)Ca(II) and thus may indicate both heterodinuclear cadmium complexes have a cadmium-carboxylate and hence have similar rate of reactions.

5.1.8 A Route to Co(II) Heterodinuclear Complexes

Due to the significant rate enhancement observed with complexes with a cobalt centre, including the macrocyclic work discussed in Chapter 4, a cobalt derived heterodinuclear complex was targeted.



32

Scheme 5.8: Synthesis of a mono-cobalt (**32**) complex. i) $Co(OAc)_2$, THF, 25 °C, 16 h.

The initial reaction saw the deprotonation of the pro-ligand with cobalt acetate, reacted at 25 °C in THF for 16 hours. The resulting acetic acid was carefully removed by multiple azeotropic washings with toluene. The solvent was removed in *vacuo* and the complex washed with hexane. This afforded a red/brown solid at 65 % yield. The complex was characterised by X-ray crystallography (Figure S146).

A single crystal of **32** was isolated via vapour diffusion of pentane into a saturated solution of complex in Toluene at -40 °C. Structural elucidation reveals the complex exists as a dimer in the solid state. Each cobalt centre adopts a pentacoordinate, trigonal bipyramidal geometry (τ = 0.58), bound by two imino-nitrogen centres and three phenolic-oxygen centres; isomorphic to the monozinc species. The metal-metal distance was measured at 3.16510(5) Å.

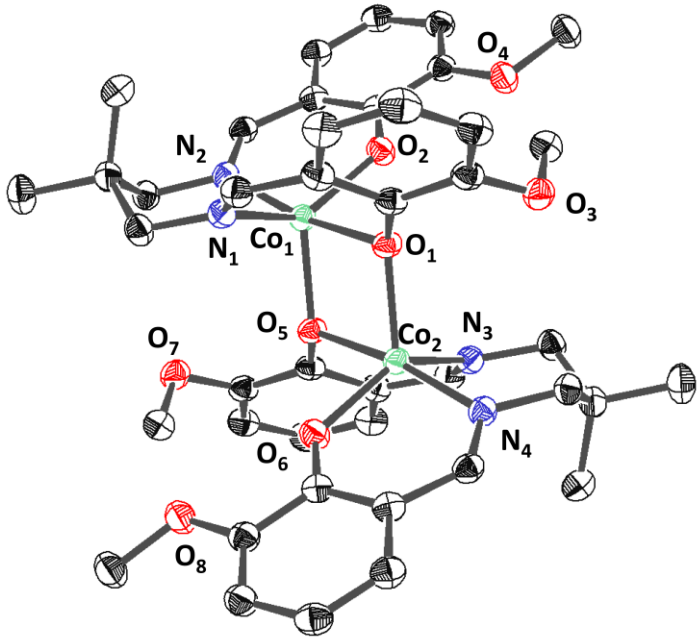


Figure 5.11: ORTEP representation of complex X, obtained by single crystal X-ray diffraction. Disorder and H-atoms have been omitted for clarity, with thermal ellipsoids represented at 40 % probability.

The monocobalt complex (**32**) resembles the structure observed for the monozinc complex (**22**). It is envisaged this complex could also be used to make a series of heterodinuclear complexes with sodium, calcium and cadmium. These complexes would be expected to give a significant rate enhancement in comparison to the zinc or magnesium heterodinuclear catalysts. An interesting target may be the CoZn complex, with cobalt providing a reactive nucleophile and the zinc providing activated epoxide could lead to a significant rate enhancement.

5.1.9 Conclusions

The successful synthesis of a series of Zn(II) and Mg(II) heterodinuclear complexes with Na(I), Ca(II) and Cd(II) coordinated by an o-vanillin derived dinucleating ligand were reported. The complexes were characterised by ^{1}H NMR spectroscopy and X-ray crystallography. The difference in the size of each binding cavity promoted the selective formation of the heterodinuclear complexes under mild conditions (25 °C). In the ROCOP of PA/CHO the homodinuclear Zn(II)Zn(II) complex proved most active with an observed activity of 150 h^{-1}, all heterodinuclear analogues proved significantly less active. The Mg(II) analogues were all less active than the Zn(II) counterparts and could be a result of the increase nucleophilicity of the Zn(II)-carboxylate in comparison to the Mg(II)-carboxylate. A mono-cobalt complex was synthesised and characterised by X-ray crystallography and could provide a useful intermediate to a future series of heterodinuclear cobalt(II) complexes.

5.2.0 References

1. https://www.plasticsinsight.com/resin-intelligence/resin-prices/polyester/ (accessed 27/03/2019).
2. Saini, P. K.; Romain, C.; Zhu, Y.; Williams, C. K., Di-magnesium and zinc catalysts for the copolymerization of phthalic anhydride and cyclohexene oxide, *Polym. Chem.,* **2014,** *5*, (20), 6068.
3. Romain, C.; Zhu, Y.; Dingwall, P.; Paul, S.; Rzepa, H. S.; Buchard, A.; Williams, C. K., Chemoselective Polymerizations from Mixtures of Epoxide, Lactone, Anhydride, and Carbon Dioxide, *J. Am. Chem. Soc.,* **2016,** *138*, (12), 4120.
4. Garden, J. A.; Saini, P. K.; Williams, C. K., Greater than the Sum of Its Parts: A Heterodinuclear Polymerization Catalyst, *J. Am. Chem. Soc.,* **2015,** *137*, (48), 15078.
5. Fieser, M. E.; Sanford, M. J.; Mitchell, L. A.; Dunbar, C. R.; Mandal, M.; Van Zee, N. J.; Urness, D. M.; Cramer, C. J.; Coates, G. W.; Tolman, W. B., Mechanistic Insights into the Alternating Copolymerization of Epoxides and Cyclic Anhydrides Using a (Salph)AlCl and Iminium Salt Catalytic System, *J. Am. Chem. Soc.,* **2017,** *139*, (42), 15222.
6. Van Zee, N. J.; Sanford, M. J.; Coates, G. W., Electronic Effects of Aluminum Complexes in the Copolymerization of Propylene Oxide with Tricyclic Anhydrides: Access to Well-Defined, Functionalizable Aliphatic Polyesters, *J. Am. Chem. Soc.,* **2016,** *138*, (8), 2755.
7. Li, J.; Liu, Y.; Ren, W.-M.; Lu, X.-B., Asymmetric Alternating Copolymerization of Meso-epoxides and Cyclic Anhydrides: Efficient Access to Enantiopure Polyesters, *J. Am. Chem. Soc.,* **2016,** *138*, (36), 11493.
8. Darensbourg, D. J.; Poland, R. R.; Escobedo, C., Kinetic Studies of the Alternating Copolymerization of Cyclic Acid Anhydrides and Epoxides, and the Terpolymerization of Cyclic Acid Anhydrides, Epoxides, and CO_2 Catalyzed by (salen)CrIIICl, *Macromolecules,* **2012,** *45*, (5), 2242.
9. Shi, Z.; Jiang, Q.; Song, Z.; Wang, Z.; Gao, C., Dinuclear iron(iii) complexes bearing phenylene-bridged bis(amino triphenolate) ligands as catalysts for the copolymerization of cyclohexene oxide with carbon dioxide or phthalic anhydride, *Polym. Chem.,* **2018,** *9*, (38), 4733.
10. Thevenon, A.; Garden, J. A.; White, A. J. P.; Williams, C. K., Dinuclear Zinc Salen Catalysts for the Ring Opening Copolymerization of Epoxides and Carbon Dioxide or Anhydrides, *Inorg. Chem.,* **2015,** *54*, (24), 11906.
11. Trott, G.; Garden, J. A.; Williams, C. K., Heterodinuclear zinc and magnesium catalysts for epoxide/CO2 ring opening copolymerizations, *Chem. Sci.,* **2019**.
12. Nagae, H.; Aoki, R.; Akutagawa, S.; Kleemann, J.; Tagawa, R.; Schindler, T.; Choi, G.; Spaniol, T. P.; Tsurugi, H.; Okuda, J.; Mashima, K., Lanthanide Complexes Supported by a Trizinc Crown Ether as Catalysts for Alternating Copolymerization of Epoxide and CO_2: Telomerization Controlled by Carboxylate Anions, *Angew. Chem. Int. Ed.,* **2018,** *57*, (9), 2492.
13. Della Monica, F.; Maity, B.; Pehl, T.; Buonerba, A.; De Nisi, A.; Monari, M.; Grassi, A.; Rieger, B.; Cavallo, L.; Capacchione, C., [OSSO]-Type Iron(III) Complexes for the Low-Pressure Reaction of Carbon Dioxide with Epoxides: Catalytic Activity, Reaction Kinetics, and Computational Study, *ACS Catal.,* **2018,** 6882.

14. Mike, S.; Sebastian, D.; Franc, M., Highly Active and Readily Accessible Proline-Based Dizinc Catalyst for CO_2/Epoxide Copolymerization*, Chem. Eur. J.,* **2017,** *23*, (65), 16472.
15. Lehenmeier, M. W.; Kissling, S.; Altenbuchner, P. T.; Bruckmeier, C.; Deglmann, P.; Brym, A.-K.; Rieger, B., Flexibly Tethered Dinuclear Zinc Complexes: A Solution to the Entropy Problem in CO_2/Epoxide Copolymerization Catalysis?*, Angew. Chem. Int. Ed.,* **2013,** *52*, (37), 9821.

Chapter 6:

Prospective and Future Work

6.1.1 Prospective and Challenges

- Mechanistic understanding
- Catalysts for PO/CO_2 without co-catalyst
- Renewable Materials
- Catalyst Recyclability

In CO_2/epoxide ROCOP catalysis, a full mechanistic understanding has not yet been reached, especially for bifunctional catalytic systems where the role of co-catalyst is still a topic for discussion.[1-2] In contrast, dinuclear catalysts allow for improved mechanistic understanding, with the best systems showing a second order rate law.[2] With a first order dependence in both catalyst and epoxide concentrations and zero order dependence in CO_2 pressure. The goal of this thesis was to improve understanding of the roles of each metal and its key finding is that both transition state entropy and enthalpy may be independently controlled by appropriate selection of metals. The ability to improve rate using heterocatalysts should be further tested with other ligand systems such as tethered beta-diimines, and metals for further validation.

The copolymer produced from PO/CO_2 (polypropylene carbonate, PPC) has become the main focus in the synthesis of polyols for polyurethanes due to its low T_g, high flexibility and industrial compatibility.[3] In the ROCOP of PO/CO_2 the most effective catalysts are bifunctional (catalyst-co-catalyst) or systems with tethered co-catalysts. The need for a co-catalyst is a major drawback as it is expensive, toxic and corrosive to steel. Dinuclear catalysts can alleviate the need for a co-catalyst, as apparent in the ROCOP of CHO/CO_2.[2-3] The application of dinuclear catalysts in the ROCOP of PO/CO_2 has been less successful, and is complicated by a competitive low energy pathway to backbiting (formation of cyclic carbonate). Understanding the backbiting side-

reaction mechanism and the effect of two metals on the energy barrier may allow optimisation of dinuclear catalysts for PO/CO_2 ROCOP.

The ROCOP of CO_2/epoxide has almost exclusively focused on epoxides which are derived from fossil fuels. As fossil fuel depletion is the scientific consensus, and an increasing public opinion to drive to more bio-renewable, recyclable and degradable materials, there is a move to 'greener' monomers. Those highlighted in light green (Figure 6.1) are able to be derived as biological metabolites, although require several steps to obtain the alkene necessary to obtain the epoxide. Those highlighted in dark green (Figure 6.1) represent monomers that exist naturally as the alkene (terpenes). Limited investigations into the ROCOP of these terpenes have been undertaken, with only a handful of catalyst reporting low activities due to the steric encumbrance around the nucleophilic epoxide centre.[4-6]

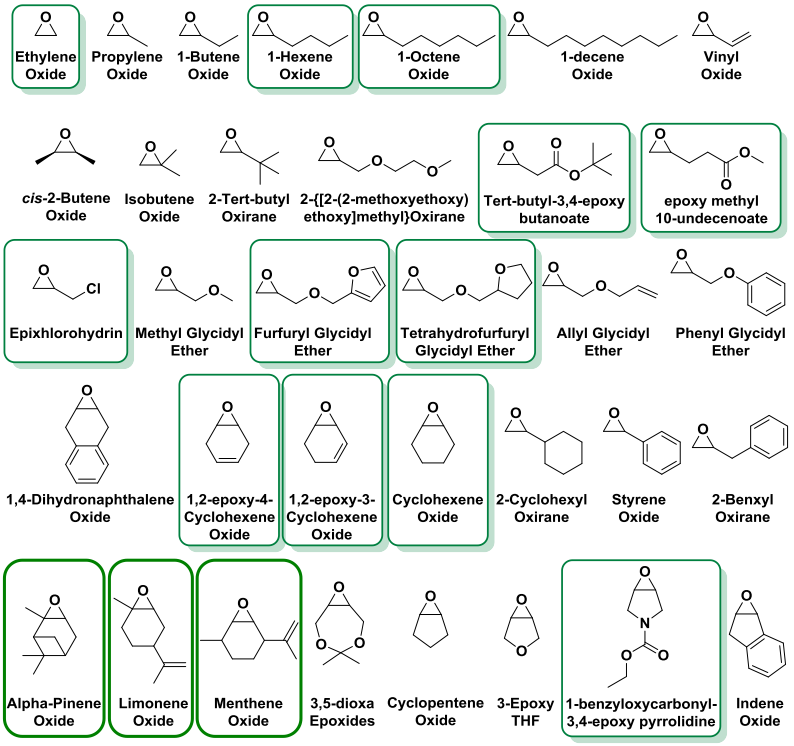


Figure 6.1: Epoxides reported in literature for CO_2 coupling. Light green (metabolites) Dark green (terpene).[4]

Currently, the best reported catalysts for the ROCOP of CO_2/epoxides have been homogeneous cobalt complexes and thus presents several challenges for commercialisation: colour, toxicity, cost, and recyclability/re-usability. One future direction would be to target heterogeneous catalysts as a means to increase thermal stability, and allow for catalyst recovery and re-usability. One strategy may be to tether active homogeneous catalysts to a solid support, thus potentially enabling recyclability of the catalyst. Furthermore, metal-organic frameworks (MOFs) based on transition metals such as Co(II) and Zn(II) may be of interest due to the close proximity of metal centres and their ability to withstand high temperature and pressure.

6.1.2 Enthalpy Driven Catalyst Design

An investigation into other Mg (II) / TM (II) catalysts may provide further rate enhancement and/or provide further insight into the requirements for a more active nucleophilic donor. In particular, both Fe(II/III) and Cr(II/III) would be of interest due to the track record of active ROCOP catalysts.[2, 7-19]

An initial investigation into the activities of TM (II) / Magnesium (II) complexes has been undertaken, in collaboration with Natalia Reis (Williams Group, Oxford). Preliminary data suggests Mg(II)Co(II) remains the most active catalyst. As yet, it is still not established why Co(II) is the best transition metal and in parallel a computational investigation into the transition state energy of each complex may provide useful insight.

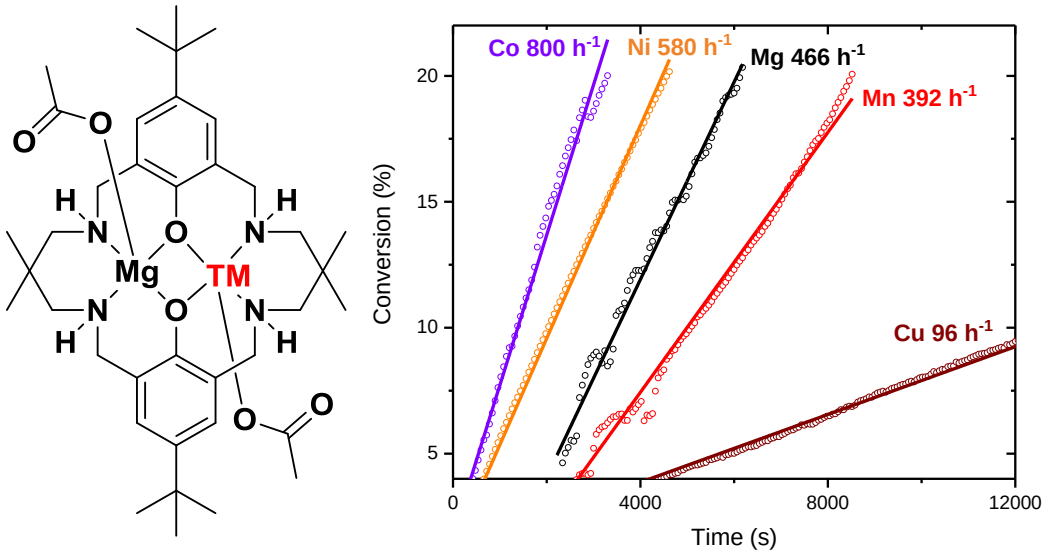


Figure 6.2: Conversion vs. Time plot for several Mg(II)TM(II)$(OAc)_2$ complexes for the ROCOP of CO_2/CHO

The best metal combination both in the field and in this thesis is Mg(II)Co(II), with Mg(II) being a highly Lewis acidic metal for epoxide binding and Co(II) providing a labile metal carbonate nucleophile to enhance epoxide ring opening. To enhance the rate further a range of ligand variations are envisaged. The features of the ligand hypothesised to give high activity originate from:

1) Ideal intermetallic separation ~ 3.0 Å.[2]

2) Amine functionalisation.

3) Flexibility to adopt a 'bowl' shape conformation.[20]

Donor R groups such as a tethered pyridine arm could be used to bind *trans* to the carboxylate intermediate and hence enhance its nucleophilicity. The amine functionality could be replaced with stronger electron donating groups such as imine or phosphaimine, futher enhancing nucleophilicity. Finally, a C_2-linker could be used in-place of the C_3-linker as a smaller binding cavity may be more suited to the smaller Co(II) centre (in comparison to Zn(II)/Mg(II)) and should enhance the binding of the amine groups.

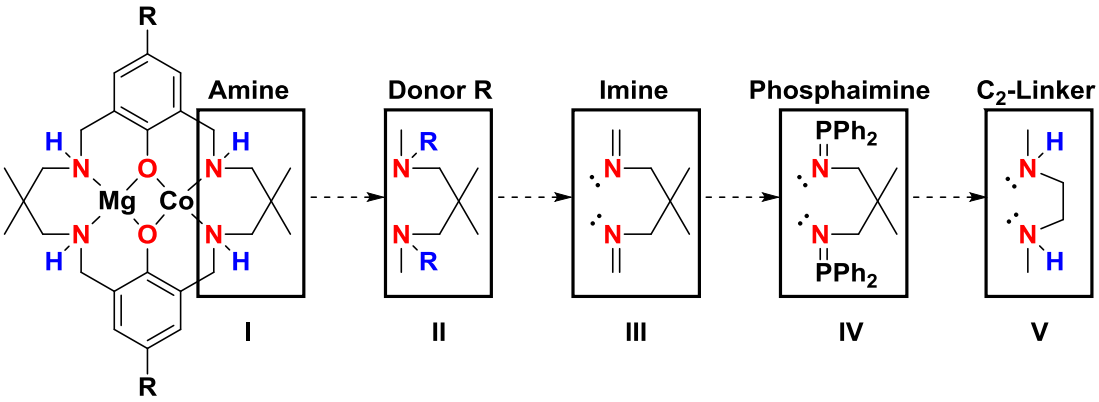


Figure 6.3: Proposed structural changes to the backbone of the Co(II) side of the macrocycle to enhance Co(II)-carbonate nucleophilicity.

Furthermore, the secondary amine group can be replaced by more donating/structurally rigid nitrogen donors in order to increase the nucleophilicity of the Co(II) and increase/reduce the steric environment around the attacking nucleophile.

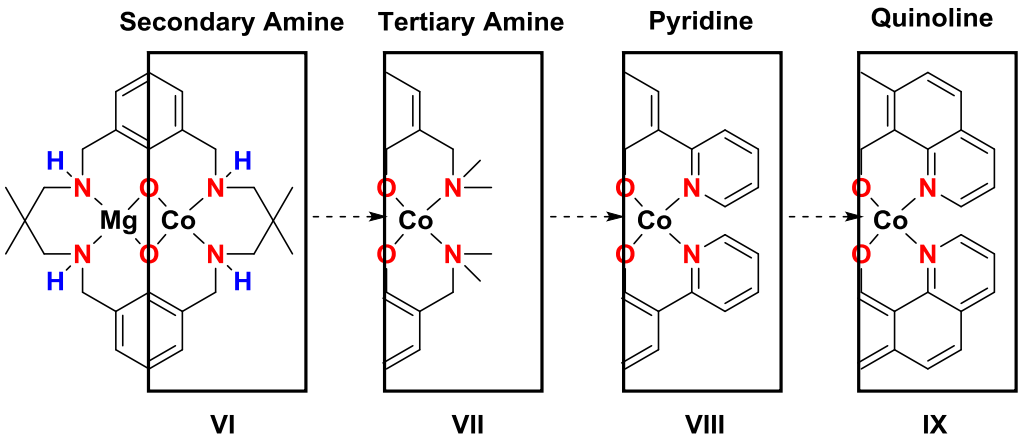


Figure 6.4: Proposed structural changes to determine effects of ligand rigidity.

6.1.3 Entropically driven Catalyst Design – Multimetallic

Attempts to reduce the transition state entropy is an approach scarcely taken, as entropic contributions in catalysis are often poorly understood and generally significantly smaller than enthalpic contributions. It may be feasibile to decrease the transition state entropy further by replacing the Mg(II) with more ionic metal centres such as Group 1, 2 or Lanthanides (III). Although this proved unsuccessful with the macrocycle studied in this thesis, due to the large ionic radius of the Group 1 and 2 metals, this substitution may be achieved with a ligand which could accommodate the larger metal centres (Figure 6.5).

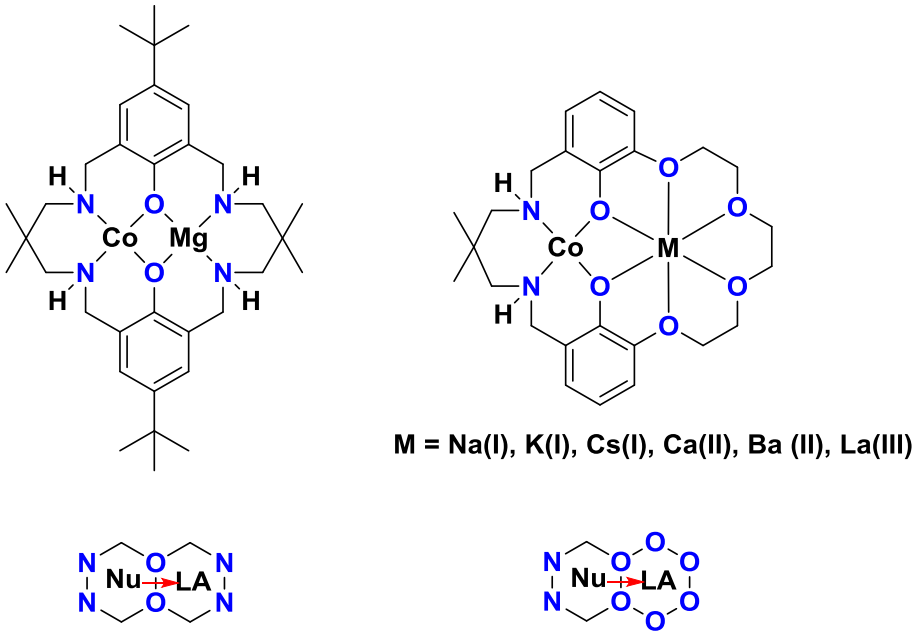


Figure 6.5: Crown-ether macrocycle suitable to accommodate large ionic metal centres.

An alternative would be to increase the number of epoxide binding configurations which could lead to successful nucleophilic attack/epoxide ring opening. Multimetallic ligands may result in improved activities due to the increased number of nucleophilic donors to attack a single coordinated epoxide at the Lewis acid.

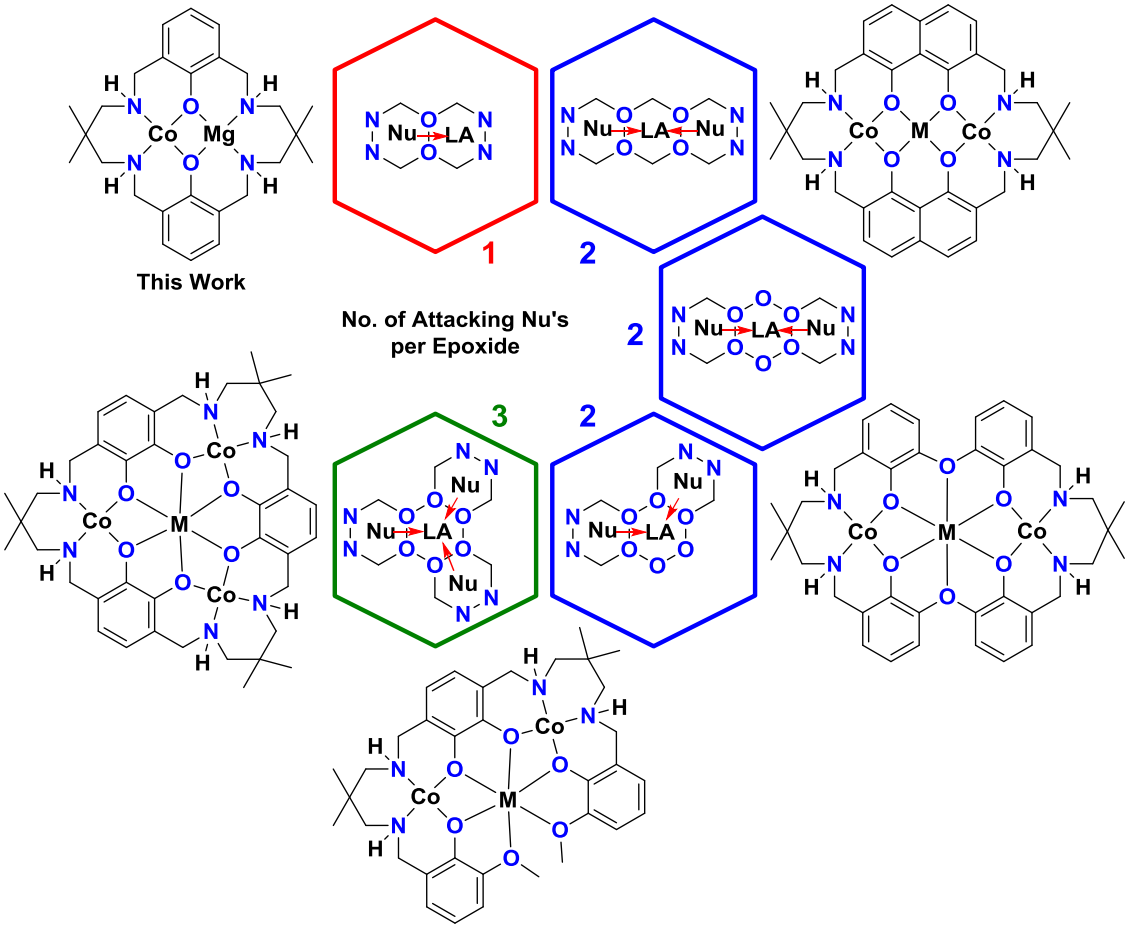


Figure 6.6: Proposed ligand structures to increase the number of attacking nucleophiles per coordinated epoxide.

6.1.4 References

1. Trott, G.; Saini, P. K.; Williams, C. K., Catalysts for CO_2/epoxide ring-opening copolymerization*, Phil. Trans. R. Soc. A.,* **2016,** *374*, (2061), 1.
2. Klaus, S.; Lehenmeier, M. W.; Anderson, C. E.; Rieger, B., Recent advances in CO2/epoxide copolymerization—New strategies and cooperative mechanisms*, Coord. Chem. Rev.,* **2011,** *255*, (13), 1460.
3. Kember, M. R.; Buchard, A.; Williams, C. K., Catalysts for CO_2/epoxide copolymerisation*, Chem. Commun.,* **2011,** *47*, (1), 141.
4. Poland, S. J.; Darensbourg, D. J., A quest for polycarbonates provided via sustainable epoxide/CO_2 copolymerization processes*, Green Chem.,* **2017,** *19*, (21), 4990.
5. Peña Carrodeguas, L.; González-Fabra, J.; Castro-Gómez, F.; Bo, C.; Kleij, A. W., AlIII-Catalysed Formation of Poly(limonene)carbonate: DFT Analysis of the Origin of Stereoregularity*, Chem. Eur. J.,* **2015,** *21*, (16), 6115.
6. Byrne, C. M.; Allen, S. D.; Lobkovsky, E. B.; Coates, G. W., Alternating Copolymerization of Limonene Oxide and Carbon Dioxide*, J. Am. Chem. Soc.,* **2004,** *126*, (37), 11404.
7. Shi, Z.; Jiang, Q.; Song, Z.; Wang, Z.; Gao, C., Dinuclear iron(iii) complexes bearing phenylene-bridged bis(amino triphenolate) ligands as catalysts for the copolymerization of cyclohexene oxide with carbon dioxide or phthalic anhydride*, Polym. Chem.,* **2018,** *9*, (38), 4733.
8. Della Monica, F.; Maity, B.; Pehl, T.; Buonerba, A.; De Nisi, A.; Monari, M.; Grassi, A.; Rieger, B.; Cavallo, L.; Capacchione, C., [OSSO]-Type Iron(III) Complexes for the Low-Pressure Reaction of Carbon Dioxide with Epoxides: Catalytic Activity, Reaction Kinetics, and Computational Study*, ACS Catal.,* **2018,** 6882.
9. Ohkawara, T.; Suzuki, K.; Nakano, K.; Mori, S.; Nozaki, K., Facile Estimation of Catalytic Activity and Selectivities in Copolymerization of Propylene Oxide with Carbon Dioxide Mediated by Metal Complexes with Planar Tetradentate Ligand*, J. Am. Chem. Soc.,* **2014,** *136*, (30), 10728.
10. Nakano, K.; Kobayashi, K.; Ohkawara, T.; Imoto, H.; Nozaki, K., Copolymerization of Epoxides with Carbon Dioxide Catalyzed by Iron–Corrole Complexes: Synthesis of a Crystalline Copolymer*, J. Am. Chem. Soc.,* **2013,** *135*, (23), 8456.
11. Buchard, A.; Kember, M. R.; Sandeman, K. G.; Williams, C. K., A bimetallic iron(III) catalyst for CO_2/epoxide coupling*, Chem. Commun.,* **2011,** *47*, (1), 212.
12. Stößer, T.; Williams, C. K., Selective Polymerization Catalysis from Monomer Mixtures: Using a Commercial Cr-Salen Catalyst To Access ABA Block Polyesters*,* **2018,** *57*, (21), 6337.
13. Kozak, C. M.; Woods, A. M.; Bottaro, C. S.; Devaine-Pressing, K.; Ni, K., A MALDI-TOF MS analysis study of the binding of 4-(N,N-dimethylamino)pyridine to amine-bis(phenolate) chromium(iii) chloride complexes: mechanistic insight into differences in catalytic activity for CO_2/epoxide copolymerization*, Faraday Discuss.,* **2015,** *183*, (0), 31.
14. Han, B.; Zhang, L.; Yang, M.; Liu, B.; Dong, X.; Theato, P., Highly Cis/Trans-Stereoselective (ONSO)CrCl-Catalyzed Ring-Opening Copolymerization of Norbornene Anhydrides and Epoxides*, Macromolecules,* **2016,** *49*, (17), 6232.
15. Chatterjee, C.; Chisholm, M. H., Influence of the Metal (Al, Cr, and Co) and the Substituents of the Porphyrin in Controlling the Reactions Involved in the

Copolymerization of Propylene Oxide and Carbon Dioxide by Porphyrin Metal(III) Complexes. 2. Chromium Chemistry*, Inorg. Chem.,* **2012,** *51*, (21), 12041.
16. Nakano, K.; Nakamura, M.; Nozaki, K., Alternating Copolymerization of Cyclohexene Oxide with Carbon Dioxide Catalyzed by (salalen)CrCl Complexes*, Macromolecules,* **2009,** *42*, (18), 6972.
17. Darensbourg, D. J.; Fitch, S. B., (Tetramethyltetraazaannulene)chromium Chloride: A Highly Active Catalyst for the Alternating Copolymerization of Epoxides and Carbon Dioxide*, Inorg. Chem.,* **2007,** *46*, (14), 5474.
18. Darensbourg, D. J.; Bottarelli, P.; Andreatta, J. R., Inquiry into the Formation of Cyclic Carbonates during the (Salen)CrX Catalyzed CO_2/Cyclohexene Oxide Copolymerization Process in the Presence of Ionic Initiators*, Macromolecules,* **2007,** *40*, (21), 7727.
19. Darensbourg, D. J.; Mackiewicz, R. M.; Rodgers, J. L.; Phelps, A. L., (Salen)CrIIIX Catalysts for the Copolymerization of Carbon Dioxide and Epoxides: Role of the Initiator and Cocatalyst*, Inorg. Chem.,* **2004,** *43*, (6), 1831.
20. Kember, M. R.; Jutz, F.; Buchard, A.; White, A. J. P.; Williams, C. K., Di-cobalt(ii) catalysts for the copolymerisation of CO_2 and cyclohexene oxide: support for a dinuclear mechanism?*, Chem. Sci.,* **2012,** *3*, (4), 1245.

Chapter 7:

Experimental Section

7.1.0 General Comments

All experimental manipulations were performed using a dual-manifold nitrogen-vacuum Schlenk line or in a nitrogen filled glovebox. All solvents and reagents were obtained from commercial sources and used as received unless stated otherwise. Common organic solvents were obtained from an SPS system, degassed by several freeze-pump-thaw cycles and further dried with 3 Å molecular sieves and stored under nitrogen. Cyclohexene oxide was dried over calcium hydride, overnight, and purified via fractional distillation prior to use and stored under an inert atmosphere. All anhydrides were obtained from commercial sources, extracted into benzene, recrystallized from chloroform, followed by sublimation. All anhydrous deuterated solvents were obtained from GOSS Scientific and dried over calcium hydride, overnight, and purified via vacuum transfer, with the exception of THF which was dried over 3 Å Molecular sieves. Deuterated MeOH, DMSO and Pyridine were obtained in individual glass ampoules and were used as received. Research-grade carbon dioxide (BOC, 99.99 %) was dried through a drierite column and two additional drying columns (Micro Torr, Model number: MC1-804FV) in series before use in copolymerisation studies.

7.1.1 NMR spectroscopy

All spectra were measured on a Bruker Avance III HD nanobay NMR equipped with a 9.4 T magnet, a Bruker Avance NMR equipped with a 11.75 T magnet and a ^{13}C detect cryoprobe or a Bruker AV 400 instrument. NMR spectra were processed and analysed using MestReNova and Bruker TopSpin software packages.

7.1.2 Elemental Analysis

Elemental analysis was determined by Mr Stephen Boyer at the London Metropolitan University. Two samples of each complex (ca. 10 mg) were submitted and results averaged.

7.1.3 Mass Spectroscopy

MALDI-ToF analysis was performed on a Micromass MALDI micro MX spectrometer. *Catalyst Matrix: trans*-2-[3-(4-*tert*-butylphenyl)-2-methyl-2-propenylidene]-malonitrile.

Polymer Matrix: Dithranol. The samples were prepared as follows: 10 mg/mL THF solution of complex and 10 mg/mL THF solution of matrix were mixed together. This mixture (2 μL) was then spotted on the MALDI-plate and allowed to dry. All preparations were carried out in a glovebox.

7.1.4 X-ray Diffraction

Imperial College London: Crystal structure data (4a) was collected and solved by Dr Andrew J. P. White. Data was collected using an Agilent Xcalibur PX 3E diffractometer, with the structures refined using the SHELXTL and SHELX-2013 program systems.

Oxford University: Crystal structure (18) was collected and solved by Dr Kirsten Christensen, all other structures were collected and solved by Dr Christopher B. Durr.

Crystalline samples were isolated in a glovebox, under a pool of fluorinated oil, and mounted on MiTeGen MicroMounts. The crystals were then cooled to 150 K, with an Oxford Cryosystems nitrogen cooling device. Data collection was carried out with an Oxford Diffraction Supernova diffractometer using, Cu Kα (λ = 1.5417 Å) or Mo Kα (λ = 0.7107 Å) radiation. The resulting raw data was processed using CrysAlisPro. Structures were solved by SHELXT and full-matrix least squares refinements based on F2 were performed in SHELXL-14, as incorporated in the WinGX package. For each methyl group, the hydrogen atoms were added at calculated positions using a riding model, with U(H) = 1.5 Ueq (bonded carbon atoms). The rest of the hydrogen atoms were included in the model, at calculated positions, using a riding model U(H) – 1.2 Ueq (bonded atom). Neutral atom scattering factors were used and included terms of anomalous dispersion.

7.1.5 Size Exclusion Chromatography (SEC)

Two mixed bed PSS SDV linear S columns were used in series, with THF, as the eluent, at a flow rate of 1 mL/min, on a Shimadzu LC-20AD instrument at 40 °C. The polymer samples were dissolved in SEC grade THF and filtered prior to analysis. Polymer molecular weight (Mn) was determined by comparison against polystyrene standards and where appropriate correction factors were applied as reported in the literature.

7.1.6 DOSY NMR Spectroscopy

A calibration plot between molecular weight and diffusion coefficient was determined using standards of molecular weight 81 $gmol^{-1}$ and 418.7 $gmol^{-1}$. A linear relationship was observed between logMW and logD.

Table 7.1: Diffusion coefficients of complexes in d_8-THF along with corresponding molecular weights.

Compound	LogD	MW (g mol^{-1})	LogMW
THF	-8.568	81	1.9040
$HN(Si(CH_3)_3)_2$	-8.763	161	2.2079
$Zn(N(Si(CH_3)_3)_2)_2$	-8.943	386	2.5868
BDIH	-8.990	419	2.6219

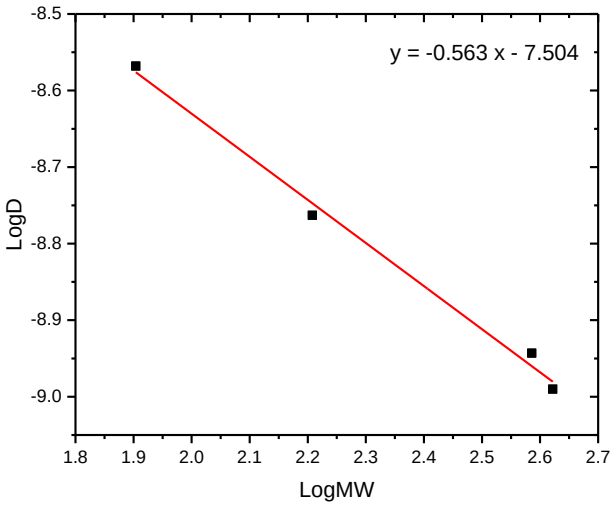


Figure 7.1: LogD vs LogMW from the ^1H DOSY NMR data represented on Table 7.1

Equation 7.1: Estimation of MW from diffusion coefficients obtained in THF.

$$\log(D) = -7.505 - (0.5626 * \log(MW)) \quad (7.1)$$

7.1.7 CO_2 Polymerisations + ATR-IR Measurements

Low Pressure (1 bar): Performed on a triple manifold Young tap Schlenk line (N_2, CO_2, and Vacuum).

High Pressure (>50 bar): Performed in a 25 mL Parr 5500 HP Compact Reactor.

In situ ATR-IR measurements were performed on a Mettler-Toledo ReactIR ic.10 spectrometer equipped with a MCT detector and a silver halide DiComp probe.

7.1.8 X-ray Photoelectron Spectroscopy

XPS data was collected and analysed by Dr. Anna Reguotz (Imperial College). The surface of the catalyst powders were characterised using X-ray photoelectron spectroscopy (XPS). The spectra were recorded on a Thermo Scientific Kα X-ray photoelectron spectrometer operating at $2x10^{-9}$ mbar base pressure. This system incorporates a monochromated, microfocused Al Kα X-ray Source (hν = 1486.6 eV) and a 180 ° double focusing hemispherical analyser with a 2D detector. The X-ray source was operated at 6 mA emission current and 12 kV anode bias and a flood gun was used to minimise sample charging. Data were collected at 20 eV pass energy using an X-ray spot size of 400 μm. All data were analysed using the Avantage software package

7.1.9 Superconducting Quantum Interference Device Magnetometry

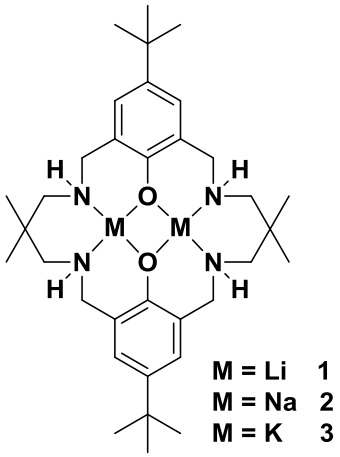
SQUID data was collected and analysed by Dr Alexander F.R. Kilpatrick (Oxford University). Magnetic measurements on powdered samples were carried out using a Quantum Design MPMS-5 magnetometer, at a field of 0.1 Tesla, at temperatures from 2-300 K. Weighed samples (ca. 30 mg) were placed into gelatine capsules and then loaded into a diamagnetic plastic straw before being put in the cryostat. Data reproducibility

was carefully checked on two independently synthesised and measured samples. Values of the magnetic susceptibility were corrected for the underlying diamagnetic increment by using tabulated Pascal constants, per bimetallic complex unit for **16** (χ_{dia} = -4.83x10^{-4} cm^{3}mol^{-1}) and **18** (χ_{dia} = -4.76x10^{-4} cm^{3}mol^{-1}). The mass magnetic susceptibility, χ_g, was multiplied by the molar mass for **16** (786.8 gmol-1) and **18** (752.2 gmol^{-1}) to obtain the magnetic susceptibility per mole of bimetallic complex, χ_m.

7.2.0 Cyclic Voltammetry

Electrochemical studies were carried out using a PalmSens EmStat Blue potentiostat under computer control. Cyclic voltammetry experiments were performed in an MBraun UNIlab glovebox, under N_2, using a three-electrode configuration: with a Au disc (2.0 mm^2) as the working electrode, a Pt wire as the counter electrode and a Ag wire as the pseudo-reference electrode. Sample solutions were prepared by dissolving the analyte (*ca.* 5 mM), in THF (10 mL), followed by addition of a supporting electrolyte [^{n}Bu$_4$N][PF$_6$]. The reported mid-peak potentials are referenced internally to that of the Fc$^+$/Fc redox couple, which was measured by adding ferrocene (*ca*. 1 mg) to the sample solution.

7.2.1 Chapter 2: Group 1 and 2, zinc (II) catalysts



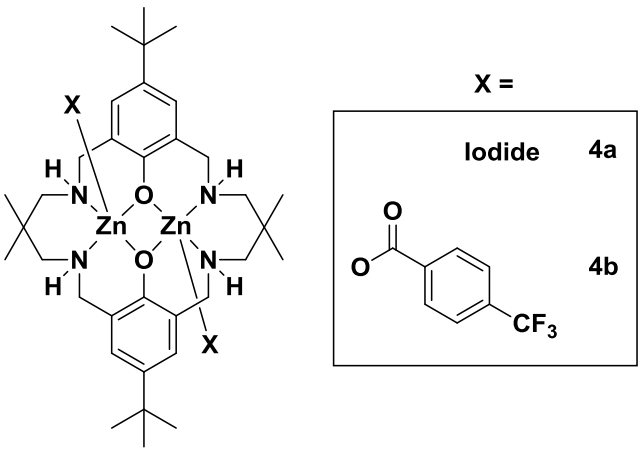
General Procedure: $M(N(Si(CH_3)_3)_2)$ (1.81 mmol) was added to a solution of H_2L (0.50 g, 0.91 mmol), in THF (10 mL), and stirred for 16 h. The solution was reduced in *vacuo* to dryness and the crude product was washed with pentane (3 x 5 mL) to afford a white solid.

Complex 1: (0.42 g, 0.75 mmol, 83 %). ^{1}H NMR (d_8-THF, 400.20 MHz, 298 K) 6.87 (s, 4H, Ph**H**) 3.57 (s, 8H, Ph-C**H**$_2$-NH) 2.46 (d, 8H, ^3J = 7.4 Hz, C**H**$_2$-C$(CH_3)_2$) 1.41 (q, 4H, ^3J = 6.3 Hz, N**H**) 1.22 (s, 18H, C(C**H**$_3)_3$) 0.89 (s, 12H, C(C**H**$_3)_2$). ^{7}Li NMR (155.52 MHz, d_8-THF, 298K) 1.07 ppm. ^{13}C{^{1}H} NMR (125.81 MHz, d_8-THF, 298K) 166.7 (ipso-**Ph**) 131.2 (ortho-**Ph**) 126.8 (para-**Ph**) 125.6 (meta-**Ph**) 59.9 (Ph-**C**H$_2$-NH) 56.3 (**C**H$_2$-C$(CH_3)_2$) 34.3 (**C**$(CH_3)_3$) 33.8 (C(**C**$H_3)_2$) 32.3 (**C**$(CH_3)_3$) 26.4 (C(**C**$H_3)_2$). Elemental Analysis for $C_{34}H_{54}Li_2N_4O_2$ (564.46 gmol^{-1}): Calculated; C, 72.3; H, 9.6; N, 9.9 %. Found: C, 72.0; H, 9.3; N, 9.9 %.

Complex 2: (0.41 g, 0.68 mmol, 75 %). ^{1}H NMR (d_8-THF, 400.20 MHz, 298 K) 6.91 (s, 4H, Ph**H**) 4.42 (t, 4H, ^3J = 9.9 Hz, Ph-C**H**$_2$-NH) 3.14 (d, 4H, ^3J = 9.6 Hz, Ph-C**H**$_2$-NH) 2.44 (d, 4H, NH-C**H**$_2$-C$(CH_3)_2$) 2.37 (t, 4H, ^3J = 10.1 Hz, NH-C**H**$_2$-C$(CH_3)_3$) 1.20 (s, 18H,

C(C**H**$_3$)$_3$) 0.94 (br. 4H, N**H**) 0.91 (s, 6H, C(C**H**$_3$)$_2$) 0.78 (s, 6H, C(C**H**$_3$)$_2$). ^{13}C{^{1}H} NMR (125.81 MHz, d$_8$-THF, 298K) 167.9 (ipso-**Ph**) 131.7 (ortho-**Ph**) 128.7 (para-**Ph**) 126.3 (meta-**Ph**) 62.0 (Ph-**C**H$_2$-NH) 55.6 (**C**H$_2$-C(CH$_3$)$_2$) 34.6 (**C**(CH$_3$)$_3$) 33.7 (**C**(CH$_3$)$_2$) 32.2 (C(**C**H$_3$)$_3$) 28.1 (C(**C**H$_3$)$_2$) 23.3 (C(**C**H$_3$)$_2$). Elemental Analysis for $C_{34}H_{54}N_4Na_2O_2$ (596.40 gmol^{-1}): Calculated; C, 68.4; H, 9.1; N, 9.4 %. Found: C, 68.7; H, 8.9; N, 9.1 %.

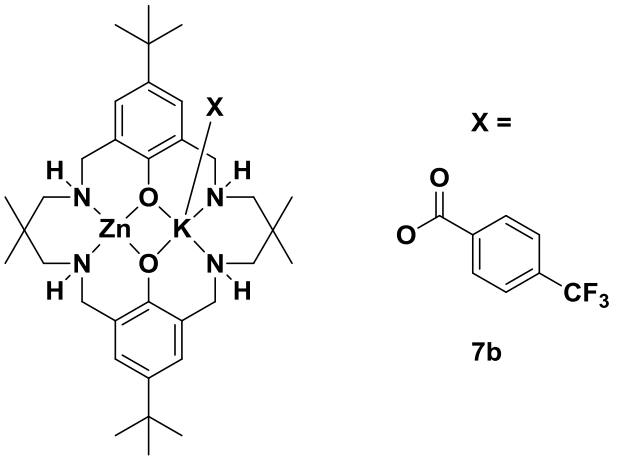
Complex 3: (0.44 g, 0.71 mmol, 78 %). ^{1}H NMR (d$_8$-THF, 400.20 MHz, 298 K) 6.81 (s, 4H, Ph**H**) 3.60 (s, 8H, Ph-C**H**$_2$-NH) 2.25 (s, 8H, C**H**$_2$-C(CH$_3$)$_2$) 1.44 (br. 4H, N**H**) 1.17 (s, 18H, C(C**H**$_3$)$_3$) 0.82 (s, 12H, C(C**H**$_3$)$_2$). ^{13}C{^{1}H} NMR (125.81 MHz, d$_8$-THF, 298 K) 166.8 (ipso-**Ph**) 130.0 (ortho-**Ph**) 127.3 (para-**Ph**) 126.3 (meta-**Ph**) 58.8 (Ph-**C**H$_2$-NH) 55.0 (**C**H$_2$-C(CH$_3$)$_2$) 34.9 (**C**(CH$_3$)$_3$) 33.7 (**C**(CH$_3$)$_2$) 32.3 (C(**C**H$_3$)$_3$) 25.8 (C(**C**H$_3$)$_2$). Elemental Analysis for $C_{34}H_{54}K_2N_4O_2$ (628.35 gmol^{-1}): Calculated; C, 64.9; H, 8.7; N, 8.9 %. Found: C, 64.8; H, 8.7; N, 9.0 %.



General Procedure to di-zinc catalysts: $ZnEt_2$ (0.91 mmol) was added to a solution of H_2L (0.50 g, 0.91 mmol) in THF (5 mL) and stirred for 2 h. ZnX_2 (0.91 mmol, X = I or benzoate) was added and allowed to stir for a further 2 h. The solution was reduced in *vacuo* to dryness and the crude product was washed with pentane (3 x 5 mL) to afford a white solid.

Complex 4a: (0.64 g, 0.69 mmol, 76 %) ^{1}H NMR (d_2-TCE, 400.20 MHz, 403 K) 7.00 (s, 4H, Ph**H**) 4.79 (s, 4H, Zn-HN-C**H**$_2$-Ph) 3.34 (s, 4H, Zn-HN-C**H**$_2$-Ph) 2.95 (s, 4H, Zn-N**H**) 2.88 (s, 4H, Zn-HN-C**H**$_2$-C$(CH_3)_2$) 2.46 (s, 4H, Zn-HN-C**H**$_2$-C$(CH_3)_2$) 1.35 (s, 18 H, C(C**H**$_3)_3$) 1.31 (s, 6H, C(C**H**$_3)_2$) 1.06 (s, 6H, C(C**H**$_3)_2$). ^{13}C{^{1}H} NMR (d_2-TCE, 125.81 MHz, 403 K) 160.6 (*ipso*-**Ph**) 140.0 (*para*-**Ph**) 128.4 (*meta*-**Ph**) 125.4 (*ortho*-**Ph**) 65.0 (Zn-HN-**C**H$_2$-C$(CH_3)_2$) 58.3 (Zn-HN-**C**H$_2$-Ph) 34.9 (**C**$(CH_3)_2$) 32.9 (**C**$(CH_3)_3$) 29.4 (C(**C**H$_3)_2$) 23.0 (C(**C**H$_3)_2$). Elemental Analysis for $C_{34}H_{54}I_2N_4O_2Zn_2$ (932.09 gmol^{-1}): Calculated; C, 43.7; H, 5.8; N, 6.0 %. Found; C, 43.5; H, 5.9; N, 6.1 %. MS (MALDI-ToF): m/z 808 $[LZnZnI]^+$ (90 %).

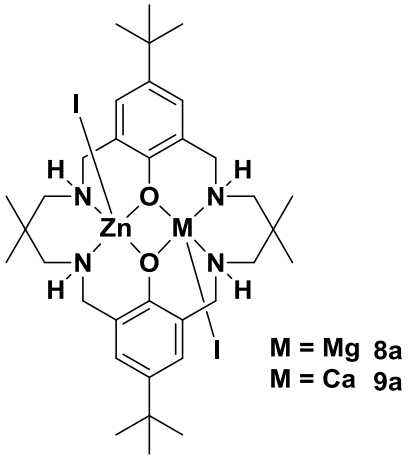
Complex 4b: (0.91 g, 0.86 mmol, 95 %) ^{1}H NMR (d_2-TCE, 500.20 MHz, 403 K) 8.23 (d, 4H, ^{3}J = 7.8 Hz, *o*-OBz) 7.78 (d, 4H, ^{3}J = 7.8 Hz, *m*-OBz) 7.00 (s, 4H, Ph**H**) 4.80 (br., 4H, Ph-C**H**$_2$-NH) 3.35 (br., 4H, Ph-C**H**$_2$-NH) 2.97 (br., 4H, N**H**) 2.87 (br., 4H, C**H**$_2$-C(CH$_3$)$_2$) 2.48 (br. 4H, C**H**$_2$-C(CH$_3$)$_2$) 1.35 (s, 18H, C(C**H**$_3$)$_3$) 1.32 (s, 6H, C(C**H**$_3$)$_2$) 1.07 (s, 6H, C(C**H**$_3$)$_2$). ^{13}C{^{1}H} NMR (d_2-TCE, 125.81 MHz, 403 K) 130.1 (*o*-OBz) 127.0 (*m*-OPh) 125.2 (*m*-OBz) 63.4 (**C**H$_2$-C(CH$_3$)$_2$) 56.5 (Ph-**C**H$_2$-NH) 33.5 (**C**(CH$_3$)$_2$) 33.3 (**C**(CH$_3$)$_3$) 31.3 (C(**C**H$_3$)$_3$) 27.9 (C(**C**H$_3$)$_2$) 21.3 (C(**C**H$_3$)$_2$). ^{19}F NMR (d_2-TCE, 376.64 MHz, 403 K): -61.6 (s, CF_3). Elemental Analysis for $C_{50}H_{62}F_6N_4O_6Zn_2$ (1056.32 gmol^{-1}): Calculated; C, 56.7; H, 5.9; N, 5.3 %. Found; C, 56.8; H, 6.0; N, 5.4 %. MS (MALDI-ToF): m/z 869 [LZn$_2$(OBz)]$^{+}$ (100 %).



7b

Complex 7b: $ZnEt_2$ (0.91 mmol) was added to a solution of H_2L (0.50 g, 0.91 mmol) in THF (5 mL) and stirred for 2 h. KX (0.91 mmol) was added and the solution was heated to 100 °C for 2 h. The solution was reduced in *vacuo* to dryness and the crude product was washed with pentane (3 x 5 mL) to afford a white solid. (0.53 g, 0.63 mmol, 70 %). ^{1}H NMR (d_8-THF, 400.20 MHz, 298 K) 8.22 (d, 2H, ^{3}J = 7.5 Hz, *o*-**OBz**) 7.63 (d, 2H, ^{3}J =7.5 Hz, *m*-OBz) 6.96 (s, 2H, Zn-Ph**H**) 6.78 (s, 2H, K-Ph**H**) 4.38 (t, 2H, ^{3}J = 11.7 Hz, Zn-HN-C**H**$_2$-Ph) 3.58 (d, 2H, ^{3}J =10.2 Hz, K-HN-C**H**$_2$-Ph) 3.38 (t, 2H, ^{3}J = 10.1 Hz, K-HN-C**H**$_2$-Ph) 3.25 (t, 2H, ^{3}J = 11.8 Hz, Zn-HN-C**H**$_2$-C(CH$_3$)$_2$) 3.11 (d, 2H, ^{3}J = 11.4 Hz, Zn-HN-C**H**$_2$-Ph) 2.67 (t,

2H, ^{3}J = 11.9 Hz, Zn-N**H**) 2.60 (d, 2H, ^{3}J = 11.9 Hz, Zn-HN-C**H**$_2$-C(CH$_3$)$_2$) 2.53-2.37 (m, 4H, K-HN-C**H**$_2$-C(CH$_3$)$_2$) 1.50 (b. s, 2H, K-N**H**) 1.22 (s, 18H, C(C**H**$_3$)$_3$) 1.21 (s, 3H, C(C**H**$_3$)$_2$) 1.02 (s, 3H, C(C**H**$_3$)$_2$) 0.94 (s, 6H, C(C**H**$_3$)$_2$). ^{13}C{^{1}H} NMR (125.81 MHz, d$_8$-THF, 298 K) 164.4 (*ipso*-**Ph**) 141.8 (*ipso*-**OBz**) 132.3 (*p*-**Ph**) 131.0 (q, $^{2}J_{C\text{-}F}$ = 30.85 Hz, *p*-**OBz**) 129.9 (*m*-**OBz**) 127.4 (*o*-**Ph**$_{Zn}$) 127.0 (m–**Ph**$_{Zn}$) 125.3 (m–**Ph**$_K$) 124.1 (*o*-**OBz**) 123.1 (*o*–**Ph**$_K$) 62.7 (Zn-HN-**C**H$_2$-C(CH$_3$)$_2$) 59.7 (K-HN-**C**H$_2$-C(CH$_3$)$_2$) 56.5 (Zn-HN-**C**H$_2$-Ph) 54.2 (K-HN-**C**H$_2$-Ph) 34.4 (quat. K-HN-CH$_2$-**C**(CH$_3$)$_2$) 33.9 (quat. Zn-HN-CH$_2$-**C**(CH$_3$)$_2$) 33.0 (C(**C**H$_3$)$_3$) 31.4 (C(**C**H$_3$)$_3$) 28.1 (K-HN-CH$_2$-C(**C**H$_3$)$_2$) 25.9 (K-HN-CH$_2$-C(**C**H$_3$)$_2$) 25.4 (Zn-HN-CH$_2$-C(**C**H$_3$)$_2$) 20.9 (Zn-HN-CH$_2$-C(**C**H$_3$)$_2$). Quaternary carbonyl and -CF$_3$ resonances were not observed. ^{19}F NMR (d$_8$-THF, 376.64 MHz, 298 K): -63.3 (s, -C**F**$_3$) Elemental Analysis for C$_{42}$H$_{58}$F$_3$KN$_4$O$_4$Zn (842.33 gmol^{-1}): Calculated; C, 59.7; H, 6.9; N, 6.6 %. Found; C, 59.9; H, 7.0; N, 6.7 %. MS (MALDI-ToF): m/z 654 [LZnK]$^+$ (95 %)



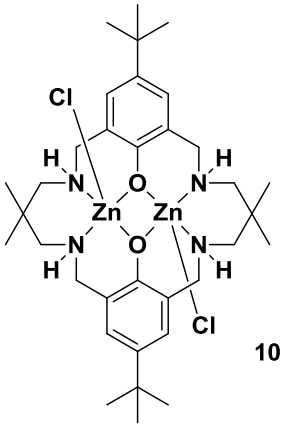
Synthesis of 8a/9a: $ZnEt_2$ (0.91 mmol) was added to a solution of H_2L (0.50 g, 0.91 mmol) in THF (5 mL) and stirred for 2 h. MX_2 (0.91 mmol) was added and the solution was heated to 100 °C for 2 h. The solution was reduced in *vacuo* to dryness and the crude product was washed with pentane (3 x 5 mL) to afford a white solid.

Complex 8a: (0.63 g, 0.71 mmol, 75 %) ^{1}H NMR (d_8 – THF, 400.20 MHz, 298 K): 6.92 (s, 4H, Mg-Ph**H** + Zn-Ph**H**) 5.09 (t, 2H, ^3J = 11.9 Hz, Mg-HN-C**H**$_2$-Ph) 4.08 (d, 2H, ^3J = 10.9 Hz, Zn-HN-C**H**$_2$-Ph) 3.23 (d, 2H, ^3J = 12.6 Hz, Zn-HN-C**H**$_2$-Ph) 3.10 (t, 2H, ^3J = 12.6 Hz, Mg-HN-C**H**$_2$-C(CH$_3$)$_2$) 3.05 (d, 2H, ^3J = 13.0 Hz, Mg-HN-C**H**$_2$-Ph) 2.86 (d, 2H, ^3J = 11.6, Mg-N**H**) 2.82 (d, 2H, ^3J = 7.7 Hz, Zn-HN-C**H**$_2$-C(CH$_3$)$_2$) 2.69 (t, 2H, ^3J = 10.5 Hz, Zn-N**H**) 2.67 (d, 2H, ^3J = 9.5 Hz, Zn-HN-C**H**$_2$-C(CH$_3$)$_2$) 2.46 (d, 2H, ^3J = 11.6 Hz, Zn-HN-C**H**$_2$-C(CH$_3$)$_2$) 1.41 (s, 3H, C(C**H**$_3$)$_2$) 1.38 (s, 3H, C(C**H**$_3$)$_2$) 1.24 (s, 18H, C(C**H**$_3$)$_3$) 0.96 (s, 3H, C(C**H**$_3$)$_2$) 0.94 (s, 3H, C(C**H**$_3$)$_2$). ^{13}C{^{1}H} NMR (d_8 – THF, 125.82 MHz, 298 K) 160.2 (*ipso*-**Ph**) 137.3 (*p*-**Ph**) 128.3 (*m*-**Ph**$_{Mg}$) 127.9 (*m*-**Ph**$_{Zn}$) 124.9 (*o*-**Ph**$_{Mg}$) 124.9 (*o*-**Ph**$_{Zn}$) 64.0 (Mg-NH-**C**H$_2$-C(CH$_3$)$_2$) 63.7 (Zn-NH-**C**H$_2$-C(CH$_3$)$_2$) 58.6 (Mg-NH-**C**H$_2$-Ph) 56.1 (Zn-NH-**C**H$_2$-Ph) 35.3 (Zn-NH-CH$_2$-**C**(CH$_3$)$_2$) 34.8 (Mg-NH-CH$_2$-**C**(CH$_3$)$_2$) 33.9 (**C**(CH$_3$)$_3$) 31.8 (C(**C**H$_3$)$_3$) 28.5 (C(**C**H$_3$)$_2$) 28.4 (C(**C**H$_3$)$_2$). Elemental Analysis for $C_{34}H_{54}I_2MgN_4O_2Zn$ (892.15 gmol^{-1}):

Calculated; C, 45.7; H, 6.1; N, 6.3 %. Found; C, 45.3; H, 5.9; N, 6.1 %. MS (MALDI-ToF): m/z 765 $[LZnMgI]^+$ (100 %).

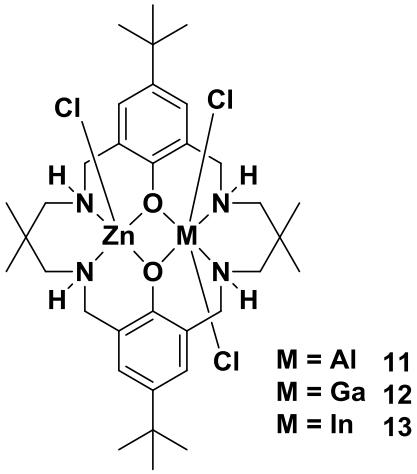
Complex 9a: (0.72 g, 0.79 mmol, 87 %). ^{1}H NMR (d_8 – THF, 400.20 MHz, 298 K): 6.81 (s, 2H, Zn-Ph**H**) 6.77 (s, 2H, Ca-Ph**H**) 4.96 (br., 2H, Zn-HN-C**H**$_2$-Ph) 4.39 (d, 2H, ^3J = 13.2 Hz, Ca-HN-C**H**$_2$-Ph) 3.45 (br., 2H, Ca-HN-C**H**$_2$-Ph) 3.18 (br., 2H, Zn-HN-C**H**$_2$-C$(CH_3)_2$) 3.00 – 2.80 (br. m, 6H, Zn-HN-C**H**$_2$-Ph, Ca-N**H**, Zn-N**H**) 2.54 (br., 2H, Ca-HN-C**H**$_2$-C$(CH_3)_2$) 2.38 (br., 2H, Zn-HN-C**H**$_2$-C$(CH_3)_2$) 2.13 (br., 2H, Ca-HN-C**H**$_2$-C$(CH_3)_2$) 1.13 (s, 18H, C(C**H**$_3)_3$) 1.00 (s, 3H, C(C**H**$_3)_2$) 0.87 (s, 6H, C(C**H**$_3)_2$) 0.69 (s, 3H, C(C**H**$_3)_2$). ^{13}C{^{1}H} NMR (d_8 – THF, 125.81 MHz, 298 K) 160.5 (*ipso*-**Ph**) 137.3 (*para*-**Ph**) 128.5 (*meta*-**Ph**$_{Ca}$) 127.5 (*meta*-**Ph**$_{Zn}$) 126.2 (*ortho*-**Ph**$_{Ca}$) 124.7 (*ortho*-**Ph**$_{Zn}$) 63.7 (Ca-NH-**C**H$_2$-C$(CH_3)_2$) 60.7 (Zn-NH-**C**H$_2$-C$(CH_3)_2$) 58.9 (Ca-NH-**C**H$_2$-Ph) 53.9 (Zn-NH-**C**H$_2$-Ph) 35.4 (Zn-NH-CH$_2$-**C**$(CH_3)_2$) 34.4 (Ca-NH-CH$_2$-**C**$(CH_3)_2$) 33.8 (**C**$(CH_3)_3$) 31.8 (C(**C**H$_3)_3$) 28.5 (C(**C**H$_3)_2$) 23.2 (C(**C**H$_3)_2$). Elemental Analysis for $C_{34}H_{54}CaI_2N_4O_2Zn$ (908.13 $gmol^{-1}$): Calculated; C, 44.9; H, 6.0; N, 6.2 %. Found; C, 45.0; H, 6.1; N, 6.0 %. MS (MALDI-ToF): m/z 782 $[LZnCaI]^+$ (100 %).

7.2.2 Chapter 3: Group 13, Zinc (II) Heterodinuclear Catalysts



10

Complex 10: $ZnEt_2$ (0.91 mmol) was added to a solution of H_2L (0.50 g, 0.91 mmol) in THF (5 mL) and stirred for 2 h. $ZnCl_2$ (0.91 mmol) was added and the solution was stirred for 2 h. The solution was reduced in *vacuo* to dryness and the crude product was washed with pentane (3 x 5 mL) to afford a white solid. (0.55 g, 0.73 mmol, 81 %). ^{1}H NMR (d_2-TCE, 400.20 MHz, 403 K) 6.99 (s, 4H, Ph**H**) 4.77 (s, 4H, Zn-HN-C**H**$_2$-Ph) 3.38 (s, 4H, Zn-HN-C**H**$_2$-Ph) 3.03 (s, 4H, Zn-N**H**) 2.82 (s, 4H, Zn-HN-C**H**$_2$-C$(CH_3)_2$) 2.50 (s, 4H, Zn-HN-C**H**$_2$-C$(CH_3)_2$) 1.40 – 1.30 (s, 24 H, C(C**H**$_3)_2$, C(C**H**$_3)_3$) 1.12 (s, 6H, C(C**H**$_3)_2$). ^{13}C{^{1}H} NMR (d_2-TCE, 125.81 MHz, 403 K) 160.5 (*ipso*-**Ph**) 140.3 (*p*-**Ph**) 128.3 (*m*-**Ph**) 124.9 (*o*-**Ph**) 64.5 (Zn-HN-**C**H$_2$-C$(CH_3)_2$) 58.7 (Zn-HN-**C**H$_2$-Ph) 35.2 (**C**$(CH_3)_2$) 34.9 (**C**$(CH_3)_3$) 32.9 (**C**$(CH_3)_3$) 29.4 (C(**C**H$_3)_2$) 25.3 (C(**C**H$_3)_2$). Elemental Analysis for $C_{34}H_{54}Cl_2N_4O_2Zn_2$ (748.22 gmol^{-1}): Calculated; C, 54.3; H, 7.2; N, 7.5 %. Found; C, 54.5; H, 7.4; N, 7.6 %. MS (MALDI-ToF): m/z 717 $[LZnZnCl]^+$ (90 %).



General Procedure to Goup 13-zinc(II) complexes: $ZnEt_2$ (0.91 mmol) was added to a solution of H_2L (0.50 g, 0.91 mmol) in THF (5 mL) and stirred for 2 h. MCl_3 (0.91 mmol) was added and the solution was heated to 100 °C for 2 h. The solution was reduced in *vacuo* to dryness and the crude product was washed with pentane (3 x 5 mL) to afford a white solid.

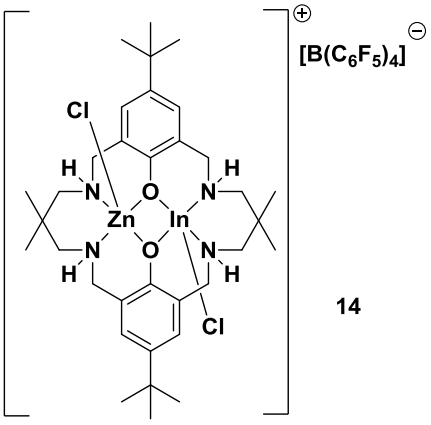
Complex 11: (0.63 g, 0.84 mmol, 95 %). ^{1}H NMR (d_3-MeCN, 400.20 MHz, 298 K): 7.06 (d, 4H, Al-Ph**H**, Zn-Ph**H**) 5.04 – 4.89 (m, 4H, Al-HN-C**H**$_2$-Ph, Zn-HN-C**H**$_2$-Ph) 3.65 (t, 2H, ^3J = 11.5 Hz, Al-N**H**) 3.35 (d, 2H, ^3J = 13.2 Hz, Zn-HN-C**H**$_2$-Ph) 3.29 (s, 2H, ^3J = 12.6 Hz, Al-HN-C**H**$_2$-Ph) 2.93 (t, 2H, ^3J = 11.5 Hz, Al-HN-C**H**$_2$-C(CH$_3$)$_2$) 2.83 (t, 2H, ^3J = 13.2 Hz, Zn-HN-C**H**$_2$-C(CH3)2) 2.78 – 2.64 (m, 4H, Al-HN-C**H**$_2$-C(CH$_3$)$_2$, Zn-HN-C**H**$_2$-C(CH$_3$)$_2$) 2.54 (t, 2H, ^3J = 12.0 Hz, Zn-N**H**) 1.36 (s, 3H, C(C**H**$_3$)$_2$) 1.27 (s, 18H, C(C**H**$_3$)$_3$) 1.07 (s, 3H, C(C**H**$_3$)$_2$) 0.93 (s, 3H, C(C**H**$_3$)$_2$). ^{13}C{^{1}H} NMR (d_3-MeCN, 125.81 MHz, 298 K) 155.0 (*ipso*-**Ph**) 141.5 (*p*-**Ph**) 129.1 (*m*-**Ph**$_{Zn}$) 127.7 (*m*-**Ph**$_{Al}$) 124.7 (*o*-**Ph**$_{Zn}$) 64.8 (Zn-HN-**C**H$_2$-C(CH$_3$)$_2$) 63.2 (Al-HN-**C**H$_2$-C(CH$_3$)$_2$) 57.1 (Zn-HN-**C**H$_2$-Ph) 56.7 (Al-HN-**C**H$_2$-Ph) 34.2 (Zn-HN-CH$_2$-**C**(CH$_3$)$_2$) 34.0 (Al-HN-CH$_2$-**C**(CH$_3$)$_2$) 33.3 (C(**C**H$_3$)$_3$) 31.6 (**C**(CH$_3$)$_3$) 27.9 (C(**C**H$_3$)$_2$) 27.7 (C(**C**H$_3$)$_2$) 22.1 (C(**C**H$_3$)$_2$) 20.4 (C(**C**H$_3$)$_2$). Elemental Analysis for $C_{34}H_{54}AlCl_3N_4O_2Zn$

(746.24 $gmol^{-1}$): Calculated; C, 54.5; H, 7.3; N, 7.5 %. Found; C, 54.2; H, 7.0; N, 7.3 %. MS (MALDI-ToF): m/z 714 $[LZnAlCl_2]^+$ (90 %)

Complex 12: (0.51 g, 0.65 mmol, 72 %). ^1H NMR (d_3-MeCN, 400.20 MHz, 298 K): 7.06 (d, 2H, ^4J = 2.63 Hz, Ga-Ph**H**) 7.03 (d, 2H, ^4J = 2.63 Hz, Zn-Ph**H**) 4.99 (t, 2H, ^3J = 12.9 Hz, Ga-HN-C**H**$_2$-Ph) 4.87 (t, 2H, ^3J = 11.9 Hz, Zn-HN-C**H**$_2$-Ph) 3.71 (t, 2H, ^3J = 11.2 Hz, Ga-N**H**) 3.26 (d, 2H, ^3J = 12.4 Hz, Ga-HN-C**H**$_2$-Ph) 3.25 (d, 2H, ^3J = 12.7 Hz, Zn-HN-C**H**$_2$-Ph) 3.03 (t, 2H, ^3J = 12.3 Hz, Ga-C**H**$_2$-C$(CH_3)_2$) 2.86 (t, 2H, ^3J = 12.8 Hz, Zn-C**H**$_2$-C$(CH_3)_2$) 2.73 (t, 2H, ^3J = 11.6 Hz, Ga-HN-C**H**$_2$-C$(CH_3)_2$) 2.66 (t, 2H, ^3J = 10.2 Hz, Zn-HN-C**H**$_2$-C$(CH_3)_2$) 2.43 (t, 2H, ^3J = 10.1 Hz, Zn-N**H**) 1.35 (s, 3H, C(C**H**$_3)_2$) 1.28 (s, 18H, C(C**H**$_3)_3$) 1.05 (s, 3H, C(C**H**$_3)_2$) 0.96 (s, 3H, C(C**H**$_3)_2$) 0.93 (s, 3H, C(C**H**$_3)_2$). $^{13}C\{^1H\}$ NMR (d_3-MeCN, 125.81 MHz, 298 K): 157.2 (ipso-**Ph**) 140.9 (*p*-**Ph**) 129.4 (Zn-*m*-**Ph**) 128.7 (Ga-*m*-**Ph**) 125.2 (Ga-*o*-**Ph**) 124.2 (Zn-*o*-**Ph**) 64.1 (Zn-HN-**C**H$_2$-C$(CH_3)_2$) 63.3 (Ga-HN-**C**H$_2$-C$(CH_3)_2$) 56.9 (Zn-HN-**C**H$_2$-Ph) 56.7 (Ga-HN-**C**H$_2$-Ph) 33.6 (**C**$(CH_3)_3$) 34.2 (**C**$(CH3)_2$) 34.0 (C(**C**H$_3)_2$) 31.7 (C(**C**H$_3)_3$) 27.9 (C(**C**H$_3)_2$) 26.3 (C(**C**H$_3)_2$) 22.0 (C(**C**H$_3)_2$) 20.5 (C(**C**H$_3)_2$). Elemental Analysis for $C_{34}H_{54}Cl_3GaN_4O_2Zn$ (788.19 $gmol^{-1}$): Calculated; C, 51.5; H, 6.9; N, 7.1 %. Found; C, 51.7; H, 6.9; N, 7.1 %. MS (MALDI-ToF): m/z 755 $[LZnGaCl_2]^+$ (100 %).

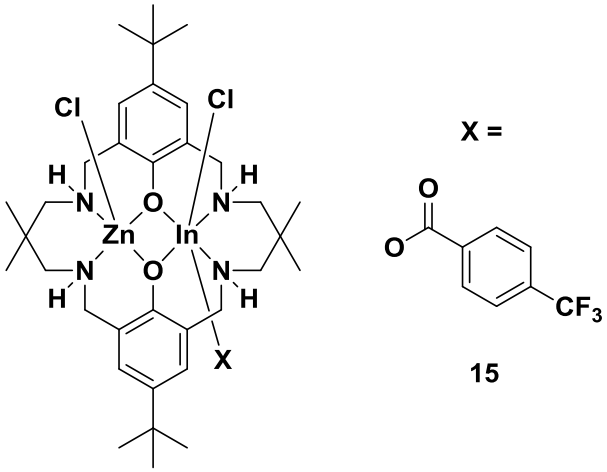
Complex 13: (0.65 g, 0.78 mmol, 86 %). ^1H NMR (d_8-THF, 400.20 MHz, 298 K) 6.99 (d, 2H, ^4J = 2.1 Hz, In-Ph**H**) 6.96 (d, 2H, ^4J = 2.0 Hz, Zn-Ph**H**) 5.15 (t, 2H, ^3J = 11.9 Hz, In-HN-C**H**$_2$-Ph) 4.98 (t, 2H, ^3J = 11.7 Hz, Zn-HN-C**H**$_2$-Ph) 3.77 (t, 2H, ^3J = 10.7 Hz, In-N**H**) 3.37 (t, 2H, ^3J = 12.0 Hz, In-HN-C**H**$_2$-C$(CH_3)_2$) 3.26 (d, 2H, ^3J = 13.0 Hz, In-HN-C**H**$_2$-Ph) 3.11 (d, 2H, ^3J = 12.3 Hz, Zn-HN-C**H**$_2$-Ph) 3.05 (t, 2H, ^3J = 12.0, Zn-HN-C**H**$_2$-C$(CH_3)_2$) 2.68 (d, 2H, ^3J = 12.0 Hz, In-HN-C**H**$_2$-C$(CH_3)_2$) 2.60 (d, 2H, ^3J = 11.4 Hz, Zn-HN-C**H**$_2$-C$(CH_3)_2$) 2.50 (t, 2H, ^3J = 11.6, Zn-N**H**) 1.31 (s, 3H, -C(C**H**$_3)_2$)) 1.25 (s, 18H, C(C**H**$_3)_3$) 1.09 (s, 3H, -C(C**H**$_3)_2$) 0.99 (s, 3H, -C(C**H**$_3)_2$) 0.95 (s, 3H, -C(C**H**$_3)_2$). $^{13}C\{^1H\}$ NMR (d_8-THF, 125.81

MHz, 298K) 159.7 (*ipso*-**Ph**) 138.8 (*p*-**Ph**) 129.4 (Zn-*m*-**Ph**) 128.4 (In-*m*-**Ph**) 126.5 (In-*o*-**Ph**) 123.8 (Zn-o-**Ph**) 63.3 (Zn-HN-**C**H_2-C(CH_3)$_2$) 61.7 (In-HN-**C**H_2-C(CH_3)$_2$) 57.0 (Zn-HN-**C**H_2-Ph) 56.1 (In-HN-**C**H_2-C(CH_3)$_2$) 35.0 (**C**(CH_3)$_2$) 34.2 (**C**(CH_3)$_2$) 34.0 (-C(**C**H_3)$_3$) 31.7 (-C(**C**H_3)$_3$) 28.9 (-C(**C**H_3)$_2$) 28.2 (-C(**C**H_3)$_2$) 21.7 (-C(**C**H_3)$_2$) 20.7 (C(**C**H_3)$_2$). Elemental Analysis for $C_{34}H_{54}Cl_3InN_4O_2Zn$ (834.16 $gmol^{-1}$): Calculated; C, 48.8; H, 6.5; N, 6.7 %. Found; C, 48.7; H, 6.6; N, 6.6 %. MS (MALDI-ToF): m/z 799 $[LZnInCl_2]^+$ (90 %).



14

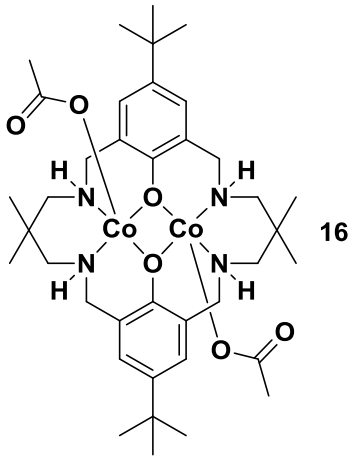
Complex 14: $K[B(C_6F_5)_4]$ (0.33 g, 0.46 mmol) was added to a solution of complex **13** (0.38 g, 0.46 mmol) in THF (5 mL) and stirred for 16 h at 25 °C. The solution was filtered and reduced in *vacuo* to dryness. The product was extracted into toluene and washed with pentane (3 x 5 mL) to afford a white solid (0.61 g, 0.41 mmol, 90 %). ^{1}H NMR (d_8-THF, 400.20 MHz, 298 K) 7.06 (s, 2H, In-Ph**H**) 7.03 (s, 2H, Zn-Ph**H**) 5.05 (t, 2H, ^{3}J = 11.9 Hz, In-HN-C**H**$_2$-Ph) 4.84 (t, 2H, ^{3}J = 11.7 Hz, Zn-HN-C**H**$_2$-Ph) 4.30 (t, 2H, ^{3}J = 10.7 Hz, In-N**H**) 3.36 (t, 2H, ^{3}J = 12.0 Hz, In-HN-C**H**$_2$-C$(CH_3)_2$) 3.28 (d, 2H, ^{3}J = 13.0 Hz, In-HN-C**H**$_2$-Ph) 3.23 (d, 2H, ^{3}J = 12.3 Hz, Zn-HN-C**H**$_2$-Ph) 2.96 (t, 2H, ^{3}J = 12.0, Zn-HN-C**H**$_2$-C$(CH_3)_2$) 2.90 (d, 2H, ^{3}J = 12.0 Hz, In-HN-C**H**$_2$-C$(CH_3)_2$) 2.75 (d, 2H, ^{3}J = 11.4 Hz, Zn-HN-C**H**$_2$-C$(CH_3)_2$) 2.69 (t, 2H, ^{3}J = 11.6, Zn-N**H**) 1.27 (s, 3H, -C(C**H**$_3)_2$)) 1.25 (s, 18H, C(C**H**$_3)_3$) 1.09 (s, 3H, -C(C**H**$_3)_2$) 1.00 (s, 3H, -C(C**H**$_3)_2$) 0.97 (s, 3H, -C(C**H**$_3)_2$). ^{11}B NMR (d8-THF, 128.39 MHz, 298 K) -16.6 (s, **B**$(ArF_5)_4$). ^{13}C{^{1}H} NMR (d_8-THF, 125.81 MHz, 298K) 158.2 (*ipso*-**Ph**) 149.2 (br. *ipso*-B**Ar**F) 147.2 (br. *p*-B**Ar**F) 139.6 (*p*-**Ph**) 137.2 (br. *m*-B**Ar**F) 135.1 (br. m-B**Ar**F) 129.1 (Zn-*m*-**Ph**) 128.3 (In-*m*-**Ph**) 125.5 (In-*o*-**Ph**) 123.1 (Zn-o-**Ph**) 63.6 (Zn-HN-**C**H$_2$-C$(CH_3)_2$) 61.3 (In-HN-**C**H$_2$-C$(CH_3)_2$) 56.0 (Zn-HN-**C**H$_2$-Ph) 55.3 (In-HN-**C**H$_2$-C$(CH_3)_2$) 34.2 (**C**$(CH_3)_2$) 33.3 (**C**$(CH_3)_3$) 30.8 (C(**C**H$_3)_3$) 27.8 (C(**C**H$_3)_2$) 27.2 (C(**C**H$_3)_2$) 20.7 (**C**$(CH_3)_2$) 19.8 (**C**$(CH_3)_2$). ^{19}F NMR (d8-THF, 470 MHz, 298 K) -132.7 (s, *o*-Ph**F**) -165.1 (t, ^{3}J = 24.4 Hz, *p*-Ph**F**) -168.5 (t, ^{3}J = 22.3 Hz, *m*-Ph**F**).



15

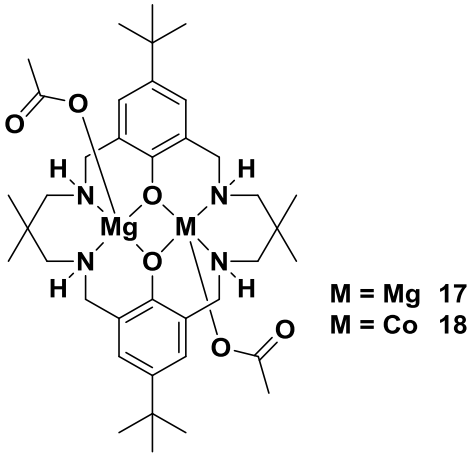
Complex 15: KOBz*p*CF_3 (0.01 g, 0.05 mmol) was added to a solution of complex **13** (0.04 g, 0.05 mmol) in THF (5 mL) and stirred for 16 h at 25 °C. The solution was filtered and reduced in *vacuo* to dryness. The product was extracted into toluene (0.5 mL) and further dried in *vacuo*. The crude product was washed with pentane (3 x 5 mL) to afford a white solid (0.05 g, 0.048 mmol, 95 %) ^{1}H NMR (d_4-MeOD, 500.20 MHz, 298 K) 7.96 (d, 2H, ^3J = 8.1 Hz, *ortho*-OBz*p*CF_3) 7.53 (d, 2H, ^3J = 8.4 Hz, *meta*-OBz*p*CF_3) 7.10 (d, 2H, ^4J = 2.5 Hz, Zn-Ph**H**) 7.07 (d, 2H, ^4J = 2.6 Hz, In-Ph**H**) 4.64 (d, 2H, ^3J =12.2 Hz, Ph-C**H**$_2$-NH) 4.25 (d, 2H, 3J = 12.2 Hz, Ph-C**H**$_2$-NH) 3.41 (d, 4H, ^3J =12.4 Hz, Ph-C**H**$_2$-NH) 3.33 (d, 2H, ^3J = 12.1 Hz, C**H**$_2$-C$(CH_3)_2$) 2.95 (d, 2H, ^3J = 12.1 Hz, C**H**$_2$-C$(CH_3)_2$) 2.78 (d, 2H, ^3J = 12.1 Hz, C**H**$_2$-C$(CH_3)_2$) 2.75 (d, 2H, ^3J = 12.1 Hz, C**H**$_2$-C$(CH_3)_2$) 1.50 (s, 3H, C(C**H**$_3)_2$) 1.43 (s, 3H, C(C**H**$_3)_2$) 1.19 (s, 18 H, C$(CH_3)_3$) 1.08 (s, 3H, C(C**H**$_3)_2$) 1.05 (s, 3H, C$(CH_3)_2$). ^{13}C{^{1}H} NMR (d_4-MeOD, 125.81 MHz, 298 K) 170.3 (**C**O_2Ph) 159.3 (ipso-O**Ph**) 139.4 (ipso-O**Bz**) 138.0 (ortho-O**Ph**) 130.0 (*ortho*-O**Bz**) 129.5 (*meta*-O**Ph**) 129.0 (*meta*-O**Bz**) 124.2 (para-O**Bz**) 124.1 (para-O**Bz**) 61.8 (**C**H$_2$-C$(CH_3)_2$) 60.3 (**C**H$_2$-C$(CH_3)_2$) 54.8 (Ph-**C**H$_2$-NH) 54.3 (Ph-**C**H$_2$-NH) 34.3 (**C**$(CH_3)_2$) 33.1 (**C**$(CH_3)_3$) 30.5 (C(**C**$H_3)_3$) 27.5 (C(**C**$H_3)_2$) 27.3 (C(**C**$H_3)_2$) 20.9 (C(**C**$H_3)_2$) 20.3 (C(**C**$H_3)_2$). ^{19}F NMR (d_4-MeOD, 376.64 MHz, 298 K): -64.4 (s, CF_3).

7.2.3 Chapter 4: Magnesium-Cobalt Heterodinuclear Catalyst



16

Complex 16: $Co(OAc)_2$ (0.32 g, 1.82 mmol) was added to a solution of H_2L (0.50 g, 0.91 mmol) in THF (10 mL) and stirred at 100 °C for 16 h. The solution was reduced in *vacuo* to dryness and the crude product was purified by several azeotropic washes with toluene (3 x 5 mL) and further washes with pentane (3 x 5 mL) to afford a pink solid (0.72 g, 0.67 mmol, 74 %). Elemental Analysis for $C_{38}H_{60}Co_2N_4O_6$ (786.32 $gmol^{-1}$): Calculated; C, 58.0; H, 7.7; N, 7.1. Found; C, 57.7; H, 7.4; N, 7.0 %. MS (MALDI-ToF): m/z 727 $[LCo_2(OAc)]^+$ (92 %). Further characterised by X-Ray Crystallography, SQUID magnetometry, Cyclic Voltammetry and X-Ray Photoelectron Spectroscopy (Appendix).

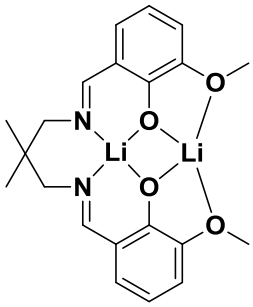


General Procedure to 17 and 18: $Mg(N(Si(CH_3)_3)_2)_2$ (0.31 g, 0.91 mmol) was added to a solution of H_2L (0.50 g, 0.91 mmol) in THF (5 mL) and stirred for 2 h. $M(OAc)_2$ (0.91 mmol) was added and the solution was stirred for a further 16 h. The solution was reduced in *vacuo* to dryness and the crude product was washed with pentane (3 x 5 mL) to afford a white (Mg) or pink (Co) solid.

Complex 17: (0.45 g, 0.62 mmol, 68 %) ^{1}H NMR (d_4-MeOD, 400.20 MHz, 298 K) 7.00 (s, 4H, Ph**H**) 4.03 (t, ^3J = 11.9 Hz, 4H, Mg-HN-C**H**$_2$-Ph) 3.21 (d, ^3J = 12.7 Hz, 4H, Mg-HN-C**H**$_2$-Ph) 2.79 (t, ^3J = 12.2 Hz, 4H, Mg-N**H**) 2.63 (d, ^3J = 9.6 Hz, 4H, Mg-HN-C**H**$_2$-C$(CH_3)_2$) 2.20 (t, ^3J = 13.5 Hz, 4H, Mg-HN-C**H**$_2$-C$(CH_3)_2$) 1.26 (s, 18 H, C(C**H**$_3)_3$) 1.24 (s, 6H, C(C**H**$_3)_2$) 1.01 (s, 6H, C(C**H**$_3)_2$). Elemental Analysis for $C_{39}H_{62}Mg_2N_4O_6$ (730.44 gmol^{-1}): Calculated; C, 64.0; H, 8.5; N, 7.7 %. Found; C, 63.6; H, 8.6; N, 7.6 %.

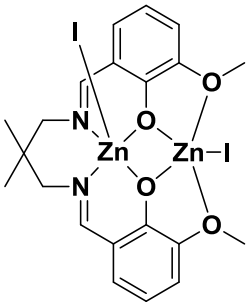
Complex 18: (0.51 g, 0.67 mmol, 74 %). Elemental Analysis for $C_{38}H_{60}CoMgN_4O_6$ (751.37 gmol^{-1}): Calculated; C, 60.7; H, 8.0; N, 7.5. Found: C, 60.5; H, 7.9; N, 7.2 %. MS (MALDI-ToF): m/z 692 $[LMgCo(OAc)]^+$ (94 %). Further characterised by X-Ray Crystallography, SQUID magnetometry, Cyclic Voltammetry and X-Ray Photoelectron Spectroscopy (Appendix).

7.2.4 Chapter 5: O-Vanillin Derived Heterodinuclear Catalysts



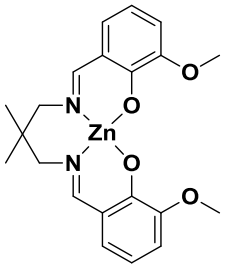
19

Complex 19: $Li(N(SiMe_3)_2)$ (0.27 g, 1.62 mmol) was added to a solution of H_2L (0.30 g, 0.81 mmol) in THF (5 mL), at 25 °C, and a colour change from yellow to colourless was observed. The solvent was reduced in *vacuo* to dryness, and the crude product was washed with pentane (3 x 5 mL) to afford a white solid (0.29 g, 0.77 mmol, 95 %). ^{1}H NMR (d_8-THF, 400.20 MHz, 298 K) 7.90 (s, 2H, **H**C=N) 6.66 (d, ^3J = 7.6 Hz, 2H, *o*-Ph**H**) 6.55 (d, ^3J = 7.3, 2H, *m*-Ph**H**) 6.18 (t, ^3J = 7.3 Hz, 2H, *p*-Ph**H**) 3.66 (s, 6H, -OC**H**$_3$) 3.16 (s, 4H, N-C**H**$_2$-) 0.66 (s, 6H, -C(C**H**$_3$)$_2$). ^{7}Li NMR (d_8-THF, 155.52 MHz, 298 K) 1.44 ppm. ^{13}C{^{1}H} NMR (d_8-THF, 125.81 MHz, 298 K) 164.5 (H**C**=N) 160.8 (ipso-Ph) 152.9 (*o*-**Ph**-OCH_3) 126.2 (*m*-**Ph**-CH=N) 122.5 (*o*-**Ph**-CH=N) 110.9 (*p*-**Ph**) 110.3 (*m*-**Ph**-OCH_3) 75.5 (N-**C**H_2-C$(CH_3)_2$) 55.4 (-O**C**H_3) 36.6 (-**C**$(CH_3)_2$) 23.0 (-C(**C**$H_3)_2$). Elemental Analysis for $C_{21}H_{24}Li_2N_2O_4$ (382.21 gmol^{-1}): Calculated; C, 66.0; H, 6.3; N, 7.3 %. Found: C, 65.9; H, 6.4; N, 7.3 %.



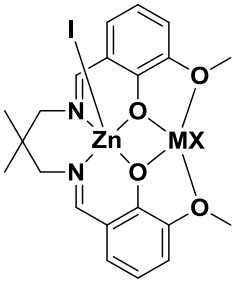
20

Complex 20: $LiN(SiMe_3)_2$ (0.23 g, 1.35 mmol) was added to a solution of H_2L (0.25 g, 0.68 mmol) in THF (5 mL). A solution of ZnI_2 (0.48 g, 2.70 mmol) was added and a pale yellow precipitate was formed. The solute was decanted and the solid was washed with THF (3 x 5 mL) then pentane (3 x 5 mL) and dried in *vacuo* to afford a pale yellow solid (0.41 g, 0.54 mmol, 80 %). ^{1}H NMR (d_8-THF, 400.20 MHz, 298 K) 7.97 (s, 2H, **H**C=N) 6.76 (d, ^3J = 7.8 Hz, ^4J = 1.5 Hz, 2H, *o*-Ph**H**) 6.67 (d, ^3J = 7.83, ^{4}J = 1.2 Hz, 2H, *m*-Ph**H**) 6.30 (t, ^3J = 8.1 Hz, 2H, *p*-Ph**H**) 4.63 (br. m, 2H, -C**H**$_2$) 3.89 (s, 6H, -OC**H**$_3$) 2.95 (br. m, 2H, -C**H**$_2$) 1.03 (s, 3H, -C**H**$_3$) 0.67 (br. s, 3H, -C**H**$_3$). ^{13}C{^{1}H} NMR (d_8-THF, 125.81 MHz, 298 K) 168.2 (H**C**=N) 160.7 (*ipso*-**Ph**) 151.7 (*o*-**Ph**-OCH_3) 126.8 (*m*-**Ph**-CH=N) 118.7 (*o*-**Ph**-CH=N) 112.1 (*p*-**Ph**) 111.9 (*m*-**Ph**-OCH_3) 73.9 (N-**C**H_2-$C(CH_3)_2$) 55.4 (-O**C**H_3) 36.5 (-**C**$(CH_3)_2$) 26.2 (-C(**C**$H_3)_2$). Elemental Analysis for $C_{21}H_{24}I_2N_2O_4Zn_2$ (749.84 gmol^{-1}): Calculated; C, 33.5; H, 3.2; N, 3.7 %. Found: C, 33.3; H, 3.3; N, 3.6 %.



22

Complex 22: $ZnEt_2$ (0.17 g, 1.35 mmol) was added dropwise to a solution of H_2L (0.5 g, 1.35 mmol) in THF (10 mL) and stirred at 25 °C for 16 h and a pale yellow precipitate had formed. The solution was filtered and the solid washed with pentane (3 x 5 mL) and dried *in vacuo* to afford a pale yellow solid (0.44 g, 1.01 mmol, 75 %). ^{1}H NMR (400.20 MHz, $CDCl_3$, 298 K) 7.87 (s, 2H, ***H**C=N*), 6.80 (dd, ^3J = 7.4 Hz, ^4J = 1.6 Hz, 2H, *Ph**H***) 6.67 (dd, ^3J = 8.0 Hz, ^4J = 1.4 Hz, 2H, *Ph**H***), 6.45 (t, ^3J = 7.7, 2H, *Ph**H***), 3.75 (s, 6H, -*OC**H**$_3$*), 3.41 (Br., 4H, N-C**H**$_2$-C$(CH_3)_2$) 0.88 (s, 6H, -C(C**H**$_3)_2$). ^{13}C{^{1}H} NMR (125.81 MHz, $CDCl_3$, 298 K) 168.8 (*H**C**=N*) 161.5 (*ipso*-**Ph**) 152.7 (*o*-**Ph**) 127.1 (o-**Ph**) 120.4 (m-**Ph**) 117.4 (m-**Ph**) 113.7 (p-**Ph**) 73.4 (N**C**H$_2$C$(CH_3)_2$) 57.2 (-O**C**H$_3$) 36.4 (NCH$_2$**C**$(CH_3)_2$). Elemental Analysis for $C_{21}H_{24}N_2O_4Zn$ (432.10 gmol^{-1}): Calculated; C, 58.1; H, 5.6; N, 6.5 %. Found; C, 57.9; H, 5.7; N, 6.4 %.



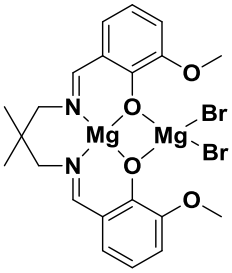
MX = NaI 23
MX = CaI_2 24
MX = CdI_2 25

General Synthesis 23-25: $ZnEt_2$ (0.07 g, 0.54 mmol) was added dropwise to a solution of H_2L (0.30 g, 0.54 mmol) in THF (5 mL) and stirred at 25 ˚C for 4 h. MX_n (0.54 mmol) in THF (2 mL) was added and stirred for a further 4 h. The solvent was reduced to dryness to afford a pale yellow solid.

Complex 23: (0.26 g, 0.45 mmol, 83 %) ^{1}H NMR (400.20 MHz, d_8-THF, 298 K) 8.00 (s, 2H, ***HC=N***) 6.74 (dd, 2H, ^{3}J = 7.61 Hz, ^{4}J = 1.6 Hz, Ph**H**) 6.66 (dd, 2H, ^{3}J = 8.0 Hz, ^{4}J = 1.5 Hz, Ph**H**) 6.28 (t, 2H, ^{3}J = 7.8 Hz, Ph**H**) 3.81 (s, 6H, -OC**H**$_3$) 0.94 (s, 6H, -C(C**H**$_3$)$_2$). Methylene protons not observed. ^{13}C{^{1}H} NMR (125.81 MHz, d_8-THF, 298 K) 169.2 (H**C**=N) 162.3 (ipso-**Ph**) 152.1 (o-**Ph**$_{Na}$) 127.5 (o-**Ph**$_{Zn}$) 118.8 (m-**Ph**$_{Zn}$) 112.2 (m-**Ph**$_{Na}$) 111.2 (p-**Ph**) 75.1 (N**C**H$_2$C(CH$_3$)$_2$) 55.4 (-O**C**H$_3$) 35.3 (NCH$_2$**C**(CH$_3$)$_2$). Methyl signal not observed. Elemental Analysis for $C_{21}H_{24}IN_2NaO_4Zn$ (583.46 gmol^{-1}): Calculated; C, 43.2; H, 4.4; N, 4.8 %. Found; C, 43.1; H, 4.5; N, 4.8 %.

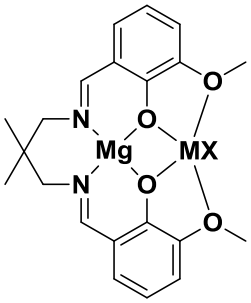
Complex 24: (0.73 g, 1.01 mmol, 75 %). ^{1}H NMR (400.20 MHz, d_8-THF, 298 K) 8.05 (s, 2H, ***HC=N***) 6.97 (dd, 2H, ^{3}J = 7.9 Hz, ^{4}J = 1.2 Hz, Ph**H**) 6.75 (dd, 2H, ^{3}J = 7.9 Hz, ^{4}J = 1.3 Hz, Ph**H**) 6.47 (t, 2H, ^{3}J = 7.8 Hz, Ph**H**) 4.34 (br. s, 3H, C**H**$_2$-C(CH$_3$)$_2$) 4.26 (s, 6H, -OC**H**$_3$) 3.14 (br. s, 2H, C**H**$_2$-C(CH$_3$)$_2$) 1.06 (s, 6H, -C(C**H**$_3$)$_2$). ^{13}C{^{1}H} NMR (125.81 MHz, d_8-THF, 298 K) 170.2 (H**C**=N) 158.2 (ipso-**Ph**) 151.5 (o-**Ph**$_{ca}$) 128.5 (o-**Ph**$_{Zn}$) 119.0 (m-**Ph**$_{ca}$) 114.7 (m-**Ph**$_{zn}$) 114.5 (p-**Ph**) 74.8 (N**C**H$_2$C(CH$_3$)$_2$) 60.3 (-O**C**H$_3$) 35.1 (NCH$_2$**C**(CH$_3$)$_2$). Elemental Analysis for $C_{21}H_{24}CaI_2N_2O_4Zn$ (725.87 gmol^{-1}): Calculated; C, 34.6; H, 3.3; N, 3.8 %. Found; C, 34.2; H, 3.1; N, 4.1 %.

Complex 25: (0.54 g, 0.68 mmol, 84 %). ^{1}H NMR (400.20 MHz, $CDCl_3$, 298 K) 8.05 (Br. s, 2H, **H**C=N) 6.82 (d, 2H, ^{3}J = 7.5 Hz, Ar**H**) 6.71 (d, 2H, ^{3}J = 7.5 Hz, Ar**H**) 6.61 (t, 2H, ^{3}J = 7.5 Hz, Ar**H**) 3.84 (s, 6H, -OC**H**$_3$) 3.66 (Br. s, 4H, NC**H**$_2$C(CH$_3$)$_2$) 1.04 (NCH$_2$C(C**H**$_3$)$_2$). ^{13}C{^{1}H} NMR (125.81 MHz, $CDCl_3$, 298 K): 171.6 (H**C**=N) 157.1 (ipso-**Ph**) 148.9 (o-**Ph**$_{Cd}$) 126.6 (o-**Ph**$_{Zn}$) 117.2 (m-**Ph**$_{Cd}$) 115.7 (m-**Ph**$_{Zn}$) 114.2 (p-**Ph**) 74.9 (N**C**H$_2$C(CH$_3$)$_2$) 54.3 (-O**C**H$_3$) 35.0 (NCH$_2$**C**(CH$_3$)$_2$) 24.6 (NCH$_2$C(**C**H$_3$)$_2$). Elemental analysis for $C_{21}H_{24}CdI_2N_2O_4Zn$ (800.03 gmol^{-1}): Calculated; C, 31.5; H, 3.0; N, 3.5 % Found; C, 31.2; H, 3.3; N, 3.2 %.



26

Complex 26: $Mg(N(Si(CH_3)_3)_2)_2$ (0.19 g, 0.54 mmol) was added to a solution of H_2L (0.30 g, 0.54 mmol) in THF (5 mL) and stirred for 2 h. $MgBr_2$ (0.10 g, 54 mmol) was added and the solution was stirred for a further 16 h. The solution was reduced in *vacuo* to dryness and the crude product was washed with pentane (3 x 5 mL) to afford a white solid (0.70 g, 1.22 mmol, 90 %). ^{1}H NMR (d_8-THF, 400.20 MHz, 298 K) 8.22 (s, 2H, **H**C=N) 6.98 (d, 2H, ^3J = 7.4 Hz, ortho-Ph**H**) 6.87 (d, 2H, ^3J = 7.4 Hz, meta-Ph**H**) 6.62 (t, 2H, ^3J = 7.7 Hz, para-Ph**H**) 4.07 (s, 6H, -OC**H**$_3$) 3.79 (br. s, 4H, -C**H**$_2$) 0.98 (s, 6H, -C**H**$_3$). ^{13}C{^{1}H} NMR (d_8-THF, 125.81 MHz, 298 K) 170.4 (H**C**=N) 154.9 (*ipso*-**Ph**) 150.8 (*o*-**Ph**-OCH_3) 127.2 (*m*-**Ph**-CH=N) 120.2 (*o*-**Ph**-CH=N) 115.8 (*p*-**Ph**) 113.8 (*m*-**Ph**-OCH_3) 74.5 (N-**C**H_2-$C(CH_3)_2$) 56.2 (-O**C**H_3) 35.8 (-**C**$(CH_3)_2$) 26.2 (-C(**C**$H_3)_2$). Elemental Analysis for $C_{21}H_{24}Br_2Mg_2N_2O_4$ (573.98 gmol^{-1}): Calculated; C, 43.7; H, 4.2; N, 4.9 %. Found: C, 43.8; H, 4.3; N, 4.7 %.



MX = NaI 29
MX = CaI_2 30
MX = CdI_2 31

General Procedure to 29-31: $Mg(N(Si(CH_3)_3)_2)_2$ (0.19 g, 0.54 mmol) was added to a solution of H_2L (0.30 g, 0.54 mmol) in THF (5 mL) and stirred for 2 h. MI_n (0.54 mmol) was added and the solution was stirred for a further 16 h. The solution was reduced in *vacuo* to dryness and the crude product was washed with pentane (3 x 5 mL) to afford a white solid.

Complex 29: (0.26 g, 0.45 mmol, 83 %) ^{1}H NMR (400.20 MHz, d_8-THF, 298 K) 8.18 (s, 2H, ***H**C=N*) 6.78 (dd, 2H, ^3J = 7.6 Hz, ^4J = 1.6 Hz, Ph**H**) 6.72 (dd, 2H, ^3J = 8.0 Hz, ^4J = 1.5 Hz, Ph**H**) 6.35 (t, 2H, ^3J = 7.8 Hz, Ph**H**) 3.97 (s, 6H, -OC**H**$_3$) 1.03 (s, 6H, -C(C**H**$_3$)$_2$). Methylene protons not observed. ^{13}C{^{1}H} NMR (125.81 MHz, d_8-THF, 298 K) 169.2 (H**C**=N) 162.3 (*ipso*-**Ph**) 152.1 (*ortho*-**Ph**) 127.5 (*ortho*-**Ph**) 118.8 (*meta*-**Ph**) 112.2 (*meta*-**Ph**) 111.2 (*para*-**Ph**) 75.1 (N**C**H$_2$C(CH$_3$)$_2$) 55.4 (-O**C**H$_3$) 35.3 (NCH$_2$**C**(CH$_3$)$_2$). Methyl signal not observed. Elemental Analysis for $C_{21}H_{24}IN_2NaO_4Zn$ (583.46 gmol^{-1}): Calculated; C, 46.5; H, 4.5; N, 5.2 % Found; C, 46.2; H, 4.6; N, 5.1 %.

Complex 30: (0.22 g, 0.39 mmol, 72 %) ^{1}H NMR (400.20 MHz, d_8-THF, 298 K) 8.24 (s, 2H, ***H**C=N*) 7.11 (d, 2H, ^3J = 8.4 Hz, Ph**H**) 6.94 (d, 2H, ^3J = 8.0 Hz, Ph**H**) 6.62 (t, 2H, ^3J = 8.4 Hz, Ph**H**) 4.35 (s, 6H, -OC**H**$_3$) 3.83 (br. 4H, -C**H**$_2$C(CH$_3$)$_2$) 0.95 (s, 6H, -C(C**H**$_3$)$_2$). ^{13}C{^{1}H} NMR (125.81 MHz, d_8-THF, 298 K) 169.8 (H**C**=N) 155.6 (*ipso*-**Ph**) 150.6 (*ortho*-**Ph**) 127.7 (*ortho*-**Ph**) 119.8 (*meta*-**Ph**) 114.4 (*meta*-**Ph**) 114.0 (*para*-**Ph**) 74.1

(N**C**$H_2C(CH_3)_2$) 59.0 (-O**C**H_3) 34.8 (NCH_2**C**$(CH_3)_2$). Elemental Analysis for $C_{21}H_{24}CaI_2MgN_2O_4$ (685.93 $gmol^{-1}$): Calculated; C, 36.7; H, 3.5; N, 4.1 % Found; C, 37.3; H, 3.3; N, 4.3 %.

Complex 31: (0.27 g, 0.35 mmol, 65 %) ^{1}H NMR (400.20 MHz, $CDCl_3$, 298 K) 7.99 (br., 2H, ***HC***=*N*) 6.76 (d, 2H, ^3J = 7.4 Hz, Ph**H**) 6.65 (d, 2H, ^3J = 7.8 Hz, Ph**H**) 6.54 (t, 2H, ^3J = 7.8 Hz, Ph**H**) 3.78 (s, 6H, -OC**H**$_3$) 3.60 (br. 4H, -C**H**$_2C(CH_3)_2$) 0.97 (s, 6H, -C(C**H**$_3)_2$). ^{13}C{^{1}H} NMR (125.81 MHz, d_8-THF, 298 K) 171.6 (H**C**=N) 157.1 (*ipso*-**Ph**) 148.9 (*o*-**Ph**) 126.6 (*o*-**Ph**) 117.2 (*m*-**Ph**) 115.7 (*m*-**Ph**) 114.2 (*p*-**Ph**) 74.9 (N**C**$H_2C(CH_3)_2$) 54.3 (-O**C**H_3) 25.7 (NCH_2**C**$(CH_3)_2$). Elemental Analysis for $C_{21}H_{24}CdI_2MgN_2O_4$ (759.87 $gmol^{-1}$): Calculated; C, 33.2; H, 3.2; N, 3.7 %. Found; C, 32.8; H, 3.4; N, 4.1 %.

Chapter 8:

Appendices

Table of Contents

8.1.1 Chapter 2: Group 1 and 2, zinc(II) heterodinuclear complexes

Figure S1: ^{1}H NMR spectrum of **1** (d_8-THF, 298 K). 262
Figure S2: 2D HSQC NMR spectrum of **1** (d_8-THF, 298 K). 262
Figure S3: 2D COSY NMR spectrum of **1** (d_8-THF, 298 K). 263
Figure S4: ^{13}C{^{1}H} NMR spectrum of **1** (d_8-THF, 298 K). 263
Figure S5: ^{7}Li NMR spectrum of **1** (d_8-THF, 298 K). 264
Figure S6: ^{1}H NMR spectrum of **2** (d_8-THF, 298 K). 264
Figure S7: 2D HSQC NMR spectrum of **2** (d_8-THF, 298 K). 265
Figure S8: 2D COSY NMR spectrum of **2** (d_8-THF, 298 K). 265
Figure S9: ^{13}C{^{1}H} NMR spectrum of **2** (d_8-THF, 298 K). 266
Figure S10: ^{1}H NMR spectrum of **3** (d_8-THF, 298 K). 266
Figure S11: 2D HSQC NMR spectrum of **3** (d_8-THF, 298 K). 267
Figure S12: 2D COSY NMR spectrum of **3** (d_8-THF, 298 K). 267
Figure S13: ^{13}C{^{1}H} NMR spectrum of **3** (d_8-THF, 298 K). 268
Figure S14: ORTEP representation of the molecular structure of **1** 269
Figure S15: ORTEP representation of the molecular structure of **2** 270
Figure S16: 2D DOSY of **1** (d_8-THF, 298 K) 271
Figure S17: 2D DOSY of **2** (d_8-THF, 298 K) 271
Figure S18: 2D DOSY of **3** (d_8-THF, 298 K) 271
Figure S19: ^{1}H NMR spectrum of **4a** (d_8-THF, 298 K). 272
Figure S20: ^{1}H NMR spectrum of **4a** (d_2-TCE, 403 K). 272
Figure S21: ^{13}C{^{1}H} NMR spectrum of **4a** (d_2-TCE, 403 K). 273
Figure S22: ^{1}H NMR spectrum of **4b** (d_8-THF, 298 K). 273
Figure S23: ^{1}H NMR spectrum of **4b** (d_2-TCE, 403 K). 274
Figure S24: ^{13}C{^{1}H} NMR spectrum of **4b** (d_2-TCE, 403 K). 274
Figure S25: ^{19}F NMR spectrum of **4b** (d_2-TCE, 403 K). 275
Figure S26: 2D DOSY NMR of complex **4a** (d_8-THF, 298 K). 275
Figure S27: 2D DOSY NMR of complex **4b** (d_8-THF, 298 K) 276
Figure S28: MALDI-ToF mass spectrum of **4a**. 276
Figure S29: MALDI-ToF mass spectrum of **4b**. 277
Figure S30: ORTEP representation of the molecular structure of **4a** 278
Figure S31: ORTEP representation of the molecular structure of **4b** 279
Figure S32: Metal redistribution reaction between **1** and **4a** (d_8-THF). 280
Figure S33: Metal redistribution reaction between **3** and **4a** (d_8-THF). 280
Figure S34: COSY NMR of product formed from metal redistribution reaction between **1** and **4a** (d_8-THF). 281
Figure S35: Metal redistribution reaction between **2** and **4a.** (d_8-THF). 281
Figure S36: ^{1}H NMR of complex **5a** prepared through sequential metalation (d_8-THF, 298 K). 282

Figure S37: ^{1}H NMR of complex **7a** prepared through sequential metalation. (d_8-THF, 298 K). 282
Figure S38: ^{1}H NMR spectrum of **5a** (d_5-pyridine, 403 K). 283
Figure S39: COSY NMR of complex **5a** (d_5-pyridine, 403 K). 283
Figure S40: ^{1}H NMR spectrum of complex **6** (d_8-THF, 298 K). 284
Figure S41: COSY NMR of complex **6** (d_8-THF, 298 K). 284
Figure S42: Metal redistribution of complex **6** towards complexes **2** and **4a** as observed by ^{1}H NMR (d_8-THF, 298 K). 285
Figure S43: ^{1}H NMR spectrum of complex **5b** (d_8-dioxane, 403 K). 285
Figure S44: COSY NMR of complex **5b** (d_8-dioxane, 403 K). 286
Figure S45: ^{1}H NMR spectrum of complex **7b** (d_8-THF, 298 K). 287
Figure S46: HSQC NMR of complex **7b** (d_8-THF, 298 K). 287
Figure S47: COSY NMR of complex **7b** (d_8-THF, 298K). 288
Figure S48: ^{13}C{^{1}H} NMR spectrum of complex **7b** (d_8-THF, 298 K). 288
Figure S49: ^{19}F NMR spectrum of complex **7b** (d_8-THF, 298 K). 289
Figure S50: 2D DOSY NMR of complex **7b** (d_8-THF, 298 K). 289
Figure S51: MALDI-ToF mass spectrum of complex **5a** 290
Figure 52: MALDI-ToF mass spectrum of complex **5b.** 290
Figure S53: MALDI-ToF mass spectrum of complex **7a.** 291
Figure S54: MALDI-ToF mass spectrum of complex **7b**. 291
Figure S55: ORTEP representation of the molecular structure of **5b**. 292
Figure S56: ^{1}H NMR spectrum of **8a** (d_8-THF, 298 K) 293
Figure S57: 2D COSY NMR of **8a** (d_8-THF, 298 K). 293
Figure S58: HSQC NMR of complex **8a** (d_8-THF, 298 K). 294
Figure S59: ^{13}C{^{1}H} NMR spectrum of **8a** (d_8-THF, 298 K) 294
Figure S60: ^{1}H NMR spectrum of **9a** (d_8-THF, 298 K). 295
Figure S61: 2D HSQC NMR of **9a** (d_8-THF, 298 K) 295
Figure S62: 2D COSY NMR of **9a** (d_8-THF, 298 K). 296
Figure S63: ^{13}C{^{1}H} NMR spectrum of complex **9a** (d_8-THF, 298 K). 296
Figure S64: 2D DOSY NMR of **8a** (d_8-THF, 298 K) 297
Figure S65: 2D DOSY NMR of **9a** (d_8-THF, 298 K) 297
Figure S66: MALDI-ToF of complex **8a**. 298
Figure S67: MALDI-ToF mass spectrum of **9a.** 298
Figure S68: ORTEP representation of the molecular structure of **8a**. 299
Figure S69: ORTEP representation of the molecular structure of **9a** 300

8.1.2 Chapter 3: Group 13-zinc(II) heterodinuclear complexes

Figure S70: ^{1}H NMR spectrum of **10** (d_2 –TCE, 403 K) 301
Figure S71: ^{13}C{^{1}H} NMR spectrum of **10** (d_2 – TCE, 403 K) 301
Figure S72: MALDI – ToF mass spectrum of **10** 302

Figure S73: ORTEP representation of the molecular structure of **10** 303
Figure S74: ^{1}H NMR spectrum of **11** (d_3 – MeCN, 298 K) 304
Figure S75: 2D HSQC NMR of **11** (d_8 – THF, 298 K) 304
Figure S76: 2D COSY NMR of **11** (d_8 – THF, 298 K) 305
Figure S77: ^{13}C{^{1}H} NMR spectrum of **11** (d_3 – MeCN, 298 K) 305
Figure S78: MALDI – ToF mass spectrum of **11** 306
Figure S79: 2D DOSY NMR of **11** (d_3-MeCN, 298 K) 306
Figure S80: ORTEP representation of the molecular structure of **11** 307
Figure S81: ^{1}H NMR spectrum of **12** (d_3 – MeCN, 298 K) 308
Figure S82: 2D HSQC NMR of **12** (d_3 – MeCN, 298 K) 308
Figure S83: 2D COSY NMR of **12** (d_3 – MeCN, 298 K) 309
Figure S84: ^{13}C{^{1}H} NMR spectrum of **12** (d_3 – MeCN, 298 K) 309
Figure S85: 2D DOSY NMR of **12** (d_3 – MeCN, 298 K) 310
Figure S86: MALDI – ToF mass spectrum of **12** 310
Figure S87: ORTEP representation of the molecular structure of **12** 311
Figure S88: ^{1}H NMR spectrum of **13** (d_8 –THF, 298 K) 312
Figure S89: 2D HSQC NMR of **13** (d_8 –THF, 298 K) 312
Figure S90: 2D COSY NMR of **13** (d_8 – THF, 298 K) 313
Figure S91: ^{13}C{^{1}H} NMR spectrum of **13** (d_8 –THF, 298 K) 313
Figure S92: 2D DOSY NMR of **13** (d_8 –THF, 298 K) 314
Figure S93: MALDI – ToF mass spectrum of **13** 314
Figure S94: ORTEP representation of the molecular structure of **13** 315
Figure S95: ^{1}H NMR spectrum of **14** (d_8-THF, 298 K) 316
Figure 96: HSQC NMR of **14** (d_8-THF, 298 K) 316
Figure S97: ^{11}B NMR spectrum of **14** (d8-THF, 298 K) 317
Figure 98: ^{13}C{^{1}H} NMR spectrum of **14** (d_8-THF, 298 K) 317
Figure S99: ^{19}F NMR spectrum of **14** (d8-THF, 298 K) 318
Figure S100: ^{1}H NMR spectrum of **15** (d_4-MeOD, 298 K) 318
Figure S101: HSQC NMR of **15** (d_4-MeOD, 298 K) 319
Figure S102: ^{13}C{^{1}H} NMR spectrum of **15** (d4-MeOD, 298 K) 319
Figure S103: 2D DOSY NMR of **15** (d_4-MeOD, 298 K) 320
Figure S104: ORTEP representation of the molecular structure of **15** 321

8.1.3 Chapter 4: MgCo Heterodinuclear Catalyst

Figure S105: ^{1}H NMR spectra of mono-zinc (chapter 2 and 3) and mono-magnesium species (chapter 4) used as intermediates for heterodinuclear synthesis 322
Figure S106: ^{1}H NMR spectrum of complex **17** (d_4-MeOH, 298 K) 323

8.1.4 Chapter 5: O-Vanillin Dervied Heterodinuclear Catalysts

Figure S107: ^{1}H NMR spectrum of **19** (d_8-THF, 298 K) 326
Figure S108: ^{7}Li NMR spectrum of **19** (d_8-THF, 298 K) 326
Figure S109: ^{13}C{^{1}H} NMR spectrum of **19** (d_8-THF, 298 K) 327
Figure S110: DOSY NMR of **19** in (d_8-THF, 298 K) 327
Figure S111: ORTEP representation of the molecular structure of **19** 328
Figure S112: ^{1}H NMR spectrum of **20** (d_8-THF, 298 K) 329
Figure S113: ^{13}C{^{1}H} NMR spectrum of **20** in (d_8-THF, 298 K) 329
Figure S114: 2D DOSY NMR of complex **20** (d_8-THF, 298 K) 330
Figure 119: ORTEP representation of the molecular structure of **20** 331
Figure 120: ORTEP representation of the molecular structure of **21** 332
Figure S121: ^{1}H NMR spectrum of **22** ($CDCl_3$, 298 K) 333
Figure S122: ^{13}C NMR spectrum of **22** ($CDCl_3$, 298 K) 333
Figure S123: 2D DOSY NMR of **22** ($CDCl_3$, 298 K) 334
Figure S124: ORTEP representation of the molecular structure of **22** 335
Figure S125: ^{1}H NMR spectrum of **23** (d_8-THF, 298 K) 336
Figure S126: ^{13}C NMR spectrum of **23** (d_8-THF, 298 K) 336
Figure S127: 2D DOSY of **23** (d_8-THF, 298 K) 337
Figure S128: ORTEP representation of the molecular structure of **23** 338
Figure S129: ^{1}H NMR spectrum of **24** (d_8-THF, 298 K) 339
Figure S130: ^{13}C{^{1}H} NMR spectrum of **24** (d_8-THF, 298 K) 339
Figure S131: ORTEP representation of the molecular structure of **24** 340
Figure 132: ^{1}H NMR spectrum of **25** (d_8-THF, 298 K) 341
Figure S133: ^{13}C{^{1}H} NMR spectrum of **25** ($CDCl_3$, 298 K) 341
Figure S134: 2D DOSY NMR of **25** (d_8-THF, 298 K) 342
Figure S135: ORTEP representation of the molecular structure of **25** 343
Figure S136: ^{1}H NMR spectrum of **26** (d_8-THF, 298 K) 344
Figure S137: ^{13}C{^{1}H} NMR spectrum of **26** (d_8-THF, 298 K) 344
Figure S138: 2D DOSY NMR of **26** (d_8-THF, 298 K) 345
Figure S139: ORTEP representation of the molecular structure of **26** 346
Figure S140: ORTEP representation of the molecular structure of **27** 347
Figure S141: ORETEP representation of the molecular structure of **28** 348
Figure S142: ^{1}H NMR spectrum of **28** (d_8-THF, 298 K) 349
Figure S143: 2D DOSY NMR of **28** (d_8-THF, 298 K) 349
Figure S144: ^{1}H NMR spectrum of **29** (d_8-THF, 298 K) 350
Figure S145: ^{13}C{^{1}H} NMR spectrum of **29** (d_8-THF, 298 K) 350
Figure S146: ORTEP representation of the molecular structure of **29** 351
Figure S147: ^{1}H NMR spectrum of **30** ($CDCl_3$, 298 K) 352
Figure S148: ORTEP representation of the molecular structure of **31** 353
Figure S151**:** Representative example of ^{1}H NMR spectrum of a typical CO_2-CHO ring opening copolymerisation forming both poly(cyclohexene oxide) and *trans*-cyclic carbonate ($CDCl_3$, 298 K). 354

Figure S152**:** Representative example of ^{1}H NMR spectrum of a typical CO_2-CHO reaction forming the *cis*-cyclic carbonate ($CDCl_3$, 298 K). 354

8.1.1 Chapter 2: Group 1 and 2, Zinc (II) Heterodinuclear Catalysts

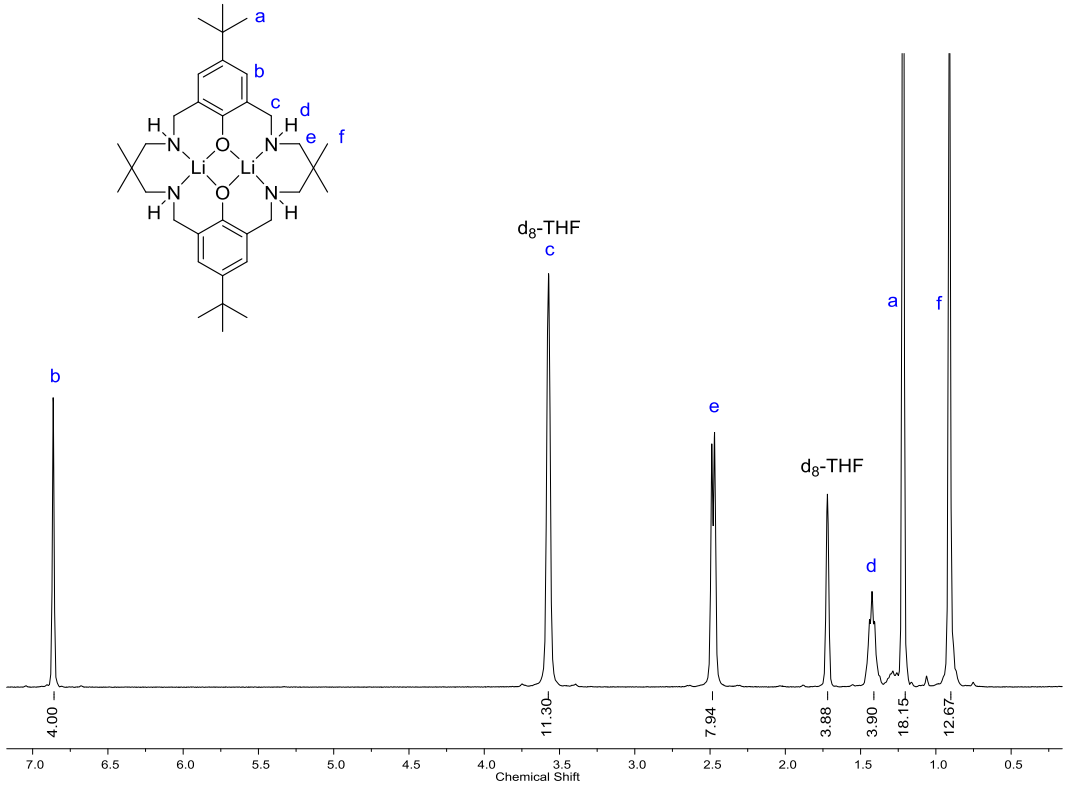


Figure S1: ^{1}H NMR of **1** (d_8-THF, 298 K).

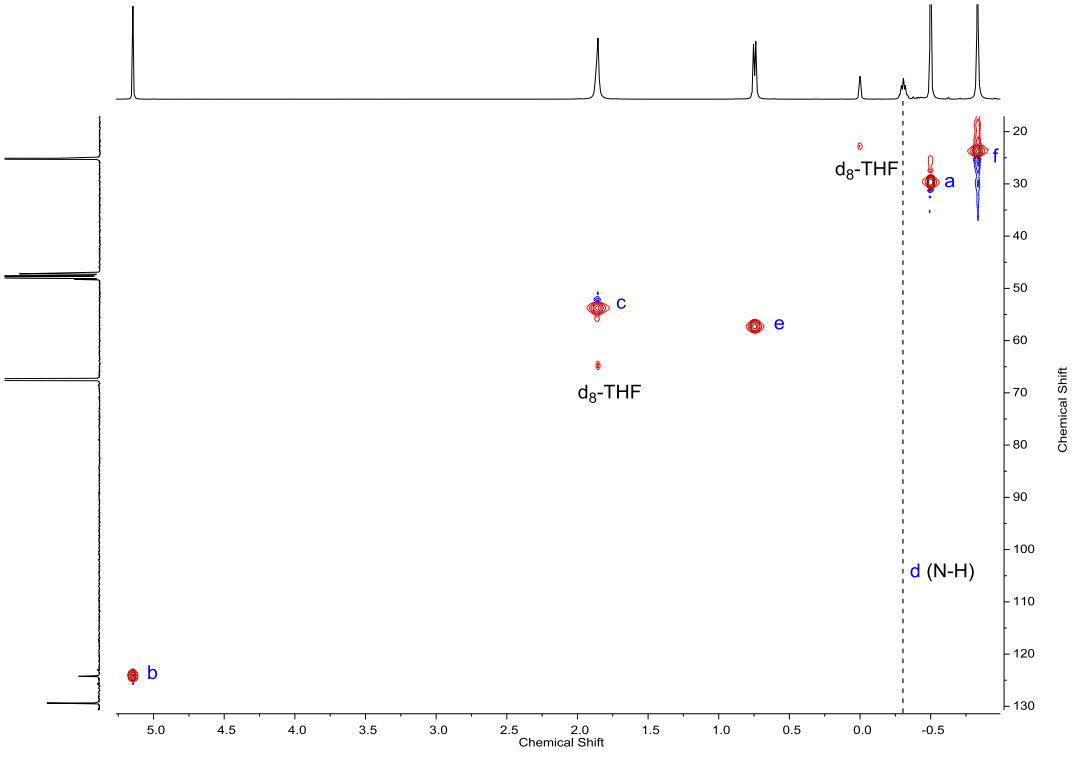


Figure S2: 2D HSQC NMR of **1** (d_8-THF, 298 K).

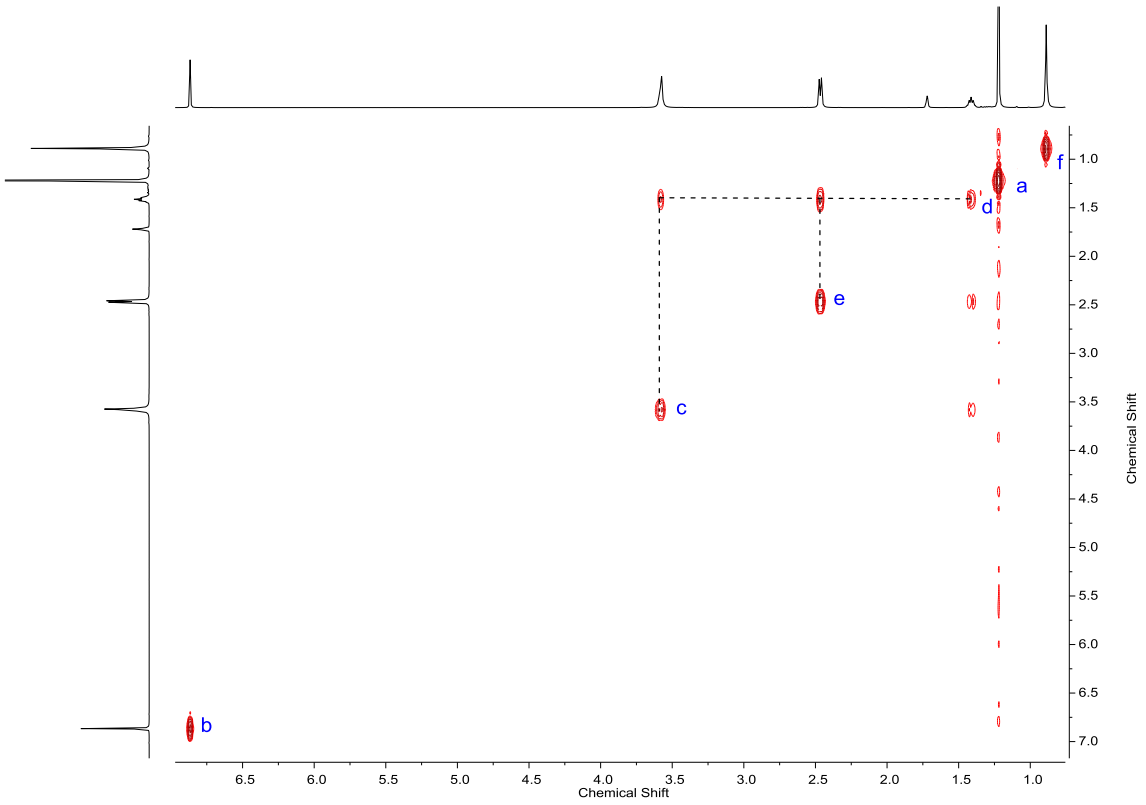


Figure S3: 2D COSY NMR of **1** (d_8-THF, 298 K).

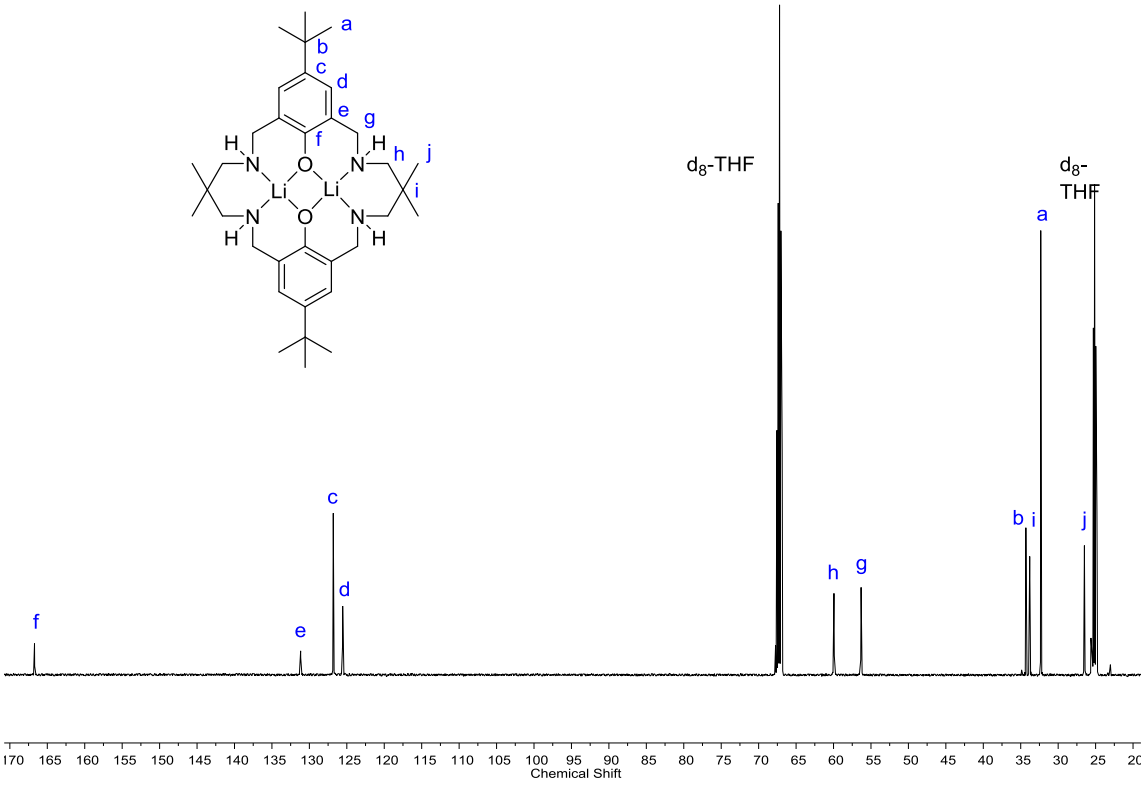


Figure S4: ^{13}C NMR of **1** (d_8-THF, 298 K).

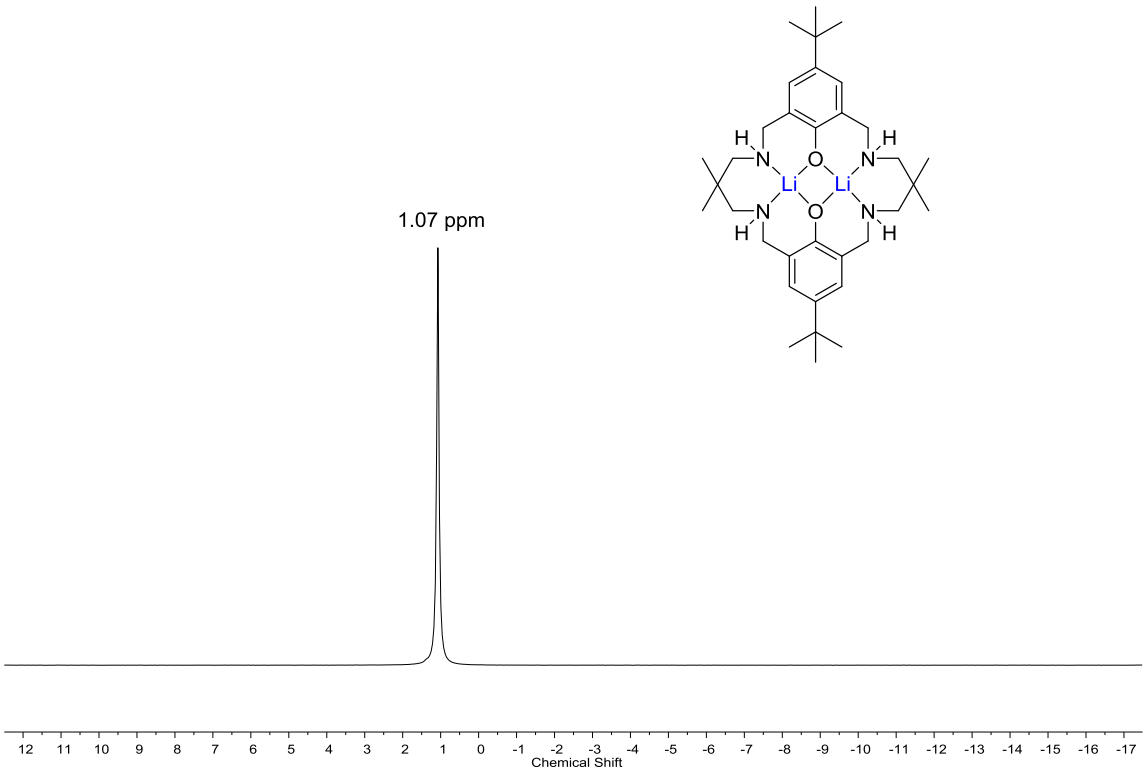


Figure S5: ^{7}Li NMR of **1** (d_8-THF, 298 K).

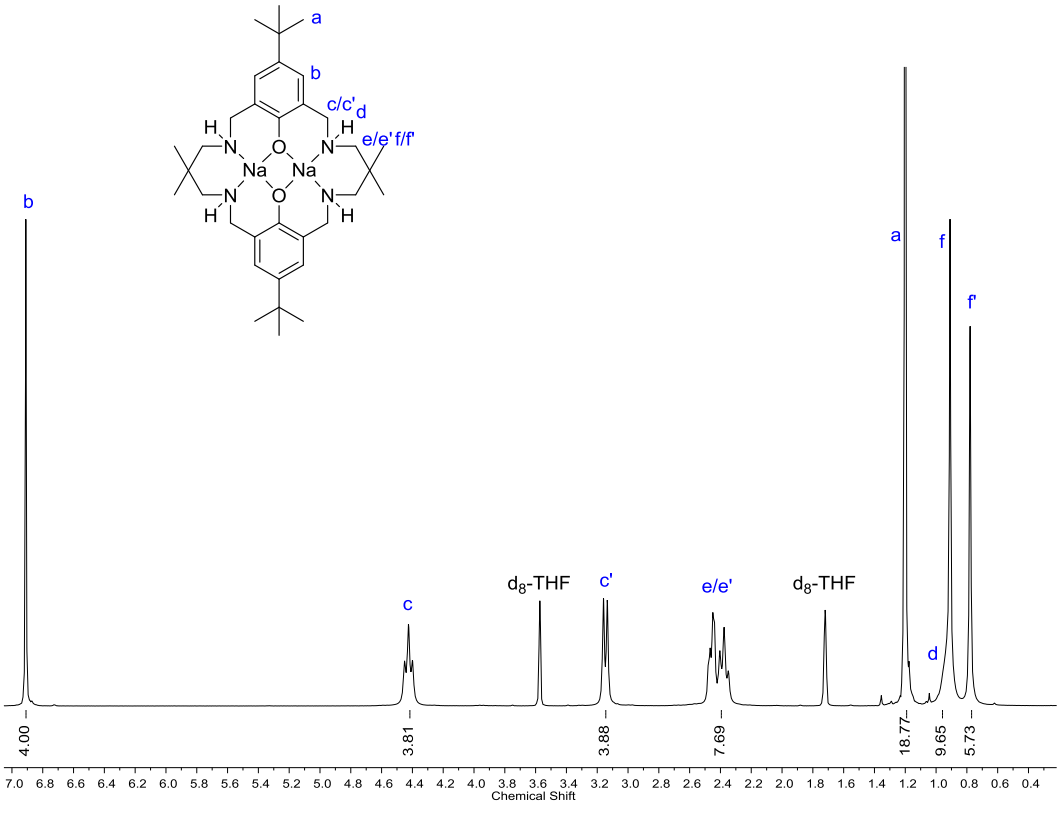


Figure S6: ^{1}H NMR of **2** (d_8-THF, 298 K).

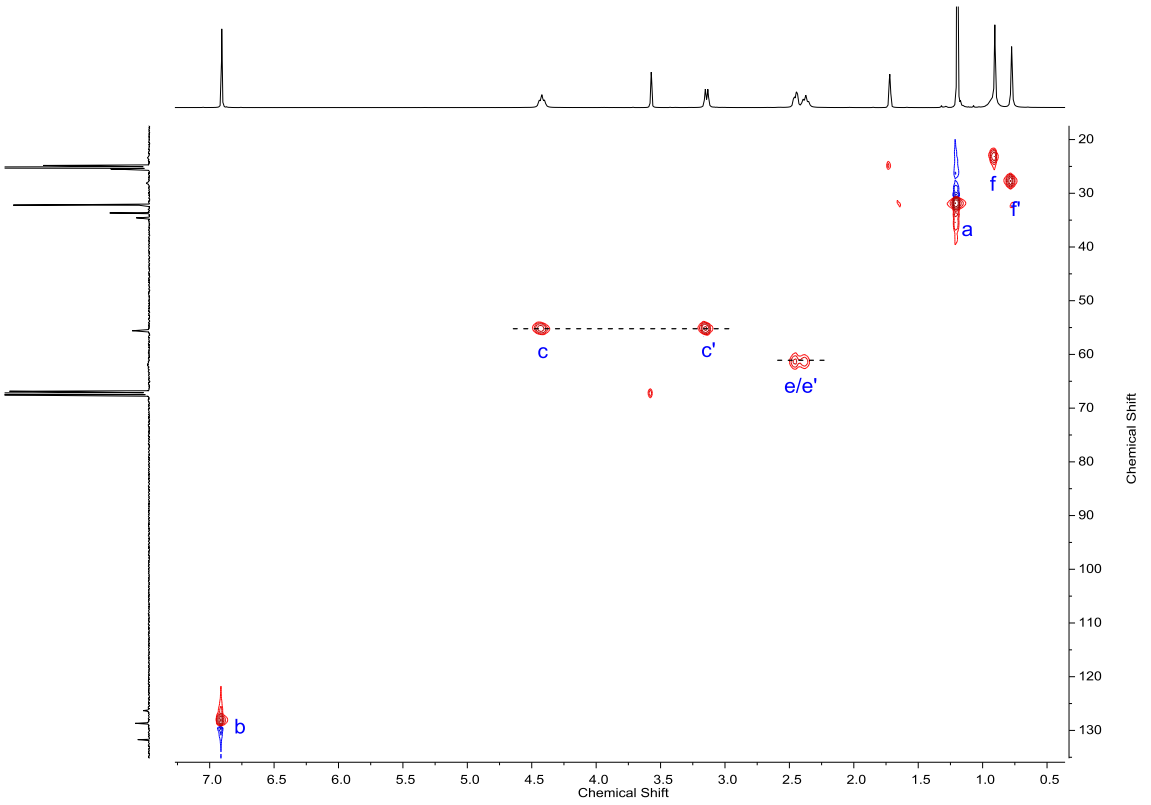


Figure S7: 2D HSQC NMR of **2** (d_8-THF, 298 K).

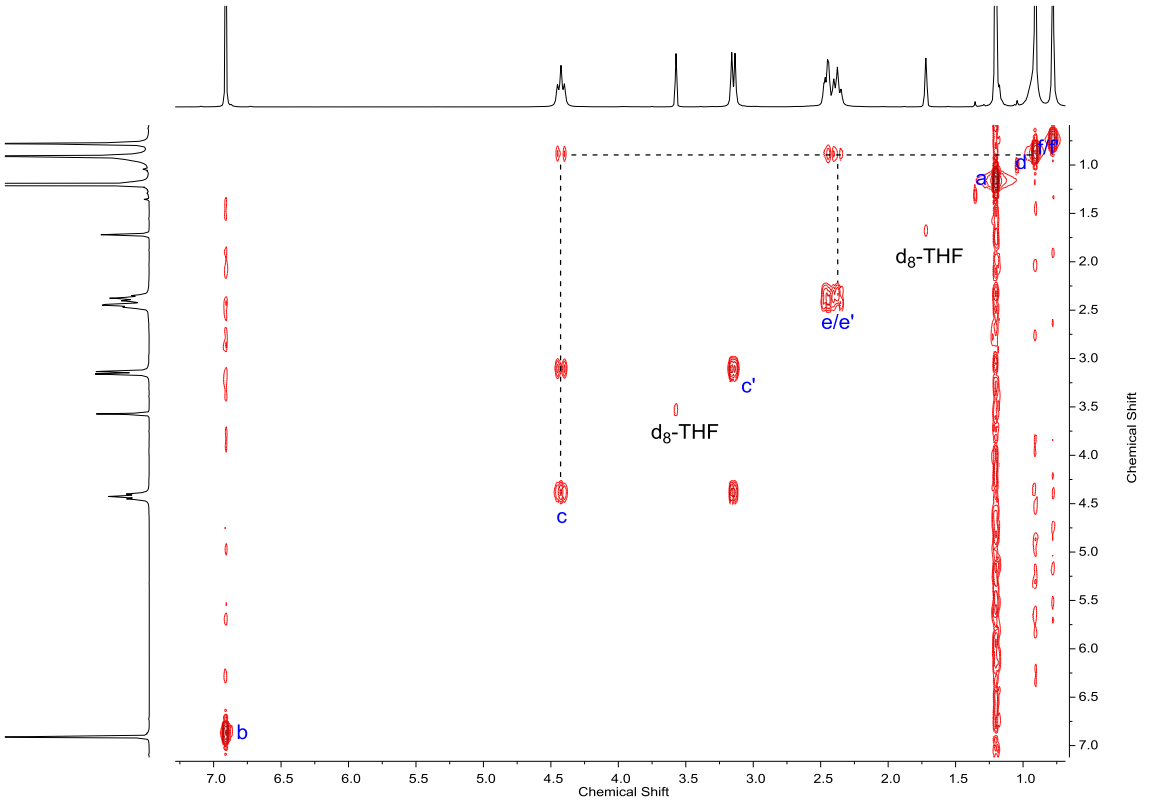


Figure S8: 2D COSY NMR of **2** (d_8-THF, 298 K).

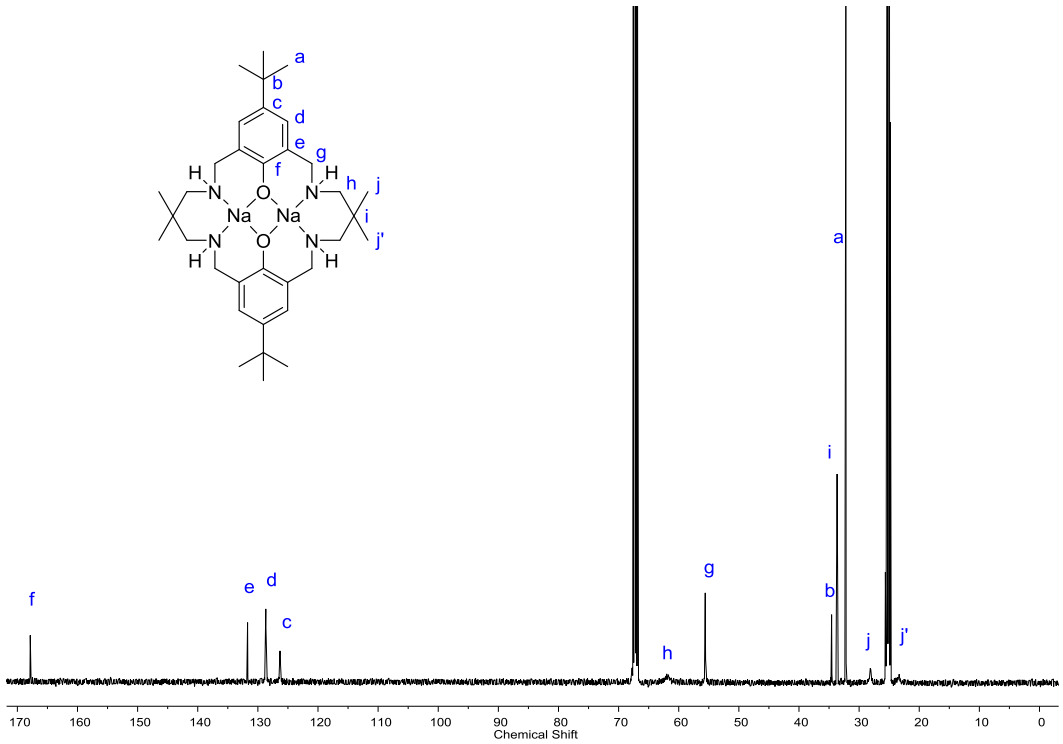


Figure S9: ^{13}C NMR of **2** (d_8-THF, 298 K).

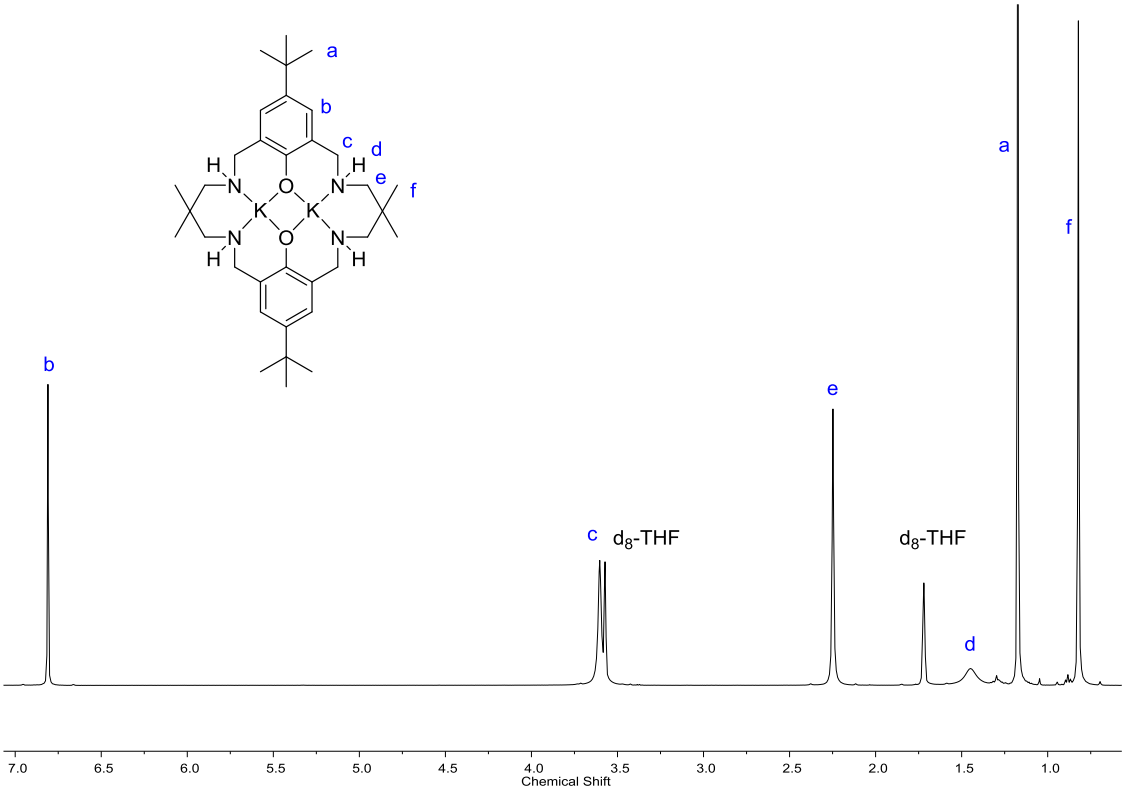


Figure S10: ^{1}H NMR of **3** (d_8-THF, 298 K).

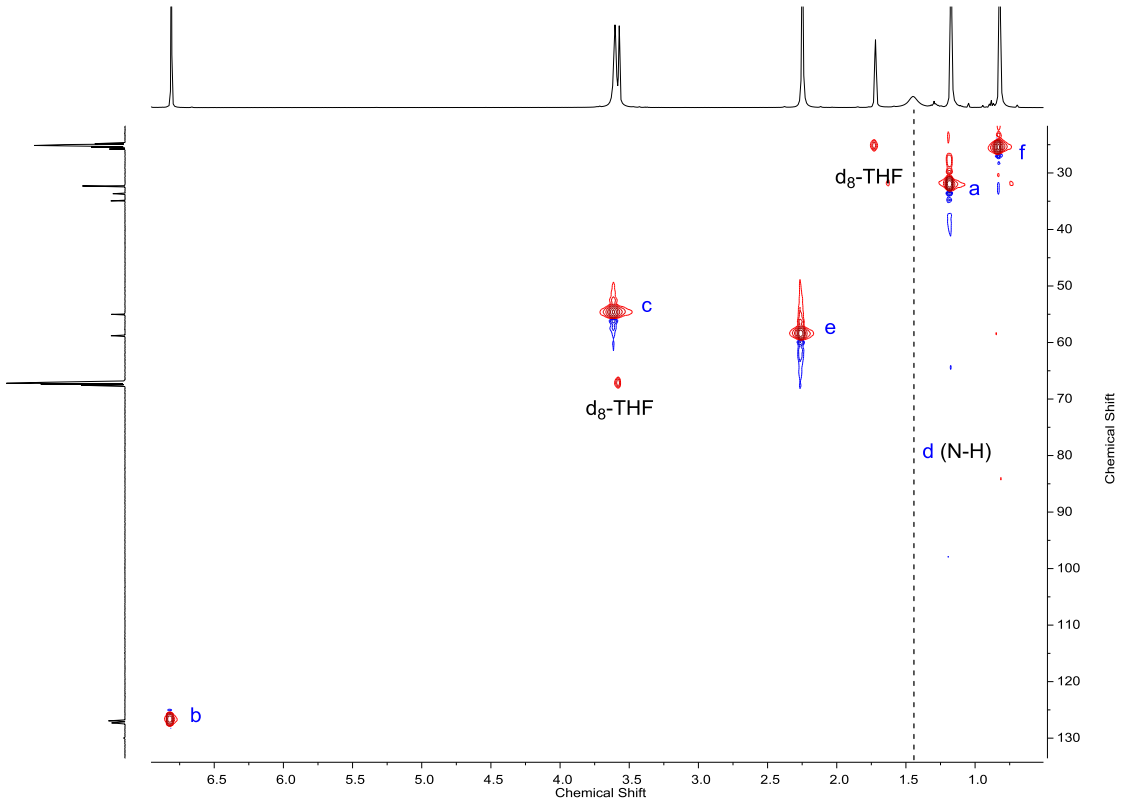


Figure S11: 2D HSQC NMR of **3** (d_8-THF, 298 K).

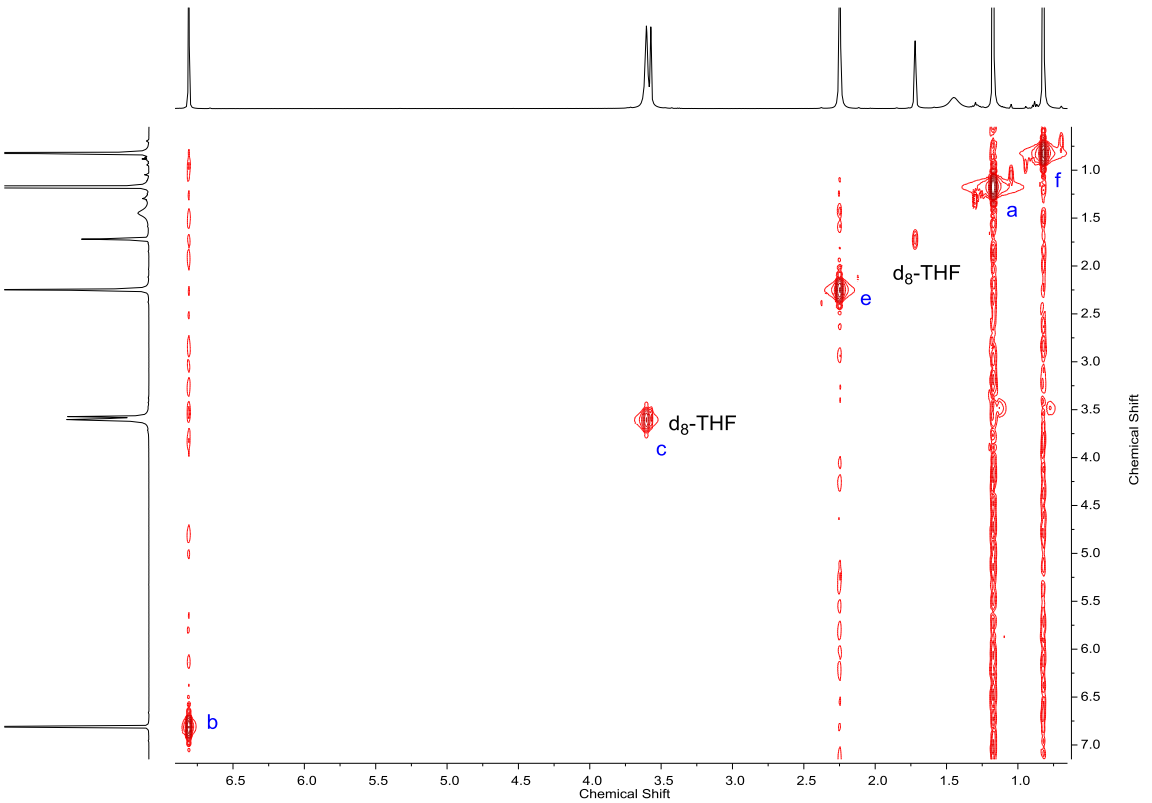


Figure S12: 2D COSY NMR of **3** (d_8-THF, 298 K).

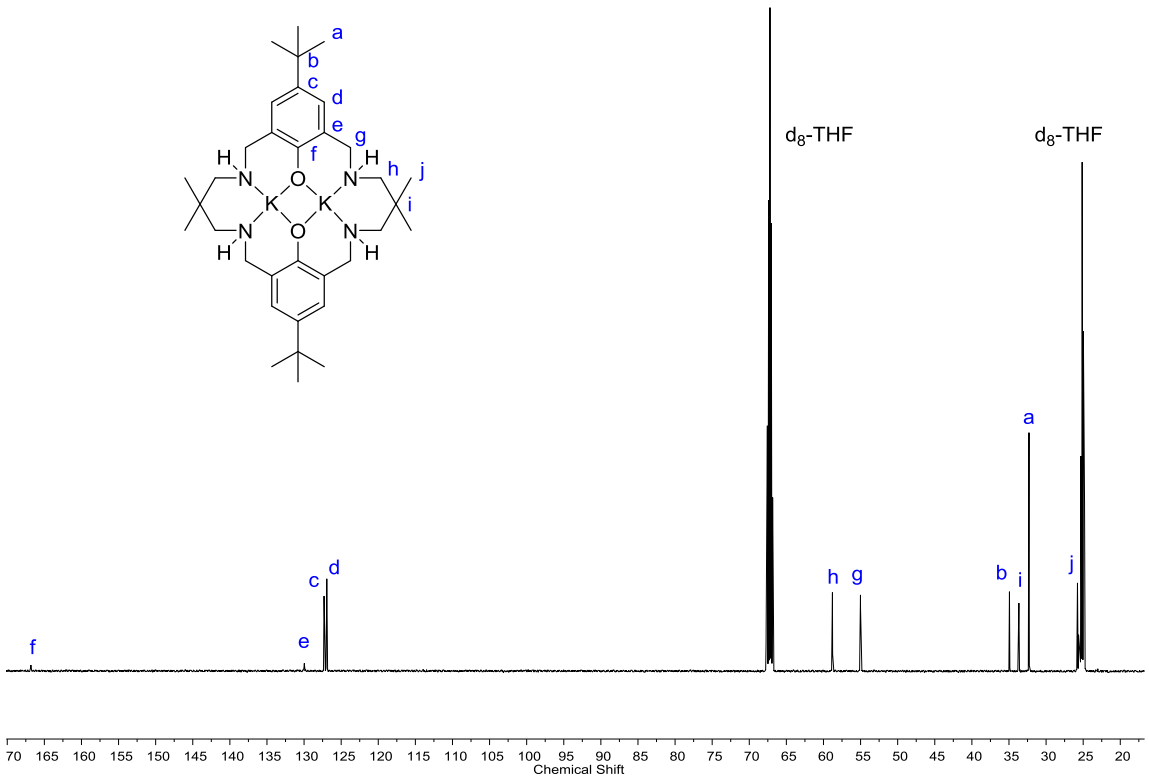


Figure S13: ^{13}C NMR of **3** (d_8-THF, 298 K).

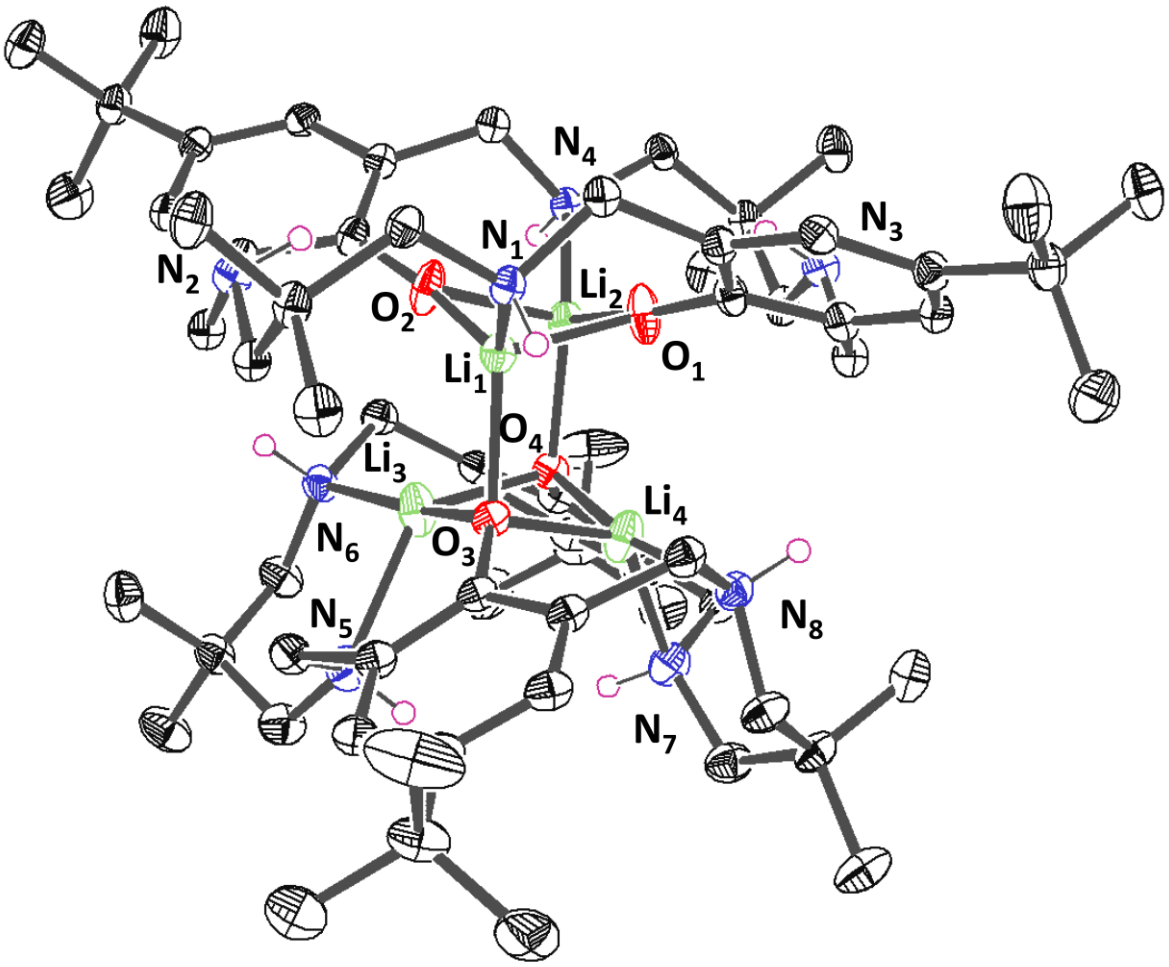


Figure S14: ORTEP representation of the molecular structure of **1**, with disorder and hydrogen atoms (excluding N-H) omitted for clarity and thermal ellipsoids represented at 40 % probability Li_1=Li_2, Li_3=Li_4.

Table S1: Selected bond lengths (Å) and angles (°) for complex **1**

Bond	Bond Length (Å)	Bond	Bond Angle (°)
N (1) – Li (1)	2.119(2)	N (1) – Li (1) – O (2)	126.90(11)
N (2) – Li (1)	3.269(2)	N (1) – Li (1) – O (1)	101.61(9)
O (1) – Li (1)	1.935(2)	N (1) – Li (1) – O (3)	117.74(10)
O (2) – Li (1)	1.883(2)	N (7) – Li (4) – O (4)	168.66(14)
O (3) – Li (1)	1.982(2)	N (8) – Li (4) – O (3)	130.84(13)
N (7) – Li (4)	2.106(2)	N (7) – Li (4) – N (8)	93.79(9)
N (8) – Li (4)	2.162(3)		
O (3) – Li (4)	1.953(2)	**Metal – Metal**	**Distance (Å)**
O (4) – Li (4)	1.965(2)		
O (1) – Li (4)	2.774(3)	Li (1) – Li (2)	2.518(4)
		Li (3) – Li (4)	2.630(4)

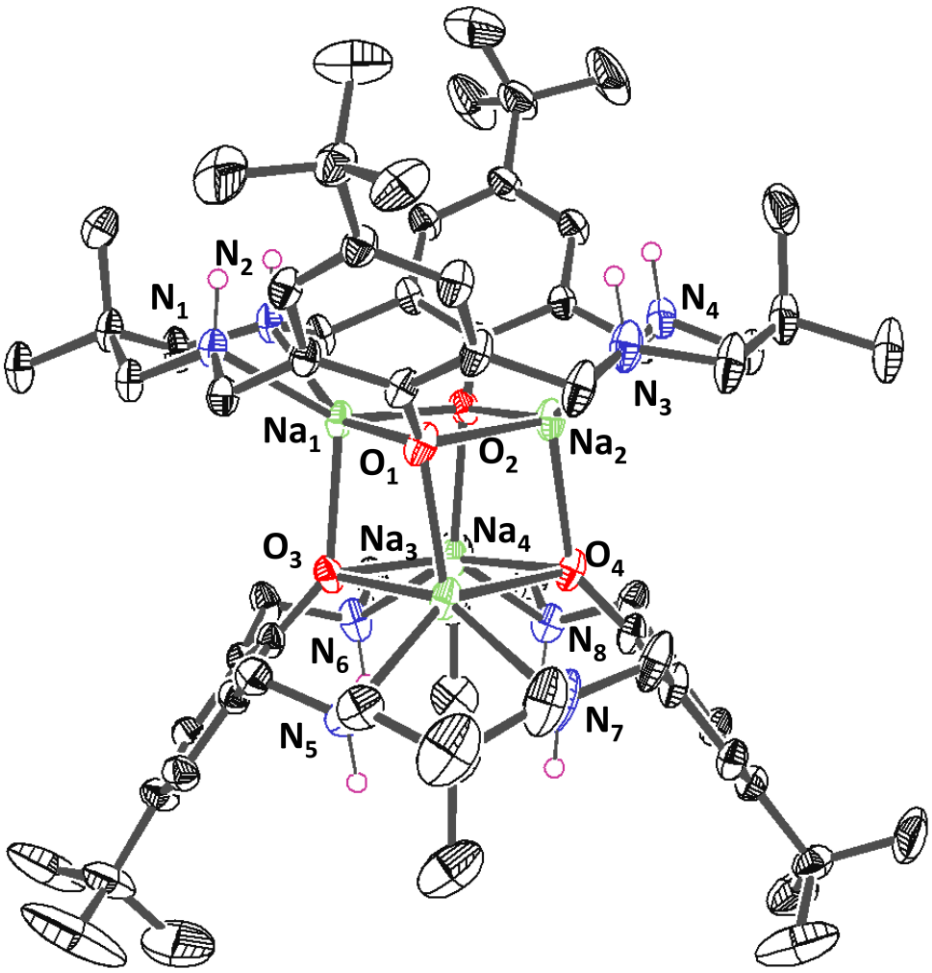


Figure S15: ORTEP representation of the molecular structure of **2**, with disorder and hydrogen atoms (excluding N-H) omitted for clarity with thermal ellipsoide representaed at 40 % probability.

Table S2: Selected bond lengths (Å) and bond angles (°) of complex **2**.

Bond	**Bond Length (Å)**	**Bond**	**Bond Angel (°)**
N (1) – Na (1)	2.426(3)	N (1) – Na (1) – O (2)	150.32(9)
N (2) – Na (1)	2.453(3)	N (2) – Na (1) – O (1)	151.66(10)
O (1) – Na (1)	2.365(3)	N (1) – Na (1) – O (3)	114.09(9)
O (2) – Na (1)	2.345(2)	N (3) – Na (2) – O (2)	150.74(10)
O (3) – Na (1)	2.289(2)	N (4) – Na (2) – O (1)	149.24(10)
N (3) – Na (2)	2.470(3)	N (3) – Na (2) – O (4)	123.44(10)
N (4) – Na (2)	2.431(3)		
O (1) – Na (2)	2.3624(15)	**Metal – Metal**	**Distance (Å)**
O (2) – Na (2)	2.376(2)		
O (4) – Na (2)	2.31461(15)	Na (1) – Na (2)	3.1364(15)

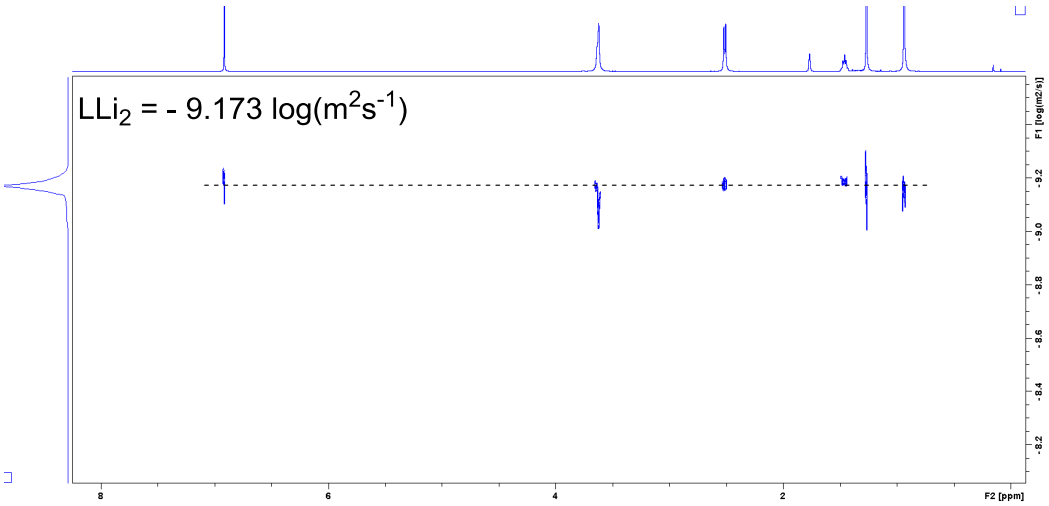


Figure S16: 2D DOSY of **1** (d_8-THF, 298 K)

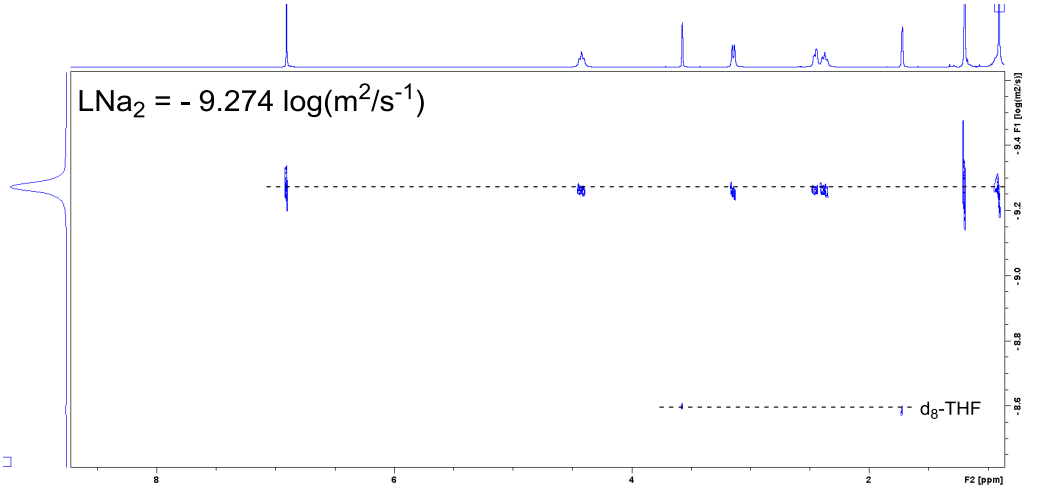


Figure S17: 2D DOSY of **2** (d_8-THF, 298 K)

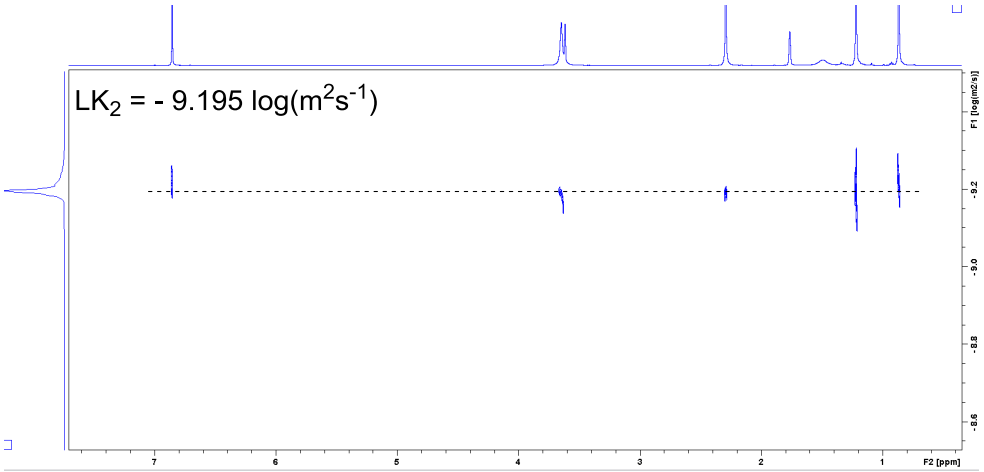


Figure S18: 2D DOSY of **3** (d_8-THF, 298 K)

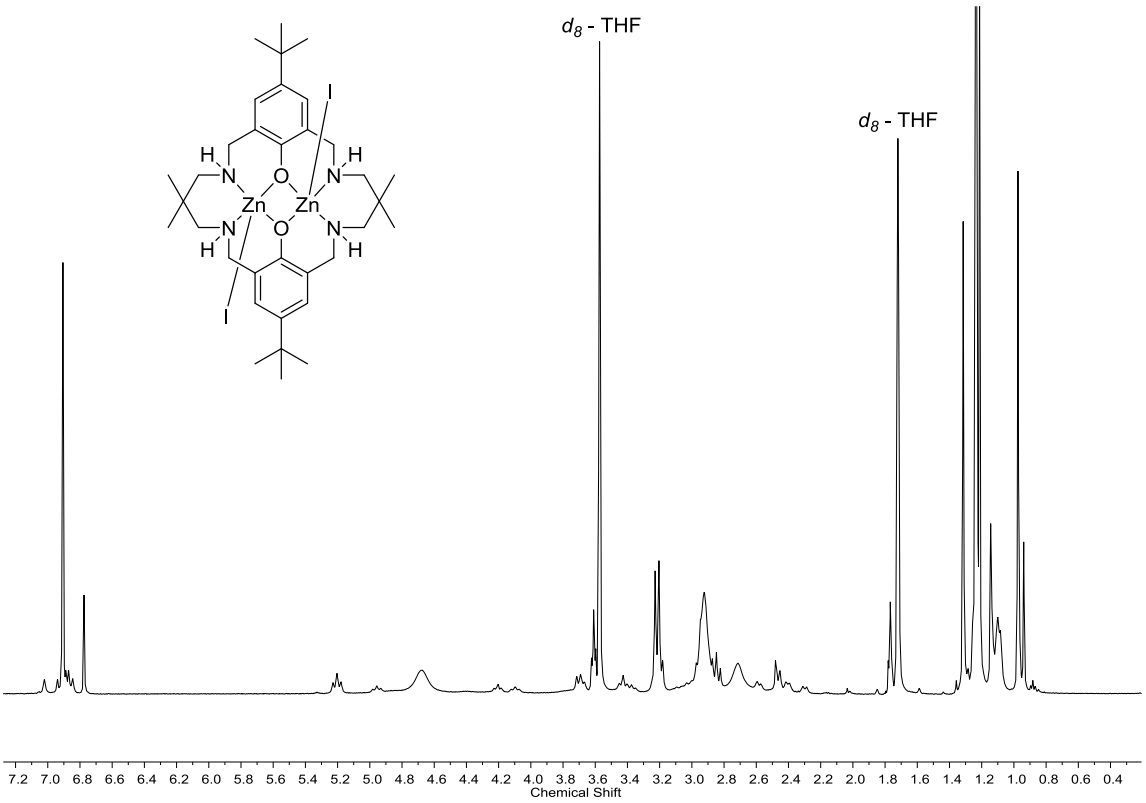


Figure S19: ^{1}H NMR of **4a** (d_8-THF, 298 K).

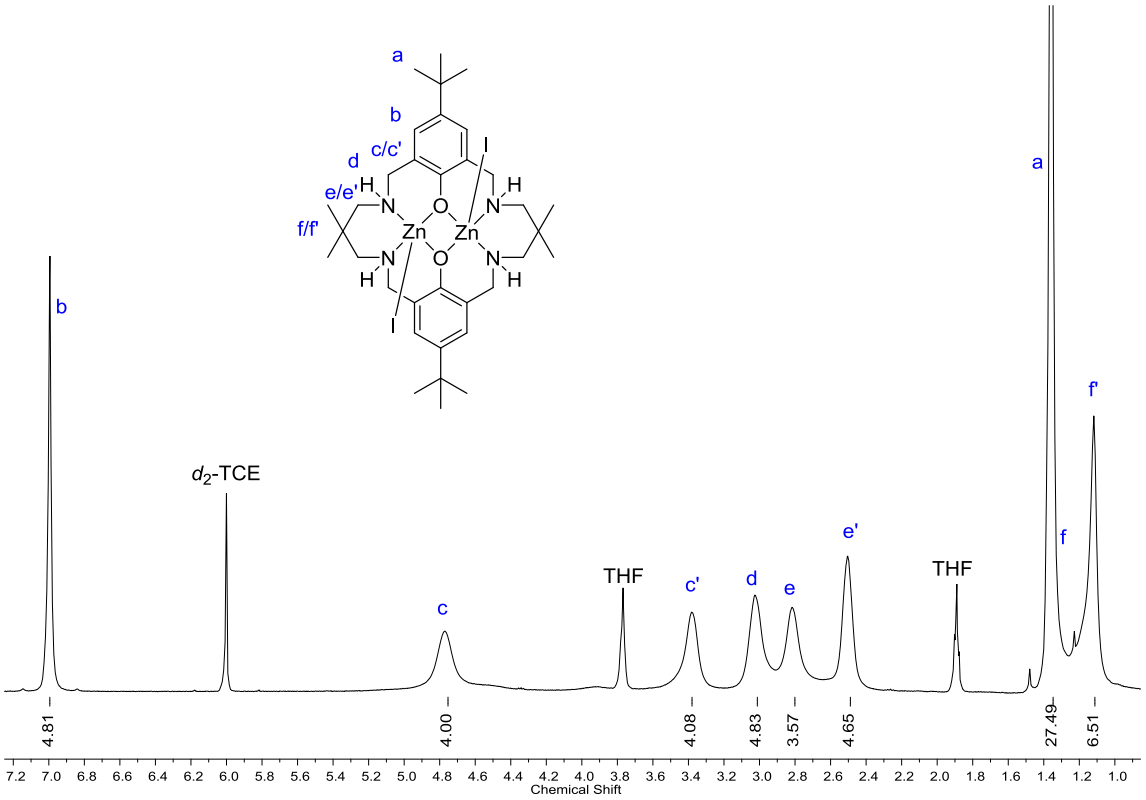


Figure S20: ^{1}H NMR of **4a** (d_2-TCE, 403 K).

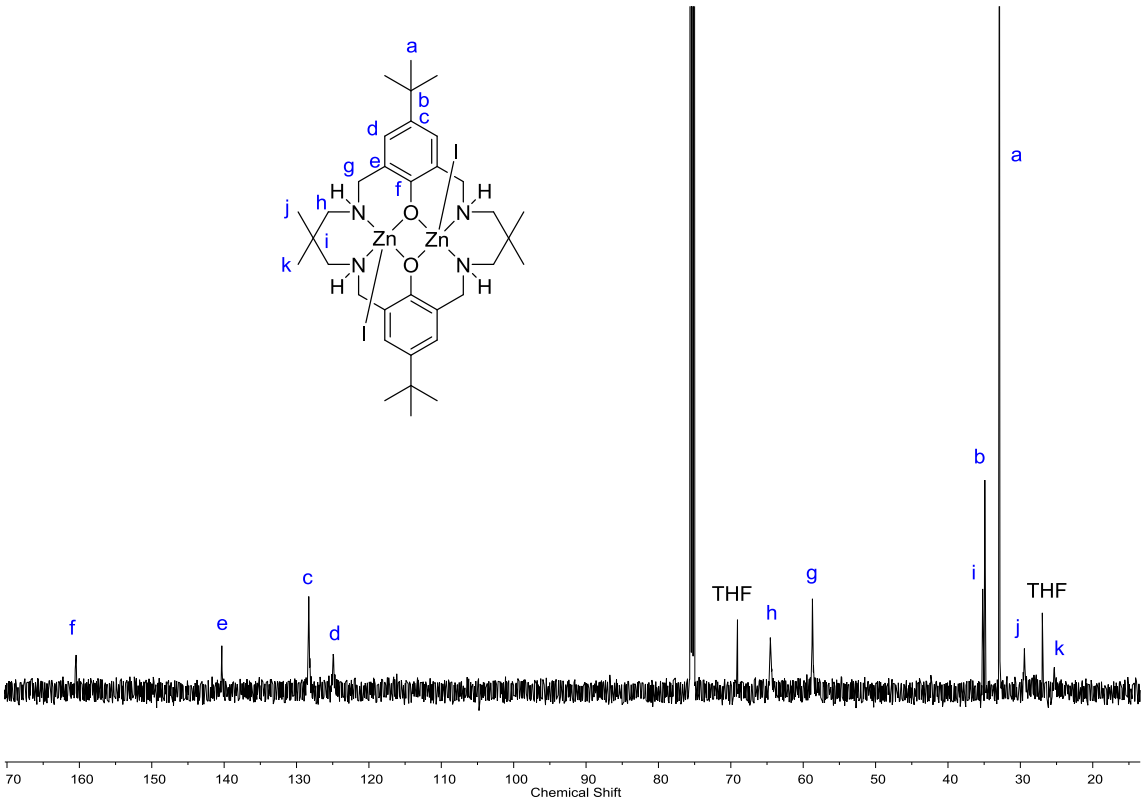


Figure S21: ^{13}C NMR of **4a** (d_2-TCE, 403 K).

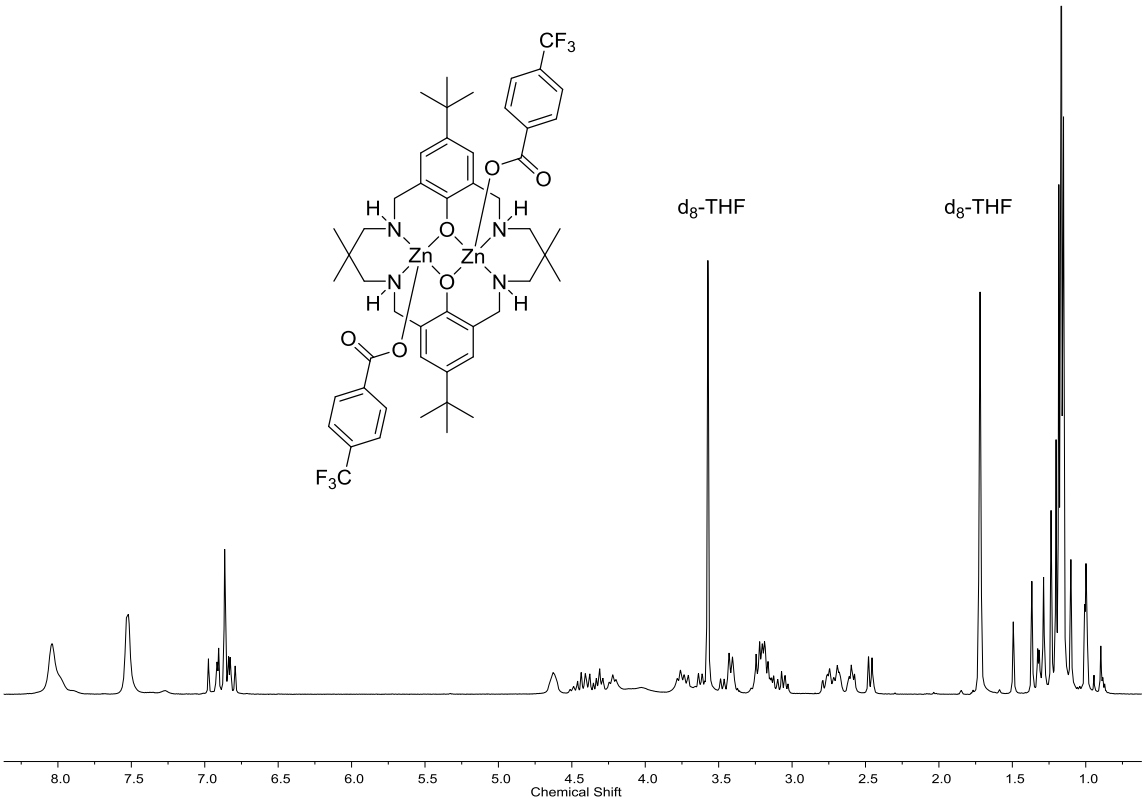


Figure S22: ^{1}H NMR of **4b** (d_8-THF, 298 K).

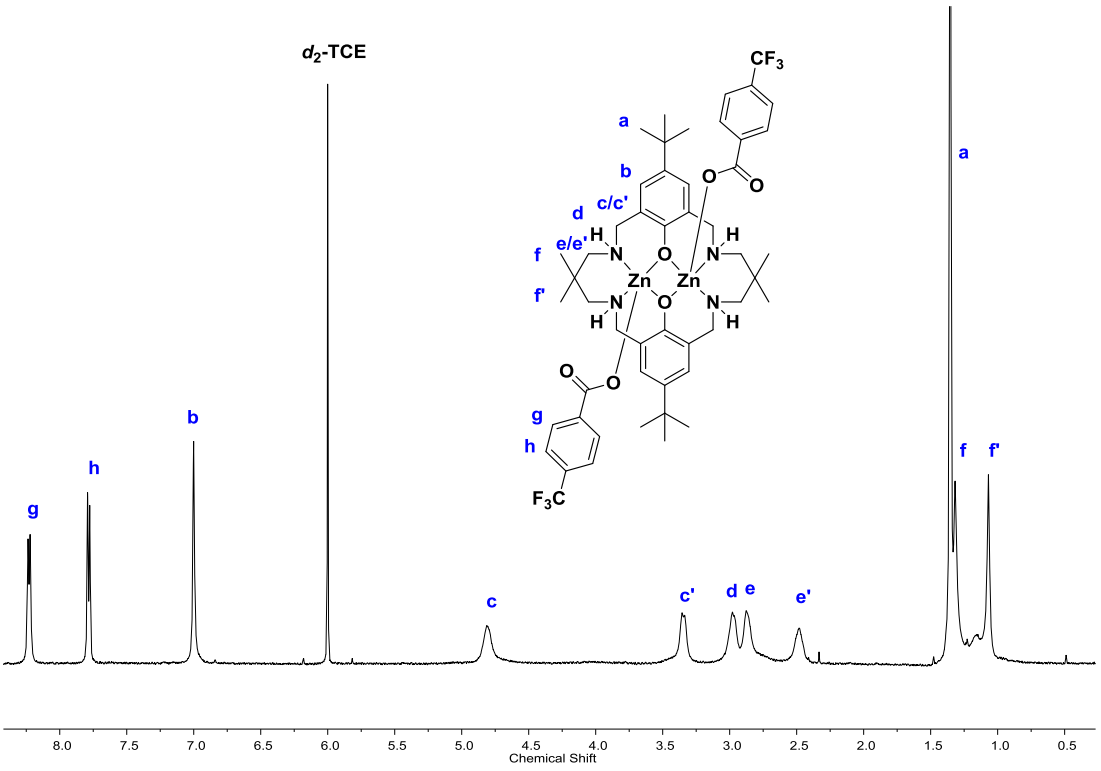


Figure S23: ^{1}H NMR of **4b** (d_2-TCE, 403 K).

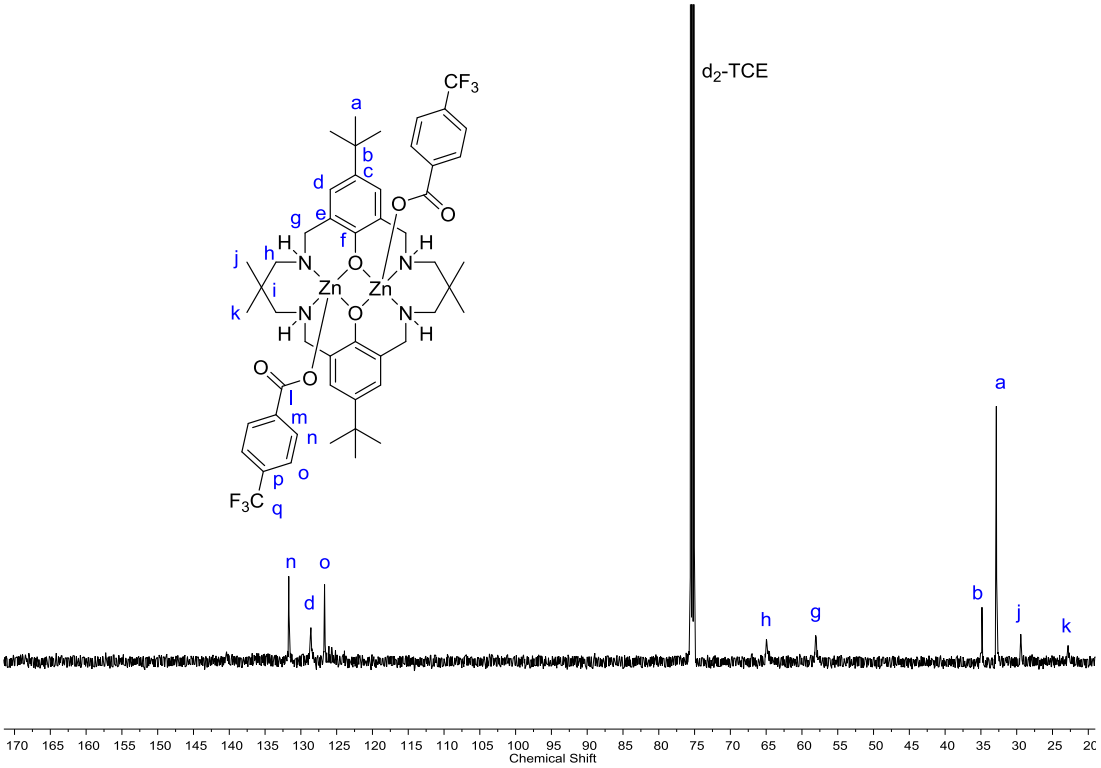


Figure S24: ^{13}C NMR of **4b** (d_2-TCE, 403 K). Unfortunately, aromatic quartenary carbons were not able to be observed in the ^{13}C NMR as previously reported with a dinuclear zinc phenyl catalyst.[1]

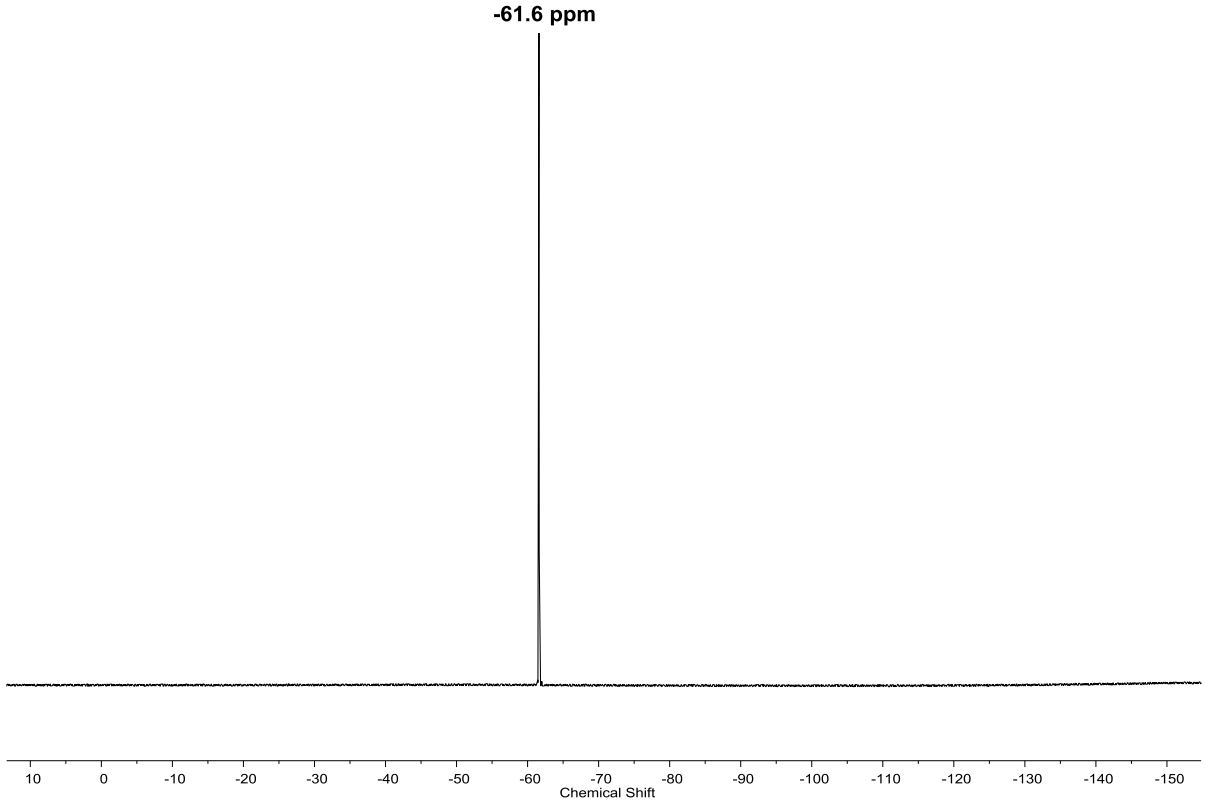


Figure S25: ^{19}F NMR of **4b** (d_2-TCE, 403 K).

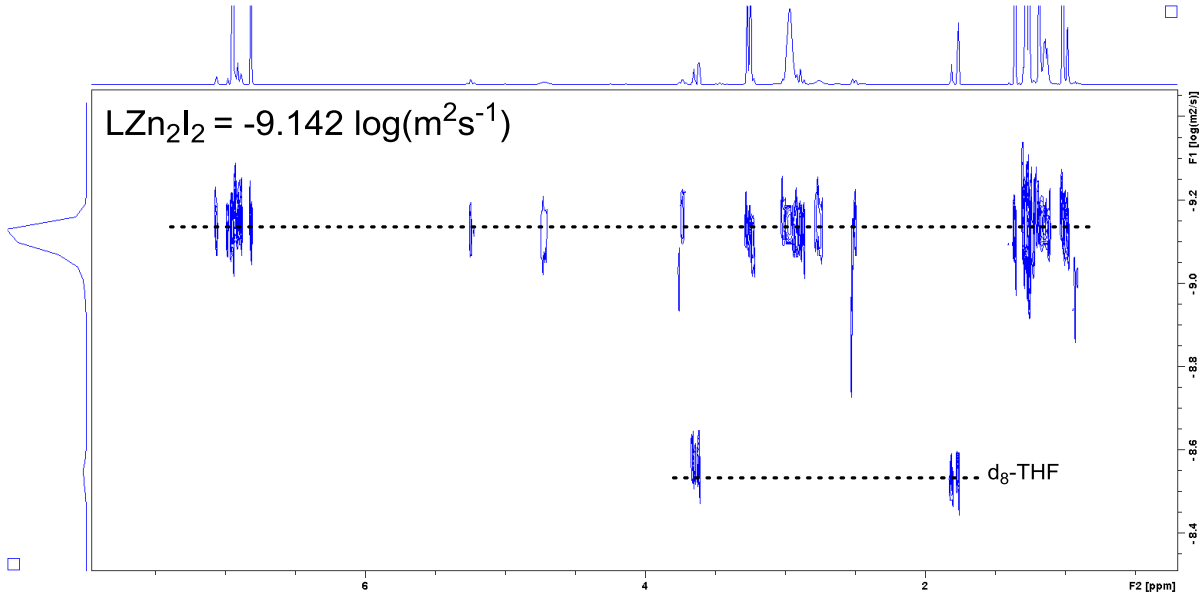


Figure S26: 2D DOSY NMR of complex **4a** (d_8-THF, 298 K).

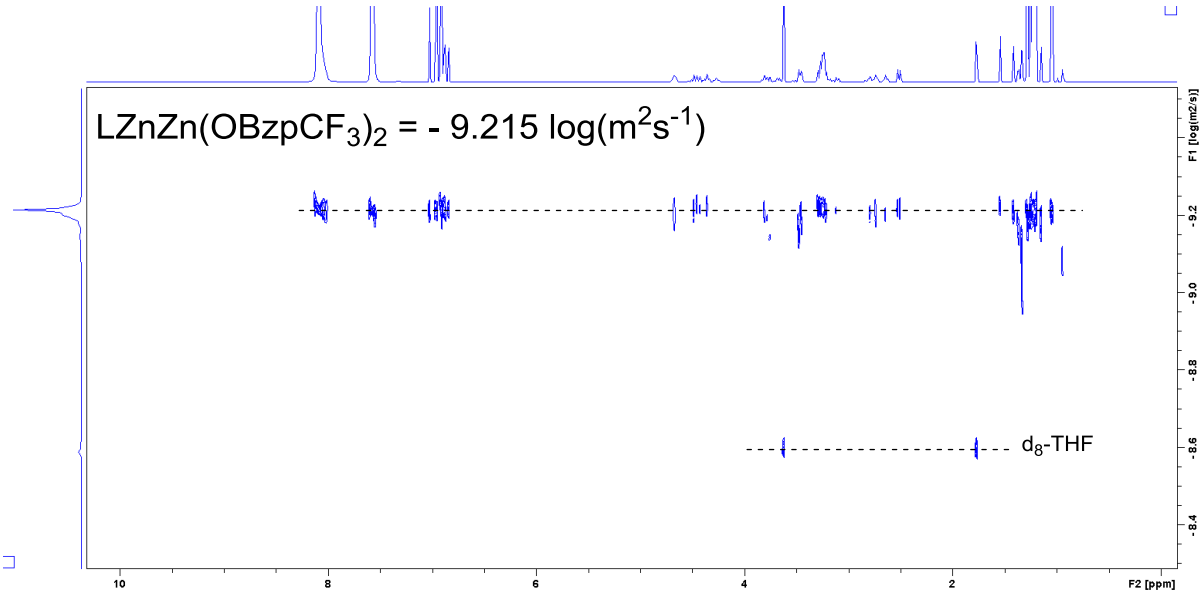


Figure S27: 2D DOSY NMR of complex **4b** (d_8-THF, 298 K)

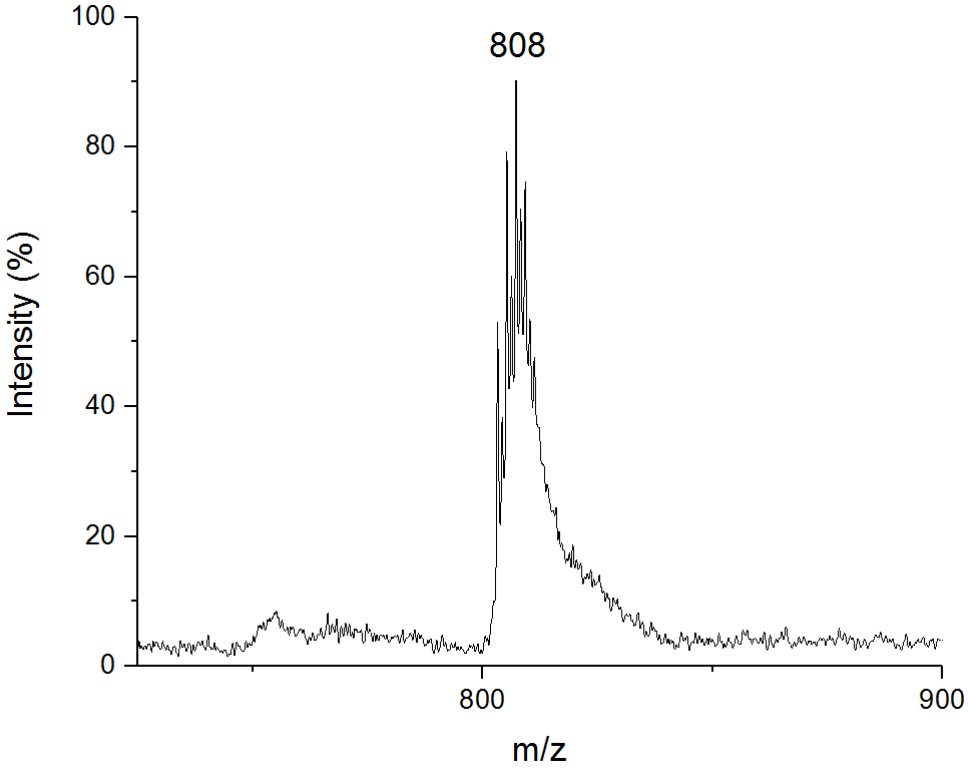


Figure S28: MALDI-ToF mass spectrum of **4a**. An m/z of 808 was observed and assigned to the complex cation $[LZn_2(I)]^+$.

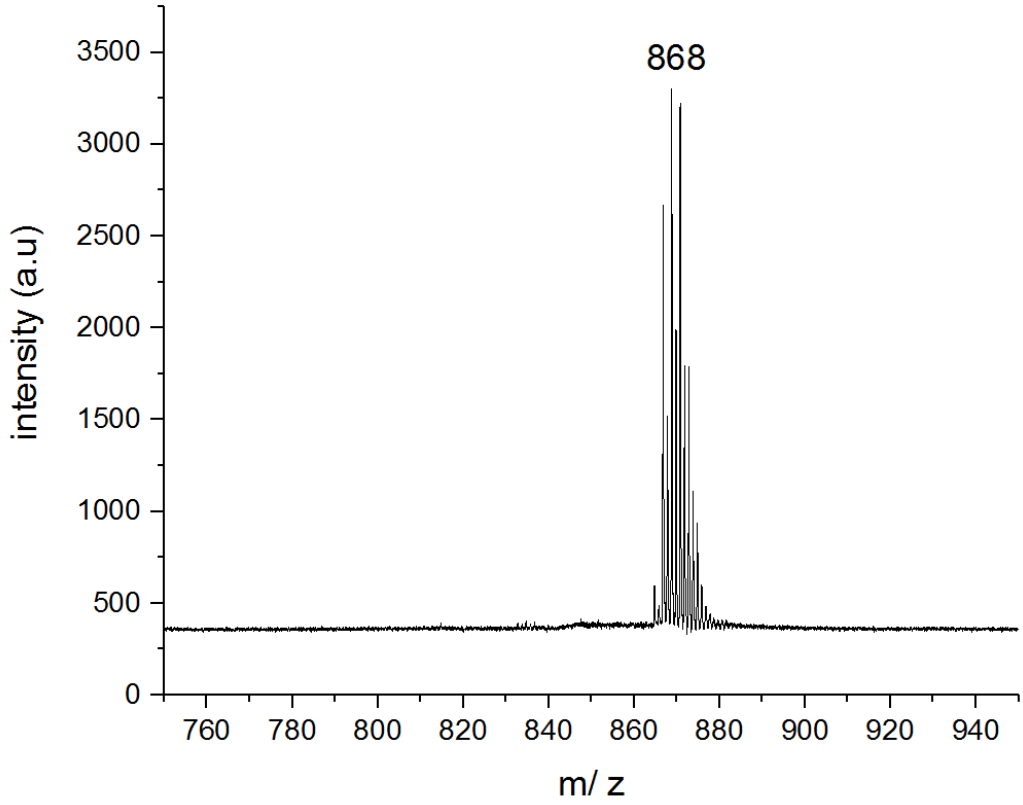


Figure S29: MALDI-ToF mass spectrum of **4b**. An m/z of 868 was obsereved and assigned to the complex cation $[LZn_2(OBzpCF_3)]^+$.

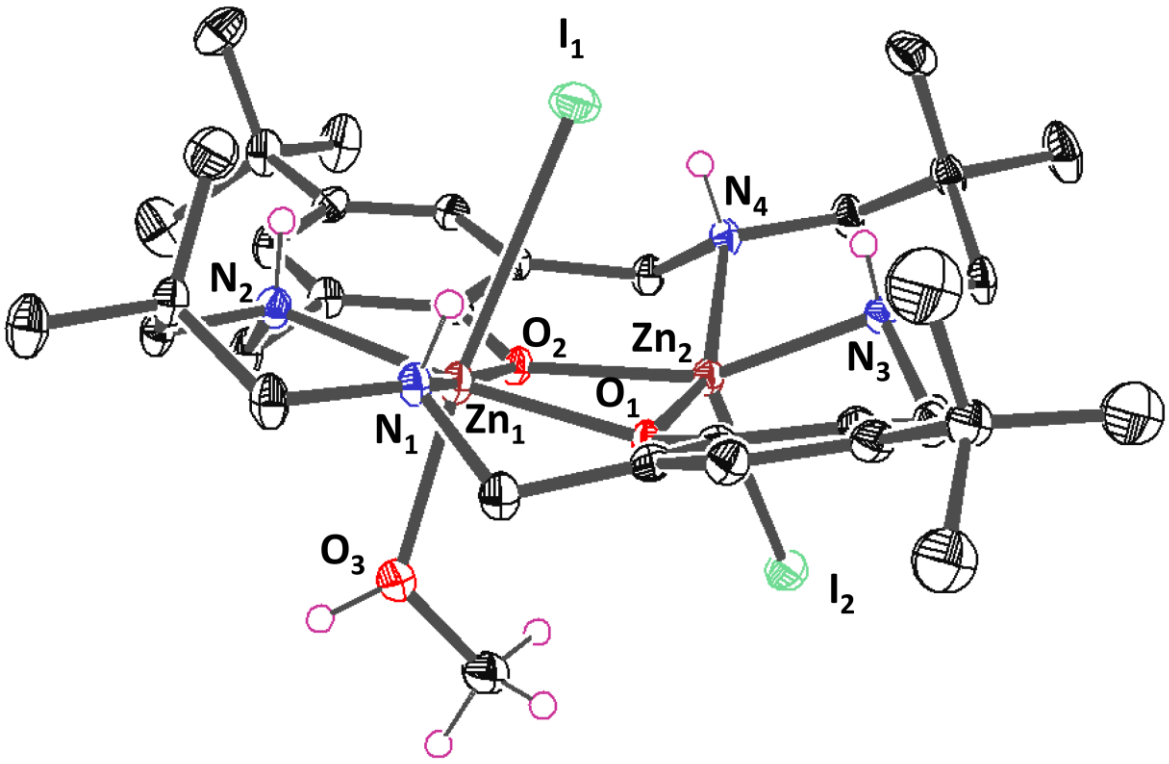


Figure S30: ORTEP representation of the molecular structure of **4a**, with disorder and hydrogen atoms (excluding N-H) omitted for clarity with thermal ellipsoids represented at 40 % probability.

Table S3: Selected bond lengths (Å) and angles (°) for complex **4a**.

Bond	Bond Length (Å)	Bond	Bond Angle (°)
N (1) – Zn (1)	2.131(3)	N (1) – Zn (1) – O (2)	151.07(9)
N (2) – Zn (1)	2.144(3)	N (2) – Zn (1) – O (1)	150.80(8)
O (1) – Zn (1)	2.087(2)	N (1) – Zn (1) – I (1)	100.95(6)
O (2) – Zn (1)	2.060(2)	N (3) – Zn (2) – O (2)	171.32(9)
I (1) – Zn (1)	2.6420(4)	N (4) – Zn (2) – O (1)	171.75(9)
N (3) – Zn (2)	2.108(3)		
N (4) – Zn (2)	2.107(3)	**Metal – Metal**	**Distance (Å)**
O (1) – Zn (2)	2.051(2)		
O (2) – Zn (2)	2.053(2)	Zn (1) – Zn (2)	3.0996(5)
I (2) – Zn (2)	3.1298(5)		
O (3) – Zn (2)	2.138(2)		

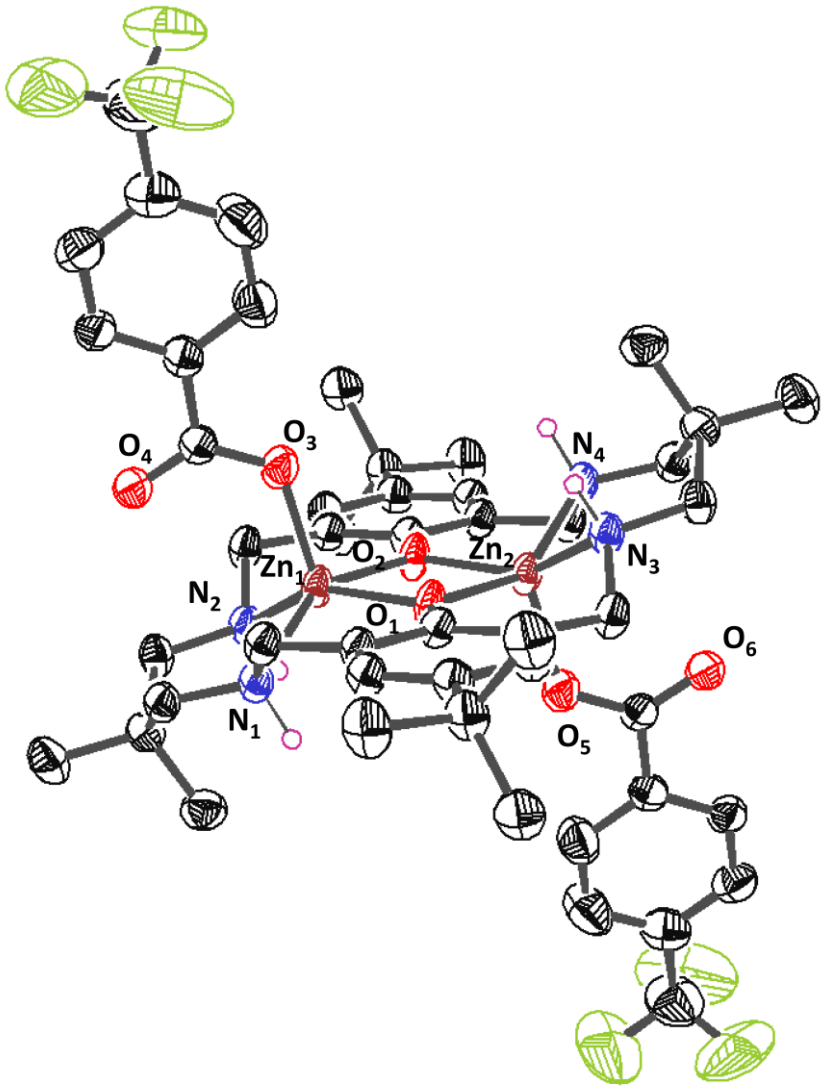


Figure S31: ORTEP representation of the molecular structure of **4b**, with disorder and hydrogen atoms (excluding N-H) are omitted for clarity with thermal ellipsodies represented at 40 % probability.

Zn_1=Zn_2.

Table S4: Selective bond lengths (Å) and angles (°) for complex **4b**.

Bond	Bond Length (Å)	Bond	Bond Angle (°)
N (1) – Zn (1)	2.106(2)	N (1) – Zn (1) – O (2)	148.47(10)
N (2) – Zn (1)	2.105(3)	N (2) – Zn (1) – O (1)	147.85(10)
O (1) – Zn (1)	2.0644(19)	O (3) – Zn (1) – I (1)	99.61(10)
O (2) – Zn (1)	2.0410(18)	N (3) – Zn (2) – O (2)	147.85(10)
O (3) – Zn (1)	1.987(3)	N (4) – Zn (2) – O (1)	148.47(10)
N (3) – Zn (2)	2.105(3)	O (5) – Zn (2) – O(1)	102.01(9)
N (4) – Zn (2)	2.106(2)		
O (1) – Zn (2)	2.0410(18)	**Metal – Metal**	**Distance (Å)**
O (2) – Zn (2)	2.0644(19)		
O (5) – Zn (2)	1.987(3)	Zn (1) – Zn (2)	3.19204(11)

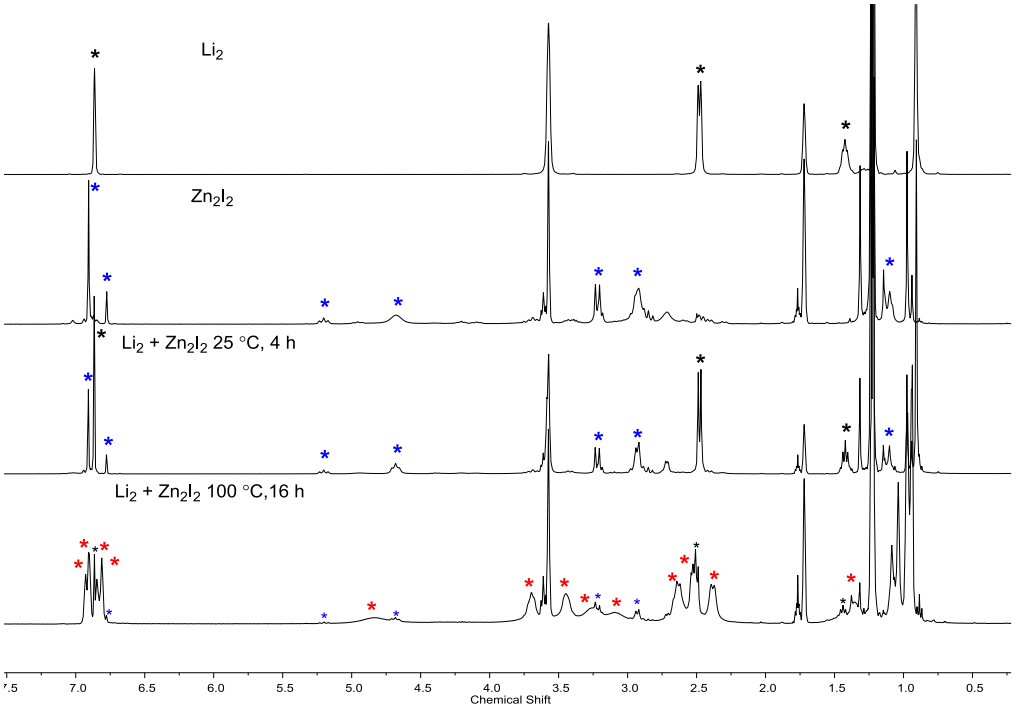


Figure S32: Metal redistribution reaction between **1** and **4a** (d_8-THF).

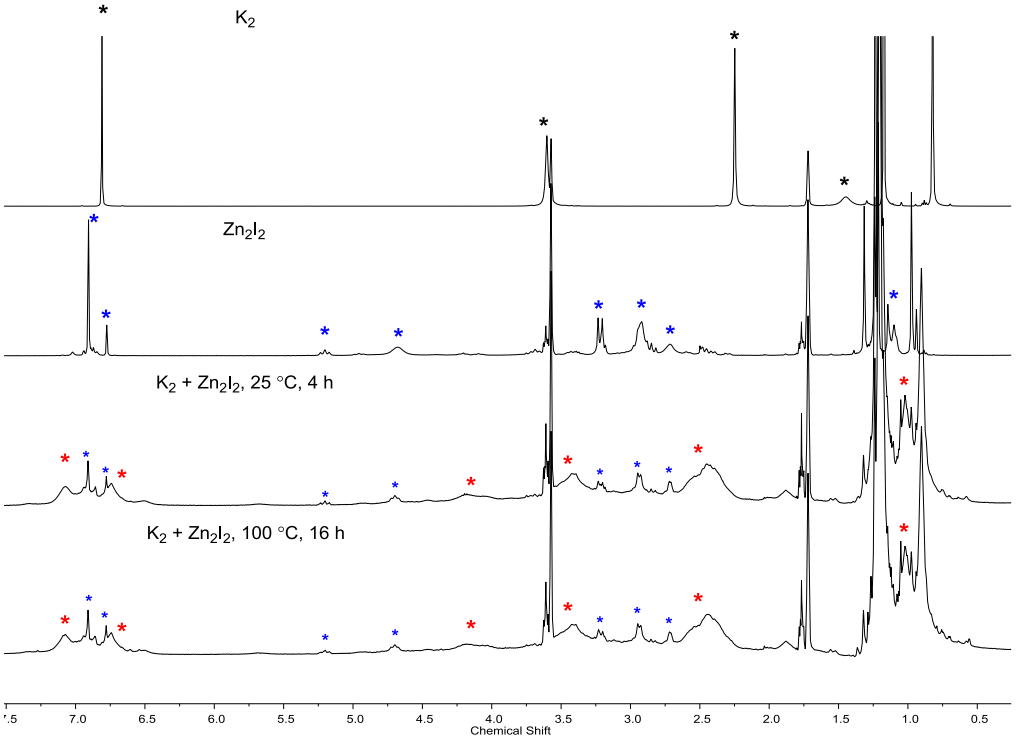


Figure S33: Metal redistribution reaction between **3** and **4a** (d_8-THF).

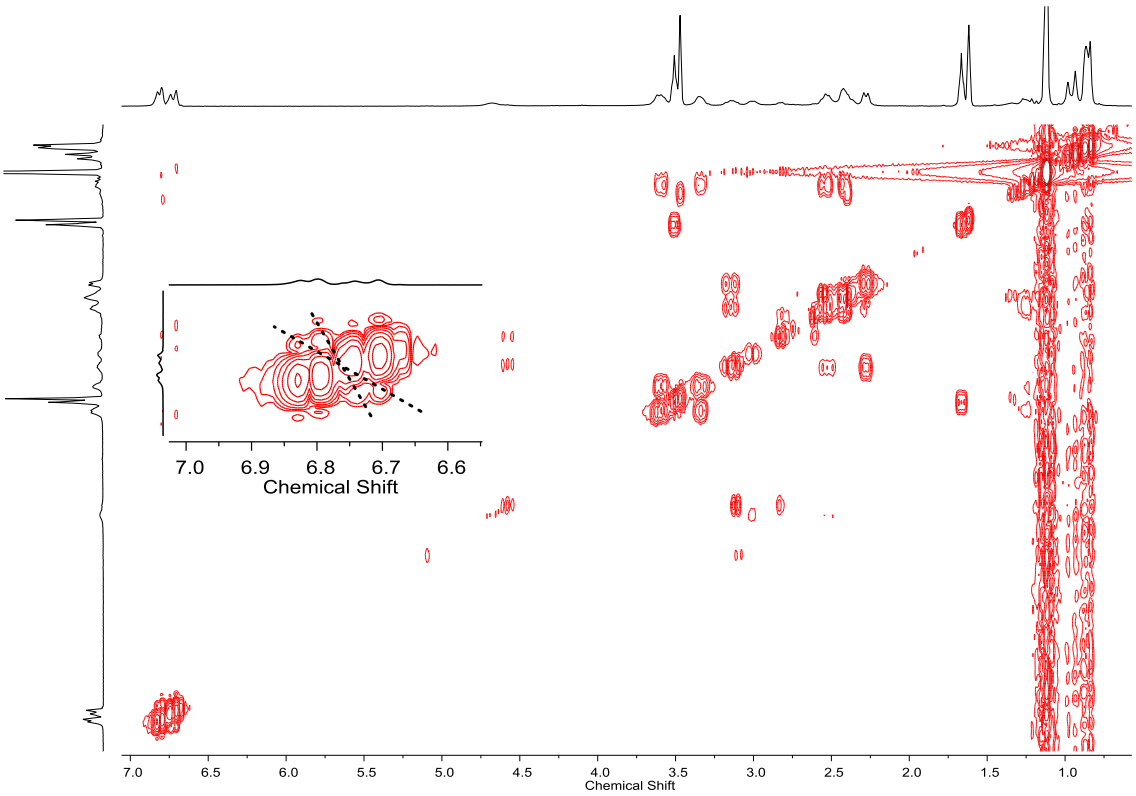


Figure S34: COSY NMR of product formed from metal redistribution reaction between **1** and **4a** (d_8-THF).

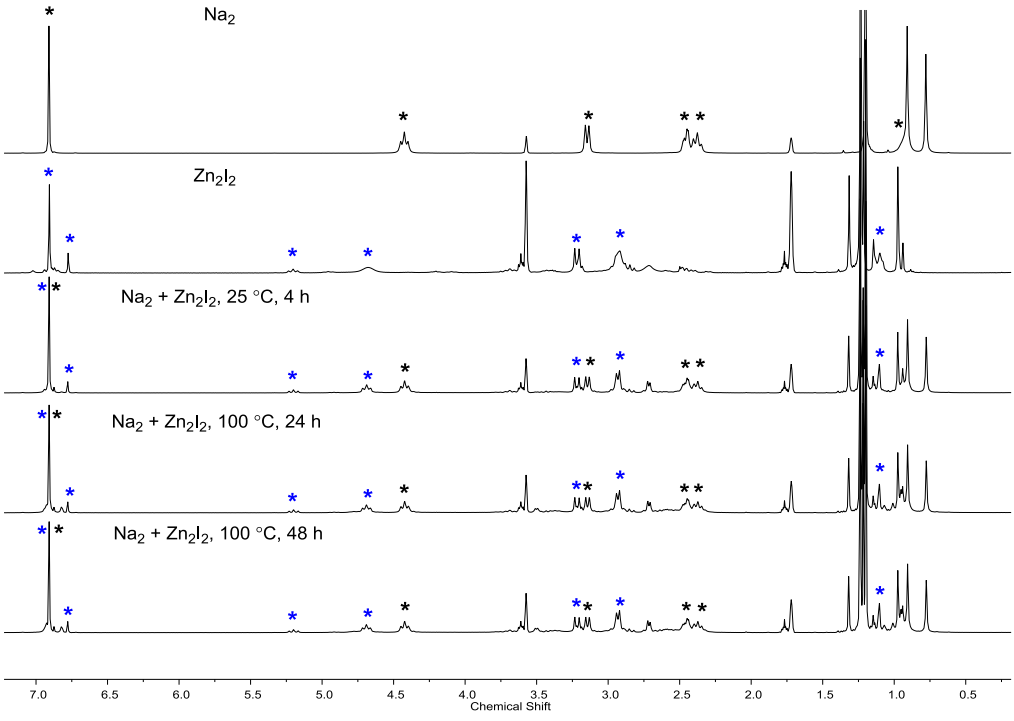


Figure S35: Metal redistribution reaction between **2** and **4a.** (d_8-THF).

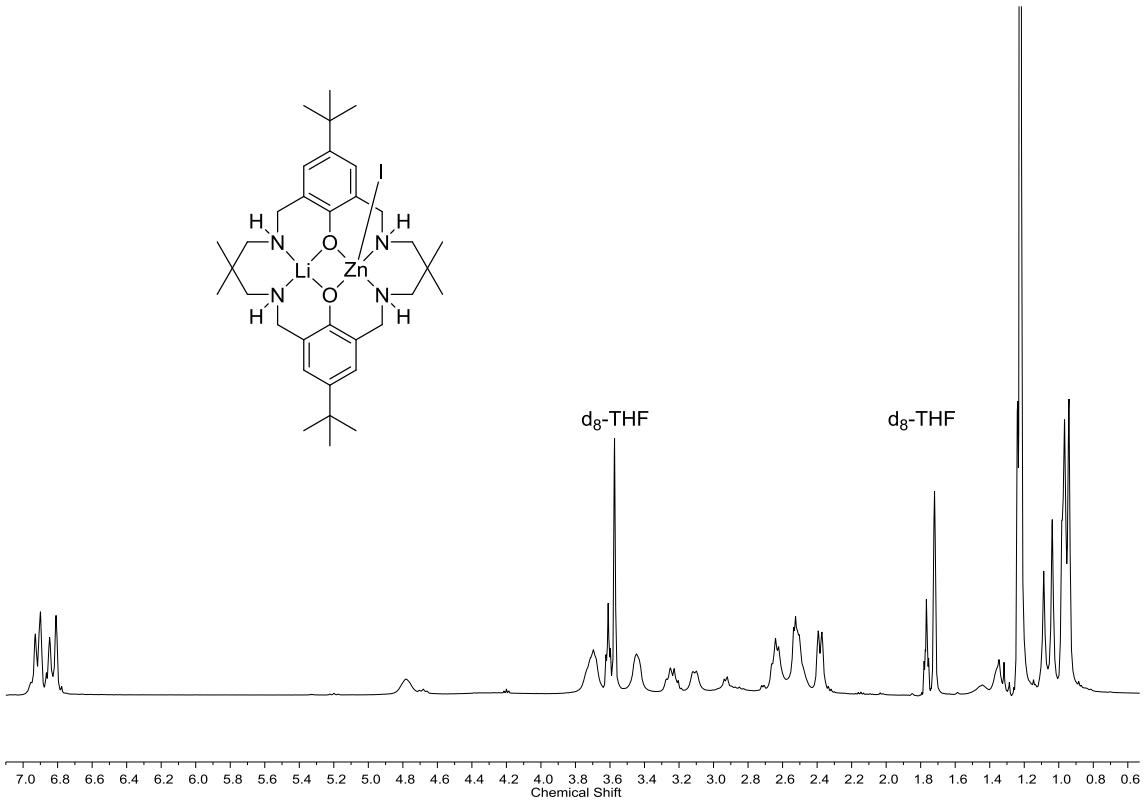


Figure S36: ^{1}H NMR of complex **5a** prepared through sequential metalation (d_8-THF, 298 K).

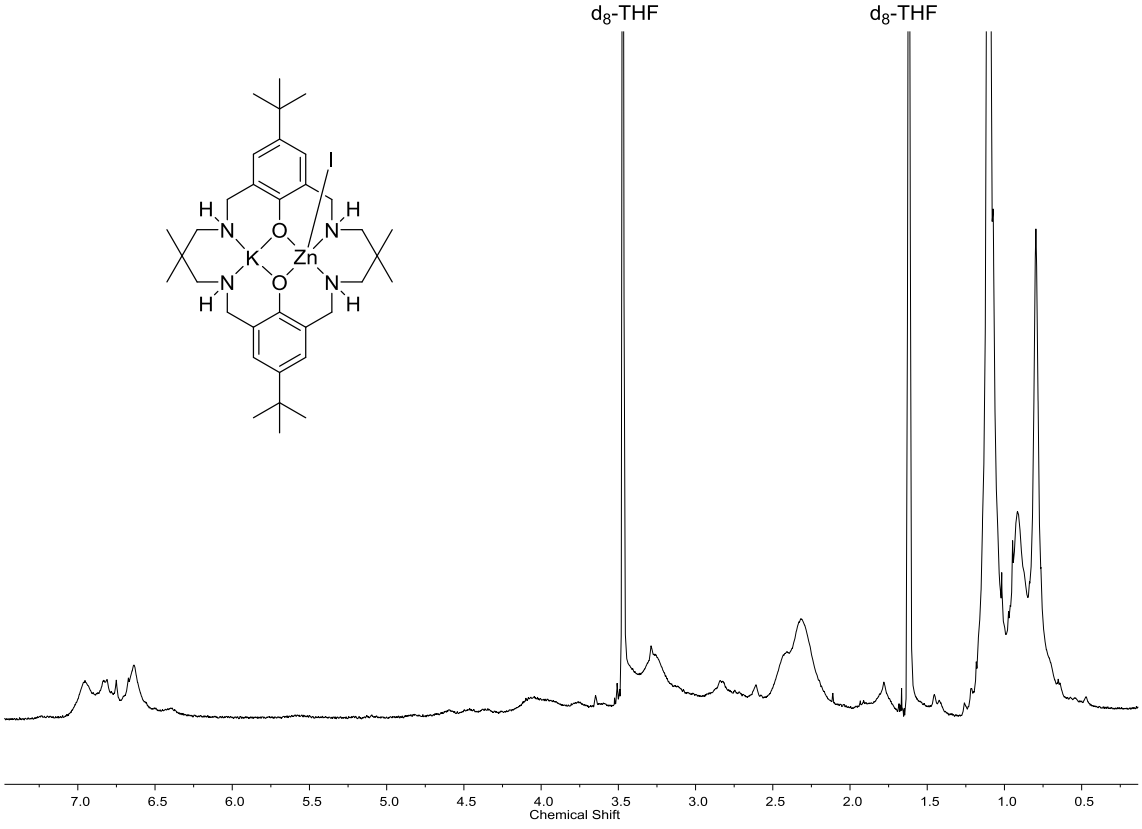


Figure S37: ^{1}H NMR of complex **7a** prepared through sequential metalation. (d_8-THF, 298 K).

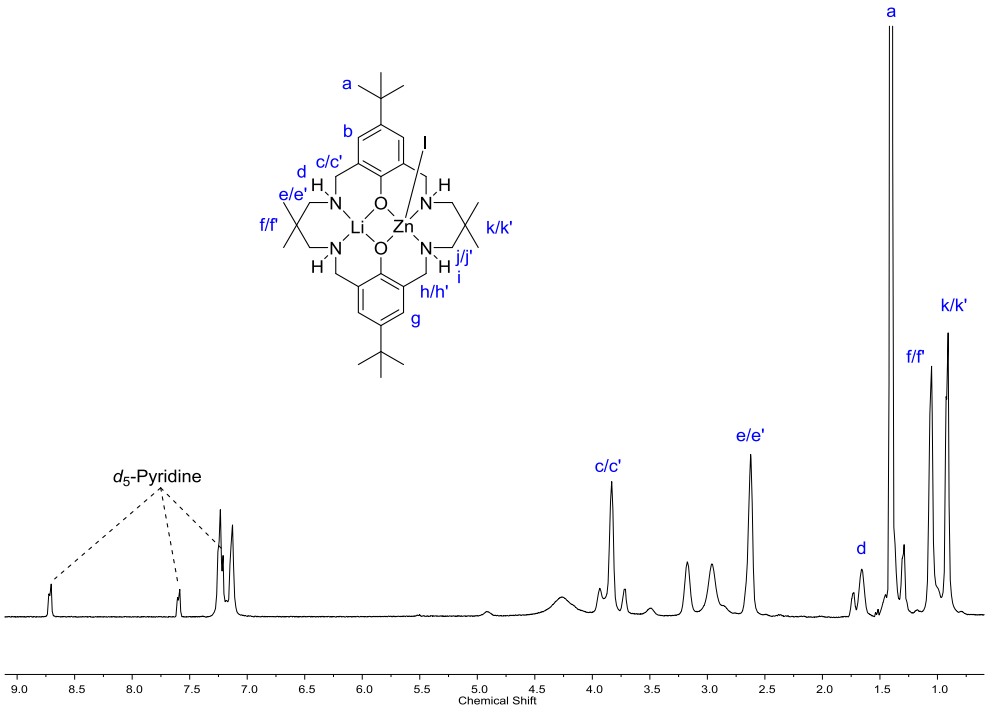


Figure S38: ^{1}H NMR spectrum of **5a** (d_5-pyridine, 403 K).

Due to multiple conformations and fluxionality of complex **5a** at room temperature, the complex was analysed by ^{1}H NMR spectroscopy in a range of high boiling organic solvents, including toluene, dioxane, tetrachloroethane, DMSO and pyridine. Although full coalescence of the proton environments are not fully observed, coupling between the phenyl proton resonances are observed in the COSY NMR, indicating heterodinuclear complex formation. (Figure S39)

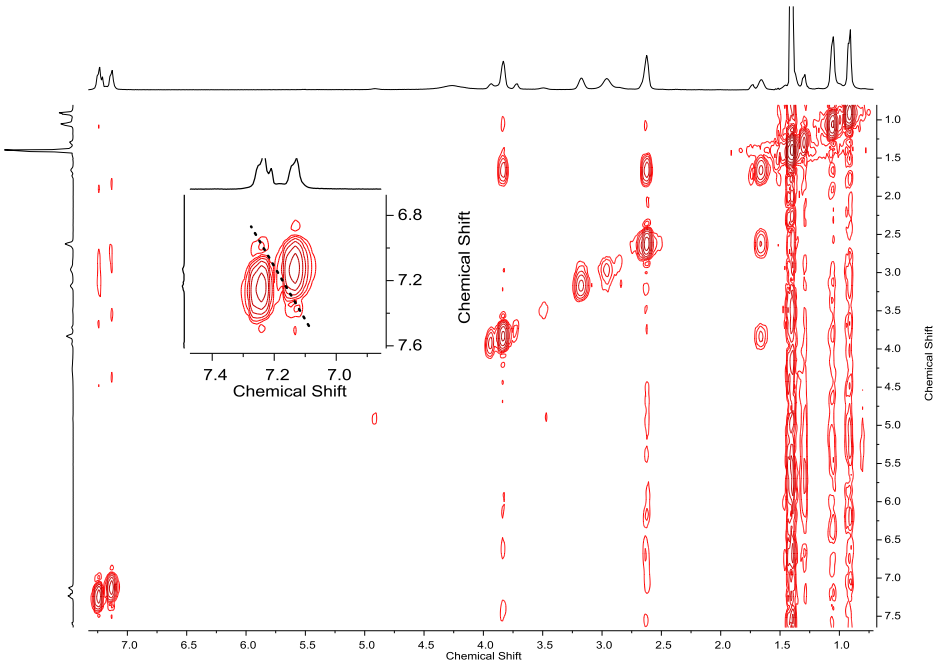


Figure S39: COSY NMR of complex **5a** (d_5-pyridine, 403 K).

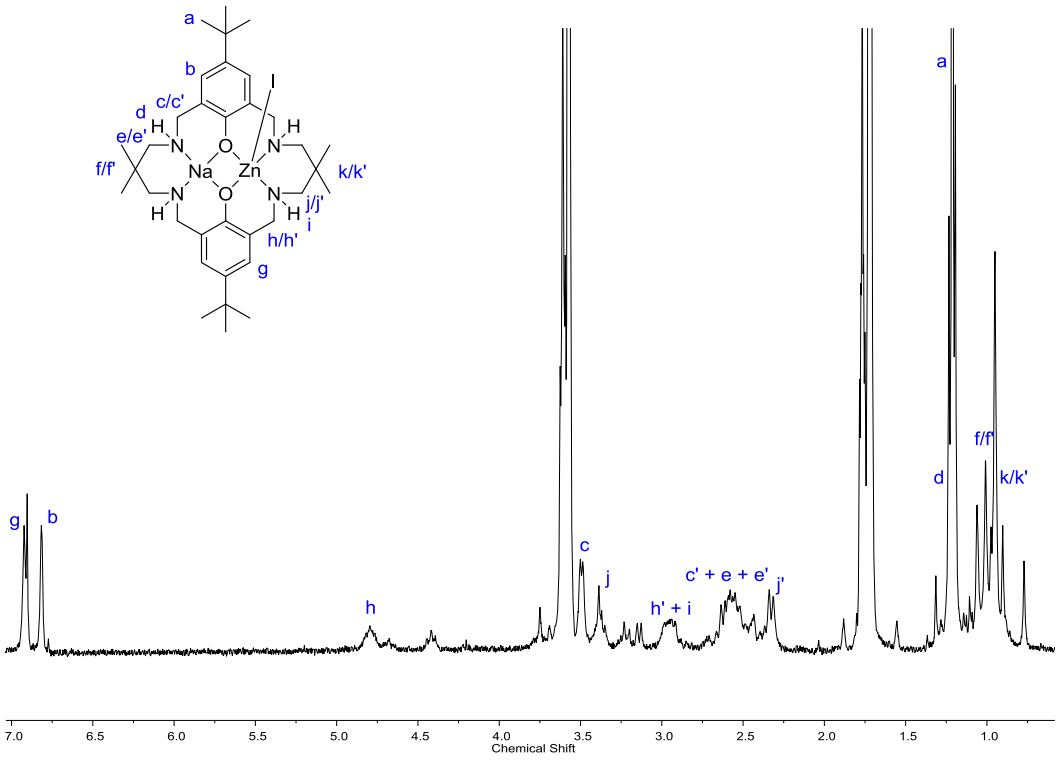


Figure S40: ^{1}H NMR of complex **6** (d_8-THF, 298 K).

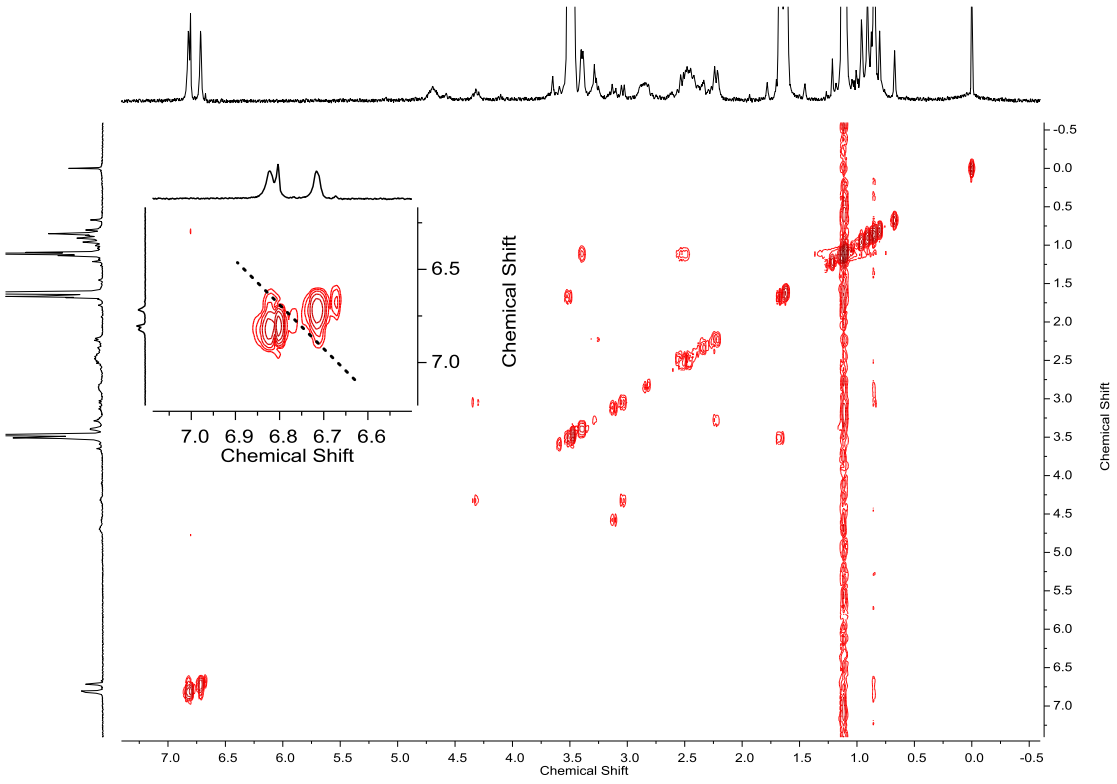


Figure S41: COSY NMR of complex **6** (d_8-THF, 298 K).

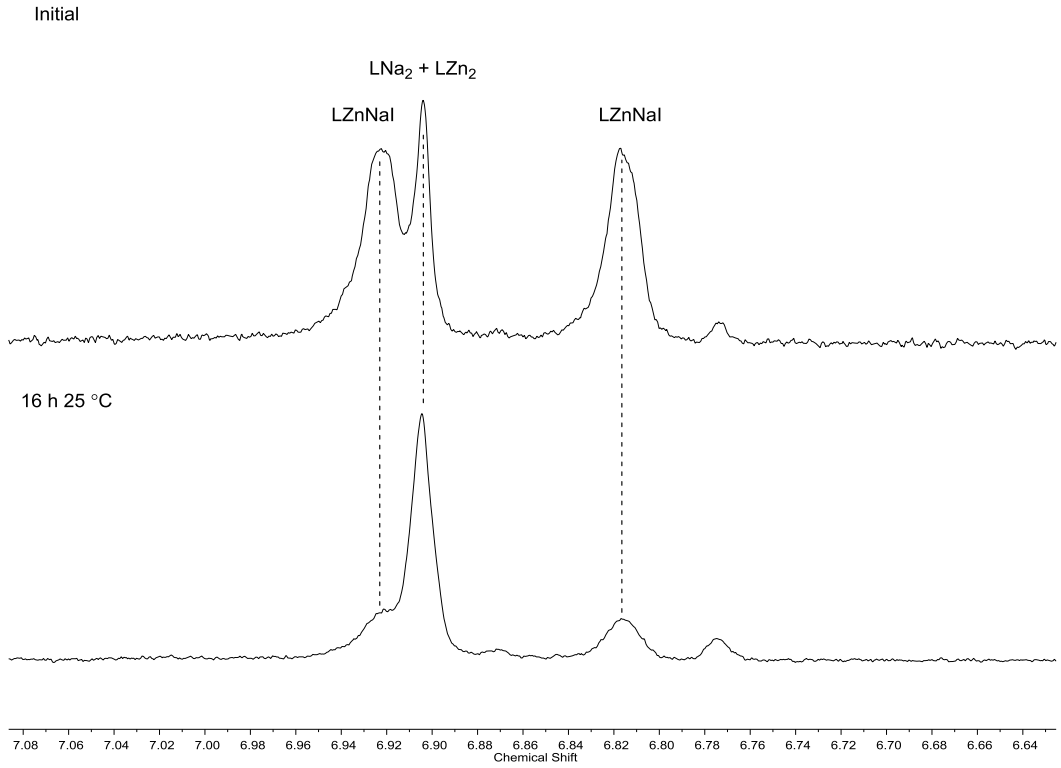


Figure S42: Metal redistribution of complex **6** towards complexes **2** and **4a** as observed in ^{1}H NMR (d_8-THF, 298 K).

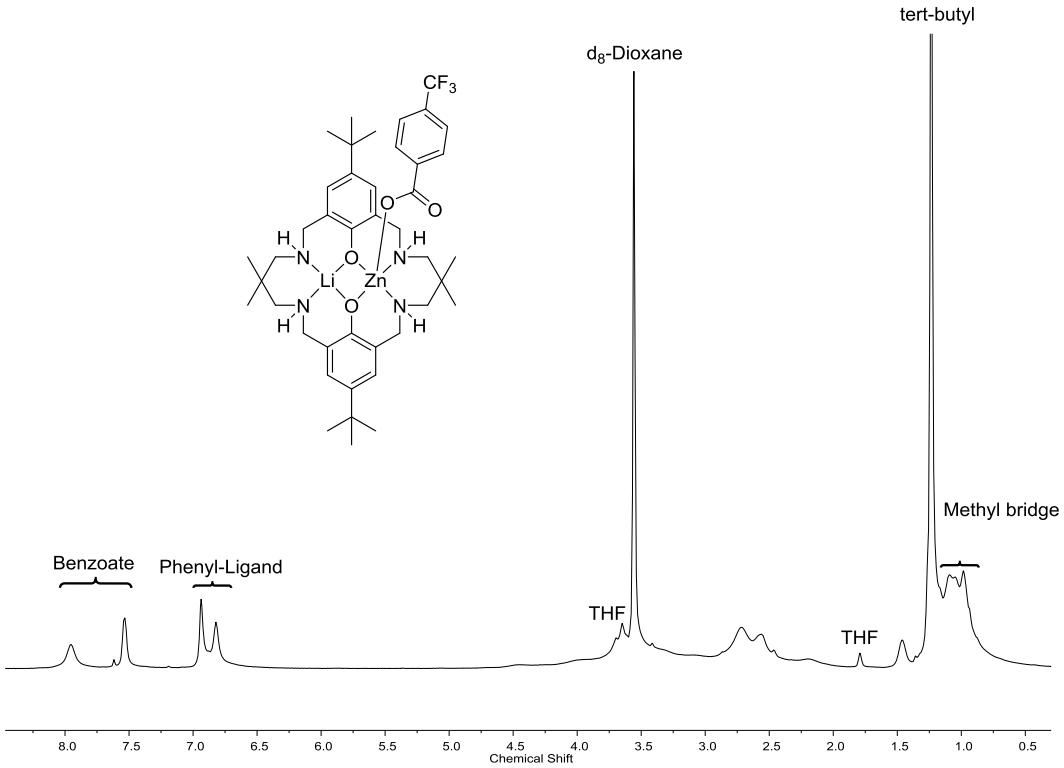


Figure S43: ^{1}H NMR of complex **5b** (d_8-dioxane, 403 K).

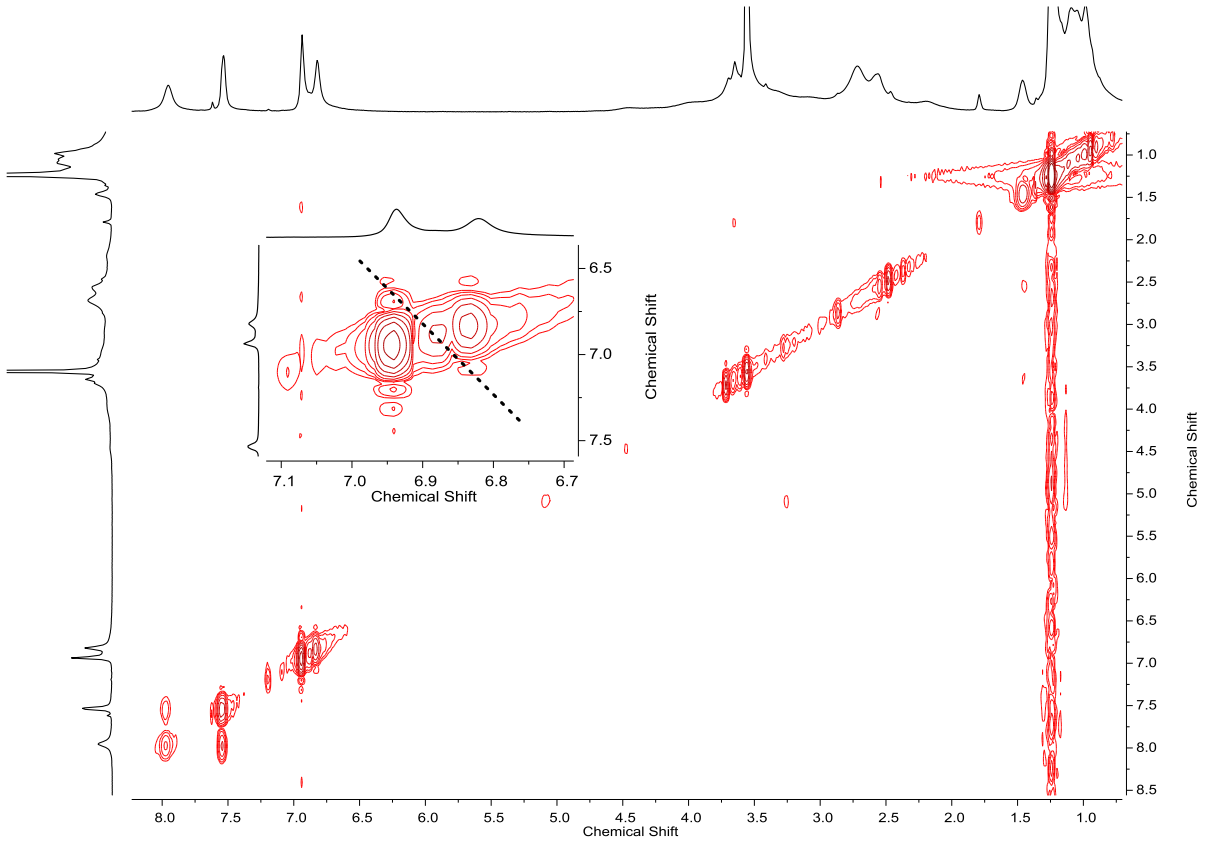


Figure S44: COSY NMR of complex **5b** (d_8-dioxane, 403 K).

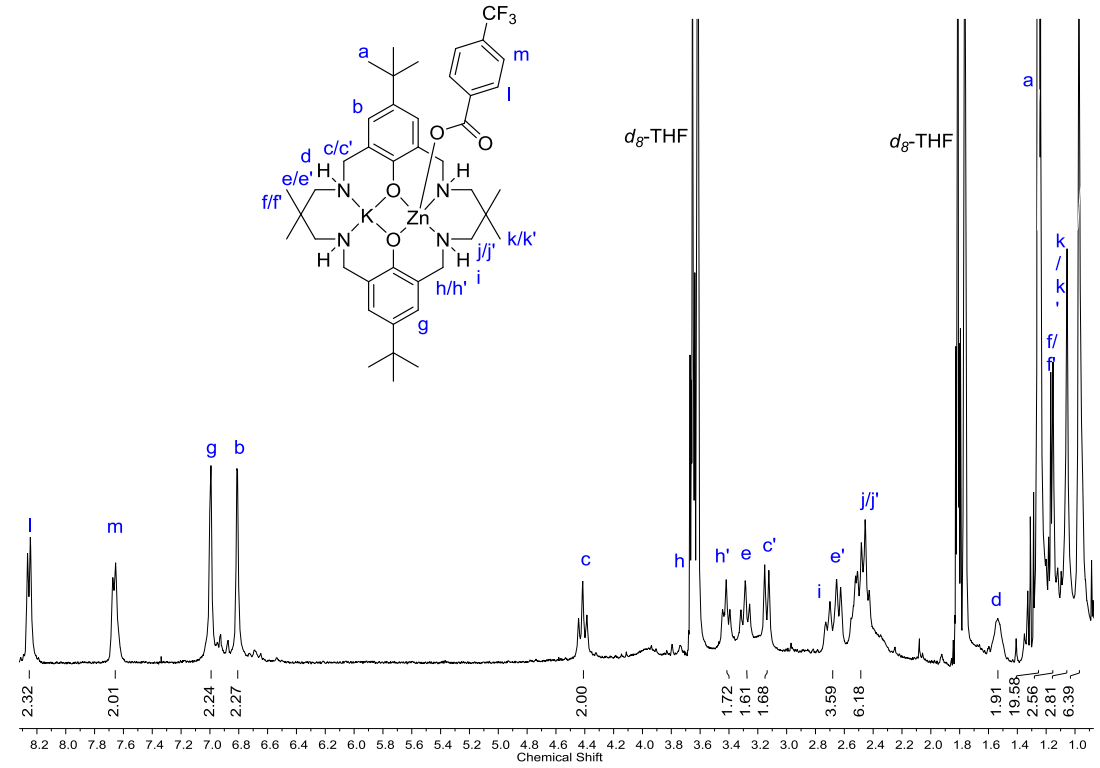


Figure S45: ^{1}H NMR of complex **7b** (d_8-THF, 298 K).

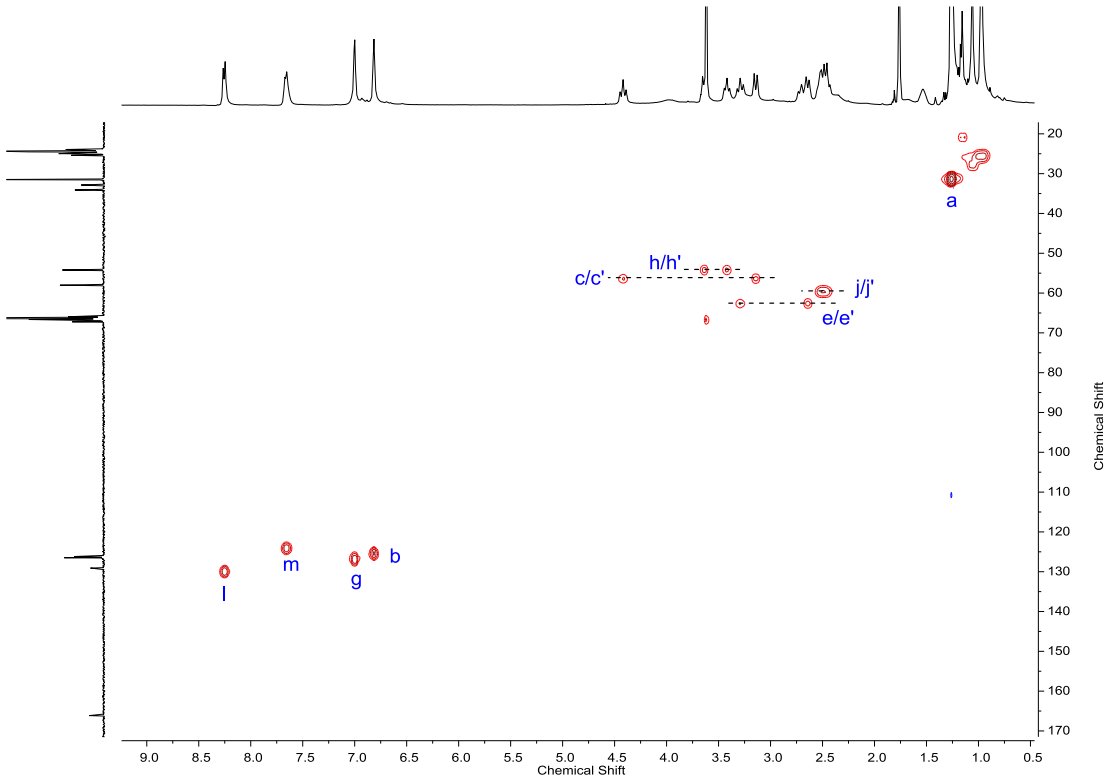


Figure S46: HSQC NMR of complex **7b** (d_8-THF, 298 K).

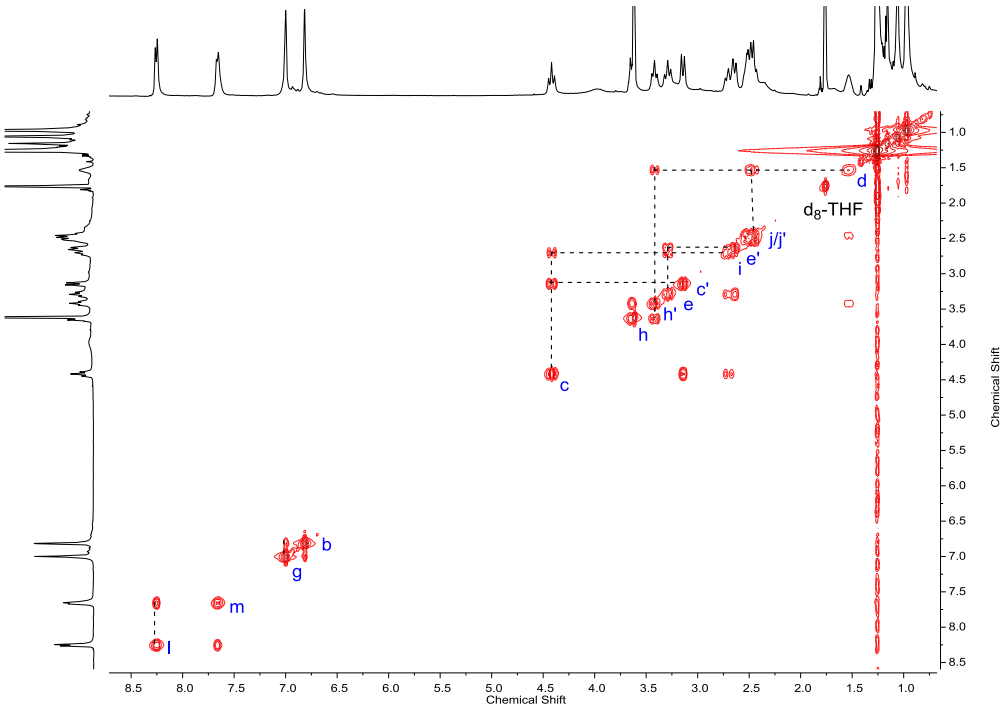


Figure S47: COSY NMR of complex **7b** (d_8-THF, 298K).

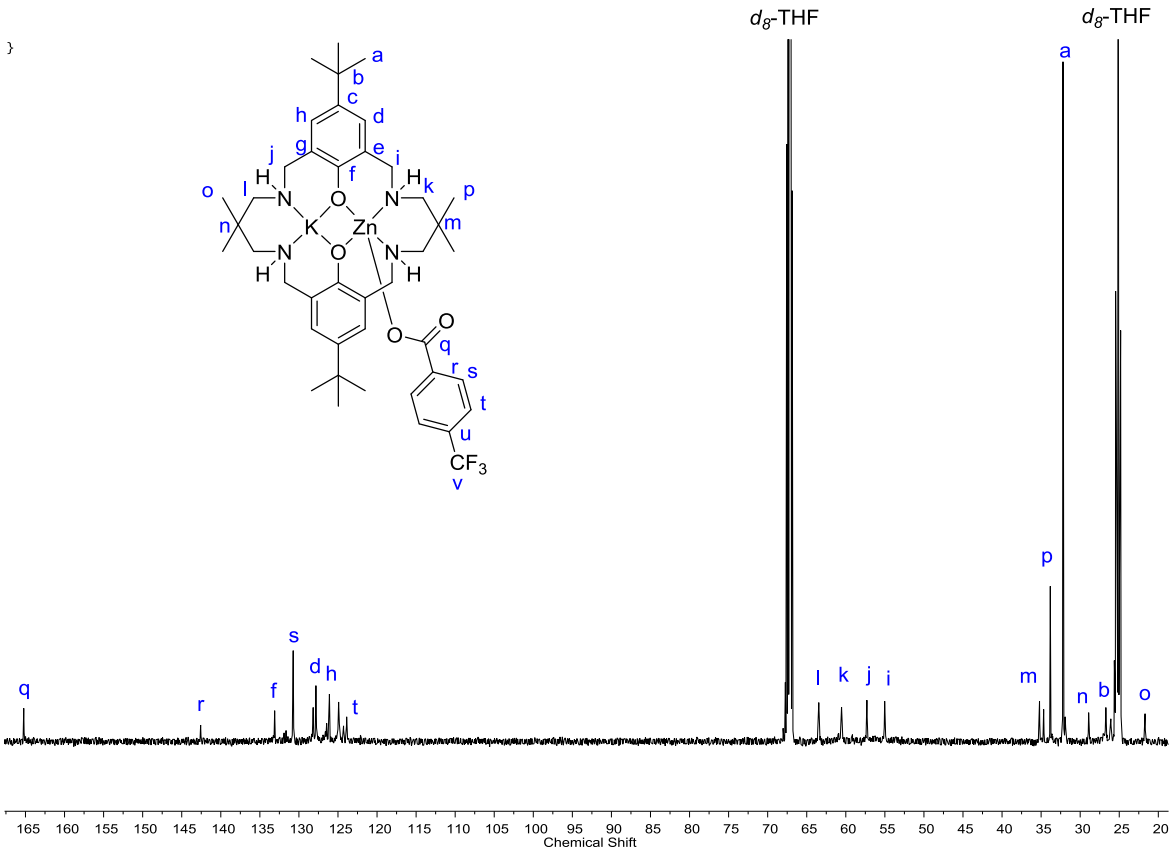


Figure S48: ^{13}C NMR of complex **7b** (d_8-THF, 298 K).

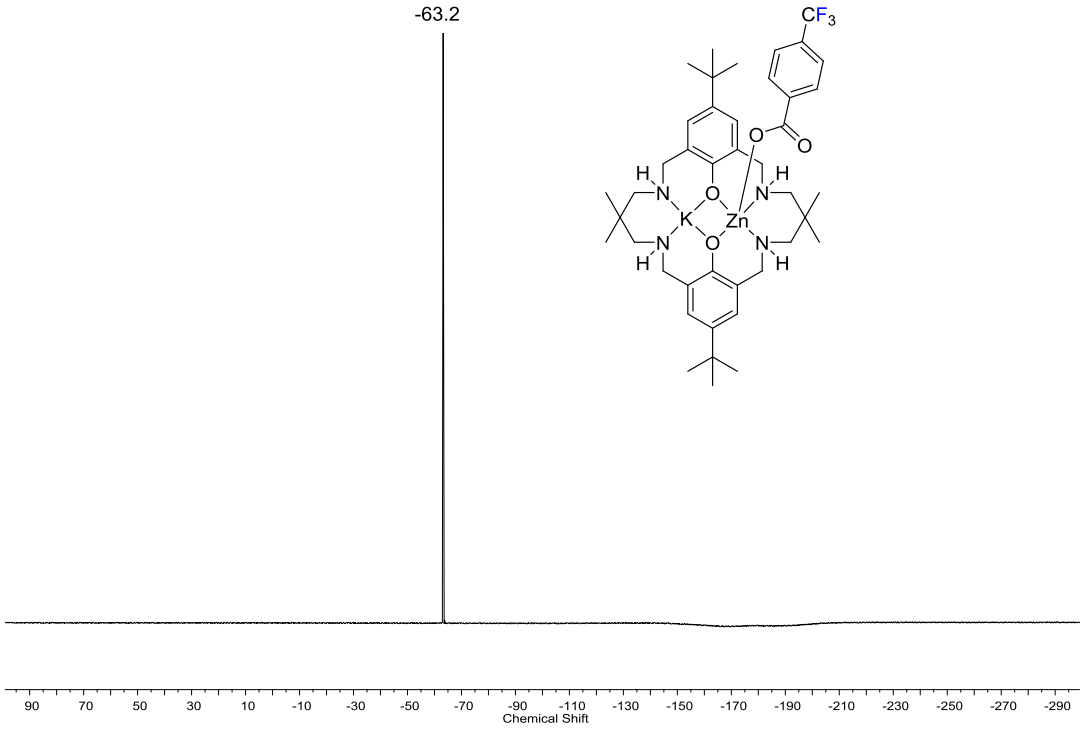


Figure S49: ^{19}F NMR of complex **7b** (d_8-THF, 298 K).

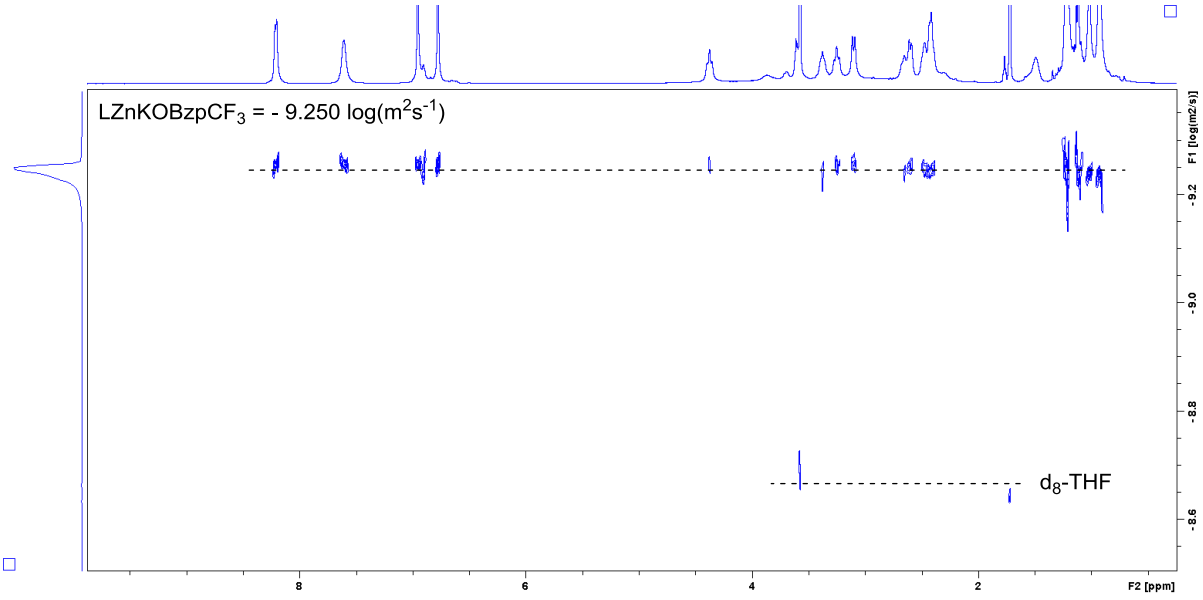


Figure S50: 2D DOSY NMR of complex **7b** (d_8-THF, 298 K).

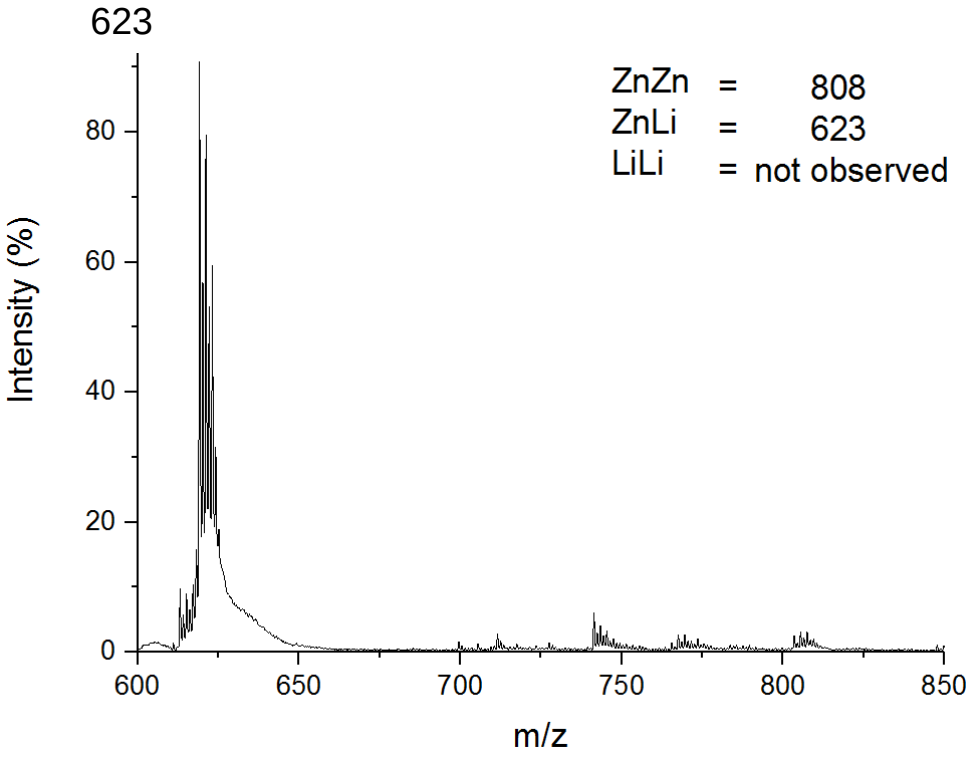


Figure S51: MALDI-ToF mass spectrum of complex **5a**

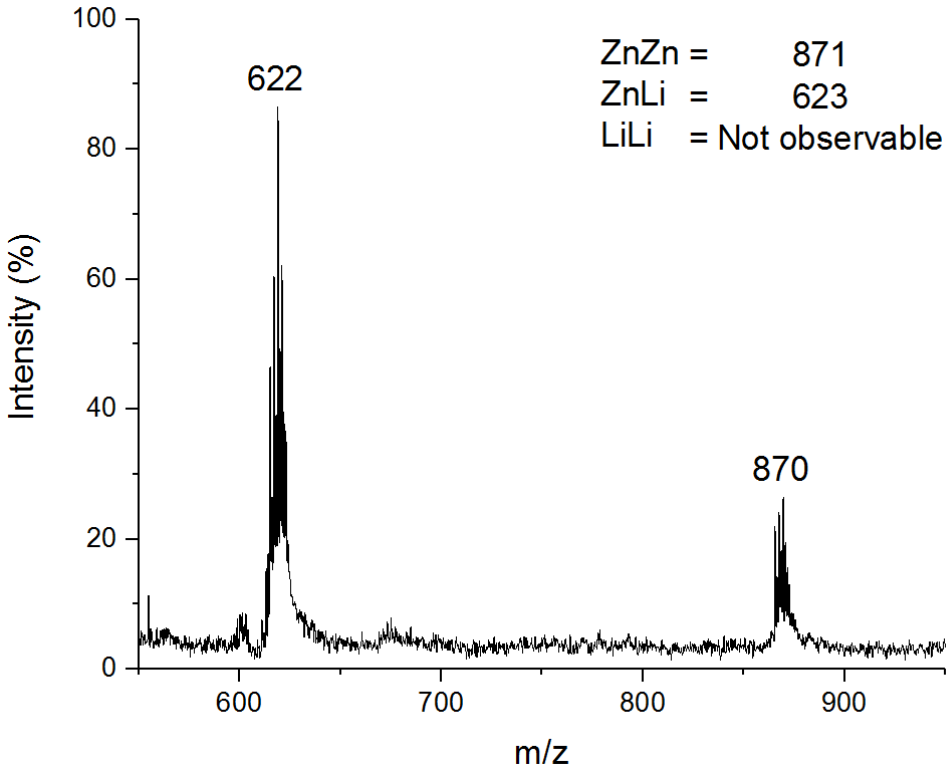


Figure 52: MALDI-ToF mass spectrum of complex **5b.**

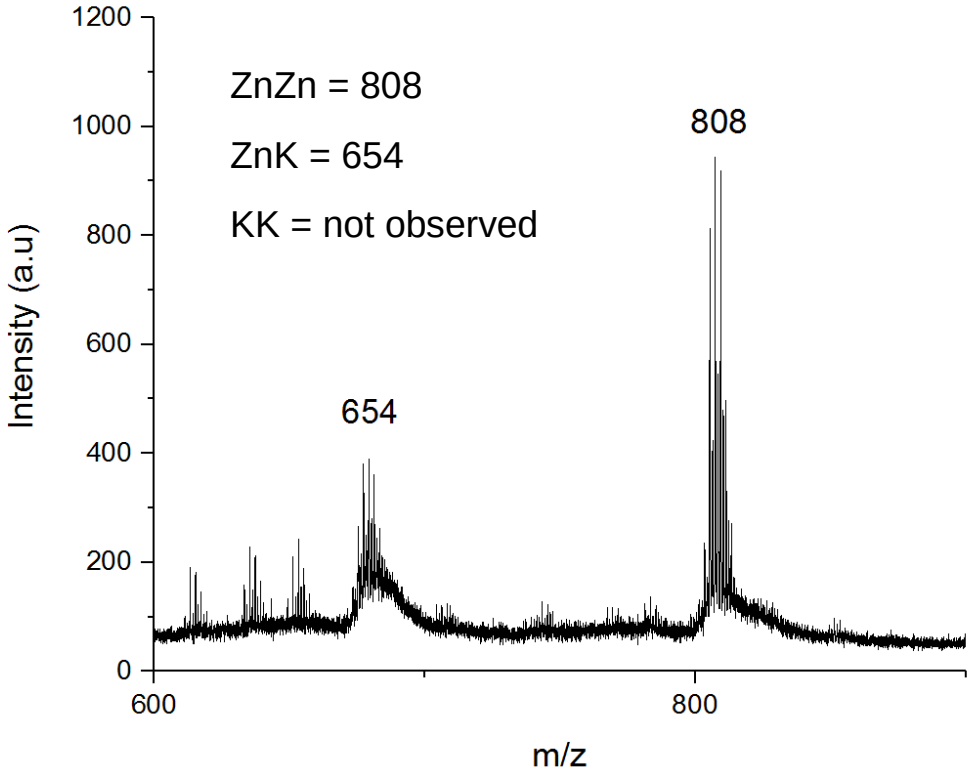


Figure S53: MALDI-ToF mass spectrum of complex **7a.**

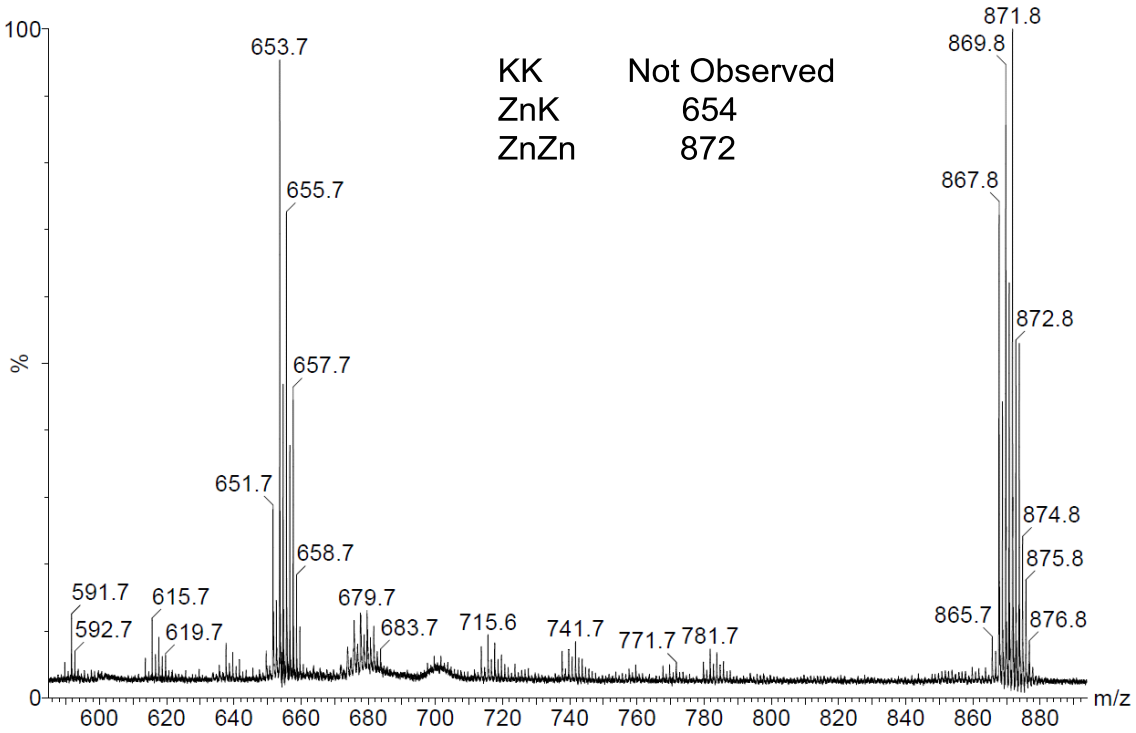


Figure S54: MALDI-ToF mass spectrum of complex **7b**.

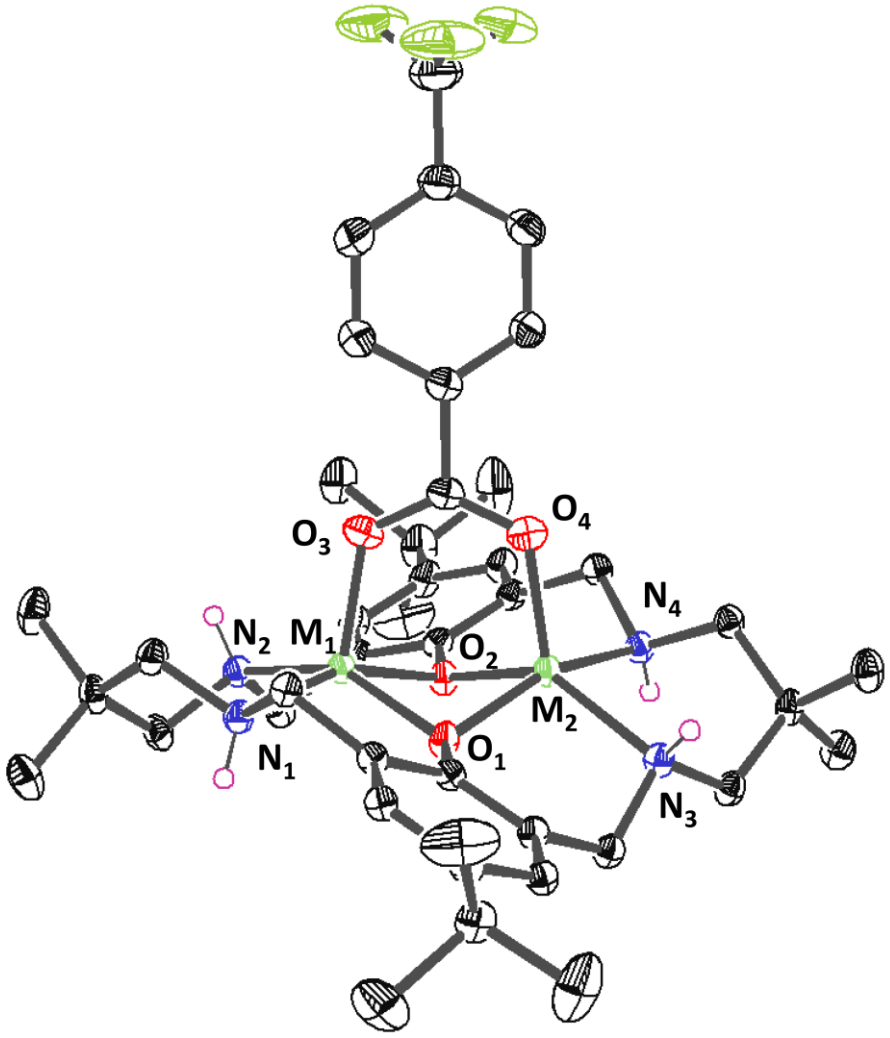


Figure S55: ORTEP representation of the molecular structure of **5b**, with disorder and hydrogen atoms (excluding N-H) omitted for clarity with thermal elipsoids represented at 40 %.

Table S5: Selected bond lengths (Å) and angles (°) for complex 5b

Bond	**Bond Length (Å)**	**Bond**	**Bond Angle (°)**
N (1) – M (1)	2.1653(16)	N (1) – M (1) – O (2)	157.9465(11)
N (2) – M (1)	2.1448(15)	N (2) – M (1) – O (1)	147.4608(17)
O (1) – M (1)	1.9838(13)	O (1) – M (1) – O (3)	102.241(3)
O (2) – M (1)	2.0026(13)	N (3) – M (2) – O (2)	142.9237(19)
O (3) – M (1)	1.9934(18)	N (4) – M (2) – O (1)	155.9289(11)
N (3) – M (2)	2.2248(17)	O (1) – M (2) – O (4)	99.605(3)
N (4) – M (2)	2.1520(17)	**Metal – Metal**	**Distance (Å)**
O (1) – M (2)	1.9880(16)		
O (2) – M (2)	1.9906(13)	M (1) – M (2)	2.8612(8)
O (4) – M (2)	2.0347(19)		

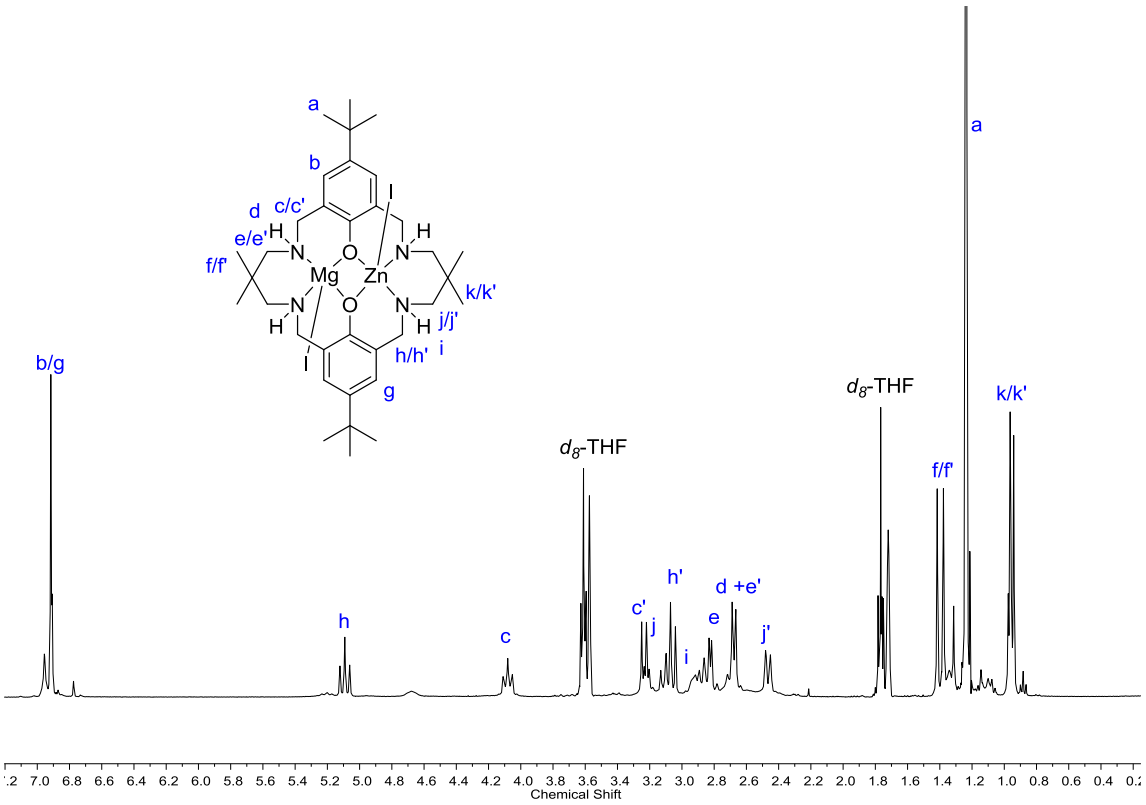


Figure S56: ^{1}H NMR of **8a** (d_8-THF, 298 K).

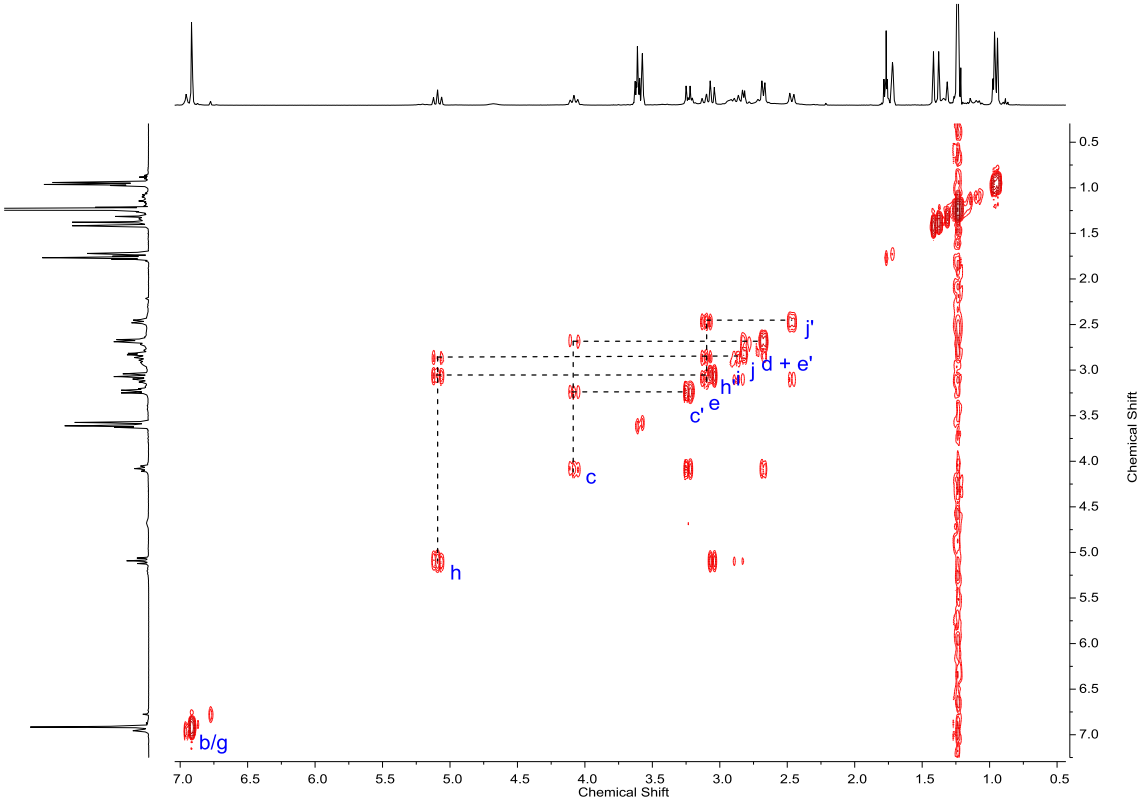


Figure S57: 2D COSY NMR of **8a** (d_8-THF, 298 K).

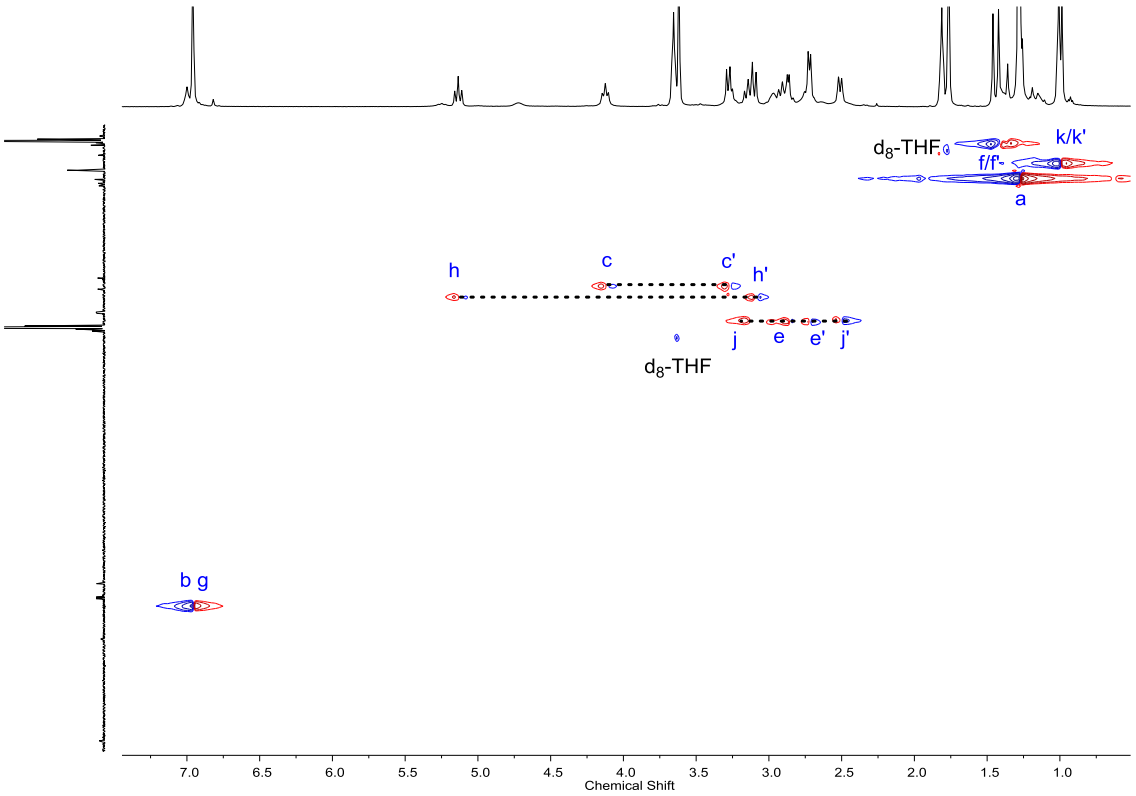


Figure S58: HSQC NMR of complex **8a** (d_8-THF, 298 K).

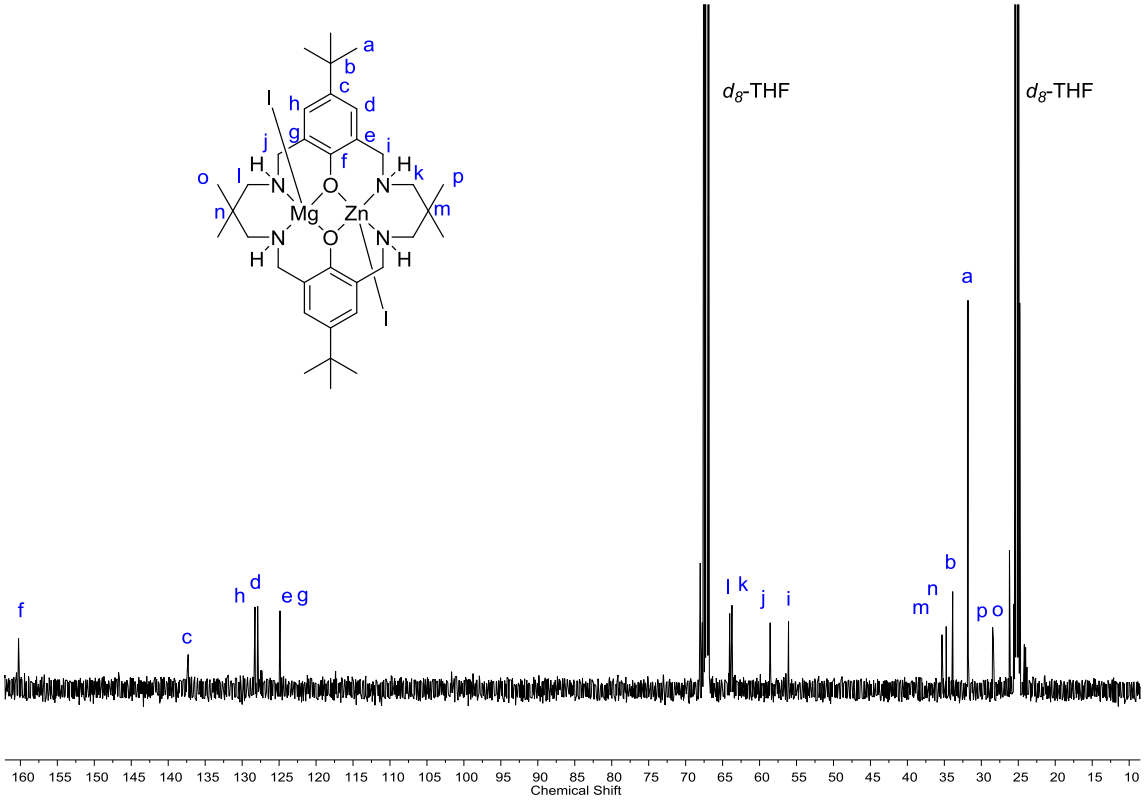


Figure S59: ^{13}C NMR of **8a** (d_8-THF, 298 K).

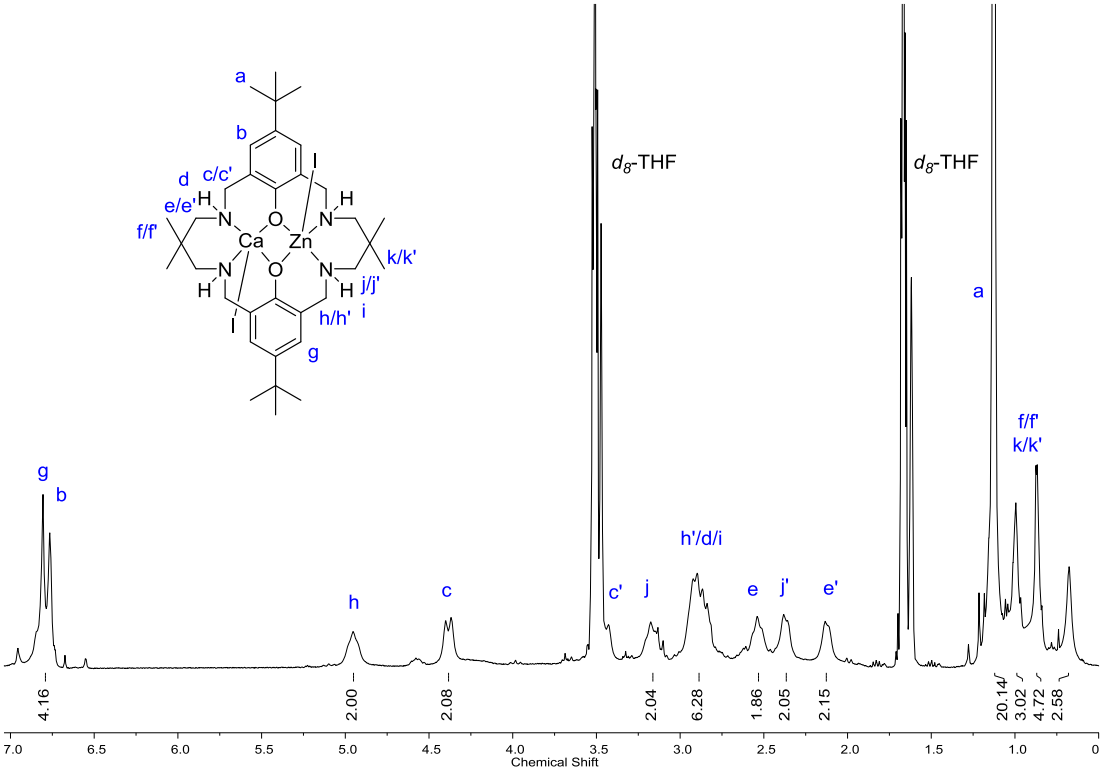


Figure S60: ^{1}H NMR of **9a** (d_8-THF, 298 K).

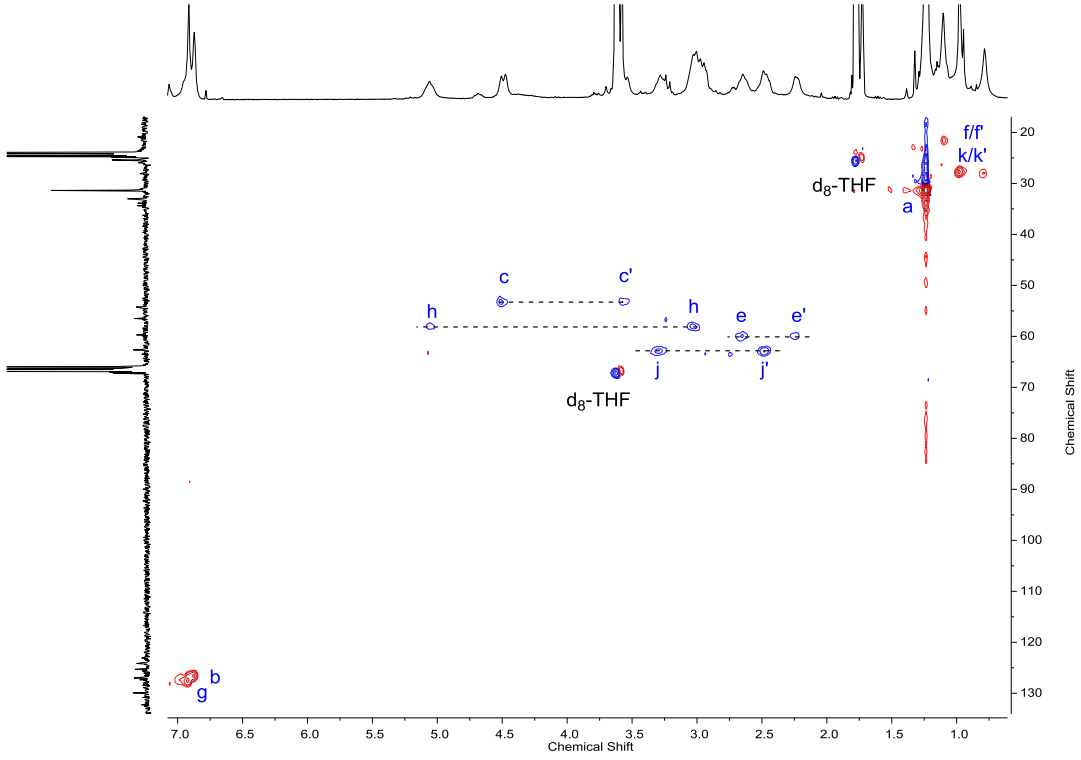


Figure S61: 2D HSQC NMR of **9a** (d_8-THF, 298 K).

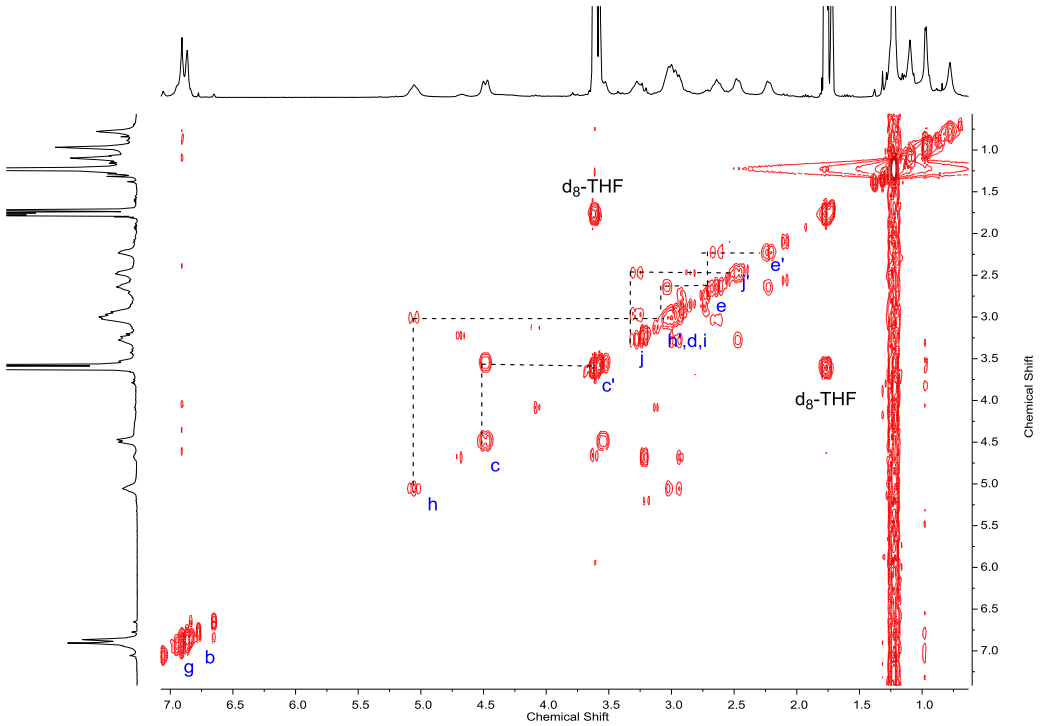


Figure S62: 2D COSY NMR of **9a** (d_8-THF, 298 K).

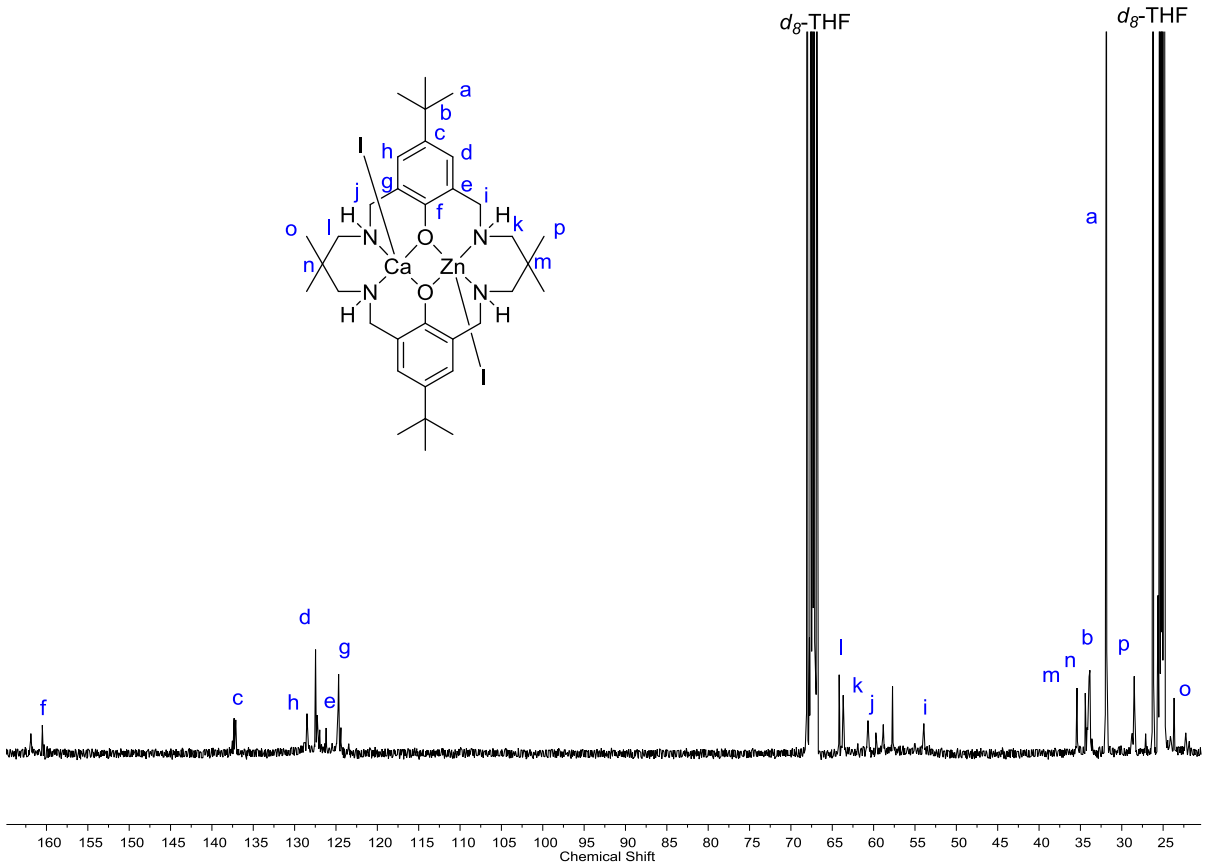


Figure S63: ^{13}C NMR of complex **9a** (d_8-THF, 298 K).

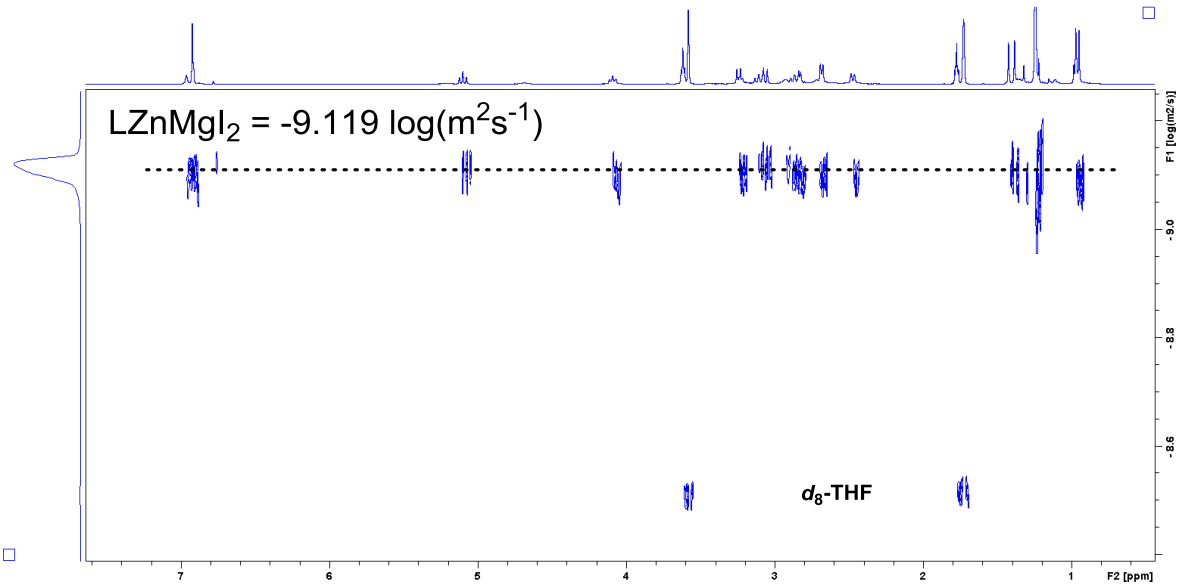


Figure S64: 2D DOSY NMR of **8a** (d_8-THF, 298 K).

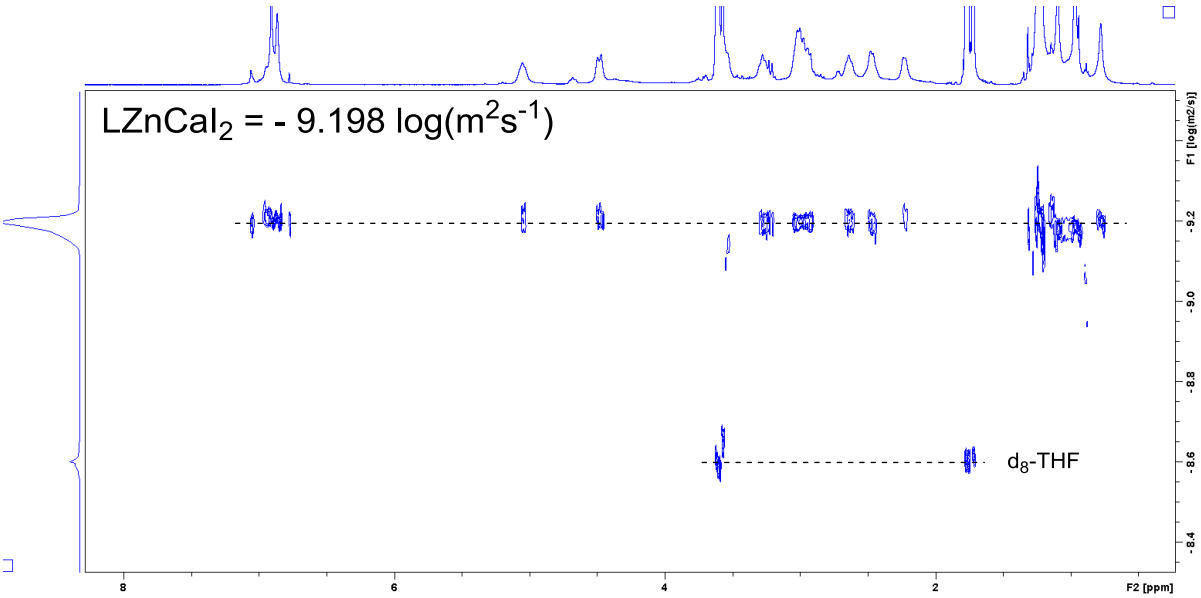


Figure S65: 2D DOSY NMR of **9a** (d_8-THF, 298 K).

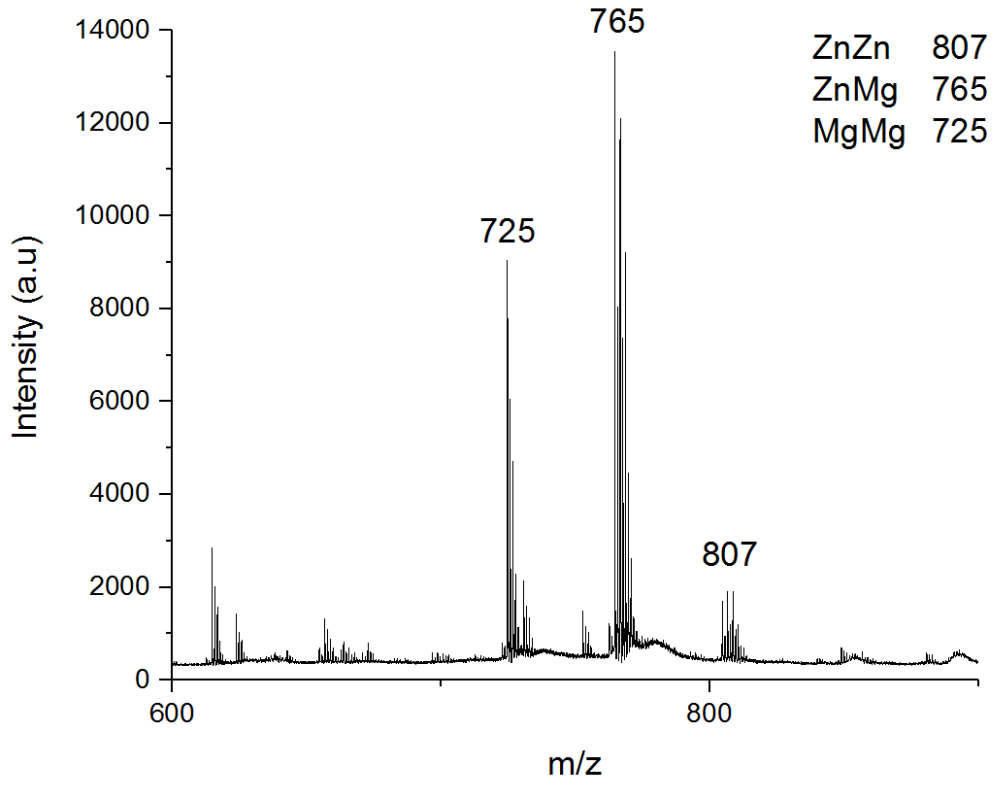


Figure S66: MALDI-ToF of complex **8a**.

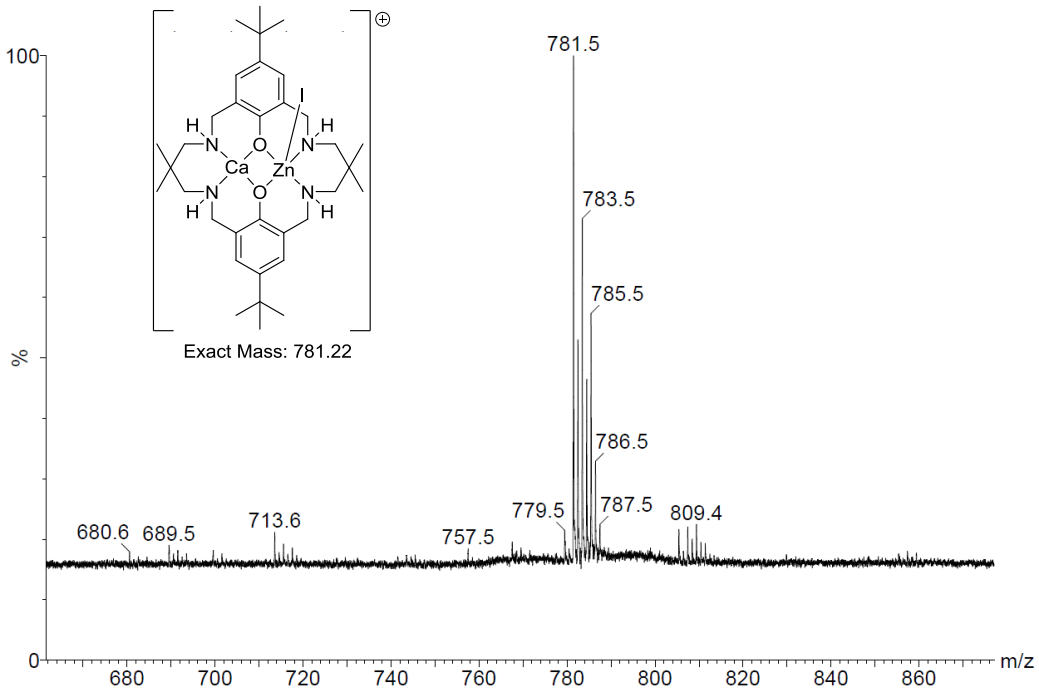


Figure S67: MALDI-ToF mass spectrum of **9a.**

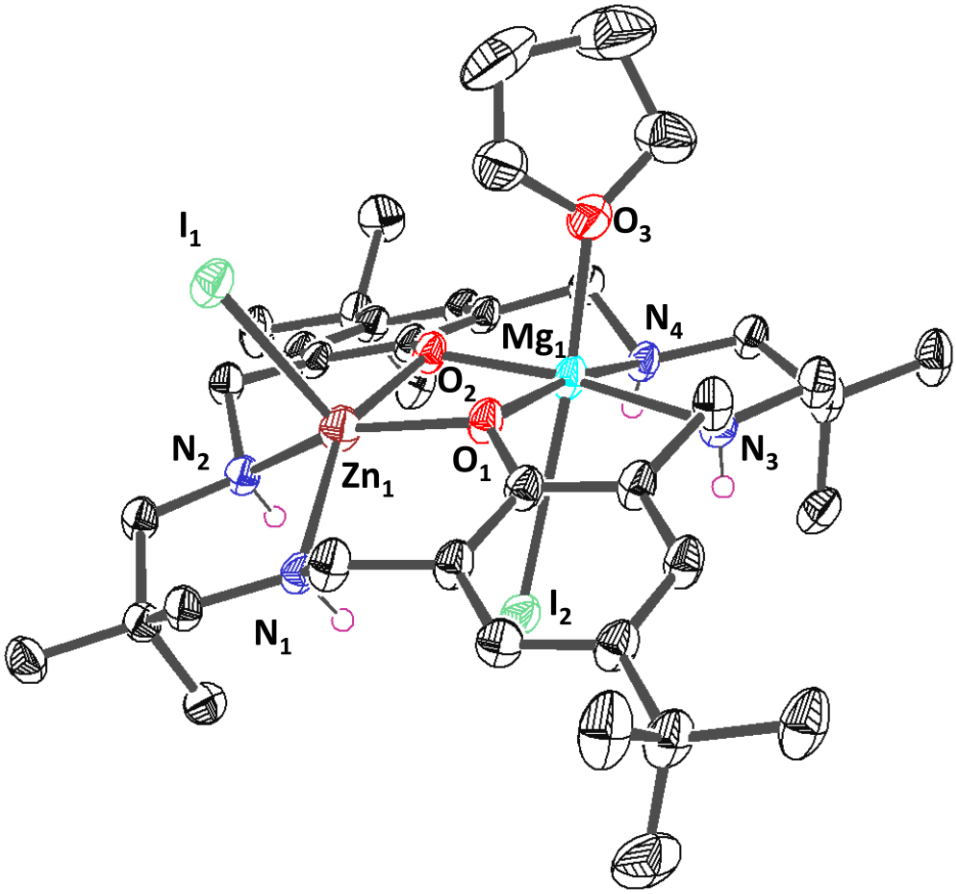


Figure S68: ORTEP representation of the molecular structure of **8a**, with disorder and hydrogen atoms (excluding N-H) omitted for clarity with thermal ellipsoids represented at 40 %.

Table S6: Selected bond lengths (Å) and angles (°) for complex **8a**.

Bond	Bond Length (Å)	Bond	Bond Angle (°)
N (1) – Zn (1)	2.136(4)	N (1) – Zn (1) – O (2)	150.02(15)
N (2) – Zn (1)	2.134(4)	N (2) – Zn (1) – O (1)	155.15(16)
O (1) – Zn (1)	2.089(3)	I (1) – Zn (1) – O (1)	103.78(11)
O (2) – Zn (1)	2.105(3)	N (3) – Mg (1) – O (2)	172.89(19)
I (1) – Zn (1)	2.6825(9)	N (4) – Mg (1) – O (1)	169.54(19)
I (2) – Zn (1)	3.59890(12)	O (3) – Mg (1) – O (1)	93.83(18)
N (3) – Mg (1)	2.149(4)	I (2) – Mg (1) – O (1)	172.83(14)
N (4) – Mg (1)	2.156(4)		
O (1) – Mg (1)	2.040(4)	**Metal – Metal**	**Distance (Å)**
O (2) – Mg (1)	2.017(4)		
O (3) – Mg (1)	2.137(5)	Zn (1) – Mg (1)	3.0616(17)
I (2) – Mg (1)	3.2158(18)		

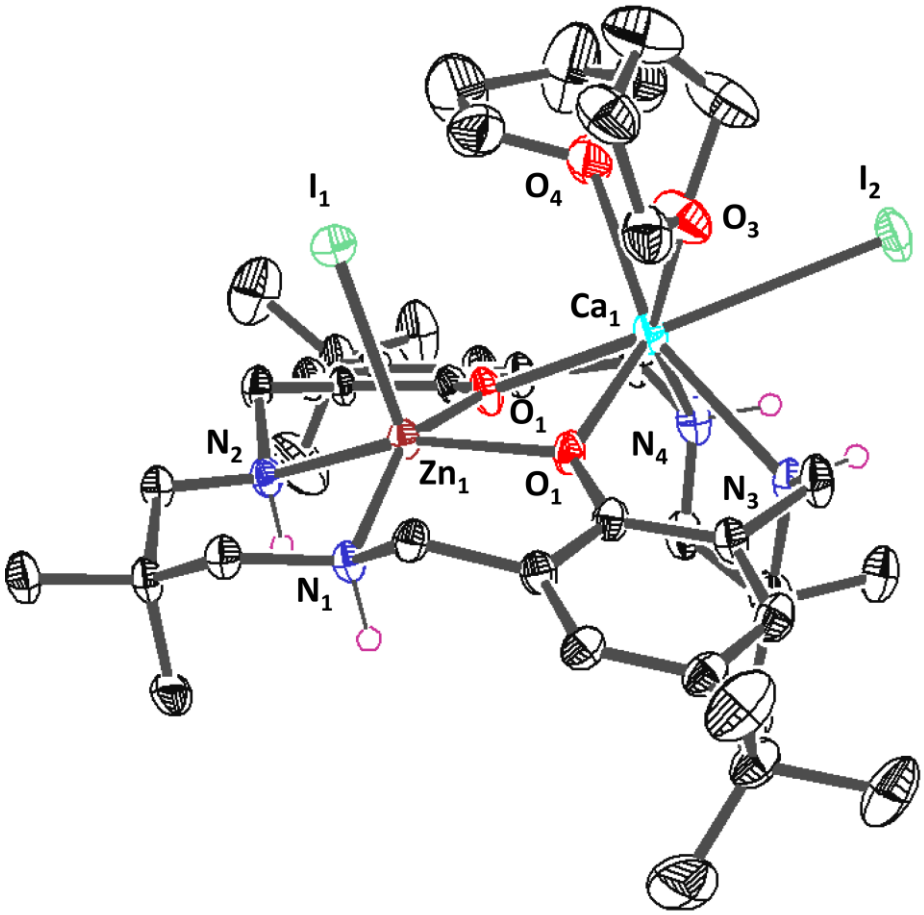


Figure S69: ORTEP representation of the molecular structure of **9a**, with disorder and hydrogen atoms (excluding N-H) omitted for clarity with thermal ellipsoids represented at 40 %.

Table S7: Selected bond lengths (Å) and angles (°) for complex **9a**.

Bond	Bond Length (Å)	Bond	Bond Angle (°)
N (1) – Zn (1)	2.126(4)	N (1) – Zn (1) – O (2)	153.43(17)
N (2) – Zn (1)	2.142(4)	N (2) – Zn (1) – O (1)	157.25(16)
O (1) – Zn (1)	2.101(3)	I (1) – Zn (1) – O (1)	101.80(11)
O (2) – Zn (1)	2.074(4)	N (3) – Ca (1) – O (2)	114.67(16)
I (1) – Zn (1)	2.6823(8)	N (4) – Ca (1) – O (1)	114.14(16)
N (3) – Ca (1)	2.494(5)	O (3) – Ca (1) – O (1)	81.72(16)
N (4) – Ca (1)	2.490(5)	I (2) – Ca (1) – O (1)	140.52(9)
O (1) – Ca (1)	2.327(4)		
O (2) – Ca (1)	2.314(4)	**Metal – Metal**	**Distance (Å)**
O (3) – Ca (1)	2.428(10)		
O (4) – Ca (1)	2.493(5)	Zn (1) – Ca (1)	3.3534(12)
I (2) – Ca (1)	3.3674(11)		

8.1.2 Chapter 3: Group 13, Zinc(II) Heterodinuclear Catalysts

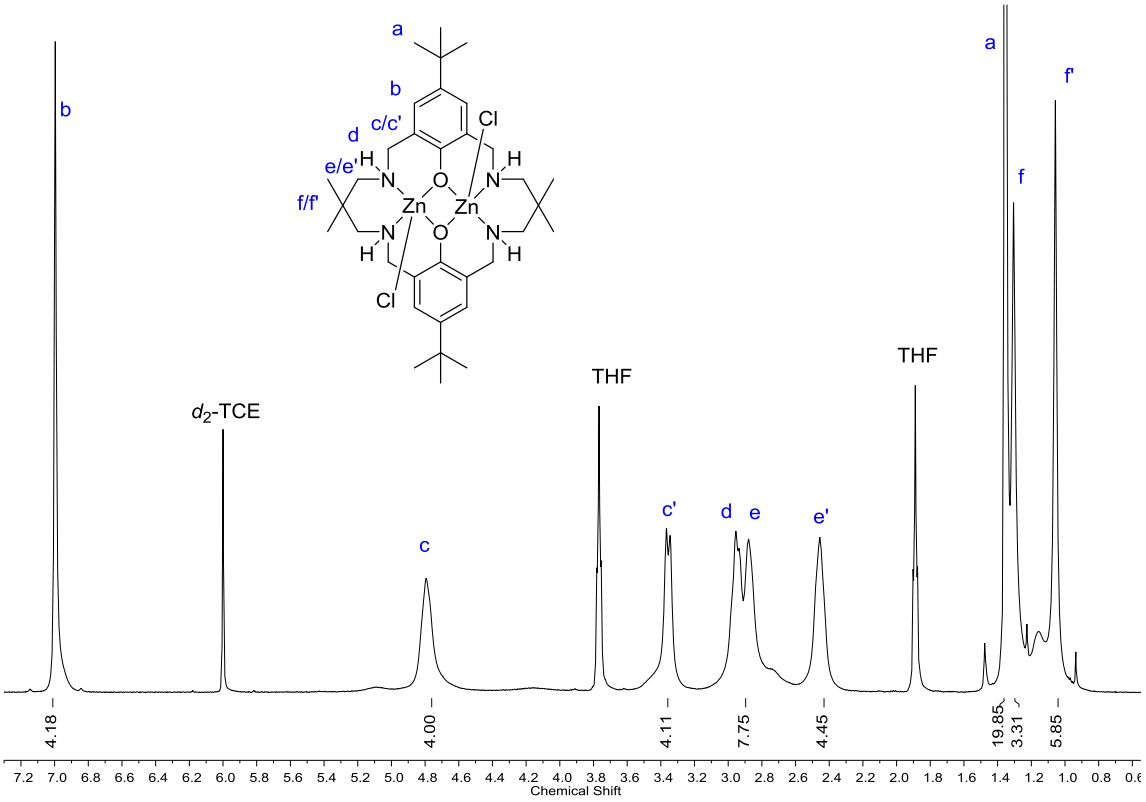


Figure S70: ^{1}H NMR of **10** (d_2 –TCE, 403 K)

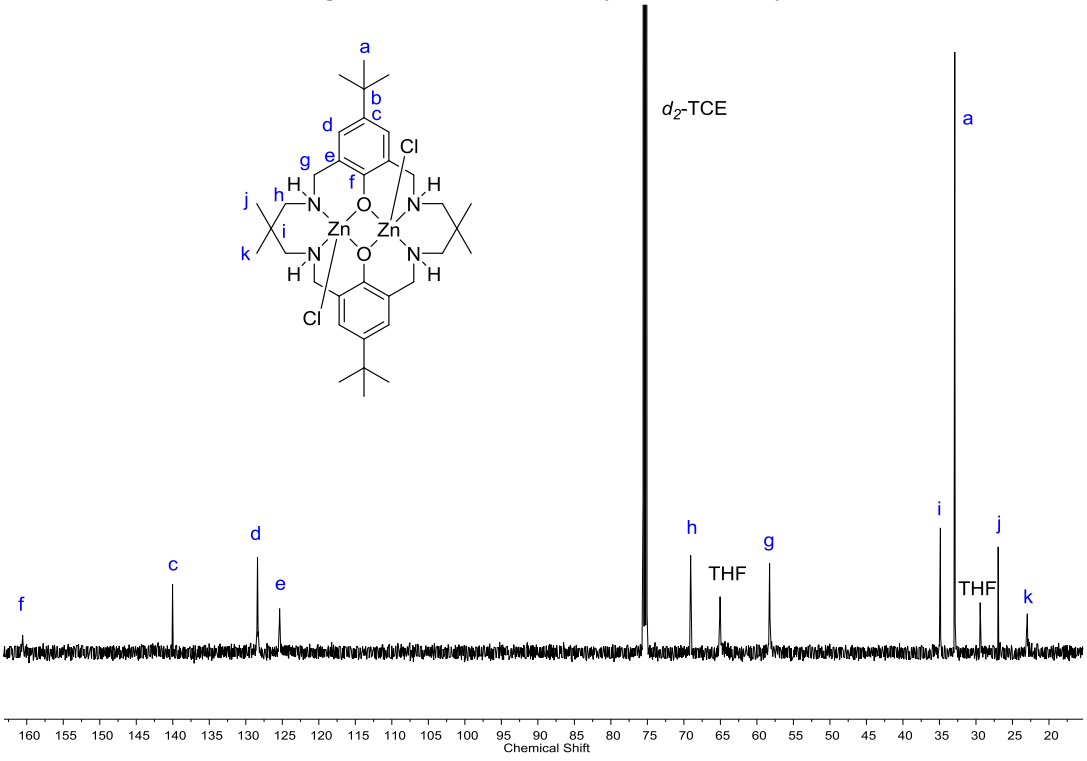


Figure S71: ^{13}C NMR of **10** (d_2 – TCE, 403 K)

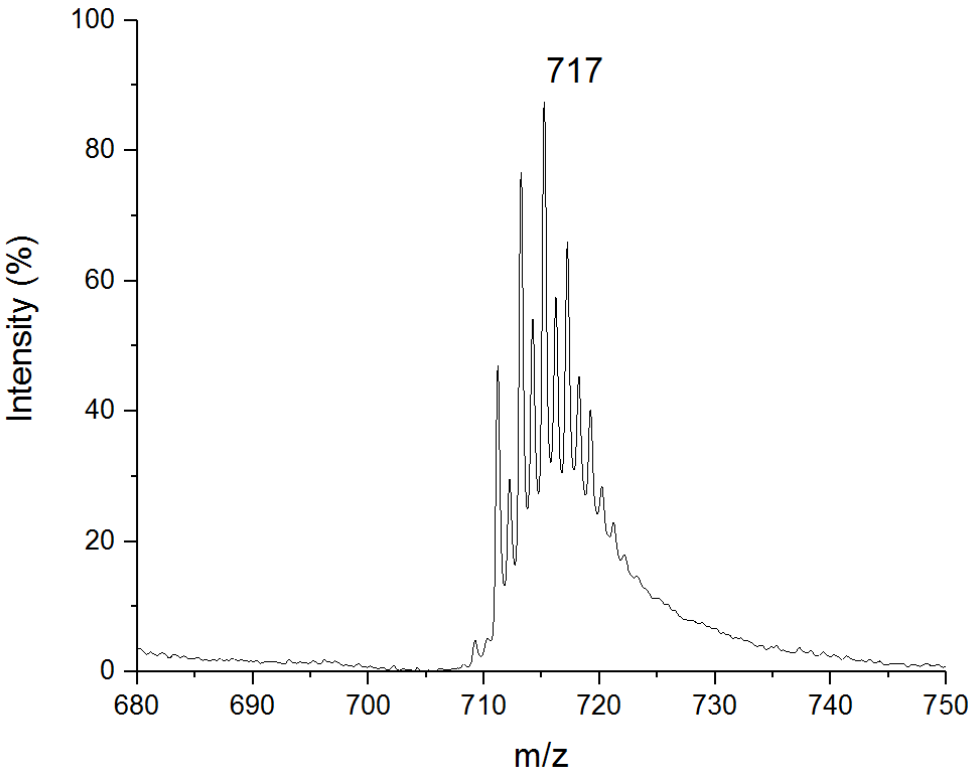


Figure S72: MALDI – ToF mass spectrum of **10**

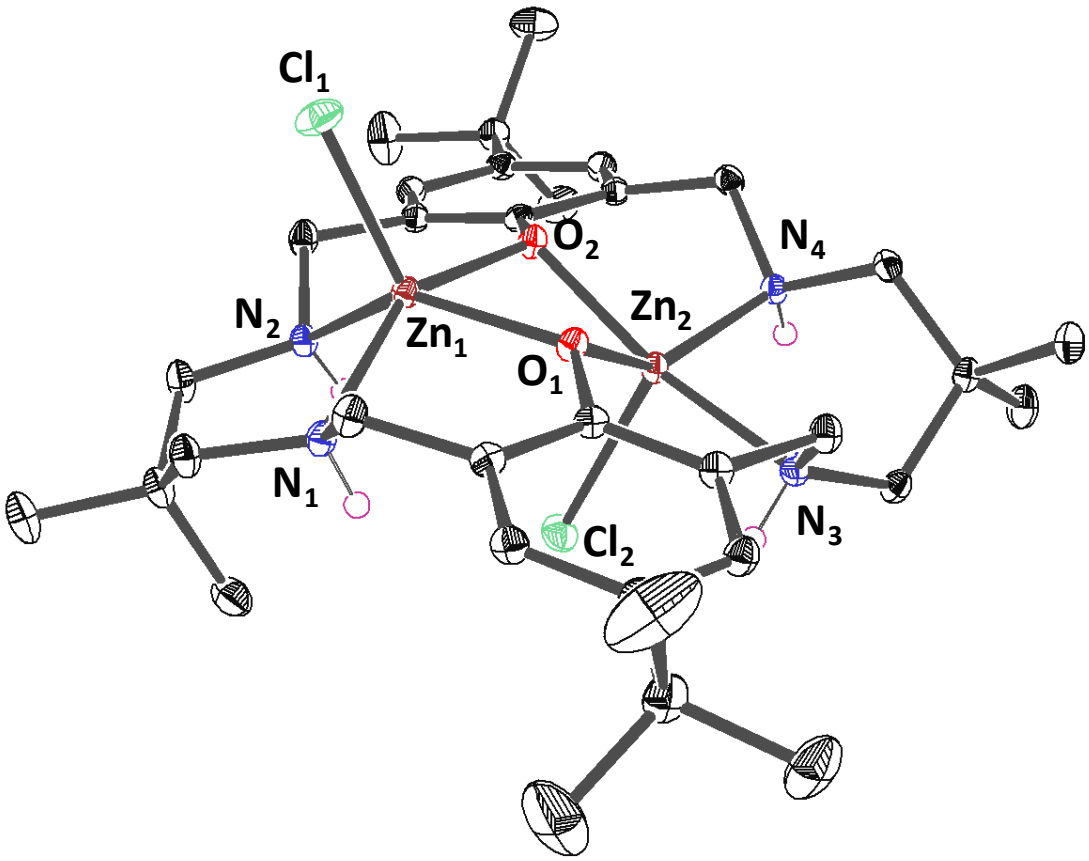


Figure S73: ORTEP representation of the molecular structure of **10** with disorder and hydrogen atoms (excluding NH) omitted for clarity with thermal ellipsoids represented at 40 % probability.

Table S8: Selected bond lengths (Å) and angles (°) for complex **10**.

Bond	**Bond Length (Å)**	**Bond**	**Bond Angle (°)**
N (1) – Zn (1)	2.1063(12)	N (1) – Zn (1) – O (2)	162.32(5)
N (2) – Zn (1)	2.1085(12)	N (2) – Zn (1) – O (1)	141.29(4)
O (1) – Zn (1)	2.0772(10)	Cl (1) – Zn (1) – O (1)	100.90(3)
O (2) – Zn (1)	2.0353(10)	N (3) – Zn (2) – O (2)	148.16(5)
Cl (1) – Zn (1)	2.3114(4)	N (4) – Zn (2) – O (1)	139.44(4)
N (3) – Zn (2)	2.1123(13)	Cl (2) – Zn (2) – O (1)	112.94(3)
N (4) – Zn (2)	2.1432(12)	**Metal – Metal**	**Distance (Å)**
O (1) – Zn (2)	2.1129(13)		
O (2) – Zn (2)	2.0486(10)	Zn (1) – Zn (2)	3.0405(3)
Cl (2) – Zn (2)	2.2588(4)		

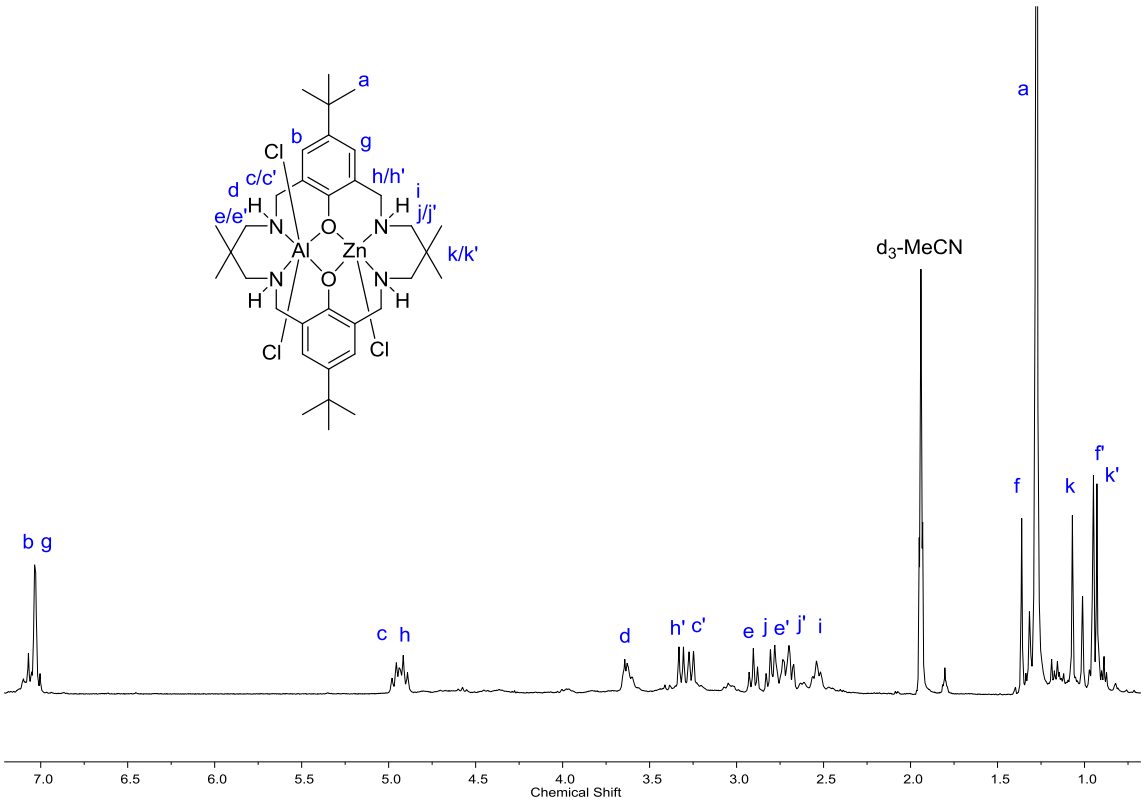


Figure S74: ^{1}H NMR of **11** (d_3 – MeCN, 298 K)

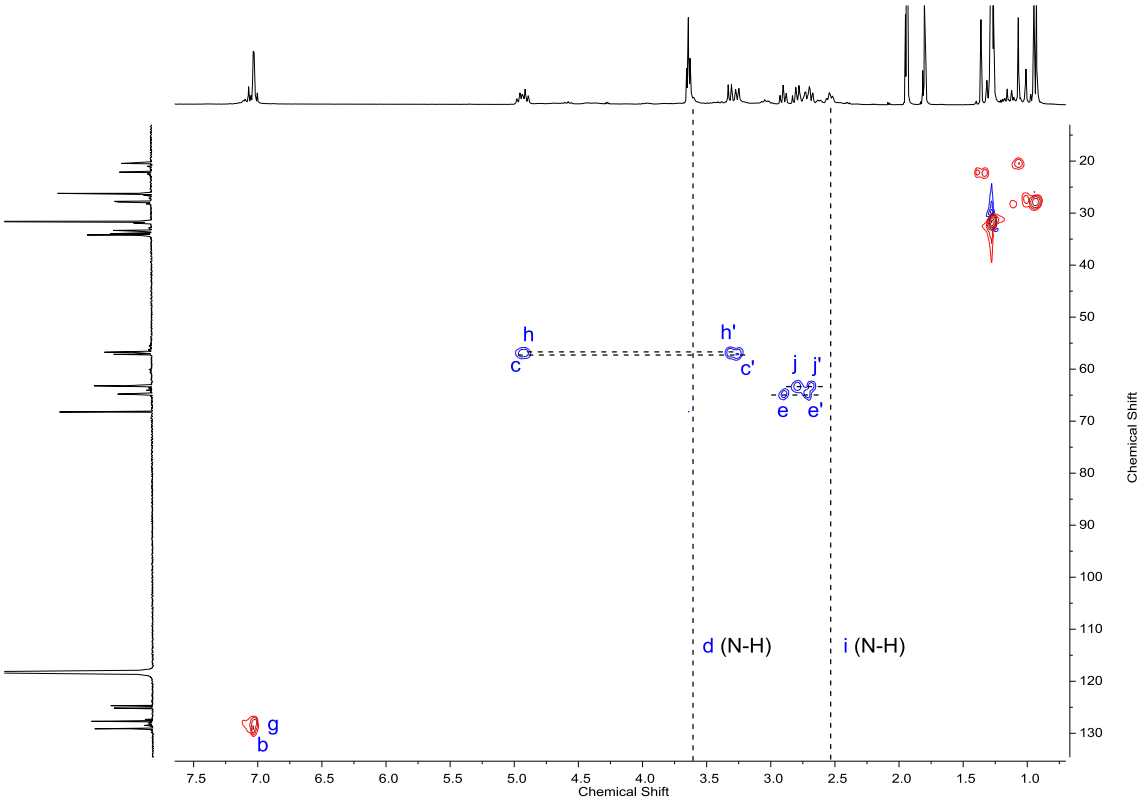


Figure S75: 2D HSQC NMR of **11** (d_8 – THF, 298 K)

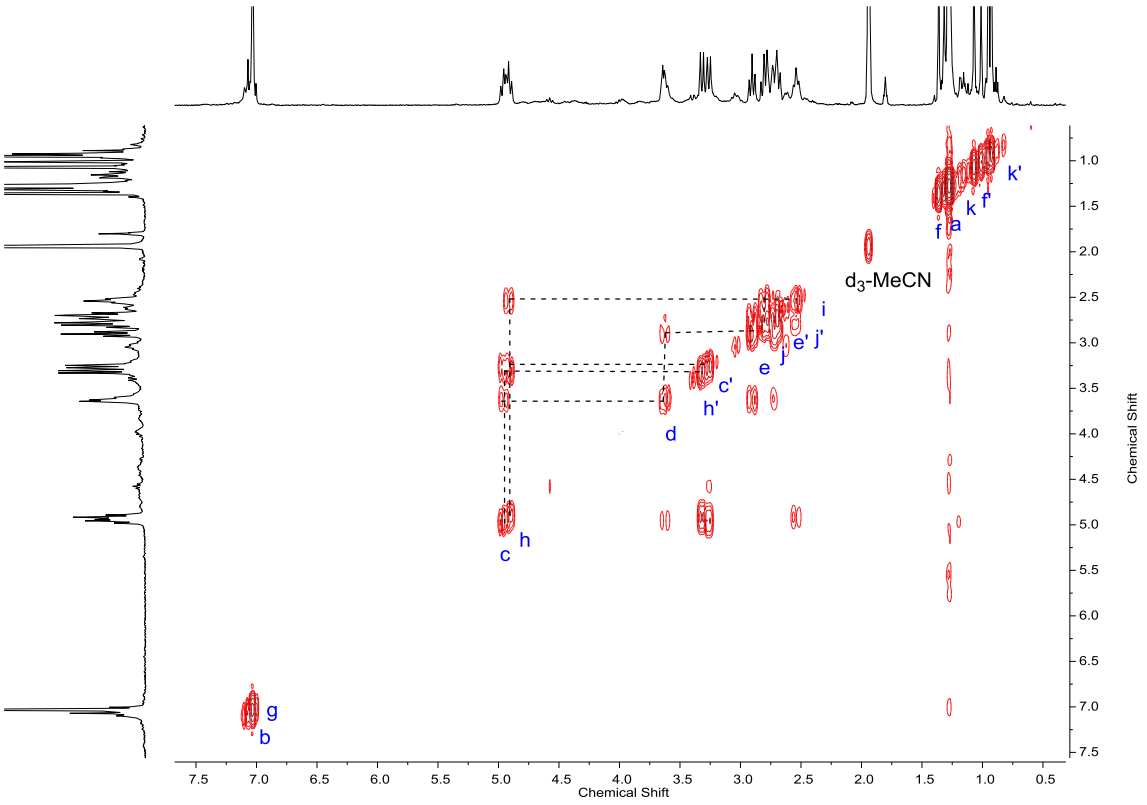


Figure S76: 2D COSY NMR of **11** (d_8 – THF, 298 K)

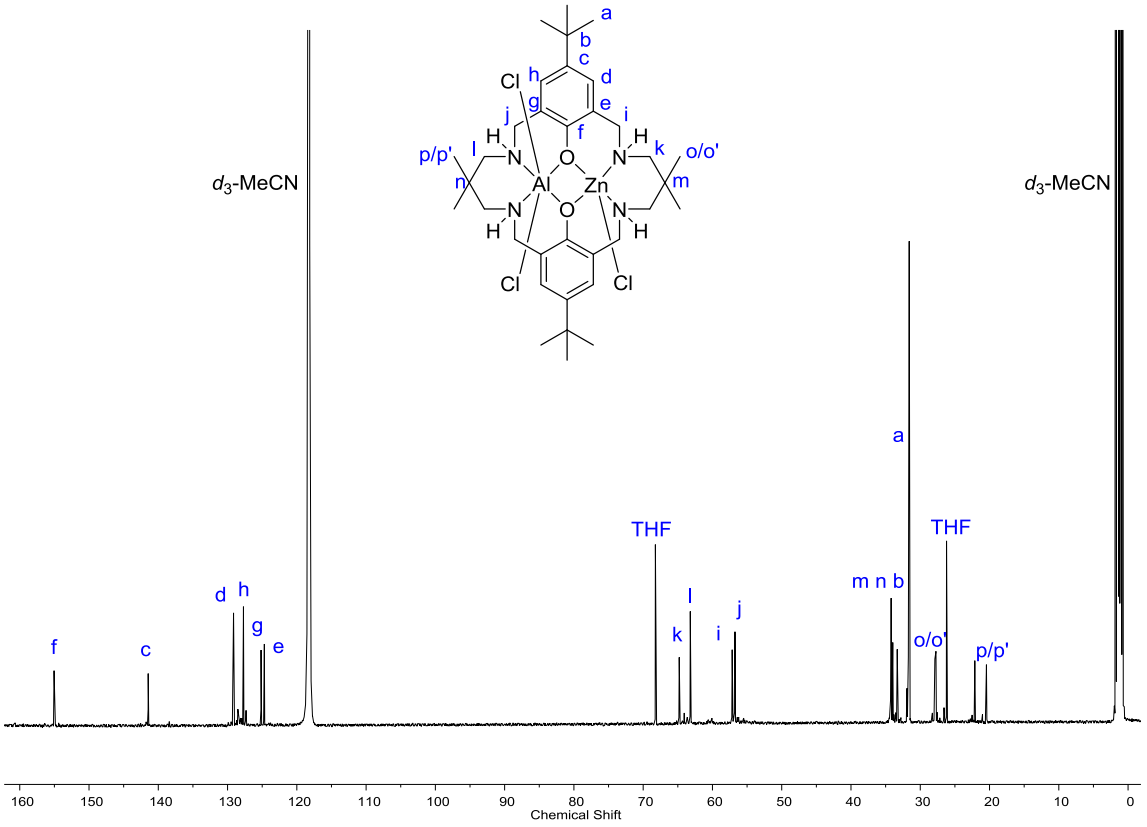


Figure S77: ^{13}C NMR of **11** (d_3 – MeCN, 298 K)

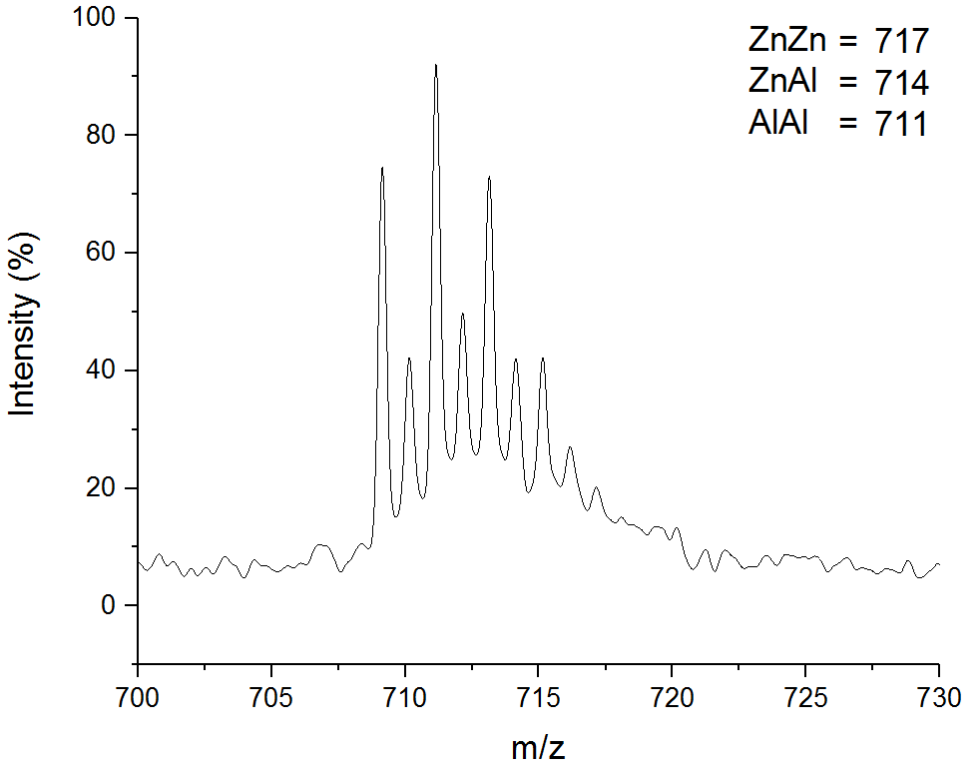


Figure S78: MALDI – ToF mass spectrum of **11**

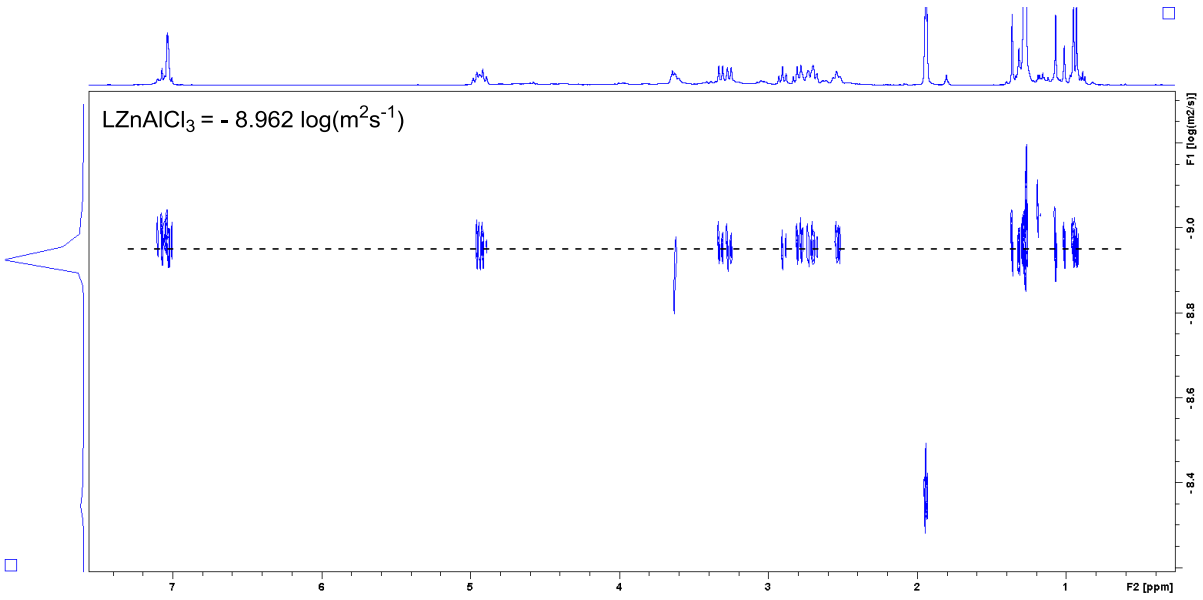


Figure S79: 2D DOSY NMR of **11** (d_3-MeCN, 298 K)

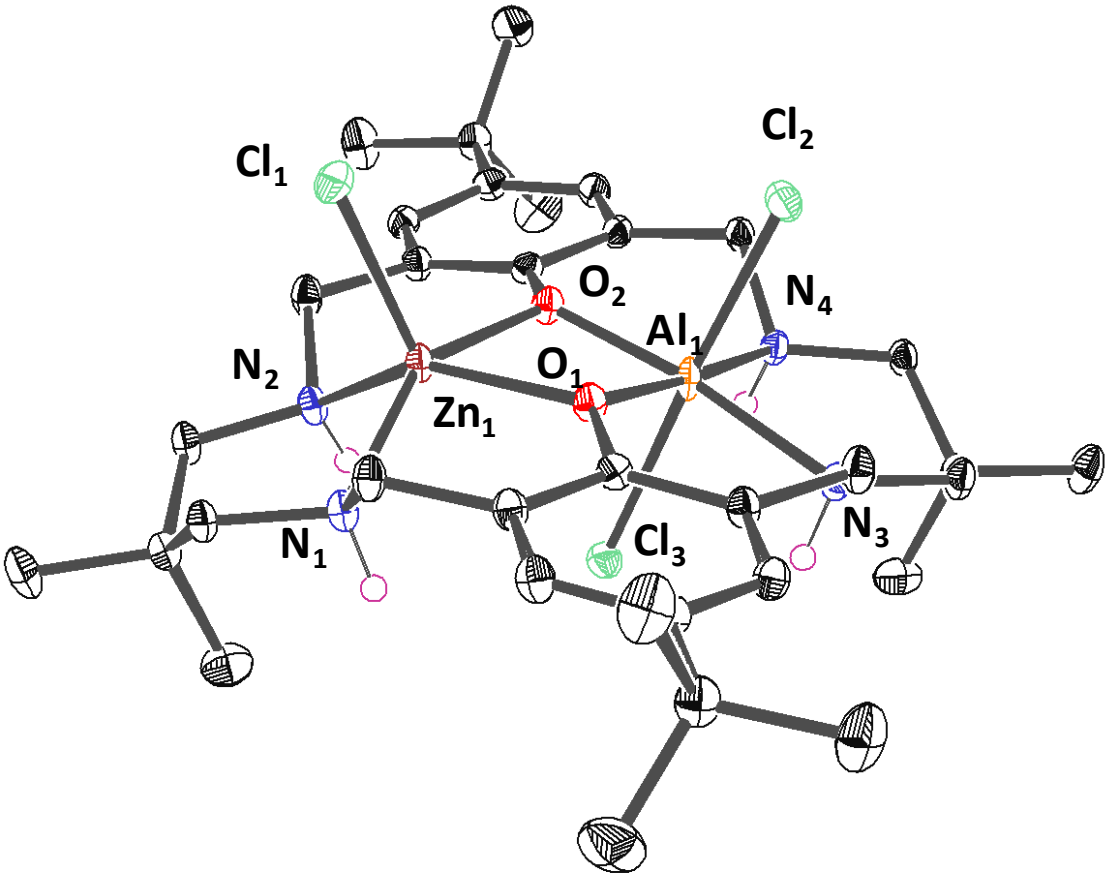


Figure S80: ORTEP representation of the molecular structure of **11** with disorder and hydrogen atoms (excluding NH) omitted for clarity with thermal ellipsoids represented at 40 % probability.

Table S9: Selected bond lengths (Å) and angles (°) for complex **11**.

Bond	**Bond Length (Å)**	**Bond**	**Bond Angle (°)**
N (1) – Zn (1)	2.089(2)	N (1) – Zn (1) – O (2)	148.60(9)
N (2) – Zn (1)	2.090(2)	N (2) – Zn (1) – O (1)	144.32(10)
O (1) – Zn (1)	2.086(2)	Cl (1) – Zn (1) – O (1)	109.20(10)
O (2) – Zn (1)	2.046(2)	N (3) – Al (1) – O (2)	172.61(17)
Cl (1) – Zn (1)	2.289(2)	N (4) – Al (1) – O (1)	175.28(18)
N (3) – Al (1)	2.093(3)	Cl (2) – Al (1) – Cl (3)	176.89(15)
N (4) – Al (1)	2.060(3)	**Metal – Metal**	**Distance (Å)**
O (1) – Al (1)	1.924(3)		
O (2) – Al (1)	1.891(3)	Zn (1) – Al (1)	3.02297(3)
Cl (2) – Al (1)	2.333(3)		
Cl (3) – Al (1)	2.412(3)		

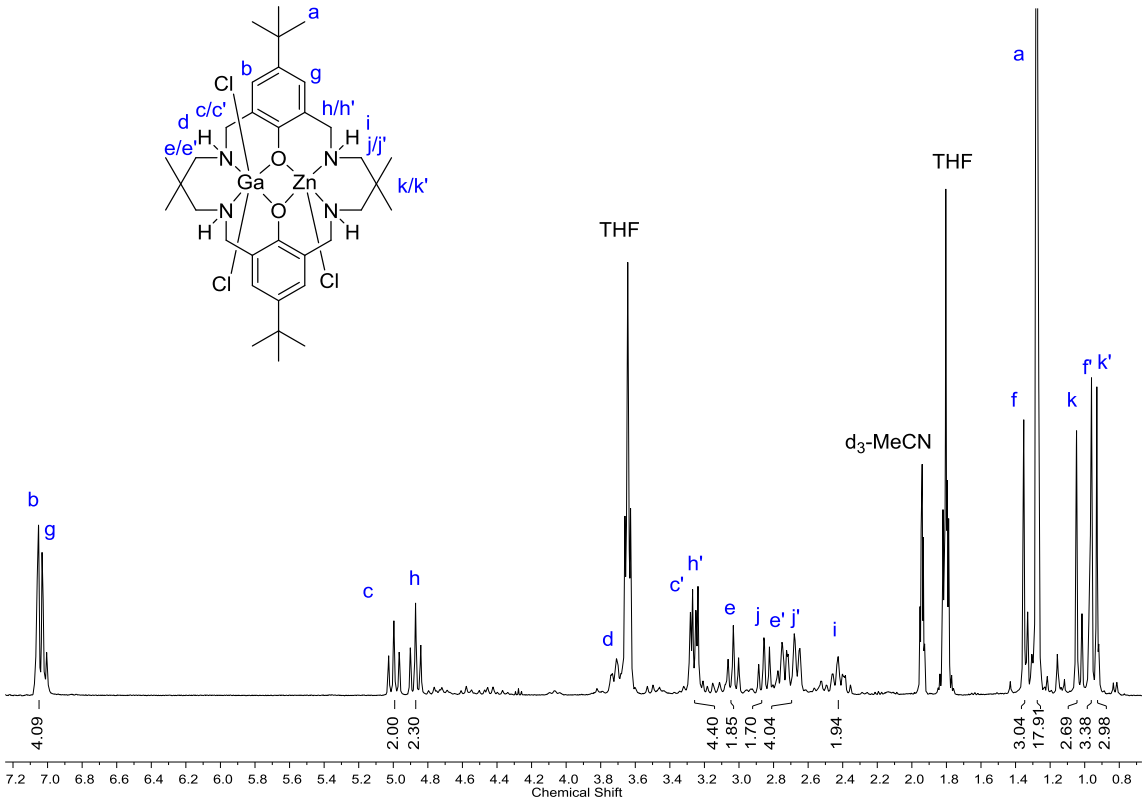


Figure S81: ^{1}H NMR of **12** (d_3 – MeCN, 298 K)

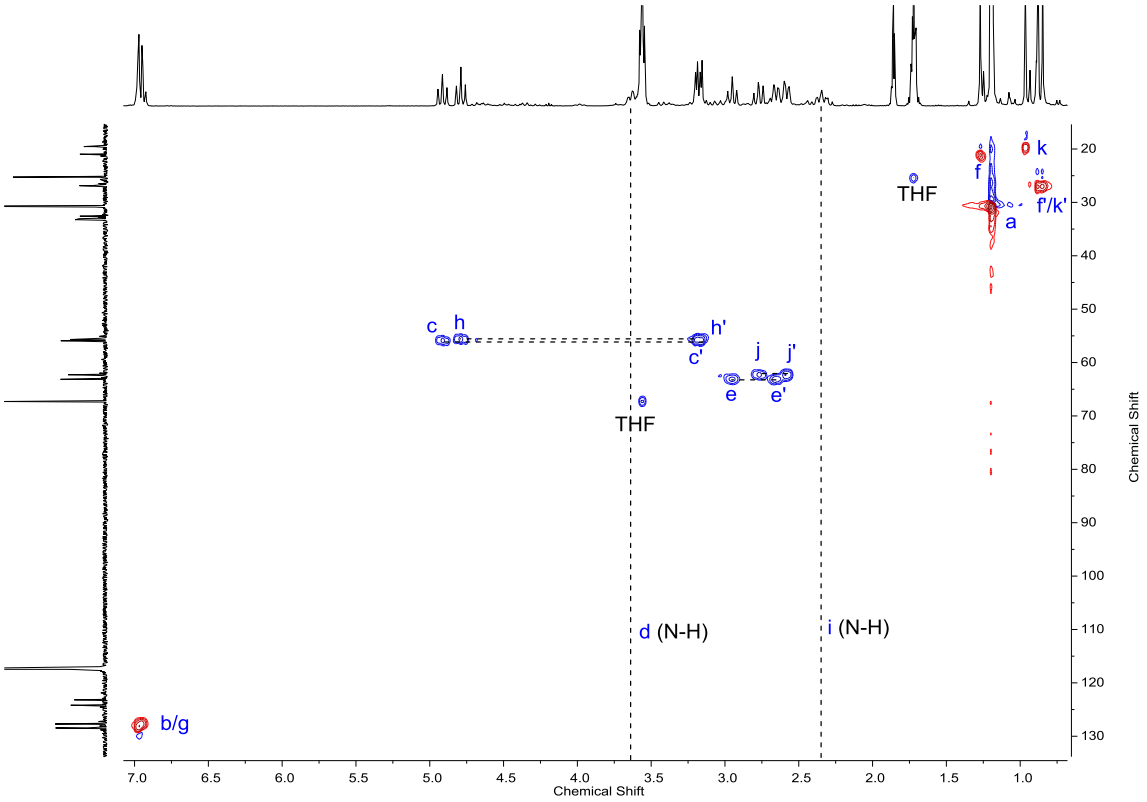


Figure S82: 2D HSQC NMR of **12** (d_3 – MeCN, 298 K)

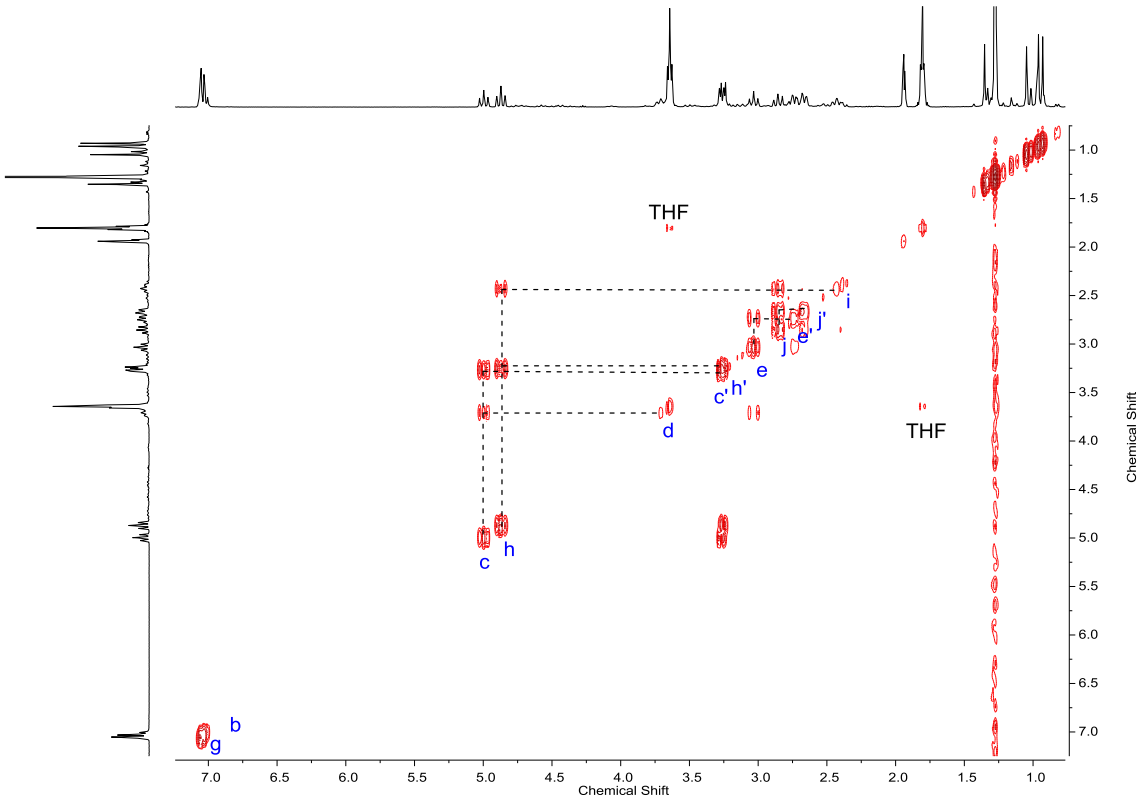


Figure S83: 2D COSY NMR of **12** (d_3 – MeCN, 298 K)

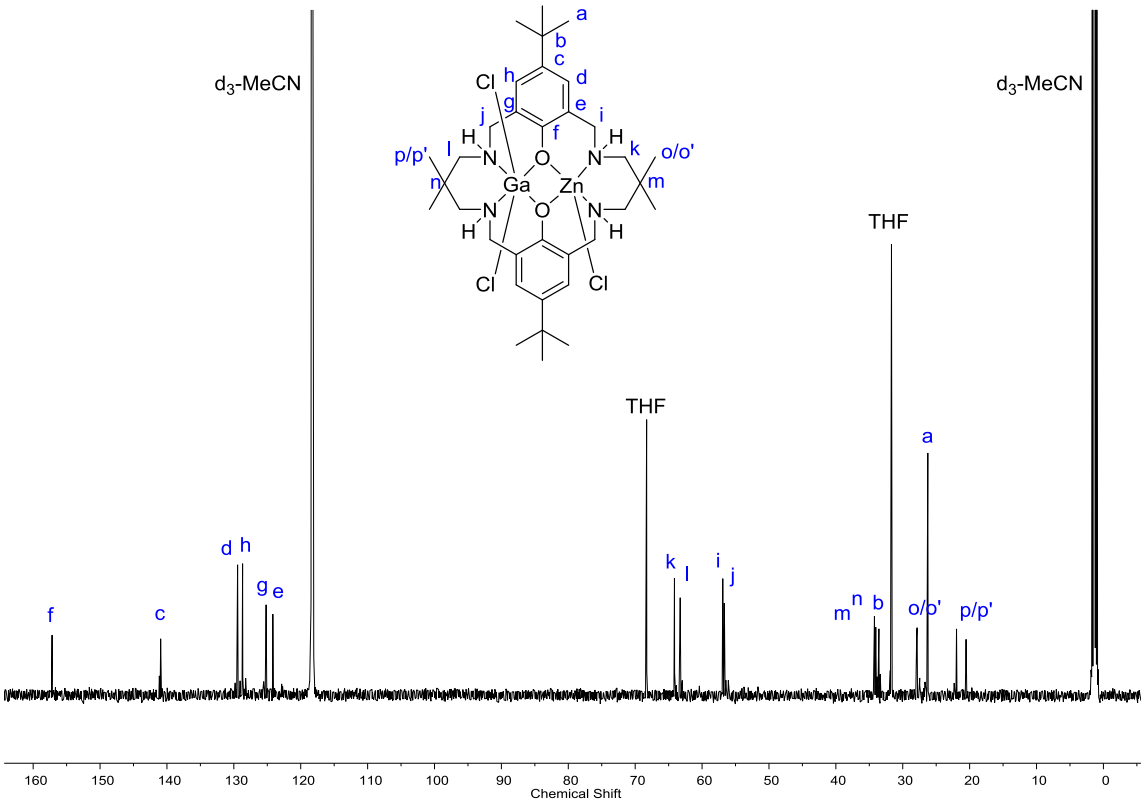


Figure S84: ^{13}C NMR of **12** (d_3 – MeCN, 298 K)

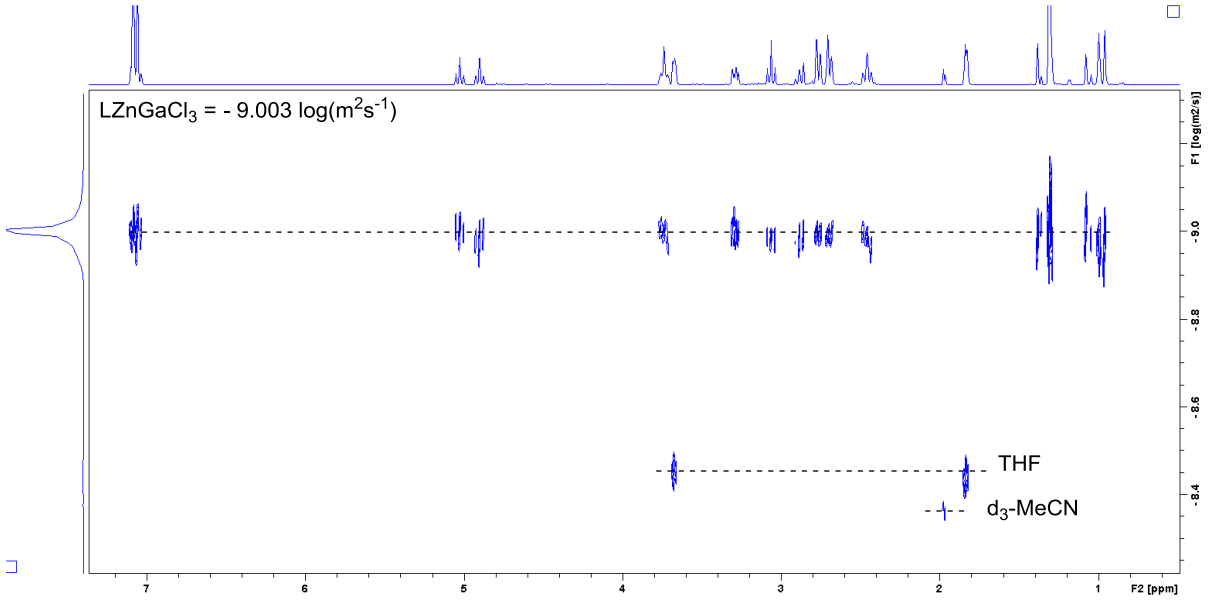


Figure S85: 2D DOSY NMR of **12** (d_3 – MeCN, 298 K)

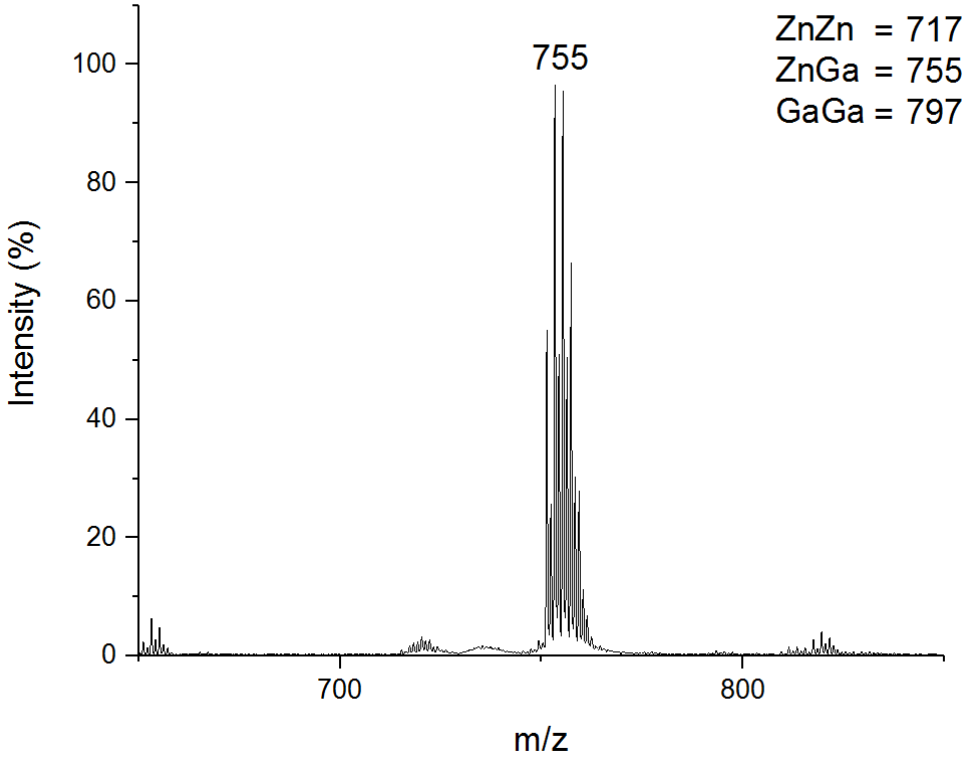


Figure S86: MALDI – ToF mass spectrum of **12**

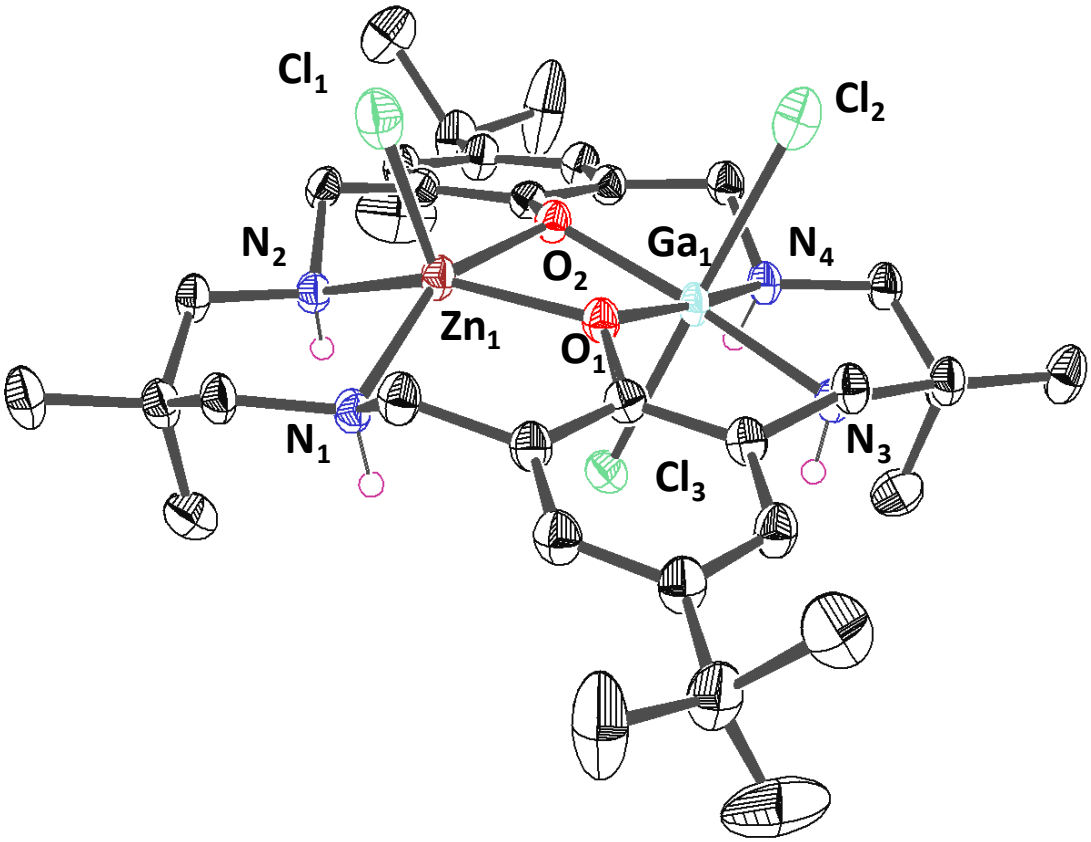


Figure S87: ORTEP representation of the molecular structure of **12** with disorder and hydrogen atoms (excluding NH) omitted for clarity with thermal ellipsoids represented at 40 % probability.

Table S10: Selected bond lengths (Å) and angles (°) for complex **12**.

Bond	**Bond Length (Å)**	**Bond**	**Bond Angle (°)**
N (1) – Zn (1)	2.133(2)	N (1) – Zn (1) – O (2)	153.77(8)
N (2) – Zn (1)	2.103(2)	N (2) – Zn (1) – O (1)	152.59(8)
O (1) – Zn (1)	2.117(2)	Cl (1) – Zn (1) – O (1)	106.35(8)
O (2) – Zn (1)	2.069(2)	N (3) – Ga (1) – O (2)	174.00(10)
Cl (1) – Zn (1)	2.1110(13)	N (4) – Ga (1) – O (1)	172.74(10)
N (3) – Ga (1)	2.062(2)	Cl (2) – Ga (1) – Cl (3)	178.73(9)
N (4) – Ga (1)	2.099(2)	**Metal – Metal**	**Distance (Å)**
O (1) – Ga (1)	2.019(2)		
O (2) – Ga (1)	2.026(2)	Zn (1) – Ga (1)	3.123(2)
Cl (2) – Ga (1)	2.5455(12)		
Cl (3) – Ga (1)	2.3721(13)		

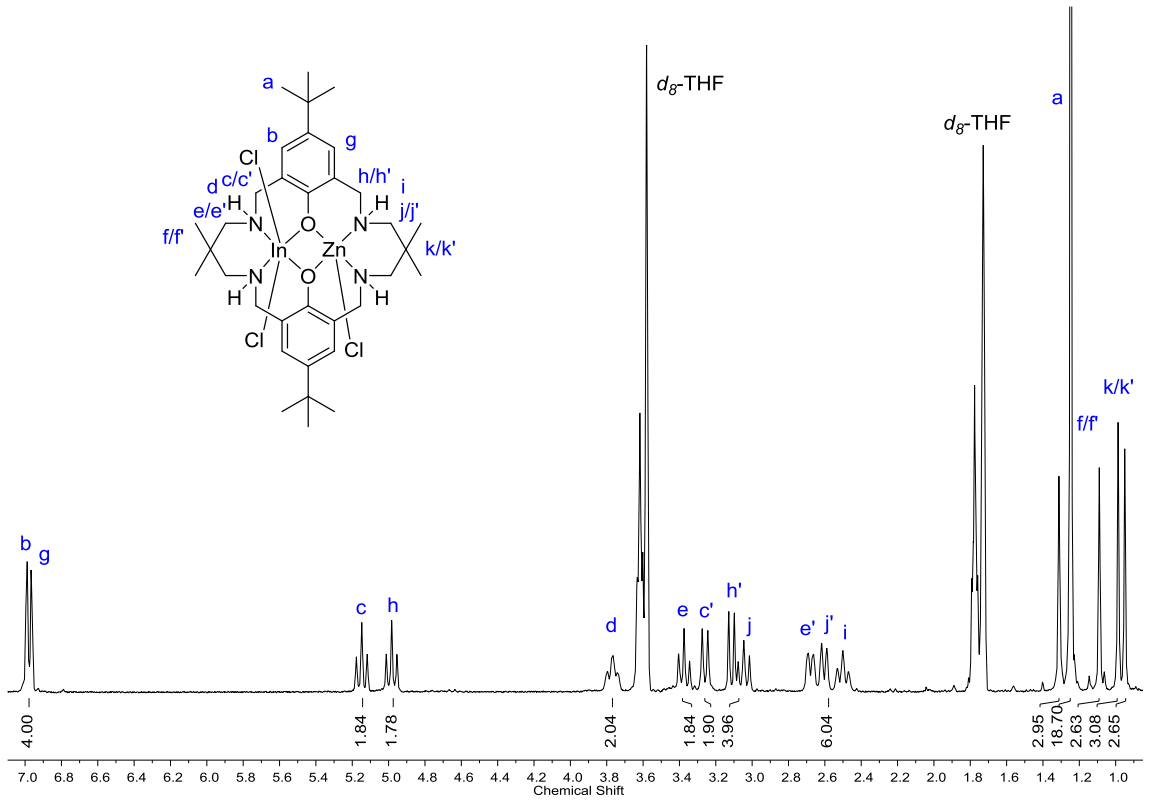


Figure S88: ^{1}H NMR of **13** (d_8 –THF, 298 K)

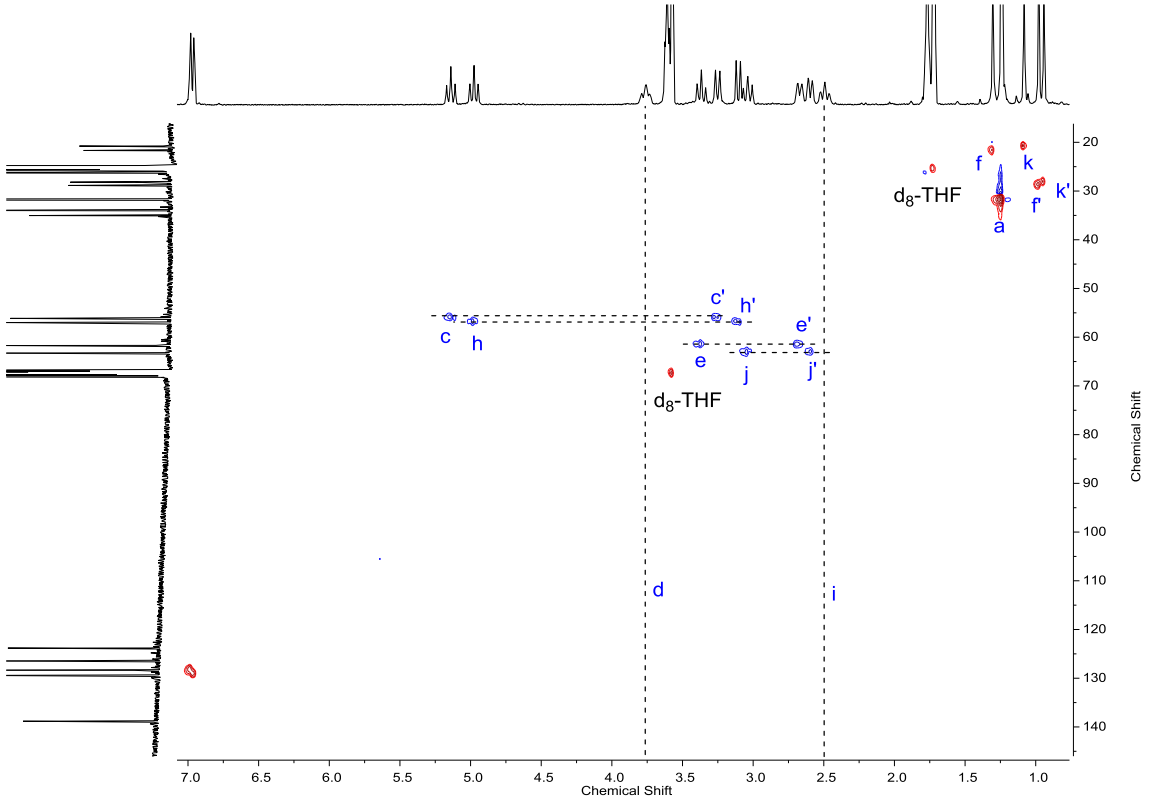


Figure S89: 2D HSQC NMR of **13** (d_8 –THF, 298 K)

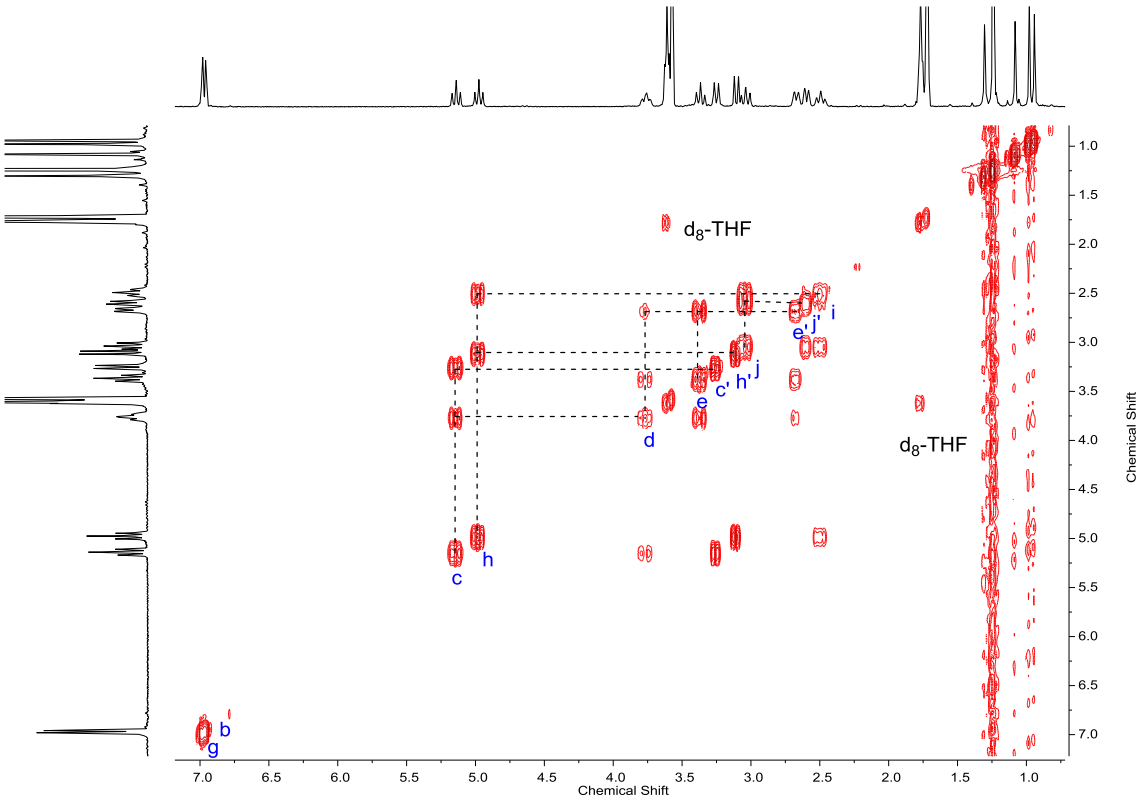


Figure S90: 2D COSY NMR of **13** (d_8 – THF, 298 K)

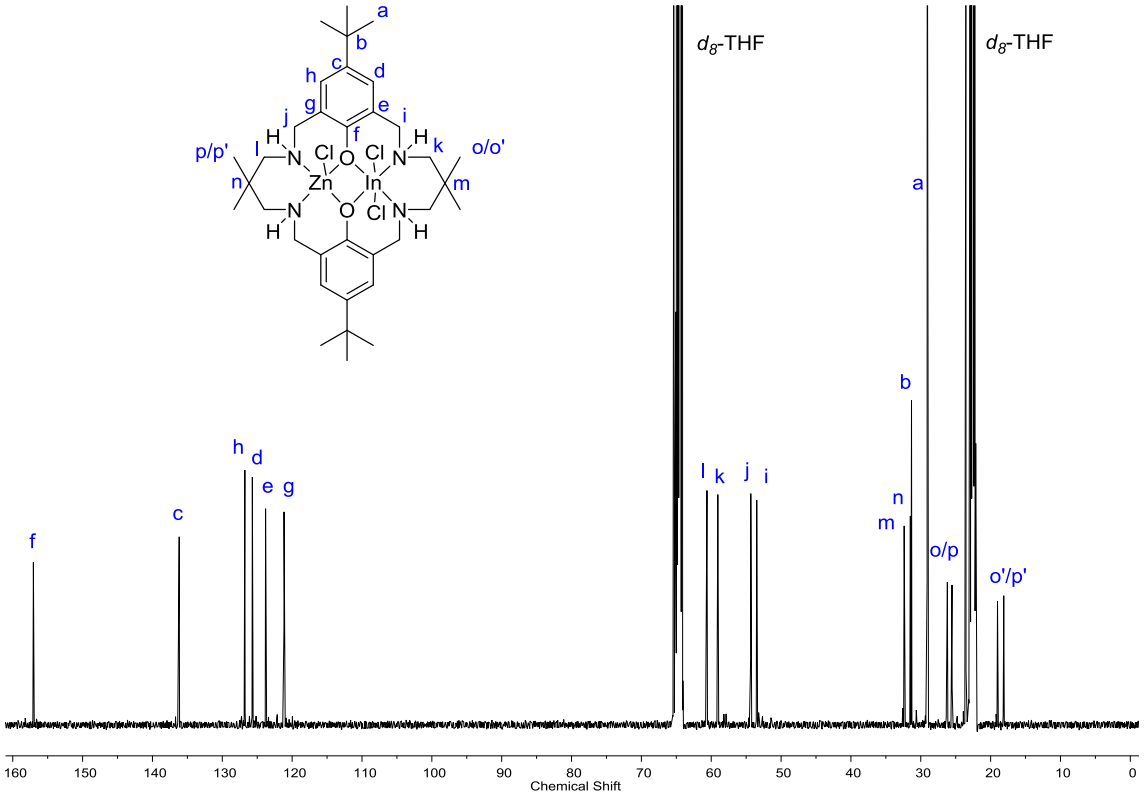


Figure S91: ^{13}C NMR of **13** (d_8 –THF, 298 K)

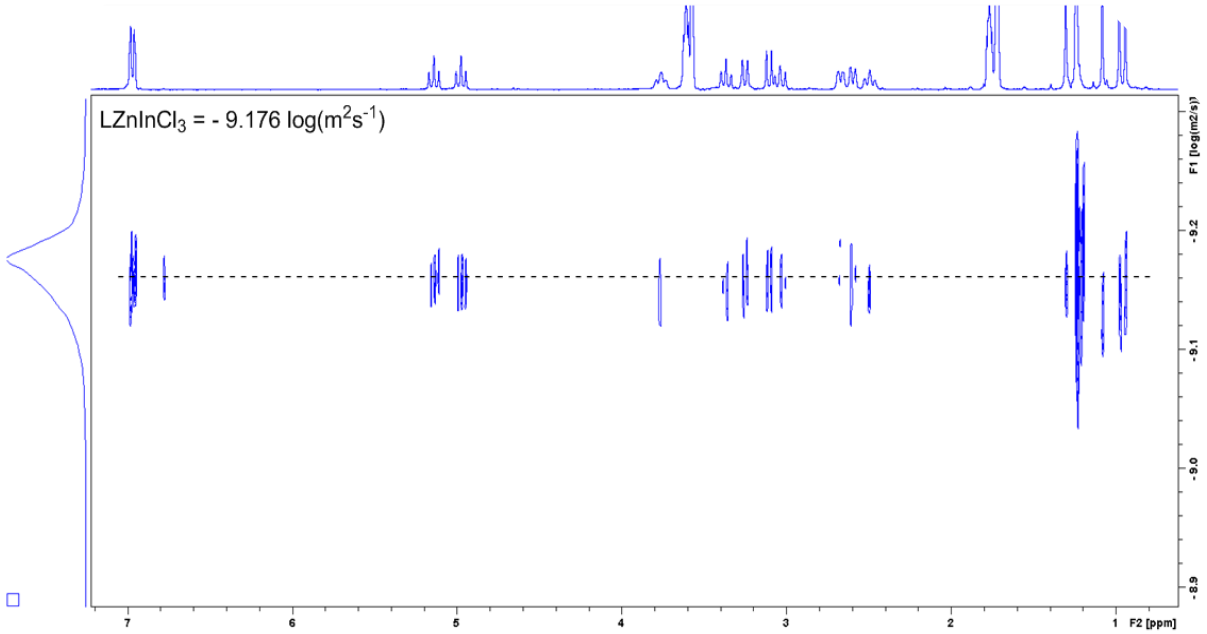


Figure S92: 2D DOSY NMR of **13** (d_8 –THF, 298 K)

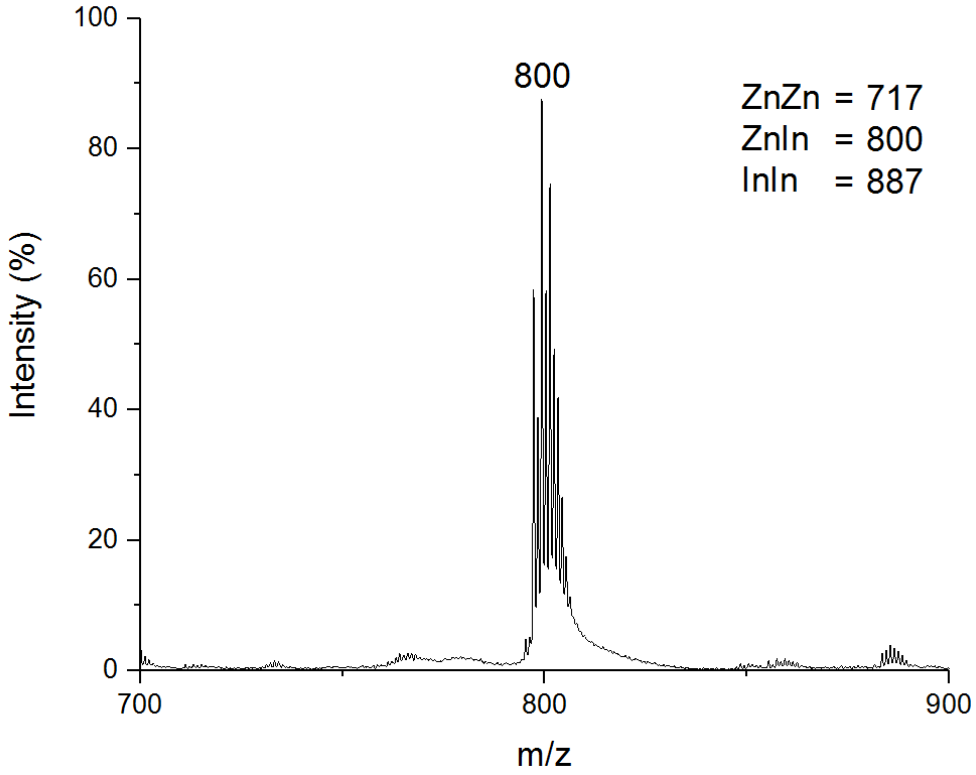


Figure S93: MALDI – ToF mass spectrum of **13**

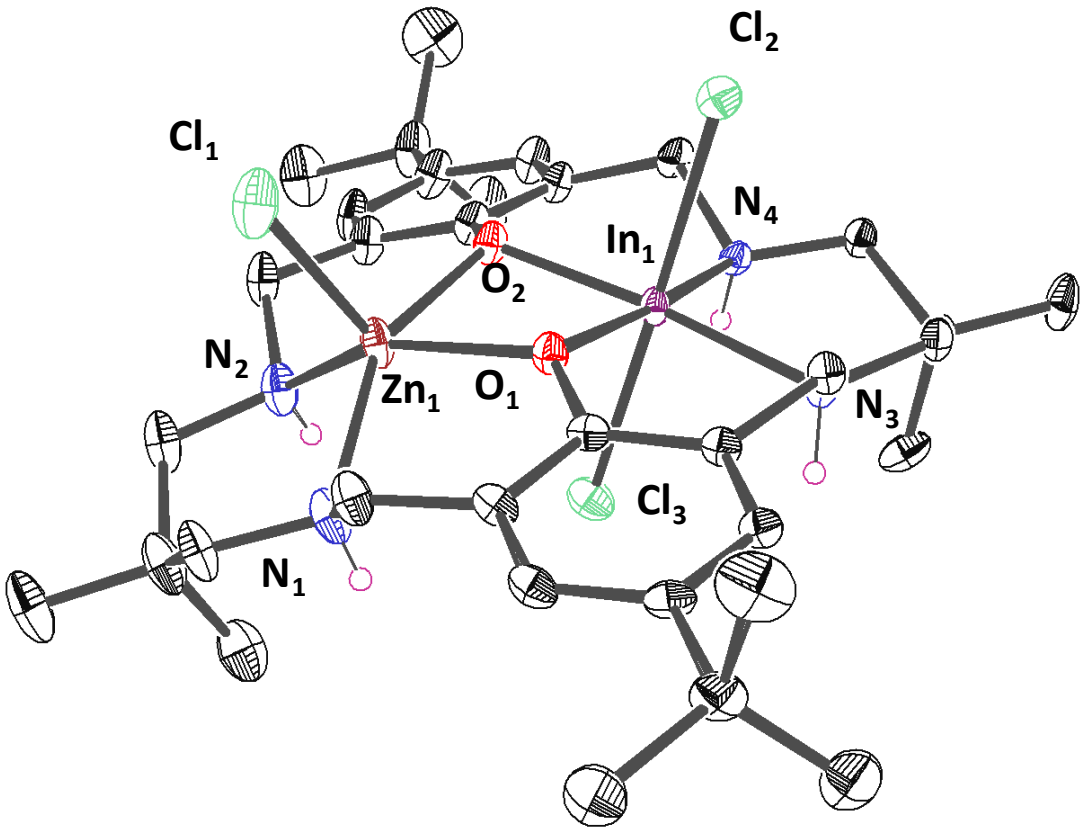


Figure S94: ORTEP representation of the molecular structure of **13** with disorder and hydrogen atoms (excluding NH) omitted for clarity with thermal ellipsoids represented at 40 % probability.

Table S11: Selected bond lengths (Å) and angles (°) for complex **13**.

Bond	**Bond Length (Å)**	**Bond**	**Bond Angle (°)**
N (1) – Zn (1)	2.238(5)	N (1) – Zn (1) – O (2)	150.17(18)
N (2) – Zn (1)	2.165(5)	N (2) – Zn (1) – O (1)	151.4(3)
O (1) – Zn (1)	2.274(5)	Cl (1) – Zn (1) – O (1)	103.5(2)
O (2) – Zn (1)	2.203(5)	N (3) – In (1) – O (2)	174.3(2)
Cl (1) – Zn (1)	2.061(5)	N (4) – In (1) – O (1)	173.38(19)
N (3) – In (1)	2.111(4)	Cl (2) – In (1) – Cl (3)	175.2(2)
N (4) – In (1)	2.094(5)	**Metal – Metal**	**Distance (Å)**
O (1) – In (1)	2.085(4)		
O (2) – In (1)	2.036(3)	Zn (1) – In (1)	3.15788(10)
Cl (2) – In (1)	2.808(3)		
Cl (3) – In (1)	2.5502(13)		

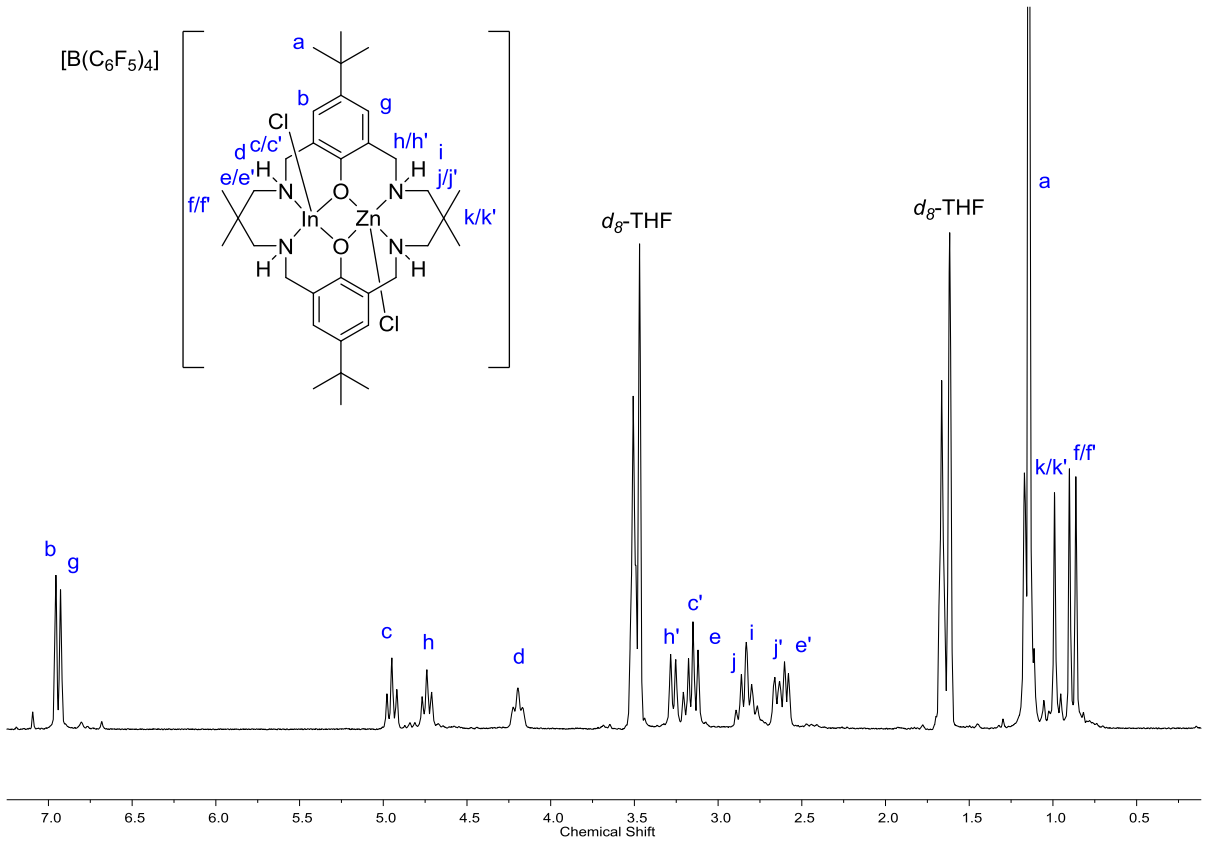


Figure S95: ^{1}H NMR of **14** (d_8-THF, 298 K)

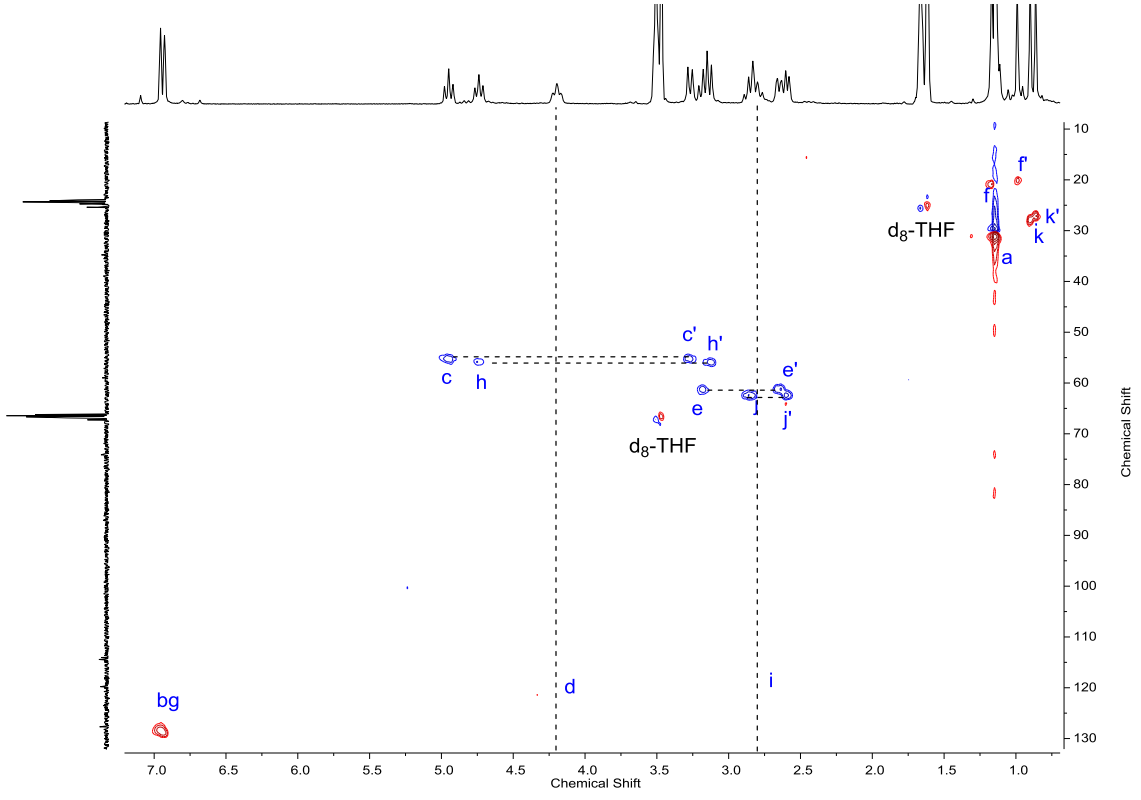


Figure 96: HSQC NMR of **14** (d_8-THF, 298 K)

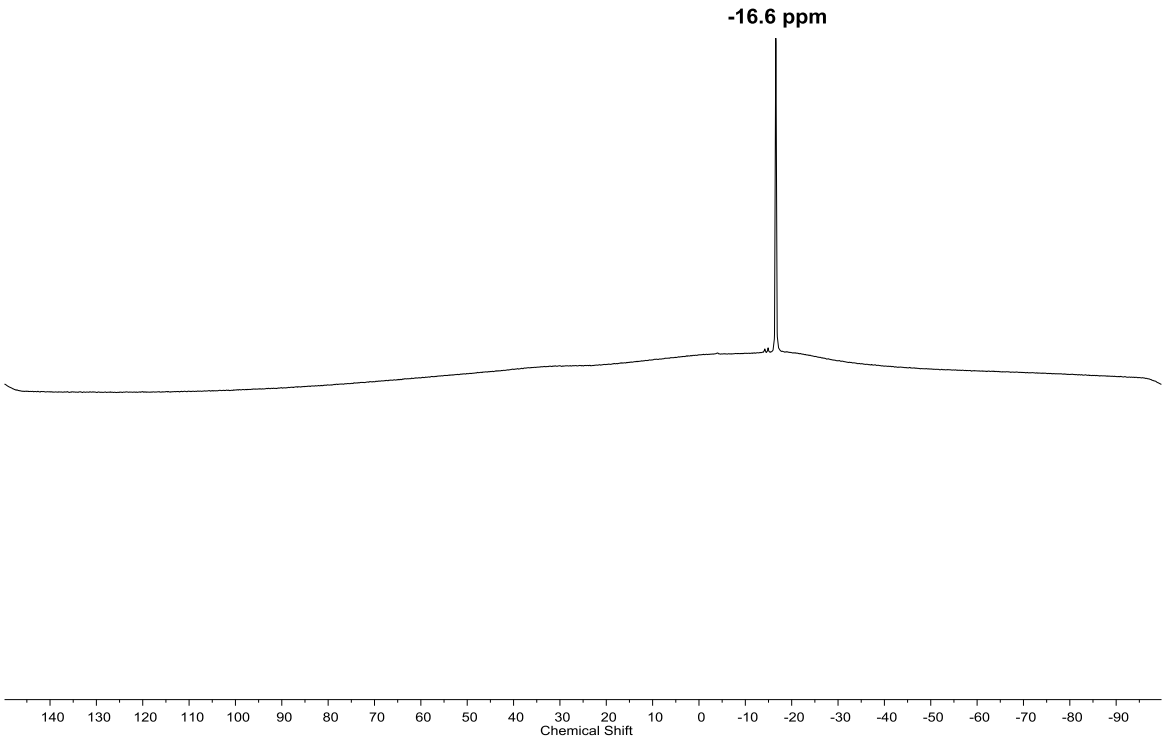


Figure S97: ^{11}B NMR of **14** (d8-THF, 298 K)

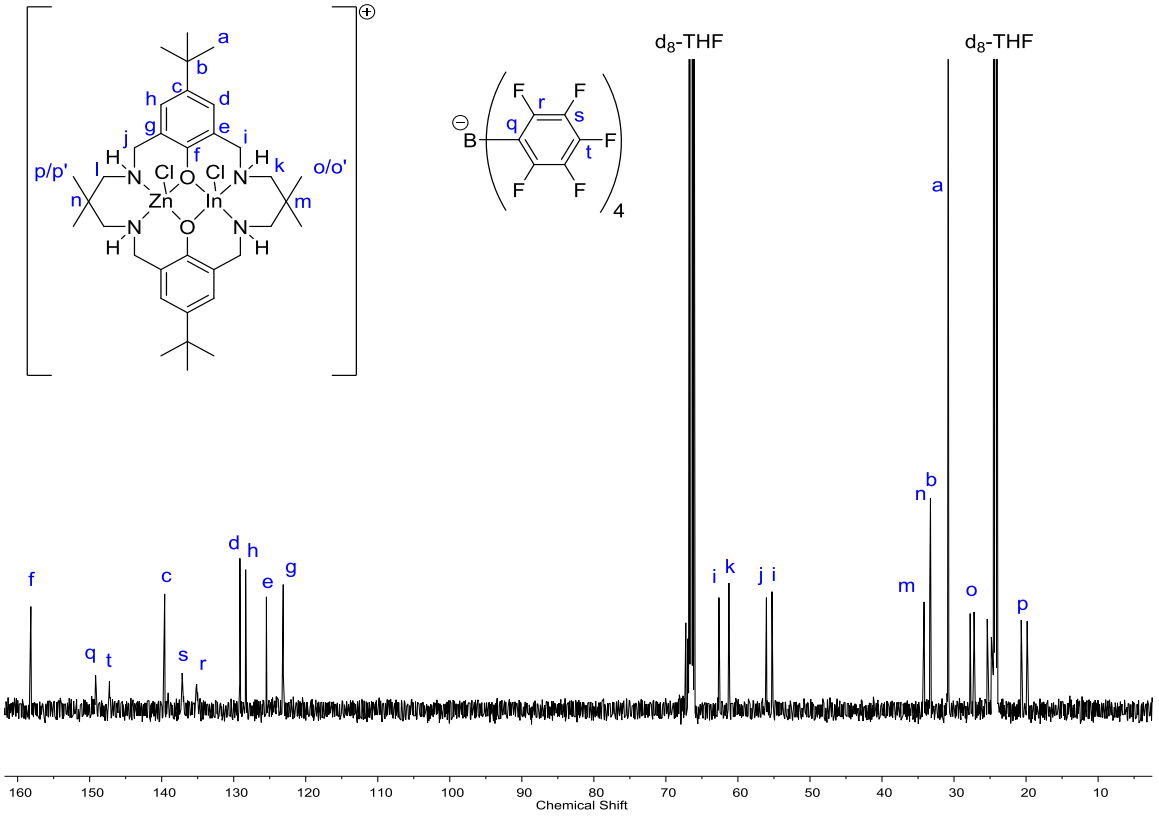


Figure 98: ^{13}C NMR of **14** (d_8-THF, 298 K)

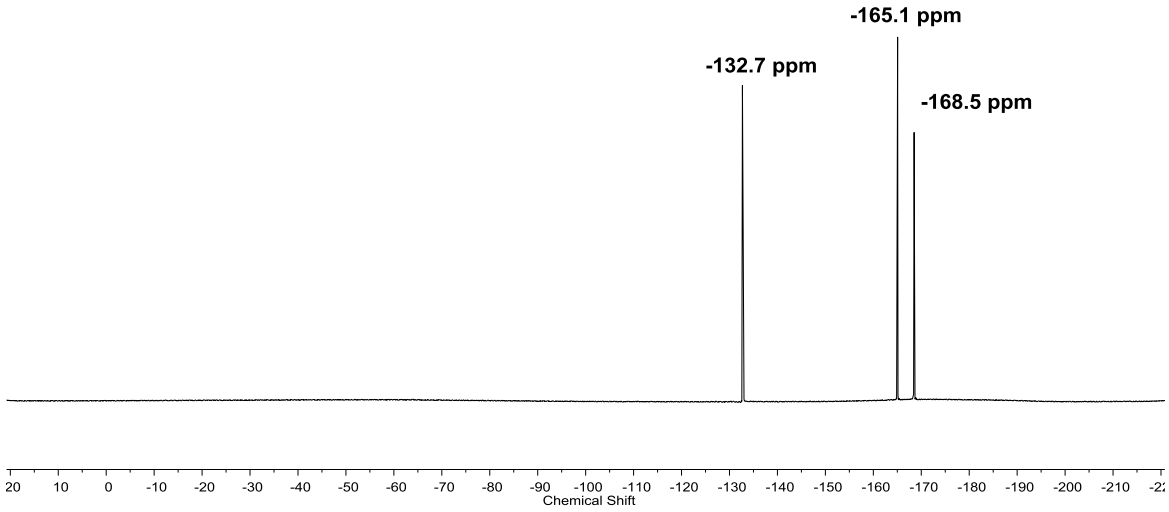


Figure S99: ^{19}F NMR of **14** (d8-THF, 298 K)

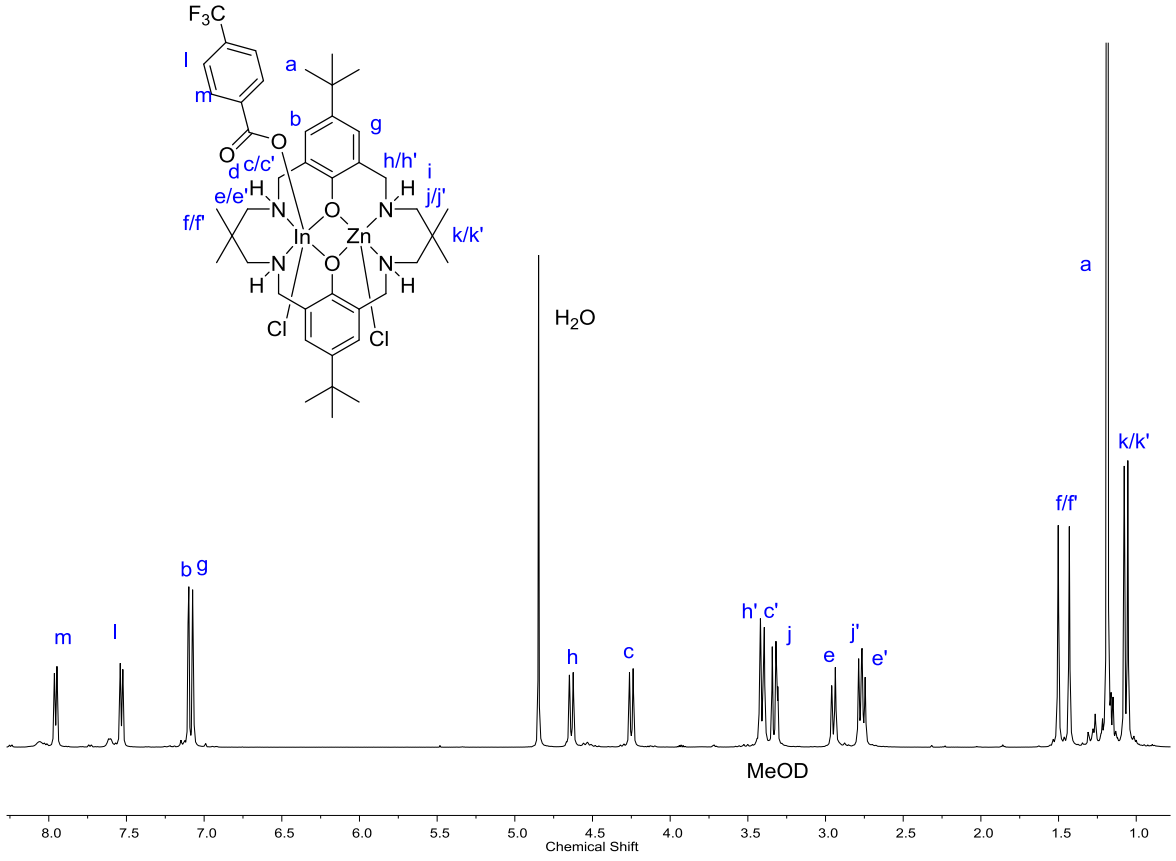


Figure S100: ^{1}H NMR of **15** (d_4-MeOD, 298 K)

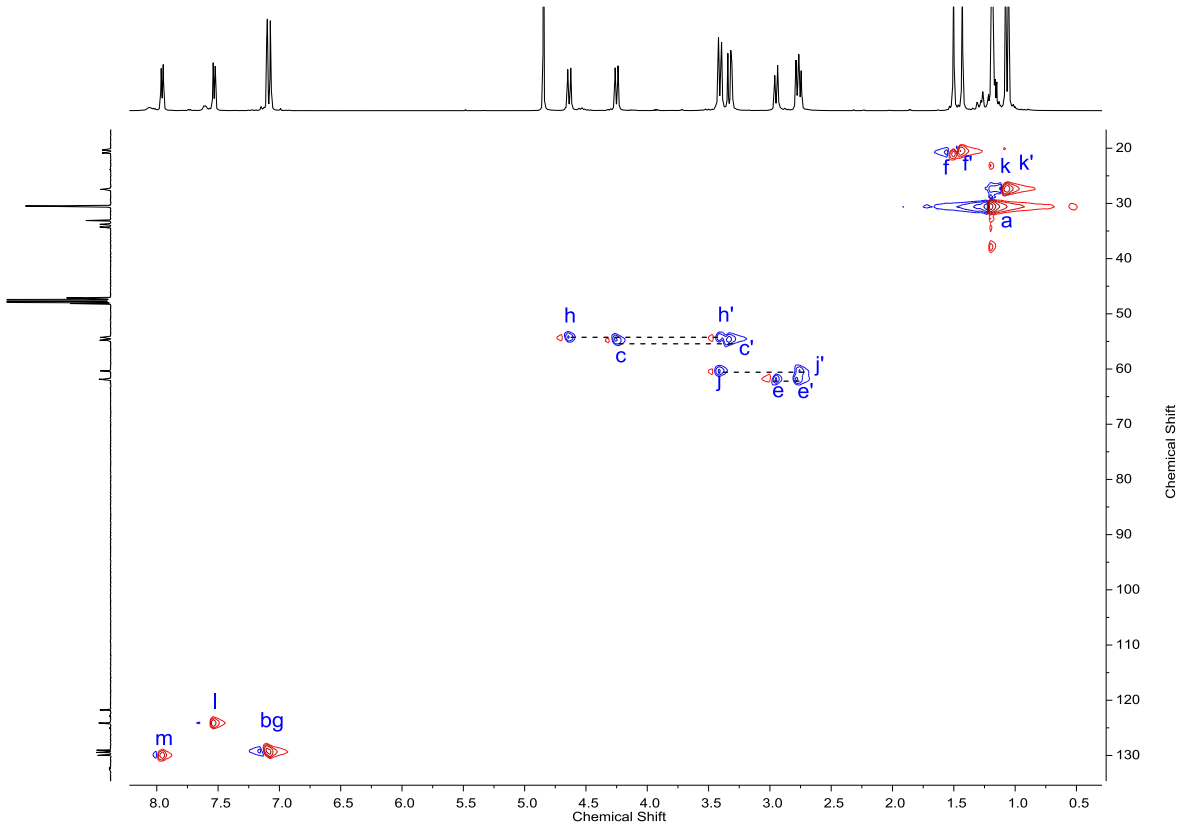


Figure S101: HSQC NMR of **15** (d_4-MeOD, 298 K)

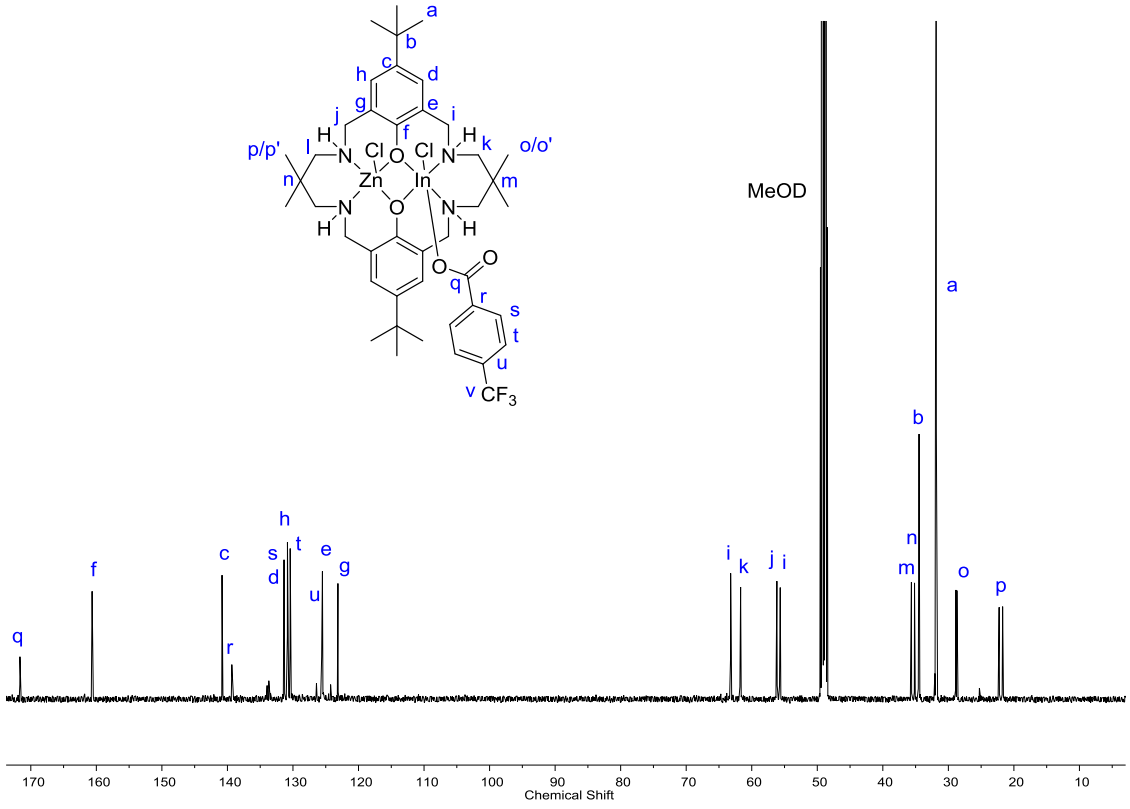


Figure S102: ^{13}C NMR of **15** (d4-MeOD, 298 K)

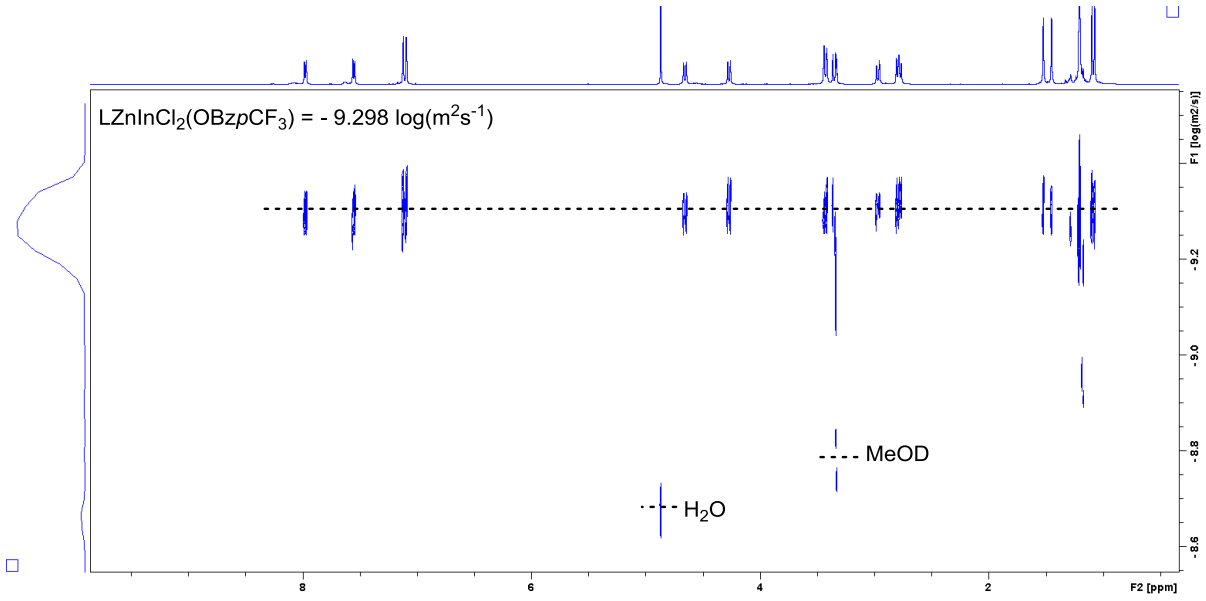


Figure S103: 2D DOSY NMR of **15** (d_4-MeOD, 298 K)

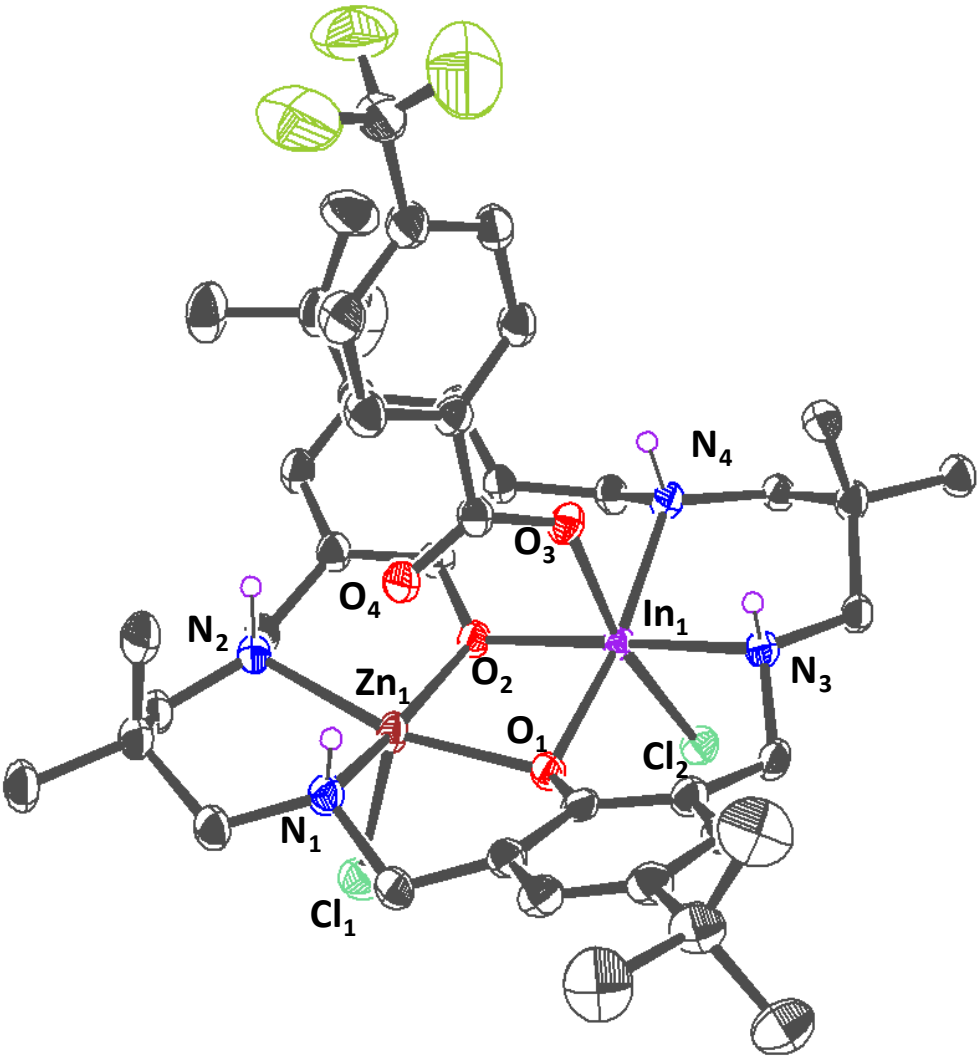


Figure S104: Connectivity moleculare structure of **15** with disorder and hydrogen atoms (excluding NH) omitted for clarity with thermal ellipsoids represented at 40 % probability.

8.1.3 Chapter 4: Magnesium-Cobalt Heterodinuclear Catalyst

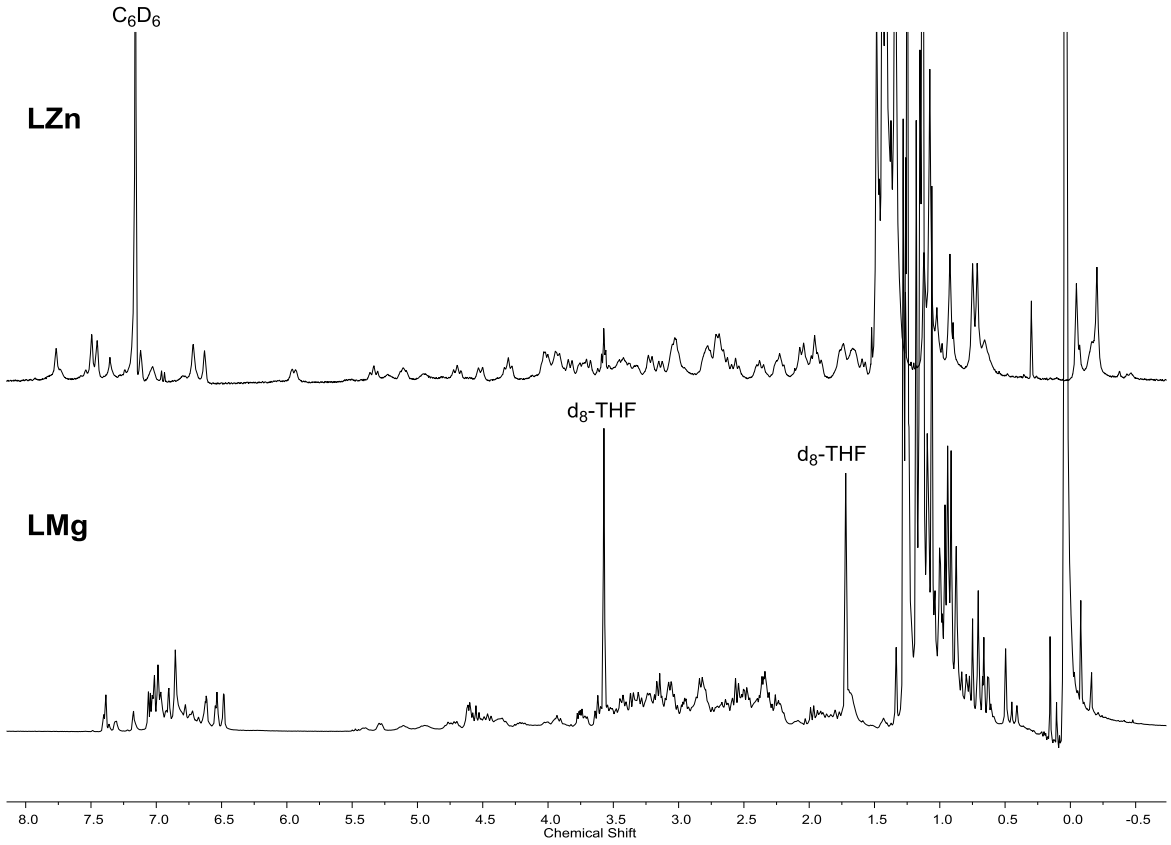


Figure S105: ^{1}H NMR spectra of mono-zinc (chapter 2 and 3) and mono-magnesium species (chapter 4) used as intermediates for heterodinuclear synthesis.

Both ^{1}H NMR spectra of the mono-metallated intermediates used in this Thesis, LZn and LMg, are extremely complex. The complexity of the mono-zinc species was previously reported to be due to the formation of several aggregates in solution as determined by DOSY NMR spectroscopy.[2]

The mono-magnesium complex was further used to form both homodinuclear complex **17** (MgMg) and heterodinuclear complex **9a** ($MgZnI_2$) which was found to yield the product with high heterocontent (> 98 %). Based on these findings, its use as a precursor for magnesium-transition metal heterocomplexes was validated.

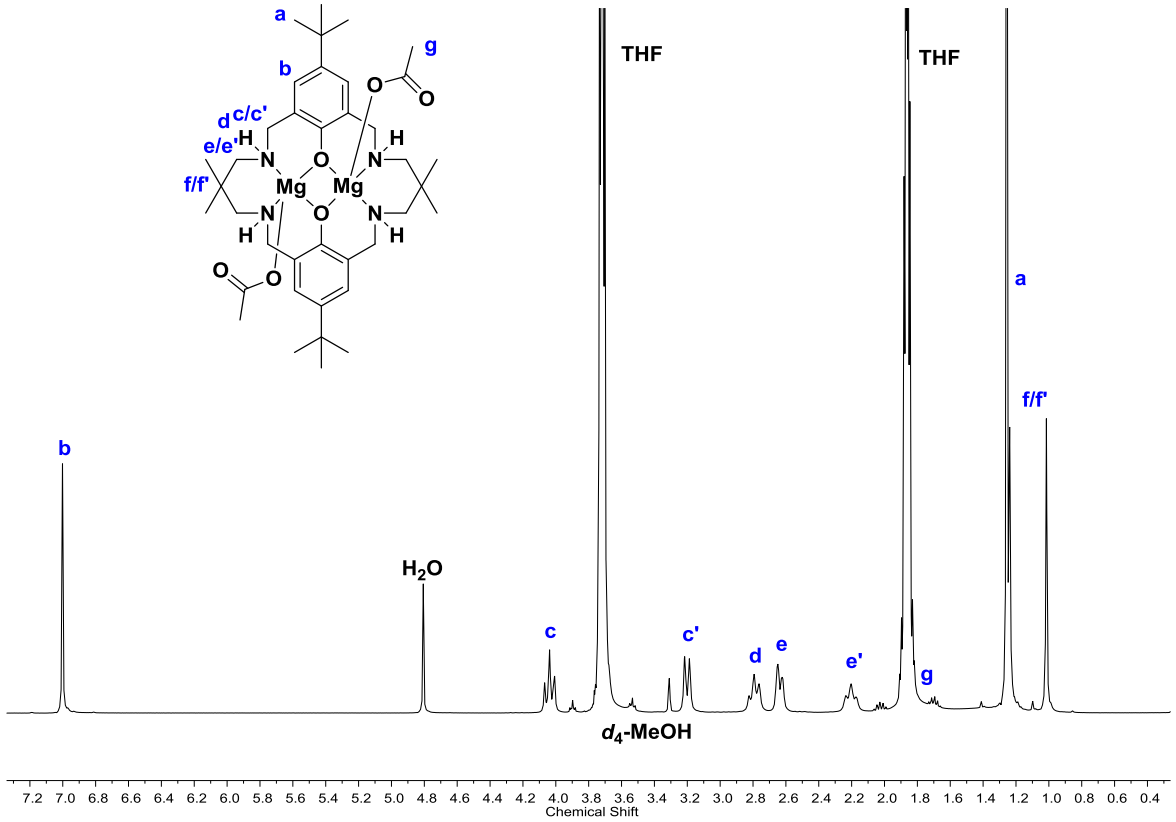


Figure S106: ^{1}H NMR of complex **17** (d_4-MeOH, 298 K)

Table S12: Linear fitting and calculated rate constants for the copolymerisation of CO_2/CHO with **MgCo**.

Temp (K)	y = mx + c	R^2	k_{obs}	k	Ln(k/T)
333	$-2.51\times10^{-5} + 0.71$	0.9928	2.51×10^{-5} ($\pm0.06\times10^{-5}$)	0.0151 (±0.001)	-10.00 (±0.02)
353	$-1.55\times10^{-4} + 0.65$	0.9810	1.55×10^{-4} ($\pm0.03\times10^{-4}$)	0.0931 (±0.002)	-8.24 (±0.01)
373	$-7.14\times10^{-4} + 0.92$	0.9933	7.14×10^{-4} ($\pm0.16\times10^{-4}$)	0.4289 (±0.001)	-6.77 (±0.01)
393	$-2.05\times10^{-3} + 1.87$	0.9972	2.05×10^{-3} ($\pm0.05\times10^{-3}$)	1.2312 (±0.027)	-5.77 (±0.01)
413	$-2.98\times10^{-3} + 0.36$	0.9949	2.98×10^{-3} ($\pm0.07\times10^{-3}$)	1.7844 (±0.039)	-5.44 (±0.01)

k_{obs} = gradient of linear fitting of the logarithm of CHO concentration vs time. k = k_{obs}/[cat]^1 where [cat] = 1.67 mM. Error in k_{obs} calculated at ±2.2 %

Table S13: Linear fitting and calculated rate constants for the copolymerisation of CO_2/CHO with **CoCo**.

Temp (K)	y = mx + c	R^2	k_{obs}	k	Ln(k/T)
333	$-1.32\times10^{-5} + 0.04$	0.9942	1.32×10^{-5} ($\pm0.03\times10^{-5}$)	0.0079 (±0.001)	-10.65 (±0.02)
353	$-1.07\times10^{-4} + 0.30$	0.9886	1.07×10^{-4} ($\pm0.02\times10^{-4}$)	0.0931 (±0.003)	-8.61 (±0.01)
373	$-4.39\times10^{-4} + 0.61$	0.9900	4.39×10^{-4} ($\pm0.10\times10^{-4}$)	0.2637 (±0.007)	-7.23 (±0.01)
393	$-9.31\times10^{-4} + 0.90$	0.9984	9.31×10^{-4} ($\pm0.20\times10^{-4}$)	0.5592 (±0.012)	-6.56 (±0.01)

k_{obs} = gradient of linear fitting of the logarithm of CHO concentration vs time. k = k_{obs}/[cat]^1 where [cat] = 1.67 mM. Error in k_{obs} calculated at ±2.2 %

Table S14: Linear fitting and calculated rate constants for the copolymerisation of CO_2/CHO with **MgMg**.

Temp (K)	y = mx + c	R^2	k_{obs}	k	Ln(k/T)
333	$-3.58\times10^{-6} + 0.30$	0.9837	3.58×10^{-6} ($\pm0.08\times10^{-6}$)	0.0022 (±0.0005)	-11.95 (±0.02)
353	$-2.78\times10^{-5} + 1.33$	0.9938	2.78×10^{-5} ($\pm0.06\times10^{-5}$)	0.0167 (±0.0004)	-9.96 (±0.02)
373	$-1.02\times10^{-4} + 0.27$	0.9989	1.02×10^{-4} ($\pm0.02\times10^{-4}$)	0.0613 (±0.0017)	-8.71 (±0.01)
393	$-4.49\times10^{-4} + 0.54$	0.9765	4.49×10^{-4} ($\pm0.10\times10^{-4}$)	0.2697 (±0.008)	-7.28 (±0.01)

k_{obs} = gradient of linear fitting of the logarithm of CHO concentration vs time. k = k_{obs}/[cat]^1 where [cat] = 1.67 mM. Error in k_{obs} calculated at ±2.2 %

Error Analysis: Least Squares Method.

$$\Delta H^{\ddagger} = R\ x\ \frac{S_{xy}}{S_x} \tag{S1}$$

$$\Delta S^{\ddagger} = R\left(\bar{y} - ln\frac{k_B}{h}\right) - (\Delta H^{\ddagger}\ x\ \bar{x}) \tag{S2}$$

Where:

$$\bar{x} = \frac{1}{n}\sum_{i=1}^{n}\frac{1}{T_i} \tag{S3}$$

$$\bar{y} = \frac{1}{n}\sum_{i=1}^{n} ln\frac{k_i}{T_i} \tag{S4}$$

$$S_x = \frac{1}{n}\sum_{i=1}^{n}\left(\frac{1}{T_i} - \bar{x}\right)^2 \tag{S5}$$

$$S_{xy} = \frac{1}{n}\sum_{i=1}^{n}(\frac{1}{T_i} - \bar{x})(ln\frac{k_i}{T_i} - \bar{y}) \tag{S6}$$

$$S = \sqrt{\sum_{i=1}^{n}(ln\frac{k_i}{T_i} - ln\frac{k_{i,fit}}{T_i})^2} \tag{S7}$$

Standard Error:

$$\sigma(\Delta H^{\ddagger}) = \frac{s}{\sqrt{S_x}} \tag{S8}$$

$$\sigma(\Delta S^{\ddagger}) = s\sqrt{\frac{1}{n} + \frac{x^2}{S_x}} \tag{S9}$$

Where Sx << n

$$\frac{\sigma(\Delta S^{\ddagger})}{\sigma(\Delta H^{\ddagger})} = \sqrt{\frac{S_x}{n} + x^2} = x = \frac{1}{n}\sum_{i=1}^{n}\frac{1}{T_i} = \frac{1}{T_{average}} = 0.0027725\ K^{-1} \tag{S10}$$

8.1.4 Chapter 5: O-Vanillin Dervied Heterodinuclear Catalysts

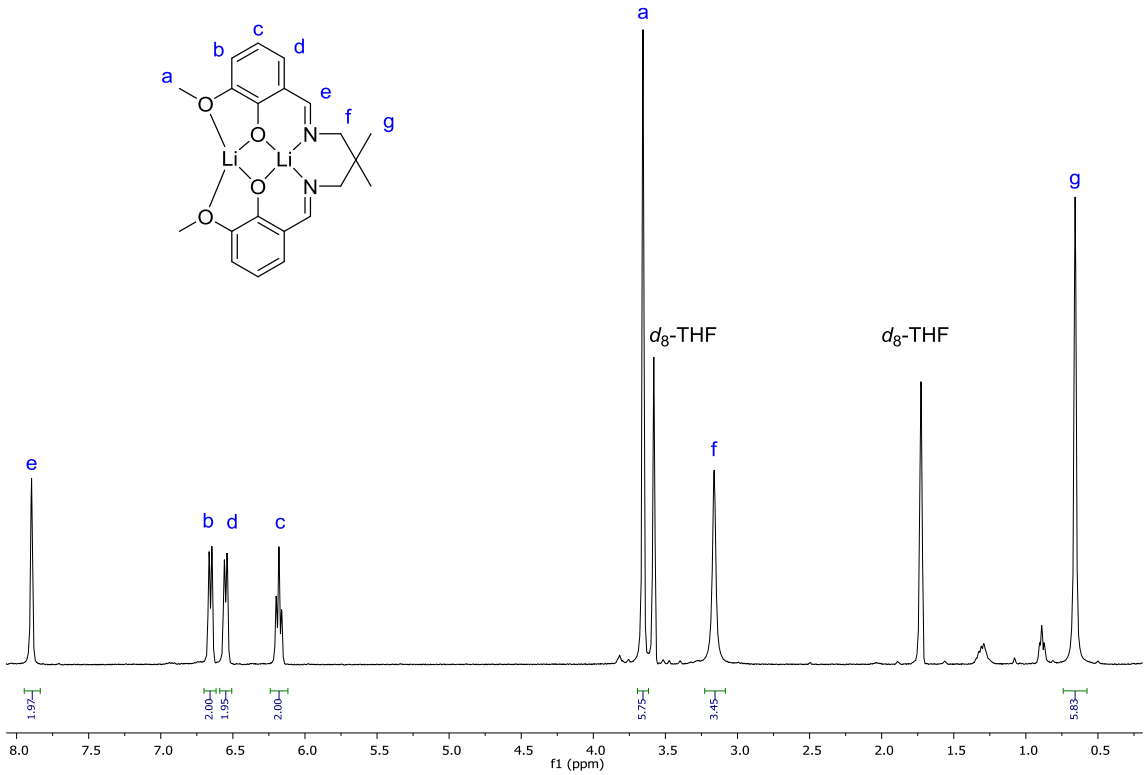


Figure S107: ^{1}H NMR of **19** (d_8-THF, 298 K)

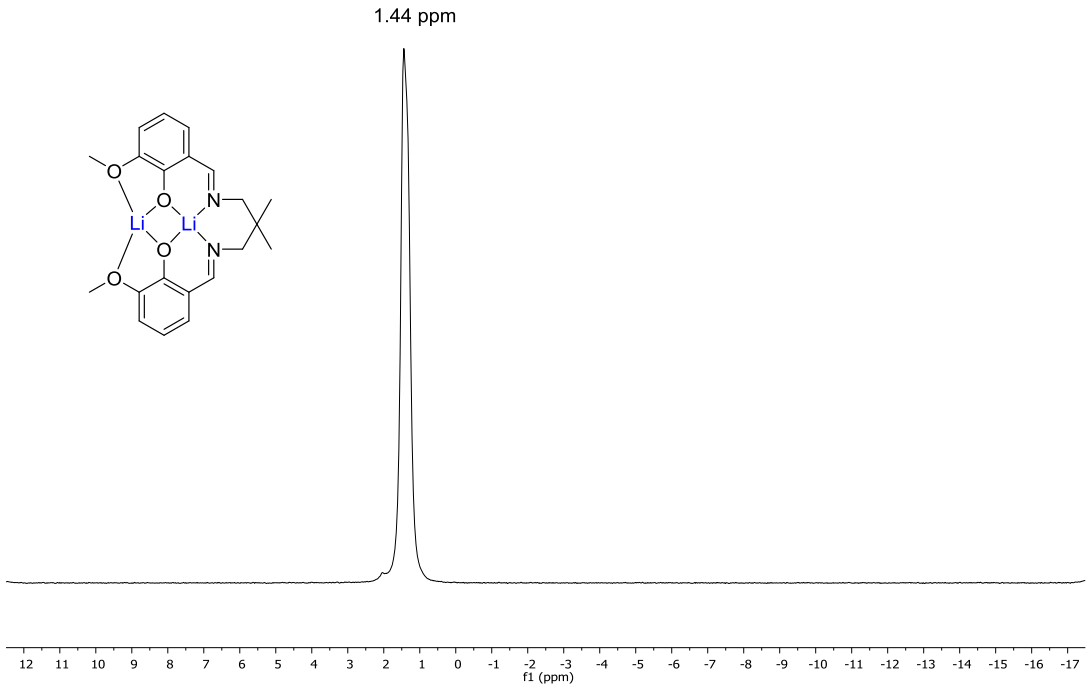


Figure S108: ^{7}Li NMR of **19** (d_8-THF, 298 K)

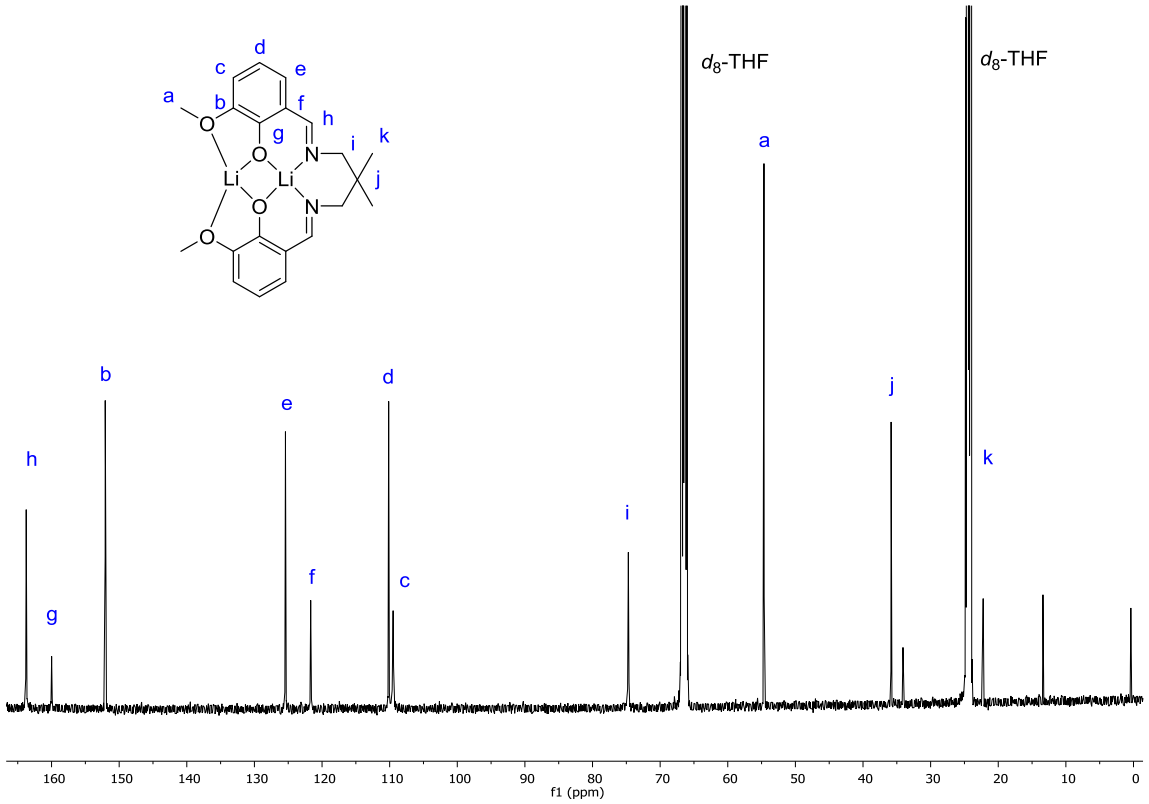


Figure S109: ^{13}C NMR of **19** (d_8-THF, 298 K)

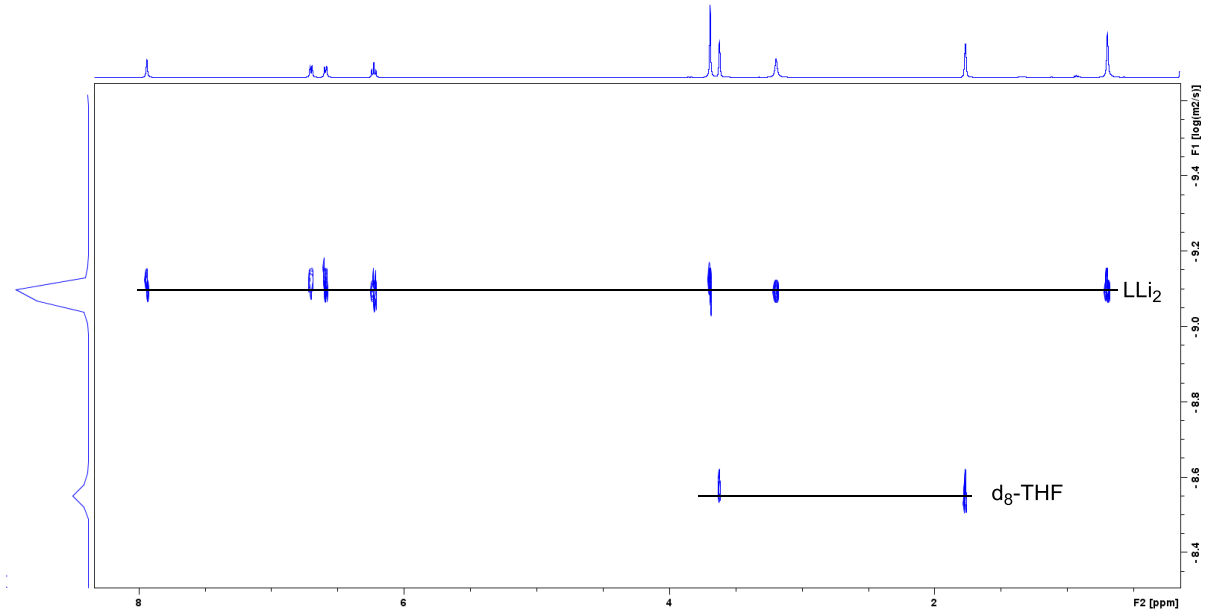


Figure S110: DOSY NMR of **19** in (d_8-THF, 298 K)

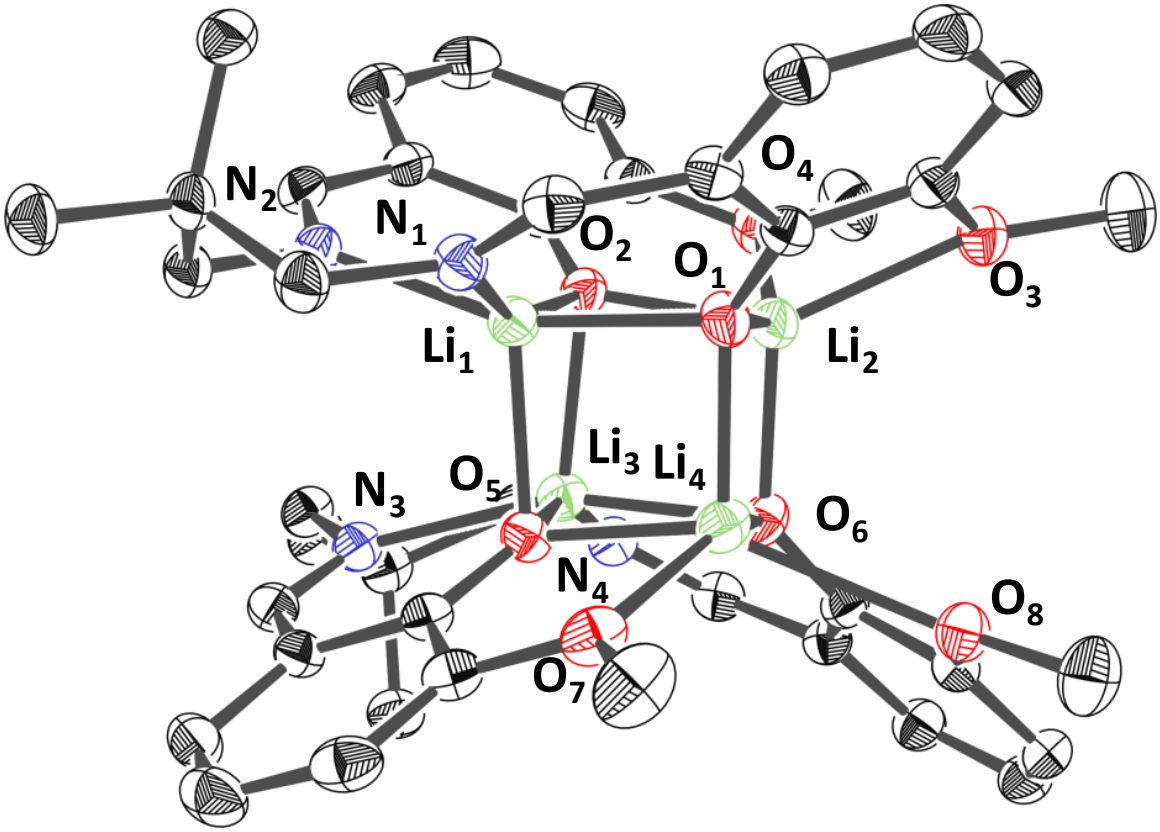


Figure S111: ORTEP representation of the molecular structure of **19** with disorder and hydrogen atoms omitted for clarity with thermal ellipsoids represented at 40 % probability.

Table S15: Selected bond lengths (Å) and angles (°) for complex **19**.

Bond	Bond Length (Å)	Bond	Bond Angle (°)
N (1) – Li (1)	2.068(7)	N (1) – Li (1) – O (2)	155.6(3)
N (2) – Li (1)	2.109(7)	N (2) – Li (1) – O (1)	159.5(3)
O (1) – Li (1)	2.028(7)	N (1) – Li (1) – O (5)	109.9(3)
O (2) – Li (1)	1.937(7)	O (3) – Li (2) – O (2)	143.5(3)
O (5) – Li (1)	2.030(6)	O (4) – Li (2) – O (1)	150.2(4)
O (1) – Li (2)	1.962(7)	O (3) – Li (2) – O (6)	114.1(3)
O (2) – Li (2)	1.905(7)		
O (3) – Li (2)	2.491(7)	**Metal – Metal**	**Distance (Å)**
O (4) – Li (2)	2.386(8)		
O (6) – Li (2)	1.922(7)	Li (1) – Li (2)	2.840(9)

.

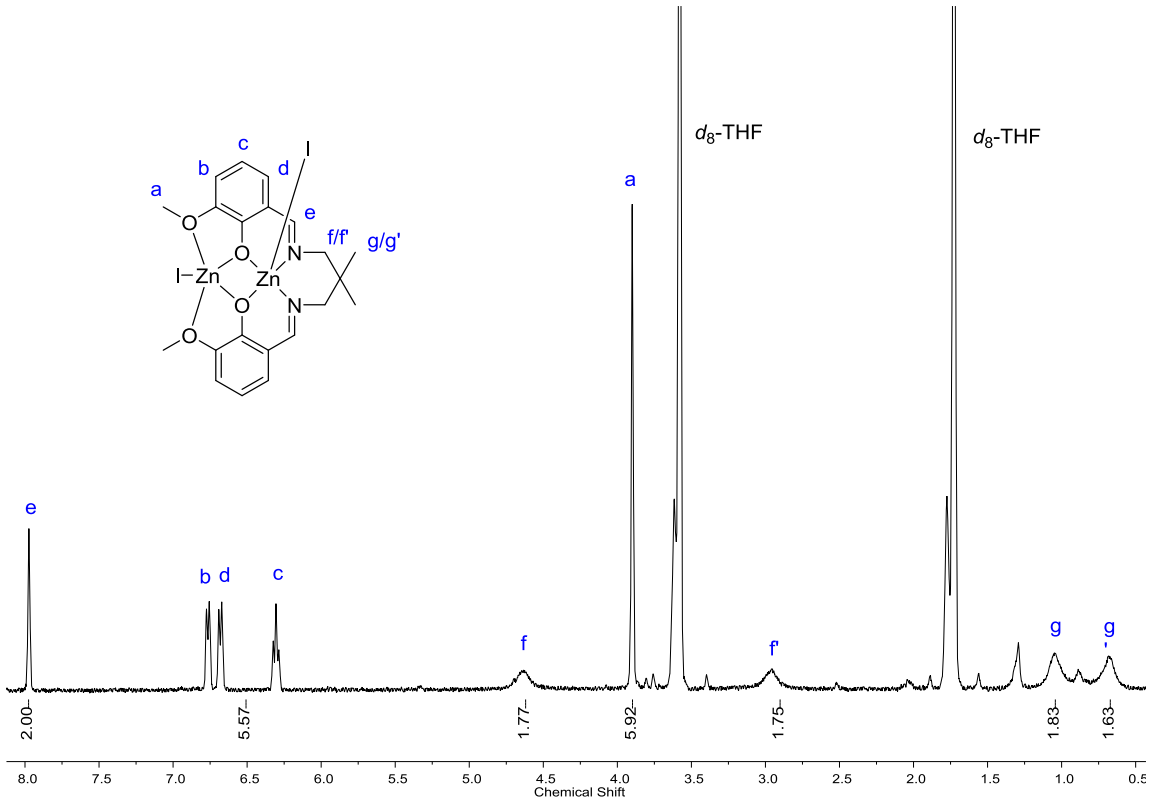


Figure S112: ^{1}H NMR of **20** (d_8-THF, 298 K)

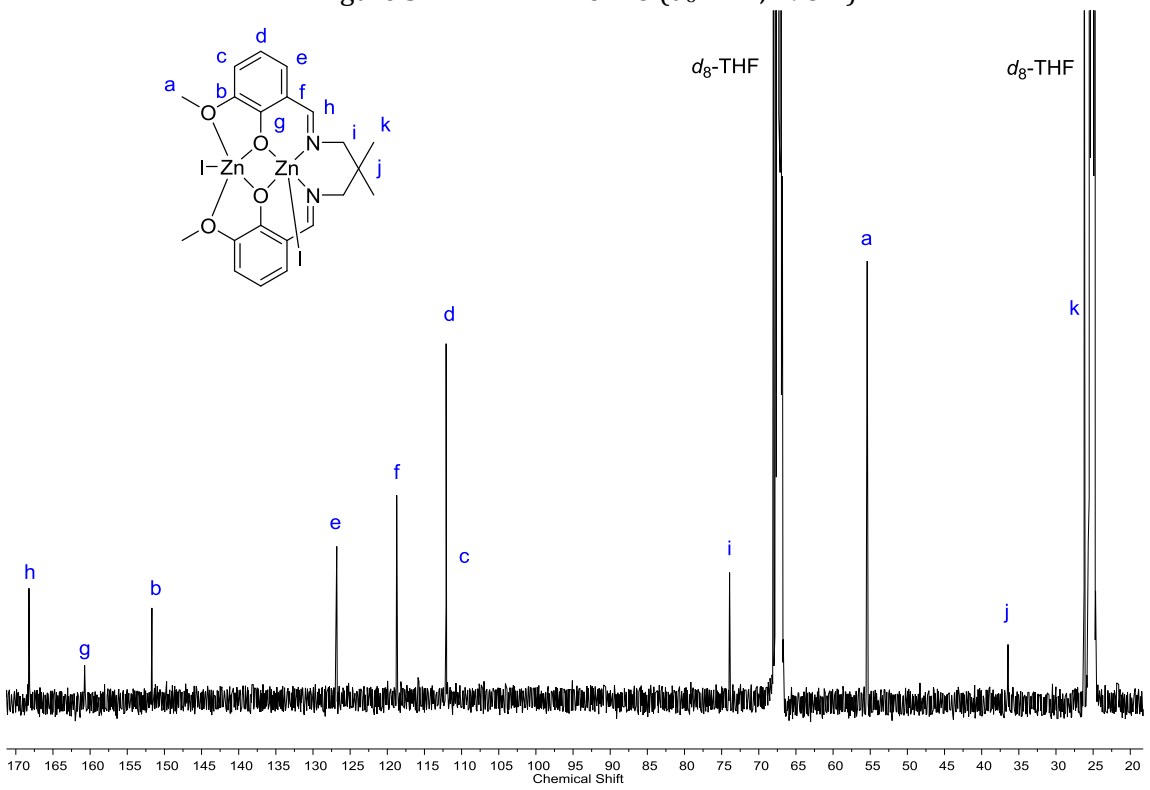


Figure S113: ^{13}C NMR of **20** in (d_8-THF, 298 K)

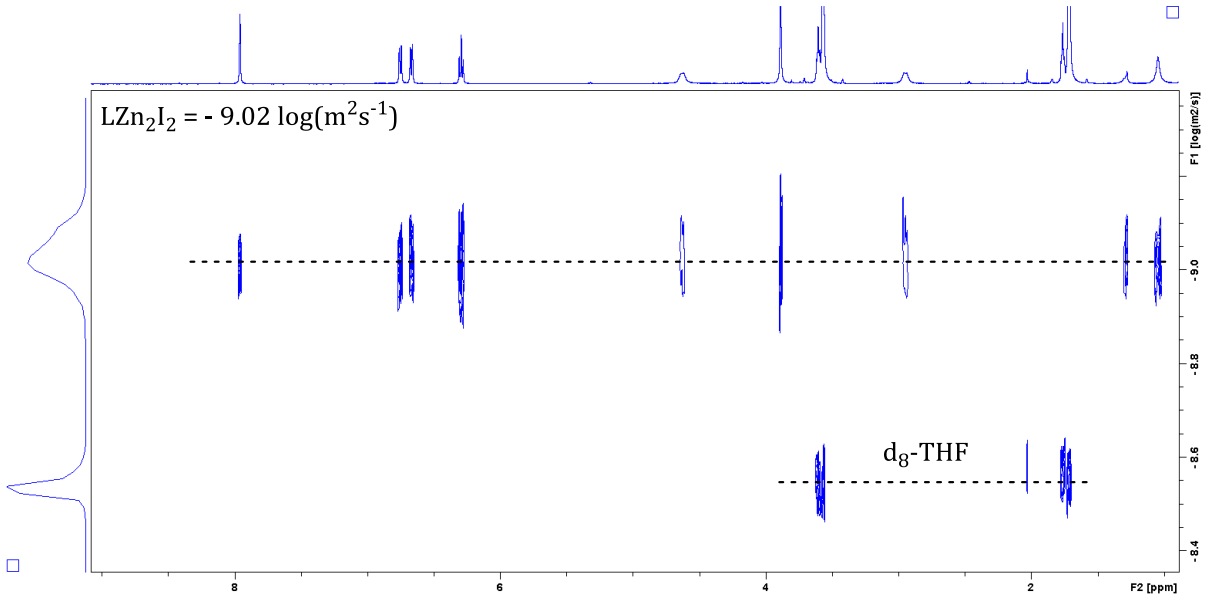


Figure S114: 2D DOSY NMR of complex **20** (d_8-THF, 298 K)

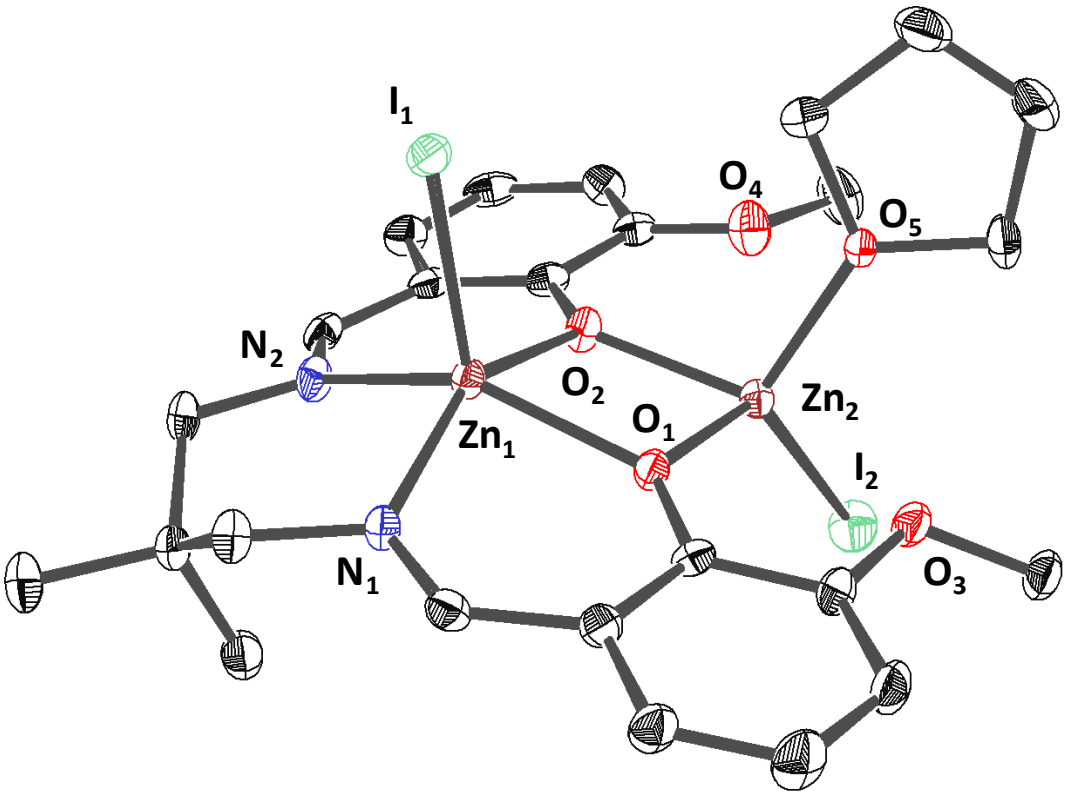


Figure 115: ORTEP representation of the molecular structure of **20** with disorder and hydrogen atoms omitted for clarity with thermal ellipsoids represented at 40 % probability.

Table S16: Selected bond lengths (Å) and angles (°) for complex **20**.

Bond	Bond Length (Å)	Bond	Bond Angel (°)
N (1) – Zn (1)	2.076(5)	N (1) – Zn (1) – O (2)	150.0(3)
N (2) – Zn (1)	2.109(7)	N (2) – Zn (1) – O (1)	142.1(3)
O (1) – Zn (1)	2.082(6)	N (1) – Zn (1) – I (1)	101.0(2)
O (2) – Zn (1)	2.070(5)	O (1) – Zn (2) – O (5)	104.0(2)
I (1) – Zn (1)	2.63297(13)	O (2) – Zn (2) – I (2)	117.84(19)
O (1) – Zn (2)	1.995(6)	O (5) – Zn (2) – I (2)	118.96(18)
O (2) – Zn (2)	2.012(6)		
O (5) – Zn (2)	2.035(7)	**Metal – Metal**	**Distance (Å)**
I (2) – Zn (2)	2.5232(12)	Zn (1) – Zn (2)	3.21325(6)

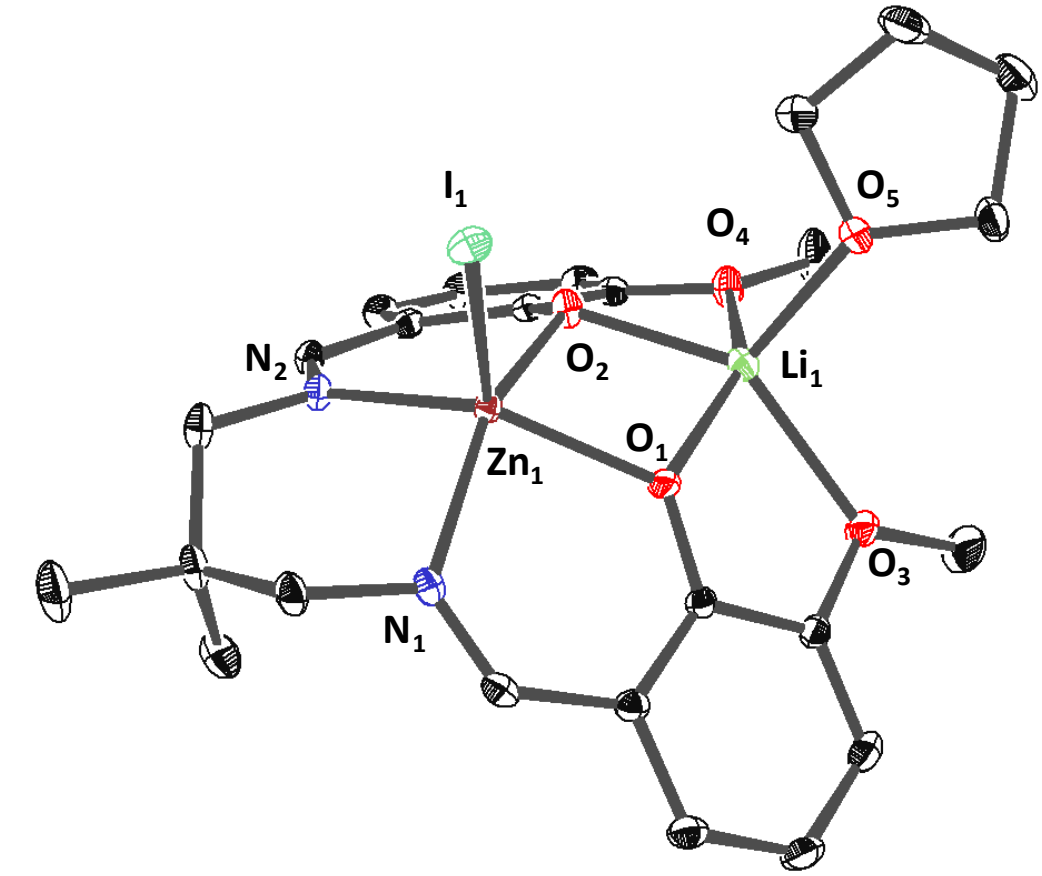


Figure 116: ORTEP representation of the molecular structure of **21** with disorder and hydrogen atoms omitted for clarity with thermal ellipsoids represented at 40 % probability.

Table S17: Selected bond lengths (Å) and angles (°) for complex **21**.

Bond	Bond Length (Å)	Bond	Bond Angel (°)
N (1) – Zn (1)	2.0990(17)	N (1) – Zn (1) – O (2)	150.09(7)
N (2) – Zn (1)	2.0862(17)	N (2) – Zn (1) – O (1)	141.82(7)
O (1) – Zn (1)	2.0165(15)	N (1) – Zn (1) – I (1)	101.66(5)
O (2) – Zn (1)	2.0389(14)	O (1) – Li (1) – O (5)	119.8(2)
I (1) – Zn (1)	2.6219(3)	O (2) – Li (1) – O (3)	142.89(19)
O (1) – Li (1)	1.933(4)	O (1) – Li (1) – O (4)	143.5(2)
O (2) – Li (1)	1.994(4)		
O (3) – Li (1)	2.196(4)	**Metal – Metal**	**Distance (Å)**
O (4) – Li (1)	2.143(4)		
O (5) – Li (1)	1.935(4)	Zn (1) – Li (1)	3.070(4)

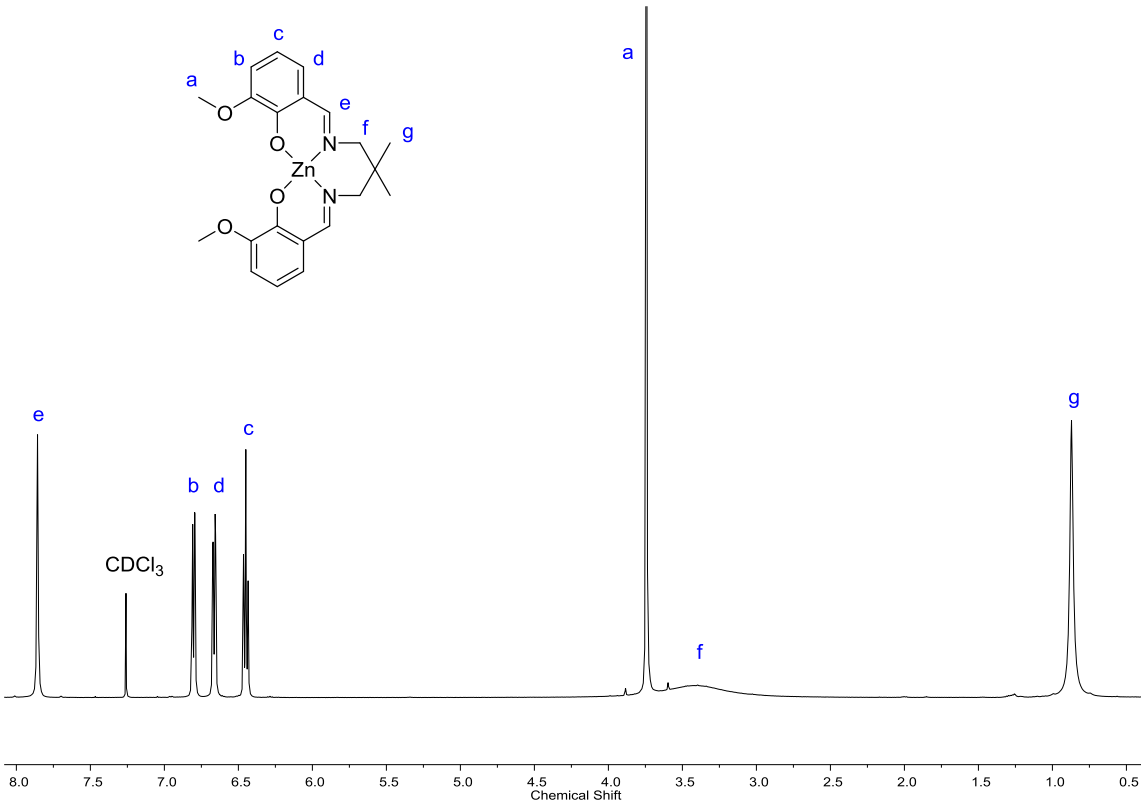


Figure S117: ^{1}H NMR of **22** ($CDCl_3$, 298 K)

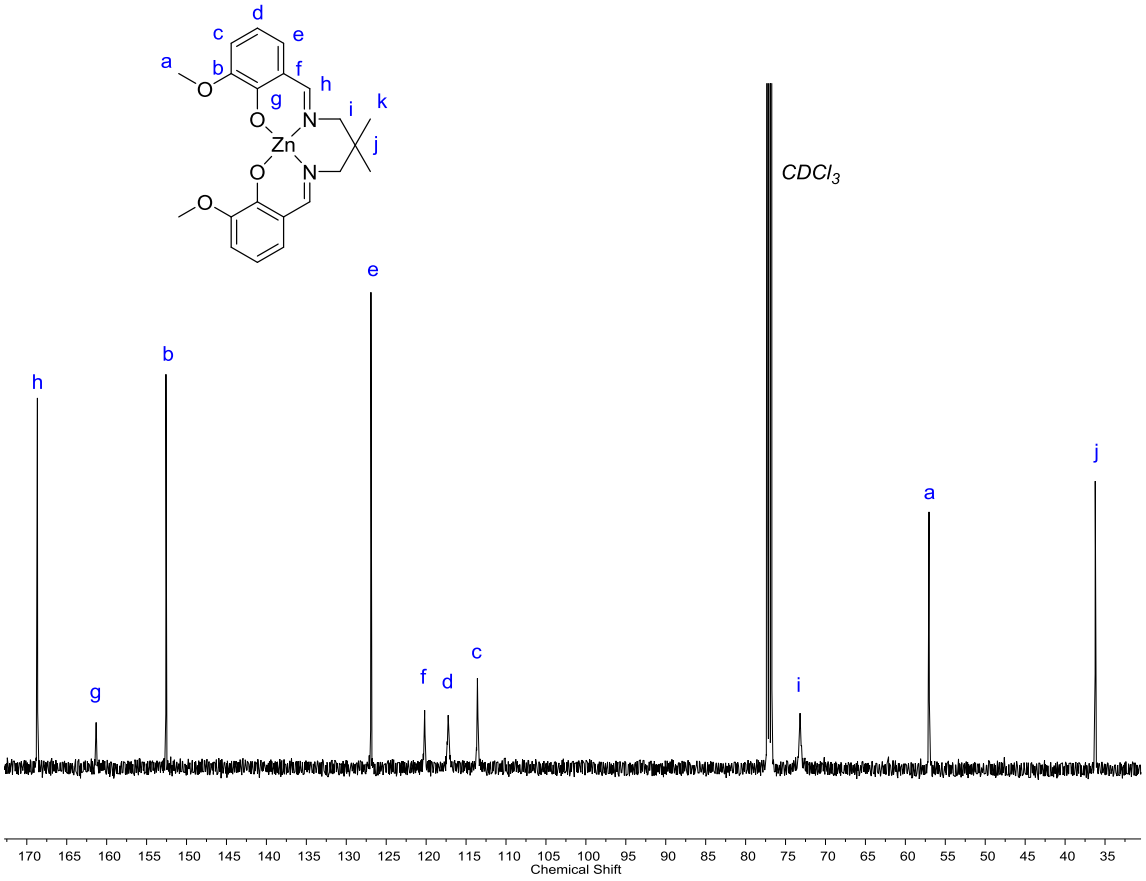


Figure S118: ^{13}C NMR of **22** ($CDCl_3$, 298 K)

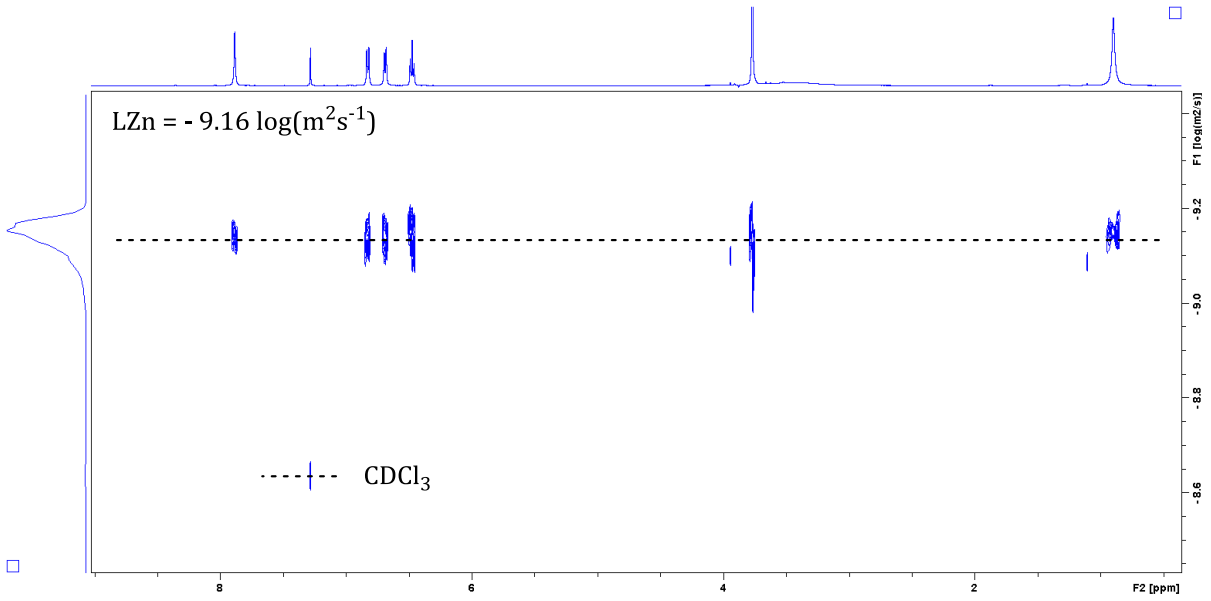


Figure S119: 2D DOSY NMR of **22** ($CDCl_3$, 298 K)

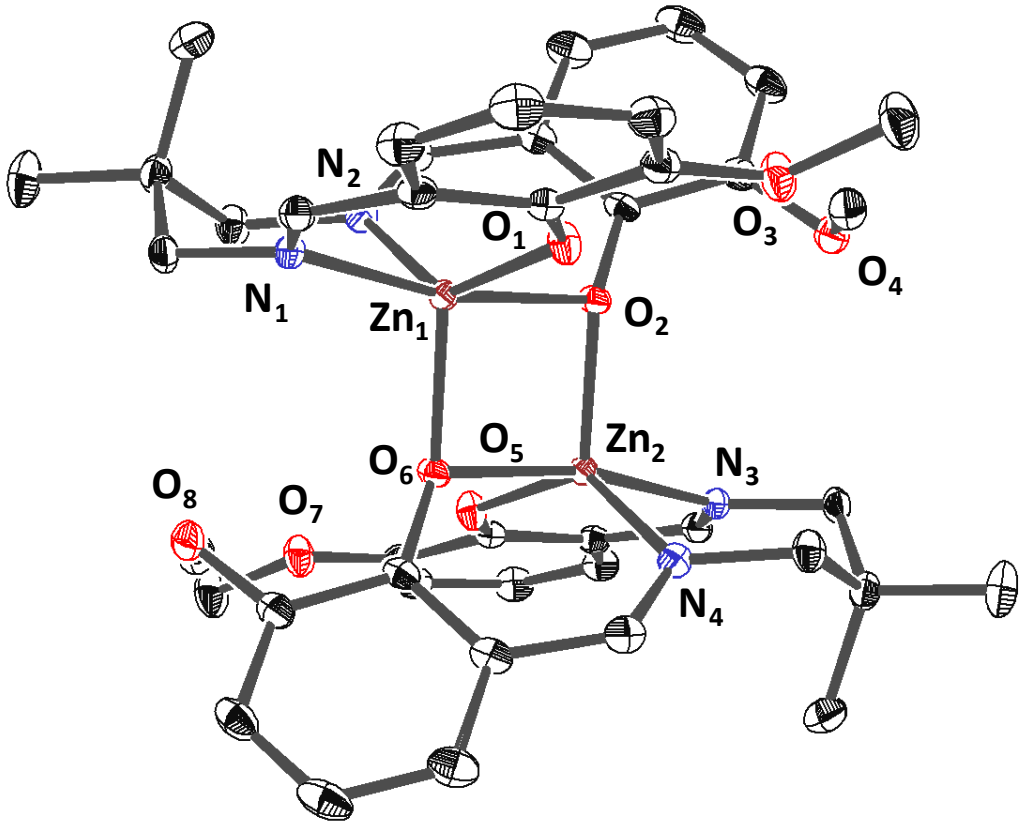


Figure S120: ORTEP representation of the molecular structure of **22** with disorder and hydrogen atoms omitted for clarity with thermal ellipsoids represented at 40 % probability.

Table S18: Selected bond lengths (Å) and angles (°) for complex **22**.

Bond	Bond Length (Å)	Bond	Bond Angel (°)
N (1) – Zn (1)	2.0741(13)	N (1) – Zn (1) – O (2)	168.70(5)
N (2) – Zn (1)	2.0977(14)	N (2) – Zn (1) – O (1)	136.66(5)
O (1) – Zn (1)	1.9575(11)	N (1) – Zn (1) – O (6)	108.35(5)
O (2) – Zn (1)	2.1437(11)	N (3) – Zn (2) – O (6)	168.70(5)
O (6) – Zn (2)	2.0102(10)	N (4) – Zn (2) – O (5)	136.66(5)
N (2) – Zn (2)	2.0741(13)	N(3) – Zn (2) – O (2)	108.35(5)
N (3) – Zn (2)	2.0977(14)		
O (5) – Zn (2)	1.9575(11)	**Metal – Metal**	**Distance (Å)**
O (6) – Zn (2)	2.1437(11)		
O (2) – Zn (2)	2.0102(10)	Zn (1) – Zn (2)	3.1217(4)

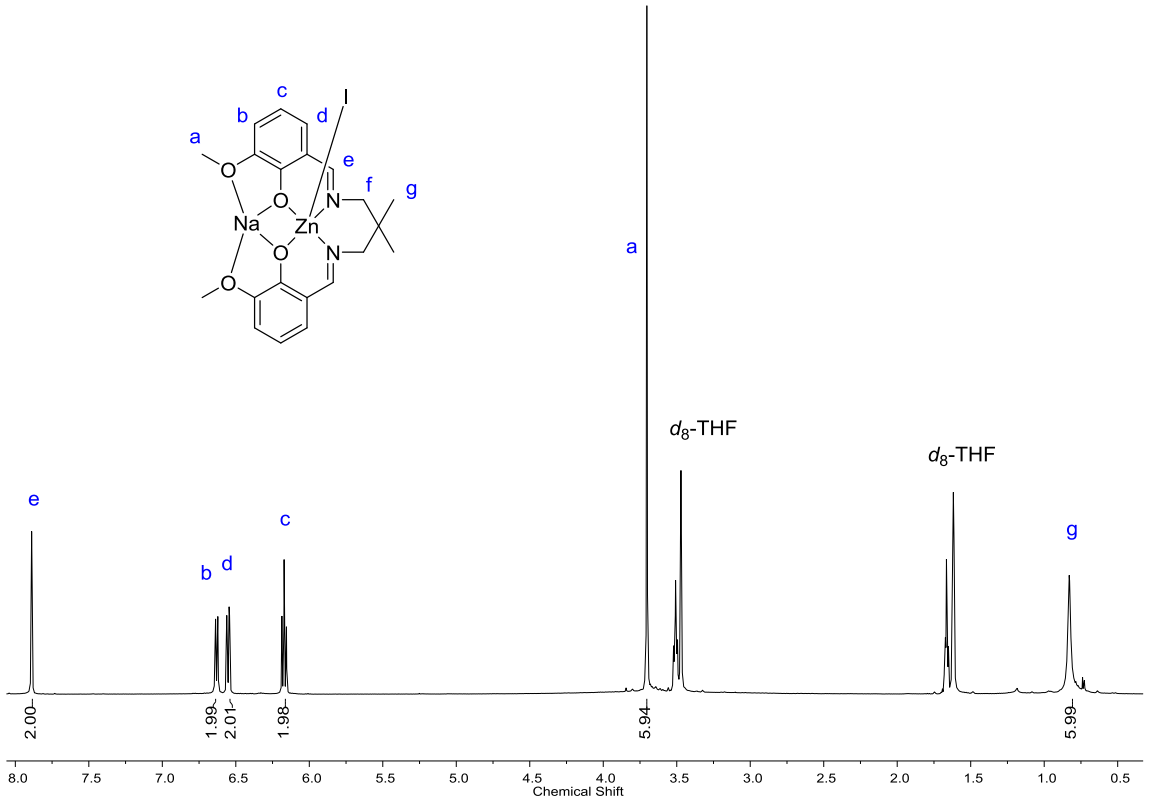


Figure S121: ^{1}H NMR of **23** (d_8-THF, 298 K)

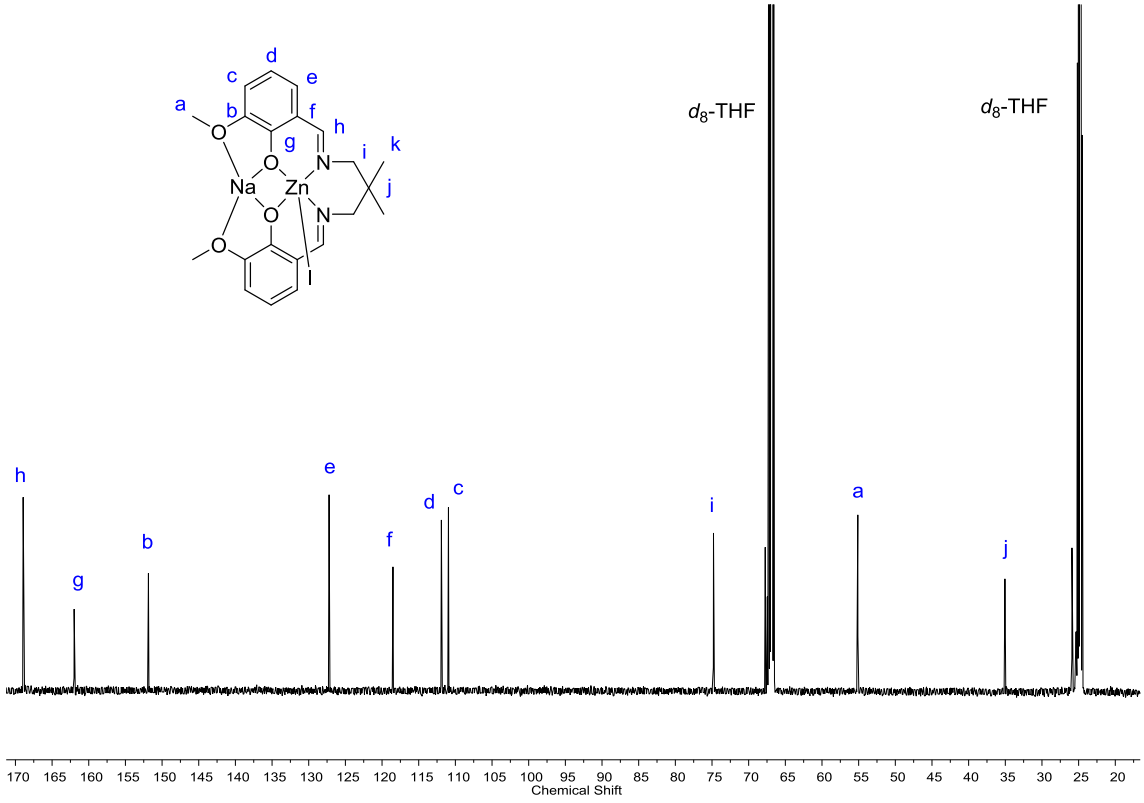


Figure S122: ^{13}C NMR of **23** (d_8-THF, 298 K)

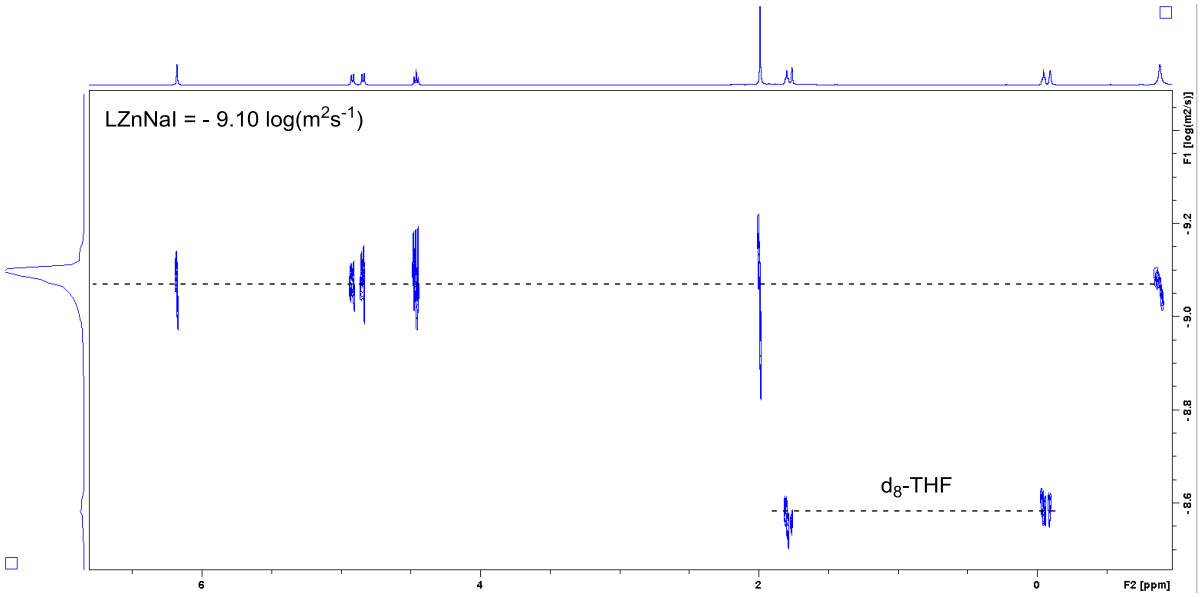


Figure S123: 2D DOSY of **23** (d_8-THF, 298 K)

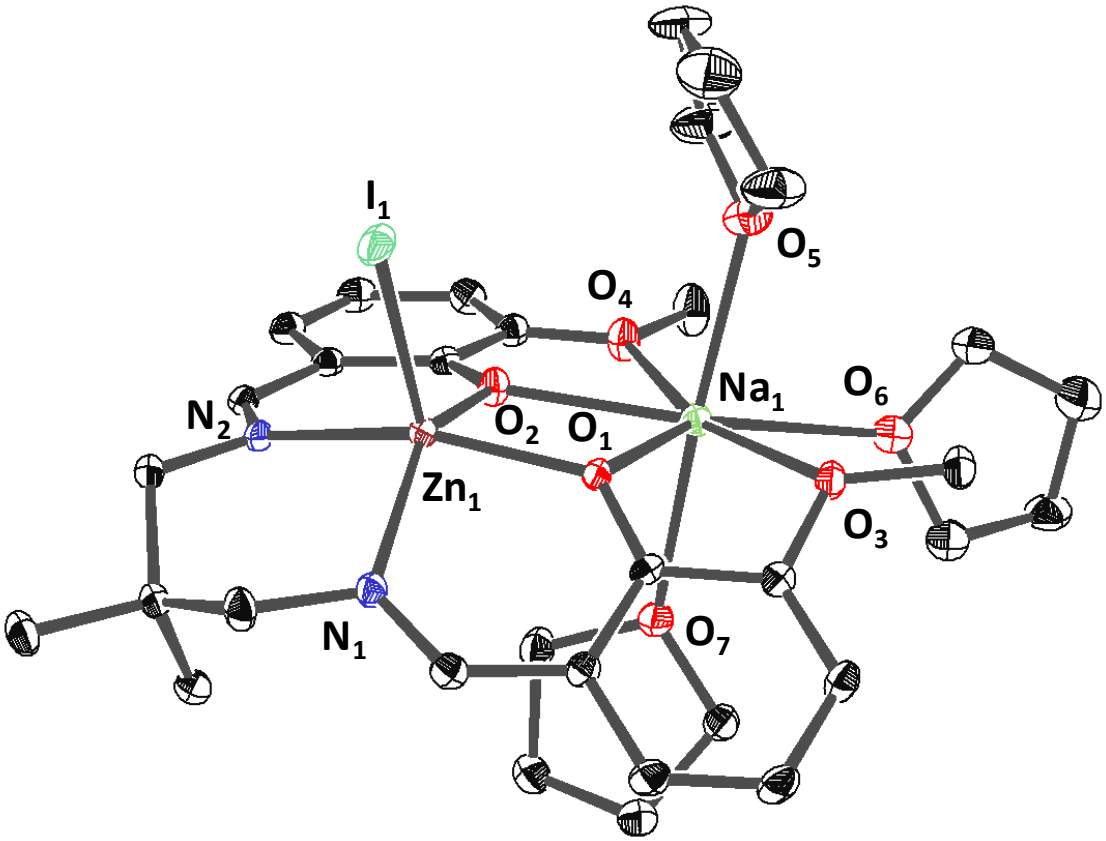


Figure S124: ORTEP representation of the molecular structure of **23** with disorder and hydrogen atoms omitted for clarity with thermal ellipsoids represented at 40 % probability.

Table S19: Selected bond lengths (Å) and angles (°) for complex **23**.

Bond	Bond Length (Å)	Bond	Bond Angel (°)
N (1) – Zn (1)	2.115(2)	N (1) – Zn (1) – O (2)	141.55(10)
N (2) – Zn (1)	2.128(3)	N (2) – Zn (1) – O (1)	157.12(10)
O (1) – Zn (1)	2.009(2)	N (1) – Zn (1) – I (1)	102.59(7)
O (2) – Zn (1)	2.050(2)	O (1) – Na (1) – O (6)	141.66(10)
I (1) – Zn (1)	2.6560(5)	O (1) – Na (1) – O (5)	101.30(10)
O (1) – Na (1)	2.388(2)	O (5) – Na (1) – O (7)	173.91(11)
O (2) – Na (1)	2.376(3)		
O (3) – Na (1)	2.497(3)	**Metal – Metal**	**Distance (Å)**
O (4) – Na (1)	2.481(3)		
O (5) – Na (1)	2.450(3)	Zn (1) – Na (1)	3.5461(13)
O (6) – Na (1)	2.650(3)		
O (7) – Na (1)	2.481(3)		

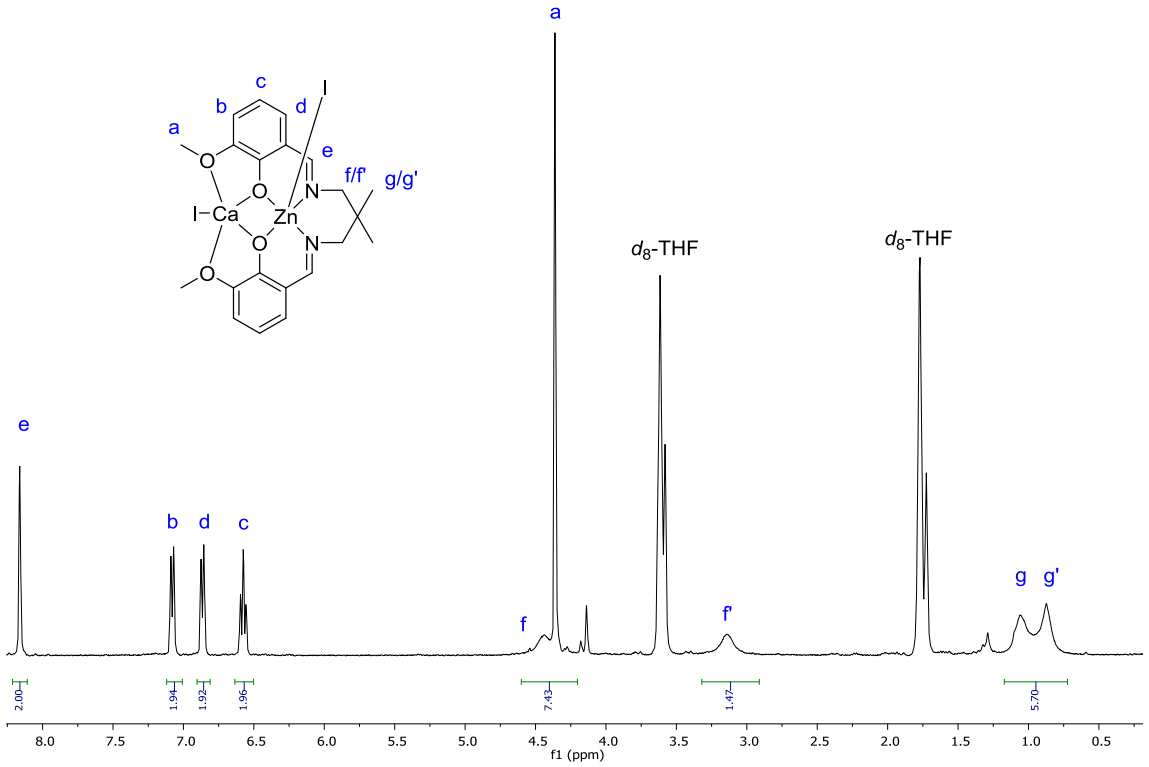


Figure S125: ^{1}H NMR of **24** (d_8-THF, 298 K)

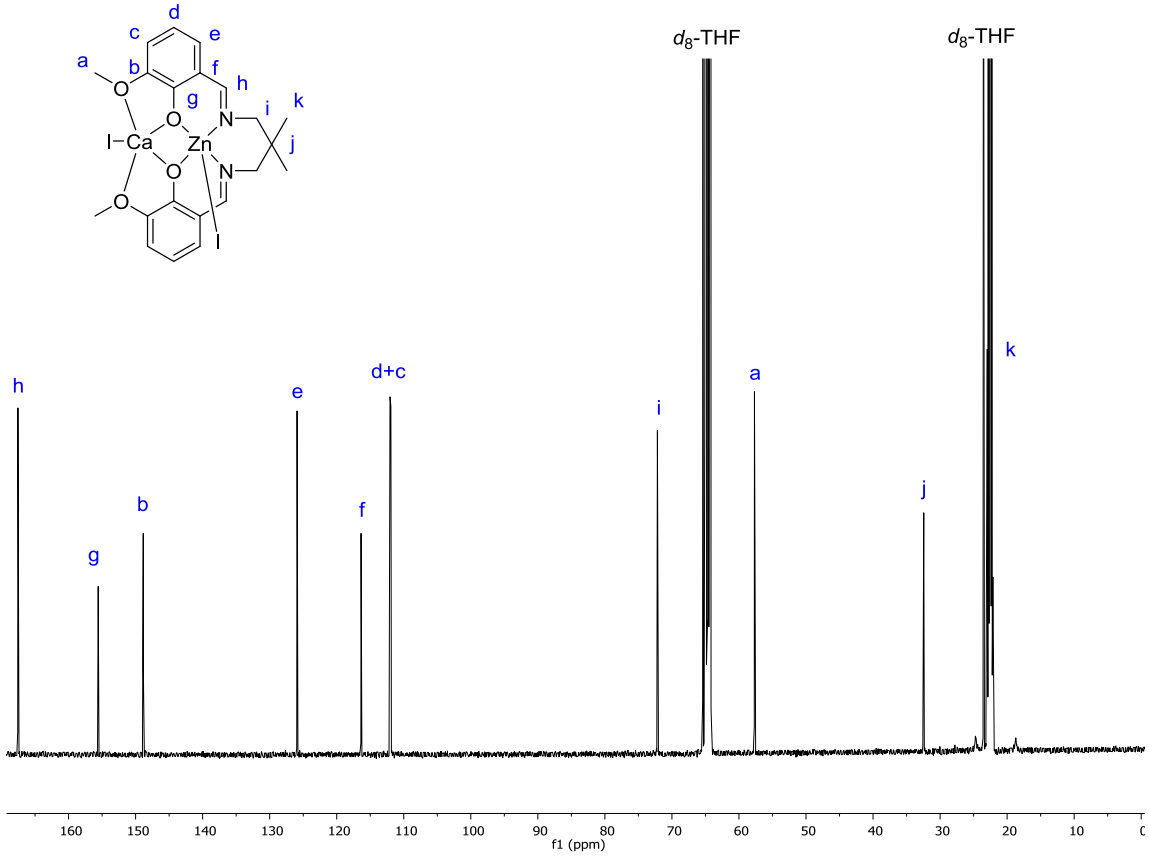


Figure S126: ^{13}C NMR of **24** (d_8-THF, 298 K)

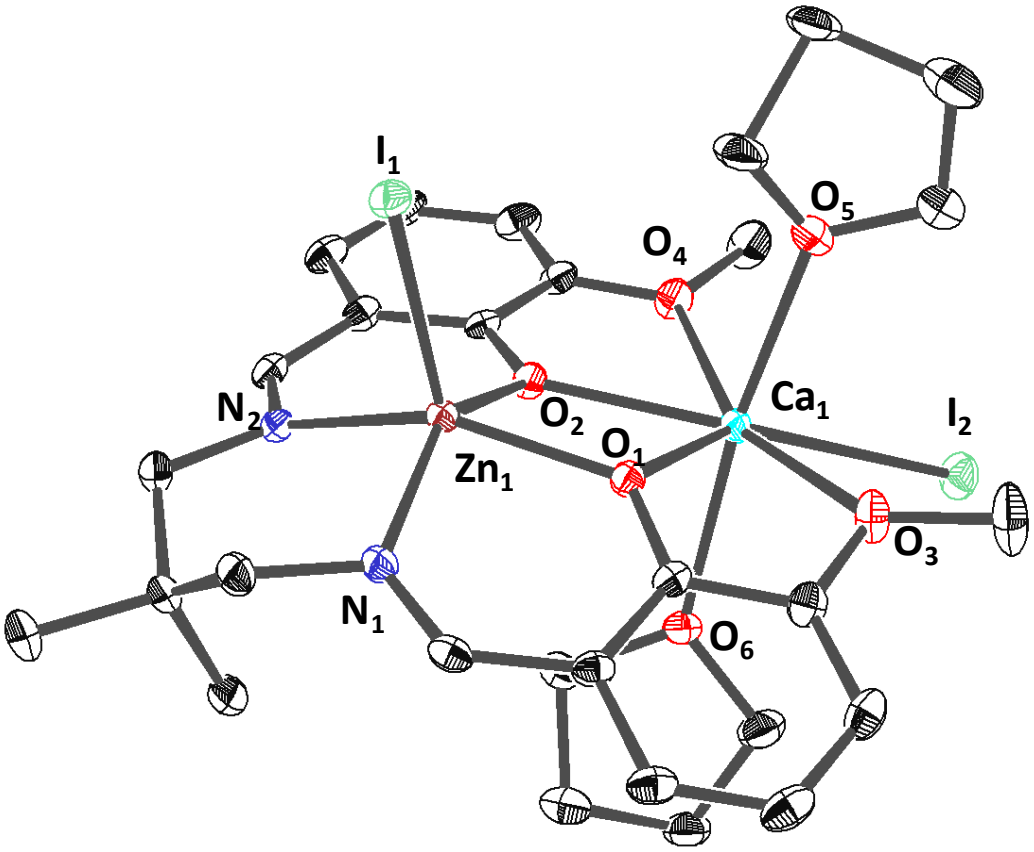


Figure S127: ORTEP representation of the molecular structure of **24** with disorder and hydrogen atoms omitted for clarity with thermal ellipsoids represented at 40 % probability.

Table S20: Selected bond lengths (Å) and angles (°) for complex **23**.

Bond	Bond Length (Å)	Bond	Bond Angel (°)
N (1) – Zn (1)	2.086(3)	N (1) – Zn (1) – O (2)	144.18(11)
N (2) – Zn (1)	2.132(3)	N (2) – Zn (1) – O (1)	149.77(11)
O (1) – Zn (1)	2.083(2)	N (1) – Zn (1) – I (1)	104.20(9)
O (2) – Zn (1)	2.043(2)	O (1) – Ca (1) – I (2)	144.46(6)
I (1) – Zn (1)	2.6313(5)	O (1) – Ca (1) – O (5)	95.22(11)
O (1) – Ca (1)	2.357(2)	O (5) – Ca (1) – O (7)	170.314(12)
O (2) – Ca (1)	2.333(2)		
O (3) – Ca (1)	2.502(3)	**Metal – Metal**	**Distance (Å)**
O (4) – Ca (1)	2.482(3)		
O (5) – Ca (1)	2.365(3)	Zn (1) – Ca (1)	3.5785(8)
O (6) – Ca (1)	2.401(3)		
I (2) – Ca (1)	3.1686(7)		

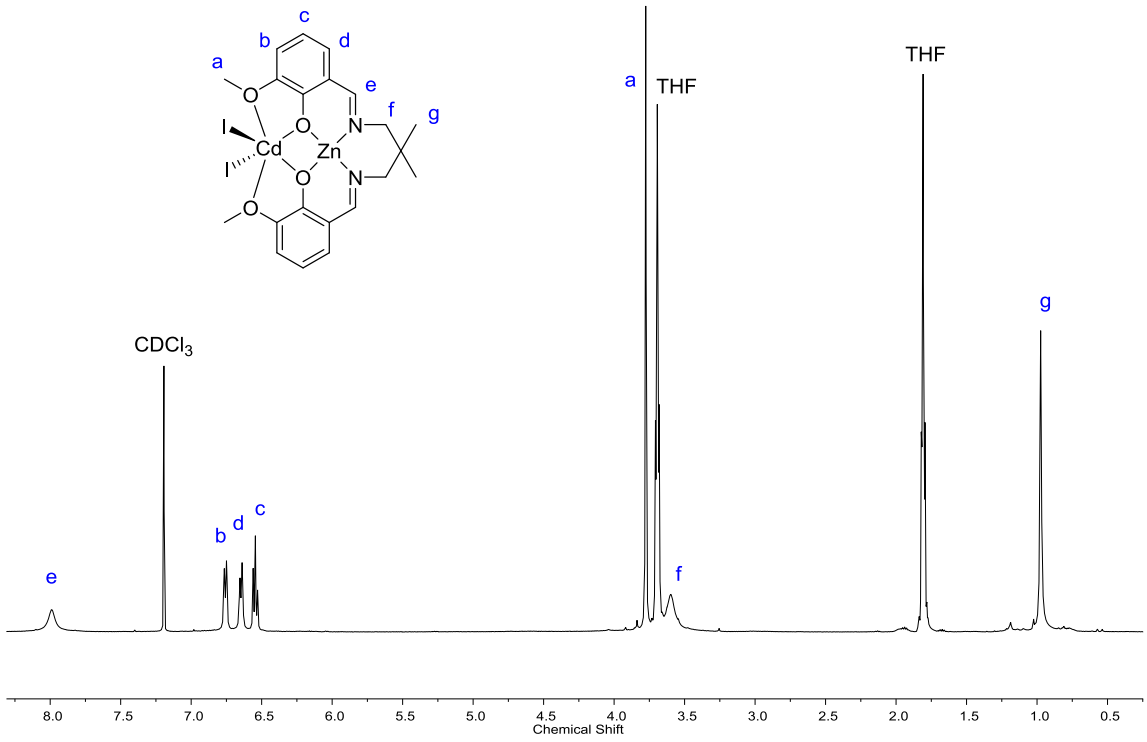


Figure 128: ^{1}H NMR of **25** (d_8-THF, 298 K)

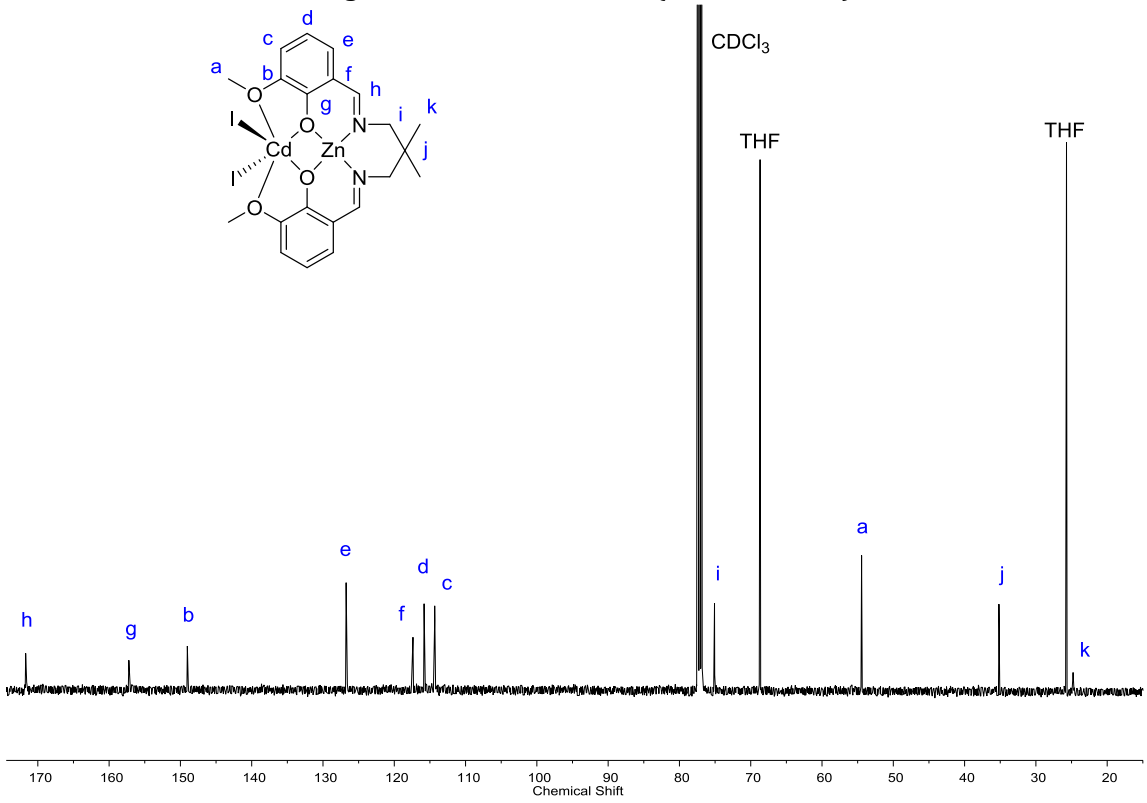


Figure S129: ^{13}C NMR of **25** ($CDCl_3$, 298 K)

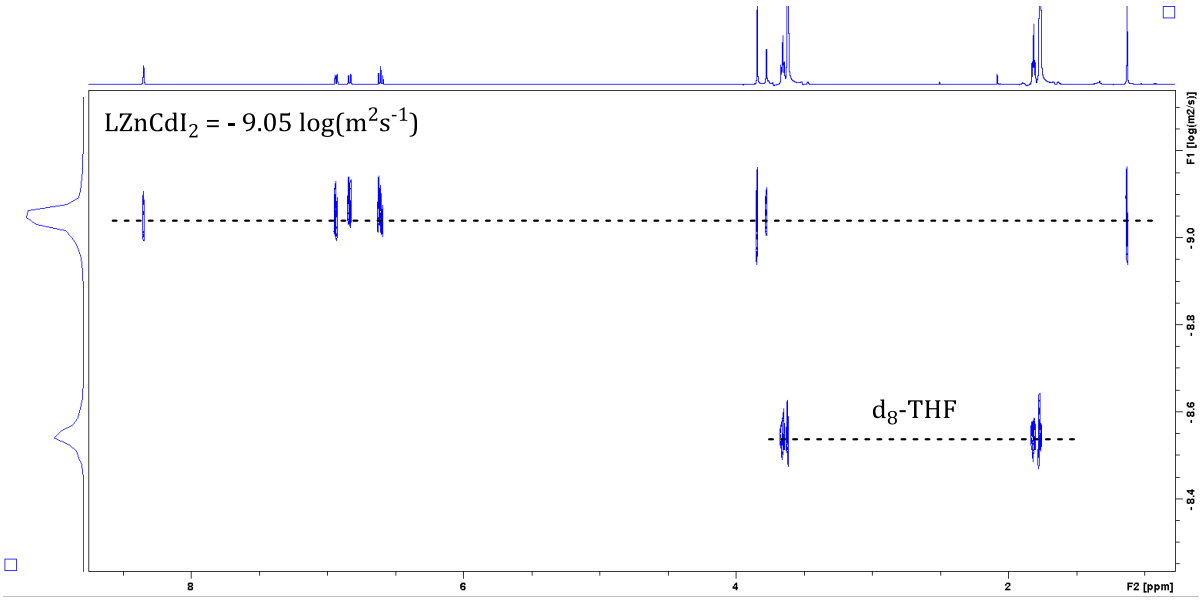


Figure S130: 2D DOSY NMR of **25** (d_8-THF, 298 K)

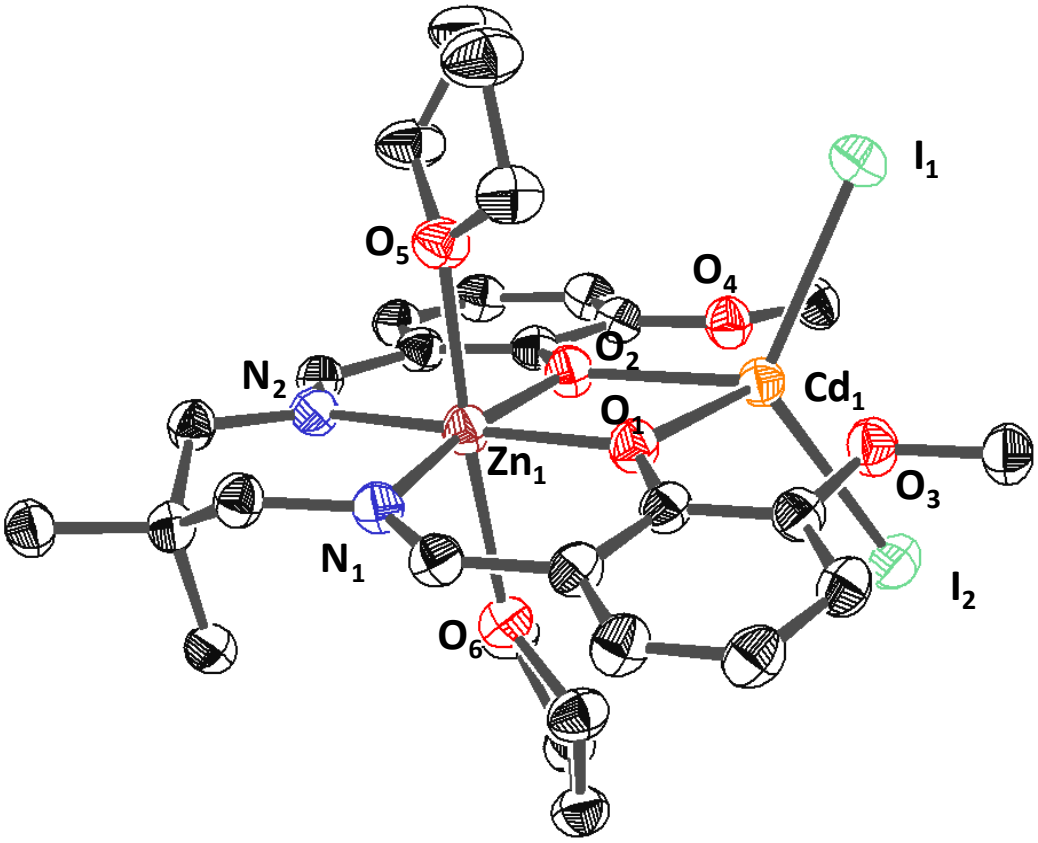


Figure S131: ORTEP representation of the molecular structure of **25** with disorder and hydrogen atoms omitted for clarity with thermal ellipsoids represented at 40 % probability.

Table S21: Selected bond lengths (Å) and angles (°) for complex **25**.

Bond	**Bond Length (Å)**	**Bond**	**Bond Angle (°)**
N (1) – Zn (1)	2.061(4)	N (1) – Zn (1) – O (2)	170.93(15)
N (2) – Zn (1)	2.057(4)	N (2) – Zn (1) – O (1)	172.99(15)
O (1) – Zn (1)	2.032(3)	O (5) – Zn (1) – O (6)	175.73(14)
O (2) – Zn (1)	2.019(3)	O (1) – Cd (1) – O (4)	134.64(11)
O (5) – Zn (1)	2.416(4)	O (1) – Cd (1) – I (2)	111.84(9)
O (6) – Zn (1)	2.191(4)	I (1) – Ca (1) – I (2)	122.381(15)
O (1) – Cd (1)	2.304(3)	**Metal – Metal**	**Distance (Å)**
O (2) – Cd (1)	2.277(3)		
I (1) – Cd (1)	2.7346(4)	Zn (1) – Cd (1)	3.4020(8)
I (2) – Cd (1)	3.7571(5)		

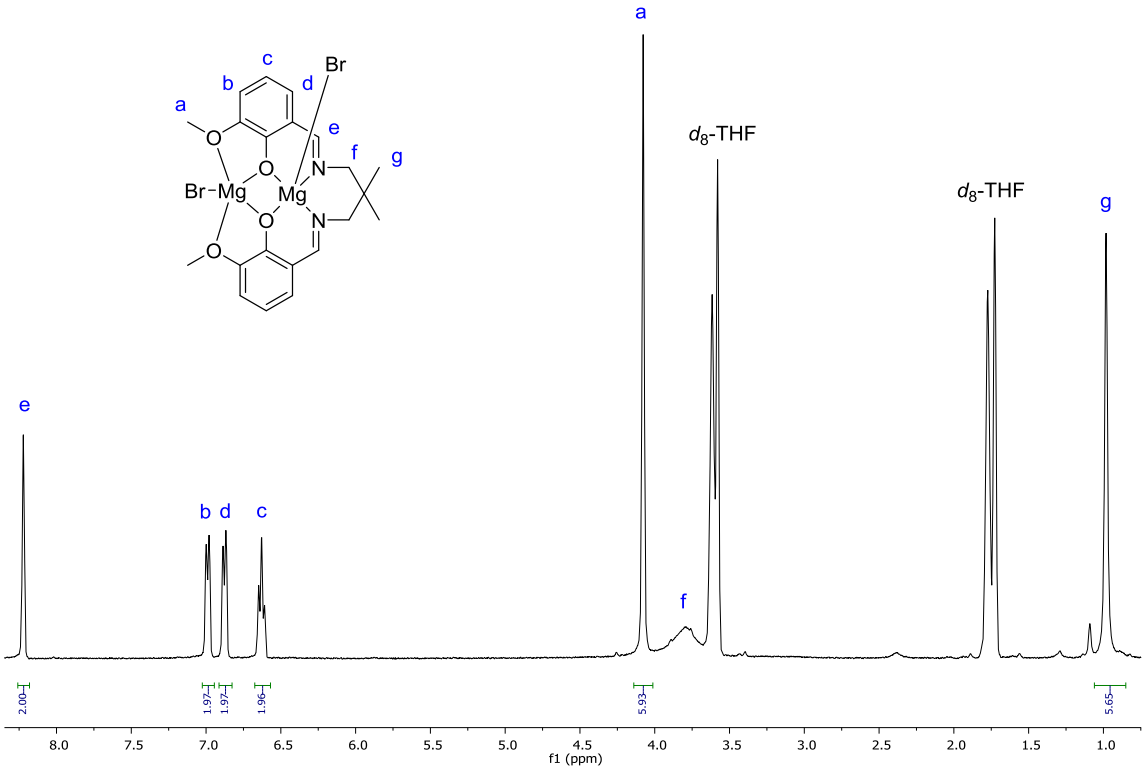


Figure S132: ^{1}H NMR of **26** (d_8-THF, 298 K)

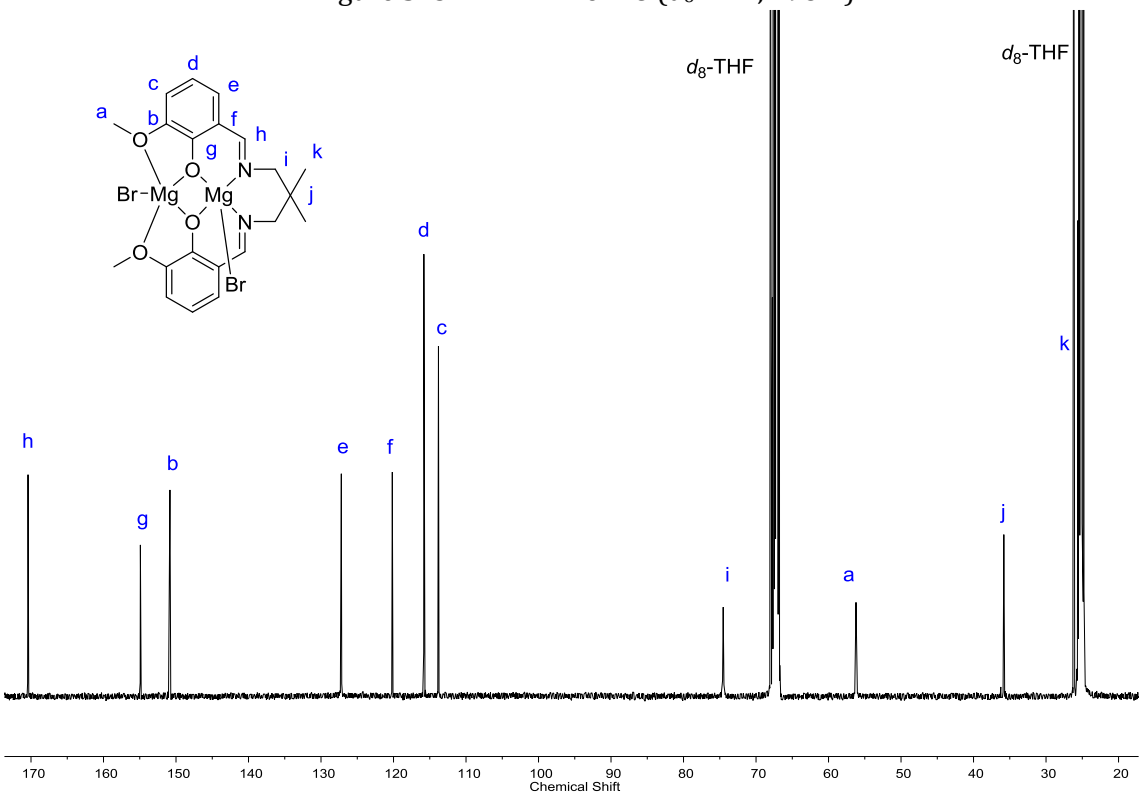


Figure S133: ^{13}C NMR of **26** (d_8-THF, 298 K)

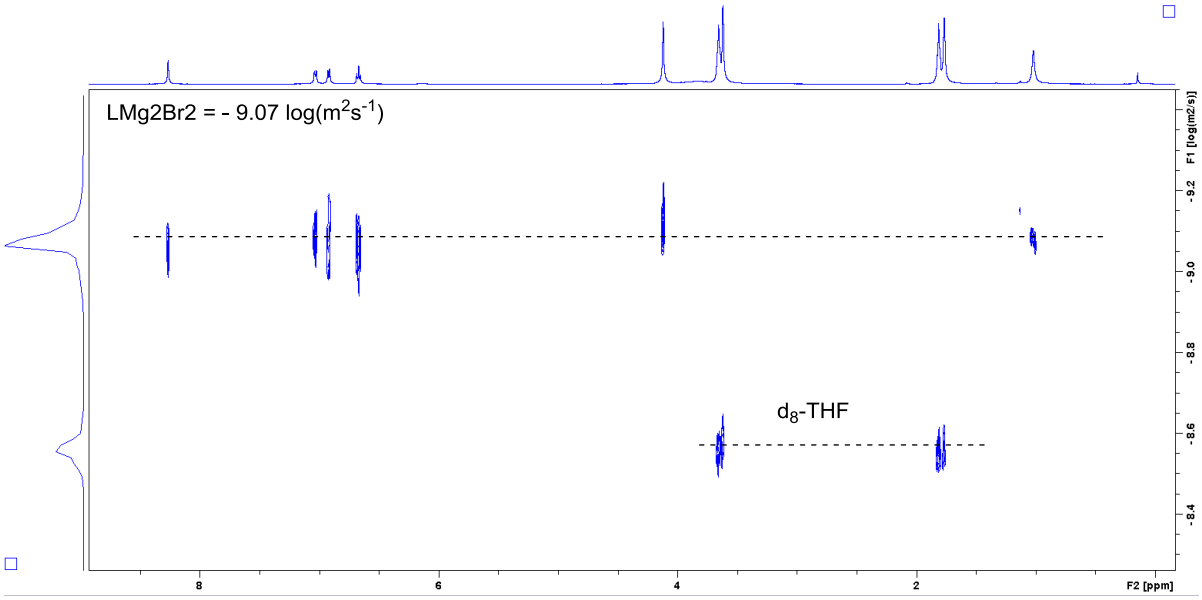


Figure S134: 2D DOSY NMR of **26** (d_8-THF, 298 K)

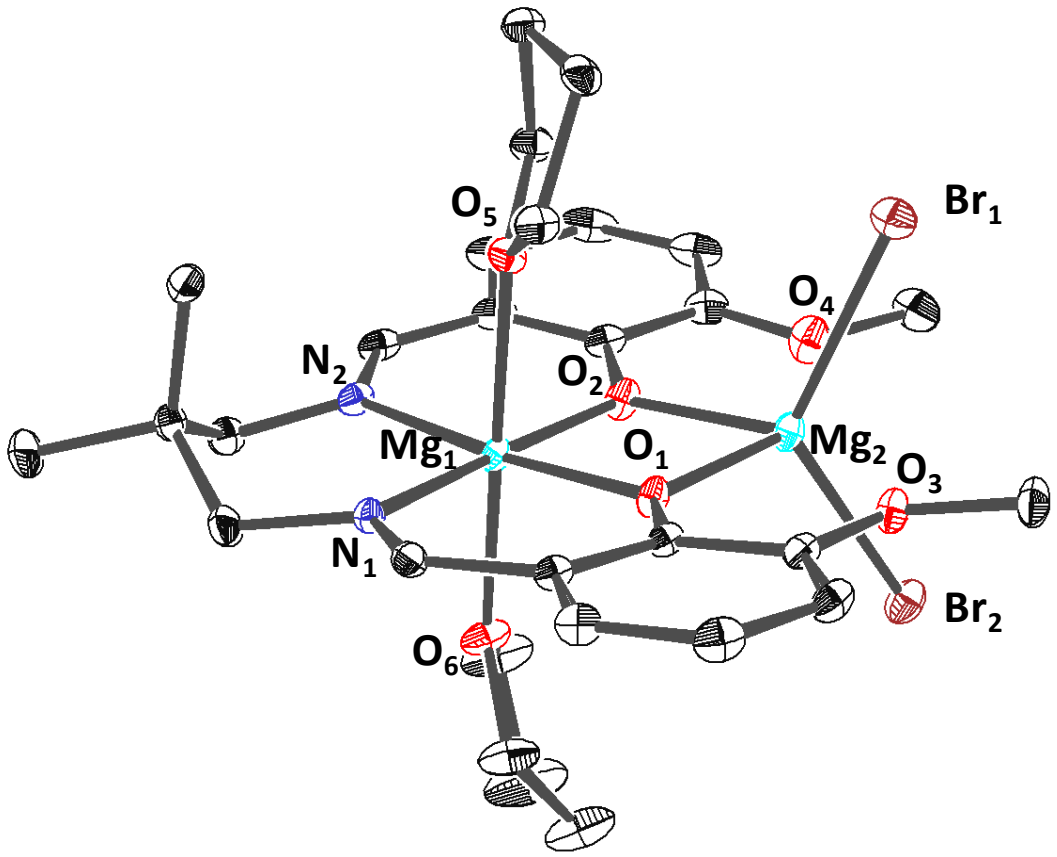


Figure S135: Connectivity molecular structure of **26** with disorder and hydrogen atoms omitted for clarity with thermal ellipsoids represented at 40 % probability.

Table S22: Selected bond lengths (Å) and angles (°) for complex **26**.

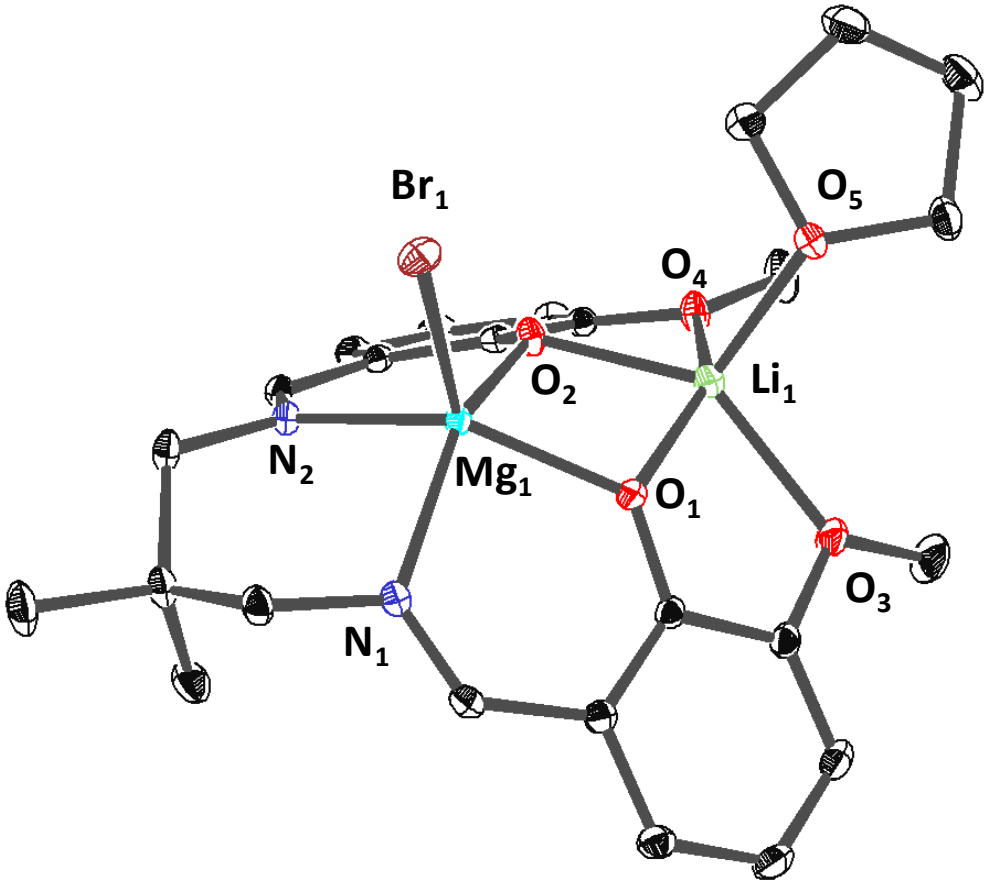


Figure S136: ORTEP representation of the molecular structure of **27** with disorder and hydrogen atoms (excluding NH) omitted for clarity with thermal ellipsoids represented at 40 % probability.

Table S23: Selected bond lengths (Å) and angles (°) for complex **25**.

Bond	**Bond Length (Å)**	**Bond**	**Bond Angle (°)**
N (1) – Mg (1)	2.1443(11)	N (1) – Mg (1) – O (2)	147.41(5)
N (2) – Mg (1)	2.1450(12)	N (2) – Mg (1) – O (1)	143.07(5)
O (1) – Mg (1)	1.9720(10)	Br (1) – Mg (1) – O (1)	101.44(3)
O (2) – Mg (1)	1.9740(10)	O (1) – Li (1) – O (4)	145.45(13)
Br (1) – Mg (1)	2.5091(4)	O (2) – Li (1) – O (3)	141.56(12)
O (1) – Li (1)	1.971(2)	O (1) – Li (1) – O (5)	117.93(13)
O (2) – Li (1)	1.999(3)	**Metal – Metal**	**Distance (Å)**
O (3) – Li (1)	2.148(3)		
O (4) – Li (1)	2.170(3)	Zn (1) – Li (1)	3.001(2)
O (5) – Li (1)	1.947(2)		

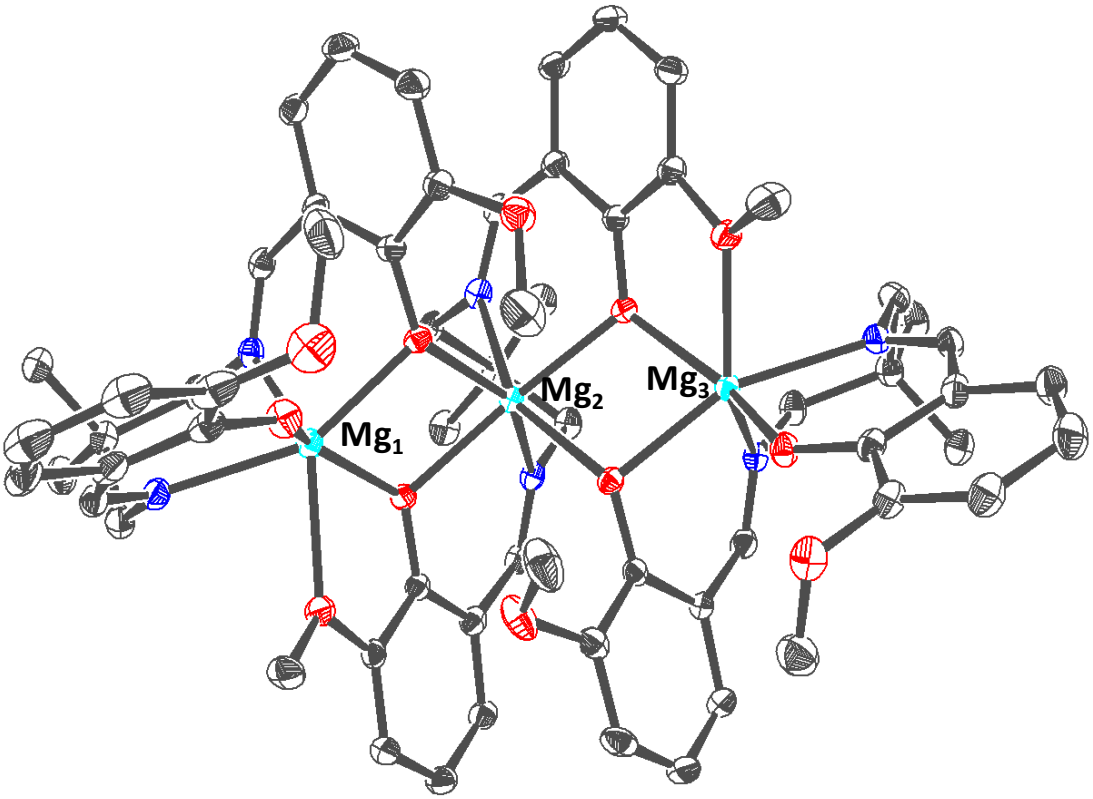


Figure S137: Connectivity structure of the molecular structure of **28** with disorder and hydrogen atoms omitted for clarity with thermal ellipsoids represented at 40 % probabiliy

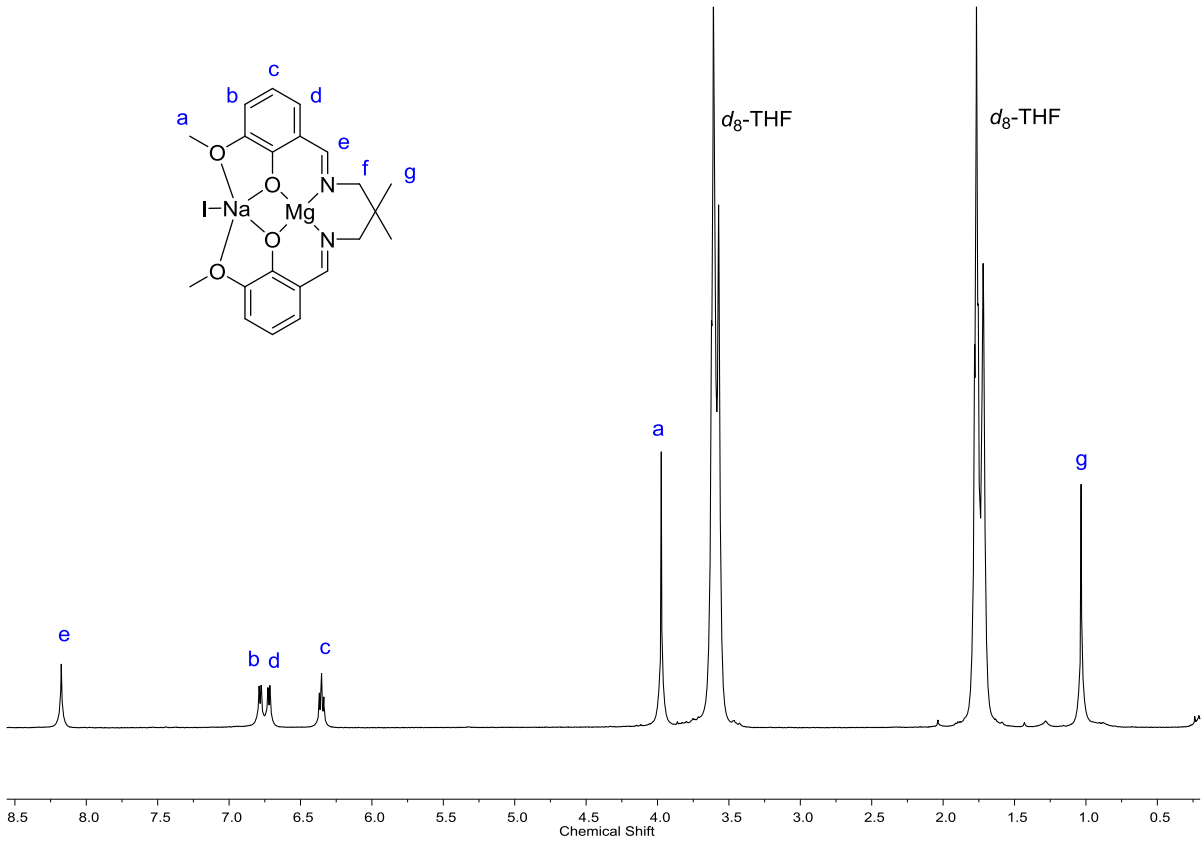


Figure S138: ^{1}H NMR of **28** (d_8-THF, 298 K)

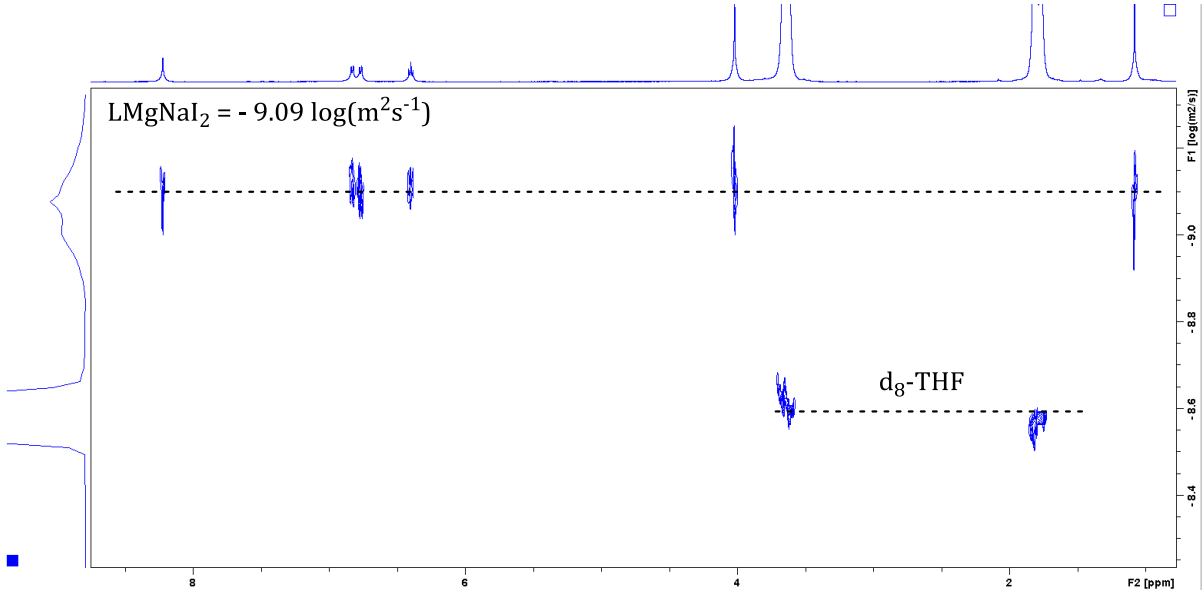


Figure S139: 2D DOSY NMR of **28** (d_8-THF, 298 K)

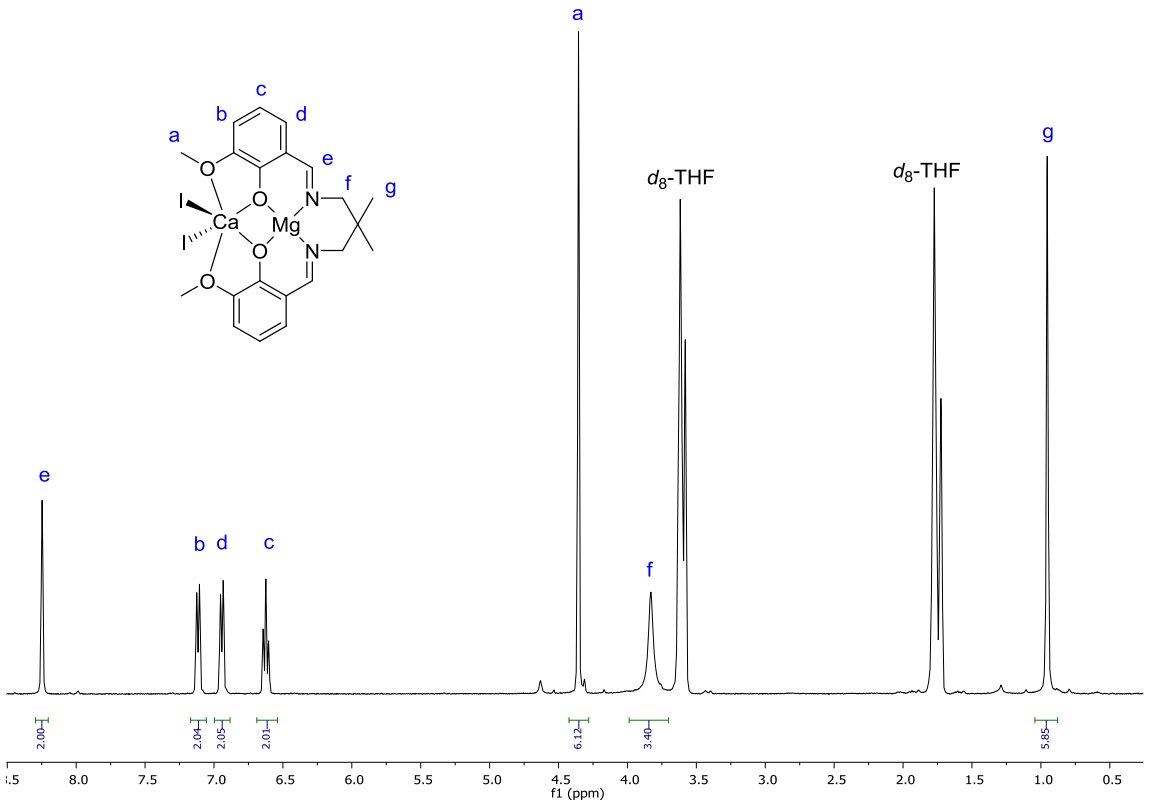


Figure S140: ^{1}H NMR of **29** (d_8-THF, 298 K)

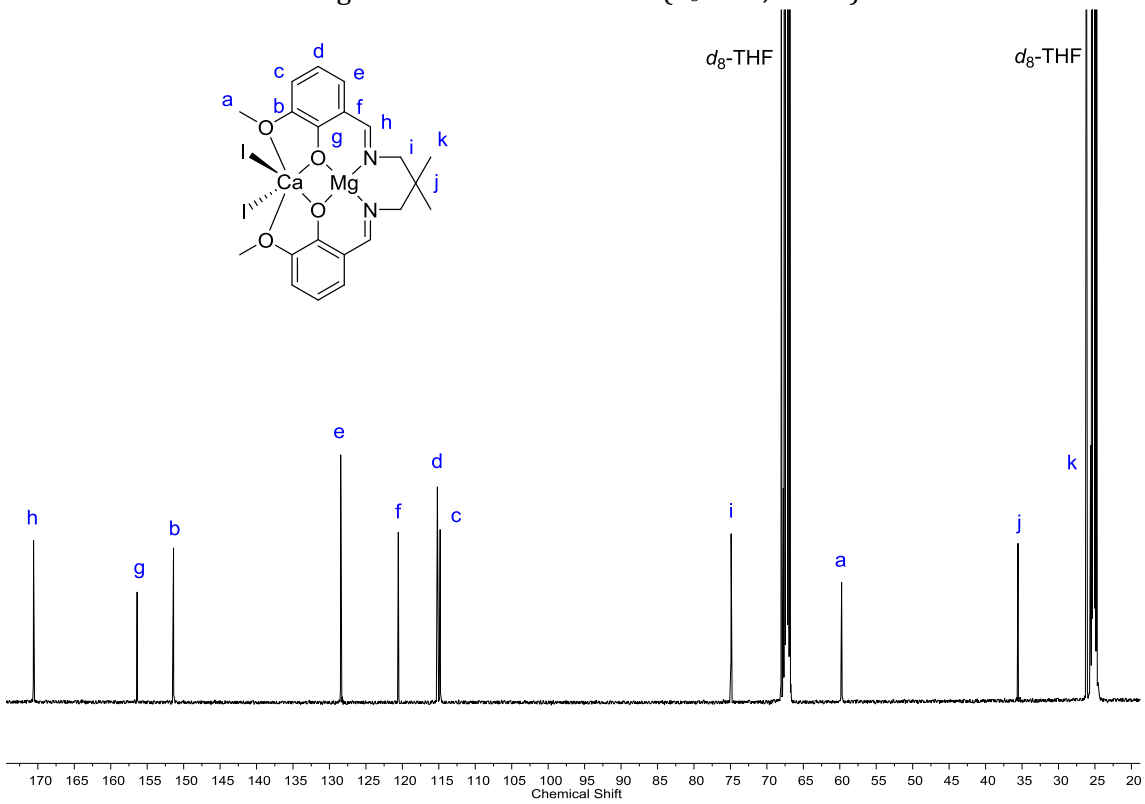


Figure S141: ^{13}C NMR of **29** (d_8-THF, 298 K)

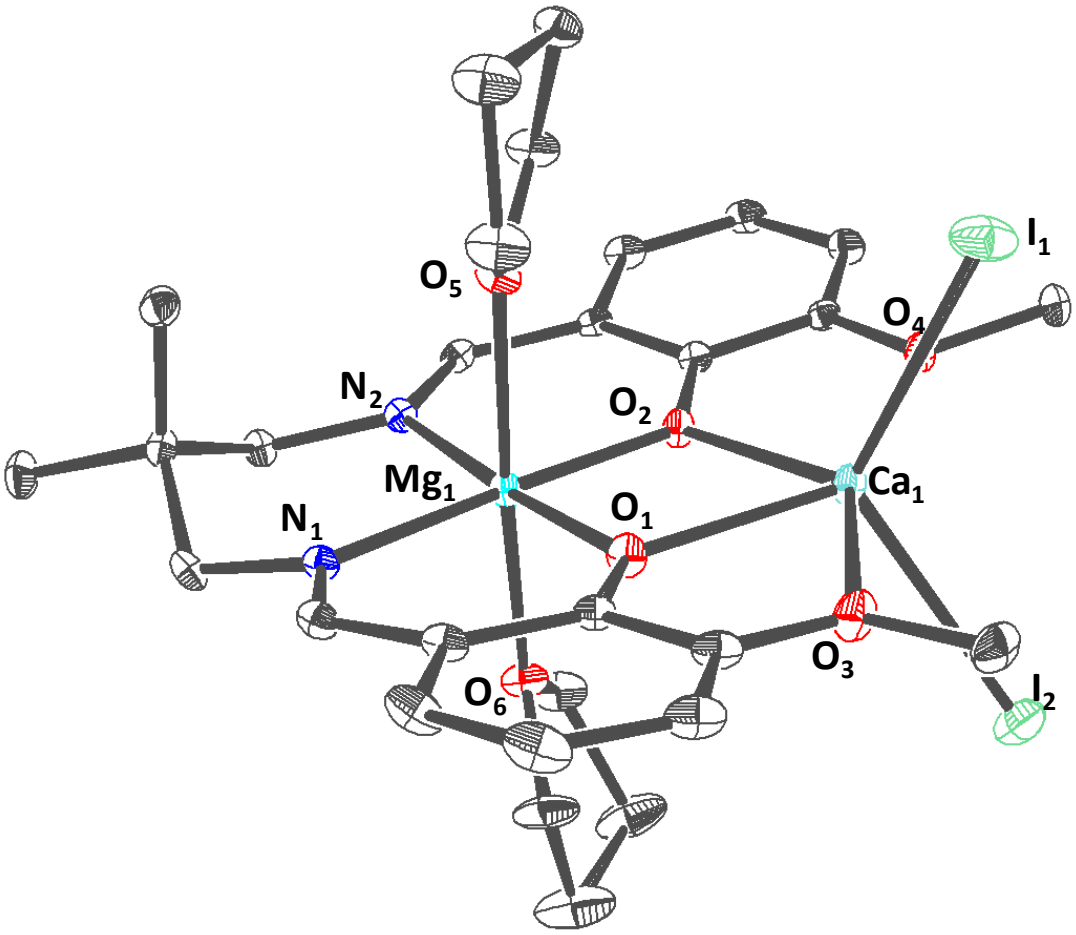


Figure S142: ORTEP representation of the molecular structure of **29** with disorder and hydrogen atoms omitted for clarity with thermal ellipsoids represented at 40 % probability.

Table S24: Selected bond lengths (Å) and angles (°) for complex **29**.

Bond	**Bond Length (Å)**	**Bond**	**Bond Angle (°)**
N (1) – Mg (1)	2.125(3)	N (1) – Mg (1) – O (2)	173.82(11)
N (2) – Mg (1)	2.104(3)	N (2) – Mg (1) – O (1)	175.09(10)
O (1) – Mg (1)	1.976(2)	O (5) – Mg (1) – O (1)	176.48(10)
O (2) – Mg (1)	1.968(2)	O (1) – Ca (1) – O (2)	134.26(8)
O (5) – Mg (1)	2.247(2)	O (1) – Ca (1) – I (2)	111.44(6)
O (6) – Mg (1)	2.133(3)	I (1) – Ca (1) – I (2)	120.73(2)
O (1) – Ca (1)	2.317(2)	**Metal – Metal**	**Distance (Å)**
O (2) – Ca (1)	2.296(2)		
O (3) – Ca (1)	2.527(2)	Mg (1) – Ca (1)	3.3470(11)
O (4) – Ca (1)	2.499(2)		
I (1) – Ca (1)	2.9770(7)		
I (2) – Ca (1)	2.9490(7)		

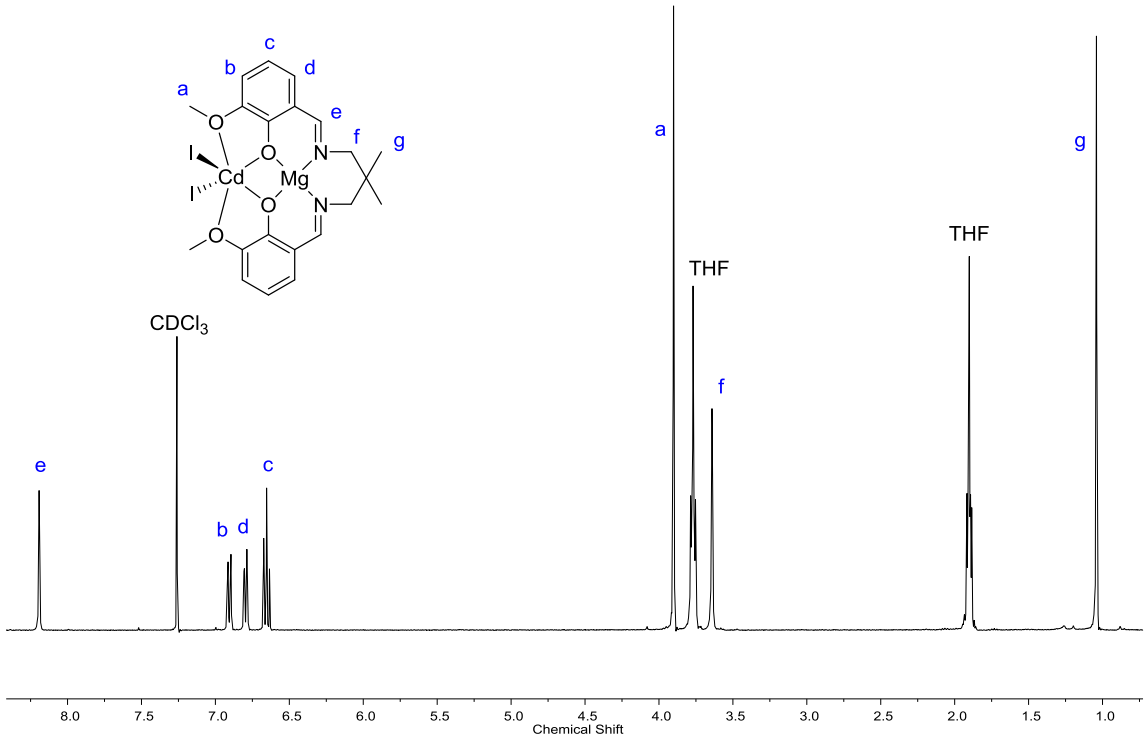


Figure S143: ^{1}H NMR of **30** ($CDCl_3$, 298 K)

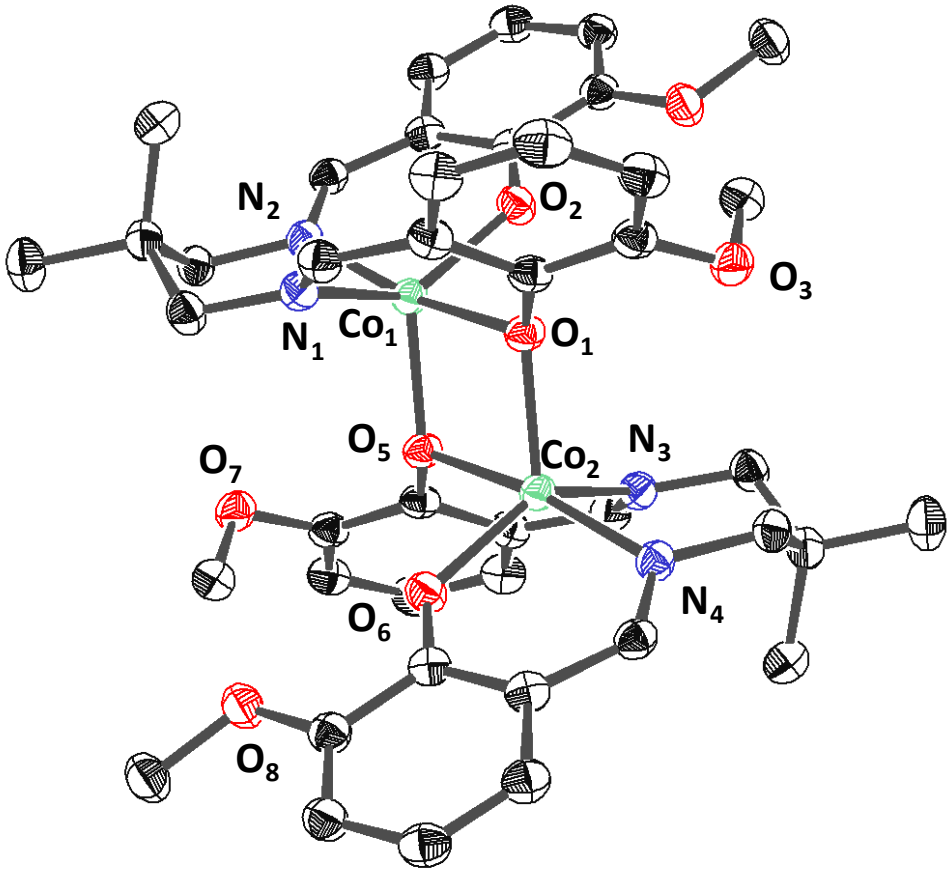


Figure S144: ORTEP representation of the molecular structure of **31** with disorder and hydrogen atoms omitted for clarity with thermal ellipsoids represented at 40 % probability, $Co_1 = Co_2$

Table S25: Selected bond lengths (Å) and angles (°) for complex **31**.

Bond	**Bond Length (Å)**	**Bond**	**Bond Angle (°)**
N (1) – Co (1)	2.07846(5)	N (1) – Co (1) – O (2)	135.2250(9)
N (2) – Co (1)	2.05460(4)	N (2) – Co (1) – O (1)	169.7854(3)
O (1) – Co (1)	2.16050(4)	N (1) – Co (1) – O (5)	101.4139(6)
O (2) – Co (1)	1.94998(3)	**Metal – Metal**	**Distance (Å)**
		Co (1) – Co (2)	3.16510(5)

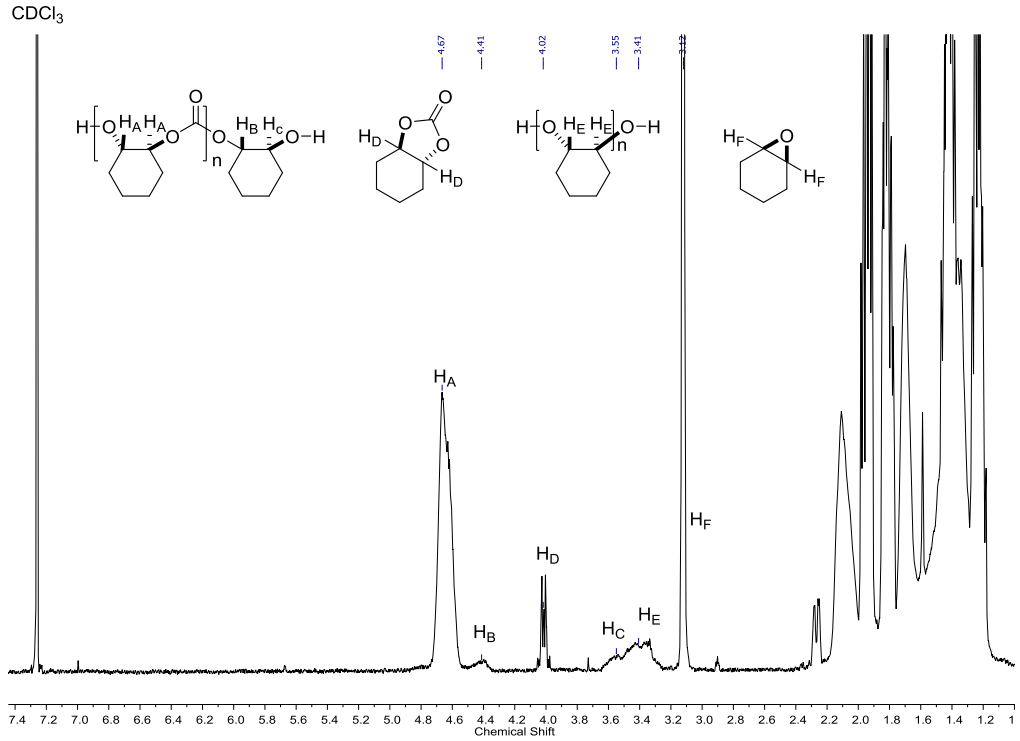


Figure S145**:** Representative example of ^{1}H NMR spectrum of a typical CO_2-CHO ring opening copolymerisation forming both poly(cyclohexene oxide) and *trans*-cyclic carbonate ($CDCl_3$, 298 K).

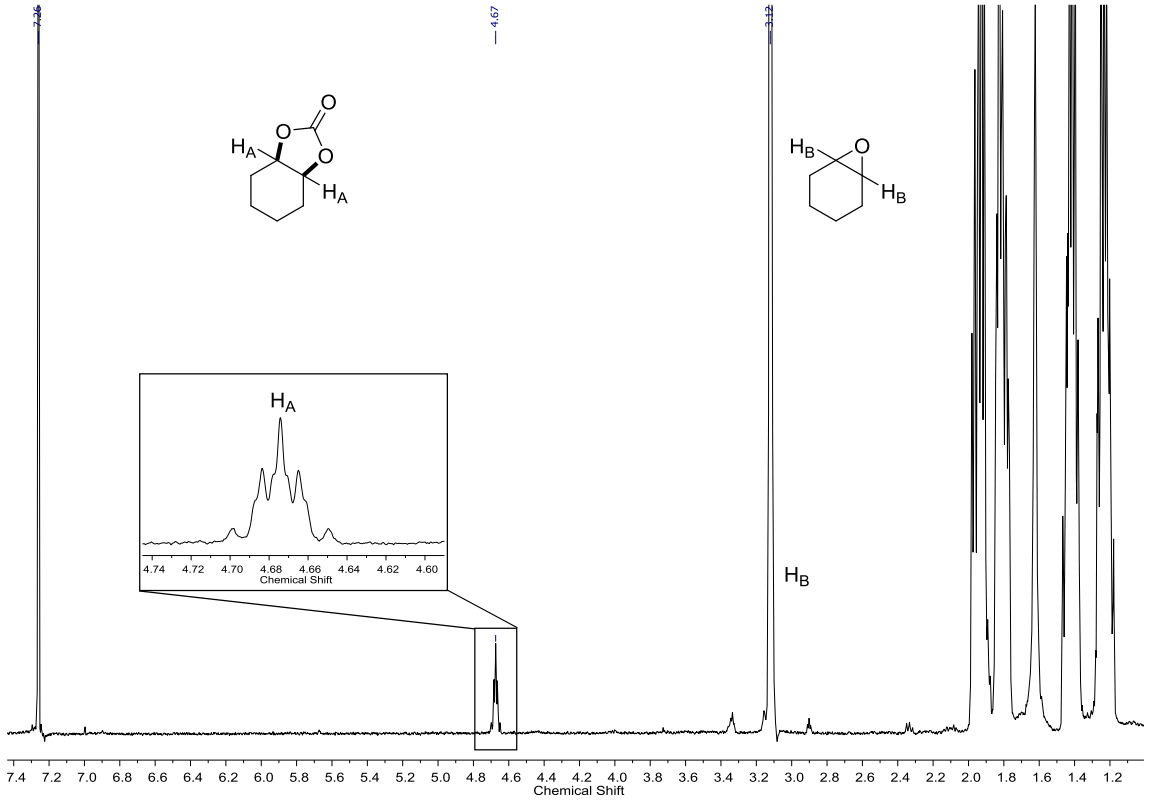


Figure S146**:** Representative example of ^{1}H NMR spectrum of a typical CO_2-CHO reaction forming the *cis*-cyclic carbonate ($CDCl_3$, 298 K).

8.1.5 References

1. Zhu, Y.; Romain, C.; Williams, C. K., Selective Polymerization Catalysis: Controlling the Metal Chain End Group to Prepare Block Copolyesters*, J. Am. Chem. Soc.,* **2015,** *137*, (38), 12179.
2. Garden, J. A.; Saini, P. K.; Williams, C. K., Greater than the Sum of Its Parts: A Heterodinuclear Polymerization Catalyst*, J. Am. Chem. Soc.,* **2015,** *137*, (48), 15078.